

Sanjay Yadav · Harish Kumar ·  
Meher Wan · Pawan Kumar Arora ·  
Yusri Yusof *Editors*

# Recent Advances in Applied Mechanics and Mechanical Engineering

Select Proceedings of ICAMME 2022

# Lecture Notes in Mechanical Engineering

## Series Editors

Fakher Chaari, National School of Engineers, University of Sfax, Sfax, Tunisia

Francesco Gherardini , Dipartimento di Ingegneria “Enzo Ferrari”, Università di Modena e Reggio Emilia, Modena, Italy

Vitalii Ivanov, Department of Manufacturing Engineering, Machines and Tools, Sumy State University, Sumy, Ukraine

## Editorial Board

Francisco Cavas-Martínez , Departamento de Estructuras, Construcción y Expresión Gráfica Universidad Politécnica de Cartagena, Cartagena, Murcia, Spain

Francesca di Mare, Institute of Energy Technology, Ruhr-Universität Bochum, Bochum, Nordrhein-Westfalen, Germany

Mohamed Haddar, National School of Engineers of Sfax (ENIS), Sfax, Tunisia

Young W. Kwon, Department of Manufacturing Engineering and Aerospace Engineering, Graduate School of Engineering and Applied Science, Monterey, CA, USA

Justyna Trojanowska, Poznan University of Technology, Poznan, Poland

Jinyang Xu, School of Mechanical Engineering, Shanghai Jiao Tong University, Shanghai, China

**Lecture Notes in Mechanical Engineering (LNME)** publishes the latest developments in Mechanical Engineering—quickly, informally and with high quality. Original research reported in proceedings and post-proceedings represents the core of LNME. Volumes published in LNME embrace all aspects, subfields and new challenges of mechanical engineering.

Topics in the series include:

- Engineering Design
- Machinery and Machine Elements
- Mechanical Structures and Stress Analysis
- Automotive Engineering
- Engine Technology
- Aerospace Technology and Astronautics
- Nanotechnology and Microengineering
- Control, Robotics, Mechatronics
- MEMS
- Theoretical and Applied Mechanics
- Dynamical Systems, Control
- Fluid Mechanics
- Engineering Thermodynamics, Heat and Mass Transfer
- Manufacturing
- Precision Engineering, Instrumentation, Measurement
- Materials Engineering
- Tribology and Surface Technology

To submit a proposal or request further information, please contact the Springer Editor of your location:

**Europe, USA, Africa:** Leontina Di Cecco at [Leontina.dicecco@springer.com](mailto:Leontina.dicecco@springer.com)

**China:** Ella Zhang at [ella.zhang@springer.com](mailto:ella.zhang@springer.com)

**India:** Priya Vyas at [priya.vyas@springer.com](mailto:priya.vyas@springer.com)

**Rest of Asia, Australia, New Zealand:** Swati Meherishi at [swati.meherishi@springer.com](mailto:swati.meherishi@springer.com)

**Indexed by SCOPUS, EI Compendex, and INSPEC.**

All books published in the series are evaluated by Web of Science for the Conference Proceedings Citation Index (CPCI).

To submit a proposal for a monograph, please check our Springer Tracts in Mechanical Engineering at <https://link.springer.com/bookseries/11693>

Sanjay Yadav · Harish Kumar · Meher Wan ·  
Pawan Kumar Arora · Yusri Yusof  
Editors

# Recent Advances in Applied Mechanics and Mechanical Engineering

Select Proceedings of ICAMME 2022



Springer

*Editors*

Sanjay Yadav  
CSIR—National Physical Laboratory  
New Delhi, Delhi, India

Meher Wan  
CSIR-National Institute of Science  
Communication and Policy Research  
(CSIR-NIScPR)  
New Delhi, Delhi, India

Yusri Yusof  
Tun Hussein Onn University of Malaysia  
Parit Raja, Malaysia

Harish Kumar  
National Institute of Technology Delhi  
New Delhi, Delhi, India

Pawan Kumar Arora  
Galgotias College of Engineering  
and Technology  
Greater Noida, Uttar Pradesh, India

ISSN 2195-4356                   ISSN 2195-4364 (electronic)  
Lecture Notes in Mechanical Engineering  
ISBN 978-981-99-2374-8       ISBN 978-981-99-2375-5 (eBook)  
<https://doi.org/10.1007/978-981-99-2375-5>

© The Editor(s) (if applicable) and The Author(s), under exclusive license to Springer Nature Singapore Pte Ltd. 2023

This work is subject to copyright. All rights are solely and exclusively licensed by the Publisher, whether the whole or part of the material is concerned, specifically the rights of translation, reprinting, reuse of illustrations, recitation, broadcasting, reproduction on microfilms or in any other physical way, and transmission or information storage and retrieval, electronic adaptation, computer software, or by similar or dissimilar methodology now known or hereafter developed.

The use of general descriptive names, registered names, trademarks, service marks, etc. in this publication does not imply, even in the absence of a specific statement, that such names are exempt from the relevant protective laws and regulations and therefore free for general use.

The publisher, the authors, and the editors are safe to assume that the advice and information in this book are believed to be true and accurate at the date of publication. Neither the publisher nor the authors or the editors give a warranty, expressed or implied, with respect to the material contained herein or for any errors or omissions that may have been made. The publisher remains neutral with regard to jurisdictional claims in published maps and institutional affiliations.

This Springer imprint is published by the registered company Springer Nature Singapore Pte Ltd.  
The registered company address is: 152 Beach Road, #21-01/04 Gateway East, Singapore 189721,  
Singapore

# **Committee Members**

## **Conference General Chair**

Prof. Yusri Yusof, Advanced Manufacturing and Materials Centre (AMMC) and Universiti Tun Hussein Onn Malaysia (UTHM), Malaysia

## **Publication Chairs**

Dr. Sanjay Yadav, CSIR-National Physical Laboratory, India

Dr. Prashant K. Jain, Indian Institute of Information Technology, Design and Manufacturing, India

Dr. Pawan Kumar Arora, Galgotias College of Engineering and Technology, India

## **Technical Program Committee Chair**

Prof. Jiang Zhu, Tokyo Institute of Technology, Japan

## **Technical Program Committee Members**

Prof. Murat Tolga Özkan, Gazi University, Turkey

Prof. Ji Wang, Ningbo University, China

Prof. Krishna Murari Pandey, National Institute of Technology Silchar, India

Prof. Morteza Mohammadzaheri, Sultan Qaboos University, Australia

Prof. Mohamed Abdel Kader El Gelany Ismail, Miami College of Henan University, Canada

- Prof. Hakan Çalışkan, Usak University, Turkey  
Prof. Hakim NACEUR, INSA Hauts-de-France, French  
Prof. I. Neethi Manickam, Francis Xavier Engineering College, India  
Prof. Ali Rahman, Southwest Jiaotong University, China  
Prof. Hage Chehade Fadi, the Lebanese Association for the Advancement of Science (LAAS), Lebanon  
A. Prof. Maxim Rahula Bharathi B, Mechanical Engineering, JNTU Kakinada, India  
A. Prof. Mohammad, Dalian University of Technology, Bangladesh  
A. Prof. Rizwan Ul Haq, Bahria University, Pakistan  
A. Prof. Saman Abdanan Mehdizadeh, Agricultural Sciences and Natural Resources University of Khuzestan, Iran  
A. Prof. Tian Soon Lee, Multimedia University, Malaysia

## Organizing Committee Members

- Dr. Kulwant Singh, Guru Kashi University, India  
Dr. Shubham Sharma, IK Gujral Punjab Technical University, India  
Dr. Haytham F. A. Isleem, Tsinghua University, Palestinian  
Dr. Masoud Taghavi, Faculty of Noshahr, Technical and Vocational University, Iran  
Dr. Man Djun Lee, Mechanical Engineering, Curtin University Malaysia, Malaysia  
Dr. Sandip Kunar, Mechanical Engineering, Aditya Engineering College, India  
Dr. Jaishankar Bharatharaj, Bharath Institute of Higher Education and Research, India & New Zealand  
Dr. Karuppaiya Sakkaravarthi, Asia-Pacific Center for Theoretical Physics (APCTP), South Korea  
Dr. Nor Hasanah Binti Abdul Shukor Lim, Universiti Teknologi Malaysia, Malaysia  
Dr. Saleh Mobayen, National Yunlin University of Science and Technology, Taiwan, China  
Dr. Md Mozasser Rahman, Universiti Tun Hussein Onn Malaysia, Malaysia  
Dr. Sugam J Shivhare, Narsee Monjee Institute of Management Studies, India  
Dr. V. Vijaya Kishore, G Pullaiah College of Engineering and Technology, India  
Dr. Morteza Mohammadzaheri, Sultan Qaboos University, Sudan  
Dr. Arockia Selvakumar. A, VIT University, India  
Dr. Mohd Arif Agam, University Tun Hussein Onn Malaysia, Malaysia

# Preface

The 3rd International Conference on Applied Mechanics and Mechanical Engineering (ICAMME 2022) was successfully held on September 23–25, 2022 in Xi'an, China (virtual conference). ICAMME 2022 provided a platform for sharing scientific research findings and cutting-edge technologies; strengthened the academic research and discussion; and promoted the industrialization cooperation of academic accomplishments.

Renowned academician Prof. Yusri Yusof from Universiti Tun Hussein Onn Malaysia (UTHM), Malaysia, served as the Conference General Chair. A total number of 100 individual participants attended the conference, divided into 3 parts, covering keynote speeches, oral presentations, and online Q&A discussions. Primarily, 30 keynote lectures were delivered along with many selected oral presentations. During the conference, three distinguished professors delivered keynote talks, namely (1) Prof. Li Guo from Hunan University, China on “Research on Acoustic Emission Intelligent Monitoring in Grinding Engineering Ceramics,” (2) Prof. Bing Li from Northwestern Polytechnical University, China on “Design and Applications of Elastic Meta-structures,” and (3) Prof. Yang Xiao from Southwestern Petroleum University, China on “New Technologies for Product Research and Development and Manufacturing in the Digital Transformation of Manufacturing Industry.” The wonderful and state-of-the-art keynote talks had triggered the heated discussion and set the ball rolling for further discussion and presentations in the conference. Moreover, the talks were highly appreciated and praised for disseminating useful and insightful knowledge.

After months of well preparation and hard work, the proceedings of ICAMME 2022 covering a bunch of high-quality papers are compiled and published in this series. These papers feature but are not limited to the following areas: Mechanics and Engineering, Force Analysis, Material Modeling, Engineering Design, Industrial Manufacturing, etc. All the papers have been checked through rigorous review processes to meet the requirements of publication.

On behalf of the organizing committee, all the Editors of the proceedings would like to express our sincere thanks to all the keynote speakers, peer reviewers, and all the participants. Particularly, we would like to acknowledge the Springer, for the

endeavor of all its colleagues in publishing this paper volume. We firmly believe that all the attendees have had fruitful discussions and gained valuable knowledge, and will enjoy the opportunity for future collaborations.

New Delhi, India

New Delhi, India

Greater Noida, India

New Delhi, India

Dr. Sanjay Yadav

Dr. Meher Wan

Dr. Pawan Kumar Arora

Dr. Harish Kumar

# Contents

<b>Nonlinear Dynamic Analysis of Elastic Robotic Arms .....</b>	1
Hongbing Wen and Shanying Jiang	
<b>Influence of the Modulus of Elasticity of the Jointed Material and Interlayers in Nodes with an Interlayer with a High TCLE .....</b>	11
Qi Li, FengMei Liu, Haitao Gao, Huang He, and Viktor Kvasnytskyi	
<b>Research on Imaging Method of Missile-Borne Infrared Lateral Window Adapting to Deflection Light Path with Large Incident Angle .....</b>	21
Qi Meng and Dong Chen	
<b>Study on the Characteristics of Rollover Injury of Passenger on the Passenger Side of an Off-Road Vehicle .....</b>	31
Lizhi Zhou, Yunbo Zhou, Ming Zhang, Jianing Bai, and Wangang Xiao	
<b>Study on the Failure Mechanism and Reliability of Silicon Aluminum Alloy Under Impact Loading .....</b>	41
Dan Li, Qiongjiao Wang, Feng Dong, Sheng Wang, and Yun Bai	
<b>Analysis of Prefabricated Fragment Intrusion Damage Based on Complete Restart Technique .....</b>	51
Jiazhi Liu, Yunbo Zhou, Ming Zhang, Jianing Bai, and Wangang Xiao	
<b>Flexible Thermal Invisibility Cloak with Meta-Structures: Design and Fabrication .....</b>	63
Zhengyu Lian, Peng Lu, and Bo Li	
<b>Research on Topology Optimization Methods for Continuum Structures .....</b>	71
Yong Wen, Xia Liu, Shufan Wang, and Shi Yang	
<b>Study on Interface and Joint Properties of Aluminum Alloy by High-Power Ultrasonic Welding .....</b>	81
Jingyun Liu, Mujiu Cheng, Fang Cheng, and Qiao Cheng	

<b>Analysis of Nozzle Flow Based on Small Disturbance Equation Using Successive Over Relaxation Method .....</b>	91
Shujia Li	
<b>On Optimal Tooth Profile Modification of Helical Gears Based on High Precision FEM .....</b>	105
Yanping Liu, Yongqiang Zhao, and Changzhan Xue	
<b>Numerical Study on Atomization Process of Transverse Jet .....</b>	113
Na Gao and Xiaobin Zhang	
<b>Mechanism of Collision and Adhesion Between Adhesive Impact Ball and Spacecraft .....</b>	121
Bingyu Xu, Shuquan Wang, and Liping Zhao	
<b>A Pose Calibration Method for Serial Robots Considering Joint Variables .....</b>	133
Lu Yang and Xiaoliu Yu	
<b>Research on Rigid-Flexible Coupling Problem of Piston-Pump Tube ...</b>	145
Yisheng Xie and Bing Cao	
<b>Route to a Chaotic State in the Wake of a NACA0015 Airfoil at Post-stall Angles of Attack .....</b>	155
Liping Sun, Ziheng Song, Jiuming Zhang, and Min Fang	
<b>Research on Kinematic Characteristics of Revolving Chain Shell Magazine .....</b>	165
Yongyong Zhu, Pengfei Yue, and Qiangwei Pang	
<b>Separate Heat Pipe Research Status of Application in Passive Cooling System .....</b>	173
Zhengfu Zhang, Kunrong Huang, and Ningkang Duan	
<b>Current Status and Prospects for Quantification of 3D Printing .....</b>	181
Yaoxin Huang and Jiaqi Chen	
<b>Development Trend of Monitoring System Application in Coal, Metal and Non-metal Mines .....</b>	193
Jialan Sun	
<b>Weighted Modal Strain Energy Damage Identification Based on Image Sequences .....</b>	201
Jiayan Zheng, Hailin Chen, Haijing Liu, Renwei Luo, and Heng Li	
<b>Solution of the Full Potential Equation on an Airfoil by Physics-Informed Neural Network .....</b>	215
Peiyuan Cong and Yunfei Gao	

<b>Analysis and Research on Magnetic Leakage Simulation of Bimetallic Composite Pipe .....</b>	227
Yilai Ma, Jinzhong Chen, Yaxing Wen, and Zhikun Xiong	
<b>Health State Assessment of Large Complex Equipment Based on Modified ER Algorithm .....</b>	239
HaiYan Li, WenLi Li, and SongBin Liu	
<b>Influence of the Modulus of Elasticity of the Jointed Material and Interlayers in Nodes with an Interlayer with a Low TCLE .....</b>	247
Qi li, FengMei Liu, Haitao Gao, Huang He, and Viktor Kvasnytskyi	
<b>Research on Aspect Ratio and Angle of Attack for Optimizing the Performance Of Airfoil NACA 24112 .....</b>	257
Ziyi Zhang	
<b>Experimental Analysis of Viscous Damping Wall Based on Free Vibration Response .....</b>	269
Junxia Sun, Nana Liu, Yingjia Wang, Yan Zhang, and Wei Wang	
<b>Design and Analysis of Turnover Function of Nursing Bed Based on Ergonomics .....</b>	277
Weiliang Zeng, Xinzui Wang, Fucheng Cao, Haibing Xin, Xihua Li, Zhaobo Li, and Hui Fu	
<b>Cumulative Damage Study of Air-Dropped Vehicles with Multiple Drops Impact .....</b>	289
Xudong Wang, Yubo Zhou, and Ming Zhang	
<b>Research on Detonation Wave Analysis Model of Composite Charge ...</b>	299
Huiming Shen, Wenli Yu, Tao Wang, Weibing Li, Jintao Wang, and Guiyun Hang	
<b>Influences of Element Types on Nonlinear Finite Element Analysis of a Concrete Column Under Near-Field Blast Loading .....</b>	311
Jie Xu, Max A. N. Hendriks, Jan G. Rots, and Apostolos Tsouvalas	
<b>Experimental Study on the Mitigation Effects of Water Mist on Quasi-Static Pressure .....</b>	323
Qi Li, Yan-Wei Chen, Liang Zhang, Ping-Hui Li, Ya-Wei Wang, and Ya-Bin Liu	
<b>Research on the Method of Compiling the Normalized Fatigue Load Spectrum of Motorized Transportation .....</b>	333
Chunjuan Shi, Zhiyong Sun, and Gang Feng	
<b>Research on the Reliability Design Method of the Typical Mechanism of Naval Gun Based on Failure Form .....</b>	341
Fei Zhao	

<b>Computer Aided Mechanical Mechanism Design for Industrial Design .....</b>	353
Yanxia Liang	
<b>Research on Parameter Identification of the Mechanical Model of Damping Wall Based on Free Vibration Response .....</b>	363
Wei Wang, Nana Liu, Yingjia Wang, Yan Zhang, and Junxia Sun	
<b>Experimental Study on Electrical Discharge Precision Orbital Machining of Closed Impeller Based on Response Surface Optimization .....</b>	373
Yicong Qiu	
<b>Influence of Vibration on Noise Measurement and Correction Method .....</b>	389
Yuan-ming Zhao, Ya-hui Song, Sheng Shen, and Gao-yu Fan	
<b>Flex-Structural Embedded Flexible Strain Sensor via 3D Printing .....</b>	403
Hongyu Han, Xumingyang Xie, Bo Li, and Facao Ren	
<b>Research on Pre-tightening Force of Filament-Wound Composite Barrel of Railgun .....</b>	411
Xuan Li	
<b>A Study on the Outfield Application of Nondestructive Testing Technologies for Stealth Coating .....</b>	427
Xiaohuan Guo, Faliang Sun, Xiaoju Yong, and Minghua Chen	
<b>Simulation Analysis of the Maneuverability Limit of a Certain Type of Military Vehicle Based on Adams/Car Under Semi-Circular Obstacles .....</b>	435
Rui Tao, Ming Zhang, Yaoyu Fu, Yunbo Zhou, Jianing Bai, Jun Zhou, and Yongguang Yu	
<b>An Extraction Method of Resistance Characteristics in Different Microchannels Using Numerical Method .....</b>	443
Yang Tang	
<b>Vibration Analysis of Airplane Wing Under Fuel Weight .....</b>	459
Zihao Zhou	
<b>Selection and Research of Common Waste Water Tank Mixer .....</b>	469
Chun-Yu Tian	
<b>Study on Grease Elasto-Hydrodynamic Lubrication of Deep Groove Ball Bearings .....</b>	477
Hao Wu, Shenghan Zhang, Haoyang Sun, Jirong Wang, and Hongxin Zhang	

Contents	xiii
<b>Influence of Shock Load on Performance of Mixed Lubrication Sliding Bearings .....</b>	<b>487</b>
L. C. Qin, X. M. Miao, H. Guo, and M. H. Shi	
<b>Experimental Study on Direct Measurement of the Air–Water Interface at High-Speed Condition .....</b>	<b>497</b>
Sheng-Zhe Shi, Teng-Jiao Sang, Fei Wei, and Gang Sun	
<b>Experimental Study on Fatigue Life of Four Typical Aircraft Connectors .....</b>	<b>505</b>
Hongwei Qiao, Yunyan Ren, and Hui Zhang	

## About the Editors

**Dr. Sanjay Yadav** born in 1962, obtained his master degree in science (M.Sc.) in 1985 and Ph.D. degree in Physics in 1990. Presently, he is working as the Editor-in-Chief (EIC) of the MAPAN: The Journal of Metrology Society of India. He is also Vice President of Metrology Society of India (MS), New Delhi as well as Vice President of Ultrasonic Society of India (USI), New Delhi. He is Former Chief Scientist and Head, Physico Mechanical Metrology Division of NPL and also Former Professor, Faculty of Physical Sciences, Academy of Scientific and Innovative Research (AcSIR), HRDG, Ghaziabad. He had taught ‘Advanced Measurement Techniques & Metrology’ course, taken practical classes and supervising graduate, master and Ph.D. students since 2011. He is the recipient of research scholarships from Ministry of Home Affairs, India (1986); CSIR, India (1988); Col. G.N. Bajpayee Award of Institution of Engineers, India (1989); Commendation Certificates from Haryana Government (1991 & 1992); JICA Fellowship of JAPAN (1998), Commendation Certificates from SASO, Saudi Arabia (2003); 3 Appreciation Certificates from Director, NPL (2005); Managing Editor, MAPAN (2006-2014); nominated as Member of APMP Technical Committee of Mass Related Quantities (TCM), Australia (2013-2019); Nominated as Country Representative in APMP, China (2019); Vice President, Metrology Society of India (2020); Member, National Advisory Committee, NCERT, Delhi (2019); Members, Testing and Calibration Advisory Committee, BIS (2019, 2020 and 2021), and very recently received a prestigious International award i.e. APMP Award for Developing Economies, China (2020). He has significantly contributed in the field of pressure metrology, biomedical instrumentation, ultrasonic transducers and instrumentation systems. His current research interests include research and developmental activities in physico mechanical measurements; establishment, realization, maintenance and up-gradation of national pressure and vacuum standards; dissemination of national practical pressure scale to users through apex level calibration, training and consultancy services; inter-laboratory comparisons, proficiency testing programme and key comparisons, implementation of Quality System in the laboratory as per ISO/IEC 17025 standard and Finite Element Analysis (FEA) and Monte Carlo Simulations for pressure

balances. He has published more than 450 research papers in the national and international journals of repute and conferences, 20 books, 14 patents and copyrights, supervised 8 PhDs (another 5 in waiting), drafted several projects, scientific and technical reports, documents and policy papers.

**Dr. Harish Kumar** is currently working as Associate Professor at the National Institute of Technology, Delhi. With more than 17 years of research and academic experience, he is Active Researcher in the area of mechanical measurement and metrology. He served as Scientist at the National Physical Laboratory, India, for more than a decade, and as Guest Researcher at the National Institute of Standards and Technology, USA, in 2016. He has authored more than 90 publications in peer-reviewed journals and conference proceedings. He is Active Reviewer for many prominent journals on measurement, metrology, and related areas and is Associate Editor of the MAPAN/Journal of Metrology Society of India, published by Springer.

**Dr. Meher Wan** is a scientist at CSIR- National Institute of Science Communication and Policy Research, New Delhi. He did his Ph.D. from University of Allahabad and was an Institute-post doctoral fellow at IIT-Kharagpur. He has been actively involved in setting up Micro/Nano-Robotics and Fabrication Facility at Advanced Technology Development Centre, Indian Institute of Technology-Kharagpur, which has a semi-clean room environment. He had been helping in making the design of facility, from pre-installation preparations to installations of sophisticated instruments. He has expertise in electron microscopy, micro-nano-fabrication technologies like Focused Ion Beam lithography, Electron beam lithography and Two photon polymerization based 3D lithography etc including micro-robotic manipulation. He is an associate Editor: Science Reporter (Popular Science Magazine), Scientific Editor: Indian Journal of Pure and Applied Physics (IJPAP), former editor: Indian Journal of Engineering and Materials Science (IJEMS).

**Dr. Pawan Kumar Arora** is a Professor at the Mechanical Engineering Department of Galgotias College of Engineering and Technology, Greater Noida, India. He received his Ph.D. in Mechanical Engineering from Jamia Millia Islamia, New Delhi, in 2014. With 22 years of academic experience, his main research areas are industrial engineering and optimization and manufacturing. Dr. Arora has published more than 50 papers in international journals and conference proceedings. He has also contributed several book chapters in different books. He has also served as editor to Smart Innovation Systems and Technologies (Springer), Material Todays: Proceedings.

**Dr. Yusri Yusof** is Professor in the Faculty of Mechanical and Manufacturing Engineering at the Universiti Tun Hussein Onn Malaysia (UTHM). He has a Ph.D. in Manufacturing, which he obtained from the University of Loughborough, United Kingdom in the year 2007. Dr. Yusri has had over 22 years' experience of teaching in higher education. Dr. Yusri has been invited 30 times as Keynote speaker local and International Conference and also served as International Committee almost

50 conferences in his area for the last 5 years. Dr. Yusri has multidisciplinary research interests and his main areas of research are CAD/CAM and STEP-NC. He has published more than 50 international technical papers, mainly in CAD/CAM and advanced manufacturing. Dr. Yusri lead about 20 grant research project involved almost RM2 million under Sciencefund (MOSTI), Prototype Research Grant (PRGS), Fundamental Research Grant (FRGS) and Internal Research Fund under Intelligent Manufacture for STEP-NC Compliant Machining projects. He has served as the Editorial Board of the International Journals and currently involved in several international bodies such as, International Association of Engineers (IAENG), Senior member of the Science and Engineering Institute (SCIEI), The World Academy of Science, Engineering and Technology (WASET) Scientific and Technical Committees, editorial & reviewers boards on Natural and Applied Sciences and Senior member of the International Association of Engineering Technology (IAET).

# Nonlinear Dynamic Analysis of Elastic Robotic Arms



Hongbing Wen and Shanying Jiang

**Abstract** In this paper, the nonlinear elastic manipulator system is taken as the research object. According to the relevant knowledge of mechanical vibration, the elastic manipulator is simplified to the mode analysis of the robotic arm by the Euler–Bernoulli beam, and the dynamic model of the system is established by using the Lagrange equation, in order to simplify the complexity of the calculation, in order to ignore some tiny amounts of the equation system and some nonlinear terms of high powers, the multi-scale method in the nonlinear vibration approximation analysis method is used to solve the dynamic model of the system. The results show that the approximate solution obtained is perfectly consistent with the analytical solution. And, the amplitude–frequency characteristic curve of the main resonance of the system is obtained, which shows that the peak value of the main resonance of the system is not only related to the amplitude of the excitation force but also related to the damping coefficient of the system.

**Keywords** Nonlinear · Elastic manipulator · Modal analysis · Multiscale method

## 1 Introduction

Under the general trend of common development of science and economy, robotic arms are gradually applied in our lives, especially in industry, agriculture, aerospace, and medical fields [1]. However, due to the existence of elastic vibration, the elastic positioning accuracy of the arm during the movement decreases, reducing the reliability of the system. Therefore, various fields must be researched in a more in-depth and intelligent direction. At present, China's manufacturing industry is in a critical period of transformation. Accelerating the pace of promoting the intelligent manufacturing industry will be of great significance to the competitiveness of China's manufacturing industry.

---

H. Wen · S. Jiang (✉)  
Shanghai Institute of Technology, Shanghai 201418, China  
e-mail: [jiangshanying@sit.edu.cn](mailto:jiangshanying@sit.edu.cn)

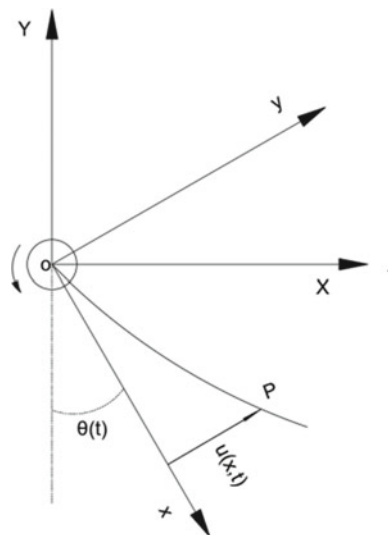
Yoshikawa et al. [2] proposed a modeling method based on virtual rigid links and passive joints. Vakil et al. [3] combined the hypothetical mode method with the Lagrangian method and proposed a new dynamic model-building method. Sayahkarajy et al. [4] reviewed the research trends of modeling and control of multi-link elastic manipulators. Cai et al. [5] studied the optimal control problem of a flexible manipulator based on a central rigid–flexible coupled arm. Yao et al. [6] studied the stability of stochastic nonlinear time-delay systems. Alhazza et al. [7] studied a multi-modal time-delayed feedback control technique to suppress the vibration of elastic beams. Zhang et al. [8] developed a phase and gain adjustment algorithm for active vibration control of elastic structures. Alhazza et al. [9] proposed a single-mode delayed feedback control strategy using piezoelectric actuators to reduce the free vibration of elastic beams. Liu et al. [10] studied the global exponential stability of neutral systems with interval time-varying delays and nonlinear disturbances.

## 2 Dynamic Modeling of Elastic Manipulator

The structure diagram of the single-link elastic manipulator is shown in Fig. 1, the joints of the manipulator are connected with the output shaft of the drive motor. In order to facilitate the modeling, the elastic manipulator is regarded as an Euler–Bernoulli beam to study and analyze its lateral vibration and bending problems.

In Fig. 1, XOY is the fixed coordinate system,  $xoy$  is the rotating coordinate system of the manipulator system, where  $\theta(t)$  is the angle between the elastic manipulator and the X-axis of the inertial coordinate system at time  $t$  during the movement,  $u(x, t)$

**Fig. 1** Structure model diagram of the robotic arm system [from self-drawn]



represents the lateral elastic deformation of  $x$  at time  $t$  at any point  $P$  on the elastic manipulator.

According to the theory of mechanical vibration, the differential equation of bending free vibration of uniform material beam is

$$\rho A \frac{\partial^2 u(x, t)}{\partial t^2} + EI \frac{\partial^4 u(x, t)}{\partial t^4} = 0 \quad (1)$$

where  $\rho$  is the density of the elastic arm material,  $A$  is the cross-sectional area of the elastic arm,  $E$  is the elastic modulus of the elastic arm material, and  $I$  is the moment of inertia of the elastic arm. The solution of the above equation can be written as

$$u(x, t) = \sum_{i=1}^{\infty} \psi_i(x) \cdot q_i(t) \quad (2)$$

where  $\psi_i(x)$  is the  $i$ th mode shape function of the elastic rod,  $q_i(t)$  is the modal coordinate corresponding to the mode shape function, which can be obtained by substituting Eq. 2 into Eq. 1

$$\rho A \psi(x) \ddot{q}(t) + EI \psi^{(4)}(x) q(t) = 0 \quad (3)$$

where  $\psi^{(4)}$  represents the fourth derivative of  $\psi$  with respect to  $x$ .

According to formula 3, we can get

$$\frac{\ddot{q}(t)}{q(t)} = -\frac{EI}{\rho A} \frac{\psi^{(4)}(x)}{\psi(x)} \quad (4)$$

Let the above formula be equal to  $-\omega^2$ , then we can get

$$q(t) = B \cos \omega t, \psi^{(4)}(x) - \beta^4 \psi(x) = 0 \quad (5)$$

where  $\beta^4 = \frac{\rho A}{EI} \omega^2$ .

According to Eq. 5 and using Euler's formula and the properties of the hyperbolic function, we can get

$$\psi(x) = D_1 \sin \beta x + D_2 \cos \beta x + D_3 \sinh \beta x + D_4 \cosh \beta x \quad (6)$$

The above formula is the mode shape function when the elastic arm vibrates.

Substituting the above equation into the boundary conditions of the elastic arm, we get

$$\psi_i(x) = \cos \beta_i x - \cos h\beta_i x + \varepsilon_i (\sin h\beta_i x - \sin \beta_i x) \quad (7)$$

where  $\varepsilon_i = \frac{\cos \beta_i l + \cos h\beta_i l}{\sin \beta_i l + \sin h\beta_i l}$ ,  $i = 1, 2, 3 \dots n$ ,  $\beta_i$  is the coefficient corresponding to the  $i$ th order natural frequency, and  $l$  is the length of the boom.

### 3 Dynamic Analysis of Elastic Manipulator

According to the schematic diagram of the mechanical arm structure, the total kinetic energy  $T$  is composed of the kinetic energy  $T_1$  of the motor shaft and the kinetic energy  $T_2$  of the mechanical arm itself, the moment of inertia of the motor is  $J_h$ , then

$$T_1 = \frac{1}{2} J_h \dot{\theta}^2(t) \quad (8)$$

The coordinates of any point  $p(X, Y)$  can be obtained from the schematic diagram of the elastic arm

$$\begin{cases} X = \sin \theta(t) \cdot x - \cos \theta(t) \cdot u(x, t) \\ Y = \cos \theta(t) \cdot x + \sin \theta(t) \cdot u(x, t) \end{cases} \quad (9)$$

Therefore, the kinetic energy of the elastic arm itself is

$$T_2 = \frac{1}{2} \rho A \int_0^l [\dot{\theta}^2(t)x^2 + \dot{\theta}^2(t)u^2(x, t) - 2x\dot{u}(x, t)\dot{\theta}(t) + \dot{u}^2(x, t)]^2 dx \quad (10)$$

The total kinetic energy of the system

$$T = \frac{1}{2} J \dot{\theta}^2(t) + \frac{1}{2} \dot{\theta}^2(t) \sum_{i=1}^n M_i q_i^2(t) - \dot{\theta}(t) \sum_{i=1}^n \sigma_i q_i(t) + \frac{1}{2} \sum_{i=1}^n M_i q_i^2(t) \quad (11)$$

where  $J = J_h + \frac{1}{3} \rho A l^3$ ,  $M_i = \rho A \int_0^l \psi_i^2(x) dx$ ,  $\sigma_i = \rho A \int_0^l x \psi_i(x) dx$ .

The potential energy  $V$  of the elastic arm includes the elastic potential energy  $V_1$  and the gravitational potential energy  $V_2$  caused by elastic deformation

$$V_1 = \frac{1}{2} EI \int_0^l \left[ \frac{\partial^2 u(x, t)}{\partial x^2} \right]^2 dx = \frac{1}{2} EI \int_0^l \left[ \frac{\partial^2 \psi_i(x)}{\partial x^2} q_i(t) \right]^2 dx = \frac{1}{2} \sum_{i=1}^n K_i q_i^2(t) \quad (12)$$

$$V_2 = - \left[ \rho Agl \left( \frac{1}{2} l \cos \theta(t) + u \left( \frac{l}{2} \right) \sin \theta(t) \right) \right] = - \frac{1}{2} \rho Agl^2 \cos \theta(t) - \rho Aglu \left( \frac{l}{2} \right) \quad (13)$$

where  $K_i = EI \int_0^l \left[ \frac{\partial^2 \psi_i(x)}{\partial x^2} \right]^2 dx$ , and  $g$  is the acceleration of gravity.

Substituting the kinetic and potential energy of the system into the Lagrangian function, we get

$$\begin{aligned} L = & \frac{1}{2} J \dot{\theta}^2(t) + \frac{1}{2} \dot{\theta}^2(t) \sum_{i=1}^n M_i q_i^2(t) - \dot{\theta}(t) \sum_{i=1}^n \sigma_i q_i(t) + \frac{1}{2} \sum_{i=1}^n M_i q_i^2(t) \\ & - \frac{1}{2} \sum_{i=1}^n K_i q_i^2(t) + \frac{1}{2} \rho A l^2 g \cos \theta(t) - \rho A g l u \left( \frac{l}{2} \right) \sin \theta(t) \end{aligned} \quad (14)$$

Applying the Lagrangian equation to get the dynamic equation of elastic manipulator:

$$\begin{aligned} J \ddot{\theta}(t) + \sum_{i=1}^n [M_i q_i^2(t) \ddot{\theta}(t) + 2M_i q_i(t) \dot{q}_i(t) \dot{\theta}(t) - \sigma_i \ddot{q}_i(t)] \\ + \frac{1}{2} \rho A g l^2 \sin \theta(t) + \rho A g l \cos \left( \frac{l}{2} \right) - \tau = 0 \end{aligned} \quad (15)$$

In the elastic manipulator system, the first-order mode is used to study the above dynamic equation, and the influence of damping factors on the system is added, the dynamic equation of the system can be expressed as

$$\begin{aligned} J \ddot{\theta}(t) + M q^2(t) \ddot{\theta}(t) + 2M q(t) \dot{q}(t) \dot{\theta}(t) - \sigma \ddot{q}(t) + \mu \dot{\theta}(t) \\ + \frac{1}{2} \rho A g l^2 \sin \theta(t) + \rho A g l \cos \left( \frac{l}{2} \right) - \tau = 0 \end{aligned} \quad (16)$$

where  $\mu$  is the damping coefficient of the system.

## 4 A Multiscale Method for the Approximate Analytical Solution of the Elastic Arm Dynamic Equation

Since it is very complicated to directly solve Eq. 17. In this paper, the multiscale method is used.

First, Eq. 17 is processed and  $\tau = 0$  is set without external control, expand  $\sin \theta(t)$  according to the Taylor series approximation and for simplicity of calculation, ignoring the high-power terms of  $\theta(t)$  and the tiny amounts, so Eq. 17 can be written as

$$\ddot{\theta}(t) + \omega_0^2 \theta(t) = \bar{\alpha}_1 q^2(t) \theta(t) + 2\bar{\alpha}_1 q(t) \dot{q}(t) \dot{\theta}(t) + \bar{\alpha}_2 \ddot{q}(t) + \bar{\alpha}_3 \dot{\theta}(t) \quad (17)$$

where  $\omega_0^2 = \frac{\rho Al^2g}{2J}$ ,  $\bar{\alpha}_1 = -\frac{M}{J}$ ,  $\bar{\alpha}_2 = \frac{\sigma}{J}$ ,  $\bar{\alpha}_3 = -\frac{\mu}{J}$ .

Introduce the parameter  $\varepsilon$ ,  $\varepsilon$  is a constant greater than 0 and less than 1, and let

$$\bar{\alpha}_1 = \varepsilon\alpha_1, \bar{\alpha}_2 = \varepsilon\alpha_2, \bar{\alpha}_3 = \varepsilon\alpha_3 \quad (18)$$

Substituting Eq. 19 into 18, we get

$$\ddot{\theta}(t) + \omega_0^2\theta(t) = \varepsilon\alpha_1q^2(t)\ddot{\theta}(t) + 2\varepsilon\alpha_1q(t)\dot{q}(t)\dot{\theta}(t) + \varepsilon\alpha_2\ddot{q}(t) + \varepsilon\alpha_3\dot{q}(t) \quad (19)$$

Let the form of the solution of Eq. 17 be

$$\theta(t, \varepsilon) = \theta_0(T_0, T_1) + \varepsilon\theta_1(T_0, T_1) + \dots \quad (20)$$

Substituting Eqs. 5 and 21 into Eq. 20, we obtain the same power coefficient equation of  $\varepsilon$  by simplification and expansion

$$\varepsilon^0 : D_0^2\theta_0 + \omega_0^2\theta_0 = 0 \quad (21)$$

$$\begin{aligned} \varepsilon^1 : D_0^2\theta_1 + \omega_0^2\theta_1 &= -2D_0D_1\theta_0 + \alpha_1D_0^2\theta_0B^2\cos^2\omega t \\ &\quad - 2\alpha_1D_0\theta_0B^2\sin\omega t\cos\omega t - \alpha_2B\omega^2\cos\omega t + \alpha_3D_0\theta_0 \end{aligned} \quad (22)$$

Write the solution of the zero-th degree approximation equation as follows:

$$\theta_0 = A(T_1)e^{i\omega_0 T_0} + \bar{A}(T_1)e^{-i\omega_0 T_0} \quad (23)$$

where  $A$  is a complex function to be determined and  $\bar{A}$  is the complex conjugate of  $A$ , substituting Eq. 24 into the right side of Eq. 23 yields

$$\begin{aligned} D_0^2\theta_1 + \omega^2\theta_1 &= -2i\omega_0D_1Ae^{i\omega_0 T_0} - \frac{1}{4}\alpha_1\omega_0^2B^2Ae^{(2\omega+\omega_0)iT_0} \\ &\quad - \frac{1}{4}\alpha_1\omega_0^2B^2Ae^{(-2\omega+\omega_0)iT_0} \\ &\quad - \frac{1}{2}\alpha_1\omega_0^2B^2Ae^{i\omega_0 T_0} - \frac{1}{2}\alpha_1\omega_0^2B^2e^{(2\omega+\omega_0)iT_0} \\ &\quad + \frac{1}{2}\alpha_1\omega_0^2B^2e^{(-2\omega+\omega_0)iT_0} \\ &\quad - \frac{1}{2}\alpha_2\omega^2Be^{i\omega T_0} + \alpha_3\omega^2Aie^{i\omega_0 T_0} + cc \end{aligned} \quad (24)$$

where  $cc$  is the complex conjugate of the terms on its left.

The case of the main resonance of the system is discussed below. On the right side of this equation, not only  $e^{i\omega_0 T_0}$  term can cause a duration term, when  $\omega = \omega_0$ , but also can produce a duration term; therefore, a duration term is generated at  $\omega \approx \omega_0$ . Let the difference between  $\omega_0$  and  $\omega$ ,  $\omega$  be the same order small quantity of  $\varepsilon$ , which

is written as

$$\omega = \omega_0 + \varepsilon\sigma \quad (25)$$

Substituting Eq. (26) into Eq. (25), we get

$$D_0^2\theta_1 + \omega_0^2 = \left( -2i\omega_0 D_1 A - \frac{1}{2}\alpha_1\omega_0^2 B^2 A - \frac{1}{2}\alpha_2\omega^2 B e^{\varepsilon\sigma} + \alpha_3\omega_0 A i \right) e^{i\omega_0 T_0} + \text{NST} \quad (26)$$

where  $\sigma$  is the tuning parameter, and  $\text{NST}$  represents the term without duration term.

Set the coefficient of duration term on the right side of the above equation to zero to eliminate the duration term, and write  $A$  in the form of a complex function

$$-2i\omega_0 D_1 A - \frac{1}{2}\alpha_1\omega_0^2 B^2 A - \frac{1}{2}\alpha_2\omega^2 B e^{\varepsilon\sigma} + \alpha_3\omega_0 A i = 0 \quad (27)$$

$$A(t) = \frac{1}{2}a(t)e^{i\phi(t)} \quad (28)$$

Write the derivative of  $A$  with respect to  $t$  as follows, and  $D_0 A = 0$

$$\frac{dA}{dt} = D_0 A + \varepsilon D_1 A + \varepsilon^2 D_2 A \quad (29)$$

Substitute Eqs. 29 and 30 into Eq. 28, and let  $\phi = \varphi - \sigma T_1$ , and separate the real and imaginary parts to get

$$\begin{cases} \dot{a} = -\frac{1}{2}\alpha_3 a + \frac{1}{2}\alpha_2 \frac{\omega^2}{\omega_0} B \sin \varphi \\ \dot{\phi} = \frac{\varepsilon\alpha_1}{4}\omega_0 B^2 + \frac{\alpha_2}{2a} \frac{\omega^2}{\omega_0} B \cos \varphi - \sigma \end{cases} \quad (30)$$

The nonzero constant solution of this equation corresponds to the steady-state periodic motion of the system, let  $\dot{a}(t) = \dot{\phi}(t) = 0$ , get constant value solutions  $a_0$  and  $\phi_0$ .

## 5 Numerical Calculation and Analysis

In this paper, the vibration law of the trajectory of the end of the elastic manipulator is mainly analyzed, and the numerical simulation is carried out by the Runge–Kutta method and compared with the obtained analytical solution. Let  $l = 1 \text{ m}$ ,  $\rho = 2700 \text{ kg/m}^3$ ,  $EI = 3.7 \text{ N m}^2$ ,  $A = 0.0025 \text{ m}^2$ ,  $J_h = 2.64 \text{ kg m}^2$ ,  $\varepsilon = 0.1$ ,  $\sigma = 0.01$ , and  $\mu = 3.7$ . The initial condition of the simulation is taken as  $q(0) = 0.1$ ,  $\dot{q}(0) = 0$ ,  $\theta(0) = 0.1$ , and  $\dot{\theta}(0) = 0.1$ . Figure 2 shows the change curve of the angular

**Fig. 2**  $\theta$  comparison of analytical and numerical solutions (from Wolfram Mathematica)

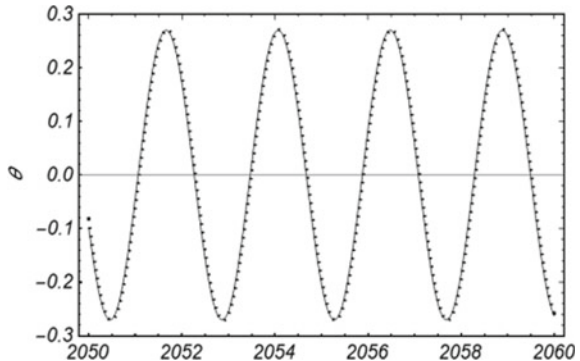
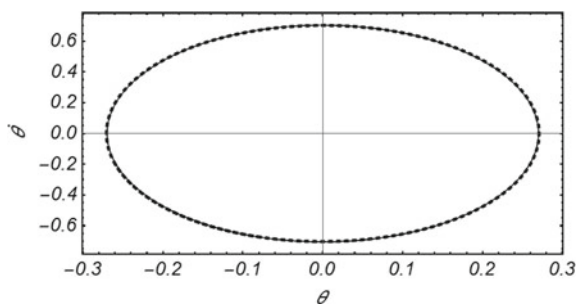


**Fig. 3**  $\theta, \dot{\theta}$  comparison of phase plane curves (from Wolfram Mathematica)



displacement of the end of the elastic manipulator with time, Fig. 3 shows the phase plane graph of the angular displacement and angular velocity of the end of the elastic arm, in which the solid line represents the numerical solution and the dashed line represents the analytical solution. It can be seen from the figure that the analytical solution is in good agreement with the numerical solution, which proves that the above analysis results are valid.

The amplitude–frequency characteristic curve determined by Eq. 30 is shown in Fig. 4, due to the multi-value caused by curve bending, the main resonance of the system appears jumping phenomenon, and the peak value of the main resonance of the system is not only related to the amplitude of the excitation force but also related to the damping coefficient of the system.

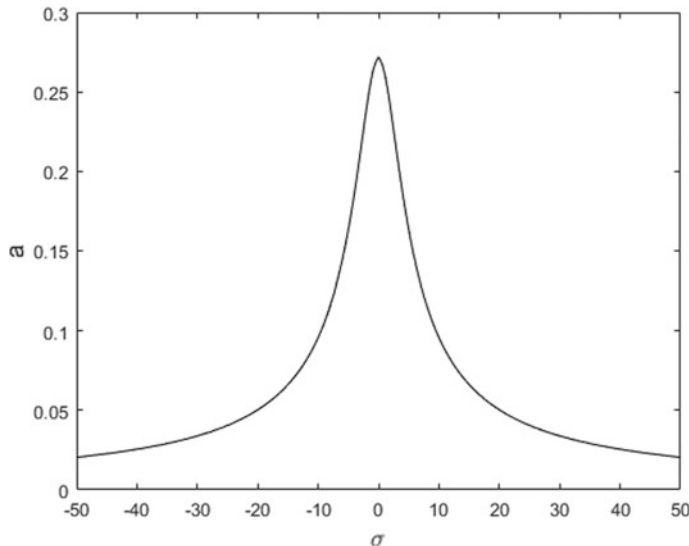


**Fig. 4** Amplitude–frequency characteristic curve of main resonance (from MATLAB)

## 6 Conclusion

- (1) The dynamic model of the elastic manipulator system is established, and the dynamic equation of the system is solved by the multiscale method. The results show that the numerical solution of the system is in good agreement with the analytical solution, which proves that the multiscale method can solve the elastic nonlinear problem. The feasibility of approximate solutions of linear dynamic systems is high.
- (2) The peak value of the main resonance of the system is not only related to the amplitude of the excitation force but also related to the damping coefficient of the system. With the change of the two, the amplitude of the system will suddenly jump.

## References

1. Wang HY, Han S (2018) Dynamic analysis of flexible joint robot. *Modern Manuf Technol Equip* 260(7):95–96
2. Yoshikawa T, Hosoda K (1991) Modeling of flexible manipulators using virtual rigid links and passive joints. *Soc Instrum Control Eng* 27(12):1389–1395
3. Vakil M, Fotouhi R, Nikiforuk PN (2012) A new method for dynamic modeling of flexible-link flexible-joint manipulators. *J Vib Acoust* 134(1)
4. Sayahkarajy M, Mohamed Z, Mohd Faudzi AA (2016) Review of modelling and control of flexible-link manipulators. *Proc Inst Mech Eng* 230(8):861–873

5. Cai GP, Hong S (2005) Research on hypothetical mode method of rotating cantilever beam. *Acta Mech Sinica* 37(1):48–56
6. Yao L, Zhang W, Xie XJ (2020) Stability analysis of random nonlinear systems with time-varying delay and its application. *Automatica* 117(C)
7. Alhazza KA, Nayfeh AH, Daqaq MF (2009) On utilizing delayed feedback for active multimode vibration control of cantilever beams. *J Sound Vib* 319:735–752
8. Zhang K, Scorletti G, Ichchou MN, Mieyeville F (2013) Phase and gain control policies for robust active vibration control of flexible structures. *Smart Mater Struct* 22(7):1–15
9. Alhazza KA, Masoud ZN, Alajmi M (2008) Nonlinear free vibration control of beams using acceleration delayed feedback control. *Smart Mater Struct* 17(1)
10. Liu Y, Lee SM, Kwon OM, Park JH (2013) Delay-dependent exponential stability criteria for neutral systems with interval time-varying delays and nonlinear perturbations. *J Frank Inst* 350(10):3313–3327

# Influence of the Modulus of Elasticity of the Jointed Material and Interlayers in Nodes with an Interlayer with a High TCLE



Qi Li, FengMei Liu, Haitao Gao, Huang He, and Viktor Kvasnytskyi

**Abstract** In this study, the influence of the modulus of elasticity of the jointed material and interlayers in the nodes with an interlayer with a high TCLE was investigated by computer simulation. To establish the general patterns of SSS formation when loading cylindrical nodes with interlayers of soft rigidity and checking the adequacy of the simulation, the average value of the elastic modulus of interlayers with a high TCLE was calculated. The results show that under thermal loading, in all variants, stresses are absent for the greater part of the node, and only in a small zone located near the interlayer near the joint edge (at the outer surface of the cylinder), and in the interlayer, a complex SSS is created. On the outer surface of the node in the greater part of the interlayer, the stiffness coefficient is at the level of 0.76, 0.80, decreasing to 0.64 near the joint in the nodes with a “soft” interlayer, and slightly increasing to 0.81 and 0.91 in the nodes with “neutral” and “hard” interlayers, respectively. The interlayer material is in the volumetric stress state throughout its entire length. This provides reliability guidance for the theory of TLP diffusion welding under large gap.

**Keywords** TLP diffusion welding · Stiffness coefficient · Interlayer

---

Q. Li · F. Liu (✉) · H. Gao (✉) · H. He

Guangdong Provincial Key Laboratory of Advanced Welding Technology, China-Ukraine Institute of Welding, Guangdong Academy of Sciences, Guang Dong, Guangzhou 510650, China  
e-mail: [liufm@gwi.gd.cn](mailto:liufm@gwi.gd.cn)

H. Gao  
e-mail: [gaoht@gwi.gd.c](mailto:gaoht@gwi.gd.c)

V. Kvasnytskyi  
National Technical University of Ukraine “Igor Sikorsky Kyiv Polytechnic Institute”, 37, Prosp. Peremohy, Kyiv 03056, Ukraine

## 1 Introduction

In the early 1970s, when Paulonic and others [1] were studying the welding of nickel-based superalloys, they proposed a new type of connection technology-transient liquid phase diffusion bonding. The technology has been successfully applied to the blade welding of turbine engine, and the high-temperature durability of the joint reaches 90% of the base material, realizing the practical application of the TLP connection technology [2]. So far, it has been widely used in nickel-based, cobalt-based, and oxide dispersion-strengthened high-temperature connections [3].

The prior studies mainly discuss the effects of factors such as TLP diffusion welding intermediate layer alloy, welding process parameters, and poor crystal orientation of welding assembly on welded joints, involving melting-reducing elements, intermediate layer alloy composition, form and thickness, welding temperature, heat preservation, welding pressure, post-weld heat treatment and poor crystal orientation of the base material, etc. [4, 5]. The appropriate intermediate layer alloy can improve the interface contact, reduce the requirements for the surface preparation quality of the welded parts and the welding pressure, improve the diffusion conditions, accelerate the diffusion rate, and achieve the purpose of reducing the welding temperature and shortening the welding time [6]. Avoid or reduce many problems such as diffusion holes and excessive thermal stress caused by the difference in physical and chemical properties between the intermediate layer and the base metal during the welding process.

There have been related theoretical studies and calculation formulas concerning the dissolution of base materials in TLP connections abroad [7]. However, after adding melting-reducing elements and strengthening elements on the basis of the composition similar to the base material, the elastic modulus of the intermediate layer will be different from that of the base material. The prior art mainly considers its phase composition and element diffusion during the welding process. The influence rule on the mechanical properties of the joint, but the influence of the elastic modulus of the intermediate layer on the stress and strain state of the joint has not been studied. Based on the preliminary research of TLP diffusion welding, this paper studies the stress and strain state law of the middle layer material for TLP diffusion welding with high elastic modulus, aiming to optimize the intermediate layer composition as an experimental reference.

## 2 Experimental Details

Considering the symmetry of the experimental samples, the top half of the sample taken from this model construction is divided into a reference. Model size: the cylinder diameter  $d = 20$  mm, the height  $h = 20$  mm, and the middle layer thickness is half of the total middle layer thickness. The overall view of the sample and the finite element (FE) of the model and the adjacent layers are shown in Fig. 1 [8].

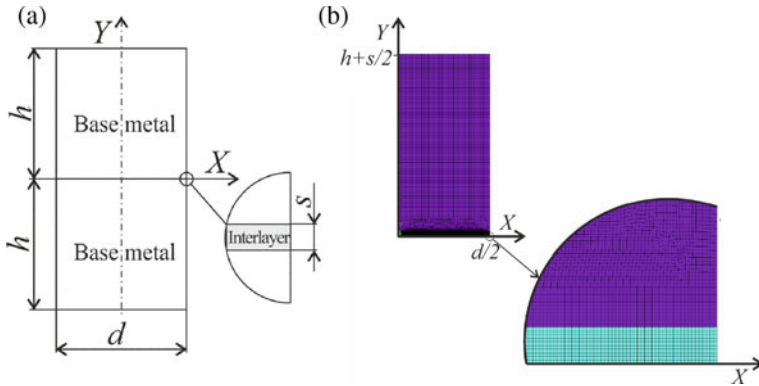


**Fig. 1** Overall view with intermediate layer specimens (a); projection of the finite element model (b)

**Table 1** The FEM model type

No. of var	TCLE <sub>intlr</sub> , $10^{-6} \cdot 1/\circ$	$E_{\text{intlr}}, 10^5 \text{ MPa}$	Thickness of interlayer, mm	Interlayer type
1	30	0.5	0.05	Neutral
2	30	0.25	0.05	Soft
3	30	1	0.05	Hard

For simulation the SSS under conditions of thermal loading (cooling) in the range 1100–1270 °C in all versions for the base metal, the average value of the elastic modulus EOM =  $0.5 \times 105$  MPa is adopted. In this case, the “soft” interlayers had a modulus of elasticity less than 2 times that of the base metal, the “neutral” layers were the same, and the “hard” ones, respectively, were two times larger Poisson’s ratio of both the main material and the interlayer was taken on the basis of extrapolation of the available data to 0.4. The thickness of the interlayer in all variants remained unchanged at 0.050 mm (Table 1).

### 3 Results and Discussion

#### 3.1 The Stress Fields in Small Areas Near the Interlayer and the Base Metal

Radial stresses in the base metal, in contrast to the nodes with interlayers with a low TCLE, are compressive (Fig. 2a, b). Staying close to zero on most of the joint (Fig. 2a), they reach at the edge of the joint with a maximum value of -48, -64, and -90 MPa in versions with soft, neutral, and hard interlayers, respectively (Fig. 2b). That is, up

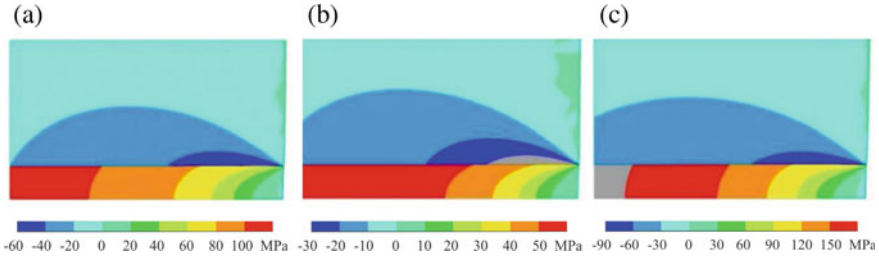


**Fig. 2** Fields of radial  $\sigma_x$  stresses in nodes with interlayers: “neutral” (a), “soft” (b), “hard” (c) near the interlayer near the outer surface of the node (x160)

to one and a half times (in proportion to the increase in the difference between the TCLE of the interlayer and the base metal) exceed the maxima in the nodes with interlayers with a low TCLE (32, 42, and 60 MPa). They also increase with increasing stiffness of the interlayer practically linearly ( $\sigma_x = -55.5 \times 10^{-5} \cdot E_{\text{intl}} - 35$ ).

In the material of the interlayer, the radial stresses, on the contrary, are tensile. On the majority of the joint they are at the level of about 64, 128, and 254 MPa (Fig. 2c) and decrease to 30, 58, and 110 MPa (Fig. 2d), that is, more than in 2 times, at the joint edge in variants with “soft”, “neutral”, and “hard” interlayers, respectively. This level is in 1.5 times higher than in nodes with interlayers with a smaller TCLE (−43, −85, and −170 MPa and −17, −26, and −56 MPa). That is, in the material of the interlayer, as its stiffness increases, the radial stresses linearly grow both at the most part inside the node ( $\sigma_x = 254 \times 10^{-5} \cdot E_{\text{intl}}$ ) and near the edge ( $\sigma_x = 109.5 \times 10^{-5} \cdot E_{\text{intl}}$ ).

Axial stresses along most of the joint, both in the main material and in the interlayer, are absent (remain at zero level) and appear compressive and increase to −27, −64, and −199 MPa only at the edge of the joint in variants with a “soft”, “Neutral”, and “hard” interlayers, respectively (Fig. 3). That is, these stresses are up to 1.5 times higher than in nodes with an interlayer with a low TCLE (18, 43 and 133 MPa) and have the opposite sign. Axial stresses, like radial stresses, also increase with increasing hardness of the interlayer material, but with a somewhat more complicated dependence ( $\sigma_y = -136 \times 10^{-10} \cdot E_{\text{intl2}} - 61.5 \times 10^{-5} \cdot E_{\text{intl}}$ ).

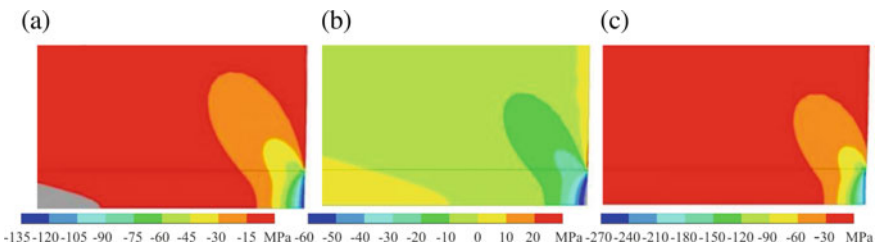


**Fig. 3** Fields of axial stress  $\sigma_y$  in the nodes with interlayers: “neutral” (a), “soft” (b), “hard” (c) near the interlayer near the outer surface of the node (x160)

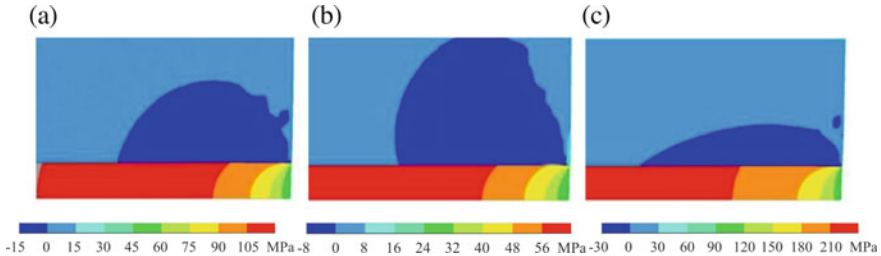


**Fig. 4** Fields of maximum principal  $\sigma_3$  stresses in nodes with interlayers: “neutral” (a), “soft” (b), “hard” (c) near the interlayer near the outer surface of the node (x160)

The main maximum stresses  $\sigma_3$  in the main metal from zero on the majority of the joint increase only near the edge (about 1 mm), reaching  $-71$ ,  $-110$ , and  $-191$  MPa in the variants with “soft”, “neutral”, and “hard” interlayers, respectively (Fig. 4a, b), which is 1.5 times higher than the maximum principal stresses in the nodes with interlayers with a low TCLE ( $47$ ,  $73$ , and  $127$  MPa).

The main maximum stresses  $\sigma_1$  in the interlayer remain at the level of  $64$ ,  $128$ , and  $255$  MPa for the most part of the joint length, they decrease to  $46$ ,  $76$ , and  $130$  MPa at the joint edge in variants with soft, neutral, and hard interlayers, respectively (Fig. 5a–c), which is about 1.5 times higher than the maximum principal stresses  $\sigma_3$  at the nodes with a low TCLE ( $-43$ ,  $-85$ , and  $-167$  MPa and  $-32$ ,  $-51$ , and  $-86$  MPa).

The circumferential stress distribution of the main material and the interlayer is similar to the radial stress. In the main metal, they are near zero at most of the joints, increasing only at their outer edges. Here they, as well as radial compressors, at the level of  $-24$ ,  $-37$ , and  $-76$  MPa (Fig. 6a, b) in variants with “soft”, “neutral”, and “hard” interlayers, respectively. This is up to 1.5 times greater than in nodes with an interlayer with a low TCLE ( $16$ ,  $26$ , and  $51$  MPa).

In the material of the interlayer, the circumferential stresses are tensile, they remain at the level of  $64$ ,  $128$ , and  $254$  MPa for the most part of the joint and decrease at the outer edge to  $46$ ,  $76$ , and  $129$  MPa, that is, also almost in 1.5 times, as well as in the nodes with interlayer with a low TCLE ( $-43$ ,  $-85$ , and  $-170$  MPa and  $-33$ ,

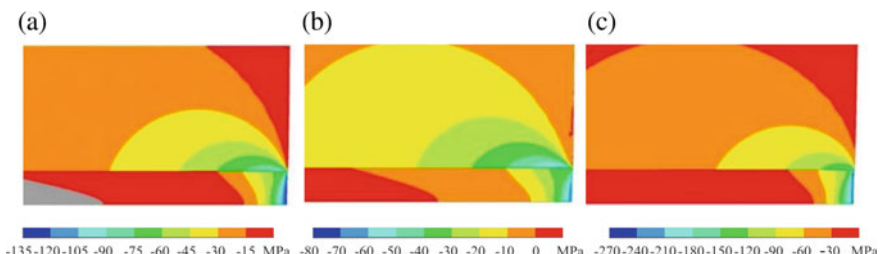


**Fig. 5** Fields of maximum principal  $\sigma_1$  stresses in nodes with interlayers: “neutral” (a), “soft” (b), “hard” (c) near the interlayer near the outer surface of the node (x160)

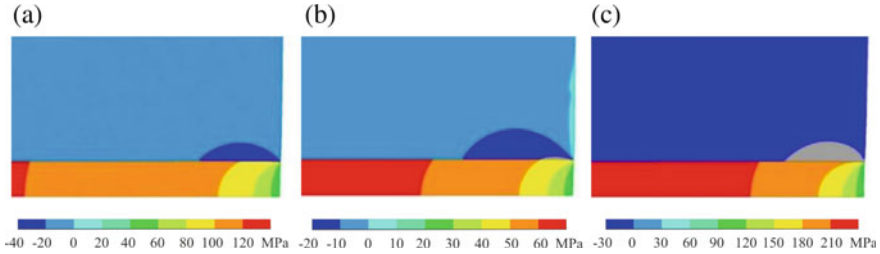


**Fig. 6** Fields of circumferential  $\sigma_{oz}$  stresses in nodes with interlayers: “neutral” (a), “soft” (b), “hard” (c) near the interlayer near the outer surface of the node (x160)

–51, and –86 MPa), in variants with soft, neutral and hard interlayers, respectively (Fig. 6).

Tangential stresses are absent for most of the joint length (about 95%), and appear and increase only at the very edge of it to 30, 47, and 77 MPa in variants with soft, neutral, and hard interlayers, respectively (see Fig. 7). That is, the maximum tangential stresses as well as normal increase as the stiffness of the interlayer increases ( $\tau_{xy} = 40.4 \times 10^{-10} \cdot E_{intl2} - 116 \cdot 10^{-5} \cdot E_{intl}$ ) and exceed similar stresses in nodes with an interlayer with a low TCLE by a factor of 1.5 (–20, –32, and –51 MPa).

Depending on an individual component,  $\sigma_{eq}$  are also distributed (Fig. 8). They are constant along most of the joint, with the level of all the variants being close to zero in the main material (Fig. 8a, b). In the interlayer, the stress level in this zone is about 64, 128, and 254 MPa in versions with “soft”, “neutral” and “hard” interlayers, respectively, (Fig. 8c, d), that is, they grow linearly with increasing stiffness of the interlayer ( $\sigma_{eq} = 254 \times 10^{-5} \cdot E_{intl}$ ). They exceed the equivalent stresses in the nodes with interlayers with a low TCLE by a factor of 1.5 (43, 85, and 170 MPa,  $\sigma_{eq} = 170 \times 10^{-5} \cdot E_{intl}$ ), that is, in proportion to the increase in the difference between the TCLE of the interlayer and the base metal.

Only near the joint edge, at about 50 layers thickness, equivalent stresses begin to gradually increase in the base metal and decrease in the interlayer, reaching a maximum of about 57, 86, and 139 MPa at the edge of the joint in the base metal, a minimum of 59, 111 and 200 MPa in the interlayer at a distance of about 2 times its

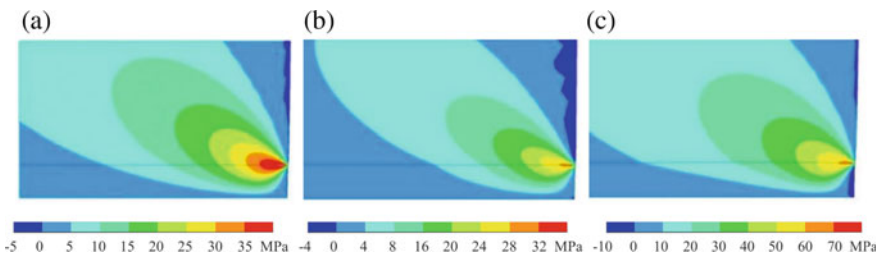


**Fig. 7** The fields of tangential stresses  $\tau_{xy}$  in the nodes with interlayers: “neutral” (a), “soft” (b), “hard” (c) near the interlayer near the outer surface of the node (x160)

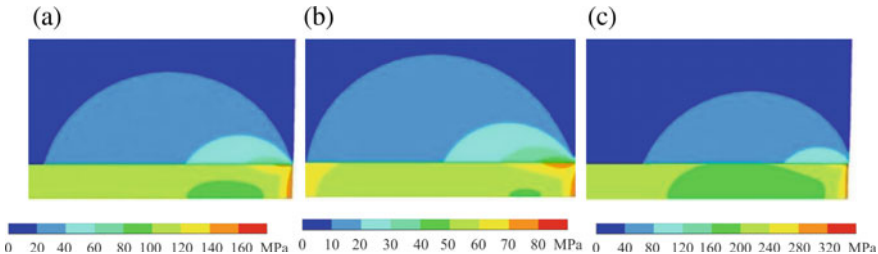


**Fig. 8** Fields of equivalent stresses  $\sigma_{eq}$  in nodes with interlayers: “neutral” (a), “soft” (b), “hard” (c) near the interlayer near the outer surface of the node (x160)

thickness from the outer surface of the unit, after which it again increases to 81, 153, and 338 MPa at its edge in versions with “soft”, “neutral”, and “hard” interlayers, respectively, which exceeds similar voltages in nodes with an interlayer with a low TCLE in 1.5 times (38, 57 and 92 MPa, 39, 72 and 132 MPa and 53, 102 and 225 MPa).

### 3.2 *The Effect of Volumetric SSS on the Strength and Plasticity of the Material in the Joint*

Figure 9 shows the graphs of the change in the stiffness coefficient in the joint zone in the base material (a, b) and the interlayer (c, d) along the entire joint (a, c) and near its edge (b, d). Analysis of the curves shows that in all variants of the nodes, both in the main material and in the interlayers, the distribution of the stiffness coefficients  $K_{stiff} = \sigma_3/\sigma_{eq}$  [9] is practically the same, that is, it does not depend on the stiffness of the interlayer.

In this case, in the main metal, over most of the joint length in its inner part, this coefficient is less than 1, gradually increasing from 0.68 on the node axis to 1 at a distance of about 1.5 mm from the edge. At the edge of the joint, it increases to 1.32, 1.34 and 1.36 in versions with “soft”, “neutral”, and “hard” interlayers, respectively (Fig. 9a, b). Comparison with the corresponding data in the nodes with an interlayer with a low TCLE (from 0.68 for most of the joint, the stiffness coefficient increases at the edge to 1.29, 1.32, and 1.36) shows that the difference lies within the real accuracy of the calculations and can be neglected.

That is, the SSS arising at thermal loading in the jointing zone in the nodes, both with the “soft” and “hard” interlayers, both with a lower and higher TCLE than in the base metal, equally reduces the strength and increases the plasticity of the base metal. On most of the joint length and leads to its hardening only near the outer surface, where the stiffness coefficient rises to 1.32–1.36 (Fig. 9b). That is, the degree of stiffness of the interlayer has practically no effect on the stiffness coefficient of the metal being joined. In the interlayer, the picture is somewhat different, for most of the joint length (up to 90%), the stiffness coefficient in the nodes with a layer of any

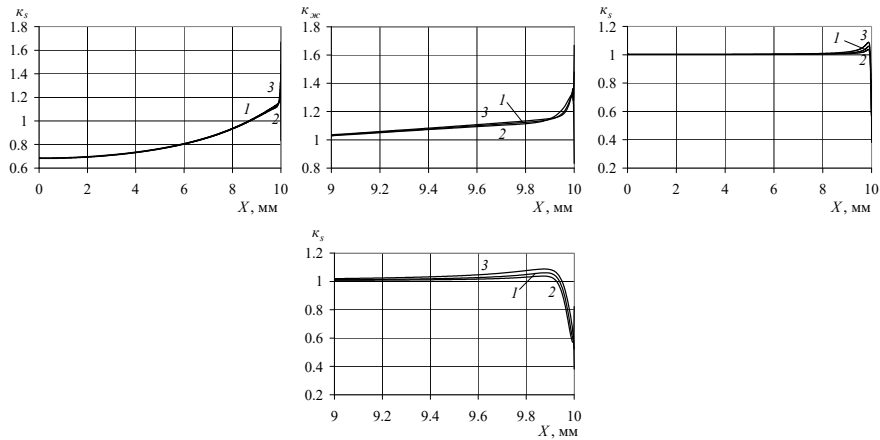


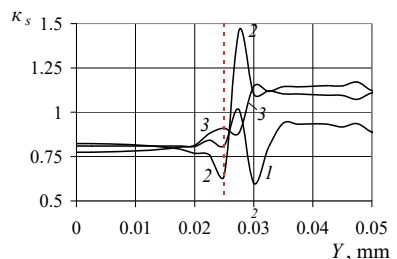
**Fig. 9** Changing the Stiffness Coefficients of the Stress State  $K_{\text{stiff}} = \sigma_3/\sigma_{\text{eq}}$  along the joint in the base metal (a, b) and  $K_{\text{stiff}} = \sigma_1/\sigma_{\text{eq}}$  and interlayer (c, d) along the entire length of the joint (a, c) and near its edge (b, d)

stiffness remains at a level close to 1. And only slightly near the joint edge, it slightly increases to 1.04, 1.06, and 1.09 (Fig. 9d) and sharply decreases to 0.57, 0.58, and 0.61 in versions with “soft”, “neutral”, and “hard” interlayers, respectively, on the side surface of the node. This practically corresponds to the nodes with an interlayer with a low TCLE (1.04, 1.06, and 1.09 for the most part of the interlayer and 0.57, 0.59, and 0.63 for the side surface of the node).

Thus, under the thermal loading of the nodes, neither the degree of stiffness of the interlayer nor the difference between the TCLE of the interlayer and the base metal in the greater or lesser side does not affect the stiffness coefficient. The distribution of the stiffness coefficient of the stress state along the generatrix near the joint is shown in Fig. 10.

On the outer surface of the node in the greater part of the interlayer the stiffness coefficient is at the level of 0.76–0.80, decreasing to 0.64 near the joint in the nodes with a “soft” interlayer, and slightly increasing to 0.81 and 0.91 in the nodes with “neutral” and “hard” interlayers, respectively, that is, the metal is somewhat softened

**Fig. 10** Changing the Stiffness Coefficients of the Stress State along the generatrix of the unit in the variants of the interlayer 1, 2, 3



here. In the main metal in the nodes with a “soft” interlayer in a very narrow zone in the immediate vicinity of the joint, the stiffness coefficient sharply increases to 1.46 and then decreases to almost 1.1, that is, the metal is somewhat hardened. In nodes with a “neutral” interlayer, it first increases to 1, then decreases to 0.6, and again increases, gradually approaching 0.95. In the nodes with a “hard” interlayer, the stiffness coefficient of the base metal at a certain distance from the joint decreases to 0.60 and then rises again, approaching 1.

## 4 Conclusions

1. The change in the combination of material rigidities in the site, as well as in the case of an interlayer with a high TCLE, does not affect the nature of its SSS, somewhat changing the stress level. In all variants, stresses are absent on most of the nodes, and only in a small zone located near the interlayer near the joint edge (at the outer surface of the cylinder), and in the interlayer itself a complex SSS is created.
2. In the interlayer, for the greater part of the joint length (up to 90%), the stiffness coefficient in the nodes with a layer of any stiffness remains at level 1. And only slightly near the joint edge, it slightly increases to 1.04, 1.06, and 1.09 and sharply decreases to 0.57, 0.58, and 0.61 in variants with “soft”, “neutral”, and “hard” interlayers, respectively, in nodes with an interlayer, with high TCLE.

**Acknowledgements** This work was supported by the National Key Research and Development Program of China (2020YFE0205300), the GDAS Special Project of Science and Technology Development (2021GDASYL-20210302008), Science and Technology Planning Project of Guangdong Province (2022B1212050001).

## References

1. Bo L, Jinbao H, Junfei T et al (2014) Diffusion welding of new aviation materials and structure. *Aviat Manuf Technol* 46(20):74–75
2. Li X, Zhong Q, Cao C et al (2003) Research on TLP diffusion welding process of DD3 single crystal alloy split blades. *Mater Eng* 06:4–7
3. Kong Q, Qu S, Shao T et al (2010) Application and development of brazing and diffusion welding technology in aircraft engine manufacturing. *Aeronaut Manuf Technol* 24:82–84
4. Li Q, Liu F, Yue X et al (2021) Effect of heat treatment on microstructure and high temperature properties of IC10 superalloy TLP diffusion welding under 80  $\mu\text{m}$  gap. *Trans China Weld Inst* 42(05):36–44
5. Yue X, Liu F, Li Q et al (2020) Effect of post-bond heat treatment on microstructure and mechanical properties of the wide gap TLP bonded IC10 superalloy with a low boron Ni3Al-based interlayer. *J Manuf Process* 54:109–119
6. Wan D, Fang W, Chen H et al (2016) Research progress of Ni-based superalloy TLP diffusion welding intermediate layer materials. *Welding* (08):20–23+73

7. Li Q, Liu F, Yue X et al (2019) Stress-strain state in elastic phase in Ni3Al superalloy with soft interlayer. IOP Conf Ser Mater Sci Eng 677:022122
8. Li Q, Xiong M, Liu F et al (2019) Influence of the residual thickness of the interlayer on the stress-strain state in the nodes with soft interlayer. IOP Conf Ser: Mater Sci Eng 677(2):022051 (12pp)
9. Kurrer KE (2009) The first fundamental engineering science disciplines: theory of structures and applied mechanics. Wiley

# Research on Imaging Method of Missile-Borne Infrared Lateral Window Adapting to Deflection Light Path with Large Incident Angle



Qi Meng and Dong Chen

**Abstract** Aiming at the problem that the conventional missile-borne infrared imaging system is easily affected by aerodynamic thermal effect, the imaging method of the infrared lateral window is studied. A set of imaging system of infrared lateral window is designed, which is suitable for deflecting light path with large incident angle. Theoretical calculation and experimental test results show that the system has fine imaging performance and can obtain good images, which verifies the feasibility of the infrared lateral window imaging method, and can provide a practical reference for similar infrared imaging in the future.

**Keywords** Deflection light path · Large incident angle · Loading conditions of bomb · Infrared detection · Lateral window imaging

## 1 Introduction

With the development of the range of contemporary military weapons and equipment and the increasing requirement of precision strike, precision guidance technology needs to adapt to a wider high-speed flight field, so it is necessary to compete for the time advantage and improve the response speed. Image Guidance Technology has the characteristics of high resolution, strong concealment, intuitive and convenient, and conforms to human visual habits, and has become an important part of modern long-range precision guidance technology [1].

Visible Light Imaging and Infrared Imaging are the two main detection methods for image guidance. Combining target tracking and recognition technology, an intelligent homing guidance system can be formed. However, Visible Light Imaging Guidance is easily limited by illumination conditions. Under complex and harsh application conditions such as high temperature and smoke, the image is prone to

---

Q. Meng (✉) · D. Chen

Laboratory of Guidance Control and Information Perception Technology of High Overload Projectiles, PLA Arm Academy of Artillery and Air Defense, Hefei, China  
e-mail: [mq9862163765@163.com](mailto:mq9862163765@163.com)

overexposure and blurring. Compared with Visible Light Imaging, harsh environments such as high temperature and smoke have less influence on Infrared imaging, and infrared images with better stability are more conducive to precise guidance. At present, some high-speed missiles at home and abroad are equipped with infrared detection systems, and the fourth generation of air-to-air missiles is one of them. Using infrared imaging guidance technology, infrared imaging can provide more and more complete target information and operational environment information, and make full use of people's judgment, recognition, and decision-making ability, so that the missile's target detection and strike ability can be greatly improved [2]. Such as AIM-9 X in the United States, ASRAAM in the United Kingdom, IRIS-T in Germany, MICA-IR in France, A-Darter in South Africa, etc. [3]. In addition, some foreign anti-ship and anti-air defense missiles have deployed infrared detection systems, such as LRASM long-range heavy-duty anti-ship missiles, NSM ship-borne anti-ship missiles, and JSM airborne anti-ship missiles of the United States [4]. High-resolution imaging and full passive guidance mode can effectively improve the ability to deal with complex battlefield environment.

At present, the flight Mach number of various high-speed missiles is constantly increasing, and the survivability and operational effectiveness of conventional missile-borne infrared imaging systems are faced with many bottlenecks and challenges: the aerodynamic thermal effect caused by supersonic flight will seriously threaten the normal operation of the photoelectric equipment on the infrared seeker, and the high-temperature effect will also cause the optical window itself to generate strong infrared radiation, which will seriously interfere with its detection imaging. To solve the above problems, window cooling systems or other methods can be used to improve the imaging environment of windows. For example, American AIM series missiles are equipped with special high-pressure nitrogen cylinders and unique low-temperature engines, which are responsible for cooling the infrared seeker [5]. However, due to the limited space and volume of missile-borne platform, the photoelectric system of detection equipment has always been integrated and modular, while the cooling system generally takes up a certain volume and consumes a lot of power, thus greatly increases the burden of the seeker. Therefore, some scholars put forward the optical side window imaging method to reduce the working pressure of cooling system. When domestic scholar Liu [6] and others studied the cooling effect of the terminal guidance side window of high-speed interceptor missile, they preliminarily put forward the main technical indexes of the optical side window and the aerodynamic thermal environment it faces; Ding [7] found that the cooling efficiency of the tangential jet is higher in the experimental study of the aero-optical effect of the high-speed optical hood, and thus discussed the cooling scheme of the infrared lateral window based on the tangential jet cooling technology. Yue Ming [8] proposed and verified the idea of designing conformal curved side windows on conformal fairing by analyzing the wave aberration of conformal curved side windows with different heat distributions. Based on the above research background, in order to find an effective method to reduce the influence of high-temperature effect on infrared window imaging, a missile-borne infrared lateral window imaging method is proposed in this paper, and the imaging method is verified by system design and experimental test.

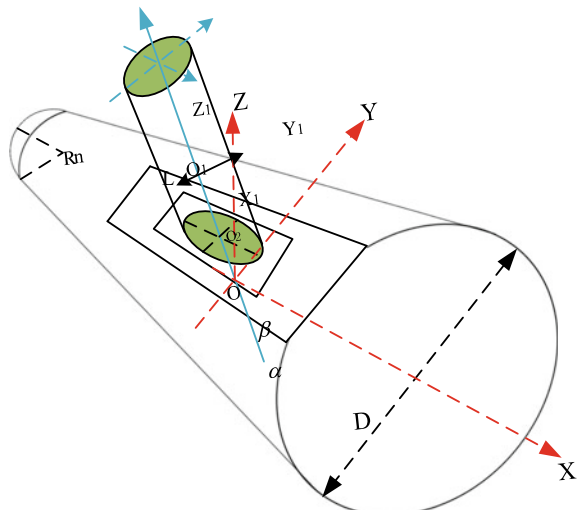
## 2 Design of Imaging System of Missile-Borne Infrared Lateral Window

### 2.1 Analysis of Imaging Problems of Infrared Lateral Window

Generally, in order to facilitate detection and imaging, infrared window is mostly deployed at the front end of the seeker, and the optical lateral window breaks through traditional detection and imaging methods. It is necessary to design a deflection light path and effectively change the light propagation path to meet the imaging requirements and achieve the expected effect similar to the traditional installation of optical windows in the front end of the seeker. Figure 1 is the imaging schematic diagram of the plane lateral window of the blunt cone warhead head. Its curvature radius of a sphere is  $R_n$ ,  $\alpha$  is the angle with the central axis of warhead,  $\beta$  is the angle between line of sight angle and infrared lateral window, so the angle between the infrared lateral window and the central axis of the warhead is  $\alpha - \beta$ . As shown in the simplified diagram of the infrared lateral window below, the geometric relationship can preliminarily determine its size, and its maximum length should be no less than  $L / \sin \beta$  and maximum width should not be less than  $L$ .

From the imaging beam, the infrared ray with a large incident angle is received by the infrared lateral window, and the imaging angle direction of the window is almost along the axial direction of the warhead. Compared with the common front-end axial imaging method, the light intensity is low and the imaging resolution is low, so it is necessary to find an effective method to change the propagation path of light and enhance the transmitted light intensity. In the dimension design, the narrow space

**Fig. 1** Imaging diagram of infrared lateral window with blunt cone of ball head



of the warhead limits the maximum length and width of the infrared lateral window, which further restricts the imaging size, and the imaging range of the lateral window is smaller. Therefore, when designing the infrared lateral window imaging system, the choice of light path must be able to adapt to the condition of large incident angle and increase the light transmittance. The increase of the deflection light path also increases the volume and complexity of inner workpiece structure. When designing the system, it is necessary to have complete imaging capability in a space smaller than the front end.

## 2.2 Deflection Light Path Design

The design starting point of deflection light path is to change the propagation direction of light beam or to adjust the imaging visual axis. According to the difference of physical principles, it can be divided into mechanical optical deflection technology, MEMS optical deflection technology, and non-mechanical optical deflection technology [9]. Among them, the mechanical optical deflection system generally changes the incident angle of the light beam by controlling the spatial position of the reflecting mirror and the transmitting mirror by inertial mechanical components, so as to achieve the purpose of optical path deflection. It has the advantages of low economic cost, relatively small manufacturing difficulty, and convenience for realizing large-angle deflection. According to the above conditions, in order to realize the large angle of incidence, the optical path is designed by the principle of reflection. As shown in Fig. 2, the combination of the transmission mirror and the reflection mirror can compress the light path, which is suitable for the characteristics of a small space layout, and has high light intensity utilization rate. Among them, the reflective imaging mirror can approach the incident window, changing the light path, further compress the space size, and realize the compression of large viewing angle, while the infrared imaging device is used for infrared imaging and information processing of capturing target.

## 2.3 System Design

According to the design principle of the above reflected light path, a lateral window imaging system is designed on the basis of Fig. 2, which mainly consists of infrared window, reflector, infrared imaging device, and mechanical connecting device. The main structural design is shown in Fig. 3. The guiding ideology of the system design is to deploy the infrared imaging device on the side wall of the seeker cone, so as to adapt to the missile-borne flight environment and reduce the aero-thermal threat. The key to the system design is how to adapt to the practical problems of large incident angle and small space layouts and improve the light transmittance while realizing the deflection of the light path.

**Fig. 2** Schematic diagram of the design principle of reflective light path (1-window front, 2-infrared window, 3-plane mirror, and 4-infrared imaging device)

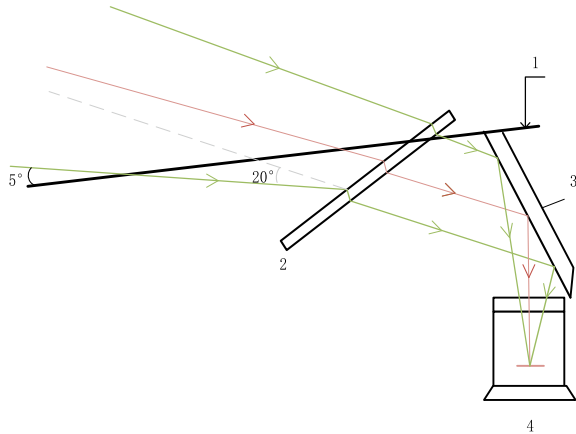
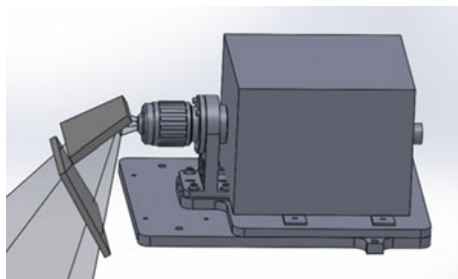


**Fig. 3** Design of the main structure of the imaging system



Aiming at the problem of large incident angle and small spatial layout, in the design of imaging system, the special-shaped structure of window mirror and reflector is designed, which is different from the conventional rectangular or circular curved surface. And the window and reflector are designed in a trapezoidal shape, so as to facilitate processing and mechanical assembly. The window is made of sapphire glass, coated on the surface, and supports infrared rays in a specific spectral range (such as 1.2–8  $\mu\text{m}$ ). The mirror is silica glass, and the surface is coated with a total reflection silver film with a reflectivity of not less than 98%. The special-shaped structure design can overcome the asymmetry of the visual field. When the lateral window is opened, the scene observation can be completed obliquely in front or obliquely below. The close mechanical connection between the mirror, the window, and the imaging mirror can adapt to low-intensity light, and the transmittance can reach about 40% in the range of 65–85 incident angles.

### 3 Imaging Quality Evaluation of Infrared Lateral Window System

After the design of the lateral window imaging system is completed, in order to better analyze the imaging quality of the system, this paper tests the system around Modulation Transfer Function (MTF), Noise Equivalent Temperature Difference (NETD), Minimum Resolvable Temperature Difference (MRTD), and other parameters, and analyzes the imaging performance of the system through astigmatism and distortion.

#### 3.1 Test Result of MTF, NETD and MRTD

First, the modulation transfer function (MTF) of the whole field of view is tested at normal temperature and high temperature ( $80^{\circ}\text{C}$ ). It can be seen that at the Nyquist frequency (i.e., The minimum sampling frequency defined to prevent signal aliasing) is more than 40% in the whole field of view at different temperatures, which also indicates that the system has good imaging quality.

Then, another test is done with the environment is  $25.4^{\circ}\text{C}$  (298.7 k), the temperature difference is  $1.0^{\circ}\text{C}$  and the pixel of the imaging unit is 0.015 mm. As can be seen from Fig. 4, for the detection of multiple sampling points, the NETD values are concentrated at around 10 Millikelvin. NETD of general infrared imaging devices is about 100 Millikelvin, and the high detection quality can reach 1 Millikelvin. The smaller the NETD value, the higher the temperature sensitivity of the imaging device, and the lower the noise. The right picture shows the measurement results of the MRTD of the infrared lateral window imaging system. It can be concluded from the figure that the first test and second tests were conducted for different spatial frequency target, and the results were 0.4 K and 0.55 K, respectively.

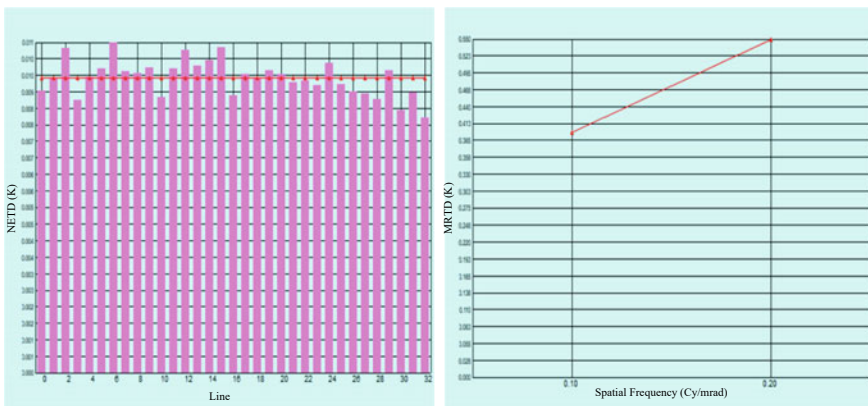


**Fig. 4** Measurement result chart of NETD and MRTD

### 3.2 Full-Field Point Array Diagram and Distortion Detection

Figure 5 shows the bitmap of the entire field of view at normal temperature and high temperature ( $80^{\circ}\text{C}$ ). The root-mean-square value of the diffuse spot in the whole field of view is less than 1.3 pixels, which indicates that the off-axis points of various colors of the optical system are basically coincident, and the chromatic aberration correction is fine.

In addition, the imaging distortion effect is also tested during the system design. As shown in Fig. 6, it can be found from the imaging distortion effect test chart of the system that the maximum distortion value of the system is less than 1.5% and the distortion rate is low. According to the test results of the above parameters, the design of the system can meet the basic requirements of infrared imaging.

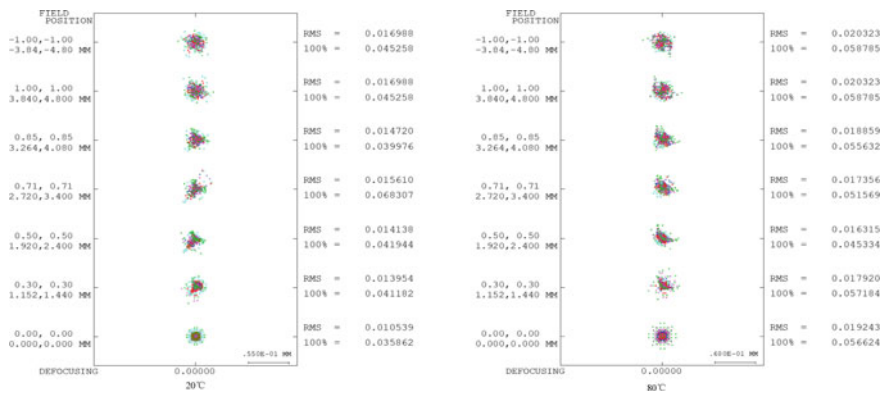
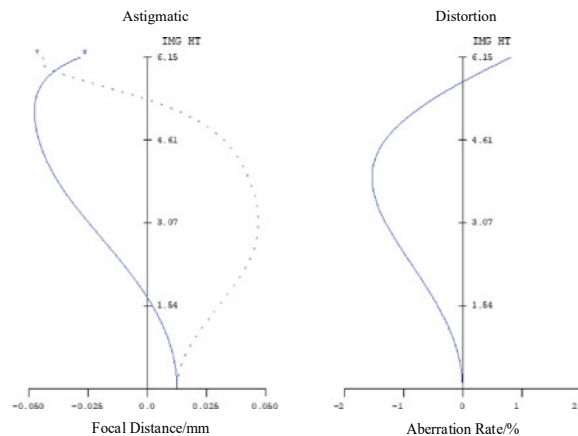


**Fig. 5** Dot diagram at normal temperature and high temperature ( $80^{\circ}\text{C}$ )

**Fig. 6** Detection diagram of the imaging distortion effect



### 3.3 Experimental Observation of Infrared Lateral Window Imaging System

Through physical observation, clear images are obtained as shown in Fig. 7. As can be seen from the figure, the red external window system can clearly capture the image information, and it is easy to distinguish the related features of the target and the background. Compared with the images obtained by the long-wave infrared camera, the side window system can adapt to the low-intensity night, and it is superior to the selected long-wave infrared camera in obtaining image data and describing the details of the scene targets. In the figure, (c) is the real-time image acquired by the traditional refrigeration medium-wave infrared camera, and (d) is the real-time image acquired by a red external window imaging system (the internal imaging equipment is also a refrigeration medium-wave infrared unit). Through the comparison between the two, it can be seen that this system can achieve the expected effect similar to the conventional front-end imaging, but the brightness of the captured image is low, because even under the action of the deflected light path, the imaging with large incident angle will lose some light transmittance, resulting in the decrease of light intensity.

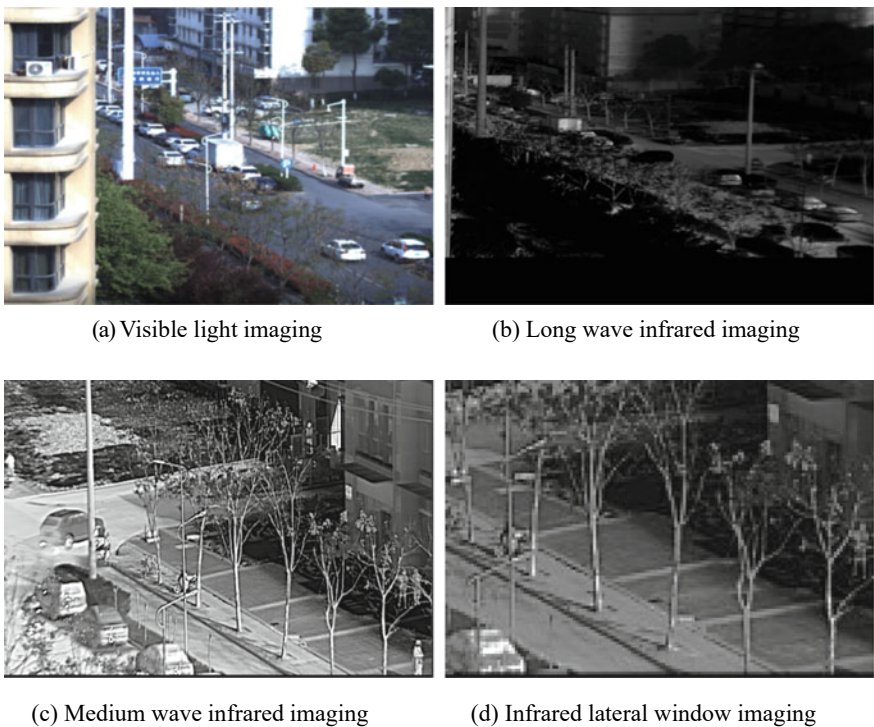


**Fig. 7** Comparison of imaging effect of real-life observation

The guiding ideology of the design of the infrared lateral window imaging system is to avoid or reduce the influence of aerodynamic heat and high temperature on imaging. By comparing the stagnation area of the head, the ideal area of the sidewall of the warhead cone is selected. However, even so, the lateral window will still be adversely affected by the temperature rise in operation. Therefore, aiming at the lateral window imaging system designed in this paper, the window high-temperature imaging experiment was also observed. The experimental condition is to select a real target with typical infrared characteristics on an indoor rotating platform, and blow it to the infrared window of the imaging system with a high-temperature hot air gun at 300 °C (about 573 K) for 2 min. After the window is heated at high temperature, observe the changes of the images acquired by the system through the monitor. The images collected during the cooling are shown in Fig. 8.

From the changes of the captured images, it can be found that under the influence of high temperature, the window increases the brightness of the captured images, the target feature information in the images gradually melts into the background, and the imaging quality is greatly reduced. These phenomena indicate that the high-temperature effect will produce strong infrared radiation, and the decrease in signal-to-noise ratio will lead to the decrease of imaging stability. Therefore, when the missile-borne infrared imaging system falls at a high speed, the window temperature caused by aerodynamic thermal effect will blur the visual field of the target, and even make the target disappear in the background. In reality, the temperature of the front window of the seeker is much higher than 300 °C. It can be inferred that the imaging stability of the conventional front window will be far lower than the

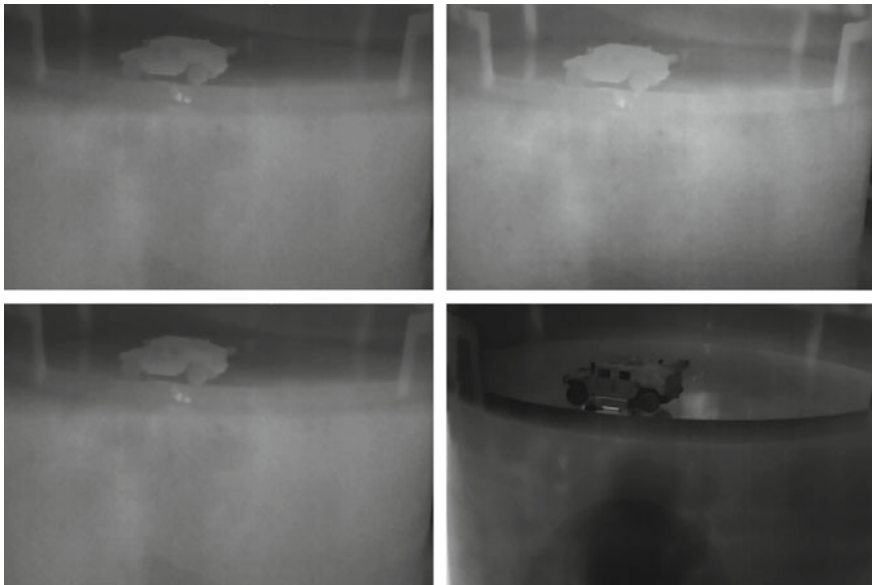


**Fig. 8** Change of images collected by high-temperature window

observation results of the uncooled system in this experiment, which further indicates that the design of the infrared lateral window imaging system can overcome the high-temperature problem from the source of image acquisition, and to some extent, can reduce the adverse effects caused by aerodynamic thermal effects.

## 4 Conclusion

A missile-borne infrared lateral window imaging system is designed, and the imaging method, system design, and imaging evaluation are introduced in detail. From the design results, the deflection light path adopted by the infrared lateral window imaging system can overcome the problems of large incident angle and small space size, and make the imaging achieve an effect similar to that of ordinary front-end axial imaging. The experimental results show that the system has good imaging performance, and can obtain fine-quality images, which verifies the feasibility of the infrared lateral window imaging method, and can provide a practical reference for similar infrared imaging in the future.

## References

1. Dong C, Zonghao T (2021) Research on heterogeneous acceleration of deep learning methods for missile-borne image processing. *Aero Weapon* 28(03):10–17
2. Ke L, Baoguo C, Lijuan L (2011) Development tendency and key technology of IR seeker for air-to-air missile. *Infrared Technol* 41(10):1117–1121
3. Heitman H-R (2015) A-darter programme nears completion. *Janes's Defence Weekly* 52(08):17
4. Huang M, Wang Y, Jiang S et al (2022) Summary of infrared terminally guided anti-ship missiles developed by united states in recent years. In: Proceedings of the 15th national conference on signal and intelligent information processing and application, pp 102–105
5. Miao R, Hao L, Jingjing L et al (2021) Research on Foreign air-to-air missiles' development in 2020. *Aero Weapon* 28(05):38–45
6. Chunsheng L, Peitian L, Jindong F (2000) Analysis of cooling effects of high-speed missile optical side window. *Infrared Laser Eng* 03:68–72
7. Haolin D, Shihe Y (2020) Research advance in aero-optical effect of high-speed optical dome. *Phys Gases* 5(03):29–40
8. Ming Y (2019) Research on side window design of conformal surface of high speed aircraft based on aero-optical effect. Harbin Institute of Technology, Hei Longjiang
9. Zhao Z (2020) Study on liquid crystal polarization grating with large deflection angle. Ji Lin: University of Chinese Academy of Sciences (Changchun Institute of Optical Precision Machinery and Physics)

# Study on the Characteristics of Rollover Injury of Passenger on the Passenger Side of an Off-Road Vehicle



Lizhi Zhou, Yunbo Zhou, Ming Zhang, Jianing Bai, and Wangang Xiao

**Abstract** In order to study the injury characteristics of the passenger-side occupant in the process of near-ground side ramp rollover, a finite element model of an off-road vehicle was established, and the acceleration of the center of mass of the vehicle rollover was obtained through simulation, and the accuracy of the model was verified through real vehicle rollover test. Hybrid III 50% male dummy was placed in the three rows of seats on the passenger side, and the restraint system was the same as that of the original vehicle, and the damage to various parts of the dummy was obtained for comparative analysis. The study shows that: the peak injury moments of different positions are similar, only the peak injury moments of the head and chest of the rear dummy appear earlier; the rear occupant's body dives and the neck is compressed, resulting in excessive axial force on the neck, and the subsequent improvement should focus on the restraint system.

**Keywords** Rollover · Dummy injury · Special vehicle · Passive car safety

## 1 Introduction

Crashes are the most common vehicle accidents while rollover crashes are the highest risk of serious injury and death in crashes [1]. In rollover accidents, the fatality rate of SUVs is more than 2.5 times higher than that of passenger cars [2]. Current rollover research is still limited by high test costs, poor reproducibility, and imperfect research [3]. Fu et al. proposed the use of a joint simulation method of multi-rigid body dynamics and finite elements, which can improve the efficiency of finite element simulation on the basis of finite element simulation accuracy [4]; Wang et al. studied the occupant injury of the driver and co-driver of a special vehicle under slope rollover

---

L. Zhou · Y. Zhou (✉) · M. Zhang · J. Bai · W. Xiao

School of Mechanical Engineering, Nanjing University of Science and Technique,  
Nanjing 210094, Jiangsu, China  
e-mail: [yunbo31983@163.com](mailto:yunbo31983@163.com)

conditions, driver-side, and co-driver-side rollover situations [5]; Ding et al. studied the special vehicle seat installation methods applicable to rollover conditions [6].

This paper focuses on the injury characteristics of the passenger-side occupant in the near-ground side ramp rollover, where the front and middle-row occupants sit facing forward and the rear-row occupants sit facing left. This paper uses Primer software for seat preload and seat belt modeling, LS-Dyna software for simulation solution to obtain the near-ground side occupant motion state during the vehicle rollover, and LS-PrePost software for post-processing to obtain the damage situation of each part of the occupant.

## 2 Establishment of Rollover Simulation Model

Hypermesh software was used to establish the rollover model of the whole vehicle. The rollover model includes three parts: the whole vehicle model, the dummy-belt model, and the ground model, and the unit is t-mm-s.

Firstly, the three-dimensional model of the whole vehicle is established, and the geometry is cleaned and simplified after importing Hypermesh. Then the model is discretized, and each component is meshed with a size of 10 mm. Finally, all parts grids are merged, and parts with wrong positions are adjusted to check and avoid initial penetration and interference of parts [7].

The dummy model is the LSTC version of Hybrid III 50% male dummy, and the seat is the original seat model, placed in the passenger-side position as shown in Fig. 1 [by author]. The constraint system is the same as the original car. The ground is modeled according to the actual test site, and the soil model uses solid cells with a grid size of 100 mm. the ramp slope is 60% and the slope height is 15 m.

Boundary conditions are imposed in Hypermesh, including gravitational acceleration of  $9.8 \text{ m/s}^2$ , initial vehicle sidelobe speed of 15 km/h, and sidelobe angular speed of 5 rad/s, as shown in Fig. 2 [by author]. The duration of this simulation is set to 3 s.

**Fig. 1** Occupant position and vehicle model. By author

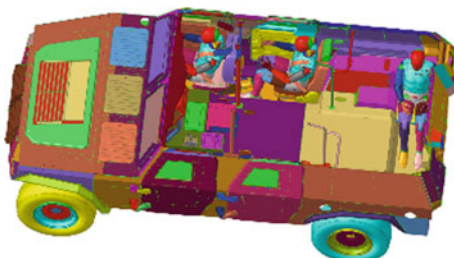
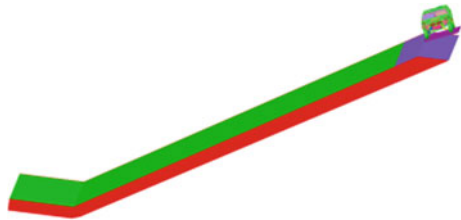


**Fig. 2** Rollover simulation schematic. By author



### 3 Model Accuracy Validation

The test collected the whole vehicle three-way acceleration of the center of mass, the whole vehicle rollover outside the high-speed camera. The whole vehicle center-of-mass acceleration sensor is shown in Fig. 3 [by author]; the vehicle after rollover is shown in Fig. 4 [by author].

As shown in Fig. 5 [by author], the X, Y, and Z acceleration curves of the vehicle center of mass are compared with those of the simulated vehicle rollover test. From the figure, it can be seen that the simulated acceleration curves of the center of mass and the acceleration curves of the test have roughly the same trend during the first roll of the vehicle. In terms of the peak size and peak time point, the peak of X-direction acceleration simulation is 49.84 g, the appearance moment is 2.48 s, the

**Fig. 3** Acceleration sensor.  
By author



**Fig. 4** Vehicle after test. By author



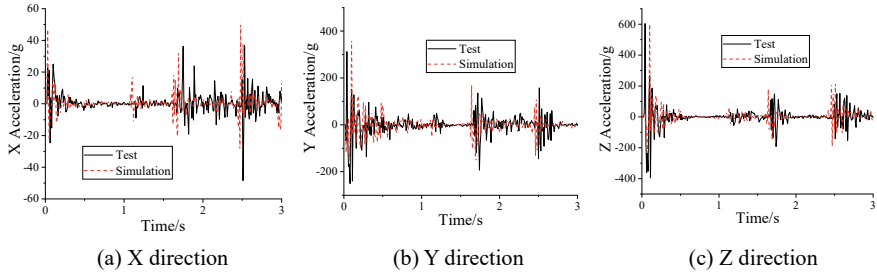


**Fig. 5** Comparison of experimental and simulated center-of-mass acceleration. By author

peak of test is 48.41 g, the appearance moment is 2.5 s, the peak error is 2.86%, the peak moment error is 0.02 s; the peak of Y-direction acceleration simulation is 360.65 g, the appearance moment is 0.1 s, the peak of test is 311.85 g, the appearance moment is 0.04 s. The peak of Y-direction acceleration simulation is 360.65 g, the appearance moment is 0.1 s, the peak of test is 311.85 g, the appearance moment is 0.04 s, the error is 13.53%, the error of peak moment is 0.06 s; the peak of Z-direction acceleration simulation is 599.2 g, the appearance moment is 0.1 s, the peak of test is 603.25 g, the appearance moment is 0.4 s, the error is 0.67%, the error of peak moment is 0.06 s.

The error may be due to the fact that the ramp used in the test is not an ideal plane and there exists a slight concave and convex curvature, so the vehicle landing position and tilt angle in the simulation are different from the test. The error is within the acceptable range, and the acceleration trend of the simulation model is in high agreement with the test results, which further verifies the reliability of the simulation finite element model.

## 4 Occupant Dynamic Response and Damage Assessment

After simulation calculations, the injuries of the passenger-side occupants during the vehicle rollover on the ramp were obtained, including the head, neck, chest, and thighs of the dummy [8]. The simulation results were filtered according to SAE J211 regulations [9], and the occupant injuries were obtained as follows in Table 1 [by author].

### 4.1 Head Injury Analysis

The indexes of head injury were head acceleration and HIC.

The head acceleration curve is shown in Fig. 6 [by author]. The peak synthetic acceleration of the head of the passenger dummy is 85.74 g at 1.1 s; the peak synthetic

**Table 1** Injuries to various parts of the occupant

	Index	Front	Middle	Rear
Head	HIC	320.67	301.8	145.2
	Acceleration	85.74 g	103 g	76.6 g
Neck	Y torque	96 N m	77N m	-43 N m
	Fz	2138 N	2520 N	7186 N
	N <sub>ij</sub>	0.62	0.7	0.83
Chest	Compression	-5 mm	6.7 mm	5.66 mm
Leg	Left	562 N	1090 N	763 N
	Right	578 N	678 N	788 N

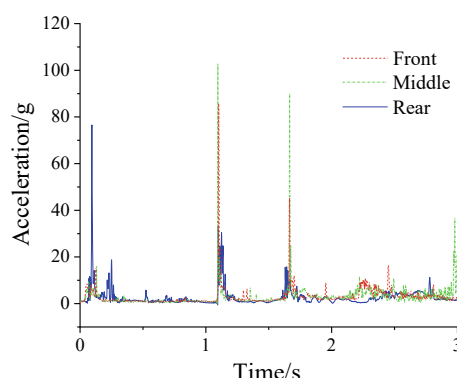
By author

acceleration of the head of the passenger rear dummy is 103 g at 1.09 s; the peak synthetic acceleration of the head of the rear lateral dummy is 76.6 g at 0.1 s. Based on the above head acceleration curve, the head HIC-36 is calculated as 320.67; the passenger rear dummy is 301.8; the rear lateral dummy is 145.2.

At 0.03 s, the vehicle tires collide with the platform car bump, at 0.1 s, the passenger seat dummy and the passenger rear-row dummy's head have a small acceleration peak due to inertia; the rear lateral dummy's head collides with the roof of the vehicle, and a maximum peak of head acceleration occurs. 1.2 s the roof collides with the ground at the connection between the roof and the side surround, the passenger seat dummy and the passenger rear-row dummy's head collides with the side surround, and a small peak of acceleration occurs. At 1.7 s, the vehicle flipped over and the whole roof was in contact with the ground, the dummy inside the car was in an inverted state and the head collided with the roof, and a small acceleration peak occurred for all positions.

**Fig. 6** Head acceleration.

By author



## 4.2 Analysis of Neck Injury

The main neck injury indicators are the force applied to the neck in three directions, the moment around the Y-axis direction, and the neck injury indicator  $N_{ij}$ .

As shown in Fig. 7a [by author], in the X-direction, the dummies at different positions did not exceed 0.6 kN although the changes were more dramatic. The X-directional positive direction of the dummy neck sensor was the front facing direction of the dummy, and the peak X-directional force in the neck of the front-row dummy was 594 N at 1.67 s; the peak X-directional force in the neck of the middle-row dummy was 2104 N at 1.67 s; and the X-directional force in the back row dummy was 233 N at 1.2 s.

The positive Y-direction is left shoulder pointing to right shoulder, as shown in Fig. 7b [by author], the peak Y-directional force of the neck of the front-row dummy is 2118 N at 1.67 s; the peak Y-directional force of the neck of the middle-row dummy is -555 N at 1.68 s; the Y-directional force of the back row dummy is -6295 N at 1.11 s.

The Z-direction is downward in the positive direction, as shown in Fig. 7c [by author]. The peak Y-directional force in the neck of the front-row dummy is 2138 N at 1.67 s; the peak Y-directional force in the neck of the middle-row dummy is 2520 N at 1.10 s; and the Y-directional force in the rear-row dummy is 7186 N at 1.11 s.

As can be seen in Fig. 8 [by author], the neck Y-directional moment oscillation varies from forward bending for positive values to backward bending for negative values, with the dummy neck mainly bending forward. The peak Y-directional moment of the neck of the passenger dummy was 96 N m at 1.77 s; the peak Y-directional moment of the neck of the passenger middle-row dummy was 77 N m at 1.72 s; the peak Y-directional moment of the neck of the rear side-facing dummy was -43 N m at 1.75 s.

The peak of the forward bend of the neck of the passenger rear seat dummy occurred at 1.1–1.2 s, which was 41.8 N m, when the head hit the roof of the car, forcing the neck of the dummy to bend forward. The peak backward bend occurred at about 1.75 s, 43 N m, when the dummy hit the back of the seat and the torso movement was restrained, and the head continued to be thrown backward, causing

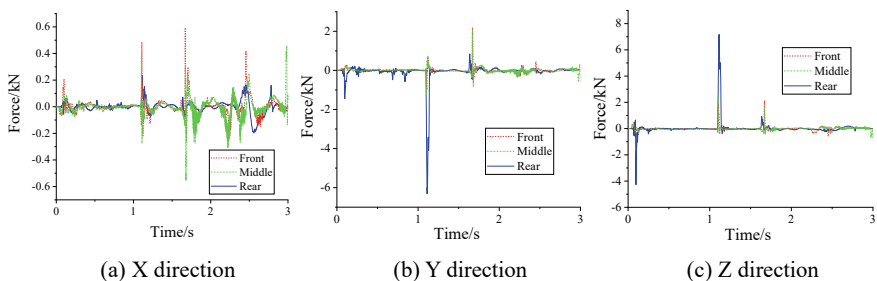
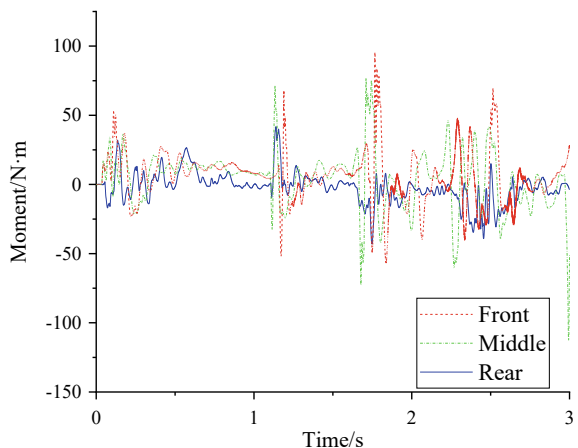


**Fig. 7** Occupant upper neck forces. By author

**Fig. 8** Occupant Y-directional neck moment.  
By author



the neck to bend backward. The peak forward and backward bending of the neck of the passenger seat and passenger middle-row dummy both occurred at about 1.7 s, when the vehicle flipped and the dummy's head impacted with the roof of the car.

#### 4.3 Analysis of Chest Injury

The main index of chest injury is chest compression. The standard of FMVSS 208 is that the chest compression amount does not exceed 76 mm.

As shown in Fig. 9 [by author] for the dummy chest compression, the peak chest compression for the passenger-side dummy was -5 mm for 1.7 s; the peak chest compression for the passenger rear dummy was 6.7 mm for 1.7 s; and the peak chest compression for the rear lateral dummy was 5.66 mm for 0.25 s.

#### 4.4 Analysis of Leg Injury

As shown in Fig. 10 [by author], the peak left leg force of the passenger-side front-row dummy was 562 N at 1.13 s and the peak right leg force was 578 N at 1.13 s; the peak left leg force of the passenger-side middle-row dummy was 1090 N at 1.13 s and the peak right leg force was 678 N at 1.13 s; the peak left leg force of the passenger-side rear-row dummy was 763 N at 1.15 s and the peak right leg force was 788 N at 1.13 s. During the late rollover period, the middle-row dummy's leg impacted with the front seat and the axial leg force peaked at 1036 N at 2.98 s for the left leg and -917 N at 2.97 s for the right leg.

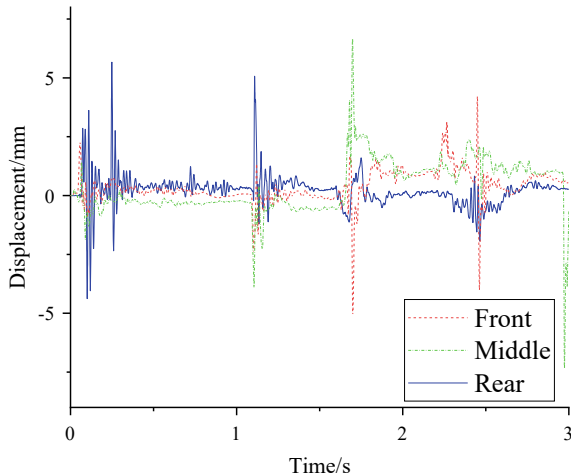


**Fig. 9** Occupant chest compression. By author

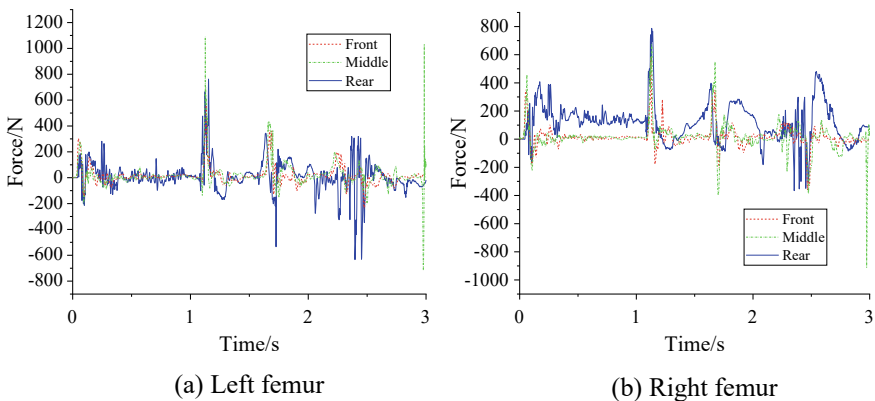


**Fig. 10** Rear lateral occupant femur forces. By author

## 5 Summary

- (1) The injury curves for same-side occupants follow the same trend, with peaks mainly concentrated at the moment when the vehicle's motion changes, with the right side of the roof being the most dangerous when it first hits the ground.
- (2) The difference in injury between left-facing and forward-facing occupants was in the head and chest, with the peak injury occurring earlier for left-facing occupants.

- (3) Rear occupant neck axial forces exceeded the standard, with the peak occurring when the vehicle was inverted. Due to the large body stiffness, the rear occupant position has little head space and the restraint system (two-point seat belt) has insufficient restraint capacity, which is typical of downward injury.
- (4) To improve the safety of rear occupants, the focus should be on restraint system improvements. Because of the tires under the occupants, it is difficult to increase headroom.

## References

1. Dobbertin KM, Freeman MD, Lambert WE et al (2013) The relationship between vehicle roof crush and head, neck and spine injury in rollover crashes. *Accid Anal Prev* 58:46–52
2. Bidez MW, Cochran JE, King D et al (2007) Occupant dynamics in rollover crashes: influence of roof deformation and seat belt performance on probable spinal column injury. *Ann Biomed Eng* 35(11):1973–1988
3. Seyed M, Jung S, Wekezer J et al (2020) Rollover crashworthiness analyses—An overview and state of the art. *Int J Crashworthiness* 25(3):328–350
4. Tiao-qí FU, Xian-Hui W, Ming Z et al (2019) Research on collaborative motion simulation environment for vehicle rollover. *Trans Beijing Inst Technol* 39(09):912–917+990. (in Chinese)
5. Wang S-D, Sun X-W, Fu T-Q et al (2019) The posture and damage evaluation of a occupant in military rolling. *Sci Technol Eng* 19(3):384–390. (in Chinese)
6. Ding R-Y, Zhou Y-B, Zhang M et al (2021) Research on protective performance of anti-shock seats in multiple working condition. *J Ordnance Equip Eng* (08):198–206. (in Chinese)
7. Hu Y-Z, Zhang B-Q, Xie S-G (2011) Vehicle safety simulation and analysis based on LS-DYNA and hyper sorks. Tsinghua University Press, Beijing, pp 68–69. (in Chinese)
8. FMVSS 208. 49 CFR Part 571—Federal Motor Vehicle Safety Standards No. 208 Occupant Crash Protection
9. SAE International std J211-1 (2003) Instrumentation for impact test-part 1-electronic instrumentation. *Soc Automot Eng*

# Study on the Failure Mechanism and Reliability of Silicon Aluminum Alloy Under Impact Loading



Dan Li, Qiongjiao Wang, Feng Dong, Sheng Wang, and Yun Bai

**Abstract** To reveal the failure mechanism of Al50Si silicon aluminum alloy under impact loading, MCM modules, and a crystal-integrated receiver/inverter were used as the research object, the pendulum-type shock response spectrum test bench was used to conduct a large number of impact loads test of 1600 g, and the fractured samples were examined by scanning electron microscopy (SEM). The results show that the Al50Si silicon aluminum alloy exhibits direct brittle fracture characteristics under a large impact loads; in order to realize the vibration impact protection of Al50Si silicon aluminum alloy, numerical simulation of the structure with impact loads was carried out using response spectrum analysis and wavelet synthesis time domain method, and the simulation method is highly accurate, with a maximum error of 2.3% compared to the experimental results. The product design has been optimized according to numerical simulation results and verified by 1600 and 2000 g impact tests, which can effectively improve the reliability of the product against large impact levels.

**Keywords** Silicon aluminum alloy · Impact loads · Structural optimization · Impact resistance reliability

## 1 Introduction

The explosive unlocking of the connecting wraps between the spacecraft and the launch vehicle, as well as the explosive unlocking of the pyrotechnics carried by the device itself, can create a severe shock environment for the device. Shock loads are characterized by short duration transients, high frequencies and high magnitudes [1, 2], which can cause damage to components containing sensitive devices (e.g., relays, crystals, microelectronic chips, etc.) as well as brittle materials [3, 4]. The ability of

---

D. Li (✉) · Q. Wang · F. Dong · S. Wang · Y. Bai  
China Academy of Space Technology (Xi'an), Xi'an 710000, Shaanxi, China  
e-mail: [lidan.tangtang@163.com](mailto:lidan.tangtang@163.com)

**Table 1** Al50Si chemical composition

Element	Si	Fe	Zn	Ca	Sn	Pb	Al
Value	49.7	0.16	0.018	0.01	0.009	0.007	All left

spacecraft components to withstand high magnitude impact loads therefore needs to be fully analyzed and evaluated prior to spacecraft launch [5].

The silicon aluminum alloy has the advantages of lower thermal expansion coefficient, higher thermal conductivity, lower density, etc. [6], and is widely used as packaging material for MCM modules. At present, the research on silicon aluminum mainly focuses on the process performance of material preparation, welding, processing, etc. [7, 8]. But there is less research on the failure mechanism of silicon aluminum alloy, especially the resistance, and there is a lack of relevant theoretical research and engineering in design.

In this paper, MCM modules and a crystal-integrated receiver/inverter with Al50Si as the base material is used as an example. The pendulum-type impact tests of 1600 and 2000 g, and the fractured samples are examined by SEM. The combined experimental-numerical simulation method was used to analyze its structural response in the shock environment, and the model was used to predict the impact resistance design, effectively achieve resistance to large number of levels of shock loads, providing theoretical support and engineering experience for the reliability design of Al50Si in the spacecraft vibration shock environment.

## 2 Materials and Methods

### 2.1 Test Material

The chemical composition of Al50Si aluminum–silicon alloy is shown in Table 1; the microstructure is shown in Fig. 1, and the average diameter of silicon particles is less than 20  $\mu\text{m}$ . Table 2 shows the mechanical property parameters of Al50Si alloy.

### 2.2 Equipment Overview

Figure 2 is a three-dimensional model of a frequency converter. The device was impact tested on a pendulum-type impact response spectrum test rig, model SP-840 MI-8008, and the response spectrum curve was collected by affixing an acceleration sensor; the fracture sample was examined by SEM; and the device was simulated numerically using the response spectrum analysis method and wavelet synthesis time domain method. Table 2 is the material parameters for each component.

**Fig. 1** Al50Si  
microstructure

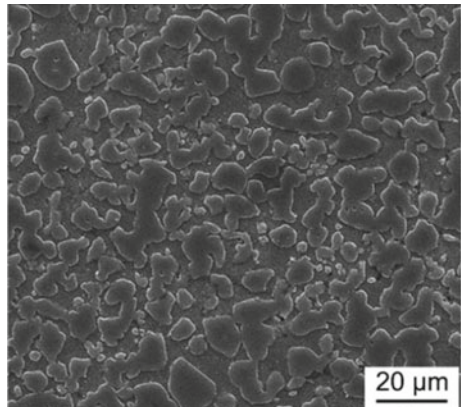
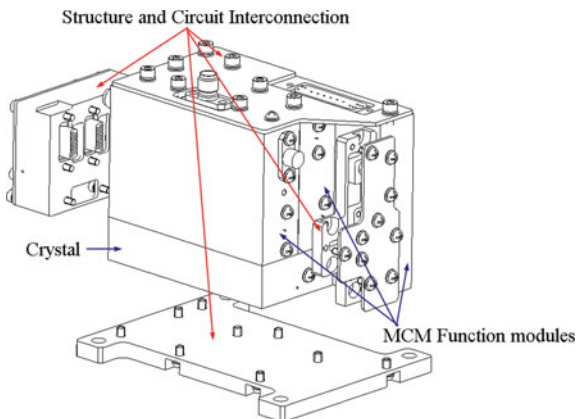


**Table 2** Material parameters for each component

Components	Material	E (MPa)	$\mu$	$\rho$ (kg/m <sup>3</sup> )	$\sigma_{0.2}$ (MPa)
MCM	Al50Si	110,000	0.3	2500	125
Partially connected	4J33	139,000	0.3	8290	343
Remaining interconnections	2A12	71,000	0.3	2700	245

**Fig. 2** A kind of frequency converter

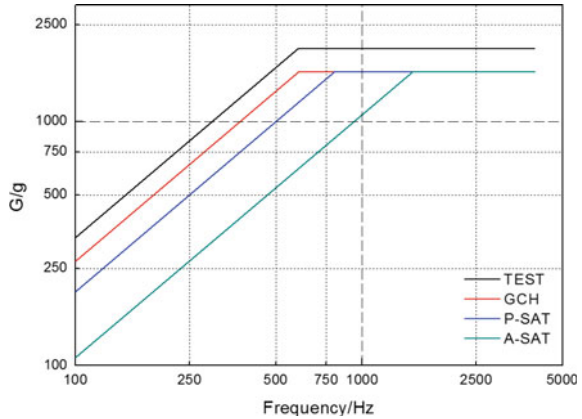


### 3 Results and Discussion

#### 3.1 Impact Tests and Numerical Simulations

Impact testing of spacecraft components is generally performed according to the impact test specification conditions [5]. As rocket thrust increases, the impact magnitude becomes larger and the severity of the impact is discerned by the maximum

**Fig. 3** Comparison of impact conditions



acceleration magnitude of the impact response spectrum for the device. Figure 3 shows a comparison of impact conditions as a frequency domain curve. In order to obtain the acceleration response of the device on the time course, the shock analysis conditions in the form of frequency domain are converted into the form of time domain, Fig. 4 shows the 1600 g time domain curve. Figure 5 shows the time domain acceleration curve at the accelerometer position, and Fig. 6 shows the numerical simulation curve at the same position, comparing the maximum acceleration and the time of maximum acceleration, the maximum relative error is 2.3%, which is a good match. Figure 7 shows the stress distribution of the structure, the maximum stress is 300 MPa, the safety margin is  $-0.72$ , the safety margin (MS) is a parameter to judge the reliability of the material, its calculation formula is shown in Eq. 1,  $\sigma$  is the yield strength of the material,  $\sigma_{\max}$  is the maximum response stress,  $f$  is the safety factor, the safety margin requirement is  $>0$ , the analysis results show that the reliability requirements are not met, the test result is the structure fracture failure. This further shows that the numerical simulation is highly accurate and the wavelet synthesis time domain method can be effective for impact load prediction (Table 3).

$$MS = \frac{\sigma}{\sigma_{\max} \times f} - 1 \quad (1)$$

### 3.2 Fracture Failure Analysis

Figure 8 shows the cracks at the bottom of the power MCM box after the 1600 g impact test. The SEM photo of the crack is shown in Fig. 9. The overall fracture morphology shows a “river pattern.” The flow direction of crack propagation, which is consistent with the cleavage fracture feature. The fracture is at the thread, indicating

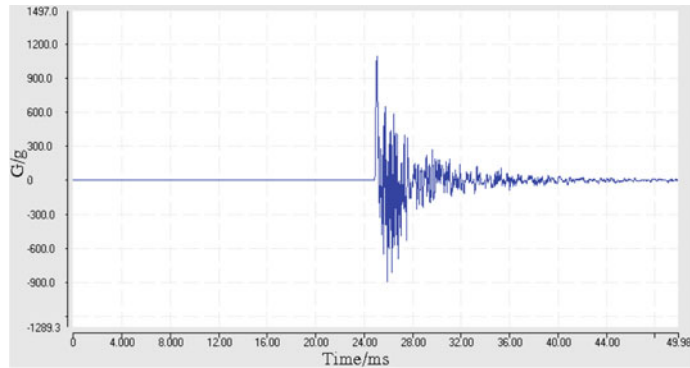


**Fig. 4** 1600 g time domain curve

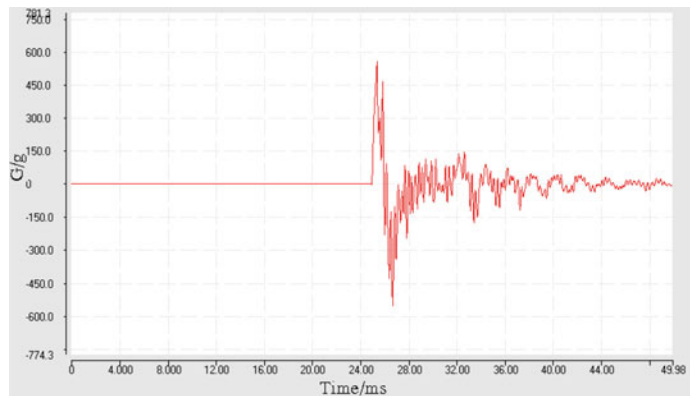


**Fig. 5** Test time domain acceleration curves 25 ms, 580 g

**Fig. 6** Numerical simulation curve 25 ms, 567 g

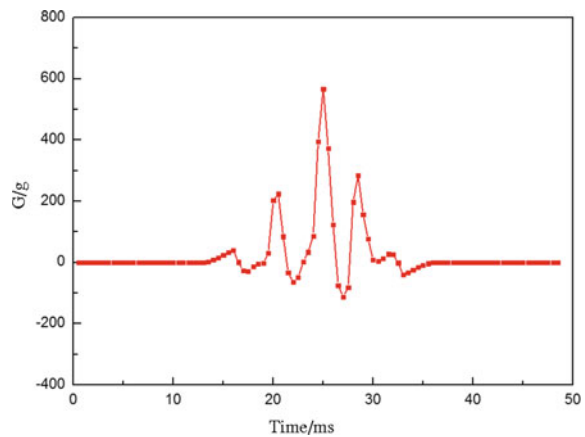


**Fig. 7** Equipment stress distribution diagram

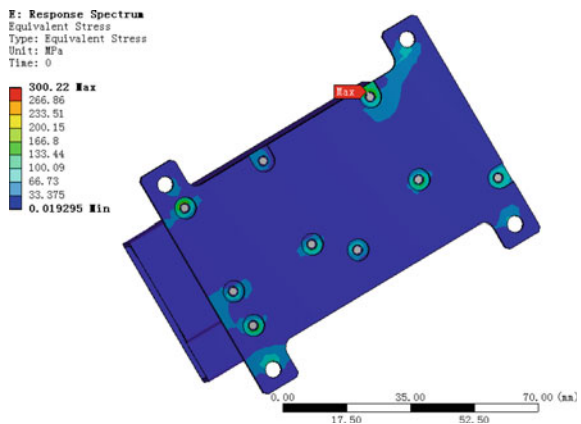


**Table 3** Comparison of experimental-numerical simulation results

	Maximum acceleration (g)	Occurrence time (ms)	MS
Numerical simulation results	567	25	-0.72
Test results	580	25	Fracture
Relative error	2.3%	0.0%	/

**Fig. 8** The damaged location after the impact test



that the stress generated in the device impact test exceeds the strength limit of the Al50Si material at the thread, resulting in a brittle fracture.

### 3.3 Structure Optimization and Validation

Analysis of the test results yielded the following reasons for the failure of the Al50Si material.

- (1) The 1600 g impact conditions exceeded the tolerance of the product.

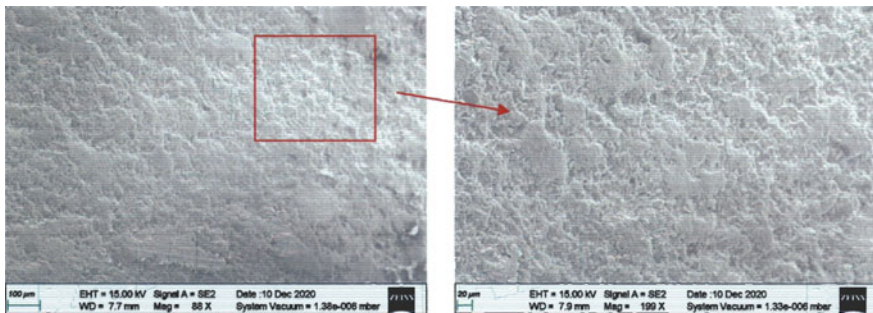


**Fig. 9** SEM photograph of the cracked area

- (2) Too few fastening screws between device and satellite deck, resulting in excessive stress at the mounting points of the Al50Si material, which does not fully guarantee the stiffness of the whole product.

According to the numerical simulation results to optimize the design of the device, combined with the above failure causes optimized structure improvement model is shown in Fig. 10. Optimized numerical simulation results are shown in Fig. 11, the maximum stress under impact load is 52 MPa, and the safety margin is 0.6, to meet the reliability requirements.

The design of the verification structural parts was tested and verified for the above optimized structure. The real module is used for the MCM3 module, and the depth of the screw holes of all silicon aluminum alloy materials is guaranteed to be the same as the actual stand-alone machine (Table 4).

The product passed the 1600 g impact test without any abnormality after the test. The impact conditions were increased to 2000 g, and after the test, there was no abnormality in the parameters of the verification part and no abnormality in the MCM3 module, which proved that the improvement measures are feasible and effective and can improve the mechanical reliability of the product against strong impact.

**Fig. 10** Improved module

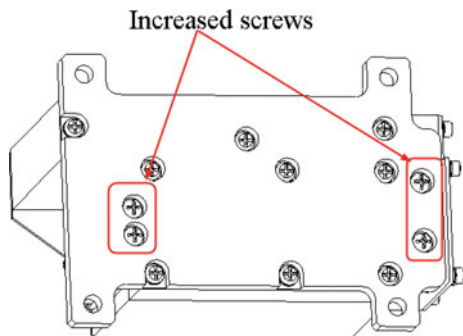


**Fig. 11** Improved impact stress distribution cloud diagram

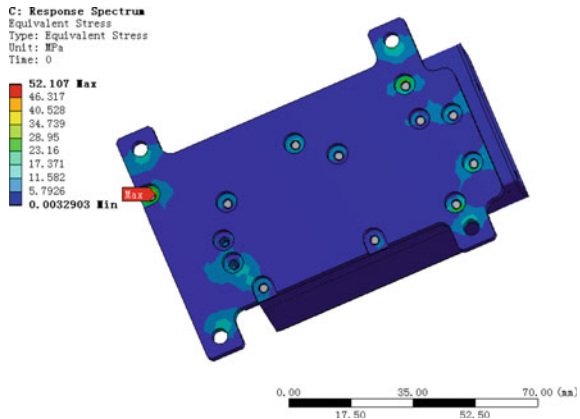


**Table 4** Comparison of verification materials with product materials

		Product	Test
MCM1	Material	Al50Si	Al50Si
	Weight	100 g	100 g
MCM2	Material	Al50Si	Al50Si
	Weight	100 g	100 g
MCM3	MCM	M-DY	M-DY
Crystals	Material	2A12	2A12
	Weight	40 g	40 g
Connected	Material	4J33	4J33
	Weight	24 g	28 g
Remaining interconnections	Material	2A12	2A12
	Weight	24 g	28 g

## 4 Conclusion

- (1) Al50Si silicon aluminum alloy exhibits direct brittle fracture characteristics under an impact load of 1600 g.
- (2) Numerical simulation of spacecraft device using response spectrum analysis and wavelet synthesis time domain method for 1600 g massive level impact mechanical environment with high accuracy and reliable and accurate results.
- (3) Reducing the stress concentration at the installation of Al50Si silicon aluminum alloy can significantly improve the impact reliability of spacecraft devices.

## References

1. Ding JF, Zhao X, Han ZY (2014) research development of spacecraft pyroshock technique. *J Astronaut* 35(12):1339–1349
2. Ma YJ, Li YL (2007) Advances in simulation techniques of pyroshock environments. *Missile Space Veh* 4:37–44
3. Zhang H, Liu TX, Li CJ et al (2014) Numerical simulation of pyrotechnic shock environment concerning pyroshock separation nut of spacecraft. *Spacecr Environ Eng* 31(4):363–368
4. Zhang JH (2005) Reviews on pyroshock environment of aerospace equipment. *Missile Space Veh* 3:30–36
5. Yang XF, Zou YQ, Deng WH et al (2017) An approach to evaluate high level shock for aerospace units. *J Astronaut* 8:872–878
6. Barooah RK, Arif AFM, Paiva JM et al (2020) Wear of form taps in threading of Al–Si alloy parts: mechanism and measurements. *Wear* 442–443(C):203153–203153
7. Kuz'min MP, Yu M, Kuz'mina PB, Kuz'min (2020) Possibilities and prospects for producing silumins with different silicon contents using amorphous microsilica. *Trans Nonferrous Metals Soc China* 30(5):1406–1418
8. Zhang SZ, Niu QL, Li S et al (2020) Research progress on the formation mechanism of Silicon–Aluminum alloy surface defects and optimization of processing technology. *Aerospace Mater Technol* 51(1):10–15

# Analysis of Prefabricated Fragment Intrusion Damage Based on Complete Restart Technique



Jiazhi Liu, Yunbo Zhou, Ming Zhang, Jianing Bai, and Wangang Xiao

**Abstract** To study the damage to the target plate under the combined action of shock wave and fragment, using the complete restart technique to extract the damage of the target plate after the action of the shock wave, and then a single fragment penetrating target plate is simulated. The Arbitrary Lagrange-Euler (ALE) algorithm and Particle Blast Method (PBM) algorithm are used to analyze the damage to the target plate by prefabricated fragments after the explosion and compare with the test to verify the feasibility of the PBM algorithm. Completely restart the target plate under the action of the shock wave generated by PBM algorithm. The Ls-dyna software is used to simulate the fragment penetration into the target plate, so as to obtain the damage of the target plate under different incidence angles. The simulation results show that the combined action of shock wave and fragment has a strong penetration ability; the end penetration capability of cylindrical fragment is greater than that of lateral penetration; the fragment penetration ability is the strongest at vertical incidence.

**Keywords** Prefabricated fragment · Complete restart · Penetration damage · Combined action · Different angles

## 1 Introduction

The explosion of the fragmentation warhead produces shock wave and a large amount of high-speed fragments, which carry enough kinetic energy to penetrate various targets and cause serious damage. Duan [1] simulated the destruction of type I sandwich panel under the combined action of shock wave and fragments. Wu [2] conducted numerical simulation analysis of the combined action of high-speed fragments and shock wave on steel plates, and the results all showed that the damage of the structure under the combined action of high-speed fragments and shock wave was

---

J. Liu · Y. Zhou (✉) · M. Zhang · J. Bai · W. Xiao

School of Mechanical Engineering, Nanjing University of Science and Technique,  
Jiangsu 210094, China

e-mail: [yunbo31983@163.com](mailto:yunbo31983@163.com)

much greater than the two alone. Domestic and foreign scholars have also carried out relevant studies on the penetration of prefabricated fragment. Jia [3] performed penetration simulations on fragment of different materials and showed that tungsten alloy fragments are more suitable as fragmentation warhead. Wang [4] studied prefabricated fragment obliquely penetrating a circular tube and showed that the critical penetration velocity is related to the angle of incidence. The current prefabricated fragment penetration analysis is only for target structures that have not undergone shock wave action, and no one has studied fragment penetrating the target plate after shock wave action.

In this paper, the feasibility of the PBM algorithm is verified by comparative analysis based on a fragment explosion test. A complete restart of the target plate after the shock wave action is performed. The Ls-dyna software is used to simulate the fragment to penetrate the target plate and obtain the damage of the fragment to the target plate at different incidence angles.

## 2 Theoretical Studies

### 2.1 Particle Blast Method (PBM) Theory

The particle blast method (PBM) is an improvement of the particle method based on molecular dynamics theory, in which the kinetic energy of individual particles no longer remains conserved, but for the whole system, the kinetic energy of the particles satisfies the statistical equilibrium law when the system reaches the equilibrium state [5]. Figure 1 depicts the interaction between the particles, and the two-particle interaction distance is defined by  $d_{\text{int}}$

$$d_{\text{int}} = (r_1 + r_2) - |x_1 - x_2| \quad (1)$$

where  $x_n$  is the coordinate vector of the center of the sphere;  $r_n$  is the radius of the spherical particle.

**Fig. 1** Schematic diagram of interaction between particles

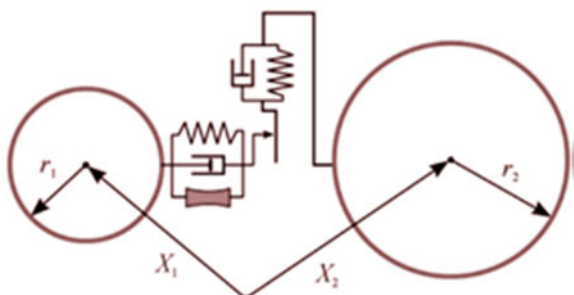


**Fig. 2** Test bench

## 2.2 Complete Restart Technique

The complete restart technique is a technique used when the original k-file is to be modified significantly, such as by adding additional PARTs or contact definitions. This is actually a completely new analysis, except that the deformation and stresses of the PARTs related to the previous analysis are taken into account, and these deformation and stresses are transferred by the keyword \*STRESS\_INITIALIZATION\_OPTION.

## 3 PBM Algorithm Validation

### 3.1 Steel Plate Bench Test

In order to verify the feasibility of the PBM algorithm, a fragments explosion test was conducted (Fig. 2). The test bench was surrounded by high-strength steel plates, and the size of high-strength steel plates was  $1000 \times 500 \times 6$  mm. The yield strength of high-strength steel was 1310 MPa. The test explosive was 550 g, cylindrical TNT charge, height to diameter ratio of 1.54, TNT diameter of 65 mm, 100 mm high, surrounded by prefabricated fragments, as shown in Fig. 3, the explosive was located in the center of the test bench, the detonation point was the center of the upper surface of the cylinder. The damage to the steel plate after the test was shown in Fig. 4.

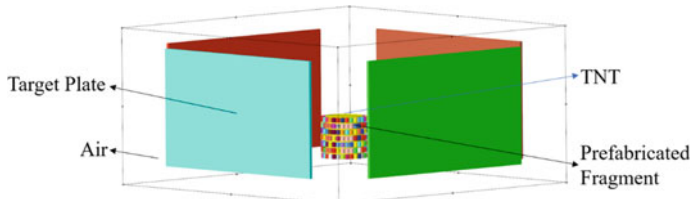
### 3.2 Simulated Analysis

ALE algorithm is used to establish finite element models of air, explosive, fragments, and target plates, as shown in Fig. 5. The Euler algorithm is used for explosive and air. The fragments and the target plate adopt Lagrange algorithm. Through

**Fig. 3** Explosive**Fig. 4** Steel plate damage

the keyword \*CONSTRAINED\_LAGRANGE\_IN\_SOLID to complete the coupling of Lagrange grid and Eulerian grid, and the keyword \*CONTACT\_ERODING\_SINGLE\_SURFACE to complete the erosion contact between prefabricated fragments and target plates, using the initial volume method to define the shape and position of the TNT. The explosive, fragments, and target plates are contained in the air domain, and the keyword \*BOUNDARY\_NON\_REFLECTION is used to set a non-reflective boundary around the air domain.

The explosive adopts \*MAT\_HIGH\_EXPLOSIVE\_BURN material ontology model [6], as shown in Table 1; the air adopts \*MAT\_NULL material ontology model [7], as shown in Table 2; the target plates material is selected as 6252 steel,

**Fig. 5** ALE algorithm simulation model

and the Johnson\_Cook ontology model [7] is selected, as shown in Table 3; the tungsten alloy fragments were treated as rigid bodies [8] with a density of 17,800 kg · m<sup>3</sup>, an elastic modulus of 357 GPa, and a Poisson's ratio of 0.303.

The simulation model of explosive particle, air particle, target plates, and fragments are established by PBM algorithm, as shown in Fig. 6. The range of air domain is defined by \*DEFINE\_PBLAST\_AIRGEO, and the geometry of explosive is established by \*DEFINE\_PBLAST\_GEOMETRY. The erosion contact between the fragments and the target plates is completed by the keyword \*CONTACT\_ERODING\_SINGLE\_SURFACE. The keyword \*PARTICLE\_BLAST is used to define the interaction mode between Lagrange grid and explosive particles. The ratio of explosive particles to air particles is 1:10. Define the density, internal energy, explosion speed, and other parameters of explosives, as shown in Table 4. Set the position of initiation point and initiation time and define the area of explosion action.

The stress clouds of the steel plates at  $t = 5$  ms for both algorithms are shown in Fig. 7, where the maximum stress of the steel plate is 1005 MPa in the ALE algorithm and 920 MPa in the PBM algorithm. The experimental damage results are consistent with the simulation results, which prove the feasibility of the PBM algorithm.

**Table 1** Explosive material parameters and state equation coefficients

P/GPa	$D/(m \cdot s^{-1})$	$\rho/(kg \cdot m^{-3})$	A/GPa	B/GPa	R <sub>1</sub>	R <sub>2</sub>	$\omega$	$E_0/(kJ \cdot m^{-3})$	V
21	6930	1630	373.77	3.734	4.15	0.9	0.35	6000	1.0

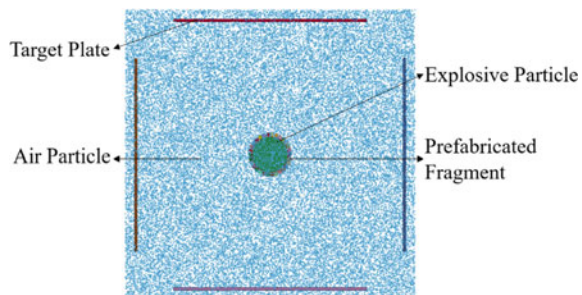
**Table 2** Air material parameters and state equation coefficients

$\rho/(kg \cdot m^{-3})$	C <sub>0</sub> /MPa	C <sub>1</sub> = C <sub>2</sub> = C <sub>3</sub> = C <sub>6</sub>	C <sub>4</sub> = C <sub>5</sub>	$E_0/(kJ \cdot m^{-3})$
1.23	-0.1	0	0.4	253

**Table 3** Material parameters of 6252 steel

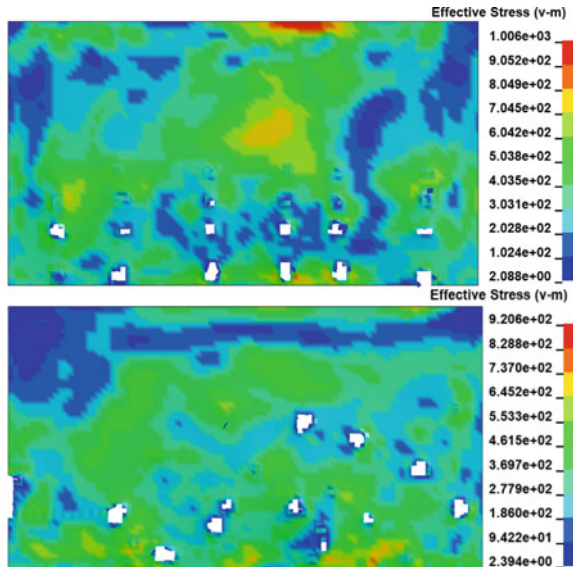
$\rho/(kg \cdot m^{-3})$	A/MPa	B/MPa	c	N
7850	1310	500	0.02	0.86

**Fig. 6** PBM algorithm simulation model



**Table 4** Explosive material parameters

$\rho /(\text{kg} \cdot \text{m}^{-3})$	$E_0 /(\text{kJ} \cdot \text{m}^{-3})$	$\gamma$	$b$	$D /(\text{m} \cdot \text{s}^{-1})$
1630	7000	1.3	0.6	6930

**Fig. 7** Steel plates von Mises stress diagrams

The simulation animations of the two algorithms in the range of 0.1–5 ms are shown in Fig. 8. The fragments dispersion in the ALE algorithm are relatively uniform, while the fragments dispersion in the PBM algorithm is more random. Figure 9 shows the curves of the energy of the steel plates under the two algorithms, including the kinetic energy of the steel plates and the absorbed internal energy, the trend of the energy of the steel plates under the two algorithms and the maximum value are close. Figures 10 and 11 show the velocity distribution curve of partial fragments, from which it can be seen that the fragments velocity of PBM algorithm is higher than that of ALE algorithm, and the fragments velocity curves of the two algorithms are basically consistent. The calculation time of PBM algorithm is only 5% of ALE algorithm, so PBM algorithm is more efficient. The simulation comparison of the two algorithms is shown in Fig. 5. The residual velocity of fragments in PBM algorithm is larger, and its penetration performance can be estimated more conservatively. Therefore, PBM algorithm has certain accuracy in the explosion simulation of fragments (Table 5).

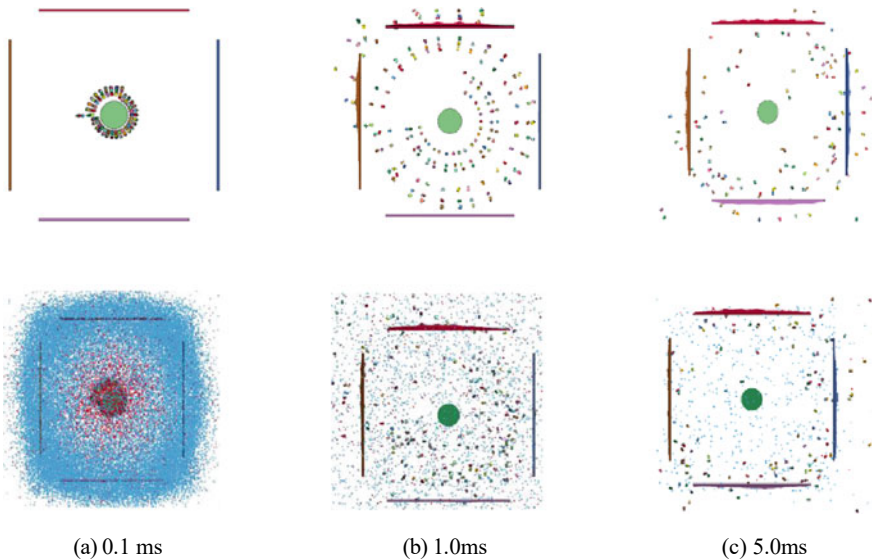


**Fig. 8** Simulation comparison between ALE algorithm (top) and PBM algorithm (bottom)

**Fig. 9** Steel plate energy curves in two algorithms

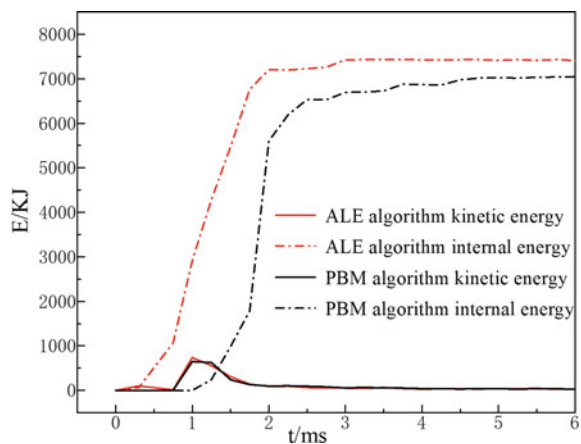


**Fig. 10** ALE algorithm speed curve

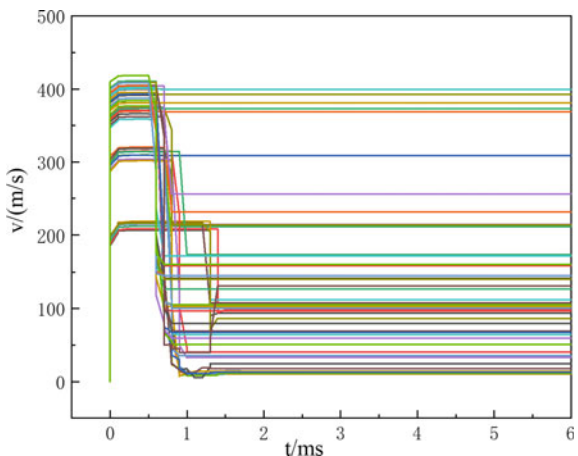


**Fig. 11** PBM algorithm speed curve

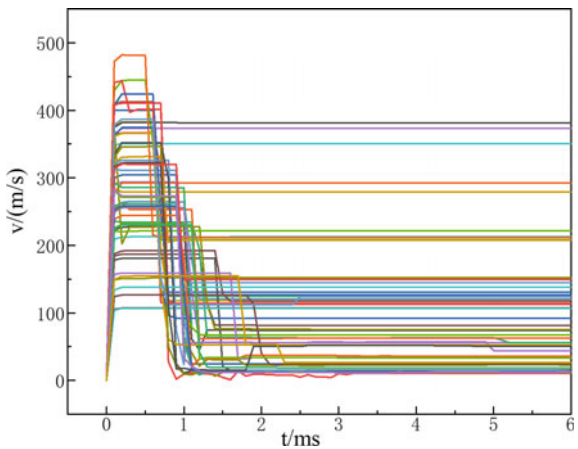


**Table 5** Simulation comparison of the two algorithms

Algorithm	Maximum stress (MPa)	Maximum internal energy (kJ)	Maximum kinetic energy (kJ)	Maximum speed(m/s)	Calculation time (s)
PBM	920	7093.7	647.1	482.1	8640
ALE	1002	7455.5	738.2	418.5	172,800

## 4 Analysis of Fragment Penetration Damage

The damage caused by the shock wave to the target plate in the above PBM algorithm was extracted using the complete restart technique, as shown in Fig. 12. The steel plate without shock wave action and steel plate after shock wave action are analyzed for penetration damage. The end-face and lateral penetration of cylindrical fragments at different incident angles ( $0^\circ$ ,  $15^\circ$ ,  $30^\circ$ ,  $45^\circ$ , and  $60^\circ$ ) are carried out to analyze the residual velocity and damage of the steel plate. The average velocity of 300 m/s calculated by the above PBM algorithm is chosen as the initial velocity for the penetration analysis.

### 4.1 End-Face Penetration Analysis of Fragments

The penetration damage caused by the end-face penetration of the steel plate at the same initial velocity and different incident angles are shown in Fig. 13. As the incidence angle increases gradually, the damage diameter caused by the fragment to the steel plate becomes larger and larger. When the fragment penetrated into the steel plate at an incident angle of  $60^\circ$ , the fragment ricochet phenomenon occurred. The stress under the combined action of the fragment and shock wave is greater than that when the fragment penetrates the steel plate alone, and the residual velocity of the fragment under the combined action is greater than that without the action of shock wave, as shown in Fig. 14.

### 4.2 Lateral Penetration Analysis of Fragments

The damage caused by the lateral penetration of the fragment into the steel plate at the same initial velocity and different incident angles is shown in Fig. 15. With the increase of incident angle, the damage diameter caused by the fragment to the steel plate becomes larger and larger. When the fragment penetrated into the steel plate at an incident angle of  $60^\circ$ , no penetration occurred, and the fragment ricochet phenomenon occurred. The remaining velocity is shown in Fig. 16.



**Fig. 12** Schematic diagram of steel plate deformation

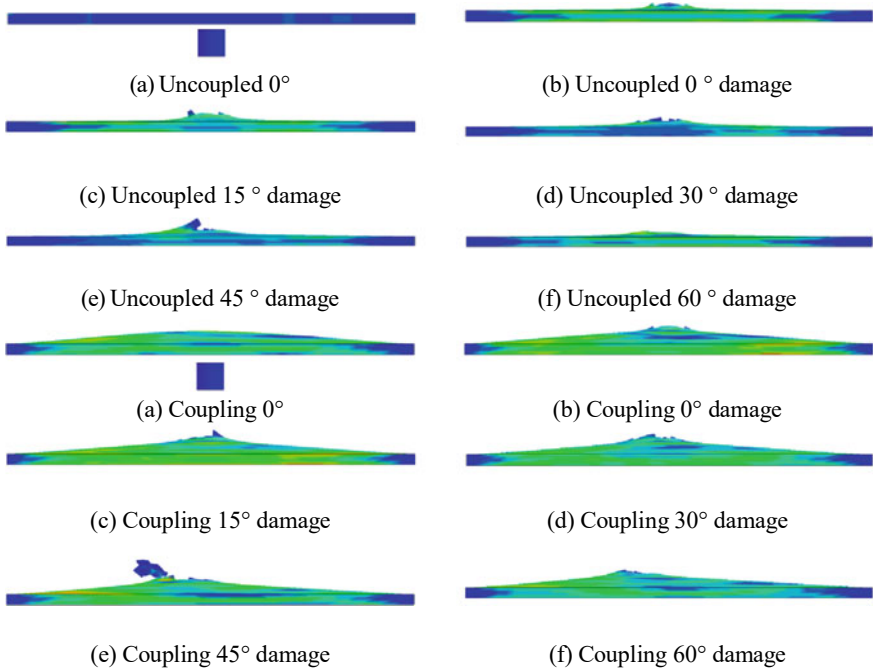


**Fig. 13** Comparative analysis of steel plate damage

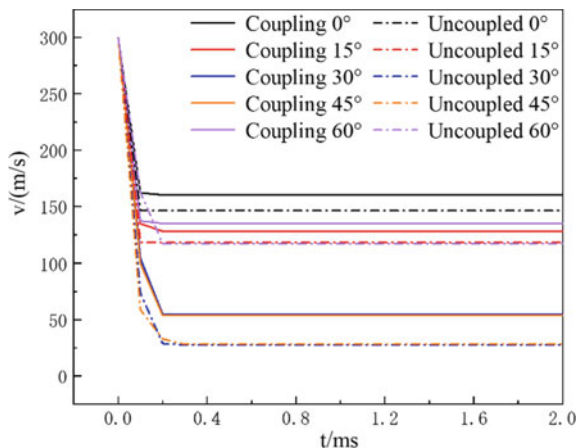


**Fig. 14** Comparison of fragment velocity curve under different incident angles in the case of end-face penetration

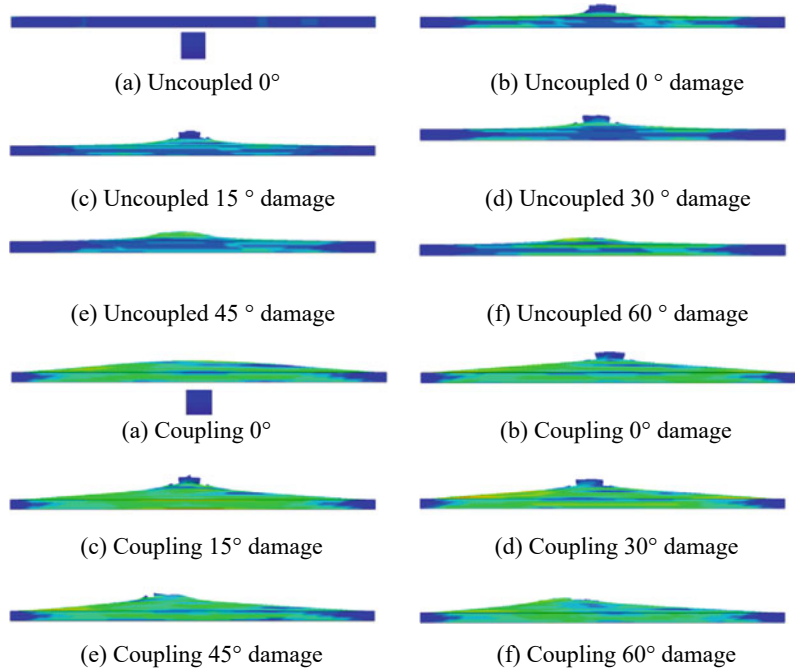
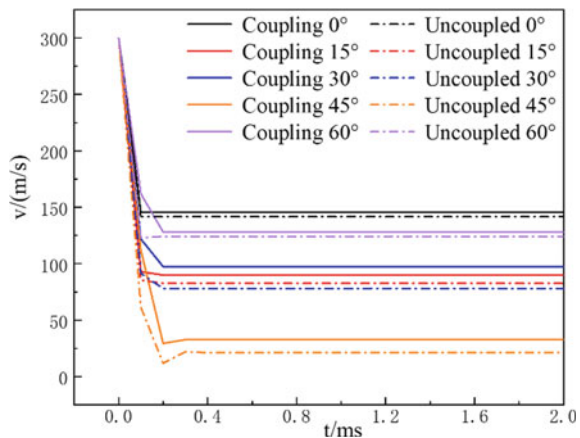


**Fig. 15** Comparative analysis of steel plate damage

**Fig. 16** Comparison of fragment velocity curve under different incident angles in the case of lateral penetration



## 5 Conclusion

- (1) This paper uses the PBM algorithm and the ALE algorithm to simulate a fragments explosion test, and the two algorithms are compared and analyzed, and then compared with the experimental results to verify the feasibility of PBM algorithm in analyzing fragment problems.
- (2) The complete restart technique is used to compare the effects of fragment alone and the combined effects of shock wave and fragment. Under the combined action of fragment and shock wave, the protection ability of steel plate decreases and the penetration ability of fragment is strong, so the attenuation effect of fragment on the velocity decreases. Therefore, the residual velocity of fragment under the combined action is smaller than that without the combined action, and the subsequent killing ability of fragment is strong.
- (3) The end-face penetration capacity of cylindrical fragment is greater than that of lateral penetration, and the damage to the steel plate is correspondingly larger. Meanwhile, the residual velocity of fragment is also larger than that of lateral penetration.
- (4) The penetration capacity of the fragment is the strongest at  $0^\circ$  vertical incidence of the steel plate. The ricochet phenomenon occurs when the fragment penetrates the steel plate at an incidence angle of  $60^\circ$ .

## References

1. Duan X, Cheng Y, Zhang P et al (2015) Numerical analysis of the damage on I-core sandwich panels subjected to combined blast and fragment loading. Chin J Ship Res. 10(6):45–59
2. Wu G, Wang X, Ji C et al (2021) Numerical simulation analysis of combined action of high-speed fragment and explosion shock wave on steel plate. Initiat Explos Devices 3:24–28
3. Jia X (2021) Simulation of fragments of different materials penetrating into air targets. Mechanical engineering and automation, pp 82–84
4. Wang Y, Li W, Zhu G et al (2019) Oblique penetration of a circular pipe target by a prefabricated fragment. Int J Struct Stab Dyn. 10(19)
5. Zhang S, Wang X, Peng B et al (2021) Numerical simulation of shock wave load based on PBM algorithm. J Ordnance Equip Eng 130–136
6. Kim SH, Chang YS, Cho YJ (2017) Parametric analyses of major nuclear components and reinforced concrete structures under FCI-induced explosive condition. Nucl Eng Des 148–158
7. Ye L, Zhou Y, Tao X et al (2021) Study on damage of honeycomb sandwich panel under the combined action of shock wave and fragment. J Ordnance Equip Eng 60–66
8. Li Y (2017) Dynamic response of corrugated hybrid sandwich plate under air blast loading. In: Huazhong University of science and technique, pp 148–158

# Flexible Thermal Invisibility Cloak with Meta-Structures: Design and Fabrication



Zhengyu Lian, Peng Lu, and Bo Li

**Abstract** Metamaterials or meta-structures are essentially a kind of artificially designed structures with certain specific physical properties or functions, which can often realize some special physical phenomena that natural materials do not possess. Thermal meta-structures can achieve some special thermal properties. Based on the transformation thermal theory and effective medium theory, this work realizes the thermal invisibility and heat flux manipulation through the integrated design of a double-layered thermal cloak meta-structure, with the flexible structural performance. The thermal simulation analysis of the thermal meta-structure was performed. The fabrication feasibility of the double-layered cloak meta-structure was studied by etching copper-clad film. Then, the thermal meta-structural properties were tested and analyzed using a self-built thermal test platform. The flexible thermal meta-structures have value in the field of human wearables and surface adaptation of geometrically complex objects.

**Keywords** Thermal invisibility cloak · Metamaterials · Thermal manipulation · Flexible structure · Design

## 1 Introduction

Manipulating thermal flow according to human desire is not always easy. According to Fourier's law, thermal energy diffuses from the high-temperature side to the low-temperature side without an external source. Nonetheless, many recent developments of metamaterials in information science have contributed to several innovative advances in thermal flow manipulation. The "metamaterial" is also called as "meta-structure". Metamaterial is essentially a kind of artificially designed structure with certain specific physical properties or functions. It can often achieve certain

---

Z. Lian · P. Lu · B. Li (✉)

School of Mechanical and Power Engineering, East China University of Science and Technology, Shanghai 200237, China

e-mail: [libo@ecust.edu.cn](mailto:libo@ecust.edu.cn)

properties or some special physical phenomena that natural materials do not have [1]. Thermal meta-structures can achieve some special thermal properties through cleverly designed and man-made structures rather than naturally occurring structures [2]. It can purposefully manipulate heat transfer parameters, such as heat transfer direction, heat flux, heat transfer speed, etc., which can provide new research and novel application directions for macroscopic thermal manipulation.

This work aims to establish the correlation between the thermal meta-structural design parameters and the corresponding thermal properties. Meanwhile, this work focuses on the preparation of flexible thermal metamaterial devices in the field of human wearable flexible devices and engineering application goals such as thermal regulation toward the surface of complex geometric objects, thereby expanding the application prospects of thermal cloak coatings, photovoltaic devices, temperature flex-sensors, human wearable flexible electronic devices, etc.

## 2 Design of Thermal Invisibility Cloak with Meta-Structures

On the basis of the coordinate transformation theory of transformation optics and the effective medium theory [3, 4], we designed a double-layered cloak thermal invisible structure. According to the theory of transformation heat, the designed thermal stealth structure is a two-dimensional planar structure. Unlike previous studies on thermal cloaks, they tend to calculate the thermal conductivity distribution of the shell with the thermal conductivity of the structural background region prespecified. Here, we use an inverse design approach that calculates the thermal conductivity of the background region with a predetermined shell structure and material. This strategy makes manufacturing easier. Based on the finite element method, we conduct a steady-state thermal simulation of the cloak thermal stealth structure. The simulated ambient temperature is room temperature (25 °C). The boundary temperature at the left end of the setting structure is 100 °C, and the boundary temperature at the right end is 0 °C. As shown in Fig. 1, the central circular space is the thermal stealth area, and the spatial range is defined as  $0 < r' < R_2$ . Before the thermal coordinate transformation, the heat flow is transmitted along a horizontal straight line both inside and outside the thermally invisible space. However, after coordinate transformation, the space of thermal stealth is transformed into two parts, namely:  $0 < r' < R_1$  region and  $R_1 < r' < R_2$  region. The heat flow is still transmitted horizontally and straightly in the outer layer of the thermal stealth space. However, after approaching the insulating layer, the heat flow bypasses the central region of  $0 < r' < R_1$  and travels along the annular region of  $R_1 < r' < R_2$ . Therefore, within the central circular space (defined as  $0 < r' < R_1$ ) of the thermally stealthy annular space, the temperature gradient is zero. It means that the transfer of heat flow from the outside has no effect on the interior area, enabling the thermal performance of the thermal cloak.

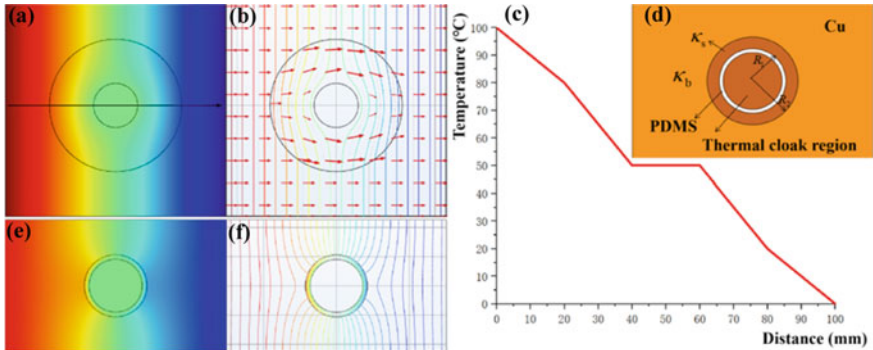


**Fig. 1** Thermal simulation results and the basic structural design of the double-layered thermal invisibility cloak: **a** surface temperature distribution; **b** heat flow and isotherm distribution; **c** temperature change curve along the direction of the central axis indicated by the black arrow; **d** schematic diagram of the basic cloak structure; **e** temperature field distribution and **f** isotherm distribution under the premise that the thermal conductivity of the background region is the same as that of the annular cloak structure (that is,  $\kappa_b = \kappa_s$ )

It can be observed from the temperature cloud map in Fig. 1 that the points in the central area of the thermal cloak structure ( $0 < r' < R_1$ ) show uniform temperature distribution and the same characteristics, and are basically kept at 50 °C. In the heat flow streamline, the streamlines of the heat flow are uniformly distributed on the substrate and remain substantially straight. The distribution density of heat flow in the outer structure region of the insulating layer ( $R_1 < r' < R_2$ ) is significantly larger than that on the substrate, and the heat flow is transmitted in an arc along the insulating layer region. In the central region ( $0 < r' < R_1$ ), there is only a very small amount of heat flow streamlines. That shows that the double-layered thermal cloak structure can effectively change the transmission direction and path of heat flow in the structure. Specifically, the heat flow transferred to the structure is changed to travel along the outer cloak region of the structure ( $R_1 < r' < R_2$ ) while bypassing the central region of the structure ( $0 < r' < R_1$ ). Therefore, the double-layer cloak structure can effectively protect the central area from the influence of external heat flow transmission. It basically does not interfere with the heat flow transmission outside the double-layer structure. This reflects the thermal characteristics of thermal stealth.

According to the theoretical calculation formula, as Function (1), [5], the designed structural parameters of  $R_1$  and  $R_2$  are 11 mm and 17 mm, and the thickness of the Polydimethylsiloxane (PDMS) insulating layer is 1.5 mm. Therefore, the required background thermal conductivity is calculated to be 161 W/m<sup>2</sup>.

$$\frac{\kappa_s}{\kappa_b} = \frac{(R_2^2 + R_1^2)}{(R_2^2 - R_1^2)} \quad (1)$$

where  $\kappa_s$  is the thermal conductivity of copper,  $\kappa_b$  is the thermal conductivity of the background region,  $R_1$  and  $R_2$  are the inner and outer radii of the shell, respectively.

Since it is very difficult for conventional materials to meet the required background thermal conductivity, we introduce the effective medium theory here to achieve the required background thermal conductivity parameters. The effective medium theory, also known as effective medium approximation theory [2]. The theory approximates the non-uniform and anisotropic material parameters using a variety of homogeneous and isotropic natural materials and arranging several materials according to some specific geometric structures. Then, according to the effective medium theory, drilling holes in the copper film and filling it with PDMS can obtain the desired background thermal conductivity. Based on the Maxwell–Garnett formula, the effective thermal conductivity is [6]:

$$\kappa_b = \kappa_{cu} \left[ 1 + \frac{2(\kappa_{PDMS} - \kappa_{cu})f}{\kappa_{PDMS} + \kappa_{cu} - (\kappa_{PDMS} - \kappa_{cu})f} \right] \quad (2)$$

where the thermal conductivity,  $\kappa_b$ , is the background thermal conductivity to be achieved through the effective medium theory. The  $\kappa_{Cu}$  is the thermal conductivity of copper, and the  $\kappa_{PDMS}$  is the thermal conductivity of PDMS. The  $f$  is the area fraction occupied by PDMS. According to the values of  $\kappa_b$ ,  $\kappa_{Cu}$ , and  $\kappa_{PDMS}$ , the area ratio,  $f$ , of PDMS in the background area was determined to be 42.06%.

In order to realize the design of the corresponding background structure, we divide the background area into square lattices with side length of 1.5 mm. Thus, we only need to design a single lattice, and then expand to the entire background region, to achieve the desired background thermal conductivity. For a single lattice, the desired thermal conductivity is achieved by filling circular holes with PDMS. Using the hole radius calculation Formula (3), the hole radius is obtained as 0.5 mm. The designed structure based on geometric parameters is shown in Fig. 2.

$$r = \sqrt{\frac{f * a^2}{\pi}} \quad (3)$$

where the  $f$  is the area fraction occupied by PDMS. The  $a$  is the side length of square lattices divided by the background region. The  $r$  is the radius of the PDMS-occupied hole. It can be seen from the temperature field, isotherm distribution, and heat flux distribution in Fig. 2 that no heat flow passes through the central stealth area of the structure after adjusting the design, and it is always maintained at 50 °C. In addition, it can be seen from the isotherm distribution that the isotherm distribution outside the thermal stealth structure is not affected. It demonstrates the performance of excellent thermal manipulation of the designed meta-structure.

Comparing Figs. 1 and 2, it can be found that although the conventional structure (Fig. 1) sets the insulating layer region to achieve constant temperature distribution in the middle region, it is obvious that the isotherm outside the structure is distorted. This

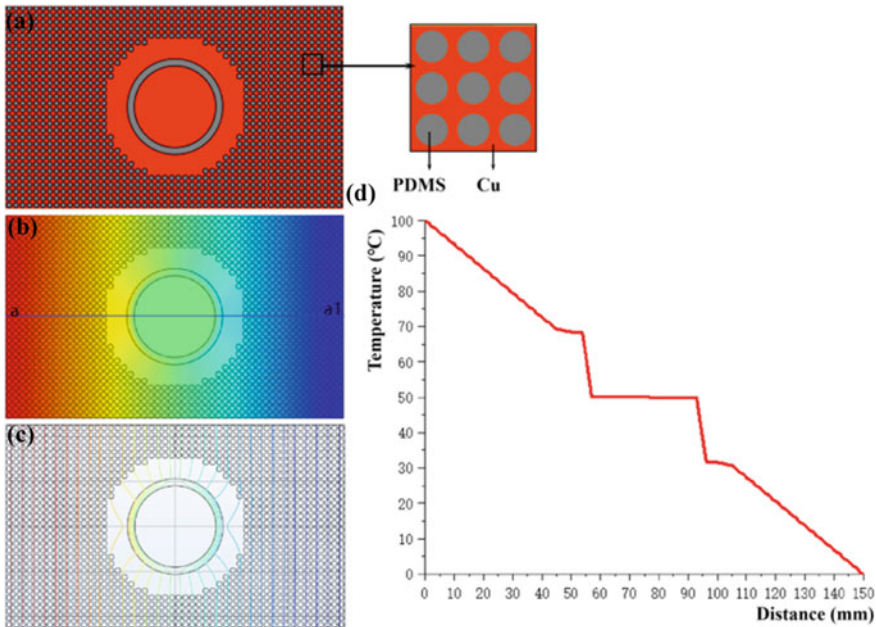


**Fig. 2** The designed double-layered thermal cloak meta-structure and its thermal simulation results: **a** schematic diagram of the structure; **b** surface temperature field distribution map; **c** surface isotherm distribution map; **d** temperature distribution along the “a—a1” line

is obviously not in line with the effect of thermal stealth. The isotherm distribution of the external area of the thermal cloak meta-structure after the improved design (Fig. 2), that is, the background area, is parallel. The natural property of parallel isotherms in the background region is not affected by the central structure.

### 3 Fabrication and Test of Flexible Thermal Invisibility Cloak

Since the designed double-layer cloak thermal stealth structure is composed of two materials, copper and PDMS, and the structure is relatively complex, we use ferric chloride to etch polyimide (PI) copper-clad film (PI thickness 25 microns, copper thickness 18 microns) to prepare Thermal stealth meta-structural specimen of a flexible double-layered cloak. The prepared samples are shown in Fig. 3. The equipment used is inkjet printer, UV light curing equipment, and heating platform.

The ferric chloride ( $\text{FeCl}_3$ ) etching preparation steps of the flexible double-layer cloak thermal stealth structure are as follows:

A layer of corrosion resist was printed by an inkjet printer, annealed at 120 °C for 20 min, and cured with UV light at a wavelength of 365 nm for 6 min. Put the copper

**Fig. 3** The fabricated flexible double-layered thermal cloak for thermal invisible performance with the designed meta-structure



film into  $\text{FeCl}_3$  etching solution to etch until the copper that needs to be filled with PDMS is completely etched away. Drop the cleaning solution (LOGI-CS01U) on the dust-free paper to wipe the surface corrosion resistance layer of the copper film until it is cleaned. PDMS filling is performed, and the PDMS solution is configured according to the mass ratio of the main agent and the hardener to 10:1. After the configuration, drop the PDMS into the pores to be filled. To reduce the convective heat transfer between the copper layer and the air, a layer of PDMS with a thickness of 1 mm was coated on the entire surface of the structure.

We use a self-built thermal test platform to conduct thermal tests on the double-layer cloak thermal stealth structure. The thermal test steps are:

Building a thermal test platform and heat the high-temperature heating platform to 100 °C.

Debugging the Compact PRO infrared thermal imager to the test state, adjust the test height to focus, and start the test when the focus is completed.

Place a section of the sample on the surface of the high-temperature platform and press it with glassware. The other section was placed in the air (20 °C). This creates a temperature gradient that allows heat transfer.

The temperature cloud images of the double-layer cloak thermal stealth structure were obtained when the thermal test was performed for 10 s, 30 s, 60 s, and 90 s, respectively, as shown in Fig. 4. It can be seen that the heat of the heating platform is gradually introduced into the sample from the part under the glass dish on the left side of the sample, and then into the thermal stealth structure of the double-layered cloak. As the thermal test progresses, the heat flow increases gradually. After the test was carried out for 90 s, the transfer of heat flow reached a steady state. The color of the temperature profile surrounding the central area of the meta-structure is essentially the same, and this area is largely free of heat intrusion. Therefore, the experimental results indicate that the modified flexible meta-structural device exhibits the thermal stealth thermal performance and thermal manipulation ability.

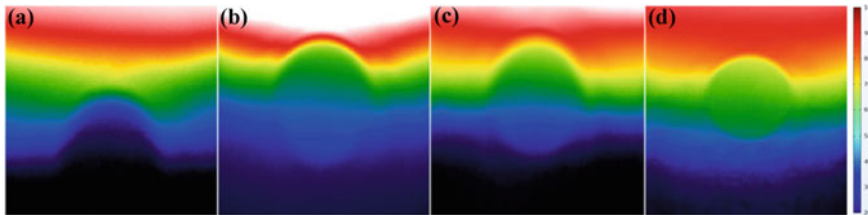


**Fig. 4** Temperature field distribution at different time nodes monitored in real time: temperature fields at **a** 10 s; **b** 30 s; **c** 60 s; **d** 90 s

## 4 Conclusion

A multi-layered annular thermal stealth structure is designed based on the theory of transformation heat. The thermal simulation of the meta-structure is carried out, and the thermal characteristics of the thermal stealth of the structure are verified. Through quantitative analysis of several regions of the meta-structure, the thermal mechanism of thermal stealth of the structure is elucidated. The fabrication and thermal testing of the structure were realized by using the form of ferric chloride etching PI copper-clad film and a self-built thermal test platform. The specific conclusions are as follows:

- (1) Based on the transformation thermal theory, the thermal stealth structure is designed as a double-layer cloak structure, and various parameters of the structure are obtained by calculation. Combined with the effective medium theory, the calculated thermal conductivity parameters of the thermal stealth structure are approximately matched by using two materials, copper and PDMS.
- (2) The thermal simulation analysis of the double-layer cloak thermal stealth structure is carried out. The simulation results of the structure are obtained under steady-state conditions, including the temperature cloud diagram and the heat flow streamline diagram. The simulation results verify the thermal stealth characteristics of the structure. Through quantitative analysis of the temperature and heat flux curves in several important regions of the structure, it was found that the heat flow transport in the double-layer cloak structure changed in direction and path relative to the heat flow transport on the substrate. That is, the transmission of heat flow in the double-layered cloak structure bypasses its central area, so that the central area is not disturbed and invaded by external heat flow.
- (3) The fabrication of double-layer cloak thermal stealth structure was realized by using the method of etching PI copper-clad film with  $\text{FeCl}_3$  and the configuration of PDMS. The thermal test was carried out on a self-built thermal test platform, and the test results were consistent with the computer simulation results. The experimental results show that ferric chloride etching PI copper-clad film can effectively realize the preparation of more complex thermal metamaterials, and it shows the effectiveness and feasibility for the flexible application potential of thermal meta-structures.

**Acknowledgements** This work is sponsored by Research Project of Shanghai Municipal Administration for Market Regulation, in China (Grant No. 2021-22), and Carbon Dioxide Peaking & Carbon Neutrality Fund from Shanghai Science and Technology Innovation Action Plan, in China (Grant No. 21DZ1207800).

## References

1. Wegener M (2013) Metamaterials beyond optics. *Science* 342(6161):939–940
2. Narayana S, Sato Y (2012) Heat flux manipulation with engineered thermal materials. *Phys Rev Lett* 108(21):214303
3. Fan CZ, Gao Y, Huang JP (2008) Shaped graded materials with an apparent negative thermal conductivity. *Appl Phys Lett* 92(25):251907–251913
4. Guenneau S, Amra C, Veynante D (2012) Transformation thermodynamics: cloaking and concentrating heat flux. *Opt Express* 20(7):8207–8218
5. Han T, Bai X, Gao D et al (2014) Experimental demonstration of a bilayer thermal cloak. *Phys Rev Lett* 112(5):054302
6. Qin J, Luo W, Yang P et al (2019) Experimental demonstration of irregular thermal carpet cloaks with natural bulk material. *Int J Heat Mass Transf* 141(10):487–490

# Research on Topology Optimization Methods for Continuum Structures



Yong Wen, Xia Liu, Shufan Wang, and Shi Yang

**Abstract** Improvements in the topology of continuum structures can effectively enhance structural performance and reduce the weight of the structure itself, resulting in significant economic benefits. This paper takes the above as a background, and addresses the complexity of the current description and algorithms of topology optimization, analyses the shortcomings of its theory, models, and algorithms, summarizes relevant experiences, discusses in depth the current basic theory and algorithms of continuum structure topology optimization, and gives conclusions on the application to bridge modeling, in the hope that it can provide a reasonable reference for workers in the same field.

**Keywords** Continuum structure · Topological optimization · Basic theory and algorithm

## 1 Introduction

In this new era, when human society is developing at a rapid pace and modern science and technology continue to advance, it has become an important research direction in various fields to improve the utilization of raw materials, bring out their basic characteristics more directly and arrange them more rationally. At the same time, the analysis from the structural point of view, the design of a more reasonable distribution of forces, and the continuous improvement of the stability and safety of the structure have now become a common concern for all engineers and product designers, and need to be given priority in the structural design. At present, there are many academic studies on topology optimization methods for continuum structures. Chinese scholars Yu Liaohong, Rong Jianhua, Zhang Guofeng, Xu Lei, Wang Xin, Li Da, and others have summarized this [1–3]. In addition to the topology optimization algorithm, the optimization solution for numerical instability problems is proposed, and sufficient

---

Y. Wen (✉) · X. Liu · S. Wang · S. Yang  
Changchun Institute of Technology, Changchun, Jilin, China  
e-mail: [tg667788@xzcstudio.com](mailto:tg667788@xzcstudio.com)

examples are provided for related theoretical research. The main optimization target for structural topology is the continuous problem structure. To distribute the optimal solution, it is necessary to continuously expand the design space. After obtaining the plate design results in the state of infinite fine rib reinforcement, it can be used as the basis for topology optimization in the subsequent stages. Based on this, it is necessary to divide the structure optimization according to the difference in design variables and perform three levels of shape optimization, size optimization, and topology optimization. At this time, the structure topology optimization can give the final boundary conditions and external load conditions. The optimization of structural topology realizes the optimization goal of performance, and then lays a better development foundation for the continuum topology optimization algorithm in the future stage.

## 2 Optimization of Topological Optimization Criterion Algorithm

### 2.1 *Optimization Steps of the Topology Optimization Criterion Algorithm for Continuum Structure Based on the SIMP Method*

Based on the SIMP material interpolation model, the details of the solution steps of the optimization criterion-based algorithm for solving the topology optimization problem of the continuum structure are as follows.

- (1) On the final definition of the design domain as well as the non-design domain, the definition needs to contain the design constraints as well as the load and other boundary and other relevant conditions. Therefore, the relative density of all cells in the design domain can be made to change continuously with the iterative process, while the relative density of all cells in the corresponding non-design domain will remain fixed, with a constant number of 0 or 1 [1].
- (2) The discrete phenomenon presented by the continuum structure can be set as a finite element mesh.
- (3) The design variables are executed by the given initialized cells, while giving all cells in the design domain a corresponding initial cell relative density quantity value.
- (4) SIMP material can be used to set the interpolation model, according to the requirements of the calculation of different discrete cells in the amount of different material properties parameters, and calculate the corresponding cell stiffness matrix information, the subsequent assembly of the total stiffness matrix of the structure as above.

- (5) In the above calculation, the SIMP material model materials will mostly be combined in the form of Poisson's ratio  $\nu = 1/3$ , the corresponding penalty factor  $p = 3$ . The unit stiffness matrix value  $k_e = p_e^p k_0$ , where  $k_0$  belongs to the standard value of the unit stiffness matrix divided by the corresponding elastic modulus value of the final unit stiffness matrix value, the total structural stiffness matrix results in  $K = \sum_{e=1}^n k_e$ .
- (6) Based on the above calculation, the final shift vector value  $U = K^{-1}F$  for calculating the actual node position of the structure can be derived after finite element analysis.
- (7) By calculating the continuum structure, its flexibility value criterion  $C$  and its gambling-winning sensitivity data can be derived.

At this time, the structural flexibility is expressed as  $C = UTKU = Z(pe)$  puetkou. During this period, the objective function needs to depend on the density  $\rho$  requirement and the structural displacement  $u$  requirement proposed by the design variables, so the gradient expression corresponding to the objective function at this time needs to contain the displacement derivative information, which is obtained with the help of the derivative calculation of the equation of equation  $KU = F$ . In such a case, the concomitant matrix method can be appropriately used to complete the final calculation of the derivative of the objective function, at which time the corresponding sensitivity expression is detailed as:  $\frac{\partial C}{\partial \rho_e} = -P(\rho_e) p^{-1} u_e$ . The material volume equation can be expressed as  $V = \sum_{e=1}^n \rho_e V_e$ , and its sensitivity is now displayed as:  $\frac{\partial V}{\partial \rho_e} = v_e$ ;  $B_e = -\frac{\partial C}{\partial \rho_e} / (\lambda \frac{\partial C}{\partial \rho_e}) = p(pe) p^{-1} u_e koue / (\lambda \cdot v_e)$ .

In the above equation,  $m$  is a factor with a moving limit and the main role is to ensure the stability of the algorithm. At the same time, in any one iteration of the calculation, a large change in the design variables will not be allowed.  $\eta$  ( $0 < \eta < 1$ ) is the damping factor, and the role is to ensure the stability of the algorithm. In most cases,  $\eta$  is taken as 0.5, and the Lagrange multiplier  $h$  will be in each step of the iterative. The Lagrangian multiplier  $h$  contained in  $B_e$  is involved in the calculation at each step of the iterative process and can be calculated by applying the dichotomous method, with reference to the structural volume constraint equation for the purpose of determining the final result [2].

If the final check result shows convergence, the next step of optimization can be performed. In the above, the following method can be applied. It can take the largest component of the neighboring design variable values of the two calculations, and then use the absolute difference between the two components as the final evaluation criterion. It is also possible to use the final design objective function of the two neighboring quantitative criteria to complete the calculation of the corresponding absolute difference equation, and use this result as the final criterion for this calculation process [3].

After the calculation, the target function value is output, and the final design variable value is given, and then the optimal topological form of the structure is obtained (as shown in the form of a density map), and then the whole calculation task [4] can be completed.

## 2.2 Optimization of Continuum Structure Topology Optimization Criterion Algorithm Based on SIMP Method

Details of the algorithm optimization implementation flowchart are shown in the content of Fig. 1.

## 3 Numerical Instability and Solution in the Algorithm

### 3.1 Instability

In general, the main factors that make topology optimization calculations prone to errors or numerical instability are problems related to porous materials (Porous), Checkerboard, mesh dependency, and local minima [5]. Among them, porous material mainly refers to the intermediate density cell volume values displayed in the calculation result area. The checkerboard lattice phenomenon mainly refers to the cells in which the material density magnitudes are shown as 1 and 0 within the computational region, and this cell is periodically distributed. Grid dependence mainly refers to the topology optimization calculation results and the calculation area range of the grid density quantitative value of the standard, after the selection of different forms of grid density, all have a direct impact on the final results, resulting in optimization calculation results of the discrepancy problem.

Conventionally, the grid density becomes larger, then the topological expression will show more fine branching structure as shown in Fig. 2. The intermediate density cells at this time as well as the tessellation calculation factors will make the results of this calculation exist less manufacturable and therefore will lose the practical significance of the engineering calculation. Therefore, the grid needs to be dependent in order to ensure that the reliability of the calculation results is more accurate and will not be significantly degraded, and it is also possible to obtain the calculation results of finer branching, but the engineering manufacturability at this time is more difficult [6].

### 3.2 Solution

In the face of the previously mentioned problems, the corresponding filtering technique was formally proposed by the scholar Sigmund, which is a new computationally simple and highly applicable heuristic algorithm that can be applied in most engineering applications with excellent results. The filtering method needs to be based on image processing techniques, and the noise factors present in the process are

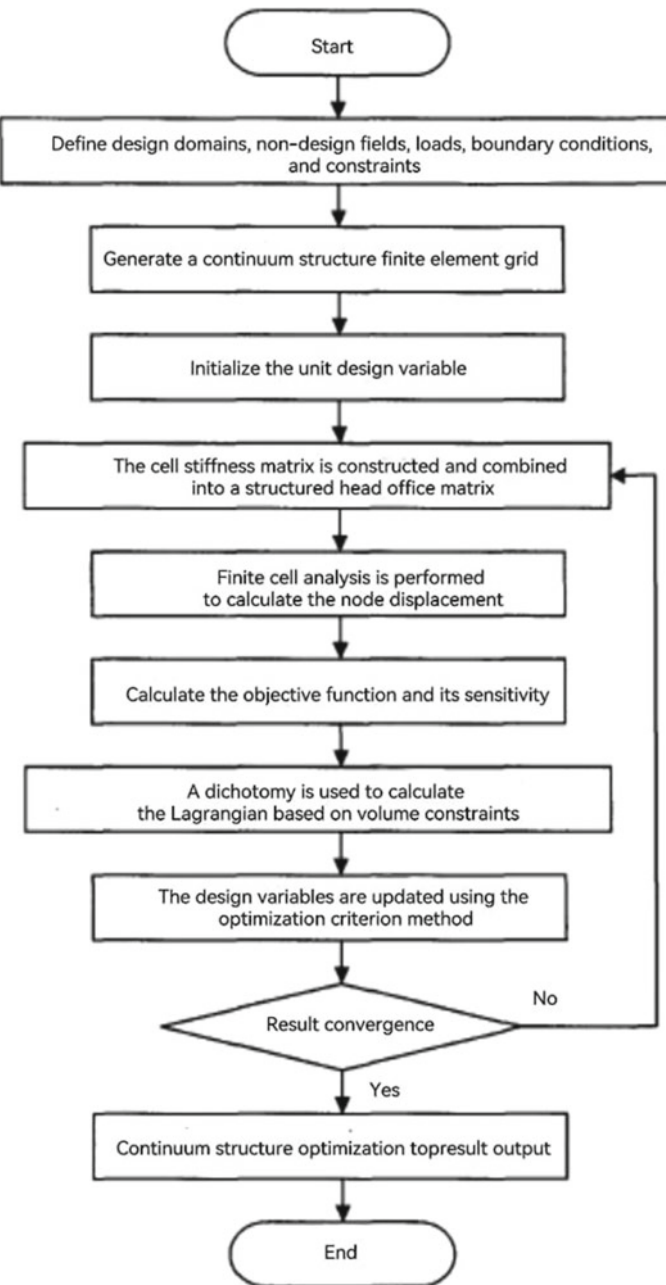


**Fig. 1** Flow chart of the continuum structure topology optimization criterion algorithm based on SIMP method

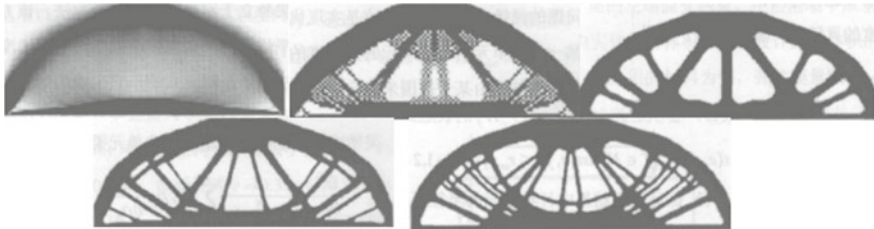


**Fig. 2** Schematic representation of porous material phenomenon, checkerboard phenomenon, and grid dependence phenomenon

filtered, and both linear factors and nonlinear forms are strongly representative after the filtering process, and the nonlinear method has better computational results at the theoretical level than the filtering effect calculated by the linear method [7].

However, this nonlinear filtering method is not recommended for use in the topology optimization process, mainly because this nonlinear method leads to an unstable optimization design and the applicability of the final results is not high. Therefore, there are two main types of existing linear filtering methods, namely, Fourier transform-based methods and convolution-based (Convolution) calculation methods. The Fourier transform is not suitable for calculation in topology optimization, mainly because it is only applicable to the calculation of more regular quadrilateral grid cells [8].

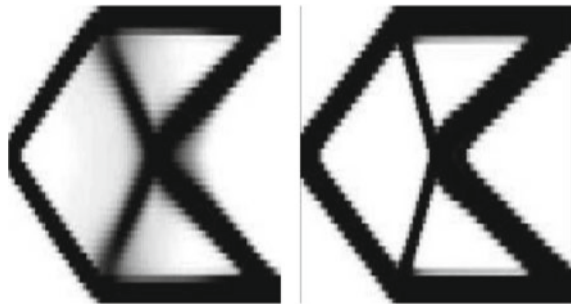
Therefore, it is necessary to use the convolution filtering technique as the main calculation method, together with the density filtering technique and the sensitivity filtering technique to complete the corresponding calculation tasks.

## 4 Example Calculation and Result Analysis

### 4.1 Effect of Different Parameters in the Optimization Algorithm

Considering the actual loading of the cantilever beam structure as shown in Fig. 3, the actual length of the initial unaccounted area is 80 cm and the width is 50 cm. At this time, the left end of the beam is in the state of solid support restraint, and at the midpoint of its free end, it can bear a concentrated force  $F$  in the direction of vertical downward, with a standard value of 1 kN within 40% of the total volume of the region. At this point, the minimum optimal topology value that can meet the requirements of structural flexibility is found. Therefore, the material properties used can be set to steel, corresponding to the modulus of elasticity standard  $E$ , corresponding to the value of 200Gpa, corresponding to Poisson's ratio standard  $\nu = 0.3$ . In the finite element analysis, the actual discrete design domain can be set to  $80 \times 50$  four-node form of quadrilateral cells. At this time, the values of penalty factor  $p$  and convolution

**Fig. 3** Cantilever density penalized topology optimized fireworks process



radius  $r_{min}$  are taken to different values, and the details of the final calculation results are shown in the content of Fig. 3.

The cantilever structure of the cantilever is shown in Fig. 3, the initial length of the missing area is set to 80 cm and the width to 50 cm. At this time, the left end of the beam is constrained by the solid support, and the middle point of the free end needs to bear the vertical downward concentration force  $F$  value of 1kN. Under this constraint, the actual volume of the corresponding structural solid material should be controlled within 40% of the total volume of the design area to ensure that the design can meet the minimum goal requirement of structural flexibility and achieve the optimal topology goal [9].

## 4.2 Other Classical Calculation Examples and Analysis of Results

Optimization of a cantilever beam model with a fixed left end and a concentrated force at the lower part of the free end can be realized (Figs. 5 and 6).

Unlike the cantilever beam model described in the previous section, the concentrated force  $F$  generated vertically downward at the free end is located in the lower region of the free end, where the constraint formally changes to a structural solid material volume not exceeding 30% of the design area volume. Therefore, all the remaining design domains involved, material parameters, etc. end up taking exactly the same criteria, so the convolution radius  $r_{min}$  in the calculation is taken as 1.5, and the grid standard of  $80 \times 50$  can be derived after the calculation. Details of the calculation results are shown in the content of Fig. 4.

The schematic diagram of the cantilever structure is shown in Fig. 4. The main difference from the cantilever model described in Fig. 3 is that the concentrated force  $F$  is located at the lower part of the free end, and the constraint volume of the solid material does not exceed 30% of the volume of the design area, and the design domain and material parameters involved in the rest are exactly the same [10].

**Fig. 4** Topological optimization evolution process of the cantilever-2 density penalty method

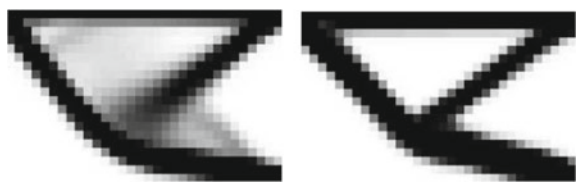


**Fig. 5** A cantilever model with the left end fixed and the free end midpoint receiving concentrated force

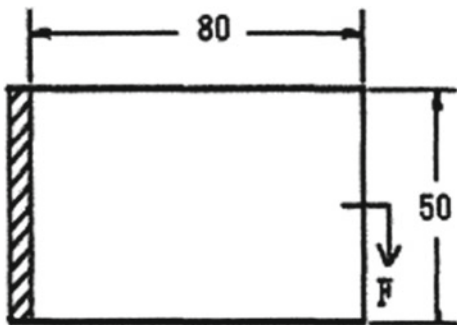
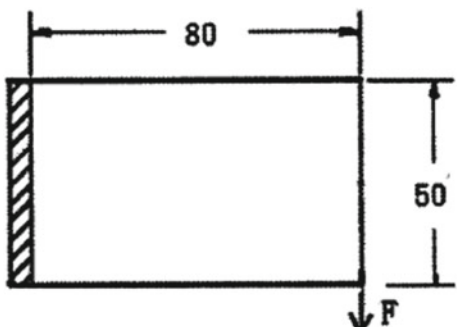


**Fig. 6** A cantilever model with concentrated force at the lower free end



## 5 Conclusion

To sum up, this paper takes the continuum structure topology optimization method as the core, and briefly describes the optimization content of the topology optimization criterion algorithm, that is, the optimization steps of the continuum structure topology optimization criterion algorithm based on the SIMP method and the continuum based on the SIMP method's optimization of the structural topology optimization criterion algorithm. At the same time, according to the numerical instability situation described in the algorithm, the corresponding final solution is given for the instability phenomenon. Finally, according to the example calculation and result analysis, the influence of different parameters in the optimization algorithm is explained, and other classic calculation examples and result analysis are listed at the same time, hoping to provide a reasonable reference for workers in the same industry.

**Acknowledgements** This work was supported by the Topic Foundation of Changchun Institute of Technology grant 320200040.

## References

1. Yu L, Rong J (2022) Boundary method overcomes the ill-conditioned load problem of topology optimization of continuum structure. *Mech Des Manuf* 01(07):107–109
2. Zhang G, Xu L, Wang X, Li D (2022) Research on partition density correction sensitivity filtering method for topology optimization of continuum structure. *Mech Sci Technol* 05(06):153–158
3. Zhang G, Xu L, Li D, Yu F (2021) Research on sensitivity filtering of continuum structure topology optimization. *Comb Mach Tool Autom Mach Technol* 08(06):129–132
4. Li Q, Li H (2021) Research on topology optimization method of continuum structure based on improved SIMP method. *Mech Electr Eng* 38(04):428–433
5. Zhan J, Peng Y, Liu M, Huang Z (2021) Topology optimization design of continuum structure based on multi-performance constraints. *Comput Integr Manuf Syst* 16(06):106–107
6. Ye H, Su P, Wang W, Sui Y (2020) Topology optimization of continuum structures under fatigue life constraints. *J Beijing Univ Technol* 46(03):236–244
7. Xu J, Ma Y (2019) Topological optimization of continuum structure under harmonic excitation by dynamic natural element method. *Vib Shock* 38(21):252–258
8. Dongdong Z, Fuqiang L, Lihui Z (2022) MicroTopology optimization of damped materials based on variable volume limit. *Appl Math Mech* 43(06):648–659
9. Teng X, Bingkun MAO, Xudong J (2019) Smooth bidirectional progressive structure optimization method for topologically optimized continuum structure frequency and dynamic stiffness. *J Agric Eng* 35(07):107–111
10. Xudong J, Keqin L, Zheng L (2019) Multi-object topology optimization of continuum structure dynamics based on the BESO method. *Mech Des* 16(05):147–152

# Study on Interface and Joint Properties of Aluminum Alloy by High-Power Ultrasonic Welding



Jingyun Liu, Mujiu Cheng, Fang Cheng, and Qiao Cheng

**Abstract** With the development of automotive lightweight, aluminum alloy and other light alloys have also developed rapidly, high-power ultrasonic welding technology is one of the branches. In this paper, Cu and Al foils with thickness of 0.3 mm are welded by high-power ultrasonic welding method. Using relevant instruments for copper alloy organization characteristics, interface temperature, and interface mechanical properties test, the corresponding results found copper–aluminum current—compound ultrasonic welding, ultrasonic power peak, welding interface temperature and interface the depth, the vertical depth of the plastic flow and increases with increasing the thickness of the IMC as auxiliary current. Too high welding pressure is not conducive to the transmission of ultrasonic energy in the workpiece, reducing the quality of the workpiece connection. During ultrasonic welding, the texture strength of copper and aluminum alloy decreases first and then increases. The texture type of copper does not vary with the welding process.

**Keywords** Aluminum copper · Ultrasonic welding · Mechanical properties

## 1 Introduction

The development and utilization of aluminum, magnesium, titanium, and other light alloys have been greatly developed in the environment of automotive lightweight, and the corresponding research on the forming of aluminum, magnesium, titanium, and other light alloys has also been rapid development, among which the light alloy welding process is one of the important fields concerned by many scholars. At present, the common welding methods include arc welding, resistance welding, friction welding, brazing, laser welding, high-frequency welding, etc., but due to the poor welding performance of aluminum, magnesium, titanium, and other light alloys, high thermal conductivity, easy to absorb hydrogen oxidation and other special points after

---

J. Liu (✉) · M. Cheng · F. Cheng · Q. Cheng  
Shenzhen Zhuohan Material Technology Co., LTD, Shenzhen 518000, Guangdong, China  
e-mail: [2438396213@qq.com](mailto:2438396213@qq.com)

heating, the welding process of light alloys has become a difficult problem hindering the application of light alloys. Ultrasonic welding technology appears under this background. The feasibility of the ultrasonic welding process and the reliability of welding parts have been confirmed by many scholars [1–3]. Ultrasonic metal welding technology is to apply vertical pressure and horizontal high-frequency vibration on the surface of the alloy, so as to make the temperature between the welding parts rapidly rise to form a firm welding joint, to achieve solid-phase connection of materials. Ultrasonic welding technology has prominent advantages: First, there is a wide range of welding materials and strong weldability, such as the welding of copper, nickel, and aluminum materials. Second, ultrasonic welding technology is not strict on the roughness of the surface of the material and the cleanliness of the material, there is no need to clean the surface of the material and remove the oxide film, welding is convenient and fast. Third, the temperature change of the ultrasonic welding process is less than 50% of the melting point of the material, to avoid serious deformation or melting of the material. Fourth, the ultrasonic welding cycle is short, the welded joint has good mechanical properties, and the damage to the welding area is small.

With the development of power ultrasonic technology and the requirement of lightweight technology, the superiority of ultrasonic welding technology is more and more obvious. Because various materials have different performance advantages, the combination of them can obtain better material performance advantages, so the development of composite materials has been widely concerned. The use of high-performance lightweight materials is one of the effective ways to improve the performance of parts and achieve the lightweight of equipment, such as aluminum alloy plate and pipe, magnesium alloy plate and pipe, and other composite materials composed of a variety of metals and nonmetals. High-performance lightweight materials are represented by aluminum and magnesium composite [4, 5]. Magnesium alloy has lighter weight, higher specific strength, and superior damping, noise reduction and heat absorption properties. Aluminum alloy has better corrosion resistance, low price, and wide application [6]. In order to give full play to the performance advantages of aluminum alloy and balance the performance of materials, the construction of aluminum alloy material has been extensively researched and developed, and is known as one of the non-ferrous metal materials with the most development potential in the twenty-first century. In the ultrasonic welding process, tensile shear strength, anti-peel strength, and welding zone hardness are important mechanical properties to test the welding effect.

**Table 1** Thermal physical properties of pure aluminum and copper

Principal	Thermal conductivity /(W · m <sup>-1</sup> °C <sup>-1</sup> )	Coefficient of thermal expansion /10 <sup>-6</sup> K <sup>-1</sup>	Specific heat capacity /(J · kg <sup>-1</sup> K <sup>-1</sup> )	Modulus of elasticity /GPa
Al	217.7	25.6	964.7	70
Cu	399	16.9	611	119

## 2 Experimental Methods

### 2.1 Experiment Material

Pure aluminum foil (Al  $\geq$  99.99wt%) and pure copper foil (Cu  $\geq$  99.5wt%) with sizes of 100 mm  $\times$  30 mm  $\times$  0.3 mm were used in the experiment. The thermophysical properties of pure aluminum and copper are shown in Table 1.

### 2.2 The Experimental Apparatus

This welding test is completed on the welding platform. During the welding process, the welding gun is fixed and the workpiece is clamped on the welding platform, and the welding is realized by moving with the platform. Ultrasonic AC TIG composite welding power supply is lorCH-V24 TIG welder produced in Germany, with square wave AC function, which can meet the aluminum alloy welding process research (Figs. 1 and 2).

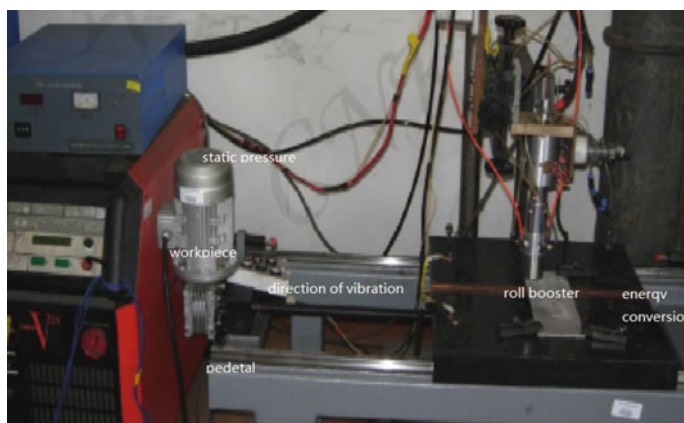


**Fig. 1** Ultrasonic welding equipment physical picture

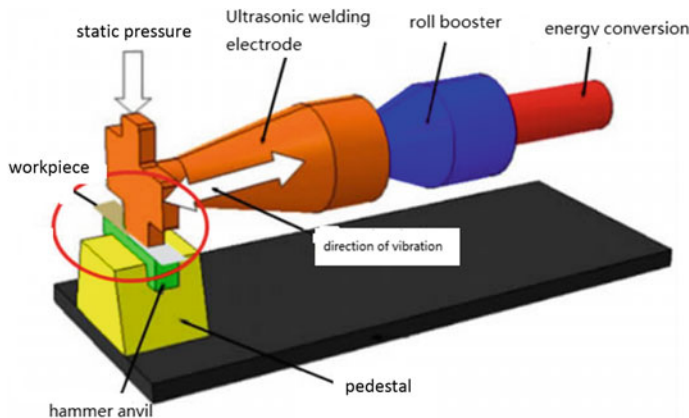


**Fig. 2** Schematic diagram of ultrasonic welding equipment

### 2.3 Experimental Methods

Nc-2020a high-power ultrasonic metal welder was used in the welding test, with a maximum power of 2000W and a vibration frequency of 20 kHz. Considering that the welding head is easy to stick aluminum, and the yield strength of the aluminum alloy is higher than that of pure copper, aluminum alloy is moved as the lower workpiece. The upper parts are pure copper. All parts are cut to 100 mm × 25 mm and are 0.3 mm thick for copper/aluminum welding. The workpiece is placed in a lap joint with a lap area of 25 mm × 25 mm. There are two kinds of welding heads with different numbers of teeth at the bottom of the tool head, which are 9 trapezoidal teeth and 10 trapezoidal teeth respectively. The end area of all welding heads is 7 mm × 5 mm. In the experiment, copper/aluminum welding uses 9 teeth welding head. For copper/aluminum welding, the process parameters are amplitude 25  $\mu\text{m}$ , welding time 0 ~ 0.7 s, welding pressure 1.45kN, and number of welding teeth 9. K type thermocouple was used to measure the interface temperature. In order to ensure the measurement accuracy, thermocouple wire with diameter of 0.1 mm was used. The temperature measurement point is 1.5 mm away from the center of the welding area. The temperature measurement method is as follows: Open a 0.5 mm semicircular hole on the upper surface of the aluminum plate, insert the thermocouple into the hole, and then embed the thermocouple wire into the material. The microstructure of the interface and its tensile fracture was observed by scanning electron microscope (SEM) equipped with an energy dispersive X-ray spectrometer. X-ray diffraction analysis was performed to further clarify the mesophase composition. The XRD spectrum ranges from 20° to 90°, the step size is 0.2°, and the scanning speed is 0.02°/s. Because ultrasonic welding zone is very irregular, it is difficult to calculate the welding zone area, tensile shear force is the main method to evaluate ultrasonic welding quality. Before welding, polish the surface of copper and aluminum workpiece with sandpaper to expose the metallic luster, and wipe it clean with acetone.

The interface structure, elemental composition, and fracture morphology of weld joints were observed and analyzed by scanning electron microscope, energy dispersive spectrometer, and X-ray diffractometer. The tensile shear force of ultrasonic welded specimens of the two kinds of joints was tested on shimadzu AGS-X micro-computer controlled electronic universal testing machine. The tensile speed is set as 2 mm/min, which can avoid the damage of joint strength and the change of interface structure. For each set of process parameters, the average value of the three tests is taken as the tensile shear force under this parameter. After that, the data such as microstructure characteristics, interface temperature, tensile strength, and Vickers hardness of Al-Cu joint were collected and analyzed by using equipment to study its characteristics.

### 3 Results and Discussion

#### 3.1 *Interfacial Structure Characteristics*

The atoms in the metal are always in the equilibrium state of thermal vibration. Under the action of high-frequency ultrasonic wave, plastic deformation of large strain rate occurs in the welding zone, resulting in many lattice defects. The temperature of welding interface rises rapidly, the balance of atoms on the interface is broken, and atoms jump from one position to another, that is, interatomic diffusion at the interface. EDS test was performed on the ultrasonic welded joint, as shown in Fig. 3. According to 3A, the hard copper side is obviously embedded in the soft aluminum side, which is the Kirkendall effect and an important embodiment of the vacancy diffusion mechanism. In the joint in Fig. 3B, Al and Cu atoms are diffused and the interface is wavy. Al in Fig. 3c crosses the interface bonding surface and a small amount of Al diffuses into the copper side. In Fig. 3D, more Cu crosses the interface and disperses into the Al side. It can be seen that The diffusion of Cu atoms is faster than that of Al atoms. Combined with Fig. 5b, all materials have a tendency to flow toward the middle. Figure 4 shows the distribution of EDS scanning elements on the interface. It can be seen that the ratio of M (Al) to M (Cu) is 2:3, predicting the existence of intermetallic compounds, and C is the residual organic matter in the sample.

At the center of the connection of the copper and aluminum joint, it can be seen that the contact interface is uneven, and the occlusion is obvious. A close connection is formed under the indentation, and the atoms are obviously diffused to each other, resulting in the phenomenon of locking and forming mechanical self-locking. With the increase of welding time, under the interaction of high-frequency vibration and pressure, aluminum and copper have uneven plastic deformation, resulting in uneven distribution of internal stress near the welding interface, and the softened metal has plastic flow under the action of uneven internal stress. At 0.2 mpa, 0.5 s, and 50%, material flow of aluminum-copper ultrasonic welded joints occurs in different

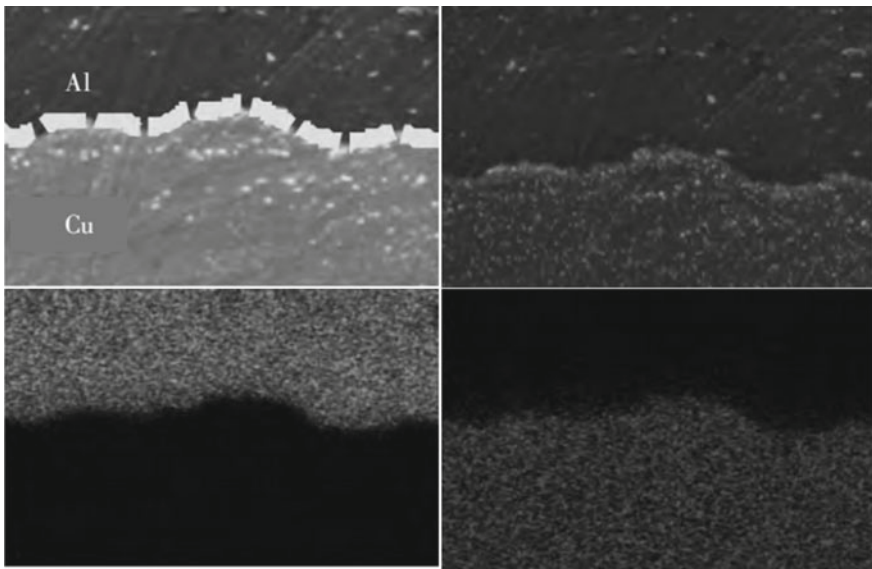
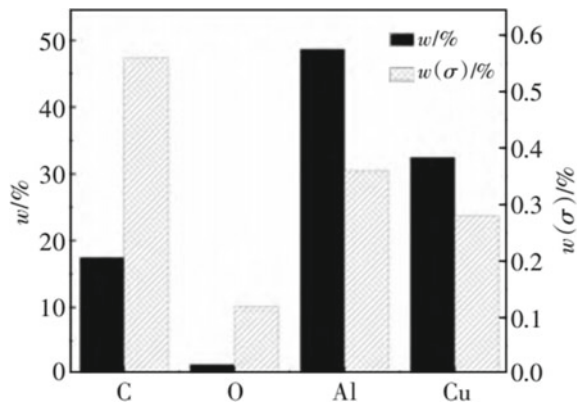


**Fig. 3** EDS results of ultrasonic welded joints (from left to right are A—Electronic images of joints; B—Joint element distribution; C—Aluminum distribution map; D—Copper distribution map)

**Fig. 4** EDS scanning element distribution on the interface



degrees at the interface. At the top of tooth of Al side, the plastic ripple of the connection interface is gentle, and there is no obvious material flow, showing a straight connection. There is a small wavy plastic flow between the two teeth, and the interface is a tiny serrated bite. The zigzag plastic deformation zone appears at the welding edge, which is helpful to improve the tensile strength of the joint. It can be known that the ultrasonic joint area presents complex and diverse structure morphology, such as straight joint, occlusion, and eddy shaped plastic flow layer. In Fig. 3b-d, there are holes of different degrees. The closer the holes are to the welding

edge, the larger the area is. The size and number of holes indicate the bonding state of the interface. According to the bonding state of the joint interface, the joint can be divided into unbonding, transition, and bonding zones.

It is observed that the flow is most obvious at the edge of the joint. The edge zone is a transition zone, where the bonding surface is extruded and vibrated, and the temperature of the interface material rises to near solid–liquid coexistence during welding, and the material gathers at the edge to strengthen the atomic flow between the aluminum and copper interface. It can be seen that the bonding mechanism of aluminum and copper is mainly mechanical occlusion and metal atom bonding. In the process of pressing the upper anvil head, the aluminum-copper interface material has plastic deformation, subjected to thermal friction and high-frequency vibration, and the material has a melting tendency. Combined with the flow and combination of elements between the interfaces, the new metal bond is formed. These micro-combinations form the interface morphology of macroscopic mechanical occlusion.

### ***3.2 Interface Temperature***

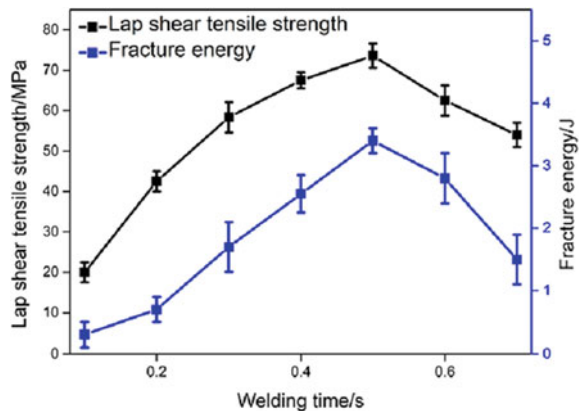
The interfacial temperature is the most direct evidence to explain the evolution of welding microstructure. The temperature of welding center is the highest in ultrasonic welding process. The temperature of welding center can be predicted by infrared temperature measurement of welding edge. The maximum edge temperature obtained by multiple tests is 230 °C. According to the relationship between welding center temperature and edge temperature established by Elangovan et al., the welding center temperature is estimated to be 330 °C. It can be seen that the temperature of the welding center is significantly lower than the low eutectic point between aluminum and copper, which can be judged as a solid-phase connection.

### ***3.3 Mechanical Property***

#### ***3.3.1 Tensile Strength***

Figure 5 shows the variation of tensile strength of copper–aluminum welded joints with welding time when the welding amplitude is 25  $\mu\text{m}$ . When the welding time is 0.1 s, due to the small input energy, the welding interface is mainly connected by local bonding. The connection area is small, and the tensile strength and fracture energy are small. With the increase of welding time, degree of distortion of work piece and welding interface temperature increase, the plastic flow interface was going on, and effective connection area increased rapidly, improving the mechanical properties of the welded joint, when the welding time is 0.3 s, copper–aluminum local mutually embedded height can reach 16.2  $\mu\text{m}$ , appear discontinuous interface of IMC. The tensile strength of welded joint reaches 58 MPa.

**Fig. 5** Evolution of tensile strength and fracture energy of copper–aluminum welded joints with welding time



When the welding time increases from 0.3 s to 0.5 s, local mechanical self-locking with maximum interlocking height of 47.8  $\mu\text{m}$  and continuous IMC thin layer with average thickness less than 1  $\mu\text{m}$  are formed at the welding interface, and fine equiaxial grains are formed due to discontinuous dynamic recrystallization. The increase of plastic flow degree, the formation of IMC thin layer, and fine equiaxed grains are beneficial to the improvement of tensile strength of welded joints. When the welding time is 0.5 s, the maximum tensile strength reaches 73.6 MPa. When the welding time increases from 0.5 s to 0.7 s, IMC increases rapidly with the increase of input energy. Too thick IMC will lead to the deterioration of mechanical properties of heterogeneous metal welded joints, and the tensile strength of welded joints begins to decrease. In addition, the high temperature generated in the welding edge area leads to local melting of the interface, which causes cracks in the welding edge area. When the welding time is 0.7 s, the tensile strength of the welded joint is only 54 MPa.

### 3.4 Webster Hardness

Figure 6 shows the hardness of the welding interface changing with welding time. It can be seen from the figure that the hardness of the welding interface is significantly higher than that of the base metal, which is mainly due to the hard and brittle intermetallic compound Cu Al<sub>2</sub> generated on the welding interface under the action of ultrasonic. And with the increase of welding energy, the thickness of IMC is thicker, so the hardness value is larger.

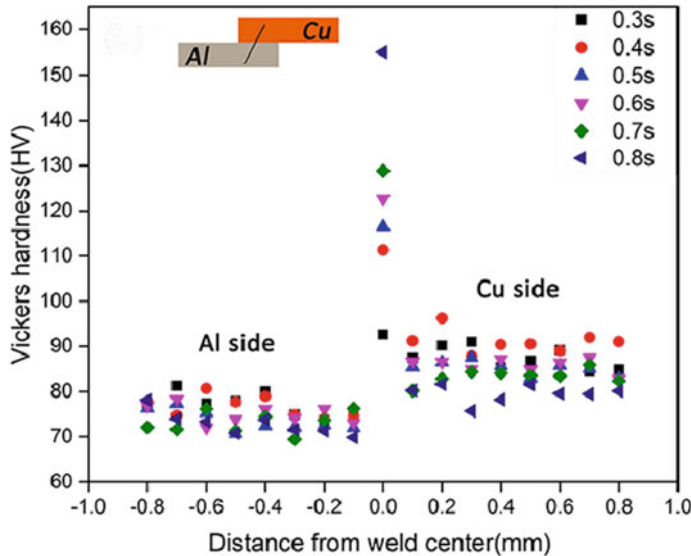


**Fig. 6** Hardness changes of ultrasonic welded joints at different welding times

## 4 Conclusion

- (1) A good al-Cu UMW joint was obtained by the experiment. The workpiece was fixed by proper welding pressure and the bonding of surface materials was promoted. The ultrasonic joint area showed complex and diverse microstructure morphology, such as straight bonding, occlusion, eddy shaped plastic flow layer, and obvious atomic diffusion phenomenon between interfaces.
- (2) The peak value of ultrasonic power, welding interface temperature, interface pressure depth, longitudinal depth of plastic flow, and IMC thickness increase with the positive increase of auxiliary current. When the auxiliary current is 3600A, the edge area of the welded joint is cracked due to local melting. The maximum tensile and shear strength of the copper/aluminum joint is 3.20kN, and the tensile failure of the joint is pull-out failure. The copper/aluminum welding interface is flat, and there is vortex plastic deformation in some areas. The simulation results show that the diffusion coefficient of Cu/Al interface under ultrasonic action is one order of magnitude larger than that under temperature action.
- (3) In the ultrasonic welding process, the plastic deformation of copper and aluminum alloy occurs, but the grain morphology and size of copper hardly change, and the texture strength of the welding interface of copper and aluminum alloy decreases first and then increases.

## References

1. Jia Y, Wen T, Huang N et al (2022) Research on aluminum alloy welding process based on high frequency and low power pulsed Laser-MIG hybrid welding. *Opt Laser Technol* 150:107899
2. Wu K, Zeng Y, Zhang M et al (2022) Effect of high-frequency phase shift on metal transfer and weld formation in aluminum alloy double-wire DP-GMAW
3. Rivai AK, Pratama KAMN, Sugeng B (2022) Microstructure investigation of mechanically alloyed 316L-6Al-0.5Y<sub>2</sub>O<sub>3</sub> oxide dispersion strengthened austenitic steel powder. IOP Publishing Ltd
4. Xiao X, Qin D, Mao Y et al (2021) Effects of pin morphology on the interface defects of the FSWed lap joints of 2A12 aluminum alloy. *J Manuf Process* 68(6):128–140
5. Xing L, Zhan M, Gao PF et al (2021) Effect of void nucleation on microstructure and stress state in aluminum alloy tailor-welded blank
6. Zhan Y, Li Y, Zhang E et al (2019) Laser ultrasonic technology for residual stress measurement of 7075 aluminum alloy friction stir welding. *Appl Acoust* 145(2):52–59

# Analysis of Nozzle Flow Based on Small Disturbance Equation Using Successive Over Relaxation Method



Shujia Li

**Abstract** De Laval nozzles are widely used in industrial areas like aerospace. This study focuses on the two-dimensional nozzle flow with small perturbation on the boundary in the purely subsonic case and the purely supersonic case. The small disturbance equations (SDE) derived from the continuity equation are used in this calculation. To get the numerical solution of velocity potential, the successive over relaxation method (SOR) with different relaxation factors is used in the iterative operation. After hundreds or thousands of iterations, the error is on the order of 10E-13. In the subsonic case, the speed of convergence is really fast with only about 300 times of iteration while the subsonic case needs more than 4500 times. The streamline plot and the velocity contour plot are finally illustrated in the paper. The simulation results reveal that the velocity field is almost triple compared to the initial speed, besides, with a slight adjustment in the shape of the boundary, the velocity field also changes a little bit.

**Keywords** Successive over relaxation method · Nozzle flow · Small disturbance equations

## 1 Introduction

De Laval nozzles and similar flow properties are widely used in mechanical areas like steam turbines and supersonic jet engines, etc. [1, 2]. SOR is an iterative method to solve linear algebraic equations and find the numerical solution by gradually reducing the deviation of each unknown value [3]. It was originally developed from the Jacobi's method, which is an iterative algorithm for determining the solutions of a strictly diagonally dominant system of linear equations [4]. Since its low efficiency, the Gauss–Seidel method was found to improve the speed of convergence [5]. By

---

S. Li (✉)

Department of Civil Engineering, Changsha University of Science and Technology, Chang Sha 410114, China

e-mail: [201902050125@stu.csust.edu.cn](mailto:201902050125@stu.csust.edu.cn)

adding the optimum accelerating factor, the SOR was eventually derived with better accuracy and faster speed of convergence [6]. The SDE is the simplification of the full potential equations while the obstacle is thin. Li et al. [2] studied the transonic shock problem for the full compressible Euler system in a general two-dimensional de Laval nozzle and solved the problem for a general class of de Laval nozzles whose divergent parts are small and arbitrary perturbations of divergent angular domains. Huang [1] used SDE to simulate the De Laval nozzle flow in the transonic case. He found that the SDE method leads to accurate performance in simulating nozzle flow. But the velocity field in the nozzle in purely subsonic and purely supersonic cases didn't show in the previous two papers. Gang [8] used the successive over relaxation iteration method to solve the linear system  $Ax = b$ . In summary, on the basis of the previous research, the SOR method will be innovatively applied to solve the SDE equation, and finally, find the velocity field of two-dimensional nozzle flow in the purely subsonic cases as well as the supersonic cases.

In Sect. 2, how SOR is derived from Jacobi's equation is presented while Sect. 3 shows how it actually uses in SDE in the supersonic case and subsonic case, respectively. Section 4 will discuss the results and followed by Sect. 5 with the conclusion.

## 2 Description of Successive Over Relaxation Method

### 2.1 Jacobi's Method

The equation  $Ax = b$  is widely used in scientific applications. For example, finite element discretization is used to solve partial differential equations like Navier–Stokes equations [7]. It can be written as

$$\begin{bmatrix} a_{11} & \cdots & a_{1n} \\ \vdots & \ddots & \vdots \\ a_{n1} & \cdots & a_{nn} \end{bmatrix} \begin{bmatrix} x_1 \\ \vdots \\ x_n \end{bmatrix} = \begin{bmatrix} b_1 \\ \vdots \\ b_n \end{bmatrix} \quad (1)$$

The principle of Jacobi's method is using the first equation and the current values of  $x_1^k, x_2^k \dots x_n^k$  to find a new value  $x_1^{k+1}$ , similar pattern can be found in the new value  $x_i^{k+1}$  by using the  $i^{th}$  line of the equation and the old values of the other variables. It can be written as

$$\begin{bmatrix} a_{11} & 0 & \cdots & 0 \\ 0 & a_{22} & \ddots & \vdots \\ \vdots & \ddots & \ddots & 0 \\ 0 & \cdots & 0 & a_{nn} \end{bmatrix} \begin{bmatrix} x_1^{k+1} \\ x_2^{k+1} \\ \vdots \\ x_n^{k+1} \end{bmatrix} + \begin{bmatrix} 0 & a_{12} & \cdots & a_{1n} \\ a_{21} & 0 & \ddots & \vdots \\ \vdots & \ddots & \ddots & a_{n-1n} \\ a_{n1} & \cdots & a_{nn-1} & 0 \end{bmatrix} \begin{bmatrix} x_1^k \\ x_2^k \\ \vdots \\ x_n^k \end{bmatrix} = \begin{bmatrix} b_1 \\ b_2 \\ \vdots \\ b_n \end{bmatrix} \quad (2)$$

By dividing A into three parts, diagonal, strict lower triangular, and strict upper triangular

$$D = \begin{bmatrix} a_{11} & 0 & \cdots & 0 \\ 0 & a_{22} & \ddots & \vdots \\ \vdots & \ddots & \ddots & 0 \\ 0 & \cdots & 0 & a_{nn} \end{bmatrix} \quad (3)$$

$$L = \begin{bmatrix} 0 & 0 & \cdots & 0 \\ a_{21} & \ddots & \ddots & \vdots \\ \vdots & \ddots & \ddots & 0 \\ a_{n1} & \cdots & a_{nn-1} & 0 \end{bmatrix} \quad (4)$$

$$U = \begin{bmatrix} 0 & a_{12} & 0 & a_{1n} \\ 0 & \ddots & 0 & 0 \\ \vdots & \ddots & \ddots & a_{n-1n} \\ 0 & \cdots & 0 & 0 \end{bmatrix} \quad (5)$$

then Jacobi's Method can be written in matrix–vector notation as

$$Dx^{k+1} + (L + U)x^k = b \quad (6)$$

$$x^{k+1} = D^{-1}(b - (L + U)x^k) \quad (7)$$

## 2.2 Gauss–Seidel Method

The difference between Jacobi's method and Gauss–Seidel method is that, in the second line of the equation, since  $x_1^{k+1}$  was found in the first line of the equation, instead of using all the old values to get  $x_2^{k+1}$  in Jacobi's method, Gauss–Seidel method uses  $x_1^{k+1}$  to replace  $x_1^k$ . Similar pattern can be found in the  $i^{th}$  line, since new  $x_1^{k+1} \dots x_{i-1}^{k+1}$  were found in previous equations, the new value  $x_i^{k+1}$  can be derived from  $x_1^{k+1} \dots x_{i-1}^{k+1}$  and  $x_{i+1}^k \dots x_n^k$ . It is described by

$$\begin{bmatrix} a_{11} & 0 & \cdots & 0 \\ a_{21} & a_{22} & \ddots & \vdots \\ \vdots & \ddots & \ddots & 0 \\ a_{n1} & \cdots & a_{nn-1} & a_{nn} \end{bmatrix} \begin{bmatrix} x_1^{k+1} \\ x_2^{k+1} \\ \vdots \\ x_n^{k+1} \end{bmatrix} + \begin{bmatrix} 0 & a_{12} & \cdots & a_{1n} \\ 0 & 0 & \ddots & \vdots \\ \vdots & \ddots & \ddots & a_{n-1n} \\ 0 & \cdots & 0 & 0 \end{bmatrix} \begin{bmatrix} x_1^k \\ x_2^k \\ \vdots \\ x_n^k \end{bmatrix} = \begin{bmatrix} b_1 \\ b_2 \\ \vdots \\ b_n \end{bmatrix} \quad (8)$$

Then Gauss–Seidel method can be written in matrix–vector notation as

$$(L + D)x^{k+1} + Ux^k = b \quad (9)$$

$$x^{k+1} = (L + D)^{-1}(b - Ux^k) \quad (10)$$

### 2.3 Successive Over Relaxation (SOR) Method

In the Gauss–Seidel method, first, keep only the diagonal term in the left

$$Dx^{k+1} = b - Lx^{k+1} - Ux^k \quad (11)$$

$$x^{k+1} = D^{-1}(b - Lx^{k+1} - Ux^k) \quad (12)$$

Subtract  $x^k$  on both sides,  $\Delta x$  in Gauss–Seidel method can be shown as

$$\Delta x = x^{k+1} - x^k = D^{-1}(b - Lx^{k+1} - Ux^k - Dx^k) \quad (13)$$

In SOR method, parameter  $\omega$  named as relaxation factor is used to accelerate the iteration [8]

$$x^{k+1} = x^k + \omega\Delta x = x^k + \omega D^{-1}(b - Lx^{k+1} - Ux^k - Dx^k) \quad (14)$$

$$\left(\frac{D}{\omega} + L\right)x^{k+1} = \frac{D}{\omega}x^k + (b - Lx^{k+1} - Ux^k - Dx^k) = \left(\left(\frac{1}{\omega} - 1\right)D - U\right)x^k + b \quad (15)$$

$$x^{k+1} = \left(\frac{D}{\omega} + L\right)^{-1}\left(\left(\frac{1}{\omega} - 1\right)D - U\right)x^k + b \quad (16)$$

$$x_i^{(k+1)} = x_i^{(k)} + \frac{\omega}{a_{ii}} \left( b_i - \sum_{j=1}^{i-1} a_{ij}x_j^{(k+1)} - \sum_{j=i}^n a_{ij}x_j^{(k)} \right) \quad (17)$$

$$i = 1, 2, \dots, n; k = 0, 1, 2, \dots$$

It can be also written as [8]

### 3 The Small Disturbance Equation

#### 3.1 Derivation

The continuity equation can be written as

$$\frac{\partial \rho}{\partial t} + \operatorname{div}(\rho \mathbf{U}) = 0 \quad (18)$$

Under the assumption that the vorticity of velocity is zero ( $\nabla \times \mathbf{U} = 0$ ), the velocity field can be described by the gradient of a scalar-valued function. The scalar value  $\phi$  is named velocity potential.

$$\mathbf{U} = \nabla \phi \quad (19)$$

So that

$$\frac{\partial \rho}{\partial t} + \operatorname{div}(\rho \nabla \phi) = 0 \quad (20)$$

In the derivation of small perturbation linearization, under the condition of constant entropy, it is possible to derive the relation

$$\frac{\rho}{\rho_0} = \left(1 - \frac{|\nabla \phi|^2}{2H_0} - \frac{\partial_t \phi}{H_0}\right)^{\frac{1}{\gamma-1}} \quad (21)$$

where  $\rho_0$  and  $H_0$  are the stagnation density and stagnation enthalpy, respectively. After substituting (21) into (20)

$$\begin{aligned} \frac{1}{c^2} (\phi_{tt} + \partial_t(|\nabla \phi|^2)) &= (1 - M_x^2)\phi_{xx} + (1 - M_y^2)\phi_{yy} \\ &+ (1 - M_z^2)\phi_{zz} - 2M_x M_y \phi_{xy} - 2M_x M_z \phi_{xz} - 2M_y M_z \phi_{yz} \end{aligned} \quad (22)$$

where

$$M_x = \frac{\phi_x}{c} \quad (23)$$

$$M_y = \frac{\phi_y}{c} \quad (24)$$

$$M_z = \frac{\phi_z}{c} \quad (25)$$

$$c^2 = (\gamma - 1) \left( H_0 - \frac{|\nabla \phi|^2}{2} - \partial_t \phi \right) \quad (26)$$

With an additional assumption that the flow is steady, it can be simplified as

$$\begin{aligned} (1 - M_x^2)\phi_{xx} + (1 - M_y^2)\phi_{yy} + (1 - M_z^2)\phi_{zz} - 2M_x M_y \phi_{xy} \\ - 2M_x M_z \phi_{xz} - 2M_y M_z \phi_{yz} = 0 \end{aligned} \quad (27)$$

Since this paper focuses on the two-dimensional flow, the influence of velocity in Y direction from the perturbation is slight enough. The speed in Y and Z directions can be ignored which means

$$\phi_y = \phi_z = 0 \quad (28)$$

So the small disturbance equation finally becomes

$$(1 - M_x^2)\phi_{xx} + \phi_{yy} = 0 \quad (29)$$

### 3.2 The Wave Equation

Before deriving the finite differences scheme of the equation, it is necessary to introduce the wave equation first. The wave equation can be written as [9]

$$\frac{\partial^2 u}{\partial t^2} - c^2 \frac{\partial^2 u}{\partial x^2} = 0 \quad (30)$$

The second-order central finite difference scheme [10] of this equation can be written as

$$\frac{u_j^{n+1} - 2u_j^n + u_j^{n-1}}{\Delta t^2} - c^2 \left( \frac{u_{j+1}^n - 2u_j^n + u_{j-1}^n}{\Delta x^2} \right) \quad (31)$$

While

$$t = n \Delta t \quad (32)$$

$$t = n \Delta t \quad (33)$$

$$x = j \Delta x \quad (34)$$

$$u_j^n = A^n e^{i\theta j} |\theta| \leq \pi \quad (35)$$

$$s = \frac{c^2 \Delta t^2}{\Delta x^2} \quad (36)$$

If the equation is stable, it means that  $|A| \leq 1$

After substituting  $u_j^n = A^n e^{i\theta j}$  into (30), it will be easily derived that the scheme will be stable only if  $s \leq 1$ .

When it comes to the small disturbance equation when the Mach number is between 1 and  $\sqrt{2}$

$$(\phi_{i+1,j} - 2\phi_{i,j} + \phi_{i-1,j}) - \frac{1}{(M_x^2 - 1)} (\phi_{i,j+1} - 2\phi_{i,j} + \phi_{i,j-1}) = 0 \quad (37)$$

Obviously  $s = \frac{1}{M_x^2 - 1} \leq 1$  is unsatisfied, in this situation, if  $\frac{\partial u^2}{\partial t^2}$  can be discretized as

$$\frac{u_j^n - 2u_j^{n-1} + u_j^{n-2}}{\Delta t^2} \quad (38)$$

Eventually, it will be found that it is stable in all the value  $s > 0$ .

### 3.3 Differential Iterative Calculation of Small Perturbation Equations

In the subsonic case, it can be easily discretized as

$$(1 - M_x^2)(\phi_{i+1,j} - 2\phi_{i,j} + \phi_{i-1,j}) + (\phi_{i,j+1} - 2\phi_{i,j} + \phi_{i,j-1}) = 0 \quad (39)$$

In the supersonic case, as mentioned earlier, it can be discretized as

$$(1 - M_x^2)(\phi_{i,j} - 2\phi_{i-1,j} + \phi_{i-2,j}) + (\phi_{i,j+1} - 2\phi_{i,j} + \phi_{i,j-1}) = 0 \quad (40)$$

In this paper, the grid size is  $96 \times 32$ , and the shape of the boundary can be described in the two function.

Lower boundary

$$fL(x) = \begin{cases} \beta \sin(\pi(x - 1)), & x \in (1, 2) \\ 0, & x \in (0, 1), (2, 3) \end{cases} \quad (41)$$

Upper boundary (Fig. 1)

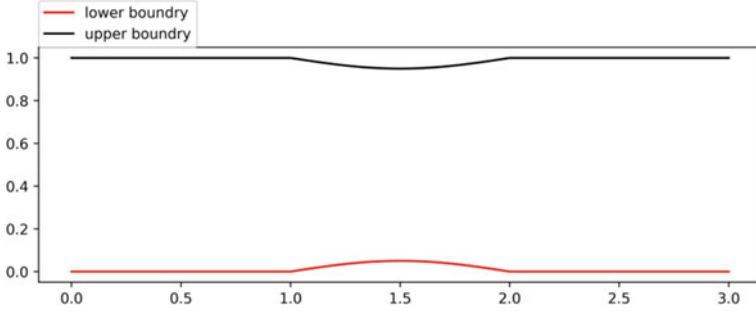


**Fig. 1** The shape of the boundary

$$fU(x) = \begin{cases} 1 - \beta \sin(\pi(x-1)), & x \in (1, 2) \\ 0, & x \in (0, 1), (2, 3) \end{cases}, \quad \beta = 0.05, 0.1 \quad (42)$$

When it comes to the calculation of upper and lower boundaries, since the obstacle is really small, it is easy to get

$$U_y = U_\infty f'(x) \quad (43)$$

Which means

$$\phi_{i,j-1} = \phi_{i,j+1} - 2hU_\infty f' L'(x), \quad j = 0 \quad (44)$$

$$\phi_{i,j+1} = \phi_{i,j-1} + 2hU_\infty f' U'(x), \quad j = 32 \quad (45)$$

So the iteration of small disturbance equations in the subsonic case can be written as

$$\begin{aligned} \phi_{i,j}^{(k+1)} &= \phi_{i,j}^{(k)} + \frac{\omega}{-2(1 + (1 - M_x^2))} \\ &\left( -(1 - M_x^2)\phi_{i-1,j}^{(k+1)} - \phi_{i,j-1}^{(k+1)} - (1 - M_x^2)\phi_{i+1,j}^{(k)} - \phi_{i,j+1}^{(k)} \right. \\ &\left. - (-2(1 + (1 - M_x^2)))\phi_{i,j}^{(k)} \right) \end{aligned} \quad (46)$$

And that in the supersonic case will be like

$$\begin{aligned} \phi_{i,j}^{(k+1)} &= \phi_{i,j}^{(k)} + \frac{\omega}{-2(1 + (1 - M_x^2))} \\ &\left( -(1 - M_x^2)\phi_{i-1,j}^{(k+1)} - \phi_{i,j-1}^{(k+1)} - (1 - M_x^2)\phi_{i-2,j}^{(k+1)} - \phi_{i,j+1}^{(k)} \right. \\ &\left. - (-2(1 + (1 - M_x^2)))\phi_{i,j}^{(k)} \right) \end{aligned} \quad (47)$$

## 4 Results and Discussion

### 4.1 Subsonic Case

See Figs. 2, 3, 4 and 5.

### 4.2 Supersonic Case

See Figs. 6, 7, 8 and 9.

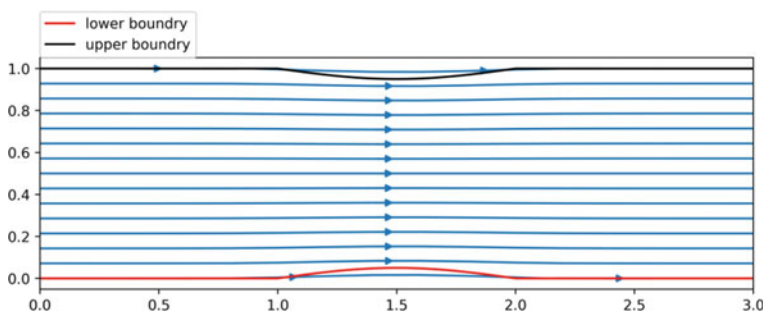


**Fig. 2** The streamline while  $M_{\infty} = 0.3$ ,  $\beta = 0.05$

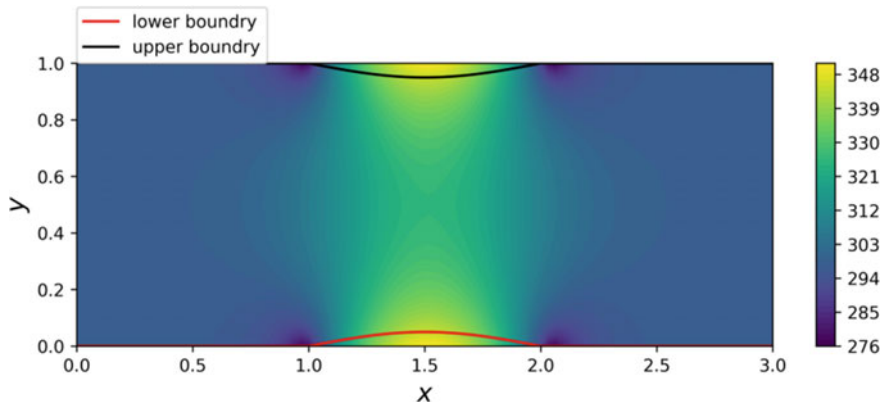


**Fig. 3** The velocity contour plot while  $M_{\infty} = 0.3$ ,  $\beta = 0.05$

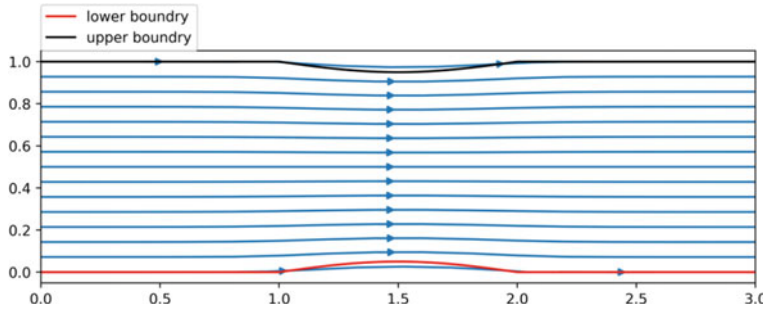


**Fig. 4** The streamline while  $M_{\infty} = 0.3$ ,  $\beta = 0.1$

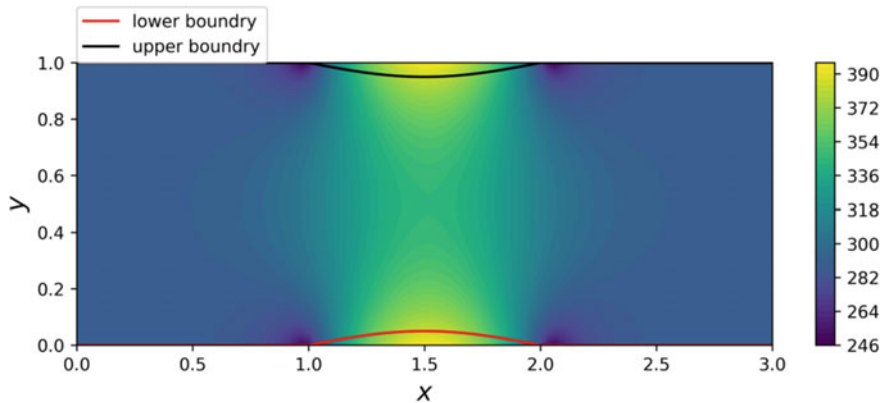


**Fig. 5** The velocity contour plot while  $M_{\infty} = 0.3$ ,  $\beta = 0.1$

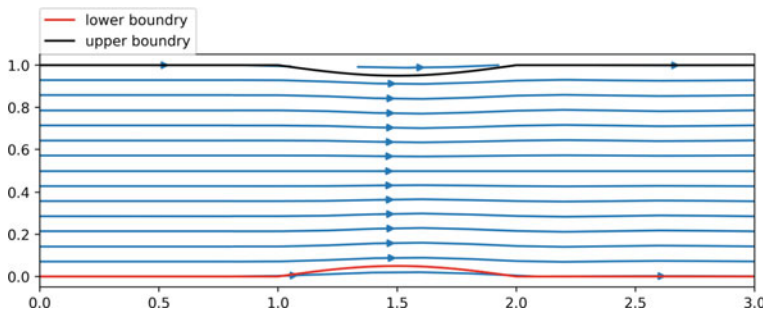


**Fig. 6** The streamline while  $M_{\infty} = 1.3$ ,  $\beta = 0.05$

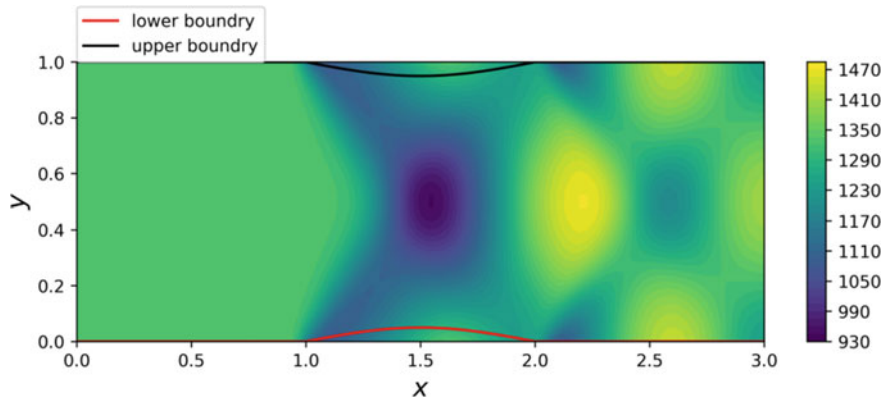


**Fig. 7** The velocity contour plot while  $M_{\infty} = 1.3$ ,  $\beta = 0.05$

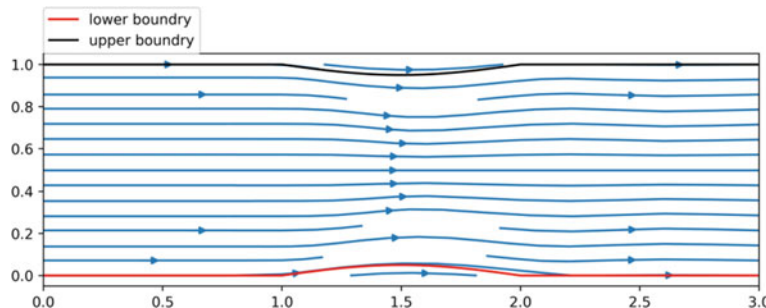


**Fig. 8** The streamline while  $M_{\infty} = 1.3$ ,  $\beta = 0.1$

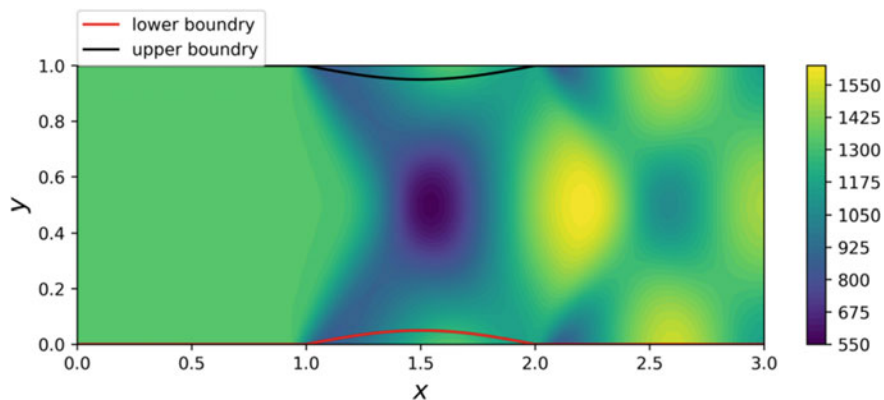


**Fig. 9** The velocity contour plot while  $M_{\infty} = 1.3$ ,  $\beta = 0.1$

### 4.3 The Accuracy

To verify the accuracy of the results, after several times of iterations, the final velocity potential will be substituted into the original equation to get the error term. Definitely, with high accuracy, the error will become really small. With the variation of the relaxation factor, the error will finally converge in different numbers with different times of iteration (Tables 1 and 2).

**Table 1** Subsonic case

Beta	Relaxation factor	Times of iteration	Error
0.05	1.9	2300	2.0e-13
0.05	1.6	9800	8.0e-14
0.05	1.3	21,000	2.6e-15
0.05	1(Gauss–Seidel method)	40,800	2.4e-15
0.1	1.9	2300	2.0e-13
0.1	1.6	11,000	8.0e-14
0.1	1.3	22,000	2.3e-15
0.1	1(Gauss–Seidel method)	41,800	2.5e-15

**Table 2** Supersonic case

Beta	Relaxation factor	Times of iteration	Error
0.05	1.4	170	0.08
0.05	1.3	190	8.30e-06
0.05	1.2	200	3.7e-14
0.05	1.1	250	4.0e-14
0.05	1 (Gauss–Seidel method)	330	4.2e-14
0.1	1.4	160	0.08
0.1	1.3	200	5.8e-11
0.1	1.2	200	3.6e-14
0.1	1.1	250	3.9e-14
0.1	1 (Gauss–Seidel method)	330	3.9e-14

## 5 Conclusion

In the subsonic case, the fastest speed can be observed near the perturbed boundary which is just under the speed of sound. By contrast, the minimum speed can be found at the beginning and end of the perturbation around 260 m/s.

In the supersonic case, the minimum speed is in the middle of the area.

With a slightly increase of the perturbation in the boundary (through changing beta in the boundary function), the velocity in the whole area changes slightly as well.

A suitable relaxation factor can both guarantee accuracy and increase the speed of iteration.

## References

1. Lopez-Acosta NP, Gonzalez-Acosta JL (2015) Study of water flow in dams using successive over-relaxation. *Tecnología y Ciencias del Agua* 6(5):43–58
2. Li J, Xin Z, Yin H (2013) Transonic shocks for the full compressible euler system in a general two-dimensional de laval nozzle. *Arch Ration Mech Anal* 207(2):533–581
3. Zhao yang S, Feng H, Jiancheng YU (2022) Influence of autonomous sailboat dual-wing sail interaction on lift coefficients. *J Ocean Univ China: Engl Ed* 21(3):13
4. Wu P, He YG, Fang GF (2013) An ameliorative algorithm of two-dimensional Poisson equation based on genetic parallel successive over-relaxation method. *Acta Phys Sin-Chin Ed* 62(2):709–712
5. Liang J, Zhang G, Qin Y (2022) Simulated analysis on nozzle dynamic characteristics based on high-order WENO scheme. *J Rocket Propuls* 20:15–19
6. Cao GY, Hill DJ (2010) Power system voltage small-disturbance stability studies based on the power flow equation. *Gener Transm Distrib Let* 4(7):873–882
7. Kagawa M (2013) A study on the meter-out velocity control of a pneumatic cylinder consideration of air temperature change effects. *Hydraul Pneum* 545:225
8. Gang L (2021) The convergence analysis of the successive over relaxation iterative method based on different splitting forms. *Henan Sci* 20(4):12–21
9. Leer BV (2009) Towards the ultimate conservative difference scheme III. Upstream-centered finite-difference schemes for ideal compressible flow-science direct. *J Comput Phys* 23(3):263–275
10. Virieux J (2017) P-SV wave propagation in heterogeneous media; velocity-stress finite-difference method. *Geophysics* 51:1933–1942

# On Optimal Tooth Profile Modification of Helical Gears Based on High Precision FEM



Yanping Liu, Yongqiang Zhao, and Changzhan Xue

**Abstract** Tooth profile modification (TPM) optimization design has got extensive attention in the design of gear system. To ensure the accuracy of the tooth contact analysis (TCA) and the optimization of the modification parameters, the paper established a 3D finite element model (FEM) of the helical gear with TPM. Loaded TCA and stress calculations of helical gears are carried out precisely. The effects of the modification parameters on transmission error (TE), mesh stiffness, tooth bending, and contact stress of the helical gear are analyzed. The tooth surface modification optimization is conducted. The results indicate that the optimized modification parameters can greatly improve the smoothness of gear transmission, which lays the foundation for the design of low vibration and noise transmission system.

**Keywords** Helical gear · FEM · Profile modification · Tooth contact analysis

## 1 Introduction

Modern industries such as aircraft, ships, and automobiles require mechanical transmission devices to develop in the direction of heavy load and high speed. As the primary means of vibration and noise reduction, tooth surface modification can greatly improve the transmission stability and contact mechanical properties of the gear system. Currently, the commonly used modification methods mainly include involute profile modification, longitudinal modification, and comprehensive modification (Fig. 1).

---

Y. Liu (✉)

Shandong University of Science and Technology, 579 Qianwangang Road, Qingdao, China  
e-mail: [liuyanpingsd@126.com](mailto:liuyanpingsd@126.com)

Y. Zhao

Harbin Institute of Technology, Nan Gang District, 92 West Dazhi Street, Harbin, China

C. Xue

Beijing Jingneng Energy Technology Research Co. Ltd., Beijing, China

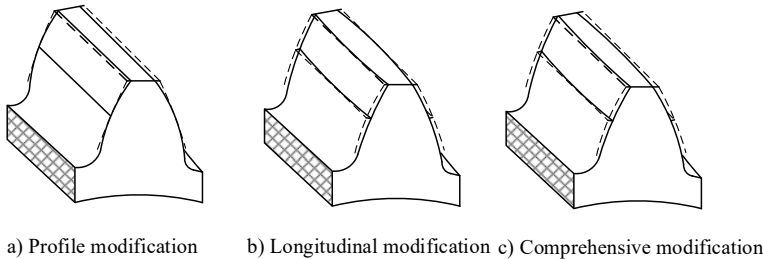


**Fig. 1** Three tooth surface modification methods of helical gear

For different modification methods, domestic and foreign scholars have conducted extensive research and achieved abundant results. Walker [1] pointed out the characteristic that the gear load changes in a step shape, and firstly proposed a gear modification technique. Based on the established 2D FEM, Wang [2] analyzed the effect of different modification amounts on the TE and mesh stiffness. Tavakol [3] measured the noise and vibration of the gear with involute modification and analyzed the effects of the tooth surface modification on the dynamic characteristics of the system. Lin [4] adopted the gear dynamics model with different modification parameters to calculate the TE and dynamic load distribution. The results indicated that the quadratic curve can adapt to a larger load working range with smaller TE. Aiming to minimize the harmonic component combination of static TE, Faggioni [5] optimized the modification types, length, and amount. To optimize the performance of vibration and noise reduction of spur gears, Bonori [6] used genetic algorithm to get the optimal modification amount and modification length of tooth tip and root. Based on two-dimensional and three-dimensional nonlinear FEM, Wagaj [7] investigated the effects of TPM parameters on the contact stress and bending stress of gears, which pointed out that by optimizing the modification parameters, the bending stress and contact stress could be greatly reduced, and the reliability of the gears could be improved. Based on the contact FEM, Wu [8] determined the parameters of the parabolic profile modification according to the deflections of the loaded gear in static state. Kortaa [9] studied the application of the response surface method in the micro-modification optimization of the spur gear tooth surface, and conducted the micro-modification optimization of the profile with the goal of minimizing the TE.

However, due to the accuracy of the gear FEM and the difficulty of element refinement, there are currently few studies on tooth surface modification based on the FEM. When the refined FEM of the gear is adopted for the contact analysis of the modified tooth surface, a gap or cut-in appears between the two tooth surfaces due to the tooth surface modification or installation error, making the finite element contact calculation difficult to converge. To ensure the accuracy of the results of contact analysis with profile modification, it's necessary to perform TCA before the finite element loaded TCA to eliminate the effect of clearance.

Based on the TCA and the FEM, this study established a high-precision three-dimensional FEM of the helical gear with surface modification. Tooth contact analyses of helical gears are carried out. Accurate TE and time-varying meshing stiffness were obtained by calculation, which provides reliable excitation parameters for subsequent dynamic characteristic analysis.

## 2 Parameters of TPM

The profile modification curve is the curve when the profile modification amount measured along the meshing line changes from the maximum modification amount  $C_a$  to 0. Currently, three kinds of modification methods are commonly used: linear modification, arc modification, and parabolic modification. This study adopts the parabolic modification as the final modified tooth profile curve. Its curve equation is

$$\delta = C_a \left[ (1 - a) \frac{x}{L} + a \left( \frac{x}{L} \right)^2 \right] \quad (1)$$

where  $\delta$  is the modification amount corresponding to the point on the meshing line whose length is  $x$  from the starting point;  $x$  is measured along the meshing line, the relative position on the modified tooth relative to the lowest point of the modification;  $L$  is the modification length measured along the meshing line;  $a$  is the parabolic modification coefficient. Spur gears usually take  $a = 0.56$ . Helical gears and herringbone gears usually take  $a = 1$ .

As a comparison, the linear modification curve used in this study is

$$\delta = C_a \left( \frac{x}{L} \right)^e \quad (2)$$

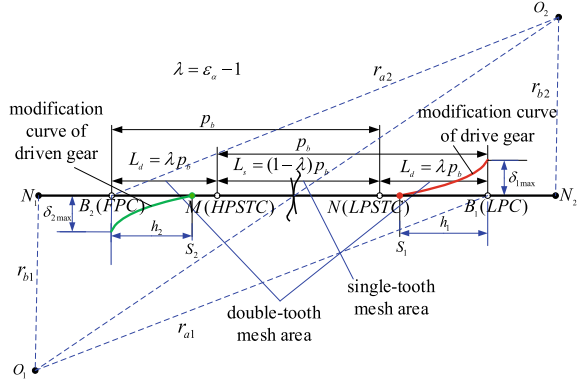
The maximum modification amount of the gear is obtained through comprehensive calculation. Then, based on this modification amount, the optimal modification amount is obtained by optimization

$$\Delta_{\max} = \delta + \delta_m + \delta_T \quad (3)$$

where  $\delta$  is the elastic deformation,  $\delta_m$  is the machining error and  $\delta_T$  is thermal deformation as follows, in which  $\Delta_\theta$  is the temperature difference between two gears, 5–10 °C in general, and  $\gamma$  is the linear expansion coefficient of material,  $\gamma = 12e^{-6}/^{\circ}\text{C}$  for steel.

$$\delta_T = \pi m_n \cos \alpha \cdot \Delta_\theta \cdot \gamma \times 10^3 (\mu\text{m}) \quad (4)$$

The TPM parameters are shown in Fig. 2.  $\varepsilon_a$  is transverse contact ratio;  $r_{bi}$  and  $r_{ai}$  are the base circle radius and tip circle radius, respectively;  $p_b$  is the length of the basal

**Fig. 2** TPM parameters

segment;  $\delta_{i \max} (i = 1, 2)$  is the maximum modification amount;  $h_i$  is the modification length;  $N_1$  and  $N_2$  are limit meshing points;  $B_1$  and  $B_2$  are the intersection points of the addendum circle and the contact line, which are the meshing start point (FPC) and end point (LPC);  $M$  is the starting point of the one tooth mesh area (HPSTC), and  $N$  is the end point of the one tooth mesh area (LPSTC);  $S_1$  and  $S_2$  are the starting points of the tip modification of gear 1 and gear 2 on the meshing line, respectively.

### 3 TPM Parameters Optimization

To facilitate the analysis of the effect of modification on gear mesh performance, the dimensionless maximum modification value and modification length coefficient of tooth profile are taken as  $C_n$  and  $L_n$ , respectively

$$\begin{cases} C_n = C_a/m_t \\ L_n = \alpha_a/\alpha_H \end{cases} \quad (5)$$

where  $m_t$  is the end module,  $\alpha_a$  is the pressure angle where the modification starts and  $\alpha_H$  is the pressure angle of the highest meshing point of single mesh area.

To analyze the effects of the maximum tip-relief on TE, long modification method is adopted for tip relief. When the dimensionless maximum modification amount is  $C_n = 0 - 0.01$ , the parametric modeling method [10] is used to establish a refined FEM of the helical gear including TPM (Fig. 3).

The effects of the profile modification on the TE are shown in Fig. 4. For linear modification and parabolic modification, when the modification length is constant, the TE decreases first and then raise with the increase of modification amount. The change of linear modification is more rapidly than that of parabolic modification. When the starting point of modification is the alternate meshing point of one and double teeth ( $L_n = 1$ ), the optimal modification amount of linear modification is

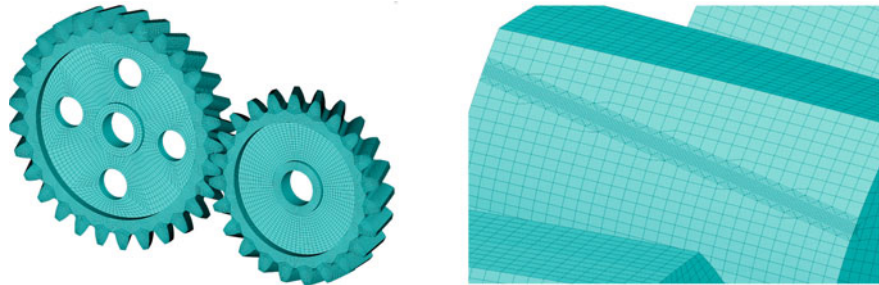


**Fig. 3** FEM of helical gear

$C_n = 0.001$  to get the minimum TE, which is  $0.45 \mu m$ . The optimal modification amount of parabolic modification is  $C_n = 0.003$  and the TE amplitude is  $0.18 \mu m$ . Because the linear modification has a second-order mutation at the transition position between the original and the modified surfaces, the contact stress is larger than that of the parabolic modification. Therefore, it is necessary to perform smooth processing at the alternate position of the modified and unmodified tooth profile, otherwise parabolic modification is better.

Compared with the linear modification, the parabolic modification of the tooth profile is less sensitive to the changes of load, modification quantity and length. The modification starts from the end of the one tooth contact range of the gears. The optimum modification amount is taken as  $C_n = 0.003$ , and the maximum modification amount is  $C_{a\min} = 13 \mu m$ . Since the normal modulus is  $m_n=4$ , the comprehensive involute error, the base circle deviation, and the tooth thickness error of the gear is taken as  $12 \mu m$ ; the maximum of the modification on the addendum is no more than  $25 \mu m$ ; the corresponding maximum modification amount coefficient is  $C_n = 0.005$ . Thus, according to the rebounding deformation modification and

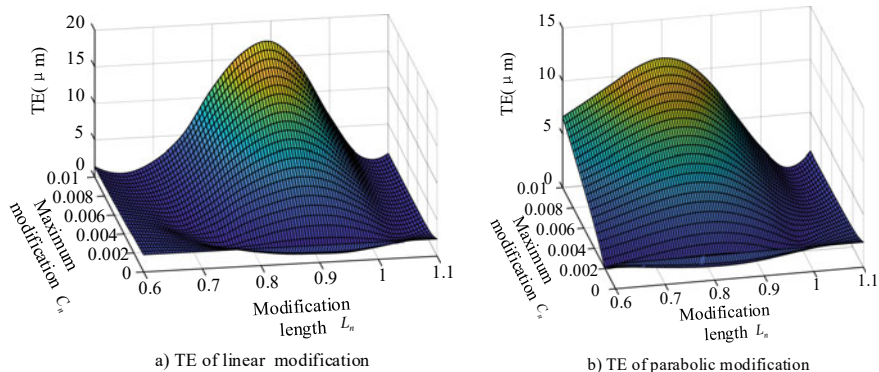


**Fig. 4** The effects of the modification on the TE

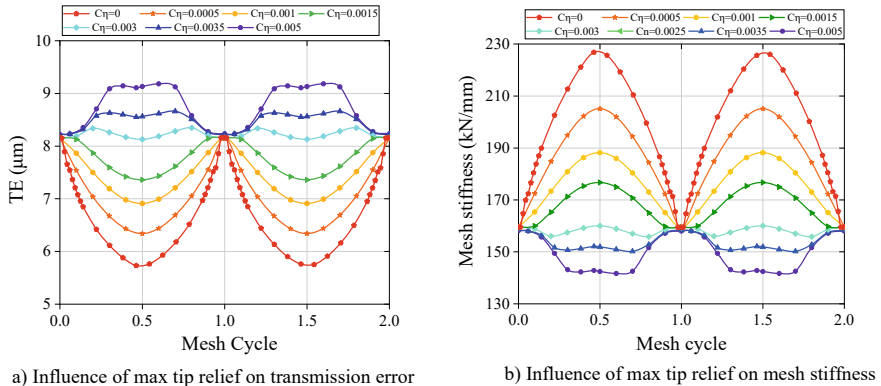


**Fig. 5** Influence of modification on TE and mesh stiffness

considering the influence of error, the value range of the maximum modification amount is determined as  $13 \mu\text{m} < C_a < 25 \mu\text{m}$ .

## 4 Loaded Tooth Contact Analysis

### 4.1 Influence of TPM on TE and Meshing Stiffness

The TE of two meshing periods under different modification quantities shown in Fig. 5a indicates that with the increase of the maximum modification, the TE decreases and becomes smoother. However, as the modification amount continues to increase, the TE of the double-toothed area is larger than that of the single-tooth area, the fluctuation of the TE curve increases. When the dimensionless maximum modification amount is  $C_n = 0.003$ , the TE is the smallest, and the TE curve of the entire meshing period is the smoothest.

The meshing stiffness is shown in Fig. 5b. Due to the overlapping degree, there is almost no non-load TE when the long tip relief is used. Therefore, the meshing stiffness is also the smoothest at this time, which is beneficial to reduce the vibration of the entire transmission system.

### 4.2 The Influence of TPM on Contact Stress and Bending Stress

When the tooth tip is not modified, since the tooth tip is involved in the contact, the contact stress of the entire meshing period on the gear teeth is shown as the red curve ( $C_n = 0$ ) in Fig. 6a. Due to the participation of the tooth tip edge in contact, the

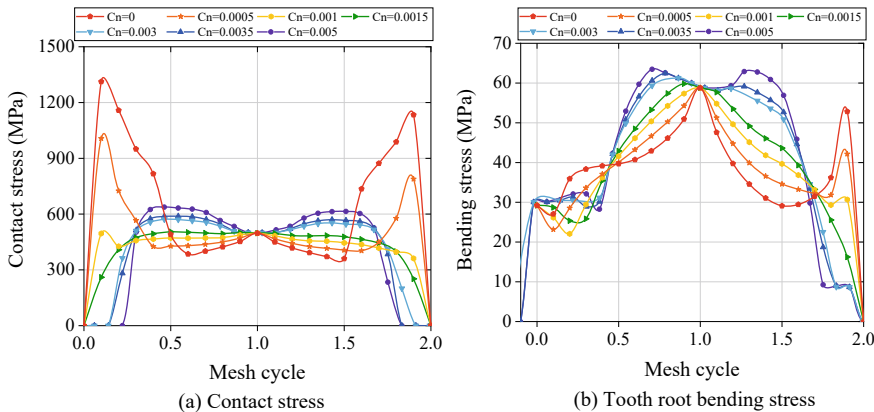


**Fig. 6** Effect of the max tip relief on contact stress and bending stress

meshing-in and meshing-out impact occurs. Then, edge contact occurs, and the tooth surface stress increases sharply, even exceeding 2 times the theoretical calculation value of the tooth surface contact stress. This causes the premature occurrence of fatigue pitting and fatigue spalling on the tooth surface, seriously affecting the service life of gears.

The tooth contact stress with different modifications is shown in Fig. 6a. As can be seen that different modification amounts not only affect the period of gear teeth entering and exiting meshing but also have a greater impact on the tooth contact stress. When the maximum modification amount is  $C_n < 0.001$ , since the modification amount is smaller than the deflection of the tooth under the current load, the tip contact still exists, and the local high stress state caused by the edge contact cannot be eliminated. When the modification amount is  $C_n = 0.0015$ , the maximum contact stress in the entire period is 505.3 MPa; no tip contact is observed; and the contact stress fluctuates relatively smoothly throughout the contact period. With the increase of modification amount, the double-toothed meshing area decreases, and the maximum contact stress increases. When the maximum modification amount is  $C_n = 0.005$ , the maximum contact stress is 637.4 MPa, which is about 26% larger than that of  $C_n = 0.0015$ . Therefore, under low-speed working conditions, the optimal dimensionless maximum modification amount is  $C_n = 0.0015$ .

Figure 6b shows the bending stress of the modified and unmodified gears. The unmodified gear teeth share the load on the gear teeth due to the entry of the adjacent gear teeth. Hence, the bending stress is smaller than the modified gear. When the tooth tip is modified, the single-tooth area increases; the tooth surface load is mainly borne by the loaded gear teeth; and the tooth root bending stress is greater than the unmodified gear. With the reduction of the modification amount, the tooth surface load can be distributed more to the adjacent gear teeth. Thus, the bending stress decreases with the reduction of the modification quantity. However, when the

modification amount ( $C_n \leq 0.001$ ) is too small, the tooth tip comes into contact, and the tooth root bending stress also increases.

## 5 Conclusions

A high-precision 3D FEM of the helical gear with TPM is established to conduct the tooth contact analysis and profile modification optimization. The influence of modification parameters on TE and meshing stiffness is investigated, and the tooth surface modification optimization is performed with the aim of minimizing the TE and meshing stiffness fluctuation. Through the modification, the non-ideal contact state is eliminated, the impact and edge contact stress are reduced, and the bearing capacity of the gear is improved. Meanwhile, the TE and the excessive fluctuation amplitude of meshing stiffness caused by excessive modification can be also avoided.

**Acknowledgements** The authors gratefully acknowledge the support of the Qingdao Postdoctoral Application Research Project. The authors also gratefully acknowledge the support of the “Key Laboratory of Helicopter Transmission Technology” of Nanjing University of Aeronautics and Astronautics through grant number HTL-O-19G08.

## References

1. Walker H (1938) Gear tooth deflection and profile modification. *Engineer* 166(4318):409–412
2. Wang J (2003) Numerical and experimental analysis of spur gears in mesh. Curtin University of Technology, Australia, pp 49–120
3. Tavakoli MS, Houser DR (1986) Optimum profile modifications for the minimization of static transmission errors of spur gears. *J Mech Des* 108(1):86–95
4. Lin HH, Townsend DP, Oswald FB (1987) Profile modification to minimize spur gear dynamic loading
5. Faggioni M, Samani FS, Bertacchi G et al (2011) Dynamic optimization of spur gears. *Mech Mach Theory* 46(4):544–557
6. Bonori G, Barbieri M, Pellicano F (2008) Optimum profile modifications of spur gears by means of genetic algorithms. *J Sound Vib* 313(3–5):603–616
7. Wagaj P, Kahraman A (2002) Influence of tooth profile modification on helical gear durability. *ASME J Mech Des* 124(9):501–510
8. Wu Y, Wang J, Han Q (2012) Static/dynamic contact FEA and experimental study for tooth profile modification of helical gears. *J Mech Sci Technol* 26(5):1409–1417
9. Korta JA, Mundo D (2017) Multi-objective micro-geometry optimization of gear tooth supported by response surface methodology. *Mech Mach Theory* 109:278–295
10. Liu Y, Zhao Y, Liu M et al (2019) Parameterized high-precision finite element modelling method of 3D helical gears with contact zone refinement. *Shock Vib* 2019:1–17

# Numerical Study on Atomization Process of Transverse Jet



Na Gao and Xiaobin Zhang

**Abstract** In order to deeply study the specific characteristics of the cross-scale phenomenon of fragmentation and atomization in the process of transverse jet atomization, this paper uses the LES turbulence model and the VTD multiphase flow model to numerically simulate the transverse jet process and analyzes the corresponding results. It can better solve the cross-scale related problems and then obtain a more suitable research method for the phenomenon of transverse jet fragmentation and atomization. The study found that the liquid column gradually narrowed along the jet direction under the action of the lateral airflow, and the liquid column was increased by the force of the lateral airflow, resulting in the expansion form of the liquid column being curved downstream. As soon as the jet enters the flow field, it forms independent droplets under the action of the air flow. With the passage of time, the stripped droplets are further broken up to form droplet particles, which are transformed from liquid phase to Lagrangian particle agglomerates. When the jet is fully developed, the surface of the liquid column is broken near the outlet to form small droplets, and then the jet is broken in a columnar shape to form a large number of ribbon-shaped liquid filaments.

**Keywords** VTD multiphase flow model · Numerical study · LES

---

N. Gao (✉)  
AVIC Aerodynamics Research Institute, Harbin 150001, China  
e-mail: [gn0427@163.com](mailto:gn0427@163.com)

Low Speed High Reynolds Number Aeronautical Key Laboratory, Harbin 150001, China

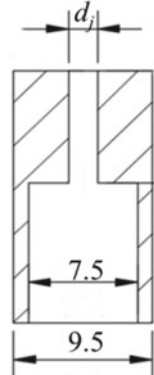
X. Zhang  
College of Aerospace and Civil Engineering, Harbin Engineering University, Harbin 150001,  
China

## 1 Introduction

As the core product of hypersonic propulsion technology, scramjet has excellent performance at high flight Mach number, so it has become the first choice of hypersonic vehicle propulsion system. Due to the high gas velocity and limited combustor length in the scramjet combustion chamber, the fuel stays in the supersonic combustion chamber for a short time. There are jet crushing and atomization processes in the combustion of liquid hydrocarbon fuel, and the ignition delay time is long. The realization of efficient atomization and good mixing is the necessary condition to ensure the stable and full combustion of fuel. The good injection characteristics and atomization quality of liquid fuel directly determine the combustion efficiency of scramjet engine. Therefore, it is necessary to study the mechanism of jet crushing process, and then establish the atomization model to predict the combustion performance of scramjet engine.

Herrmann [1] first proposed a multi-scale simulation method based on Level Set; Kim [2] used an improved Level Set method to directly solve the two-phase fluid, and when the closed interface volume is less than 2 times the cell, the droplet is converted to LPT droplets, so as to realize the conversion of Euler phase to discrete items; Tomar [3] also used similar methods and added mesh adaptation. Based on the open-source software Gerris, considering the liquid film breaking and droplet fusion process, a multi-scale simulation of atomization breakage was carried out using the method of two-way coupling of VOF model and LPT model. Madsen [4] et al. used two turbulence models combined with two two-phase flow models to compare and study centrifugal swirl pressure nozzles and found that the simulation results of the coupled VOF model were closer to reality under the assumption of laminar flow. LES combined with VOF model has obvious effects in simulating free shear flow and capturing phase interface. Liu [5] also used LES combined with VOF model to achieve the function of capturing large-size liquid filament droplets. At the same time, the LPT method was used to track the droplets that exist in the flow field smaller than the grid size; in the discrete droplet tracking based on the Euler-Lagrange framework, Shafaei [6] used OpenFOAM software to study the jet atomization phenomenon of the nozzle. Among them, the Rosin-Rammler distribution function was used for the primary fragmentation of the liquid jet; in the secondary fragmentation stage, K-H, R-T, KH-RT, and TAB models are compared. The simulation results show that the KH-RT model has reasonable atomization characteristics. Later, Yang [7] also implemented a new algorithm through OpenForm software, which is to couple the convection algorithm with the LPT method to optimize the conversion process from continuous phase large droplets to LPT discrete droplet particles. Broumand [8, 9] used the hybrid Euler-Lagrange method to establish a liquid jet trajectory model in the subsonic cross-flow of gas and studied the effect of the jet Reynolds number on the liquid column shedding mass and atomization height. The form of logarithmic function establishes the relational expression of predicting liquid column and droplet plume area respectively. In order to verify the prediction model of the liquid column trajectory in the transverse jet established in the previous study, Broumand [10] also

**Fig. 1** Nozzle structure  
(unit: mm)<sup>[self-drawn]</sup>



studied some near-field characteristics of the transverse liquid jet in the subsonic uniform cross-flow through experimental results, such as jet structure, columnar. The prediction results of trajectory and fracture length are basically consistent with experimental data and empirical formulas.

## 2 Numerical Simulation Method

### 2.1 Physical Model and Meshing

In this paper, the experiment of Broumand [10] is used as the background, and the size of the computational domain is taken as  $140 \times 140 \times 10$  mm, and the feasibility of the cross-scale model in the process of transverse jet atomization and crushing is studied. The boundary conditions are taken as the working conditions in the test: the air flow velocity is 65 m/s, the N8 nozzle (Fig. 1), the nozzle diameter  $d_j = 2$  mm,  $L$  is 8 mm, the cavity diameter is 7.5 mm, and the water at the outlet of the water nozzle is 7.5 mm. The speed is 12 m/s. According to the flow rate, the inlet speed at the bottom of the nozzle is set to 0.8533 m/s. The physical properties of air and water are parameters under standard conditions. The mesh adopts a structured mesh, and the vicinity of the nozzle and the inside of the nozzle are locally refined, and the mesh division is shown in Fig. 2.

### 2.2 Mathematical Model

The specific expression form of the cross-scale VTD model applied in this paper is as follows.

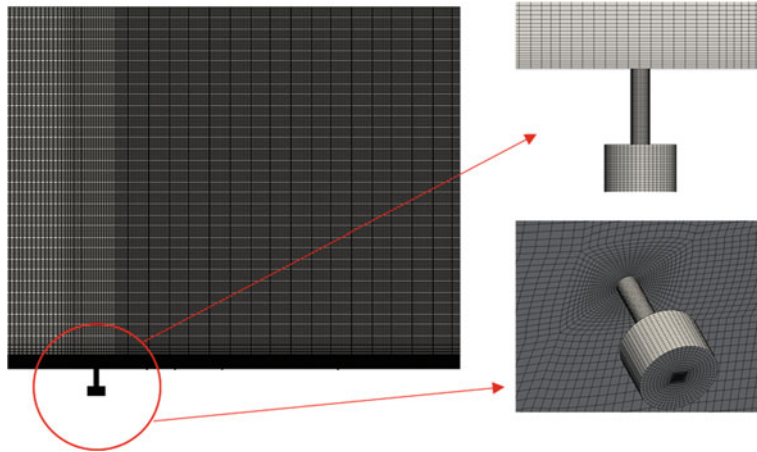


**Fig. 2** Meshing<sup>[self-drawn]</sup>

Let the main phase be air and the secondary phase be water, then there are the following three possibilities according to the existence of the  $\alpha$  value:

$\alpha = 1$ , Grid cells are all liquid phase;

$0 < \alpha < 1$ , Gas-liquid interface exists in grid cells;

$\alpha = 0$ , No liquid phase exists in grid cells. The transport equation of volume content can be expressed as:

$$\frac{\partial}{\partial t}(\tilde{\alpha}\bar{\rho}) + \nabla(\tilde{\alpha}\bar{\rho}u) = 0 \quad (1)$$

Among them,  $\tilde{\alpha}$  represents the volume fraction of liquid in the calculation grid. Equations (2) and (3) represent fluid density and viscosity, respectively.

$$\bar{\rho} = (1 - \tilde{\alpha})\rho_g + \tilde{\alpha}\rho_l \quad (2)$$

$$\bar{\mu} = (1 - \tilde{\alpha})\mu_g + \tilde{\alpha}\mu_l \quad (3)$$

In the secondary crushing stage, the motion equation of the discrete phase particles can be obtained by solving the momentum equation.

$$\frac{du_p}{dt} = F_D(u - u_p) + \frac{g(\rho_p - \rho)}{\rho_p} + F \quad (4)$$

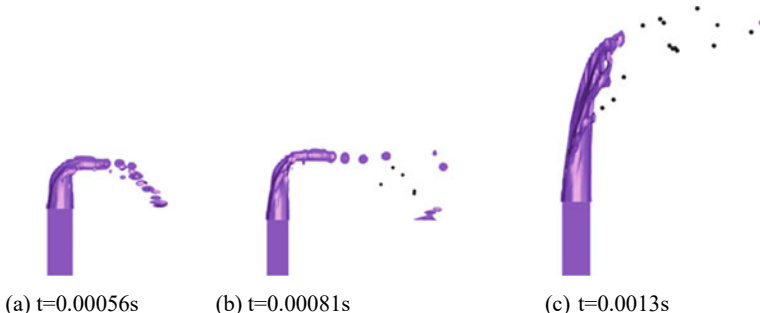
$$F_D = 18\mu C_D Re_p / (24\rho_p d_p^2) \quad (5)$$

Among them,  $u_p$ ,  $\rho_p$ , and  $d_p$ , respectively, represent the velocity, density, and particle size of the discrete item droplet particles,  $Re_p$  represents the liquid Reynolds number,  $F$  represents other forces, and drag coefficients  $C_D$ .

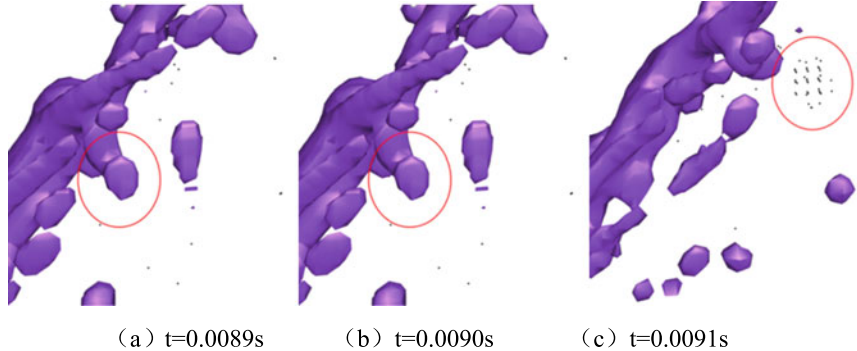
### 3 Computational Results and Analysis

Figure 3a–c shows the process of the liquid column gradually narrowing along the jet direction under the action of the lateral airflow. Combined with the side view in Fig. 7, it can be seen that the liquid column gradually widens in the y-axis direction, and the windward side increases. The lateral airflow is blocked by the liquid column, and the velocity in the stagnation zone is 0, which causes the pressure on the liquid column on the windward surface to increase. The column is squeezed so that the liquid column becomes wider and thinner. As the deformation of the liquid column intensifies, the force of the lateral airflow increases, which causes the expansion of the liquid column to bend downstream.

The main function of the VTD model in the jet problem is to study the primary and secondary fragmentation processes. Figure 4 shows the process of droplets from deforming and peeling to complete fragmentation. From Fig. 4a, it can be seen that the jet just enters the flow field. Independent droplets are formed under the action of the airflow. The analysis shows that the airflow is blocked by the liquid column to form a high-pressure zone, and flows to the side of the liquid column along the direction of the two-phase interface, causing the liquid column to be shared by the air and the surface is broken and peeled. Thus forming independent droplets peeled from the surface of the liquid column. The volume equivalent sphere size of these first stripped droplets is much smaller than the liquid column. When  $t = 0.0091$  s, the stripped droplets are further broken to form droplet particles. The volume equivalent sphere size has met the transformation requirements of VTD. This droplet will no longer be recognized by VOF, and thus transform from the liquid phase to pull Agglomerates of Grange particles.



**Fig. 3** The droplet peeling process in the initial stage<sup>[self-drawn]</sup>



**Fig. 4** Fracture process of droplet peeling<sup>[self-drawn]</sup>

It can be seen from the label in Fig. 4a that the liquid column has been constricted, and the droplets in Fig. 4b formally fall off, and the fallen droplets in Fig. 4c disappear and are replaced by a large number of droplet particles. At the moment when the liquid column breaks, the flow field parameters change greatly. Observing the changes in the flow field is beneficial to the study of jet atomization and fragmentation. Figures 5, 6 and 7, respectively, show the velocity vector distribution, z-axis direction velocity distribution, and pressure distribution where the liquid column breaks. In Fig. 5, the lateral velocity of the airflow is blocked at the constriction of the liquid column. After the liquid column is broken, the lateral airflow will flow around the ends of the exfoliated droplets.

Figure 8 shows the distribution of the liquid mist when the jet is fully developed. Figure 8a shows the complete liquid mist distribution of the lateral jet numerical simulation under the VTD model. The black particles represent the DPM droplet

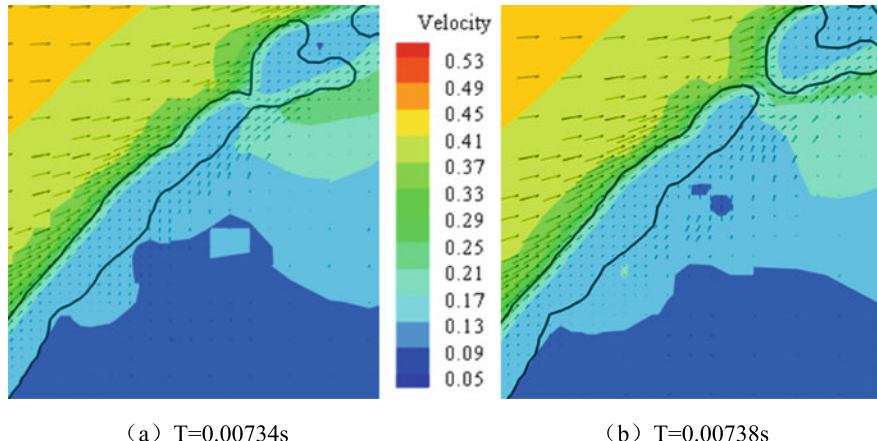


**Fig. 5** Velocity (unit: m/s) vector distribution in the x-axis direction<sup>[self-drawn]</sup>

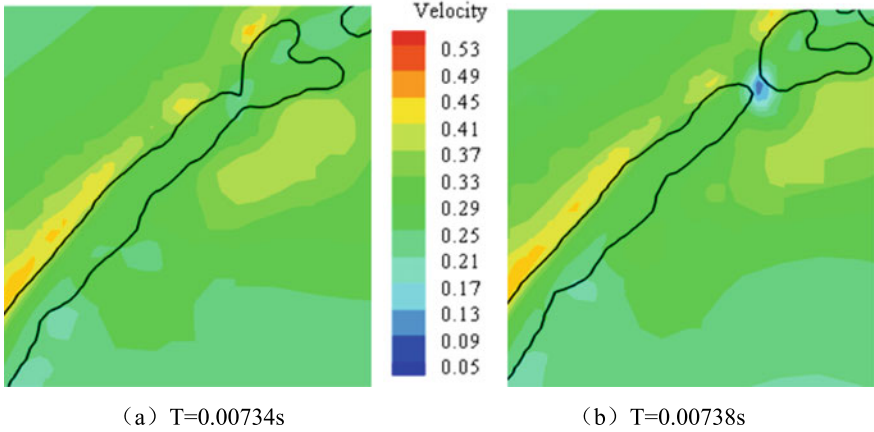


**Fig. 6** Velocity (unit: m/s) distribution in the z-axis direction<sup>[self-drawn]</sup>

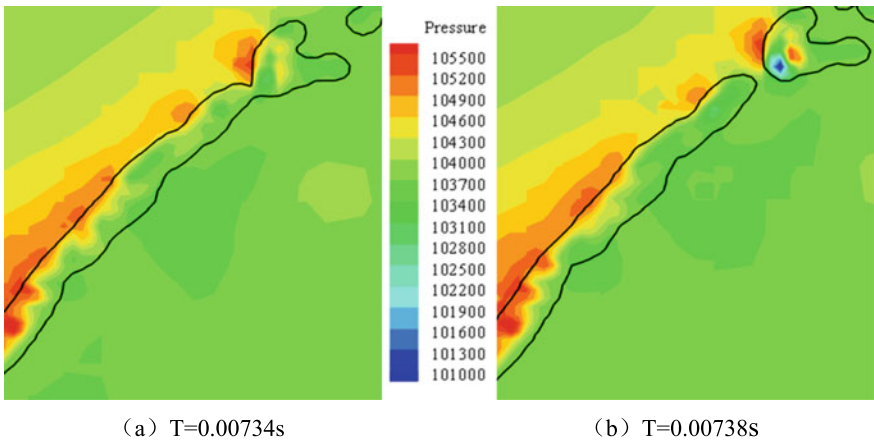


**Fig. 7** Pressure (unit: Pa) distribution<sup>[self-drawn]</sup>

particles; Fig. 8b is a single schematic diagram showing the distribution of the liquid phase of the VOF, including the main liquid column of the jet and the droplets formed by one break; Fig. 8c is a schematic diagram showing the particle distribution of DPM droplets alone, which is composed of the second droplet fragmented. The liquid column is broken near the outlet to form small droplets, and then the jet column breaks to form a large number of ribbon-like liquid filaments. There are a large number of droplet particles produced by secondary crushing under the main flow of the column, and the number of droplets increases with Fig. 8b.

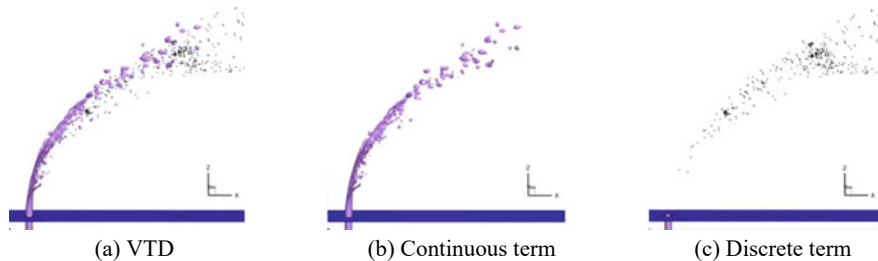


**Fig. 8** Liquid mist distribution at the fully developed stage<sup>[self-drawn]</sup>

## 4 Conclusion

Based on the adaptive mesh technology of phase gradient, VTD model can well simulate the transverse jet droplet breaking process, that is, it can study the primary and secondary crushing process and show the droplet's process from deformation spalling to complete crushing. The distribution of liquid mist when the jet is fully developed is given.

## References

1. Herrmann M (2005) Refined level set grid method for tracking interfaces. Ann Res Briefs 3–18
2. Kim D, Herrmann M, Moin P (2006) The breakup of a round liquid jet by a coaxial flow of gas using the refined level set grid method. In: 59th Annual meeting of the APS division of fluid dynamics, pp FB-010. Bull Am Phys Soc Florida
3. Tomar G, Fuster D, Zaleski S et al (2010) Multiscale simulations of primary atomization. Comput Fluids 39(10):1864–1874
4. Madsen J, Hjertager BH, Solberg T (2004) Numerical simulation of internal flow in a large-scale pressure-swirl atomiser. ILASS-Europe 183–188
5. Liu C, Lei F, Zhou L (2014) A new multiscale simulation method for primary atomization. J Natl Univ Defense Technol 36(3):25–31
6. Shafaei M, Mahmoudzadeh S (2017) Numerical investigation of spray characteristics of an air-blast atomizer with dynamic mesh. Aerosp Sci Technol 70:351–358
7. Yang D (2018) Numerical simulation method of supersonic two-phase combustion based on flamelet model. Dissertation, Harbin Engineering University
8. Broumand M, Birouk M (2015) A model for predicting the trajectory of a liquid jet in a subsonic gaseous crossflow. Atom Sprays 25(10):871–893
9. Broumand M, Birouk M (2016) Two-zone model for predicting the trajectory of liquid jet in gaseous crossflow. AIAA J 54(5):1499–1511
10. Broumand M, Birouk M (2017) Effect of nozzle-exit conditions on the near-field characteristics of a transverse liquid jet in a subsonic uniform cross airflow. Phys Fluids 29(11):113303

# Mechanism of Collision and Adhesion Between Adhesive Impact Ball and Spacecraft



Bingyu Xu, Shuquan Wang, and Liping Zhao

**Abstract** In the non-cooperative space object close-proximity tracking problem, a method of utilizing an impact ball to collide with the object is proposed to change the angular momentum and estimate the inertial parameters of the object. This paper investigates the mechanism of the collision and the adhesion between the impact ball and the spacecraft are studied. Firstly, the structure of the impact ball is analyzed. The impact ball is designed as a rubber ball with a radius of 20 mm. The surface of the ball is a bionic Parthenocissus structure. The sponge-like hole of the structure contains bionic mussel secretion with high adhesion. Secondly, the minimum relative velocity of the impact ball penetrating the spacecraft is calculated. When the relative velocity of the impact ball is less than the minimum relative velocity, the spacecraft will not be penetrated by the ball. Finally, the adhesion performance of the impact ball after the collision is analyzed. Numerical calculation shows that after the collision, the maximum adhesion force is greater than the maximum rebound force. The impact ball can adhere to the surface of the spacecraft after the collision.

**Keywords** Impact ball · Penetrating velocity · Adhesion analysis

## 1 Introduction

In the close-proximity tracking missions of non-cooperative spacecraft [1–3], the identification of the inertial parameters of the non-cooperative spacecraft is a crucial problem. The difficulty is that if the inertial matrix of the object is not diagonal, six parameters of the inertial matrix cannot be estimated solely relying on vision. To increase the excitation information in the identification, reference [4] proposed the

---

B. Xu · S. Wang (✉) · L. Zhao

Technology and Engineering Center for Space Utilization, Chinese Academy of Sciences, Beijing, China

e-mail: [shuquan.wang@csu.ac.cn](mailto:shuquan.wang@csu.ac.cn)

B. Xu

University of Chinese Academy of Sciences, Beijing, China

method of using an impact ball to collide with the object and change the angular velocity of the object. In reference [4], the impact ball was assumed to be ejected from the tracking spacecraft, and adhere to the surface of the object after the collision. In this paper, the mechanism of the impact ball and essentially how it adheres to the spacecraft after the collision are analyzed.

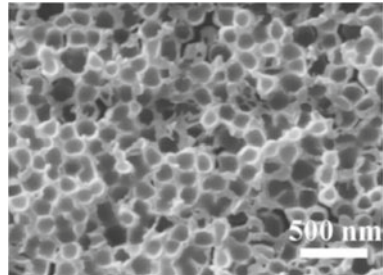
The materials used in spacecrafts mainly include aluminum alloy, titanium alloy, and glass fiber-reinforced plastic. In this paper, it is assumed that the outer shell of the spacecraft is made of aluminum alloy. After the collision between the impact ball and the spacecraft, the impact ball is required to adhere to the aluminum alloy surface of the object. Some bionic materials with adhesion are being investigated to make impact balls. According to the contact type between the organism and the object, the adhesive bionic structure can be divided into two types. One type is bristle adhesion, and the other is epidermal pad adhesion.

In the type of bristle adhesion, the adhesion force depends on the van der Waals force between the bristle structure and the surface of the object. The gecko is a typical creature that relies on bristle adhesion and friction force to crawl on the ceiling and vertical walls. Based on this principle, researchers have made some bionic gecko structures. Mo et al. [5] designed the bionic gecko foot by fusing polyurethane and silicone rubber, which had high adhesion and low elastic modulus. Sitti [6] cast the artificial bristles by fusion of the silicone rubber and polyimide, and the adhesion force of each bristle reached 100nN.

The principle of the type of epidermal pad adhesion is that when the organism contacts an object, the epidermal pad can be extended and generate some secretory fluid to the end of the adhesion pad. Secretory fluid plays an important role in the adhesion mechanism. Ants, tree frogs, and Parthenocissus belong to the type of epidermal pad adhesion. Zhou et al. [7] designed an ant-like adhesion structure. The material of the structure was silica gel, and the pattern of the structure was designed as a surface with grooves and pits. Honey water was selected as the secretory fluid. Wu et al. [8] selected organic silica gel to make the bionic tree frog paw material. The adhesion performance of the material is very similar to that of the skin tissue of the tree frog. He et al. [9, 10] selected polystyrene as the bionic material and developed columnar and spongy structures, which are similar to the structure of the Parthenocissus chuck. The surface configuration of the structure is shown in Fig. 1. In addition to the bionic structure, many adhesive materials have been developed in the industry and can be used as secretion in epidermal pad adhesion. Kinloch et al. [11] found that the adhesive strength of epoxy resin in carbon fiber composites was up to 100 MPa. Waite et al. [12, 13] designed the anti-mussel material. The adhesion force of the anti-mussel material in slate reached 8.5 GPa.

As discussed above, a variety of materials and structures can be used to design the adhesive impact ball. In this paper, the material and structure of the impact ball are discussed at first. Then, to prevent the ball from puncturing the spacecraft after the collision, the minimum relative velocity of the ball is obtained through theoretical calculation. If the relative velocity of the ball is less than the minimum punctured velocity, the spacecraft will not be punctured after the collision. Finally, the adhesion mechanism of the impact ball after the collision is studied.

**Fig. 1** The surface configuration of the Parthenocissus-like structure



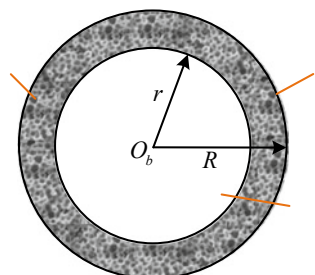
## 2 Material and Structure of the Impact Ball

This section discusses the material and structure of the impact ball. According to literature research, the type of bristle adhesion depends on the structure of the surface of the object. If the bristle adhesion structure is used in the design of the impact ball, it will be difficult for the impact ball to be ejected from the launching structure. Therefore, the skin pad adhesion principle is adopted to design the impact ball.

The intersecting surface of the impact ball is shown in Fig. 2. The rubber material with viscoelasticity is selected as the manufacturing material. The radius  $R$  of the impact ball is set as 20 mm. The surface of the ball is set as a spongy bionic Parthenocissus structure as designed in reference [9], and the spongy interior is wrapped with an adhesive secretion. Biomimetic mussel material with high adhesive capacity as designed in reference [13] is selected as the secretion. After the collision between the ball and the spacecraft, the pressure increases and the rubber ball deforms to increase the contact area. At the same time, the secretion flows out to increase the adhesive force.

To ensure that the impact ball adheres to the surface of the spacecraft after the collision, the adhesion force brought by the secretion should be greater than the maximum rebound force after the collision. The adhesion capacity of the impact ball is analyzed in Sect. 4. The rebound force is related to the relative velocity. So, the minimum relative velocity of the ball when the spacecraft is punctured by the ball is calculated in Sect. 3 at first.

**Fig. 2** Intersecting surface of the impact ball



### 3 Impact Penetration Analysis

After the collision, the ball may puncture the spacecraft if the relative velocity of the ball is too fast. If the thickness of the spacecraft shell is given, whether the spacecraft is punctured is affected by the kinetic energy of the impact ball. In this section, the minimum relative velocity when the impact ball punctures the spacecraft after the collision is calculated. If the initial relative velocity is less than the threshold, the spacecraft will not be punctured.

It is assumed that the outer shell of the spacecraft is made of aluminum alloy, and the impact ball is made of rubber. The performances of the aluminum alloy shell and the rubber ball are shown in Table 1.  $l_t$  is the thickness of the aluminum alloy shell.  $R_b$  is the radius of the rubber ball. BHN is the Brinell thickness of the aluminum alloy shell.  $\rho_t$  is the density of the aluminum alloy shell.  $\rho_b$  is the density of the rubber ball.  $E$  represents the elastic modulus of the aluminum alloy shell.

The impact kinetic energy of the ball is set as  $E_b$ . In references [14, 15], the relationship between the thickness of the aluminum alloy shell  $l_t$  and the impact kinetic energy  $E_b$  is given as:

$$l_t = 9.43d_b^{(1/18)} BHN^{-0.25} \left(\frac{\rho_b}{\rho_t}\right)^{0.5} \left(\frac{1}{C}\right)^{2/3} \left(\frac{12}{\pi\rho_b}\right)^{1/3} (E_b)^{1/3} \quad (1)$$

where  $d_b$  is the diameter of the rubber ball, and  $C$  is the sound velocity in the aluminum alloy shell and is calculated by:

$$C = \sqrt{E/\rho_t} \quad (2)$$

Derived from Eq. (1), the expression of  $E_b$  is written as:

$$E_b = \frac{l_t^3}{9.43^3 d_b^{(1/6)} BHN^{-0.75} \left(\frac{\rho_b}{\rho_t}\right)^{1.5} \left(\frac{1}{C}\right)^2 \left(\frac{12}{\pi\rho_b}\right)} \quad (3)$$

The relationship between the impact kinetic energy  $E_b$  and the impact relative velocity  $v_0$  is written as:

**Table 1** Material properties of aluminum alloy shell and rubber ball

Aluminum alloy shell	Value	Rubber ball	Value
$l_t$ (mm)	0.1	$R_b$ (mm)	20
BHN(MPa)	196	–	–
$\rho_t$ ( $\text{kg}/\text{m}^3$ )	2700	$\rho_b$ ( $\text{kg}/\text{m}^3$ )	0.93
$E$ (GPa)	70	–	–

**Table 2** Summary of parameters in Sect. 3

Parameter	$C$ (m/s)	$E_b$ (J)	$m_b$ (kg)	$v_0$ (m/s)
Value	5092	0.1055	$3.12 \times 10^{-5}$	82.27

$$E_b = \frac{1}{2} m_b v_0^2 \quad (4)$$

where  $m_b$  represents the mass of the impact ball and is calculated by:

$$m_b = \rho_b V_b = \frac{4\pi}{3} \rho_b R_b^3 \quad (5)$$

where  $\rho_b$  is the density of the rubber ball, and  $V_b$  represents the volume of the impact ball.

Derived from Eq. (4), the relative velocity  $v_0$  is calculated by:

$$v_0 = \sqrt{2 E_b / m_b} \quad (6)$$

The numerical results of  $C$ ,  $E_b$ , and  $m_b$  are summarized in Table 2. Substituting the values of  $E_b$  and  $m_b$  into Eq. (6), the value of  $v_0$  is obtained:

$$v_0 = 82.27 \text{ m/s} \quad (7)$$

It means that the spacecraft, with a single-layer and 0.1 mm thickness aluminum alloy shell, is punctured if the relative velocity of the ball is larger than 82.27 m/s.

## 4 Analysis of Adhesion Mechanism After Collision

In this section, the adhesion mechanism of the impact ball after the collision is analyzed. According to the principle of epidermal pad adhesion, adhesive secretion plays an important role in the adhesion mechanism. To ensure that the impact ball adheres to the surface of the spacecraft after the collision, the adhesion force between the ball and the spacecraft should be larger than the maximum rebound force after the collision. In this section, the maximum rebound force between the impact ball and the aluminum alloy shell is calculated at first. Then the adhesive mechanism brought by the secretion inside the ball is analyzed.

## 4.1 Rebound Force

The process of an elastic collision can be divided into two phases. The first phase is from the contact between two objects to the maximum compression deformation of the object, which is called the compression phase. The second phase is from the recovery of compression deformation to the end of the collision, which is called the recovery phase. Since the design scenario in this paper is that the ball adheres to the surface of the object after the collision, only the maximum rebound force in the compression phase is calculated in this paper.

The time when the ball contacts the object is set as the initial time  $t_0$ . This section analyzes the maximum rebound force between two balls when  $t > t_0$  at first. Then the maximum rebound force between a ball and a plane is deduced. Finally, the maximum rebound force between the aluminum alloy shell and the rubber ball is obtained.

**Collision Between Two Balls.** The schematic diagram of the collision between two balls is shown in Fig. 3.  $O_1$  and  $O_2$  represent the center of the balls, respectively.  $R_1$  and  $R_2$  represent the radius of the balls, respectively.  $v_{r_0}$  is the initial relative velocity. The compression distance is written as  $\delta$ . The rebound force is written as  $F_R$ . When the maximum compression distance  $\delta_{\max}$  is reached, the contact area between two balls is a circle with the center of  $O_c$  and the radius of  $r_{\max}$ . In Fig. 3, four points ( $M_1$ ,  $M_2$ ,  $N_1$ , and  $N_2$ ) are used to show the outermost contact area between two balls when the compression distance is maximum.

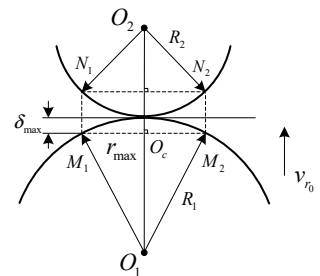
The relationship between the compression distance  $\delta$  and the contact force  $F_R$  is written as [16]:

$$\delta = \left( \frac{9\pi^2}{16} \frac{F_R^2 (k_1 + k_2)^2 (R_1 + R_2)}{R_1 R_2} \right)^{1/3} \quad (8)$$

where the expressions of  $k_1$  and  $k_2$  are:

$$k_1 = \frac{1 - \mu_1^2}{\pi E_1}, \quad k_2 = \frac{1 - \mu_2^2}{\pi E_2} \quad (9)$$

**Fig. 3** Collision between two balls



where  $\mu_1$  and  $\mu_2$  represent the Poisson's ratio of the balls,  $E_1$  and  $E_2$  represent the Young's modulus of the balls, respectively. Poisson's ratio and Young's modulus are physical quantities characterizing the properties of materials, which only depend on the material type.

Derived from Eq. (8), the contact force  $F_R$  is calculated by:

$$F_R = n\delta^{3/2} \quad (10)$$

where the expression of  $n$  is:

$$n = \frac{4}{3\pi(k_1 + k_2)} \sqrt{\frac{R_1 R_2}{R_1 + R_2}} \quad (11)$$

Integrating Eq. (8), the maximum compression distance  $\delta_{\max}$  is deduced [17] and written as:

$$\delta_{\max} = \left( \frac{5M}{4n} v_{r_0}^2 \right)^{2/5} \quad (12)$$

where the expression of  $M$  is:

$$M = \frac{m_1 m_2}{m_1 + m_2} \quad (13)$$

where  $m_1$  and  $m_2$  are the mass of the balls, respectively.

Substituting Eq. (12) into Eq. (10), the maximum contact force between two balls is obtained:

$$F_{R\max} = n\delta_{\max}^{3/2} = n \left( \frac{5M}{4n} v_{r_0}^2 \right)^{2/3} \quad (14)$$

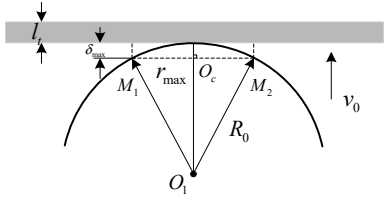
It can be seen from Eq. (14) that for inelastic collision, the collision contact force is related to the mass, radius, relative velocity, Young's modulus, and Poisson's ratio of the materials.

**Collision Between Ball and Plane.** The collision between an impact ball and an aluminum alloy plane is shown in Fig. 4. Some simplifications are used to derive the formula of the compression distance  $\delta$ :  $R_1 = R_0$ ,  $R_2 \rightarrow \infty$ ,  $m_1 = m_0$ ,  $m_2 = \infty$ ,  $v_{r_0} = v_0$ . Then the expression of the compression distance  $\delta$  is deduced and written as:

$$\delta = \left( \frac{9F_R^2}{16R_0} \left( \frac{1 - \mu_1^2}{E_1} + \frac{1 - \mu_2^2}{E_2} \right) \right)^{1/3} \quad (15)$$

The maximum compression distance  $\delta_{\max}$  is calculated by:

**Fig. 4** Collision between a ball and an aluminum alloy plane



$$\delta_{\max} = \left( \frac{5m_0}{4n_0} v_0^2 \right)^{2/5} \quad (16)$$

where the expression of  $n_0$  is:

$$n_0 = \frac{4\sqrt{R_0}}{3\pi(k_1 + k_2)} \quad (17)$$

So, the maximum contact force  $F_{R\max}$  is calculated by:

$$F_{R\max} = n_0 \delta_{\max}^{3/2} = n_0 \left( \frac{5m_0}{4n_0} v_0^2 \right)^{3/5} \quad (18)$$

According to the interaction of forces, the maximum rebound force is equal to the maximum contact force  $F_{R\max}$ .

**Maximum Rebound Force.** The material of the impact ball is chosen as rubber, and the material of the spacecraft shell is assumed to be aluminum alloy. The material properties of the aluminum alloy shell and the rubber ball [18] are shown in Table 3. Substituting the values of  $E_1$ ,  $\mu_1$ ,  $E_2$  and  $\mu_2$  into Eq. (9), the values of  $k_1$  and  $k_2$  are obtained:

$$\begin{aligned} k_1 &= 3.54 \times 10^{-8} \text{ m}^2/\text{N} \\ k_2 &= 4.05 \times 10^{-12} \text{ m}^2/\text{N} \end{aligned} \quad (19)$$

The radius of the impact ball is set as 20 mm, then  $R_0 = 0.02\text{m}$ . Substituting the values of  $R_0$ ,  $k_1$ , and  $k_2$  into Eq. (17), the value of  $n_0$  is obtained:

$$n_0 = 1.69 \times 10^6 \text{ N/m}^{3/2} \quad (20)$$

**Table 3** Material properties of rubber and aluminum alloy

Rubber ball	Value	Aluminum alloy	Value
$E_1$ (GPa)	0.007	$E_2$ (GPa)	70
$\mu_1$	0.47	$\mu_2$	0.33
–	–	$v_0$ (m/s)	5

**Table 4** Summary of parameters in Sect. 4

Parameter	$k_1$ (m <sup>2</sup> /N)	$k_2$ (m <sup>2</sup> /N)	$n_0$ (N/m <sup>3/2</sup> )	$F_{R\max}$ (N)
Value	$3.54 \times 10^{-8}$	$4.05 \times 10^{-12}$	$1.69 \times 10^6$	4.84

Numerical results of the parameters in this section are summarized in Table 4. According to Sect. 3, when the relative velocity of the impact ball is less than 82.27 m/s, the spacecraft will not be punctured. In this paper, the initial relative velocity is assumed as 5 m/s. The mass of the impact ball can be obtained from Table 2:  $m_0 = 3.12 \times 10^{-5}$  kg. Substituting the values of  $n_0$ ,  $m_0$ , and  $v_0$  into Eq. (18), the value of  $F_{R\max}$  is obtained:

$$F_{R\max} = 4.84 \text{ N} \quad (21)$$

It can be seen from Eq. (21), the maximum rebound force between a rubber ball, with the radius of 20 mm, and a spacecraft, made of a 0.1 mm thickness aluminum alloy shell, is 4.84 N. To ensure that the ball adheres to the surface of the spacecraft after the collision, the maximum adhesion force of the secretion must be larger than the maximum rebound force. In the following context, the maximum adhesion force is calculated.

## 4.2 Adhesion Force

In the type of epidermal pad adhesion, the epidermal pad is generally a viscoelastic material. When the contact force increases, the pad is deformed and the contact area increases. The maximum adhesion force  $F_{A\max}$  is equal to the product of the maximum contact area  $S_{\max}$  and the adhesion pressure  $P$ :

$$F_{A\max} = S_{\max} P \quad (22)$$

As shown in Fig. 4, the radius of the maximum contact area is written as  $r_{\max}$ . The maximum contact area  $S_{\max}$  is calculated by:

$$S_{\max} = \pi r_{\max}^2 = \pi (R_0^2 - (R_0 - \delta_{\max})^2) \quad (23)$$

Substituting Eq. (16) into Eq. (23), the value of  $S_{\max}$  is obtained:

$$S_{\max} = 2.52 \times 10^{-5} \text{ m}^2 \quad (24)$$

The bionic mussel material in reference [13] is selected as the secretion of the impact ball. It means the value of  $P$  is obtained:

$$P = 8.5 \text{GPa} = 8.5 \times 10^5 \text{N/m}^2 \quad (25)$$

Substituting Eqs. (24) and (25) into Eq. (22), the value of  $F_{A\max}$  is obtained:

$$F_{A\max} = 21.39 \text{N} \quad (26)$$

As can be seen from Eqs. (21) and (26), the maximum rebound force  $F_{R\max}$  is 4.84N, and the maximum adhesion force  $F_{A\max}$  is 21.39N. The maximum adhesion force is larger than the maximum rebound force. Therefore, the impact ball can adhere to the surface of the spacecraft after the collision under given conditions.

## 5 Conclusion

This paper investigates the mechanism of the collision and the adhesion between the impact ball and the spacecraft. To ensure that the impact ball will not puncture the spacecraft and can adhere to the surface of a spacecraft after the collision, the material and structure of the impact ball are analyzed and designed in this paper. In summary, the impact ball is designed as a ball with a radius of 20 mm. The material of the ball is chosen as rubber, and the structure of the ball is designed as a bionic Parthenocissus structure. The bionic mussel material with high adhesion is placed inside the ball and used as the secretion to increase the adhesion. Assuming that the spacecraft shell is made of aluminum alloy and the thickness of the aluminum alloy is larger than 0.1 mm, the minimum relative velocity when the impact ball punctures the spacecraft shell is 82.27 m/s. If the relative velocity is less than 82.27 m/s, the spacecraft will not be punctured. The relative velocity of the impact ball is assumed to be 5 m/s. At the moment, the maximum adhesion force after the collision is larger than the maximum rebound force. As a conclusion, the impact ball can adhere to the surface of the spacecraft after the collision.

**Acknowledgements** This work was supported by the Pathfinding project of Chinese Academy of Sciences under grant number XDA30010500 and the National Natural Science Foundation of China under grant number 61903354.

## References

1. Zhu L, Wang S (2021) Rotating object rotating object specific tracking based on orbit-attitude coordinated adaptive control. *J Guid Control Dyn* 44(2):266–282
2. Mao Q, Wang S (2019) Arbitrary angular separation relative motion in near-circular orbits with similar periods. *J Guid Control Dyn* 42(8):1709–1725
3. Ji M, Wang S, Zhao Z (2018) Synchronized attitude and position control for spacecraft tracking non-cooperative space object. In: 2018 IEEE/CSAA guidance, navigation and control conference, August 10–12, Xiamen, China

4. Xu B, Wang S (2017) Vision-based moment of inertia estimation of non-cooperative space object. In: 10th International symposium on computational intelligence and design, Hangzhou, China, December 9–10
5. Guidong M (2008) Bionics research on adhesive material of gecko-like robot sole. Nanjing University of Aeronautics and Astronautics. (In Chinese)
6. Sitti M (2003) High aspect ratio polymer micro/nano-structure manufacturing using nanoembossing, nanomolding and directed self-assembly. In: Proceedings of the 2003 IEEE/ASME international conference on advanced intelligent mechatronics, Kobe, Japan
7. Zhou Q (2008) Research on driving principle and mechanical modeling of bionic micro wet Sucion robot. Tongji University. (In Chinese)
8. Bin W (2010) Preparation and mechanical properties of bionic viscous materials. Nanjing University of Aeronautics and Astronautics. (In Chinese)
9. Tianxian H (2012) Study on the adhesion of Parthenocissus sucker. South China University of Science and Engineering. (In Chinese)
10. Li Z (2014) Isolation, purification, structural characterization and adhesion properties of Parthenocissus suction cup polysaccharide. South China University of Science and Engineering. (In Chinese)
11. Kinloch AJ (1987) Adhesion and adhesives: science and technology. Chapman and Hall, London
12. Lee H, Lee BP, Messersmith PB (2007) A reversible wet/dry adhesive inspired by mussels and geckos. *Nature* 448:338–341
13. Waite JH (1987) Nature's underwater adhesive specialist. *ChemTech* 17:692–697
14. Gongshun G, Xunyang D, Guan H (2018) Protection performance of double-wall structure of Al-plate subjected to impact effect of Hig velocity projectiles based on kinetic energy dissipation. *Chin J Mater Res* 32(4):241–246
15. Wang Y, Cao X, Chen H (2015) Evaluation of measurement uncertainty in Brinell hardness test of aluminum alloy materials. *Phys Exam Test* 33(4):14–16
16. Broberg KB (1956) Shock waves in elastic and elastic-plastic media. Stockholm
17. Cai Z, Yang C (1995) Theoretical calculation and measurement of collision time between a ball and a plate. *Lab Res Explor* 3:28–31. (In Chinese)
18. Bangguo L (2001) Quantitative calculation of collision during collision. *J Nantong Inst Technol* 17(4):7–9 (In Chinese)

# A Pose Calibration Method for Serial Robots Considering Joint Variables



Lu Yang and Xiaoliu Yu

**Abstract** The kinematic parameter error of serial robots is the main factor affecting their positioning accuracy, while kinematic parameter calibration is one of the effective methods to improve their positioning accuracy. This paper explores the calibration method for the positioning accuracy of end-effector of serial robots, to provide a calibration method including joint screw and joint variables. First, an actual kinematic model in exponential form is established in comprehensive considerations of kinematic parameter errors. Second, by differentiating the kinematic model, the paper proposes the linearized model between pose error, joint screw error, and joint variable error of end-effector of serial robot. Finally, the calibration simulation test is carried out using an industrial robot. The experimental results show that this method can effectively improve the positioning accuracy of the end effector of the serial robot.

**Keywords** Kinematic parameter · Exponential product · Joint variable · Positioning accuracy

## 1 Introduction

Positioning accuracy remains an important indicator of evaluating the working performance of serial robots and contains repeated positioning accuracy and absolute positioning accuracy. Serial robots now have a great capacity for repeated positioning accuracy but perform worse in absolute positioning accuracy subject to comprehensive error caused by processing, assembly, wear and tear, and the weight and loading

---

Authors: Yang Lu (1983–), male, born in Changzhou, Jiangsu, postgraduate, studying robot learning

---

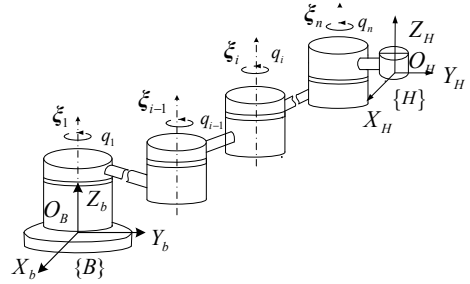
L. Yang (✉) · X. Yu  
School of Mechanical Engineering, Anhui University of Technology, Ma’anshan, China  
e-mail: [15984354@qq.com](mailto:15984354@qq.com)

of robots [1–3]. At present, kinematic parameter calibration is the most frequent approach to improving the absolute positioning accuracy of robots [4, 5].

D-H parametric method and exponential product equation are frequently used in research on the kinematic parameter calibration of serial robots. The calibration model is established based on D-H parametric method, but strangeness would occur when two adjacent joint axes of robots are parallel or nearly parallel. Some researchers tried to solve strangeness by including additional parameters, but these attempts resulted in new problems in the model, such as indirect deduction and complex forms [6–9]. In response to the problems mentioned above, this paper conducted relevant studies on kinematic parameter calibration based on exponential product equations. Since the exponential map from Lie Algebra to Lie Group is smooth and diffeomorphic in a small neighborhood, the kinematic model based on the exponential product is smooth and changing for joint movements, thus avoiding strangeness. In studies on kinematic parameter calibration, researchers suggested constructing a geometric error calibration model according to the kinematic equation of serial robots based on the Lie Algebra global exponential product equation. However, joint screw, joint variables, and initial pose error of the end-effector cannot be identified in sync in the error calibration model [10]. Besides, joint variable errors vary for the same serial robot, and this difference would cause greater positioning error in the end-effector in response to a robot's longer arms [11]. Meanwhile, the presence of joint variable errors on robots makes their corresponding joint axes inconsistent with Pippel rules; as a result, robot controllers cannot plan a precise motion trajectory for robots [10]. To solve these problems, scholars converted these identified geometric errors into joint variable errors to compensate for the pose error of robots and proposed a kinematic equation based on a global exponential product and an error compensation calibration model [12]. To meet the constraint conditions of robot joints, the calibration model was orthogonalized in the process of identifying kinematic parameters and did not calibrate robot poses on end.

Hence, this paper attributes robot joint variable errors to the system error on the ground that the joint variable error of serial robots remains unchanged in zero position and provides a pose error model containing joint screw and joint variable error. Moreover, the pose is made more accurate on the end-effector of the serial robot by updating the coordinate values of the joint screw through the adjoint matrix in the process of identifying kinematic parameters [13]. The error calibration model in exponential form is well-structured and user-friendly as an explicit expression. Pose calibration tests were performed using Robot KUKAKR500 and Industrial Robot HH150 to verify whether the model is effective and correct.

**Fig. 1**  $n$ -DOF serial robot  
[self-drawn]



## 2 Kinetic Model of Serial Robot

### 2.1 Theoretical Kinematic Model

The serial robot is shown in Fig. 1. A basic coordinate system  $\{B\}$  and a coordinate system  $\{H\}$  were established on the foundation and end respectively, the theoretical kinematic equation of a serial robot whose degree of freedom (DOF) was  $n$  is presented as follows:

$$f_{(q)}^n = e^{\hat{\xi}_1 q_1^n} e^{\hat{\xi}_2 q_2^n} e^{\hat{\xi}_3 q_3^n} \dots e^{\hat{\xi}_n q_n^n} f_{st} \quad (1)$$

Therein,  $\hat{\xi}_i$  stands for the robot's  $i$ -numbered joint screw,  $q_i^n$  for the robot's  $i$ -numbered joint variable, and  $f_{st}$  for the robot's pose matrix of end-effector in zero position. Equation (1) can be described by the exponential form of the initial transformation screw  $\xi_{st}$  as follows:

$$f_{(q)}^n = e^{\hat{\xi}_1 q_1^n} e^{\hat{\xi}_2 q_2^n} e^{\hat{\xi}_3 q_3^n} \dots e^{\hat{\xi}_n q_n^n} e^{\hat{\xi}_{st}} \quad (2)$$

### 2.2 Actual Kinematic Model

Serial robot in actual production is found with joint screw error, joint variable error, and initial pose error on the end. A serial robot is assumed with a joint variable error  $\delta q_i$  on the  $i$ -numbered joint to make the actual value of the joint screw deviate from the theoretical value, the same as adjoint transformation in Lie Group for joint screw [14] to conclude the equation below:

$$\begin{aligned}
\hat{\xi}_1^a &= \hat{\xi}_1 \\
\hat{\xi}_2^a &= \exp(\hat{\xi}_1 \delta q_1) \hat{\xi}_2 \exp(-\hat{\xi}_1 \delta q_1) \\
&= Ad \exp(\hat{\xi}_1 \delta q_1) \hat{\xi}_2 \\
&\dots \\
\hat{\xi}_n^a &= Ad \exp(\hat{\xi}_1 \delta q_1) \dots (\hat{\xi}_{n-1} \delta q_{n-1}) \hat{\xi}_n
\end{aligned} \tag{3}$$

Then the actual pose on the end-effector for the serial robot is:

$$\begin{aligned}
f_{(q)}^a &= e^{\hat{\xi}_1^a(q_1^a + \delta q_1^a)} e^{\hat{\xi}_2^a(q_2^a + \delta q_2^a)} e^{\hat{\xi}_3^a(q_3^a + \delta q_3^a)} \dots e^{\hat{\xi}_n^a(q_n^a + \delta q_n^a)} e^{\hat{\xi}_{st}} \\
&= e^{\hat{\xi}_1^a q_1^a} e^{\hat{\xi}_2^a q_2^a} e^{\hat{\xi}_3^a q_3^a} \dots e^{\hat{\xi}_n^a q_n^a} e^{\hat{\xi}_1^a \delta q_1^a} e^{\hat{\xi}_2^a \delta q_2^a} e^{\hat{\xi}_3^a \delta q_3^a} \dots e^{\hat{\xi}_n^a \delta q_n^a} e^{\hat{\xi}_{st}} \\
&= e^{\hat{\xi}_1^a q_1^a} e^{\hat{\xi}_2^a q_2^a} e^{\hat{\xi}_3^a q_3^a} \dots e^{\hat{\xi}_n^a q_n^a} e^{\hat{\Gamma}}
\end{aligned} \tag{4}$$

Therein,  $e^{\hat{\Gamma}} = e^{\hat{\xi}_1^a \delta q_1^a} e^{\hat{\xi}_2^a \delta q_2^a} \dots e^{\hat{\xi}_n^a \delta q_n^a} e^{\hat{\xi}_{st}}$  represents the actual value of poses.

According to Eq. (2) and Eq. (4), the initial pose error on the end of the serial robot can be regarded as a source of joint variable error. The joint axes of serial robots subject to geometric error lead to a deviation between the actual pose and the theoretical pose. The actual value  $\hat{\xi}_i^a$  and theoretical value  $\hat{\xi}_i^n$  can be described by the adjoint matrix of a certain rigid transformation  $e^{\hat{\eta}_i}$  [15] as follows:

$$\hat{\xi}_i^a = Ad(e^{\hat{\eta}_i}) \hat{\xi}_i^n \tag{5}$$

$$\text{Therein, } e^{\hat{\eta}_i} = \begin{bmatrix} R_{\eta_i} & p_{\eta_i} \\ 0 & 1 \end{bmatrix}, Ad(e^{\hat{\eta}_i}) = \begin{bmatrix} R_{\eta_i} & 0 \\ \hat{p}_{\eta_i} R_{\eta_i} & R_{\eta_i} \end{bmatrix} Ad(e^{\hat{\eta}_i}) = \begin{bmatrix} R_{\eta_i} & 0 \\ \hat{p}_{\eta_i} R_{\eta_i} & R_{\eta_i} \end{bmatrix}.$$

The screw coordinates of rotary joints, after being transformed by the adjoint matrix, should still meet the joint constraint conditions [16] below:

$$\|\omega_i^a\| = \|R_{\eta_i} \omega_i^a\| = \|\omega_i^n\| = 1 \tag{6}$$

$$(\omega_i^a)^T v_i^a = (R_{\eta_i} \omega_i^a)^T (\hat{p}_{\eta_i} R_{\eta_i} \omega_i^n + R_{\eta_i} v_i^n) = 0 \tag{7}$$

Hence, the actual kinematic model can be represented as:

$$\begin{aligned}
f_{(q)}^a &= Ad(e^{\hat{\eta}_1}) e^{\hat{\xi}_1^n q_1^a} Ad(e^{\hat{\eta}_2}) e^{\hat{\xi}_2^n q_2^a} Ad(e^{\hat{\eta}_3}) e^{\hat{\xi}_3^n q_3^a} \dots Ad(e^{\hat{\eta}_n}) e^{\hat{\xi}_n^n q_n^a} e^{\hat{\Gamma}} \\
&= e^{\hat{\eta}_1} e^{\hat{\xi}_1^n q_1^a} e^{-\hat{\eta}_1} e^{\hat{\eta}_2} e^{\hat{\xi}_2^n q_2^a} e^{-\hat{\eta}_2} e^{\hat{\eta}_3} e^{\hat{\xi}_3^n q_3^a} e^{-\hat{\eta}_3} \dots e^{\hat{\eta}_n} e^{\hat{\xi}_n^n q_n^a} e^{-\hat{\eta}_n} e^{\hat{\Gamma}}
\end{aligned} \tag{8}$$

### 3 Error Analysis of Serial Robot

#### 3.1 Error Model

Geometric error reaches 90% of total pose errors for serial robots in actual production [17]. The error model of the serial model can be generalized by differentiating the kinematic equation [18]:

$$\delta f f^{-1} = \left( \frac{\partial f}{\partial \xi} \delta \xi + \frac{\partial f}{\partial \xi_{st}} \delta \xi_{st} + \frac{\partial f}{\partial q} \delta q \right) f^{-1} \quad (9)$$

Since the robot's initial pose error on end can be regarded as a source of joint variable error, the POE-based error model for the serial robot can be altered as:

$$\delta f f^{-1} = \left( \frac{\partial f}{\partial \xi} \delta \xi + \frac{\partial f}{\partial q} \delta q \right) f^{-1} \quad (10)$$

The Actual Kinematic Model (8) is included in the Error Model (10) to obtain:

$$\begin{aligned} & (\delta f f^{-1})^\vee \\ &= \left( \delta \left( e^{\hat{\eta}_1} e^{\hat{\xi}_1^n q_1^a} e^{-\hat{\eta}_1} e^{\hat{\eta}_2} e^{\hat{\xi}_2^n q_2^a} e^{-\hat{\eta}_2} e^{\hat{\eta}_3} e^{\hat{\xi}_3^n q_3^a} e^{-\hat{\eta}_3} \dots e^{\hat{\eta}_n} e^{\hat{\xi}_n^n q_n^a} e^{-\hat{\eta}_n} e^{\hat{\Gamma}} \right) \right. \\ &\quad \left. \left( e^{\hat{\eta}_1} e^{\hat{\xi}_1^n q_1^a} e^{-\hat{\eta}_1} e^{\hat{\eta}_2} e^{\hat{\xi}_2^n q_2^a} e^{-\hat{\eta}_2} e^{\hat{\eta}_3} e^{\hat{\xi}_3^n q_3^a} e^{-\hat{\eta}_3} \dots e^{\hat{\eta}_n} e^{\hat{\xi}_n^n q_n^a} e^{-\hat{\eta}_n} e^{\hat{\Gamma}} \right)^{-1} \right)^\vee \\ &= \left( \delta \left( e^{\hat{\eta}_1} e^{\hat{\xi}_1^n q_1^a} e^{-\hat{\eta}_1} \right) \left( e^{\hat{\eta}_1} e^{-\hat{\xi}_1^n q_1^a} e^{-\hat{\eta}_1} \right) \right)^\vee \\ &\quad + Ad \left( e^{\hat{\eta}_1} e^{\hat{\xi}_1^n q_1^a} e^{-\hat{\eta}_1} \right) \left( \delta \left( e^{\hat{\eta}_2} e^{\hat{\xi}_2^n q_2^a} e^{-\hat{\eta}_2} \right) \left( e^{\hat{\eta}_2} e^{-\hat{\xi}_2^n q_2^a} e^{-\hat{\eta}_2} \right) \right)^\vee \\ &\quad + \dots + Ad \left( \prod_{i=1}^{n-1} e^{\hat{\eta}_i} e^{\hat{\xi}_i^n q_i^a} e^{-\hat{\eta}_i} \right) \left( \delta \left( e^{\hat{\eta}_n} e^{\hat{\xi}_n^n q_n^a} e^{-\hat{\eta}_n} \right) \left( e^{\hat{\eta}_n} e^{-\hat{\xi}_n^n q_n^a} e^{-\hat{\eta}_n} \right) \right)^\vee \end{aligned} \quad (11)$$

Therein:

$$\begin{aligned} & \left( \delta \left( e^{\hat{\eta}_i} e^{\hat{\xi}_i^n q_i^a} e^{-\hat{\eta}_i} \right) \left( e^{\hat{\eta}_i} e^{-\hat{\xi}_i^n q_i^a} e^{-\hat{\eta}_i} \right) \right)^\vee = \left( \delta \left( e^{\hat{\eta}_i} \right) e^{\hat{\xi}_i^n q_i^a} e^{-\hat{\eta}_i} \left( e^{\hat{\eta}_i} e^{-\hat{\xi}_i^n q_i^a} e^{-\hat{\eta}_i} \right) \right)^\vee \\ &+ \left( e^{\hat{\eta}_i} \delta \left( e^{\hat{\xi}_i^n q_i^a} \right) e^{-\hat{\eta}_i} \left( e^{\hat{\eta}_i} e^{-\hat{\xi}_i^n q_i^a} e^{-\hat{\eta}_i} \right) \right)^\vee + \left( e^{\hat{\eta}_i} e^{\hat{\xi}_i^n q_i^a} \delta \left( e^{-\hat{\eta}_i} \right) \left( e^{\hat{\eta}_i} e^{-\hat{\xi}_i^n q_i^a} e^{-\hat{\eta}_i} \right) \right)^\vee \\ &= \left( \delta \left( e^{\hat{\eta}_i} \right) \left( e^{-\hat{\eta}_i} \right) \right)^\vee + Ad \left( e^{\hat{\eta}_i} \right) \left( \delta \left( e^{\hat{\xi}_i^n q_i^a} \right) \left( e^{-\hat{\xi}_i^n q_i^a} \right) \right)^\vee \\ &- Ad \left( e^{\hat{\eta}_i} e^{\hat{\xi}_i^n q_i^a} e^{-\hat{\eta}_i} \right) \left( \delta \left( e^{\hat{\eta}_i} \right) \left( e^{-\hat{\eta}_i} \right) \right)^\vee \\ &= \left( I_6 - Ad \left( e^{\hat{\eta}_i} e^{\hat{\xi}_i^n q_i^a} e^{-\hat{\eta}_i} \right) \right) \left( \delta \left( e^{\hat{\eta}_i} \right) \left( e^{-\hat{\eta}_i} \right) \right)^\vee + Ad \left( e^{\hat{\eta}_i} \right) \left( \delta \left( e^{\hat{\xi}_i^n q_i^a} \right) \left( e^{-\hat{\xi}_i^n q_i^a} \right) \right)^\vee \end{aligned} \quad (12)$$

Therein, the explicit expression [19] of  $(\delta(e^{\hat{\eta}_i})e^{-\hat{\eta}_i})^\vee$  is:

$$\begin{aligned}
 & \left( \delta(e^{\hat{\eta}_i})e^{-\hat{\eta}_i} \right)^\vee \\
 &= (I_6 + \frac{4 - a_i \sin a_i - 4 \cos a_i}{2a_i^2} \Omega_i + \\
 & \quad \frac{4a_i - 5 \sin a_i + a_i \cos a_i}{2a_i^3} \Omega_i^2 + \\
 & \quad \frac{2 - a_i \sin a_i - 2 \cos a_i}{2a_i^4} \Omega_i^3 + \\
 & \quad \frac{2a_i - 3 \sin a_i + a_i \cos a_i}{2a_i^5} \Omega_i^4) \delta \eta_i \\
 &= k_i \delta \eta_i
 \end{aligned} \tag{13}$$

Therein,  $\Omega_i = \begin{bmatrix} \hat{\omega}_i & 0 \\ \hat{v}_i & \hat{\omega}_i \end{bmatrix}$ ,  $a_i = \|\omega_i\| = (\omega_{i_1}^2 + \omega_{i_2}^2 + \omega_{i_3}^2)^{1/2}$ ,  $\eta_i = \begin{bmatrix} \omega_i \\ v_i \end{bmatrix}$ .

Then the explicit expression of the linearized model of the kinematic equation containing joint constraint conditions is:

$$\begin{aligned}
 & (\delta f f^{-1})^\vee \\
 &= \left( I_6 - Ad\left(e^{\hat{\eta}_1} e^{\hat{\xi}_1^n q_1^a} e^{-\hat{\eta}_1}\right) K_1 \delta \eta_1 + Ad\left(e^{\hat{\eta}_1}\right) \xi_1^n \delta q_1 \right. \\
 & \quad \left. + Ad(C_i) \left[ \left( I_6 - Ad\left(e^{\hat{\eta}_2} e^{\hat{\xi}_2^n q_2^a} e^{-\hat{\eta}_2}\right) K_2 \delta \eta_2 + Ad\left(e^{\hat{\eta}_2}\right) \xi_2^n \delta q_2 \right] \right. \\
 & \quad \left. + \dots \right. \\
 & \quad \left. + Ad\left(\prod_{i=1}^{n-1} C_i\right) \left[ \left( I_6 - Ad\left(e^{\hat{\eta}_n} e^{\hat{\xi}_n^n q_n^a} e^{-\hat{\eta}_n}\right) K_n \delta \eta_n + Ad\left(e^{\hat{\eta}_n}\right) \xi_n^n \delta q_n \right] \right]
 \end{aligned} \tag{14}$$

Therein,  $C_i = e^{\hat{\eta}_i} e^{\hat{\xi}_i^n q_i^a} e^{-\hat{\eta}_i}$ ,  $\delta(e^{\hat{\xi}_i^n q_i^a})(e^{-\hat{\xi}_i^n q_i^a}) = \xi_i^n \delta q_i \delta(e^{\hat{\xi}_i^n q_i^a})(e^{-\hat{\xi}_i^n q_i^a}) = \xi_i^n \delta q_i$ .

When the actual pose value  $f_{(q)}^a$  and theoretical pose value  $f_{(q)}^n$  are approximate, the equation is:

$$\begin{aligned}
 [\delta f f^{-1}]^\vee &= \left[ (f_{(q)}^a - f_{(q)}^n) (f_{(q)}^n)^{-1} \right]^\vee \\
 &= \left[ f_{(q)}^a (f_{(q)}^n)^{-1} - I_4 \right]^\vee
 \end{aligned} \tag{15}$$

Linearized Eq. (14) can be described as the matrix below:

$$y = Hx \quad (16)$$

Therein,  $y = [\delta f f^{-1}]^\vee \in R^{6n}$ ;  
 $x = [\delta \eta_1^T, \delta \eta_2^T, \dots, \delta \eta_n^T, \delta q_i]^T \in R^{6n+1}$ ;  
 $H = [J_1, J_2 \dots J_n, J_{n+1}] \in R^{6 \times 6(n+1)}$ ;

The following shows the definition of matrix  $H$  in all sequences:

$$J_m = \begin{cases} [(I_6 - Ad(C_m))K_m, Ad(e^{\hat{\eta}_m})\xi_m^n] \\ Ad\left(\prod_{i=1}^{m-1} C_m\right)[(I_6 - Ad(C_m))K_m, Ad(e^{\hat{\eta}_m})\xi_m^n] \end{cases} \quad 1 < m \leq n$$

### 3.2 Identification of Error Model

The linearized equation in a matrix of k group is generalized as Eq. (16) by manipulating a serial robot into moving to the k-numbered calibration pose in the workspace for its actual pose. The combination of all equations leads to the kinematic parameter calibration equation:

$$Y = \begin{bmatrix} y_1 \\ y_2 \\ \vdots \\ y_k \end{bmatrix} = \begin{bmatrix} J_1 \\ J_2 \\ \vdots \\ J_k \end{bmatrix} x = J^* x \quad (17)$$

The least square method is used to solve  $x$  to obtain:

$$x = (J^{*T} J^*)^{-1} J^{*T} Y \quad (18)$$

The workflow of kinematic parameter calibration is illustrated in Fig. 2.

## 4 Simulation Test

### 4.1 Simulation: Robot KUKARK500

To verify the effectiveness and correctness of the kinematic calibration model for the serial robot, simulation tests were performed based on the model by calibrating and verifying Robot KUKAKR 500 whose DOF was 6. Specifically, 50 groups of joint variables were randomly generated in the robot's workspace and applied to the simulation test of kinematic parameter calibration. The theoretical and actual

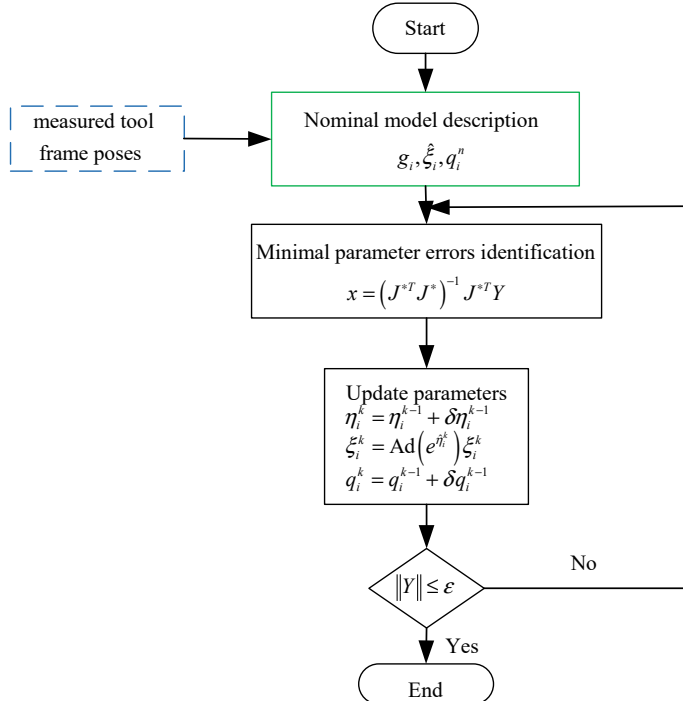


**Fig. 2** Workflow of parameter identification [self-drawn]

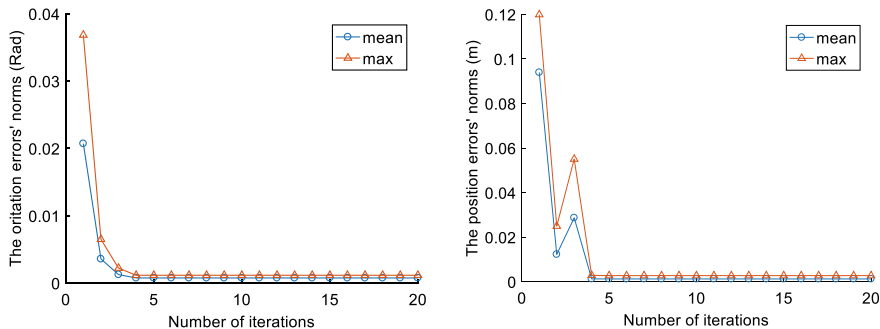
kinematic parameters as presented in Fig. 1 were put into Eq. (8), respectively, to calculate the theoretical and actual kinematic values of the robot pose of the end-effector, and the actual value was used as the measured value for the end-effector to calculate its pose error. Furthermore, the end-effector's pose volume and position volume were set in the evenly distributed noises  $[-0.001, 0.001]$  (rad) and  $[-0.1, 0.1]$  to simulate the actual measuring error. The results of kinematic parameters are shown in Table 1, and the pose error model and position error model are in the iterative process in Fig. 3. Sharp reductions were found in the pose error on the end of Robot Kukakr500.

#### 4.2 Simulation: Industrial Robot HH150

Industrial Robot HH150 was used to serve the calibration simulation test to verify that the kinematic calibration model can be applied widely. Specifically, 50 groups of joint variables were randomly generated in the robot's workspace and applied to the simulation test of kinematic parameter calibration. The theoretical and actual kinematic parameters as presented in Fig. 2 were put into Eq. (8), respectively, to

**Table 1** Results of parameter calibration [self-drawn]

Parameter	$\xi = [\xi_1 \ \xi_2 \ \xi_3 \ \xi_4 \ \xi_5 \ \xi_6]$	$\delta q$
Theoretical value	$\begin{bmatrix} 0 & 0 & 0 & -1 & 0 & -1 \\ 0 & 1 & 1 & 0 & 1 & 0 \\ -1 & 0 & 0 & 0 & 0 & 0 \\ 0 & -1.045 & -2.345 & 0 & -2.29 & 0 \\ 0 & 0 & 0 & -2.29 & 0 & -2.29 \\ 0 & 0.5 & 0.5 & 0 & 1.525 & 0 \end{bmatrix}$	$\begin{bmatrix} 0 \\ 0 \\ 0 \\ 0 \\ 0 \\ 0 \end{bmatrix}$
Calibration value	$\begin{bmatrix} -0.0087 & 0.0118 & 0.0101 & -0.9974 & -0.0053 & -0.9999 \\ 0.0016 & 0.9999 & 0.9999 & 0.0078 & 0.9875 & 0.00004 \\ -0.9999 & 0.0057 & 0.0047 & -0.0709 & 0.1575 & 0.0052 \\ -0.0020 & -0.9724 & -2.2722 & 0.0180 & -2.2606 & 0.00005 \\ 0.0431 & 0.0084 & 0.0204 & -2.1763 & -0.2525 & -2.3007 \\ 0.0002 & 0.5511 & 0.5006 & 0.0123 & 1.5075 & 0.00078 \end{bmatrix}$	$\begin{bmatrix} 0.2 \\ 0.5 \\ 0.3001 \\ 0.2987 \\ -0.3001 \\ 0.6001 \end{bmatrix}$
Actual value	$\begin{bmatrix} -0.0087 & 0 & -0.0019 & -0.9999 & -0.0061 & -0.9999 \\ 0.0017 & 0.9999 & 0.9999 & -0.0043 & 0.9999 & 0.00002 \\ -0.9999 & 0.0059 & 0.0051 & -0.00002 & -0.00004 & 0.0053 \\ -0.0021 & -1.0445 & -2.3452 & -0.099 & -2.2889 & -0.00006 \\ -0.0087 & -0.0030 & -0.0070 & -2.2905 & -0.0139 & -2.3007 \\ 0.00003 & 0.5002 & 0.5011 & -0.0068 & 1.52617 & 0.00035 \end{bmatrix}$	$\begin{bmatrix} 0.2 \\ 0.5 \\ 0.3 \\ 0.3 \\ -0.3 \\ 0.6 \end{bmatrix}$

**Fig. 3** Pose error of end-effector in the process of parameter iterations [self-drawn]

calculate the theoretical and actual kinematic values of the robot pose of the end-effector, and the actual value was used as the measured value for the end-effector to calculate its pose error. The whole simulation process was similar to Simulation I, regardless of external factors. The identification results are shown in Table 2, and

the pose error model and position error model are in the iterative process in Fig. 4. Sharp reductions were found in the pose error at the end of HH150.

**Table 2** Results of parameter calibration [self-drawn]

Parameter	$\xi = [\xi_1 \ \xi_2 \ \xi_3 \ \xi_4 \ \xi_5 \ \xi_6]$	$\delta q$
Theoretical value	$\begin{bmatrix} 0 & 0 & 0 & -1 & 0 & -1 \\ 0 & 1 & 1 & 0 & 1 & 0 \\ 1 & 0 & 0 & 0 & 0 & 0 \\ 0 & 0 & -1.2 & 0 & -1.2 & 0 \\ 0 & 0 & 0 & -1.2 & 0 & -1.883 \\ 0 & 0.35 & 0.35 & 0 & 1.399 & 0 \end{bmatrix}$	$\begin{bmatrix} 0 \\ 0 \\ 0 \\ 0 \\ 0 \\ 0 \end{bmatrix}$
Calibration value	$\begin{bmatrix} 0.0087 & -0.00002 & -0.0019 & -0.9999 & -0.0060 & -0.9999 \\ -0.0016 & 0.9999 & 0.9999 & -0.0044 & 0.9999 & 0.00007 \\ 0.9999 & 0.0058 & 0.0051 & 0.0002 & -0.0027 & 0.0052 \\ 0.0003 & 0.0004 & -1.2002 & 0.0052 & -1.1989 & -0.00008 \\ -0.0004 & -0.0020 & -0.0040 & -1.2007 & -0.0109 & -1.2085 \\ -0.000003 & 0.3500 & 0.3511 & -0.0062 & 1.4000 & 0.0004 \end{bmatrix}$	$\begin{bmatrix} 0.1533 \\ 0.4932 \\ 0.2912 \\ 0.4228 \\ -0.2928 \\ 0.4476 \end{bmatrix}$
Actual value	$\begin{bmatrix} 0.0087 & 0 & -0.0019 & -0.9999 & -0.0061 & -0.9999 \\ -0.0017 & 0.9999 & 0.9999 & -0.0044 & 0.9999 & 0.00002 \\ 0.9999 & 0.0059 & 0.0051 & -0.00002 & -0.00004 & 0.0052 \\ 0.0003 & 0.0005 & -1.2002 & 0.0052 & -1.1989 & -0.00005 \\ -0.0004 & -0.0021 & -0.0041 & -1.2006 & -0.0073 & -1.2085 \\ 0.000003 & 0.3503 & 0.3511 & -0.0063 & 1.4000 & 0.0003 \end{bmatrix}$	$\begin{bmatrix} 0.2 \\ 0.5 \\ 0.3 \\ 0.3 \\ -0.3 \\ 0.6 \end{bmatrix}$

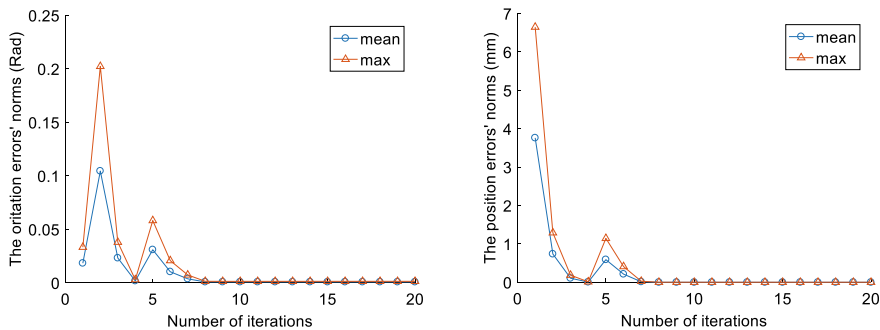


**Fig. 4** Pose error of end-effector in the process of parameter iterations [self-drawn]

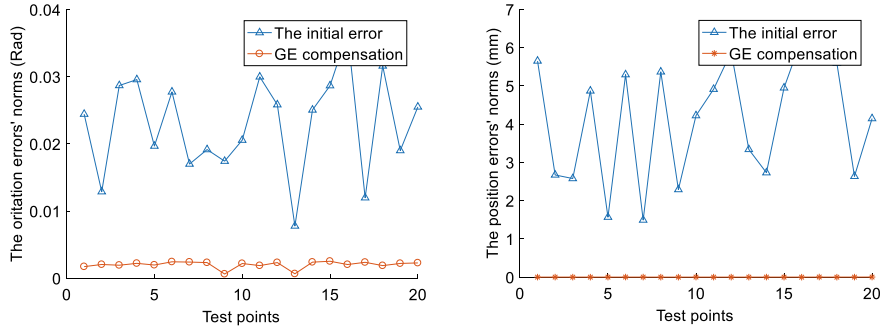


**Fig. 5** Pose error of end-effector on test points [self-drawn]

### 4.3 Verification Test

20 groups of joint variables were randomly generated in the workspace of Robot HH150 and applied to the verification test of calibration results. The theoretical and actual kinematic parameters as presented in Table 2 were put into Eq. (8), respectively, to calculate the theoretical and actual kinematic values of the end-effector, and the end-effector's calibration compensation value was calculated based on the calibration and identification results of kinematic parameters. As shown in Fig. 5, sharp reductions were found in the pose error of the end-effector of Robot HH150, which verified the correctness and effectiveness of the kinematic parameter calibration model. For the robot end-effector, the maximum pose error model and average pose error model, respectively, dropped from 0.0365 rad and 0.0230 rad to 0.0025 rad and 0.0020 rad, while the maximum position error model and average position error model declined from 6.2292 mm and 4.1266 mm to 0.0045 mm and 0.0021 mm, respectively.

## 5 Conclusion

- (1) This paper carried out geometric error analysis for serial robots and constructed a relevant kinematic model containing joint screw and joint variables. Geometric errors were defined as joint screw errors and joint variable errors in this paper to propose a pose error model, with joint constraint conditions considered. The model renews joint screw coordinates through the adjoint matrix, improves the positioning accuracy of the robot pose on end, and resists external interference better for the calibration model in the process of parameter iterations. The error calibration model is well-structured and user-friendly as an explicit expression.

- (2) Simulation tests were performed with Robot KUKAKR500 and Industrial Robot HH150. Test data revealed that kinematic parameters identified by parameters could effectively compensate for the pose error of robots, and verified that the calibration model was effective and correct.

## References

- Chu YJ (2022) A kinematic calibration method of robots based on a tool coordinate system. *China Mech Eng*
- Gao H, Zhang ML, Zhang XJ (2017) Review of key technologies of absolute positioning accuracy for robot arms. *Appl Res Comput* 34(9):7
- Lienenluke L, Grandel L, Storms S, et al (2018) Model-based process planning for milling operations using industrial robots. In: 2018 3rd International conference on control and robotics engineering (ICCRE)
- Chen J, Chao LM (1987) Positioning error analysis for robot manipulators with all rotary joints. In: IEEE international conference on robotics & automation. IEEE, pp 539–545
- Wang S, Jia Q, Chen G, et al (2019) Complete relative pose error model for robot calibration. *Ind Robot* 46(3)
- Hayati S, Mirmirani M (2010) Improving the absolute positioning accuracy of robot manipulators. *J Field Robot* 2(4):397–413
- Judd RP, Knasinski AB (1987) A technique to calibrate industrial robots with experimental verification. *IEEE Trans Robot Autom* 6(1):20–30
- Stone HW, Sanderson AC (1988) Statistical performance evaluation of the S-model arm signature identification technique. In: Proceedings. 1988 IEEE international conference on robotics and automation, 1988. IEEE
- Zhuang H, Roth ZS, Hamano F (2002) A complete and parametrically continuous kinematic model for robot manipulators. *IEEE Trans Robot Autom* 8(4):451–463
- Yang K. Research on error modeling, parameter identification and error compensation based on Lie Algebra. Huazhong University of Science and Technology
- Hu P, Jin GG, Sui XW (2013) Research on error calibration algorithms of the shoulder joint in the zero position through 6-DOF flexible measurement. *J Tiangong Univ* 1:4
- Wang W, Wang G, Yun C (2014) Kinematic calibration method for serial robot based on exponential product equation
- Jiang Z, Gao W, Yu X (2020) An improved robot calibration method using the modified adjoint error model based on POE. *Adv Robot* 34(19):1–10
- Wang W, Wang L, Yun C (2017) Design of a two-step calibration method of kinematic parameters for serial robots. *Chin J Mech Eng* 30(2):438–448
- Gao WB (2013) Research on a method that can reshape robot structure and parameter calibration. University of Chinese Academy of Sciences
- Murray RM, Shastry S, Li Z et al (2018) A mathematical introduction to robotic manipulation. CRC Press Inc
- Wu Y, Klimchik A, Caro S, et al (2015) Geometric calibration of industrial robots using enhanced partial pose measurements and design of experiments. *Robot Comput Integr Manuf*
- He RB (2011) Research on kinematic calibration method for serial structure based on exponential product equation. Huazhong University of Science and Technology
- Okamura K, Park FC (1994) Kinematic calibration and the product of exponentials formula. Springer, Netherlands, p 11

# Research on Rigid-Flexible Coupling Problem of Piston-Pump Tube



Yisheng Xie and Bing Cao

**Abstract** In order to study the rigid-flexible coupling problem of piston-pump tube during the pressurization stage of the secondary light gas gun, based on the Adams rigid-flexible contact theory and considering the elasticity of the pump tube, a piston-pump tube dynamic model and a piston-pump tube are established. contact collision model, and the dynamic simulation of the coupling process between the piston and the pump tube is carried out on the software platform, and the piston velocity curve and the vibration characteristics of the pump tube are obtained. The results show that the speed of the piston is significantly reduced by the contact force during the movement, and the high-speed piston will cause the pump tube to vibrate, and the longitudinal vibration is more obvious. The research results provide a theoretical reference for the research of piston speed and the optimal design of vibration reduction of pump tube.

**Keywords** Rigid-flexible coupling · Contact collision · Dynamic simulation

## 1 Introduction

The pump tube is an important part of the secondary light gas gun. The energy generated in the primary air chamber pushes the piston in the pump tube to continuously compress the light gas in the light gas chamber. When the pressure of the diaphragm reaches a predetermined value, the diaphragm ruptures, and the high-pressure gas drives the projectile to start moving [1]. When the piston moves at high speed in the pump tube, the contact force between the piston and the pump tube will affect the speed of the piston, resulting in energy loss, making the speed of the projectile drop and failing to achieve the expected target. At the same time, the continuous contact and collision of the piston and the pump tube will cause the vibration of the pump

---

Y. Xie (✉) · B. Cao  
Nanjing University of Science and Technology, Nanjing 210094, China  
e-mail: [xyx1379@126.com](mailto:xyx1379@126.com)

tube, resulting in flexible deformation, which will have a certain impact on the life of the pump tube.

When studying the motion of a rigid body in a flexible tube, establishing a contact collision model can simulate the actual motion more realistically. Machado et al. [2] analyzed the main problems associated with common compliant contact force models and used damping terms to enhance Hertz's law in analyzing these models. Hu et al. [3] proposed a dissipative contact force model based on the Hertzian contact law for collision analysis in multibody dynamics. Chen et al. [4] proposed a method of transmitting the interaction force between the projectile and the flexible barrel through a simulated barrel composed of a virtual body. The influence of movement patterns. Based on the flexible body contact theory in Adams, Guo et al. [5] established the contact model between the belt and the front centering part of the projectile and the inner bore of the barrel, and obtained the muzzle vibration and the corresponding projectile motion response data when the projectile was coupled. Di et al. [6] added a contact model when establishing the coupled dynamic model of the moving projectile and the elastic barrel, which more realistically reflected the vibration of the lower barrel excited by the moving projectile. Shen et al. [7] established the rigid-flexible coupling model of the barrel and the contact-collision model between the shell, armature and guide rail, and more accurately obtained the effect of the rigid-flexible coupling effect of the shell on the system dynamics during the launch of the electromagnetic gun impact of the response.

At present, most of the research methods of secondary light gas guns are based on classical internal ballistics theory and aerodynamic principles. In this study, the method of rigid-flexible coupling dynamic analysis is used to establish a piston-pump tube contact collision model, and consider the actual working conditions, the flexible deformation of the pump tube under the constraint of four fixed supports is analyzed, which provides a new research method for the secondary light gas gun.

## 2 Theoretical Basis

### 2.1 Dynamic Equation of Flexible Pump Tube

Reference [5] uses the first kind of Lagrange equation to establish the dynamic equation of the flexible pump tube, and firstly establishes the generalized coordinates of the flexible pump tube.

$$\zeta = [L, \Omega, q]^T \quad (1)$$

In Eq. (1),  $L$  is the Cartesian coordinate of the undeformed node in the flexible pump tube in the inertial coordinate system,  $L = [x, y, z]^T$ ,  $\Omega$  is the orientation angle of the Siamese base on the node relative to the inertial reference frame when

it is not deformed,  $\Omega = [\psi, \theta, \varphi]^T$ ,  $\mathbf{q}$  is the modal coordinate,  $\mathbf{q} = [\mathbf{q}_1, \mathbf{q}_2, \dots, \mathbf{q}_m]^T$ ,  $m$  represents the number of modes.

Bringing Eq. (1) into the Lagrange equation to get the dynamic equation of the flexible pump tube.

$$\mathbf{M}\ddot{\zeta} + \dot{\mathbf{M}}\dot{\zeta} - \frac{1}{2} \left[ \frac{\partial \mathbf{M}}{\partial \zeta} \dot{\zeta} \right]^T \dot{\zeta} + \mathbf{K}\zeta + \mathbf{G} + \mathbf{D}\dot{\zeta} + \left[ \frac{\partial \psi}{\partial \zeta} \right]^T \lambda = \mathbf{Q} \quad (2)$$

In Eq. (2),  $\mathbf{M}$  is the mass matrix of the elastomer,  $\psi$  is the constraint equation,  $\lambda$  is the Lagrange operator corresponding to the constraint equation,  $\zeta$  is the generalized coordinate,  $\mathbf{Q}$  is the generalized force projected onto the generalized coordinates,  $\mathbf{K}$  is the overall stiffness matrix,  $\mathbf{G}$  is gravity,  $\mathbf{D}$  is the modal damping matrix.

## 2.2 Contact Collision Model

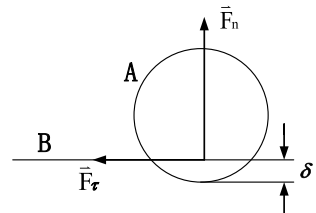
The interaction force between the piston and the pump tube during the movement is transmitted through the contact force.

The contact between the piston and the pump tube is established according to the Hertz contact theory. The Hertz elastic collision model in Adams is shown in Fig. 1. When the contact surface begins to penetrate, the calculation formula of the collision force is shown in Eq. (3).

$$F_n = k\delta^n + step(\delta, 0, 0, d_{max}, c_{max})\dot{\delta} \quad (3)$$

In Eq. (3),  $F_n$  is the collision force,  $k$  is the stiffness coefficient,  $\delta$  is the penetration depth of the contact surface.  $n$  is the force index,  $step$  function is the Heaviside function approximated by a third degree polynomial,  $d_{max}$  is the maximum permissible penetration depth,  $c_{max}$  is the maximum transient damping coefficient. When the penetration depth of the contact point is less than the critical value, the damping coefficient is a cubic function of the penetration amount. When the penetration depth reaches  $d_{max}$ , the damping coefficient also reaches the maximum value  $c_{max}$ .

**Fig. 1** Hertz elastic collision model



### 3 Piston-Pump Tube Dynamics Model

The object of this study is the pump tube of a secondary light gas gun and the piston part in the pump tube. The material of the pump tube is 40Cr. The inner diameter is 180 mm. The outer diameter is 340 mm. The density  $\rho = 7800 \text{ kg/m}^3$ . The elastic modulus  $E = 211 \text{ GPa}$ . The length of the pump tube in the effective moving part of the piston is 18 m. The material of the piston is nylon. The weight is 25 kg, and the side area is  $S = 0.025 \text{ m}^2$ . The initial inflation pressure of the launch chamber is  $P_0 = 12 \text{ MPa}$ . The inflation pressure of the light air chamber in the pump tube is  $P_p = 0.12 \text{ MPa}$ . The piston moves horizontally in the pump tube without rotational movement. As Eqs. (4) and (5), the law of the gas pressure at both ends of the piston changing with the displacement is the empirical formula of reference [8].

$$F_A(x) = Sp_0[V/(V + S(x_0 - x))]^{k_0} \quad (4)$$

$$F_p(x) = Sp_p(x_0/x)^{k_1} \quad (5)$$

The dynamic model of the piston pump tube is shown in Fig. 2. In order to obtain an accurate rigid-flexible coupling dynamic model of the piston-pump tube, the barrel model is considered as a flexible body. Firstly, I used Solidworks 3D modeling software to build a piston-pump tube model, and then used the finite element software Abaqus to perform modal analysis on the pump tube model. The model has a total of 70,300 elements and 119,134 nodes. In the case of considering the actual working conditions, a fixed support point is set every 6 m to replace the fixed support to fix the pump tube. I set up the Frequency analysis step in linear perturbation to extract the first 20 modes of the pump tube under this constraint.

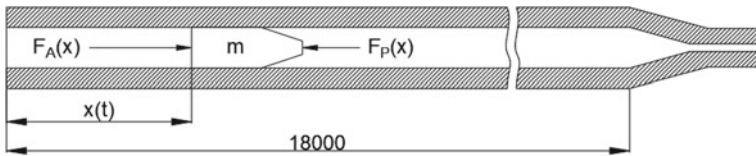


**Fig. 2** Piston-pump tube dynamics model

**Table 1** Initial parameters

Parameters	Value	Parameters	Value
Pump tube material	40Cr	Contact stiffness coefficient/ $10^6$	3.8
Piston material	Nylon	Contact damping coefficient/ $10^4$	1.0
Piston mass/kg	26	Static friction coefficient	0.3
Piston initial velocity/(m/s)	0	Coefficient of kinetic friction	0.1

## 4 Dynamic Simulation of Piston-Pump Tube Model

### 4.1 Parameter Settings

After completing the modal analysis in the finite element software Abaqus, the resulting modal neutral file (MNF file) was imported into Adams. In Adams, the fulcrum is fixedly constrained to constrain the piston in the pump tube. Three mark points are set on the central axis of the inner circle of the pump tube, and the three mark points are, respectively, located at the center points of each of two fixed supports, which are used to express the vibration characteristics of the pump tube during the movement of the piston. The displacement-dependent gas pressures  $F_A$  and  $F_P$  are defined using the displacement function and the CUBSPL difference function. The movement direction of the piston is along the positive direction of the X-axis, and the direction of the gravitational acceleration is along the positive direction of the Y-axis. The initial parameter input values of this simulation are shown in Table 1.

Since the duration of the movement of the piston is very short, about 70 ms, the calculation step is set to one millionth of a second, which can accurately reflect the vibration characteristics of the pump tube during the movement of the piston. Since this analysis does not consider the process of the piston entering the cone, in order to save the calculation cost, a measurement is added to the model to calculate the movement distance of the piston, and then the sensor function in the Adams simulation software is used to stop the simulation before the piston enters the cone.

### 4.2 Dynamic Simulation Results

The simulation situation of the rigid-flexible coupling dynamic analysis of the piston-pump tube in Adams is shown in Figs. 3 and 4.

The speed change of the piston in the compression process of the rigid pump tube and the flexible pump tube with and without considering the contact force is shown in Fig. 5. The maximum speed of the piston of the rigid pump tube without

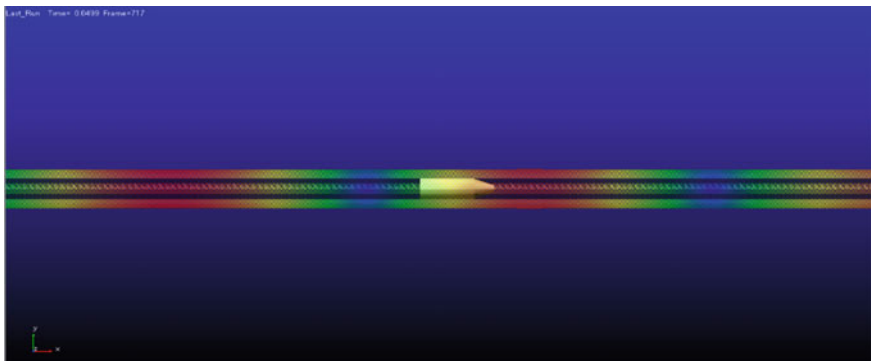


**Fig. 3** Pump tube is a flexible simulation example

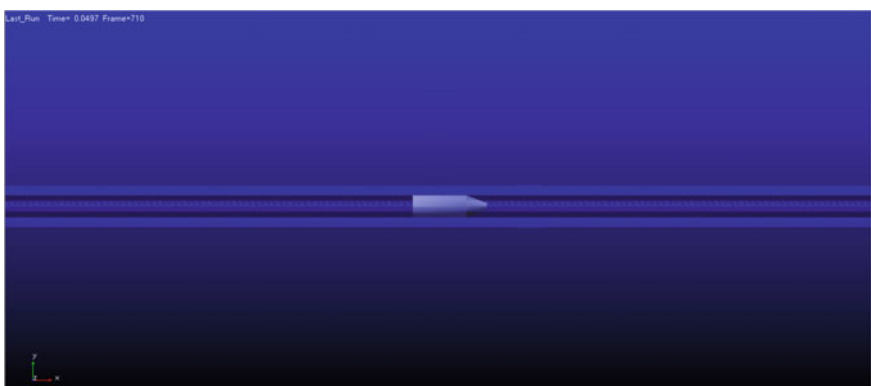


**Fig. 4** Pump tube is a flexible simulation example

considering the contact force (theoretical calculation value) can be up to 398.72 m/s, the maximum speed of the piston considering the contact force of the rigid pump tube can reach 353.44 m/s, and the maximum speed of the piston considering the contact force of the flexible pump tube can reach 353.28 m/s.

The calculation results of the contact force between the flexible pump tube and the piston are shown in Figs. 6 and 7. During the movement of the piston, there have been many contact and collisions with the pump tube. The maximum value of the contact force in the Y direction occurs at the initial moment when the piston squeezes into the pump tube, reaching 2630.07 N, and there will be a sudden and large increase at the second and third fixed supports. At the second fixed support, it reached 1857.65 N and at the third fixed support, it reached 1643.23 N. The maximum value of the contact force in the Z direction also occurred at the initial moment when the piston squeezed into the pump tube, reaching 2575.96 N, and there was a sudden and large increase near the first fixed support, reaching 1612.19 N.

**Fig. 5** Velocity curve of piston

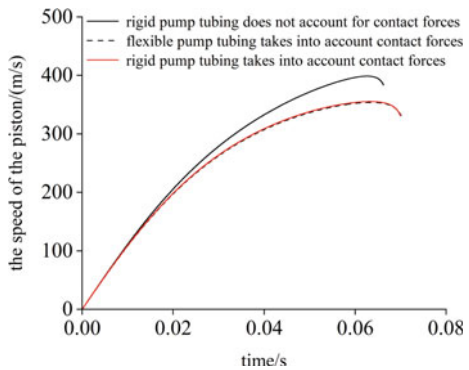


**Fig. 6** Contact force curve of Y-direction

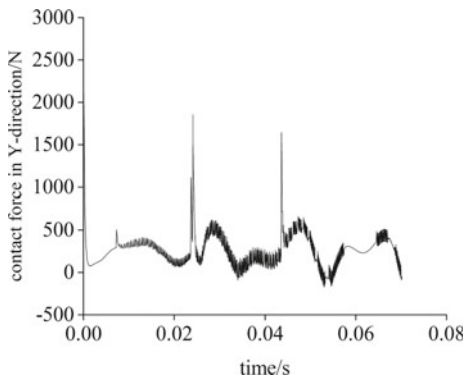
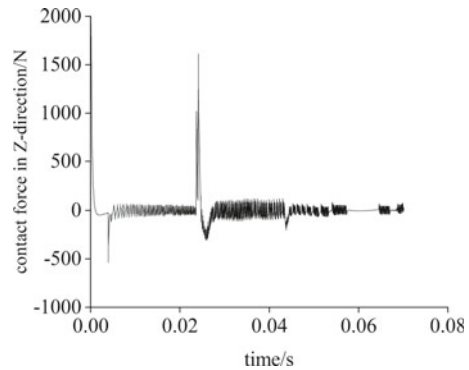


**Fig. 7** Contact force curve of Z-direction



The vibration characteristics of the flexible pump tube during the piston movement are shown in Figs. 8 and 9. In the Y-direction, the maximum amplitude of marker 1 is  $1.31 \times 10^{-4}$  m, the maximum amplitude of marker 2 is  $2.45 \times 10^{-4}$  m, and the maximum amplitude of marker 3 is  $2.59 \times 10^{-4}$  m. In the Z-direction, the maximum

**Fig. 8** Displacement curve of flexible curve of flexible

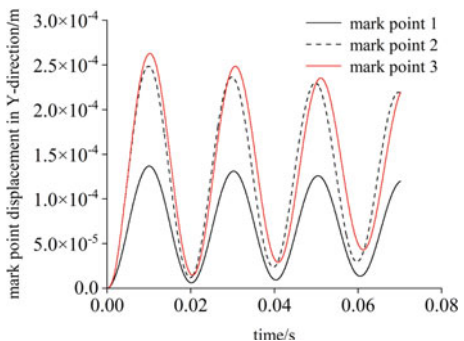
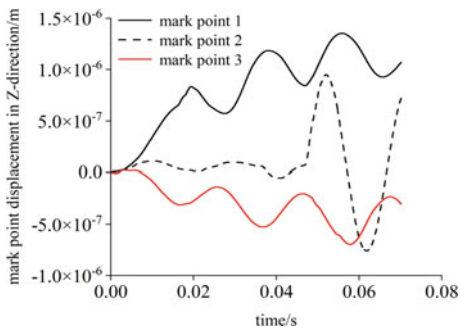


**Fig. 9** Displacement pump tube mark point in Y-direction pump tube mark point in Z-direction



amplitude of marker 1 is  $1.35 \times 10^{-6}$  m, the maximum amplitude of marker 2 is  $9.50 \times 10^{-7}$  m, and the maximum amplitude of marker 3 is  $6.97 \times 10^{-7}$  m.

## 5 Conclusions

The following conclusions are obtained by simulating the dynamics of the compression process of the piston in the pump tube.

The high-speed movement of the piston in the pump tube will cause flexible deformation of the pump tube, and the flexible deformation has little effect on the speed of the piston. In the example considering the contact force, the piston speed is reduced by 11% compared to when the contact force is not considered. Therefore, the main reason for the impact on the piston speed is the contact force between the piston and the pump tube. The friction force is an important factor affecting the contact force. Therefore, the material of the piston and the material of the pump tube will have a very important influence on the speed of the piston. The lateral and longitudinal displacements of some important points in the pump tube were measured during the movement of the piston, and the vibration characteristics of the

pump tube were obtained. The launch tube section and the middle section vibrate more than the section near the launch chamber. This study provides a research method for the vibration reduction design of the pump tube.

## References

1. Zhang D, Tang R, Lin J, Zhang X, Zhu Y (2004) Development of a new type of gas-driven secondary light gas gun. *J Ordnance Eng* (01):14–18
2. Machado M, Moreira P, Flores P, et al (2012) Compliant contact force models in multibody dynamics: evolution of the Hertz contact theory. *Mech Mach Theory Dyn Mach Syst Gears Power Trans Robots Manipul Syst Comput Aided Des Meth* 5399–121
3. Hu S, Guo X (2015) A dissipative contact force model for impact analysis in multibody dynamics. *Multibody Syst Dyn* 35(2):131–151
4. Chen S, Wang L, Shi W (2013) Contact collision dynamics in the rigid-flexible coupling model of bullets. *J Naval Eng Univ* 25(04):97–102
5. Guo B, Liu J (2013) Research on the coupling of bullets and guns with elastic barrels. *Mech Strength* 35(03):297–301
6. Di C, Qin J, Fang Y, Yang Y (2019) Analysis of coupled vibration characteristics of bullets considering the initial deflection of the barrel. *Mech Strength* 41(02):504–508
7. Shen J, Li J, Feng X, Liu G, Chen G, Tian X, Yan X (2020) Electromagnetic launch dynamics of ultra-high-speed projectiles. *Sci Technol Eng* 20(12):4730–4734
8. Lin J (1995) Analysis of launch parameters of non-powder-driven secondary light gas guns. *Explos Shock* (03):229–240

# Route to a Chaotic State in the Wake of a NACA0015 Airfoil at Post-stall Angles of Attack



Liping Sun, Ziheng Song, Jiuming Zhang, and Min Fang

**Abstract** We perform two-dimensional simulations of unsteady flow separation around a NACA0015 airfoil. The effects of Reynolds number and the angle of attack of the airfoil were studied. With the increase in the angles of attack and the Reynolds number, it reveals a route of the transition in the wake of NACA0015 foil from steady to chaotic flow. We find that the flow transits from steady flow to a chaotic state by a sequence of successive period-doubling bifurcations. Our results provide physical insight into the wake transition of an airfoil from steady to chaotic flow.

**Keywords** Wake transition · NACA0015 airfoil · Steady flow · Route to chaotic

## 1 Introduction

The flows around bluff bodies have been extensively studied experimentally, numerically, and theoretically. In the general experiment and theory of dynamics, Williamson [1–3] observed two-stage transitions in the wake of a circular cylinder and characterized the physical mechanism of the discontinuities in the St–Re relationship. It was reported that the wake transited from laminar to some three-dimensional instability modes. In recent years, Zhang et al. [4] studied the wake transition past

---

L. Sun (✉)

China Energy Technology and Economics Research Institute, China Energy Investment Corporation Ltd., Beijing 102211, China  
e-mail: [sunliping@zju.edu.cn](mailto:sunliping@zju.edu.cn)

Z. Song

State Key Laboratory of Water Resource Protection and Utilization in Coal Mining, Beijing 102209, China

J. Zhang

SEU Institute of Energy Engineering Design, Zhongli Science Park, No. 3 Street, Shangdi Information Industry Base, Beijing 100085, China

M. Fang

Sungrow, High-Tech Industry Development Zone, Hefei 230088, China

an inclined flat plate and provided the transient route from steady flow to a chaotic state. Jackson [5] found that the flow around an airfoil exhibits the similar behavior to that over a bluff body such as a circular at a very low Reynolds number and with some angle of attack. Based on previous studies, Deng et al. [6] and Sun et al. [7] numerically studied the wake transition of a pitching foil and heaving foil and performed the wake of a flapping foil transient from two- to three-dimensional flow with the increase of Reynolds number and the flapping amplitude. Meneghini et al. [8] investigated the flow in the wake of a stalled NACA0012 airfoil at the angle of attack of 20°. Deng et al. [9, 10] performed two-dimensional simulations of unsteady flow separation around a NACA0015 airfoil under low-Reynolds number, they found some different branches on the Strouhal–Reynolds number relationship curves and demonstrated that the flow around the airfoil transits to a chaotic state, which is similar to the results of Zhang et al. [4].

Though the wake dynamics, transitions of the flows over circular or square cylinders have been extensively studied. However, there is very little research on the dynamics of airfoil wake, especially on the dynamics of airfoils at fixed angles of attack. In this paper, we study how the flow transits from steady to a chaotic state and how the flow structures evolve into turbulent flow. We particularly investigate the effects of the Reynolds number and the effects of the angle of attack to the wake transition. The Reynolds number we studied here is in the range of  $100 \leq Re_d \leq 1200$  and the angle of attack is in the range of  $10^\circ \leq \alpha \leq 25^\circ$ . With the increase of  $Re_d$  and  $\alpha$ , we show the transition route and provide a transition process with a sequence of successive period-doubling bifurcations.

## 2 Numerical Method

Assuming that the fluid is Newtonian and incompressible, we use the open-source CFD code OpenFOAM [11, 12] to simulate the unsteady flow around an airfoil. In the Navier Stokes equation, the time dependent part is solved by the finite volume method, and there is no turbulence model needs to be used due to the Reynolds number is low. The integral form of the governing (conservation) equations defined in an arbitrary volume  $V$  bounded by a closed surface  $S$  states

$$\frac{d}{dt} \int_V \rho U dV + \oint_S ds \cdot \rho U U = \oint_S ds \cdot (-p I + \nu \nabla U) \quad (1)$$

where  $\rho$  is the density,  $U$  is the fluid velocity, and  $\nu = \mu/\rho$  is the kinematic viscosity.

There are two control parameters that are the angles of attack  $10^\circ \leq \alpha \leq 25^\circ$  and the Reynolds number  $Re_d = Ud/\nu$ , where  $U$  is the velocity of the free-stream flow, the  $d = C \sin \alpha$  is the feature length,  $\nu$  is the kinematic viscosity of the fluid. Here, a systematical study was carried out.

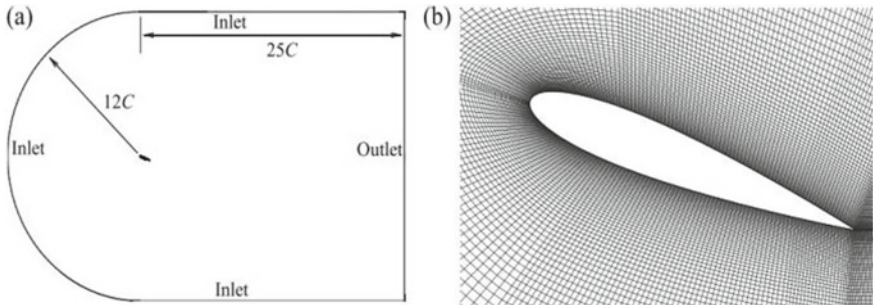


**Fig. 1** Schematic of fluid flow through a NACA0015 airfoil. **a** Computational domain; **b** grid distributions near the NACA0015 airfoil

We consider the flow system as an incompressible fluid and fix the velocity on the airfoil to be zero. A uniform velocity is set at the inlet boundary, and past a NACA0015 airfoil with the angles of attack shown in Fig. 1. The radius of the semicircle is  $12C$ , and the rectangle is with the dimensions of  $25C$ . As an example,  $\alpha = 20^\circ$  in Fig. 1b.

### 3 Results

#### 3.1 The Effect of Reynolds Numbers

We first study the transition route of the airfoil from steady to chaotic flow as the increase of Reynolds Numbers  $Re_d$  with a fixed angle of attack and analyze the evolution process between different flow regimes, as shown in Fig. 2.

When  $\alpha = 20^\circ$ , with the increase of Reynolds number  $Re_d$ , the flow turns from initially stable steady flow to periodic steady flow after Hopf bifurcation, period-doubling flow, Quasi-periodic flow, etc., and finally transition to chaotic flow, which is similar to the turbulent flow. Similar results were obtained by Zhang et al. [4] who presented the results of flow past an inclined flat plate.

Based on the overview of the flow state in the  $f$ - $Re_d$  plane shown in Fig. 3, we perform its flow characteristics in detail using the power spectral density (PSD) in the Fourier transform in order to deeply study the periodic characteristics of the flow and the transition process between the flow states.

In Fig. 3, we show the power density spectrum (PSD) of lift (first column), the phase space distribution of velocity components ( $u, v$ ) (second column), and the Lissajous-Figure of hydrofoil lift drag (third column) as a function of Reynolds number. At the same time, the corresponding instantaneous vortex structure is shown in Fig. 4, respectively.

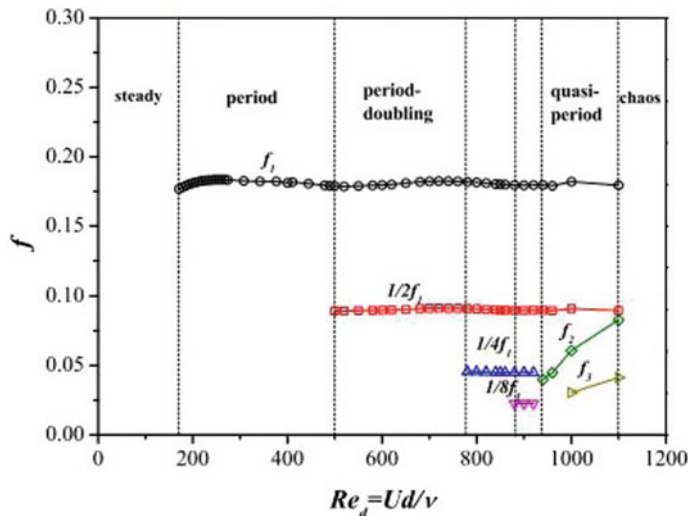


**Fig. 2** The sketches of the transition from steady to chaotic flow and schematics of the successive bifurcations leading to chaos versus  $Re_d$  at  $\alpha = 20^\circ$ . The critical parameters of the Hopf bifurcation are marked with black  $\circlearrowleft$ , representing the dominant frequency in the flow field; the first period-doubling bifurcation is marked in red  $\square$ ; the bifurcation in the quasi-periodic region is marked in green  $\diamond$

When the Reynolds number  $Re_d$  is small, at  $Re_d = 460$ , the flow lies in periodic steady flow, and the peaks in the power spectral density (PSD) correspond to a primary frequency  $f_1$  and its related sub-harmonic frequencies such as  $f_1$ ,  $2f_1$ ,  $3f_1$ , etc. The phase space distribution of the corresponding velocity component ( $u \cdot v$ ) and the Lissajous figure of the lift-drag force both show one limit cycle in the phase space, the flow exhibits a frequency-locking phenomenon. The corresponding vortex structure is shown in Fig. 4a. It can be seen that the wake is a typical Karman vortex street wake.

As  $Re_d$  increases to 600, a period-doubling bifurcation occurs, resulting in a peak of  $f_1/2$  in the power spectral density (PSD) and branching into two connected limit cycles in phase space distribution. Continue to increase the Reynolds number, when  $Re_d = 800$ , the sub-harmonic  $f_1/4$  is excited in the flow, at the same time, there are four limit cycles in the phase space distribution and the Lissajous figure. The corresponding vortices in the wake are in the “T + S” mode, that is, the flow pattern combined with three vortices and one single vortex.

Further increase  $Re_d$ , at  $Re_d = 920$ , the sub-harmonics  $f_1/8$  appears in the power spectral density (PSD), and there are eight cycles in the phase space distribution. The corresponding vortex structure is a typical “T + S” mode state (Fig. 4d). At  $Re_d = 940$ , the sub-harmonic  $f_1/16$  appears in the flow field, and similarly, 16 closed loops can be seen in the phase space distribution. With the further increase of  $Re_d$ , the flow field will be filtered, that is, some sub-harmonic frequencies containing less power, such as  $f_1/8$ ,  $f_1/16$ , etc., are filtered out. For example, when  $Re_d = 960$ , the

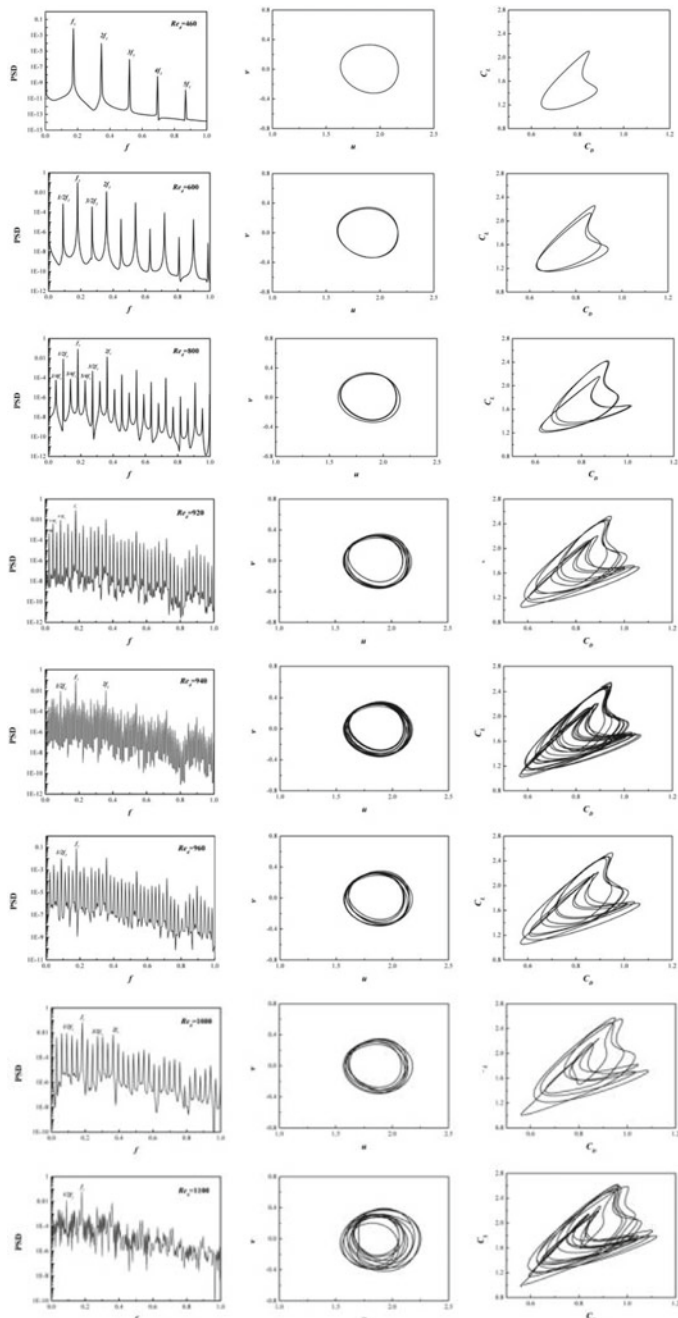


**Fig. 3** For  $\alpha = 20^\circ$ , the power density spectrum (PSD) of lift (first column), the phase space distribution of velocity components ( $u$ ,  $v$ ) (second column), and the Lissajous-Figure of hydrofoil lift drag (third column) as a function of Reynolds number. From top to bottom are:  $Re_d = 460, 600, 920, 1000, 1100$

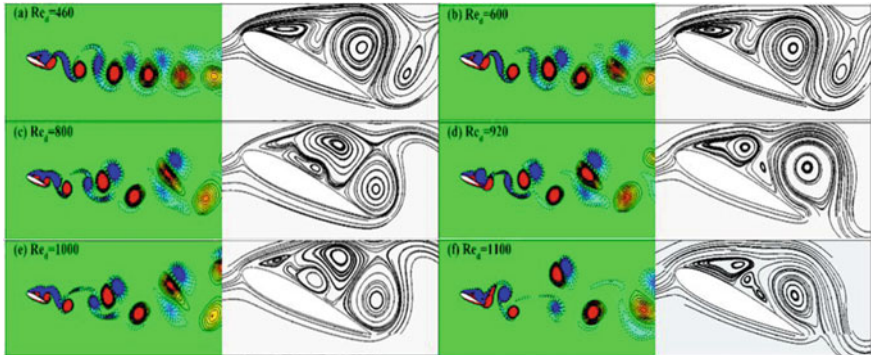


**Fig. 4** For  $\alpha = 20^\circ$ , the vortex structure cloud map and the corresponding streamlines (right column) near the airfoil under different  $Re_d \cdot Re_d = 460, 600, 800, 920, 1000, 1100$

sub-harmonic frequency  $f_1/16$  disappears, that is, it is filtered out, the peak value of the power spectrum mainly contains the main  $f_1/2$ ,  $f_1/4$ ,  $f_1/8$  etc. The corresponding closed limit cycles in the phase space distribution are reduced from 16 to 8.

Continue to increase the Reynolds number, when  $Re_d = 1000$ , the sub-harmonic frequencies of  $f_1/16$ ,  $f_1/8$  and  $f_1/4$  are filtered out, and the second main frequency  $f_2$  is excited at the same time, the spectral peaks occur in a relation of  $m_1 f_1/2 + m_2 f_2$ , where  $m_1$  and  $m_2$  are both integers. In the corresponding wake vortex, the “T + S” mode will be damaged to a certain extent, the “T” mode tends to be transformed into the “P + S” mode. When  $Re_d$  increased to the transition boundary of quasi-periodic wake and turbulent flow, for example  $Re_d = 1100$ , the third main frequency  $f_3$  is excited, the spectral peaks occur in a relation of  $m_1 f_1/2 + m_2 f_2 + m_3 f_3$ , the corresponding closed limit cycles in the phase space distribution also changed significantly.

In summary, with the increase of  $Re_d$ , the flow transitions from the initial stable steady flow to Hopf bifurcation to period-doubling flow, Quasi-periodic flow, etc., and finally to chaotic and turbulent flow. In the process of transformation, the peak frequency of the corresponding power spectral density can be expressed as:  $m_1 f_1$ ,  $m_1 f_1/2$ ,  $m_1 f_1/4$ ,  $m_1 f_1/8$ ,  $m_1 f_1/16$ ,  $m_1 f_1/2 + m_2 f_2$  and  $m_1 f_1/2 + m_2 f_2 + m_3 f_3$ , etc. where  $m_1$ ,  $m_2$ , and  $m_3$  are both integers.

### 3.2 The Effect of Angle of Attack

In addition, we also study the effect of the angle of attack on the flow structure and the wake transition at a fixed Reynolds number. Figure 5 shows the power spectral density (PSD) of lift at different angles of attack at  $Re_d = 600$ . The corresponding instantaneous vortex structure is shown in Fig. 6. Similar conclusions can be found by observing the effect of Reynolds number in previous studies.

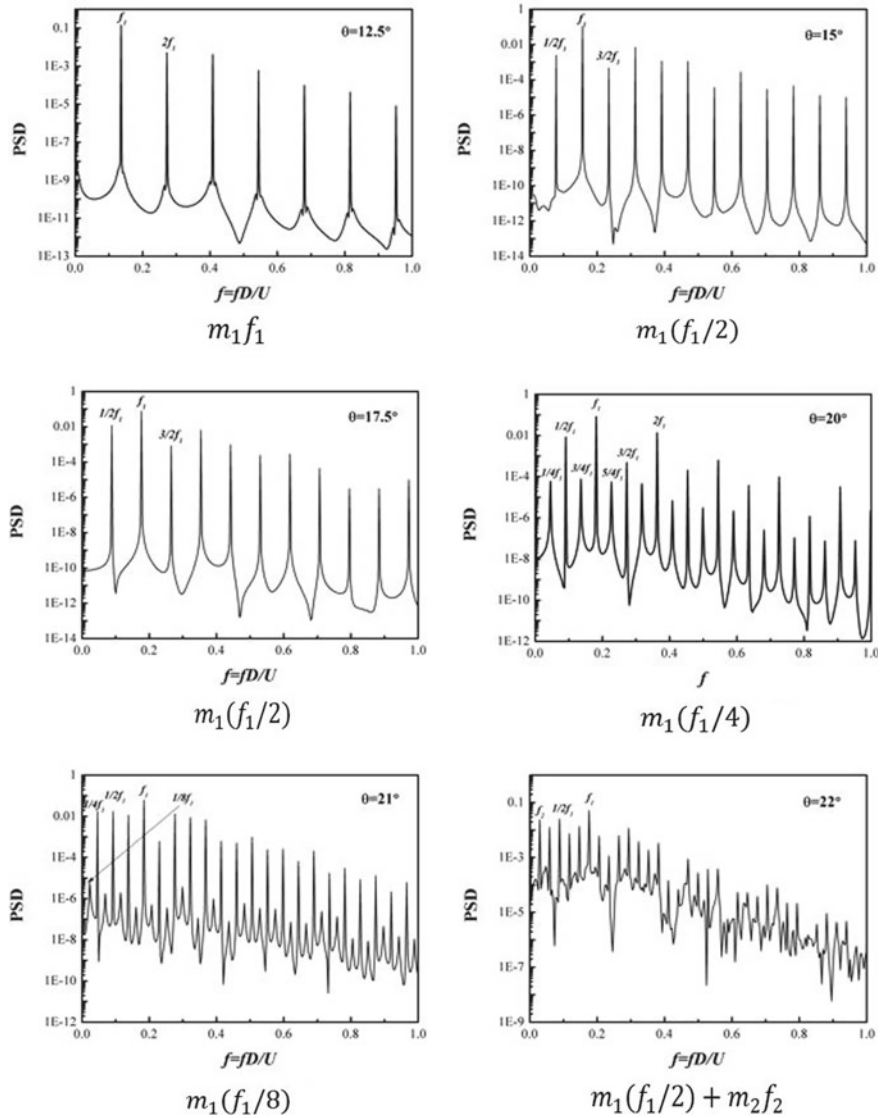


**Fig. 5** For  $Re_d = 600$ , the power spectrum density (PSD) of the velocity component in the  $y$  direction at different angle of attack. From left to right, top to bottom, the angles of attack are:  $\alpha = 12.5, 15, 17.5, 20, 21, 22^\circ$

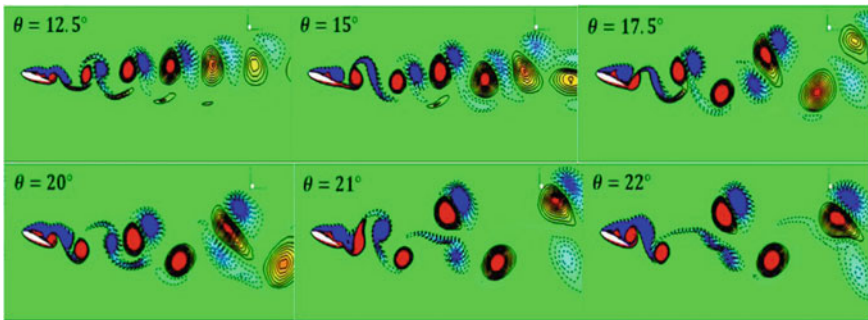


**Fig. 6** For  $Re_d = 600$ , the instantaneous vorticity contours near the airfoil at different angles of attack  $\alpha$ . From left to right, top to bottom are:  $\alpha = 12.5, 15, 17.5, 20, 21, 22^\circ$

When the angle of attack is small, at  $\alpha = 12.5^\circ$ , the flow lies in periodic steady flow and the peaks in the power spectral density (PSD) correspond to a primary frequency  $f_1$  and its related sub-harmonic frequencies such as  $f_1, 2f_1, 3f_1$  etc. And for the corresponding wake, the vortices exist in pairs, that is, the typical Karman vortex street wake.

With the increase of the angle of attack, when and a period-doubling bifurcation occurs, resulting in a peak of  $/2$ . Corresponding to the wake, there are two adjacent pairs of vortices in which period is  $T$  in the basic flow, the positive and negative vortices tend to pair, where.

When, the sub-harmonic  $/4$  is excited in the flow, and the vortices in the wake are in the “T + S” mode, that is, the flow pattern combined with three vortices and one single vortex. And when, the sub-harmonic  $/8$  is excited in the flow.

Further increase  $\alpha$ , similar conclusions can be found by observing the effect of Reynolds number in previous studies, which means that the flow will transition from steady to chaotic flow. For example, at  $\alpha = 22^\circ$ , the sub-harmonics  $f_1/4$  and  $f_1/8$  in the power spectral density (PSD) disappear, and the second main frequency  $f_2$  is excited at the same time, the spectral peaks occur in a relation of  $m_1 f_1/2 + m_2 f_2$ . In the corresponding wake vortex, the “T + S” mode will be damaged to a certain extent, the “T” mode tends to be transformed into the “P + S” mode, and the three single vortices tend to be transformed into a pair of vortices and a single vortex. Further, as increase in  $\alpha$ , the power spectrum density will be the broadband continuous spectrum, and the flow tends to be a chaotic state, as shown in the previous studies.

## 4 Conclusions

In summary, the transition route from steady to chaotic state for flow behind a NACA0015 airfoil at post-stall angles of attack has been studied. It also revealed a transition process via the sequential occurrence of a sequence of successive period-doubling bifurcations and the various incommensurate bifurcations. The results obtained in this study provide the physical insight into the wake transition phenomenon from steady to chaotic flow.

**Acknowledgements** We warmly thank Postdoc Jinghang Lin at Yale University for fruitful discussions. This work was supported by the Science and Technology projects of China Energy Investment (Grant Number GJNY-21-139).

## References

1. Williamson CHK (1988) The existence of two stages in the transition to three-dimensionality of a cylinder wake. *Phys Fluids* 31(11):3165–3168
2. Williamson CHK (1996) Three-dimensional wake transition. *J Fluid Mech* 328:345–407
3. Williamson CHK (1996) Three-dimensional vortex dynamics in bluff body wakes. *Exp Thermal Fluid Sci* 12(2):150–168
4. Zhang J, Liu NS, Lu XY (2009) Route to a chaotic state in fluid flow past an inclined flat plate. *Phys Rev E* 79(4):045306
5. Jackson CP (1987) A finite-element study of the onset of vortex shedding in flow past variously shaped bodies. *J Fluid Mech* 182:23–45
6. Deng J, Sun L, Shao X (2015) Dynamical features of the wake behind a pitching foil. *Phys Rev E* 92(6):063013
7. Sun L, Deng J, Shao X (2018) Three-dimensional instabilities for the flow around a heaving foil. *Phys Rev E* 97(1):013110
8. Meneghini JR, Carmo BS, Tsiloufas SP et al (2011) Wake instability issues: from circular cylinders to stalled airfoils. *J Fluids Struct* 27(5–6):694–701
9. Deng J, Sun L, Shao X (2017) Floquet stability analysis in the wake of a NACA0015 airfoil at post-stall angles of attack. *Phys Fluids* 29(9):094104
10. Deng J, Sun L, Shao X (2019) Wake dynamics of low-Reynolds-number flow around a two-dimensional airfoil. *Phys Fluids* 31(2):024102
11. Jasak H (1996) Error analysis and estimation for the finite volume method with applications to fluid flows
12. Jasak H, Jemcov A, Tukovic Z (2007) OpenFOAM: a C++ library for complex physics simulations//International workshop on coupled methods in numerical dynamics. IUC Dubrov Croat 1000:1–20

# Research on Kinematic Characteristics of Revolving Chain Shell Magazine



Yongyong Zhu, Pengfei Yue, and Qiangwei Pang

**Abstract** To study the kinematic characteristics of revolving chain shell magazine with time-varying inertia parameters, the rigid body dynamics model of the shell magazine system is deduced by considering the change of the equivalent moment of inertia of the shell cartridge at different positions of the chain. Under the changeable condition of the motion law of the driving sprocket, the time-varying characteristics of the equivalent moment of inertia and the output torque that the driving motor needs to satisfy are analysed. Results show that, compared with constant velocity and constant deceleration, the amplitude of change pace of the equivalent moment of inertia of the shell magazine is small under the trapezoidal motion law. The research results can provide theoretical guidance for the structural design and driving control rules of the rotational shell magazine.

**Keywords** Revolving chain shell magazine · Time-varying characteristics · Equivalent moment of inertia · Driving torque

## 1 Introduction

The revolving chain shell magazine is the key mechanism to realize the automatic transfer of ammunition [1]. Driven by the driving sprocket, the shells move one by one to the lower opening of the hoister. The driving law of the revolving magazine determines the movement time node of the shell in a firing cycle, and affects the action time interval of the ammunition feeding mechanism and the position error of the shell. In consideration of the fact that in the actual working process of the revolving magazine, the decrease of the load of the ammunition causes the decrease of the moment of inertia of the magazine, which leads to the increase of the residual

---

Y. Zhu (✉) · Q. Pang  
Naval University of Engineering, Wuhan 430033, China  
e-mail: [zyy99515@126.com](mailto:zyy99515@126.com)

P. Yue  
92941 Unit, People's Liberation Army of China, Huludao 125000, China

velocity of the shell after it moves in place. In order to reduce the position error of the ammunition transferred by the magazine, it is necessary to study the kinematic characteristics of the revolving magazine [2].

Based on the theory of guaranteed cost control, Hou and Ma [3] proposed a nonlinear robust control algorithm for an uncertain magazine system. In order to improve the dynamic performance of the magazine system, Zou et al. [4, 5] proposed an adaptive robust control algorithm with an integral synovial surface. The research on the scheme design of the automatic magazine and the parallel motion sequence of the mechanism has always been the focus to the scholars. Wang et al. [6] put forward the structural design scheme for the intermittent transmission drum system, lifting system and distributing system. Liu et al. [7] constructed the shell drum model by using the gear transmission mechanism and calculated the input torque of the transmission gear.

In this paper, the revolving chain shell magazine is simplified as a single degree of freedom plane revolving rigid body. Considering the equivalent moment of inertia of a single cartridge at different positions of the chain, the time-varying inertia parameters of the magazine system are analyzed. Through numerical simulation, the output torque of the motor under different sprocket rotation law is studied.

## 2 Dynamic Model

The main structure of the revolving chain shell magazine includes: drive motor, reduction gearbox, driving sprocket, driven sprocket, projectile chain and projectile cartridge. The cartridge and the cartridge are connected in series to form a chain, which is fixed on the transmission chain by a pin shaft. By using the equivalent method, the chain shell magazine is simplified as a plane revolving rigid body model, and the following assumptions are made: (1) the shell and the cartridge are regarded as a rigid body, and the center of mass of the rigid body coincides with the center of the cartridge. (2) The shell moves in plane without considering its longitudinal vibration. (3) The mass of the elastic chain is equivalent to a part of the cartridge without considering the influence of the elasticity and clearance of the chain. (4) The influence of contact collision between cartridges is not considered.

Taking the driving sprocket as the equivalent component, the motion parameters of the revolving shell magazine system are treated equivalently. As shown in Fig. 1, the rigid body dynamic model of the revolving chain shell magazine is established. The moment of inertia of the motor rotor is  $J_p$ , the total transmission ratio is  $i_p$ , the moment of inertia of the reduction gear mechanism is  $J_r$ , the transmission ratio between the reduction gear and the driving sprocket is  $i_r$ , and the number of cartridges is  $n$ . Under the condition of ammunition loading, the mass of the  $i$ th cartridge is  $m_i$ , the moment of inertia is  $J_i$ , the center of mass velocity is  $v_i$ , and the angular velocity is  $\dot{\varphi}_i$ . The number of sprockets is  $N$ , the moment of inertia of the  $j$ th sprocket is  $J_{Lj}$ , the angular displacement is  $\varphi_j$ , the angular velocity is  $\dot{\varphi}_j$ , the angular displacement of the driving sprocket is  $\varphi$ , the angular velocity is  $\dot{\varphi}$ .

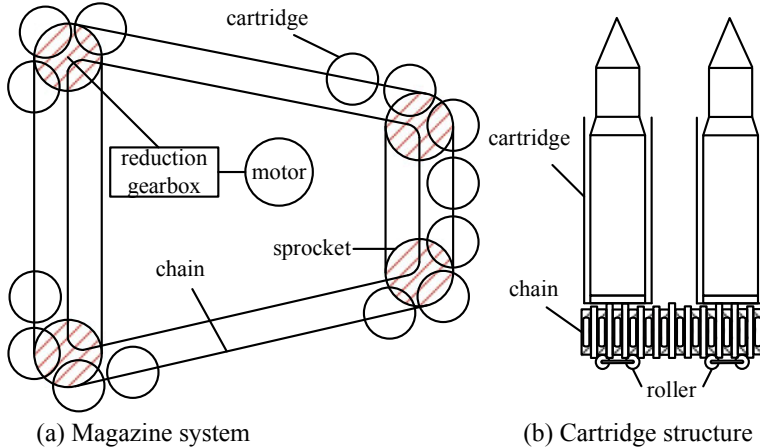


**Fig. 1** Schematic diagram of magazine structure

The equivalent method of the multi rigid body system with single degree of freedom is used to establish the dynamic equation of the model. The kinetic energy of the system can be expressed as

$$T = \frac{1}{2} J_p i_p^2 \dot{\phi}^2 + \frac{1}{2} J_r i_r^2 \dot{\phi}^2 + \sum_{j=1}^N \left( \frac{1}{2} J_{Lj} \dot{\phi}_j^2 \right) + \sum_{i=1}^n \left( \frac{1}{2} J_i \dot{\phi}_i^2 + \frac{1}{2} m_i v_i^2 \right) \quad (1)$$

The work done by the external force to the shell magazine consists of two parts, one is the work done by the output torque of the motor, the other is the work done by the external disturbance torque of the magazine. The virtual work done by the external force can be expressed as

$$\delta W = (M_e(t) - T_L) \delta \varphi \quad (2)$$

where  $M_e(t)$  is the output torque of the motor and  $T_L$  is the external disturbance torque.

According to the Lagrange equation of the second kind, the dynamic equation of the system can be obtained from (1) and (2)

$$J_e \ddot{\varphi} + \frac{1}{2} \frac{dJ_e}{dt} \dot{\varphi} = M_e(t) - T_L \quad (3)$$

In the formula, the equivalent moment of inertia of the driving motor is  $J_e$ , according to the equal kinetic energy of the system before and after the equivalent, the equivalent moment of inertia  $J_e$  can be obtained

$$J_e = J_p i_p^2 + J_r i_r^2 + \sum_{j=1}^N \left( J_{Lj} \frac{\dot{\phi}_j^2}{\dot{\phi}^2} \right) + \sum_{i=1}^n \left( J_i \frac{\dot{\phi}_i^2}{\dot{\phi}^2} + m_i \frac{v_i^2}{\dot{\phi}^2} \right) \quad (4)$$

It can be seen from the above formula that it is a time variable affected by the number of shell loading and the angle of the driving sprocket.

### 3 Analysis of Equivalent Moment of Inertia of Cartridge

When the magazine is working driven by the feeding motor, the cartridge advances to a working position through the chain transmission mechanism in each working cycle. The working cycle is divided into motion-stop-motion. In the stop state, the shell and the hoister are handed over to complete the continuous feeding of the hoister. As shown in Fig. 2, A and B represent the center of the roller, and C represents the center of mass of the cartridge. In order to solve the velocity of the center of mass of the cartridge, segment AB of the chain link can be regarded as a connecting rod for plane motion, and the connecting line OA forms a crank, in which the roller A moves on the arc track, the roller B moves on the horizontal track, and the instantaneous center of velocity of the connecting rod is the point  $O_1$ . The distance between A and B is  $l$ , the rotation center of sprocket is the point  $O$ , the indexing circle radius of sprocket is  $R$ , and the center of mass of shell is located at the midpoint of AB connecting rod. The included angle of  $AO_1$  and  $O_1B$  is  $\alpha$ , assuming that the tangent position of the arc track and linear track is D, the angle  $\alpha$  means the angle that roller A rotates relative to sprocket center O. The angle between connecting rod AB and horizontal line is  $\beta$ , and the speed of the connecting rod endpoint A is  $v_A = R\dot{\phi}$ .

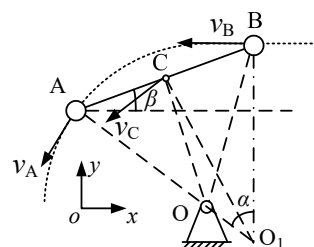
According to the principle of chain transmission, it can be seen that

$$R = \frac{Zp}{2\pi} \quad (5)$$

where  $Z$  is the number of sprocket teeth and  $p$  is the sprocket pitch.

The distance between roller A and instantaneous center  $O_1$  of velocity is  $l_1$ , which can be expressed as

**Fig. 2** Schematic diagram of cartridge movement



$$l_1 = l \cos \beta / \sin \alpha \quad (6)$$

Furthermore, the angular velocity of the connecting rod around the instantaneous center  $O_1$  of velocity is obtained

$$\omega_d = \frac{v_A}{l_1} = \frac{R\dot{\phi} \sin \alpha}{l \cos \beta} \quad (7)$$

The distance between the center of mass C and the instantaneous center  $O_1$  of velocity is

$$l_2 = \sqrt{\frac{l^2}{4} + l_1^2 - ll_1 \cos\left(\frac{\pi}{2} - \alpha + \beta\right)} \quad (8)$$

The equivalent moment of inertia of the cartridge can be expressed as

$$J_d = (J_c + J_n + ml_2^2) \left( \frac{\omega_d}{\dot{\phi}} \right)^2 \quad (9)$$

By substituting Eqs. (7) and (8) into Eq. (9), we can get

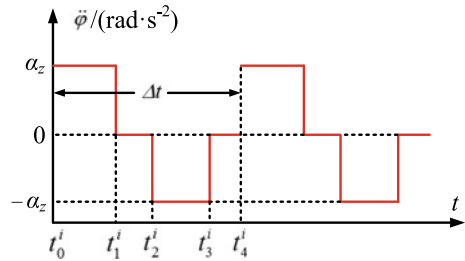
$$J_d = \frac{ml^2(\cos^2 \beta + \sin \alpha \cos \beta \sin(\beta - \alpha))}{(l/R)^2 - (1 - \cos \alpha)^2} + \frac{(J_c + ml^2/4) \sin^2 \alpha}{(l/R)^2 - (1 - \cos \alpha)^2} \quad (10)$$

where  $J_c$  is the moment of inertia of the cartridge around the center of mass, and  $r$  is the radius of the cartridge. According to the geometric relationship in Fig. 2, we can get the  $0 < \alpha < \arccos\left(1 - \frac{l^2}{2R^2}\right)$ ,  $\beta = \arcsin \frac{R(1-\cos\alpha)}{l}$ , when teeth number of the sprocket is small, the moment of inertia of the cartridge changes greatly from the straight section of the track to the transition section.

#### 4 Numerical Simulation About Influence of Driving Sprocket on the Motion Law

The numerical calculation is carried out for a revolving chain shell magazine. The selected parameters are as follows: the number of shells is  $n = 16$ , the mass of shells is  $m = 100$  kg when the shells are loaded in the shells, the moment of inertia of shells relative to the axis of the center of mass is  $J_c = 0.4225$  kg·m<sup>2</sup>, and the mass of shells is  $m' = 12$  kg when the shells are not loaded in the shells, the moment of inertia of the cartridge relative to the axis of the center of mass is  $J'_c = 0.05$  kg·m<sup>2</sup>. The number of sprocket is  $N = 4$ , the moment of inertia of sprocket is  $J_L = 0.6$  kg·m<sup>2</sup>, the radius of indexing circle of sprocket is  $R = 0.2$  m, the moment of inertia of reduction gearbox is  $J_r = 0.5$  kg·m<sup>2</sup>, the total transmission ratio is  $i_p = 5$ , and the transmission ratio

**Fig. 3** Rotation law of driving sprocket



from the reduction gearbox to the driving sprocket is  $i_r = 2.5$ . In a working cycle time, the time of projectile chain stepping motion is 0.5 s, and the working interval is 0.1 s, that is to say  $\Delta t = 0.6$  s. The step distance of the projectile chain is  $d = 0.21$  m, and the length of single link is  $l = 0.12$  m.

As shown in Fig. 3, the rotation angular velocity law of the driving sprocket under trapezoidal control, the time from the shell position before the exit to moving to the exit position is  $\Delta t$ . The time of the first shell moving to the position before the exit is  $t_0^i$ , corresponding to the time node of the last shell leaving the exit is  $t_4^{i-1}$ , in the period of time  $t_0^i \sim t_1^i$ , the driving sprocket rotates uniformly with angular acceleration of  $\alpha_z$ ; In the period of time  $t_1^i \sim t_2^i$ , the driving sprocket rotates at a constant speed, and the angular acceleration is 0; In the period of time  $t_2^i \sim t_3^i$ , the driving sprocket rotates with constant deceleration, and the angular acceleration is  $-\alpha_z$ ; During the period of time  $t_3^i \sim t_4^i$ , the driving sprocket stops rotating, and a shell on the chain passes through the ammunition outlet and moves to the lower outlet of the hoister, so as to realize the one-time ammunition transportation cycle of the revolving chain magazine. After time  $t_4^i$ , the number of shells in the magazine will be reduced by one, and the next ammunition transportation cycle will start.

In a cycle time, assuming that the driving sprocket of the full loaded magazine rotates at a constant speed, the trapezoidal motion and the constant deceleration rotation, the numerical simulation is carried out to study the influence of the sprocket motion law on the equivalent moment of inertia and driving torque of the system. The time under trapezoidal control law is  $\Delta t_1 = 0.15$  s,  $\Delta t_2 = 0.20$  s,  $\Delta t_3 = 0.15$  s respectively. Figure 4 shows the variation law of the magazine's equivalent moment of inertia with time. Figure 5 shows the angular velocity curve of the driving sprocket, and Fig. 6 shows the motor output torque curve.

As shown in Fig. 4, in a cycle, the change law of the equivalent moment of inertia of the magazine with time is a concave function. Compared with the driving sprocket moving at a constant speed and at a constant deceleration, the amplitude of the change speed of the equivalent moment of inertia of the magazine is smaller under the trapezoidal motion law, which indicates that the change of the motor load is more gentle. As shown in Fig. 5, under the trapezoidal control law, the starting point speed of the driving sprocket is 0, which is more in line with the actual movement of the sprocket. Moreover, under this movement law, the mechanism collision problem caused by the residual velocity of the cartridge is not considered, which is conducive to reducing the position error of the ammunition transferred by the magazine and

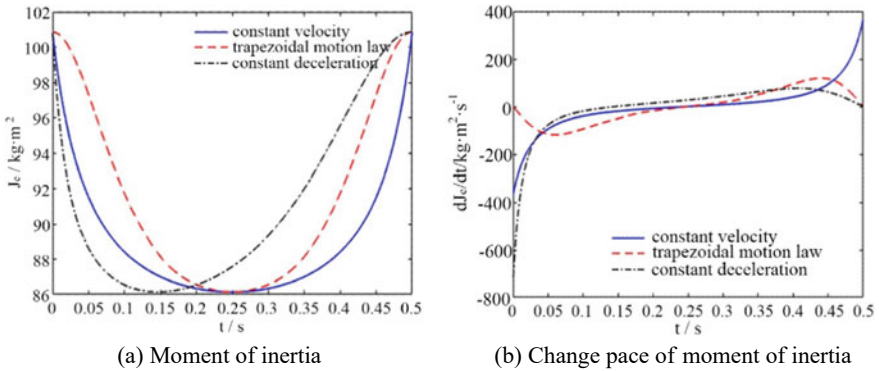


**Fig. 4** Change law of moment of inertia

**Fig. 5** Angular speed of driving sprocket

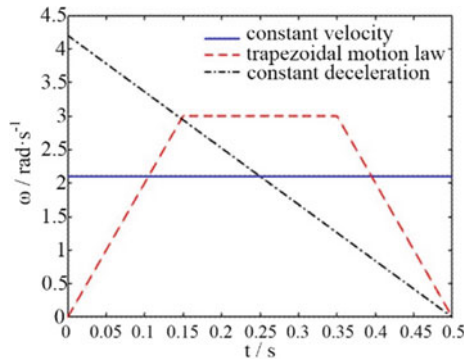
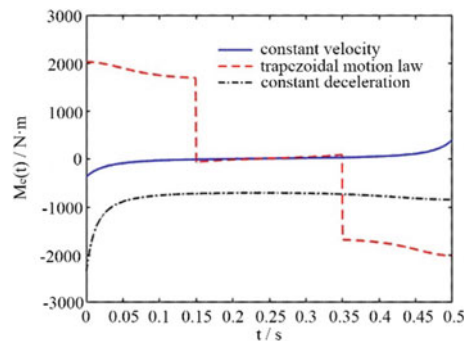


**Fig. 6** Change law of driving torque



improving the reliability of the ammunition feeding action. As shown in Fig. 6, in order to realize the trapezoidal motion law of the driving sprocket, the output torque of the motor needs to meet a piecewise function control law with large fluctuation

range, which puts forward higher requirements for the servo control system of the motor.

## 5 Conclusion

In this paper, the revolving chain shell magazine is simplified as a plane rotating rigid body, and the calculation method of the equivalent moment of inertia of the cartridge at different positions is given. Combined with the numerical simulation example, the influence of the driving torque by the motion law of the driving sprocket and the inertia parameters is analyzed. The following conclusions are obtained: the trapezoidal motion law is more in line with the actual motion of the magazine, compared with the uniform velocity and uniform deceleration. The change law of equivalent moment of inertia is gentler, and the corresponding motor driving torque meets the piecewise function control law.

## References

1. He W (2021) Design and dynamic simulation research of a chain rotary magazine. Xi'an Technological University
2. Wang R, Chen H, He W (2021) Design and simulation of chain automatic magazine. Foreign Electron Meas Technol 40:49
3. Hou B, Ma J (2009) Optimal guaranteed cost control algorithm for automatic chain shell magazine. Acta Armamenarii 30:1164
4. Zou Q, Qian L, Xu Y, Jiang Q, Liu Y (2014) Adaptive robust control of rotational chain shell magazine. Acta Armamenarii 35:1922
5. Zou Q, Qian L, Xu Y, Jiang Q, Yang H (2015) Adaptive fuzzy sliding mode control of rotational shell magazine. J Southeast Univ (Nat Sci Ed) 45:63
6. Wang G, Wang L, Meng X, Hu S (2009) Study on naval gun shell-feeding system design and experiment. Acta Armamenarii 30:518
7. Liu J, Li H, Li Q (2015) Design and force analysis of cannon drum transmission system. J Mech Transm 39:67

# Separate Heat Pipe Research Status of Application in Passive Cooling System



Zhengfu Zhang, Kunrong Huang, and Ningkang Duan

**Abstract** As an efficient heat transfer tool, heat pipes have been widely used in many aspects. As a branch of heat pipes, separate heat pipes have also played a good role in many industries. This paper summarizes the application of split heat pipes in passive containment cooling systems at home and abroad and the related research status, and looks forward to the future development prospects and hopes of this direction. At the same time, a new structure of split heat pipes is proposed.

**Keywords** Separate heat pipe · Passive cooling system · Evaporation section · Downcomer · Containment heat dissipation

## 1 Introduction

From the Chernobyl nuclear accident in the last century to the Fukushima nuclear accident in this century, the safety of nuclear power plants has attracted the attention of all sectors of society, and the containment, as the ultimate safety barrier of nuclear power plants, plays an important role. A nuclear reactor will release a lot of radioactive material and a lot of heat when it is working, so it needs to be isolated from the outside world with a containment. When the containment is about to have an accident, a large amount of heat will be generated inside it. If it cannot be exported in time, it will inevitably lead to unbearable consequences. Therefore, under accident conditions, how to cool down the containment and depressurize it is a problem worthy of research in all aspects.

The heat pipe is more capable of heat transfer and heat dissipation than general conductors, and its closed structure, stable heat transfer and other characteristics make it widely used in related micro heat dissipation scenarios such as electronic

---

Z. Zhang · K. Huang (✉) · N. Duan

School of Mechanical Engineering, University of South China, Hengyang 421000, Hunan, China  
e-mail: [473531165@qq.com](mailto:473531165@qq.com)

Z. Zhang  
e-mail: [zzforce2014@163.com](mailto:zzforce2014@163.com)

component cooling, as well as large-scale high-intensity heat dissipation scenarios such as nuclear reactor containment. Compared with the traditional heat pipe, the special separated structure of the separated heat pipe makes it more flexible in placement and layout, so it has good adaptability for some special application scenarios.

## 2 Fundamentals of Split Heat Pipes

The general heat pipe is mainly composed of pipe body, working medium and liquid absorption core. The pipe body is made of copper, stainless steel and other metal materials. Generally, the body of a general heat pipe is made of one or more materials into an integrated structure. Compared with ordinary heat pipe, the separated heat pipe usually does not have the structure of the wick, and does not need to rely on the suction of the wick for backflow. At the same time, the special feature of the separated heat pipe is its special structure of separating the evaporating end and the condensing end, which is different from the integrated structure of the traditional heat pipe. Therefore, the structure of each section of the whole separated heat pipe is not necessarily made of one material. As shown in Fig. 1, the separated heat pipe is divided into four parts: evaporation section, condensation section, liquid line, and vapor line. Usually, the evaporation end is placed in the scene where heat dissipation is required, and the evaporation end is heated at a high temperature to vaporize the liquid working medium in it, and at the same time, the heat is brought. The vaporized working medium evaporates and rises along the vapor line to the condensation section, exchanges heat in the condensation section, and finally the condensed working medium will return to the evaporation section through the liquid line. The whole process does not need other external energy to drive, and it circulates naturally to achieve continuous heat conduction, take away the heat in the working scene and reduce its temperature.

## 3 Application of Separated Heat Pipe in Nuclear Containment Heat Dissipation

During the continuous operation of nuclear power equipment, the loss of cooling of the reactor core will cause the inside of the containment to heat up instantaneously, which will cause a large amount of high-temperature steam leakage, over-temperature and over-pressure of the shell, and the rupture of the containment. For the heat dissipation of the nuclear containment, the split heat pipe has good compatibility. Due to the extremely strict airtightness requirements of nuclear containment, it is difficult for all conventional heat sinks to meet the requirements. For the separate heat pipe, the evaporation section can be placed inside the containment, and the condensation

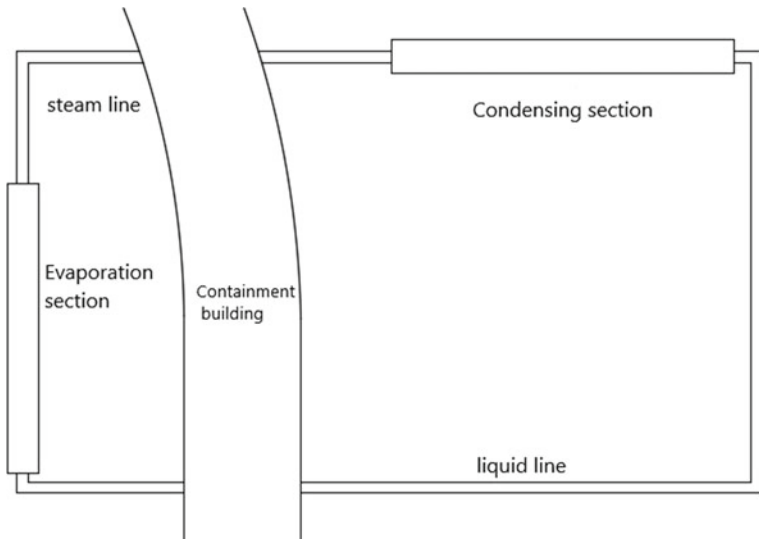


**Fig. 1** Structure of split heat pipe in passive cooling system

section can be placed outside the containment, so that the entire system can achieve heat transfer inside and outside the containment without affecting the safety of its structure. Jia and others [1] discussed the related scientific research progress of using heat pipe cooling technology in pressurized water reactor nuclear power plants, and at the same time determined that the separated gravity heat pipe is highly feasible in pressurized water reactor nuclear power plants. Li et al. [2] demonstrated the feasibility in principle of the separated heat pipe as a passive cooling system of the containment by means of experiments, that is, the system can export a large amount of heat in the containment in a short time when an accident occurs, so as to cool it down. Buck. Tian et al. [3] verified the feasibility of this passive cooling system, that is, the self-starting of the separate heat pipe cooling system is realized by using a large amount of heat generated under the condition of water loss inside the containment, so there is no need to drive by other external energy sources.

### **3.1 Application of Separated Heat Pipe in Passive Cooling System**

In China's existing third-generation nuclear reactor designs, such as AP1000, Hualong No. 1, etc., the concept of "passive" has been introduced into the design of the containment cooling system [4–6]. Passive containment cooling system (PCCS) has been widely used in third-generation nuclear power technology because it can greatly reduce the dependence on active equipment such as diesel generators and

water pumps under accident conditions. Tao et al. [7] proposed a set of PCCS using the separated heat pipe technology. The evaporation section components of the separated heat pipe were placed in the middle of the containment and attached to the shell wall, and the thermal hydraulic behavior of the system was analyzed by means of the systematic program R ELAP5. An independent analysis was performed. The heat transfer process of the passive containment cooling system is a typical coupled heat transfer process. Yuan [8] conducted a theoretical analysis of the coupled heat transfer process and its characteristics. Based on FLUENT, the coupled heat transfer of the passive containment cooling system was analyzed. The process is investigated numerically, and it is confirmed that the partition solution method still has good convergence properties when applied to complex heat transfer processes.

The separated heat pipe is the main functional component of the passive cooling system to exchange and transfer heat. Cheng et al. [9] conducted a transient characteristic test on the passive containment cooling system based on the loop heat pipe technology, which verified that the system has good startup characteristics, can realize the smooth export of heat in the containment under accident conditions, and can realize the rapid reduction of containment pressure in the startup phase. Although the whole system has a working condition area with flow instability, it has no significant impact on the pressure trend in the containment. Ma [10] built a natural circulation system based on a loop heat pipe, and conducted a systematic overall study to investigate the steady-state operating characteristics and the steady-state operation characteristics of the loop heat pipe system in a new generation of passive containment cooling systems under different working conditions. The dynamic operating characteristics are studied and analyzed. Kuang et al. [11] used the VOF model in Fluent to simulate and conduct in-depth research on the boiling heat transfer process at the evaporating end of the separate heat pipe, thereby demonstrating the feasibility of the model, and also effectively simulating the flow pattern in the tube evolutionary process. Li et al. [12] conducted an experimental study on the passive containment heat transfer system based on the separated heat pipe heat exchanger. Sun et al. [13, 14] first simulated the natural convection heat transfer of the environment in the nuclear power containment containing heat pipes, and then arranged the separated heat pipe evaporation components on the top inner wall of the containment, and placed them at an oblique angle. At the same time, Sun et al. [15] also simulated the flow boiling behavior of the evaporation section of a large separated heat pipe with an inner diameter of 80 mm. They found that the external convection heat transfer coefficient and the external fluid temperature are the main factors affecting the heat transfer coefficient. The total mass flow has little influence on the heat transfer coefficient. The obliquity of the evaporation section has a certain influence on the heat transfer effect. The heat transfer effect is better when the obliquity is 50–80°.

Wang [16] noticed that there is thermal stratification in the inner space after the containment breach accident, and studied it, and also analyzed various related factors that affect the heat transfer effect of the containment wall. For different jet flow rates, the main effect on thermal stratification in the containment is to change the thickness of the isothermal zone.

Hua [17] designed a new type of split heat pipe passive containment cooling system on the basis of predecessors. He improved the single row of evaporative end pipes into multiple rows of pipes and arranged them in a cross. At the same time, the start-up characteristics and transient flow characteristics of the passive containment cooling system are simulated and analyzed by the thermal-hydraulic program. Compared with the conventional system, the system can complete a natural cycle in a shorter time, and has very good starting characteristics and heat dissipation capacity. Hu et al. [18] analyzed the heat transfer performance of the separated heat pipe with R134 as the working fluid through experimental research.

Luo [19] introduced the header-type separated gravity heat pipe into the passive cooling system. By establishing the two-phase evaporative boiling model of the R134a working fluid on the CFD platform, the flow pattern in the evaporation section of the separated heat pipe, the flow distribution characteristics between the branch pipes, and the heat transfer coefficient law in the pipe were studied when R134a was used as the working fluid. Yang [20] studied the numerical simulation of boiling heat transfer in the evaporation section of the separated heat pipe, combined with the actual working conditions of the passive containment cooling system, carried out a parameter sensitive analysis of the heat transfer in the evaporation section of the cooling heat pipe, and clarified the relationship between heat transfer and flow pattern.

### 3.2 Study on Other Applications of Separated Heat Pipes

The research on the application of large separated heat pipes in nuclear containment has never stopped, and some other aspects of separated heat pipes are also of reference significance for passive cooling systems. Ji et al. [21] studied the heat transfer characteristics of a parallel separated gravity heat pipe through numerical simulation and design experiments, and found that the fluid in the parallel heat pipe is more inclined to flow into the branch pipe close to the incoming main pipe, thus determining that the traditional parallel design cannot ensure the uniformity of two-phase flow in the heat pipe.

For the optimization of separated heat pipe, the core component of the passive cooling system, and some other types of heat pipes can be referred to. Liu et al. [22] put forward a new structure of thermosyphon, adding a built-in tube in the thermosyphon to improve the two-phase flow pattern in the thermosyphon. This new structure provided many new ideas for later scholars. Kuang et al. [23] proposed a new pulsating heat pipe (PHP) based on this, that is, a built-in pipe was inserted into the single loop pulsating heat pipe. In this way, the flow mode of the liquid and steam plug is changed to improve the heat transfer performance of the heat pipe. The results show that the new pulsating heat pipe with 70% liquid filling rate has the best thermal performance. Compared with the classical pulsating heat pipe without built-in pipe, the heat transfer performance is improved by 14%.

Using Liu et al.'s [22] ideas for reference, as shown in Fig. 2, if a downcomer is built in the evaporation end pipe of the separated heat pipe of the passive cooling system, the liquid working medium at the evaporation end will be stratified, and the working medium at the outside of the downcomer will rise when heated. When reaching the height of the downcomer, the working medium without vaporization will return to the bottom through the downcomer to achieve secondary heating, so as to enhance the overall heat transfer effect. Unfortunately, this structure of separated heat pipes with built-in tubes has not been used in passive cooling systems for the time being, but other scholars have applied it to heat dissipation in other nuclear safety aspects. Kuang et al. [23] designed a separate heat pipe (BTSHP) with built-in downcomer in view of the poor performance of large independent heat pipes (SHP) in the spent fuel pool in long-term heat transfer applications. Through experiments and simulations, they found that the maximum thermal resistance of BTSHP was lower than that of SHP, which proved that BTSHP was more suitable for long-distance heat transfer applications than SHP. At the same time, when the cooling air flow rate increases, the double flow single heat source heat pump can further release its latent heat by reducing the proportion of liquid entering the built-in pipe, thus obtaining better performance than the single heat source heat pump.

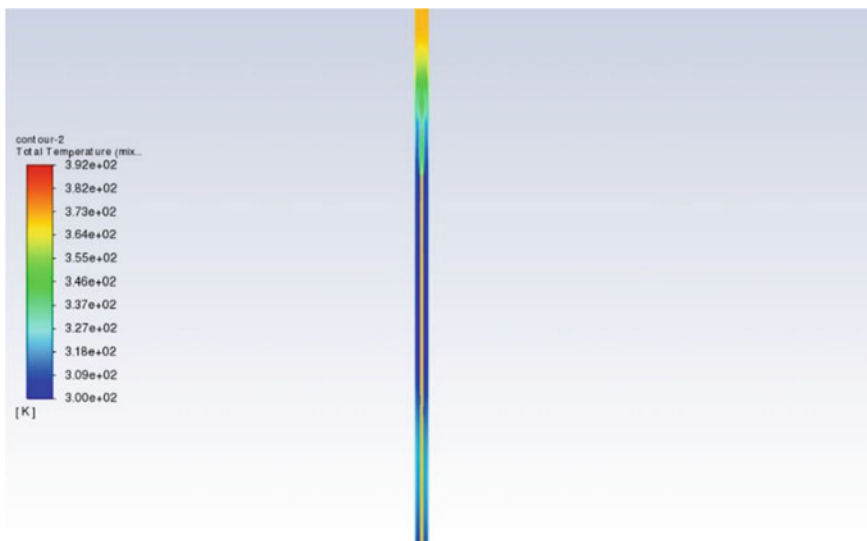


**Fig. 2** Fluent simulation diagram of separated heat pipe with built-in pipe

## 4 Outlook

As a mature heat dissipation tool, the separated heat pipe has attracted the attention of the majority of practitioners in related industries. With the increasing heat dissipation demand of various industries, and the continuous development of materials, heat transfer and other disciplines, optimizing their manufacturing materials, heat transfer working fluids, and heat pipe structures, there will be considerable and even breakthrough research progress in this field in the future. Because the separated heat pipe and the passive cooling system used for nuclear containment heat dissipation have a good phase, the separated heat pipe in this application will also be known by more researchers in the heat dissipation direction with the in-depth research of more scholars, and at the same time promote its development, so that it will have higher heat dissipation requirements, faster heat dissipation efficiency and stronger heat dissipation performance in the future.

## References

1. Jia N, Wang H, Yuan Y (2018) Research progress of heat pipe cooling technology applied to pressurized water reactor nuclear power plants. *Sci Technol Vis* 32:220–223
2. Li Y, Cheng C, Zhang G et al Experimental study on passive containment cooling system of advanced pressurized water reactor
3. Tian W, Yu B, Sun H (2021) Research on heat transfer performance of separated heat pipe in passive cooling system. *Petrochem Equip* 50(03)
4. Lee SW, Baek WP, Chang SH (1997) Assessment of passive containment cooling concepts for advanced pressurized water reactors. *Ann Nucl Energy* 24(6):467–475
5. Yi F, Gu C (2016) Introduction to active and passive safety system of Hualong No. 1. *Mod Manuf* 12:56–57
6. Gu J (2016) “Hualong No. 1” safety system configuration strategy. *China Nucl Power* 4:350–355
7. Tao J, Cheng C, Xie X, Liang X, Chen J (2018) Research on passive containment cooling system using separate heat pipes. *At Energy Sci Technol* (8)
8. Yuan Z (2017) Research on thermal hydraulic numerical method of passive containment cooling system. Harbin Engineering University
9. Cheng C, Wen Q, Lu D et al (2017) Experimental study on transient characteristics of passive containment cooling system. *Nucl Power Eng* 38(1)
10. Ma C (2019) Experimental study on passive containment cooling system of loop heat pipe. Shandong University
11. Kuang Y, Yi C, Wang W et al (2015) Heat transfer performance analysis of a large-scale separate heat pipe with a built-in tube. *Ann Nucl Energy* 75:158–167
12. Li J, Li X, Zhu C et al (2018) Experimental study on heat transfer system of passive containment based on split heat pipe heat exchanger. *At Energy Sci Technol* (3)
13. Sun H, Yu B, Tu S, Li Y (2019) Fluid flow and heat transfer simulation of the tube bundle in the evaporation section of the separated heat pipe in the nuclear power containment. *Petrochem Equip* 48(2)
14. Sun H, Yu B, Tu S (2018) Simulation of natural convection heat transfer in nuclear power containment with heat pipe cooling. *Chem Mach* 45(6)
15. Sun H, Yu B, Tu S (2018) Simulation of flow boiling in evaporation section of separate heat pipe in nuclear power containment. *Chin J Power Eng* 38(11)

16. Wang Y (2017) Experimental study on heat transfer characteristics of passive containment cooling system for small reactors. North China Electric Power University
17. Hua X (2018) Numerical study on passive containment cooling system of advanced pressurized water reactor. Chongqing University
18. Hu Y, Wang B, Yi C, Wang W (2014) Analysis of heat transfer performance of separate heat pipe with R134a as working fluid. *Low Temp Supercond* 42(12)
19. Luo Y (2020) Two-phase flow and heat transfer in a header-type separated gravity heat pipe. Shanghai Jiaotong University
20. Yang H (2017) Numerical simulation of boiling heat transfer in evaporating section of separated heat pipe. Shandong University
21. Ji L, Zhang W, Lin Y (2022) Numerical simulation and experimental study of parallel separated gravity heat pipe. *J Tianjin Urban Constr Univ* 28(3)
22. Liu G, Shan Y, Hongding H (1991) Heat transfer performance of a new two phase closed thermosyphon. *Chem Eng (China)* 19:27–31
23. Kuang Y, Yi C, Wang W et al (2020) Heat transfer performance analysis of a large-scale separate heat pipe with a built-in tube. *Appl Therm Eng* 114716

# Current Status and Prospects for Quantification of 3D Printing



Yaoxin Huang and Jiaqi Chen

**Abstract** One of the most active areas of research today is 3D printing technology. Since the 1980s, the development of 3D printing technology has aroused interest worldwide and has begun to influence people's thinking and way of life. Today, 3D printing technology has advanced and is used in many different fields such as aerospace, military and academia. Although the term "3D printing" is widely known, few are familiar with its basic principles. However, numerous studies have shown that mass production 3D printing is not yet feasible. There are not many ways to mass-produce 3D printed products. This article will summarize the current development status of 3D printing technology from the status of 3D printing technology, the classification of 3D printing technology, and the advantages and disadvantages of 3D printing technology, and look forward to its future development prospects. Through the research of this paper, it will provide a certain reference for the future development of 3D printing technology.

**Keywords** 3D printing · Quantification · Aerospace

## 1 Introduction

Bergmann et al. [1] analyzed the breakthroughs of international enterprises represented by the 3D system company in 3D printing small batch and low-cost production, and pointed out the shortcomings of domestic 3D printing technology. She

---

Y. Huang and J. Chen contributed equally.

---

Y. Huang (✉)

Mechanical Design and Manufacturing and Their Automation, Shantou University,

Shantou 515063, China

e-mail: [19yxhuang5@stu.edu.cn](mailto:19yxhuang5@stu.edu.cn)

J. Chen

Aerospace Engineering, University of Manchester, Manchester M13 9PL, UK

forecasted the future development trend of intelligent, mass production and precision of 3D by analyzing Wohlers Report 2011. Billiet et al. [2] proposed that the personalized customization of 3D printing enables this technology to prepare corresponding medical products according to patients' conditions to help patients recover, which will have a good prospect in the medical field. Bose et al. [3] pointed out that the continuous progress of 3D printing in the pharmaceutical field will help the development of talents in this field.

Three-dimensional (3D) printing is a manufacturing process used to transform digital items into physical models [4]. The technology, also known as additive manufacturing, constructs arbitrary geometries by gradually depositing materials on top of a digital design. This form of production can be accomplished in a variety of ways. The most fundamental method entails placing the raw materials on a platform in a two-dimensional layout and gradually stacking them, layer by layer until the structure is complete. Similar to 2D printers in that 3D printers must adhere to electronic blueprints known as Computer-Aided Design files; 3D printers must also adhere to electronic blueprints ("CAD files"). Users can produce CAD files by designing from scratch or scanning an object, then editing and sharing them over the internet [5]. The integration of 3D printing technology and computer construction modelling technology has significantly expedited the evolution of information-based manufacturing technology toward network customization and digitization [6]. Since the 1980s, 3D printing technology has acquired worldwide attention and begun to permeate people's perceptions and daily lives. Today, 3D printing technology has been refined and implemented in a variety of fields, including industry, medicine, academia, aerospace and the military. Although many individuals are familiar with the term '3D printing', they are unfamiliar with its fundamentals.

This essay's primary objective is to analyze the advantages and disadvantages of 3D printing, as well as its potential for the future mass manufacturing.

## 2 The State of 3D Printing

After thirty years of research and development, the three-dimensional printing (3DP) manufacturing process is now widely used. It is becoming easier for individuals, as well as small businesses and startups, to design and manufacture their own products, thanks to the growing availability of 3D printing software for product design and the ability to manufacture parts using 3D printing equipment that is relatively inexpensive. Products can be designed and manufactured by anyone, including private individuals. The utopian view is that in the not-too-distant future, private individuals will be responsible for the design and printing of many products using 3D technology. Many products' designs and 3D printing processes will eventually be carried out in the comfort of one's own home by private individuals [7]. In 2020, the global spread of the new crown epidemic has resulted in a lack of medical protective equipment in certain nations. Currently, 3D printing has played a part in saving lives. Creative teams, Internet celebrities, and university institutions in the United States, the United

Kingdom, and other countries have used 3D printers to create masks, medical face shields, goggles, and other epidemic prevention equipment, thereby alleviating the shortage of medical protective equipment in various locations; the epidemic has also caused global supply chains. Beginning in mid- to late-March, several facilities in North America and Europe have been shut down one by one, greatly impacting the availability of industrial parts. In addition to the supply chain, the sales and logistics channels of layer-by-layer circulation have been severely impacted, cutting off the supply of many goods' components and parts [6]. 3D printing, which is characterized by rapid, small-batch, mold-free, and flexible production, overcomes these supply chain bottlenecks and paves a new way to tackle supply difficulties; data from AliExpress, the largest B2C cross-border e-commerce site in China [8]. It demonstrates that domestic 3D printer sales were flourishing throughout the outbreak and that since the outbreak, 3D printer sales on the platform have doubled compared to 2019 levels. According to "Wohlers Report 2021" data, in 2020, the revenue from 3D printing services will be approximately 7.454 billion US dollars, accounting for 59.29%, a year-on-year increase of 20.3%; the global 3D printing equipment achieved sales of 3.014 billion US dollars, accounting for 23.97%, roughly the same as 2019's 3.013 billion US dollars; global 3D printing material sales were 2.105 billion US dollars, compared with 1.916 billion US dollars [9].

### 3 Types of 3D Printing

In today's society, 3D printing has entered the public consciousness, and people are continually researching new 3D printing techniques [10]. Currently, FDM (Fused Deposition Modeling), SLA (Stereolithography), Binder jetting technologies, and powder bed fusion processes are the most widely used printing techniques on the market [10].

#### 3.1 *FDM (Fused Deposition Modeling)*

**Historical perspective and evolution.** Scott Crump invented the technology known as FDM or Fused Deposition Modeling, patented it in 1989, and founded Stratasys, Inc with his wife Lisa. Mr Crump was CEO of the company for 25 years until the company's merger with Objet Ltd. in 2012. Crump is currently Chief Innovation Officer, sits on the Stratasys Board of Directors, and is Chairman of the Stratasys Executive Committee. Figure 1 is a schematic diagram of the FDM [11].

**Working principle.** The FDM method melts and extrudes plastic wires through a high-temperature nozzle [7]. The wires are then layered, cooled, and solidified on a platform or processed product, and the solid is accumulated layer by layer. Metal 3D printing offers new design opportunities for metallic components. Frequently, it is used to convert multi-part metal assemblies into a single component or lightweight part with internal channels or hollowed-out characteristics (Fig. 2).

**Fig. 1** Schematic diagram of FDM

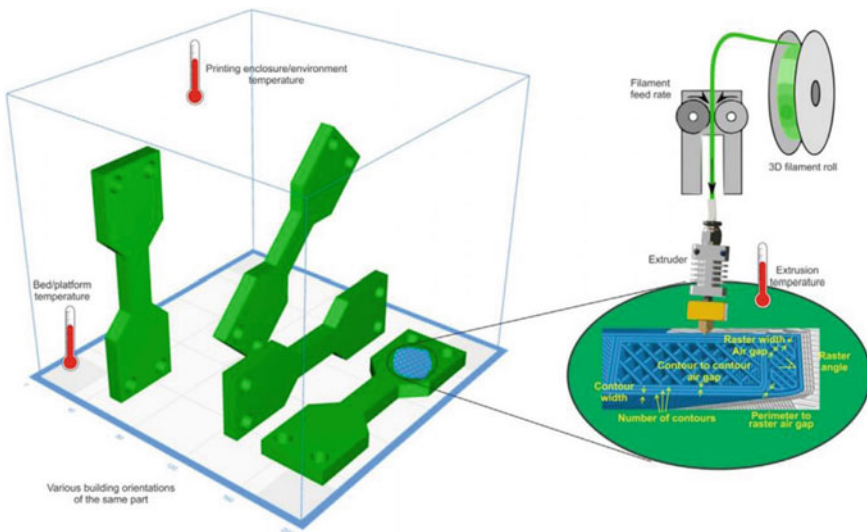
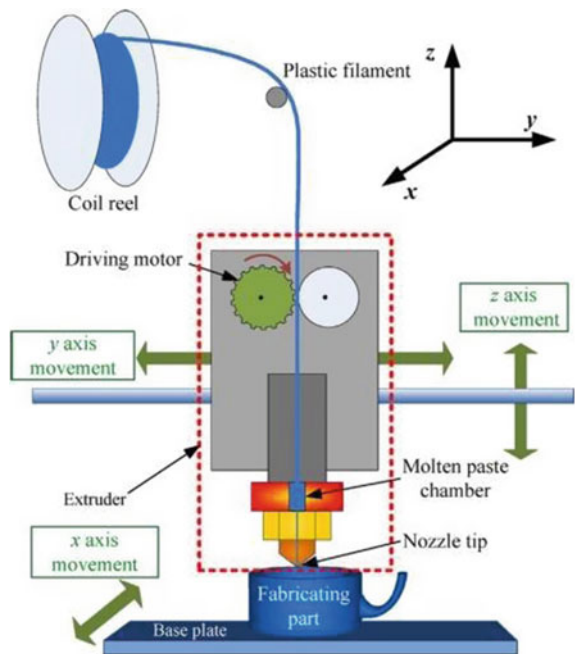


**Fig. 2** FDM process parameters at different places

**Pressure-assisted systems.** For this system, it uses low viscosity materials which results in low accuracy. It also needs a longer production time compared with the Screw assisted systems.

**Screw-assisted systems.** It is built of high viscosity materials, is more precise, and has a shorter production time than the previous system [8]. However, it should be noted that this system is incompatible with living cells for medical purposes.

**Advantages and limitations.** Build speed: dependent on feed rate and plotting speeds; Part anisotropy: isotropic properties in the  $x$ - $y$  plane are possible; Accuracy: limited to 0.078 mm in high-cost printers.

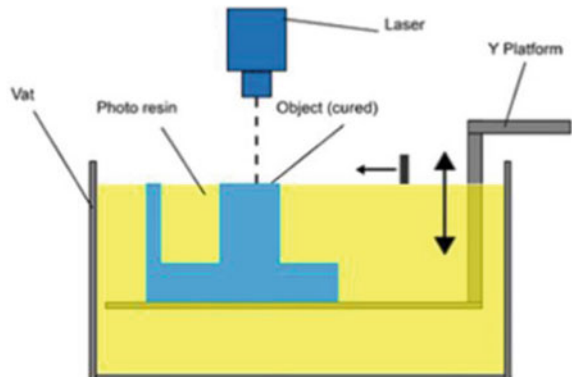
### 3.2 SLA-Vat Photopolymerization

**Working principle.** It is important to note that some machines use a blade that moves between the layers to provide a smooth resin base on which to build the next layer after all of these steps have been completed, the vat is emptied of resin, and the object is removed. The first step in the process is to build the platform and lower it down from the top of the resin vat by layer thickness. The next step is for the UV light to cure the resin layer by layer while the platform continues to move down. Figure 3 is a schematic diagram of SLA [12].

**Materials.** Thermoplastic polymers and photopolymers are the two types of polymers that can be utilized in the production of materials [6]. However, since photopolymers cannot be melted, it is impossible for them to be materials that can be reversed. In the case of photopolymers, the solidification process begins with the formation of a liquid resin, followed by an increase in viscosity.

**Advantages and limitations.** Flexibility: support many different machine configurations and size scales; Built speed: inherent speed advantage over laser scan SL; Accuracy: typical dimensional accuracies for SL machines are often quoted as a

**Fig. 3** Schematic diagram of SLA



ratio of an error per unit length and can go below 0.002 in./in; Materials: limited to acrylates and epoxies for commercial materials; Degradation: most photocured parts are known to age; Post curing: post-processing required; Strength and Durability: low impact strength and durability.

### 3.3 Binder Jetting

**Working principle.** BJ printing is also known as powder bed printing and printing with an inkjet head. In 1993, Sachs and coworkers were the ones who came up with the idea and got the patent for it. The conventional two-dimensional printing process will instead be extended to the three-dimensional space. In actual use, it involves the employment of one or more nozzles for the purpose of injecting a liquid adhesive onto the surface of a bed of powder in order to subsequently bind the powder together. The nozzles travel along a predetermined path in order to deposit a fine layer of powder before stopping. After all of the layers have been stacked atop one another in this manner, a three-dimensional object is created. Figure 4 is a schematic diagram of adhesive jetting.

**Materials.** Printing machines use almost exclusively waxy polymers, acrylic photopolymers and plasters. Research into the development of additional materials is currently underway.

**Continuous stream (CS) versus Drop on Demand (DOD).** Advantages: CS deposition has a high throughput rate; Limitations: materials must be able to carry a charge and the fluid deflected into the catcher must be either disposed of or reprocessed.

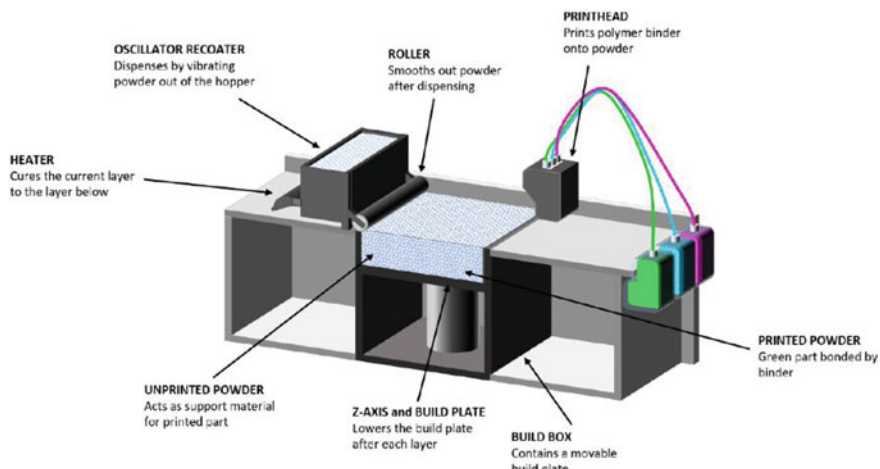
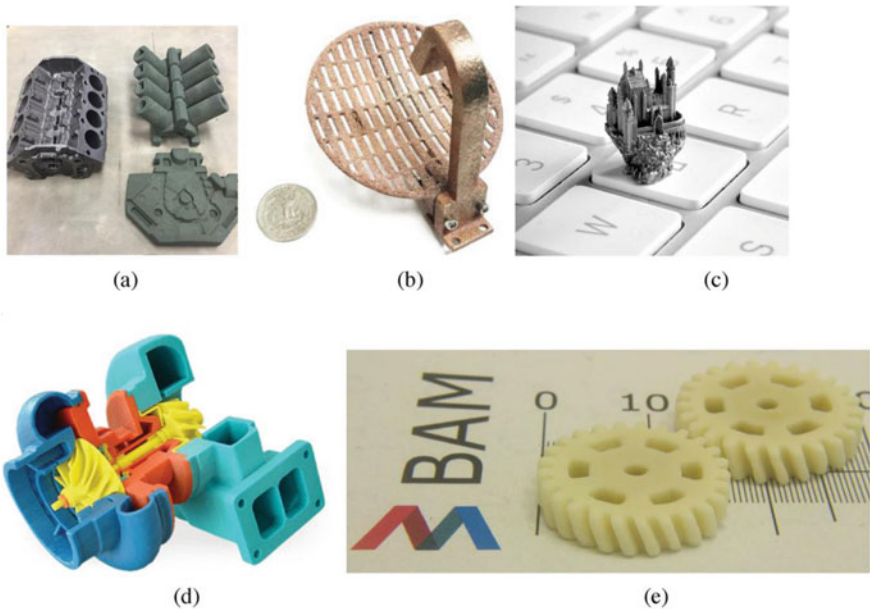


Fig. 4 Binder jetting



**Fig. 5** Examples of the different material processed by BJ printing suited for various applications

**Advantages:** DOD produces smaller drop sizes and also a higher placement accuracy in comparison to CS methods.

**Advantages and limitations.** Advantages: Low cost, High speed, Scalability: multiple printheads, Multiple materials and print in colours, Water can be used as the binder, induced microporosity; Limitations: Limited choice of materials: only waxes and photopolymers are commercially available; Limited part accuracy: particularly for large parts; Low mechanical properties of produced parts (Fig. 5).

### 3.4 Powder Bed Fusion-SLS

**Working principle.** On the building platform, a layer of material is initially laid down, with a typical thickness of 0.1 mm. The initial section or layer of the model is melted by the laser, and after that, a roller is used to sprinkle the next layer of powder on top of the one that came before it. Although the unmelted powder is not removed until the post-processing stage, it is still present in the environment.

**Materials.** All materials that can be melted and re-solidified can be used in PBF processes including polymers, metals and ceramics.

**Advantages and limitations.** Advantages: Complex geometries: enhanced by loose powder; Mechanical properties: higher compared to other additive manufacturing

systems; Surface finish and accuracy: lower compared to vat photopolymerization processes; Shrinkage: dependent on used material but generally around 3–4%; Productivity: lower compared to other additive manufacturing processes.

## 4 Advantages of 3D Printing

The current society is becoming more familiar with the technology of 3D printing, which is used in a wide range of fields and simplifies the construction of a great number of complicated models as well as turns flat surfaces into three-dimensional structures. The benefits and drawbacks of the 3D printing technology will be the topic of our next conversation.

### ***4.1 An Increase in the Productiveness of Production***

Computers can be used by 3D printers to directly carry out the production of various parts or models, and the process does not require the assistance of any other equipment to be finished. In contrast to conventional factories, the production of components when multiple people work on a single device or even a number of production lines in tandem in order to assemble, and 3D printers do not need to assemble, making them not only more productive but also helping to save a significant amount of money in terms of both labor and the cost of raw materials.

### ***4.2 An Efficient Management of Expenses***

Traditional industries oftentimes participate in the production of new items or components, and as a result, they are required, according to the various products' needs, to introduce new machinery and talent. This not only results in increased costs but also makes pricing very difficult to understand. As long as people master the technology behind it, they can directly print products with 3D printers, which is not only convenient, but also has the potential to reduce production costs and control production costs more effectively.

### ***4.3 Easily Portable and Capable of Being Relocated***

3D printers are not the same as traditional production equipment, which is usually large and cumbersome, is not portable, and transportation is a very difficult process. 3D printers, on the other hand, are mobile and portable, and they can produce larger

products with greater physical strength than their own larger products. Traditional production equipment, on the other hand, is subject to the limitations imposed by the machine tool regardless of the size of the product. In addition, when compared to its production equipment, the 3D printer is much smaller, and it does not need to be placed in a dedicated factory in order to be used. It can be used in the comfort of one's own home or office. There is no need to stop relying on synthetic models, animals, and physical laboratories because it is now possible to produce anatomical bodies with realistic touch and behavior using a 3D printer like the J750 Digital Anatomy 3D printer from the well-known 3D printing brand Stratasys. This enables practitioners to experiment and train anywhere they choose. This not only means that costs associated with training and procurement will be reduced, but it also means that. It also raises the ethical standards because it eliminates the need to conduct surgical trials on animals in order to test surgical equipment.

There are actually quite a few benefits associated with 3D printing; however, these benefits can vary depending on the specific application, the type of consumables that are supported by the 3D printer, and the underlying principles of the 3D printing technology. Consequently, certain products need to be evaluated on an individual basis. However, there is no doubt that the application of 3D printing to improve the competitiveness of enterprises has gradually become a common trend in a variety of industries, and as a result, the future development and application of the technology behind 3D printing is something that is definitely worth looking forward to.

## 5 Limitation

Within the confines of a single build operation, it is not possible to print a component in a different color or at a different resolution. When it comes to research, design verification, or reverse engineering goals for the use of 3D printing systems in final designs, this is not really a significant limitation. However, it does limit the use of parts in certain non-engineering applications. It is difficult to achieve a high level of precision, complexity, and strength because the materials that are currently available for 3D printing are limited. The majority of these materials are plaster, plastic, and resin. Because of this, 3D printing can only be used for some products with low precision. Because the price of 3D printers is still very high, the use of 3D printers to manufacture goods results in a cost that is significantly higher than the cost of large-scale enterprises after the scale of production is evenly spread to each item. The latter mass production is also faster than the manufacturing speed of 3D printing. For metal materials, the 3D printing technology has not yet reached its maturity stage. In addition, the price cost of the device makes it difficult to grow demand. 3D printing is not suitable for the direct manufacturing of high-precision instruments, the latter still needs to be processed by hand, because 3D printing is done through the material layer by layer stack up, so each layer has a certain thickness, which also led to its precision being difficult to reach the same height with the traditional

manufacturing methods. Additionally, the product performance defects of the 3D printing technology cannot be compensated for the time being.

## 6 Development Prospects

### 6.1 Aerospace

In the aerospace industry, the capacity of 3D printing technology to adjust to challenging working conditions and produce high-precision products is absolutely necessary. Therefore, in the future, 3D printing could be used in the aerospace industry to create mechanical parts that are more complex and advanced, thereby improving the defects that are created by traditional manufacturing. US aerospace researchers also successfully applied 3D printing technology to the manufacture of rocket engine jets in 2021. Reports indicate that engine jets made using 3D printing technology not only have higher quality and performance than those made using traditional industry but also significantly reduce manufacturing costs, as well as the amount of work and cycle time. This was accomplished by applying 3D printing technology to the manufacturing of rocket engines.

### 6.2 Medical Treatment

To this day, the technology of 3D printing has been put to extensive use in the field of medicine. For instance, it has been used to print surgical aids, human organs, and individualized prostheses. The materials that are used for 3D printing are also not harmful to living organisms in any way. Only medical CT scans can be used to obtain the appropriate image data, and such specialized models have a higher degree of adaptability and can better repair missing parts of the body. It is important to keep in mind that the 3D printing technology uses data to create solid geometric models, so only medical CT scans can be used to obtain the appropriate image data.

### 6.3 Material

The increasing availability of new printing materials is one of the primary factors driving the development of new uses for 3D printers. Plastic is still the most common material used in 3D printing, but metal materials are growing rapidly, with their usage rate increasing to around 36%. Ceramic materials, polymer materials, and metal materials are the primary types of materials used in 3D printing. Polymer materials are also used. The widespread use of metal materials has been a driving force behind

the growth in sales of industrial-grade 3D printers. This has caused 3D printing to expand from the consumer-grade market to the high-end manufacturing market, and this expansion of 3D printing's application areas will continue.

#### ***6.4 The Demand for Personalized Products***

Consumers are looking for products and services that are more tailored to their specific requirements as the economy and living standards continue to advance. The use of 3D printing in conjunction with other technologies, such as robotics and artificial intelligence, will allow for increased manufacturing line flexibility and the production of individualized goods at reduced costs. At the same time, it will make it possible for customers to design the form and dimensions of their models according to the specifications they desire, model them, and then create solids using the technology of three-dimensional printing. The development of 3D printers, materials, and post-processing technologies will continue to contribute to the growth of the 3D printing industry's market size in the future. This will allow the industry to accommodate a larger customer base.

### **7 Conclusion**

3D printing has the potential to easily satisfy people's creative ideas and needs at a very low cost and faster manufacturing speed. Additionally, it has the potential to provide people on the path to artistic creation with more ideas and more powerful assistance. Printing in three dimensions (3D printing) will become the primary driving force behind the technological advancements that will drive the new changes that will occur in society as time goes on. The 3D printing technology possesses the qualities of having a precise structure, having good integrity, and being relatively inexpensive. As a result, it is capable of producing a series of products with a high economic value. These products find widespread application in a variety of fields, including the manufacturing of machinery, the construction industry, medicine, aerospace, and aviation. The modern social order places an emphasis on putting the needs of the customer ahead of all other considerations in order to produce more satisfying goods for those customers. The use of three-dimensional printing not only makes it possible to produce goods that are tailored to the specific requirements of individual customers, but it also significantly lowers the costs associated with the manufacture of goods, mitigates the dangers posed by market competition, and, to some extent, raises both the consumption levels and the living standards of average people. Even though the contribution of 3D printing technology to global manufacturing is negligible, the development and application of 3D printing technology is also influenced by a variety of factors. This is because of the nature of the technology. However, as research into 3D printing continues and technological advancements are

made, its application areas will expand, printing materials will become more diverse, and printing devices will become more functional. This will soon have a profound impact on the conventional production methods that are currently in use.

## References

1. Bergmann C, Lindner M, Zhang W (2010) 3D printing of bone substitute implants using calcium phosphate and bioactive glasses. *J Eur Ceram Soc* 30(12):2563–2567
2. Billiet T, Gevaert E, Schryver TD (2013) The 3D printing of gelatin methacrylamide cell-laden tissue-engineered constructs with high cell viability. *Biomaterials* 35(1):49–62
3. Bose S, Vahabzadeh S, Bandyopadhyay A (2013) Bone tissue engineering using 3D printing. *Mater Today* 16(12):496–504
4. Chee K, Chua C (2020) 3D printing of smart materials: a review on recent progresses in 4D printing. *Virtual Phys Prototyp* 20:10–15
5. Chenxi L, Hongjun K, Jinzhu W, Ningning C, Xiaohong W (2021) 3D printing and its application in the field of medicine. *J Mater Eng* 66–76
6. Leukers B, Irsen SH (2005) Hydroxyapatite scaffolds for bone tissue engineering made by 3D printing. *J Mater Sci - Mater Med* 16(12):1121–1124
7. Lam C, Mo XM, Teoh SH (2002) Scaffold development using 3D printing with a starch-based polymer. *Mater Sci Eng, C* 20(1–2):49–56
8. Macdonald E, Salas R, Espalin D (2014) 3D printing for the rapid prototyping of structural electronics. *IEEE Access* 2(2):234–242
9. Ventola CL (2014) Medical applications for 3D printing: current and projected uses. *P & T: Peer-Rev J Formulary Manag* 39(10):704
10. Wang X (2012) 3D printing technology and industry development and prospect analysis. TP751A, 1009-2374 (2012) 26-0003-3
11. Figure 1. Schematic of fused deposition modeling process. Source: [18] (no date) ResearchGate. [https://www.researchgate.net/figure/Schematic-of-fused-deposition-modeling-process-Source-18\\_fig1\\_324601411](https://www.researchgate.net/figure/Schematic-of-fused-deposition-modeling-process-Source-18_fig1_324601411)
12. Wu C, Fan W, Zhou Y (2012) 3D-printing of highly uniform CaSiO<sub>3</sub> ceramic scaffolds: preparation, characterization and in vivo osteogenesis. *J Mater Chem* 22(24):12288–12295

# Development Trend of Monitoring System Application in Coal, Metal and Non-metal Mines



Jialan Sun

**Abstract** With the development of mining in the direction of improving quality, the management of mines has become more and more scientific, and it is particularly important to use high-tech monitoring and monitoring methods to carry out information-based high-quality safety management. The optimization, efficiency and safety of mine management work promote the long-term development of my country's energy industry. This paper starts with the necessity of the safety monitoring and monitoring system of coal mines and metal and non-metal mines, and systematically analyzes the safety monitoring and monitoring systems of coal mines and metal and non-metal mines. Status, similarity, optimization and development direction.

**Keywords** Safety monitoring system · Monitor · Mining

## 1 Introduction

Mining generally refers to conventional energy mining, that is, resource mining such as coal mines, metal and non-metal mines. Due to the great differences in geological conditions in the mining areas, various disasters are diverse. Although various accidents have generally shown a downward trend in recent years, major accidents still occur frequently and even rebound. With the changes in resource mining depth, mining scale, mining scope and mining intensity in recent years, most of the geological layers have experienced geological tectonic movements, the geological conditions are extremely complex, and the degree of disaster will be more prominent. Therefore, preventing emergencies is a necessary guarantee for safe production, and how to effectively curb the occurrence of accidents is a major issue

---

J. Sun (✉)  
Beijing University of Technology, Beijing, China  
e-mail: [29388951@qq.com](mailto:29388951@qq.com)

Ccteg China Coal Research Institute, Beijing, China

that needs to be solved urgently. Mine monitoring system is a safety monitoring and monitoring technology used in resource mining to prevent hazards from occurring.

## 2 The Necessity of Safety Monitoring and Monitoring Technology

Coal is an important industrial fuel in China. With the continuous high-level development of the coal mining industry, the demand for coal increases accordingly. Enterprises must ensure the safety of workers while pursuing production efficiency. Most of the coal mining in my country takes place underground, the natural environment is very complex, the mining conditions are extremely changeable, and many disasters may occur in mines. Coal mines large and small in my country actively respond to the national requirements and are successively equipped with coal mine safety monitoring and monitoring systems, 24 h a day which work to prevent accidents and casualties. The safety monitoring and monitoring system can automatically collect and process all kinds of underground water, fire, gas, dust, methane, carbon monoxide and other harmful gases, realize real-time monitoring and early warning, and play a significant role in ensuring coal mine safety and preventing natural disasters.

Metal and non-metal mines refer to all mines except coal mines, coal-based pyrite mines, and coal mines, associated mines, and oil mines. Non-coal mines refer to mining enterprises that mine metal ores, radioactive ores, and as petrochemical raw materials, construction materials, auxiliary raw materials, refractory materials and other non-metallic minerals (except coal). Non-coal mines have no risk of gas explosion, but are otherwise not fundamentally different from coal mines. Collapse and roof fall accidents are the most common, accounting for more than 40% of the total deaths in metal and non-metal mines, followed by water penetration and poisoning [1].

With the development of informatization, it has entered a new era. The production environment of coal mines, metal and non-metallic mines is increasingly dependent on the safety monitoring and monitoring system and has a wide range of applications. Its main function is to timely and accurately collect all kinds of required information, play an important role in monitoring and early warning, prevent and reduce many mine accidents, and avoid danger to workers. The country has put forward higher standards and requirements for the safety production of mining. The previous safety monitoring and monitoring system cannot meet the needs of mining production. While various safety monitoring systems provide efficient and convenient services, the system is real-time and stable. Sexual issues are also becoming more prominent.

### 3 Analysis of Status Quo of Mine Monitoring System and Selection of Monitoring Parameters

#### 3.1 Analysis on the Status Quo of Mine Monitoring System

Analysis of the Status Quo of Mine Monitoring System Coal mines, metal and non-metallic mines have the same principles and methods for mine field division, but because of the different reasons for the formation of minerals, there are many types of ground pressure management methods during mining, backfill mining methods, and the need for surface protection, different values, except for a few similarities with coal mining methods in production practice, such as the complex occurrence conditions of non-coal deposits, the complex and changeable shape and occurrence of ore bodies, and the types of ore and the majority of coal mining methods. However, the monitoring systems of coal mines, metal and non-metal mines are basically divided into digital monitoring and monitoring systems and video monitoring and monitoring systems [2].

The digital monitoring and monitoring system mainly collects some parameters in mining and forms real-time curves and graphs, and alarms when abnormal conditions occur. The video monitoring and monitoring system realizes the monitoring and monitoring of mining safety by collecting on-site video. At present, mining 5G technology has large bandwidth, low latency, fast speed, high concurrency, and strong anti-interference ability, which is very suitable for safety monitoring of mining.

The key influencing factors of accidents in the mining of coal mines, metal and non-metal mines are: (1) Disasters caused by the movement of geological layers. (2) Disasters are formed due to hidden structures between geological layers, or mining fractures that directly lead to adjacent geological layers with hidden danger sources. By monitoring the signs of specific factors of the geological layer, according to the common methods of judging the mining risk and the methods in the precautionary rules, we can grasp the changes, and monitor the changes to judge whether there is an accident.

Therefore, a core industrial Ethernet switch is basically set in the ground dispatching center of the mine monitoring and control system to construct the industrial Ethernet backbone network, and each monitoring subsystem and video signal are connected to the ring network switch according to the principle of proximity, that independently operate in the network segment, and connect with the mine LAN.

Mine monitoring and control system is mainly composed of various sensors, mining cameras, signal converters, communication substation, communication master station, PC, data analysis software and other parts. Each communication substation receives the real-time data of the monitoring points, transmits the data to the communication master station, and then transmits the data to the monitoring center through the industrial ring network. Each main station and substation is equipped with explosion-proof power supply to ensure normal power supply even if the equipment is cut off (Figs. 1 and 2).

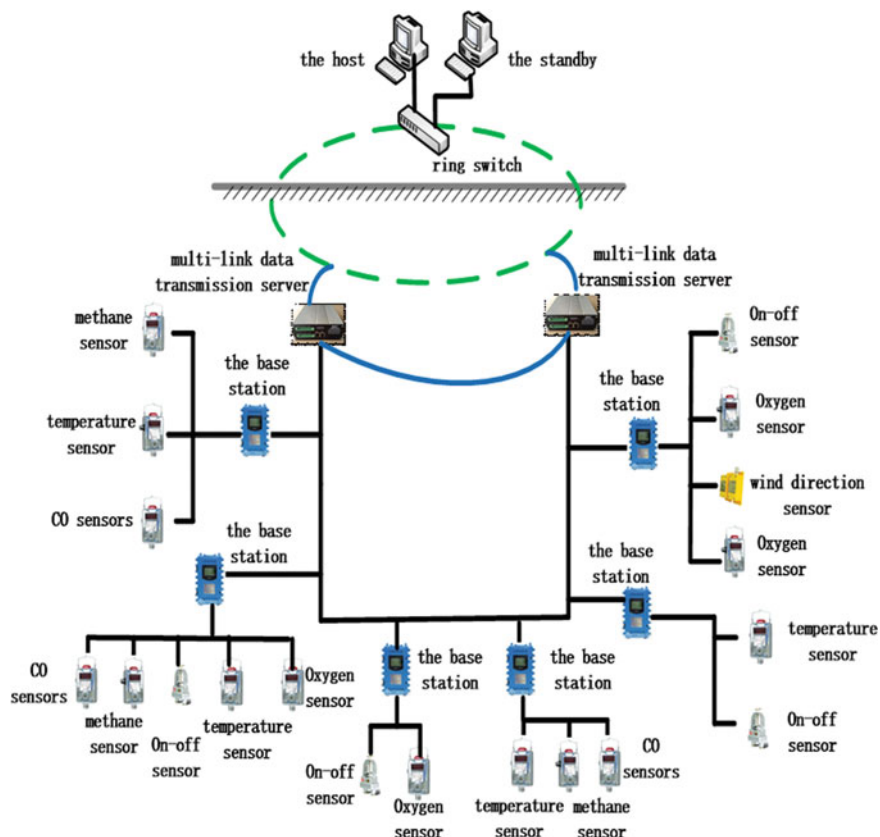


**Fig. 1** Schematic diagram of digital monitoring system

### 3.2 Selection of Monitoring Parameters

The principle of selecting the monitoring parameters of the mining monitoring system is mainly through the dynamic monitoring of the parameters, which can realize the timely, fast and efficient grasp of the mining area, especially the changes in the hazardous areas, and give active early warning based on real-time data, so as to improve the mining efficiency. The district provides effective hazard basic data, and takes corresponding preventive measures in advance to prevent the formation of sudden hazard threats by analyzing the formation causes and influencing factors of each hazard point, the location relationship with other hazard points, and the impact on other hazard factors. Therefore, each monitoring element must be rational, scientific, monitorable and timely.

Due to the different functions of various mining monitoring systems on the market, it is impossible to effectively and comprehensively monitor all the hazard

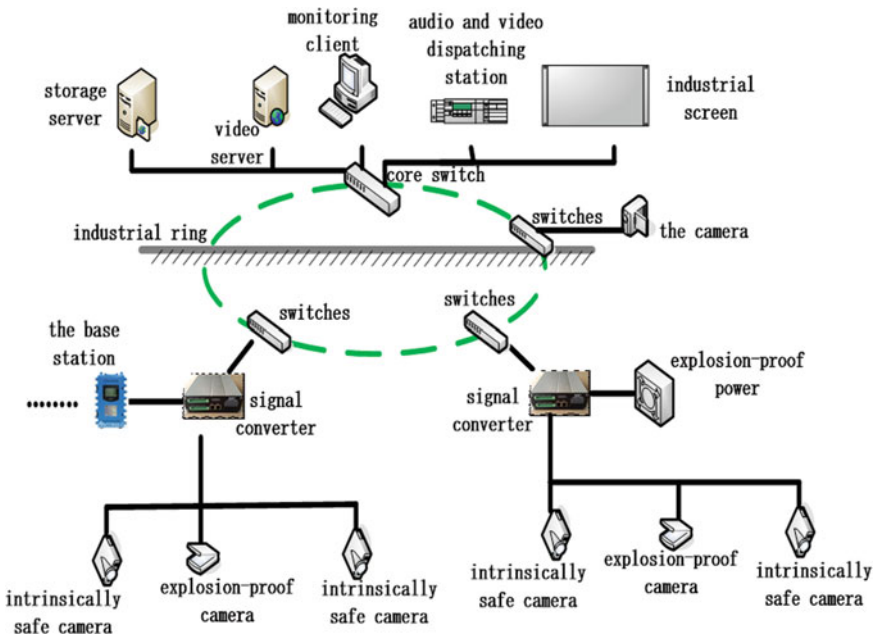


**Fig. 2** Schematic diagram of video monitoring system

factors in the mining area. Therefore, the multi-system integration and system linkage capabilities also need to be improved.

In that mine monitor and control system, the key monitoring object include air volume, temperature, water level, CO, CO<sub>2</sub>, O<sub>2</sub>, CH<sub>4</sub>, dust, smoke and other parameters, and the operation parameters of electromechanical equipment are also need to be monitored and controlled, so as to realize the real-time monitoring of the mine mining safety production situation.

#### 4 Early Warning System Function

The early warning function of mining the monitoring system can further improve the safety of mining and effectively inhibit the occurrence of various safety accidents. Therefore, it is necessary to develop a new generation of intelligent equipment and optimize software functions.

## 4.1 System Hardware Features

The monitoring system of coal mine, metal and non-metal mine mainly realizes multi-parameter real-time data monitoring. The hardware part mainly includes the data acquisition equipment, monitoring and acquisition system and data transmission equipment installed at each parameter monitoring point in the production line during the mining process. All monitoring data is sent to the monitoring center server.

The research and development of a new generation of intelligent sensors, each monitoring substation can preprocess the collected data and signals, the monitoring master station can accurately process all kinds of data and signals, the substation, master station and equipment controller are integrated, the actual base station can diagnose and correct itself, intelligent control equipment, and reduce the occurrence rate of safety accidents.

## 4.2 System Software Features

The monitoring and early warning software for coal mines, metal and non-metal mines mainly consists of six parts: web data display, speech synthesis, client data display, network publishing, dual-machine hot backup, and communication programs. Real-time online monitoring of various indicators of water, fire, dust, methane, carbon monoxide and other harmful gases; the system monitoring data can be self-collected, self-analyzed, self-divided, self-backed up, and digitized in the form of charts and curves, dynamic display and output in graphical form; a separate power supply can be configured for the system to ensure stable power supply; the system can improve the efficiency of data transmission; The system has the ability to recover data quickly; System data can be completely saved; the system has functions such as index overrun self-alarm, double-click hot standby automatic switch, man-machine dialogue, self-diagnosis, software fault tolerance, real-time multitasking and other functions.

The software interface function design mainly includes data collection, chart query, real-time over-limit warning and system management, etc. The business logic algorithm relationship is set according to their corresponding industry standards, technical requirements and performance testing methods.

## 5 Conclusion

The overall function of monitoring system should be considered from practicality. Based on the principles of rationality, scientificity, monitorability and timeliness, and combined with the systematic analysis of the key influencing factors of hazard occurrence, the important monitoring parameters were determined.

Through the monitoring data and curve analysis of the monitoring and control system on-site application, it is possible to fully understand the geological dynamics of the mining area, master the changing laws of the hazard sources in the mining area, obtain the possible causes of the hazards in time, and realize the effective monitoring and early warning of the hazard factors in the mining process through digital means.

With the advent of the era of artificial intelligence, the mining of coal mines, metal and non-metal mines also conforms to the trend and realizes intelligence. In the future, the system will not only be used for monitoring, but also widely for controlling production. The premise of building intelligent mining is to build an intelligent monitoring system. Then it would require upgrading the current system, using more control elements, leveraging cloud computing to centrally manage and monitor data. It is necessary to accumulate experiences through a lot of on-site practice to achieve intelligence, normalization and standardization [3–5].

## References

1. Yuan B (2022) Study on early warning system of metal mine accident. *Mod Occup Saf* (05):70–72
2. Lu D (2022) Exploration of underground mine safety management informatization. *Xinjiang Youse Jinshu* 45(02):18–19
3. Xu J (2022) Current situation and development trend of coal mine safety monitoring and control technology. *Energy Energy Conserv* (03):92–94
4. Lu D (2022) Non-coal underground mine accident investigation and control mechanism. *Xinjiang Youse Jinshu* 45(03):13–14
5. Yang Y (2022) Construction path of non-coal mine safety environment culture. *Labour Prot* (01):40–41

# Weighted Modal Strain Energy Damage Identification Based on Image Sequences



Jiayan Zheng, Hailin Chen, Haijing Liu, Renwei Luo, and Heng Li

**Abstract** The vibration of structures is a very common phenomenon, and obtaining vibration information of bridges can effectively analyze their health status. To identify local damage to the structure, using a camera to capture vibrations of the structure, this study uses the optical flow method to calculate the displacement, frequency, and mode shape of the structure from spatiotemporal sequence images. A local weighted modal strain energy change rate index can be calculated, and structural damage can be identified by comparing the energy change rate before and after damage. A cantilever beam was employed to test the way. The results show that the optical flow method correlates well with numerical simulation results, with a maximum error of 5% based on structure frequency. With a weighted modal strain energy change rate index, it is easier to determine the damage location; Comparing different damage degrees of the same unit yields the size of the damage degree.

**Keywords** Frequency · Weighted modal strain energy · Optical flow method

## 1 Introduction

Structural vibration characteristics can provide information about the health of a structure. Detection approaches that are traditional have the disadvantages of being labor-intensive, inefficient, and interfering with traffic flow. Using other monitoring approaches that integrate new materials and technologies [1, 2] is, however, limited by many factors, including cost, convenience, and adaptability. To identify the damage to the structure conveniently and efficiently, in recent years, modal analysis has become the focus of many scholars at home and abroad in damage identification based on

---

J. Zheng · H. Chen (✉) · R. Luo · H. Li  
Chongqing Jiaotong University, Chongqing 400074, China  
e-mail: plusdada@126.com

H. Liu  
China Merchant Chongqing Communications Technology Research and Design Institute Co. Ltd.,  
Chongqing 40076, China

dynamic characteristics. As a result of its careful consideration of the frequency, element stiffness, and other factors of the structure, modal analysis has become increasingly popular for identifying damage to structures.

Damage to a structure changes its modal frequencies. Cawley and Adams [3] suggested that when a structure has single damage, damage identification is achieved using the ratio between the frequency change before and after the damage. Liu Wenguang et al. [4] identified cracks in cantilever beams using natural frequencies. NIUZR [5] proposed a probabilistic damage detection algorithm for shear steel frames and truss structures. And the feasibility and effectiveness of the method are verified by experimental and numerical analysis. Using natural frequencies to identify damage to structures has the advantage of being easy to measure and highly accurate. However, based solely on frequency, it is not possible to determine where small or multiple damages are located.

Based on modal analysis, researchers [6, 7] proposed a modal strain energy damage identification index, which greatly settled the problem of limitations of natural frequency detection in modal analysis. In the field of damage identification, modal strain energy has gradually become the focus of attention due to its superior performance and good identification effect. However, when the modal strain energy loss is affected by the external environment, resulting in its injury, positioning accuracy is not high. Several modal strain energy damage identification algorithms were compared by Wang et al. [8] Nick et al. [9] determined the damage locations of steel girder bridges using the damage index method of modal strain energy. The Bayesian data fusion modal strain energy change rate theory was proposed by Wei Jun et al. [10] to improve the damage identification capability of traditional strain energy methods. A digital image correlation approach was used by Liang Peng [11] to improve the accuracy of modal strain energy identification. It was suggested by Miao Bingrong et al. [12] to adopt modal strain energy change rate as well as optimization technology to settle the problem of insufficient quantitative analysis. However, the above studies ignore the effect of frequency and do not consider the consistency of dynamic characteristic changes in identifying structural damage.

To better solve the issue of local damage identification of structures, by combining the modal strain energy with the frequency, the resulting proposed damage identification way [13, 14] identifies the local damage of an engineering structure more accurately. In this study, based on the modal analysis theory, the vibration information of the structure is captured by a camera. And the optical flow method [15] is adopted to track the dynamic displacement of the structure in the Spatio-temporal sequence images to obtain the displacement, frequency, and vibration pattern of the structure. The local weighted modal strain energy change rate index can be employed to verify the validity and accuracy of the approaching index in identifying damage to cantilever beam structures and to provide a reference for damage assessment. The damage identification can be achieved by calculating the local weighted modal strain energy change rate index of the structure. In this research, a cantilever beam structure was tested to verify the effectiveness and accuracy of the method and to provide a reference for damage identification of the structure.

## 2 Weighted Modal Strain Energy

The stiffness of the structure will change due to the damage. While the structural mass is almost constant. Thus, the change of mass matrix is neglected. According to the vibration characteristic equation of the structure  $[K - \lambda M]\Phi = 0$ :

$$[(K + \Delta K) - (\lambda_i + \Delta\lambda_i)M](\phi_i + \Delta\phi_i) = 0 \quad (1)$$

$\Delta K = \sum_{j=1}^L \alpha_j K_j, (-1 < \alpha_j < 0)$ ;  $\Delta\phi_i = \sum_{j=1}^m c_{ij} \phi_j$ . Where  $\phi_i$  and  $\lambda_i$  are the modal modes and inherent frequencies of the  $i$ -th order.  $m$  denotes the number of modal orders considered.  $L$  denotes the total number of units of the structural system.  $\alpha_j$  denotes the local unit stiffness matrix.  $c_{ij}$  denotes the modal mode change factor.

In the no-damage system  $\phi_r^T K = \lambda_r \phi_r^T M$ ,  $(K + \lambda_i M)\phi_i = 0$ . Therefore, we can obtain:

$$c_{ir} = \frac{-\phi_r^T \Delta K \phi_i}{(\lambda_r - \lambda_i)} \quad (2)$$

The modal strain energy (MSE) of the  $i$ -th and  $j$ -th elements before and after damage to the structure are

$$MSE_{ij}^u = \phi_i^T K \phi_i \text{ and } MSE_{ij}^d = \phi_{di}^T K \phi_{di} \quad (3)$$

The superscripts  $u$  and  $d$  indicate the undamaged and damaged conditions, respectively.  $MSE_{ij}^u$  and  $MSE_{ij}^d$  are the cells' modal strain energies of the  $i$ -th and  $j$ -th elements of the undamaged and damaged structure, respectively. The damage condition of the structure is usually not known until the structure is tested. Thus, the unit stiffness matrix of the damaged structure can be replaced by the unit stiffness of the undamaged one.

The modal strain energy change (MSEC) after damage occurs in the  $i$ -th and  $j$ -th elements is:

$$MSEC_j^i = \phi_{di}^T K_i \phi_{di} - \phi_i^T K_i \phi_i \quad (4)$$

Resolved:

$$MSEC_j^i = 2\phi_i^T K_i \left( \sum_{r=1}^m \frac{-\phi_r^T \nu K \phi_i}{\lambda_r - \lambda_i} \phi_r \right), r \neq i \quad (5)$$

Assuming that only one  $p$ -cell exists damage in the structure, substituting  $\Delta K = \sum_{j=1}^L \alpha_j K_j, (-1 < \alpha_j < 0)$  into Eq. (5) yields.

$$MSEC_j^i = -2\alpha_p \sum_{r=1}^m \frac{1}{\lambda_r - \lambda_i} \phi_r^T K_p \phi_i \phi_i^T K_j \phi_r, r \neq i \quad (6)$$

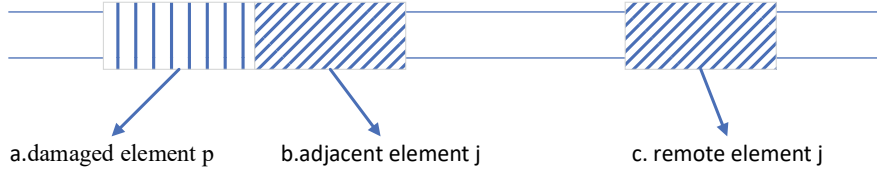


**Fig. 1** Relationship between damage element  $p$  and target element  $j$

In the structural system, most of the elements of the two vectors  $\phi_r^T K_p$  and  $K_j \phi_r$  are 0. The few elements related to the stiffness matrix  $K_p$  or  $K_j$  degrees of freedom are not 0.

The formula has the following conditions:

1. (1) If  $j = p$ , i.e., cell  $j$  is the damaged cell as in the case of *a* in Fig. 1. Then the two vectors  $\phi_r^T K_p$  correspond to the non-zero part of  $K_j \phi_r$  one by one. Currently,  $MSEC_j^i$  is a great value.
2. If  $j \neq p$ , but the damage cell  $p$  is adjacent to the  $j$  cell as in the *b* case in Fig. 1. Then  $\phi_r^T K_p$  corresponds to the non-zero part of the two vectors of  $K_j \phi_r$  locally. That is, the  $MSEC_j^i$  result is smaller.
3. If  $j \neq p$ , the computational unit is far from the damaged unit as in the case of *c* in Fig. 1. Then the non-zero parts of the two vectors  $\phi_r^T K_p$  and  $K_j \phi_r$  do not correspond to each other. That is,  $MSEC_j^i$  is very small.

It can be seen that the modal strain energy change of the cell is a more sensitive parameter for the local damage to the structure. That is, it can be employed to determine the damage location of the structure. However, in actual experiments, the low-order modal data of the structure are easier to be measured. The higher-order modal data are more susceptible to the influence of the measurement points, boundary conditions, and noise, respectively. To locate the local damage to the structure more accurately, the weighted modal strain energy (AMSE) is introduced:

$$AMSE_{ij}^u = \phi_i^T K \phi_i / \omega_i \text{ and } AMSE_{ij}^d = \phi_{di}^T K \phi_{di} / \omega_i^d \quad (7)$$

where  $\omega_i$  and  $\omega_i^d$  are the  $i$ -th order inherent frequencies before and after damage to the structure. The weighted modal strain energy takes into account the effect of the intrinsic frequency. It adopts the intrinsic frequency to reduce the effect of higher-order modes when superimposed. The rate of change of modal strain energy for this cell of the  $i$ -th modal  $j$  element is

$$AMSEC_R_{ij} = \frac{|AMSE_{ij}^d - AMSE_{ij}^u|}{AMSE_{ij}^u} \quad (8)$$

### 3 Optical Flow Method

The velocity field of the local displacement in the video or image sequence is estimated by the optical flow. It characterizes the change in motion between 2 frames of images. The vector target from the initial position to the end of the motion is characterized by it. There are 2 basic assumptions for the calculation of optical flow: ① The assumption of luminance invariance. The brightness of the objects in the adjacent frames in the image is constant ② Small motion assumption. The object motion in the adjacent frames is small enough.

Let the grayscale value of the image point  $(x, y)$  be  $I(x, y, t)$  at time  $t$ , and the position of the image point be  $(x + \Delta x, y + \Delta y)$  and the grayscale value be  $I(x + \Delta x, y + \Delta y, t + \Delta t)$  at time  $t + \Delta t$ . According to hypothesis ①, the basic equation of the optical flow is:

$$I(x, y, t) = I(x + \Delta x, y + \Delta y, t + \Delta t) \quad (9)$$

A Taylor expansion is performed on the right end of Eq. (9) at  $(x, y, t)$ . By assumption ②, removing the higher order minima yields:

$$I_x u + I_y v + I_t = 0 \quad (10)$$

where  $I_x$  and  $I_y$  are the gradients of the image gray scale in space, respectively.  $I_t$  is the derivative of the image gray scale in time.  $u$  and  $v$  are the components of the optical flow vector, respectively. That is the displacement of 2 adjacent frames in the  $x$  and  $y$  directions.

Equation (10) is the basic equation of the optical flow field, which is also called the constraint equation. Since the equation contains two unknown variables  $u$  and  $v$ , only employing the constraint equation to settle  $u$ , and  $v$  is not possible. Thus, other additional constraints need to be introduced.

### 4 Numerical Simulation Analysis of Cantilever Beam Damage

#### 4.1 Finite Element Model and Calculation Condition of Cantilever Beam

Numerical analysis of a rectangular cantilever beam with a length  $L = 1.2$  m and a section size  $0.044\text{ m} \times 0.002\text{ m}$  is carried out employing a finite element software. Figure 2 shows the fixed end A and the free end B. Its structural material is steel, and Table 1 shows its physical properties. A numerical simulation calculation is performed using 16 grids of the same length along the axial direction, and 17 element

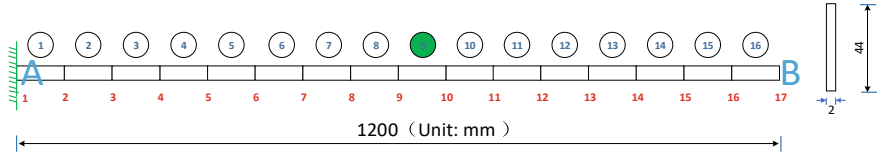


**Fig. 2** Diagram of the cantilever beam structure

**Table 1** Physical parameters of the cantilever beam

Length (m)	Height (m)	Thickness (m)	Density ( $kg/m^3$ )	Elastic Modulus (GPa)	Poisson's Ratio
1.2	0.044	0.002	7850	210	0.3

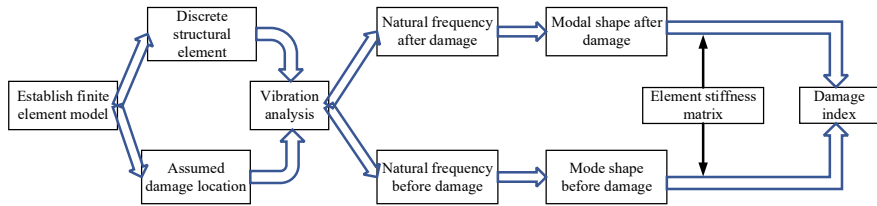


**Fig. 3** Flow chart of finite element damage identification

nodes. We select a linear reduction element with 8 nodes (C3D8R). The structural damage occurred in unit 9. In this study, the stiffness reduction method is adopted to simulate three working conditions with damage degrees of 15, 30, and 45%.

## 4.2 Process of Damage Identification

To obtain the natural vibration frequency of the structure and the main mode shapes of each order, vibration analysis and calculation are employed in this study. The weighted modal strain energy of the cell is then calculated using Eq. (7) and substituted into the damage index for damage identification. An illustration of the specific damage identification process can be found in Fig. 3.

## 4.3 Result Analysis

**Natural Frequency.** The relative rate of change of the  $j$ -th frequency before and after the injury is  $\Delta f_j = \frac{f_j - f_j^d}{f_j}$ , where  $f_j$  and  $f_j^d$  are the  $j$ -th order frequencies

before and after the injury, respectively. Table 2 shows the natural frequencies under different damage conditions for the cantilever beam's first three orders. A beam's natural frequencies decrease when damage occurs, and the frequency change rate increases as the degree of damage increases; When the damage level of unit 9 is 45%, its first-order frequency relative change rate  $\Delta f_j$  is 0.0071, its second-order  $\Delta f_j$  is 0.0231, and it's third-order  $\Delta f_j$  is 0.0016.

**Regularized vibration patterns.** Under the mass-normalized mode shape, Fig. 4 shows the first three-order displacement values of the 17 equal points under different damage conditions. As the damage degree increases, the mode shape difference increases as well. When the damage level of unit 9 is 45%, its first-order mode shape difference of 0.0051, a second-order of 0.0205, and a third-order of 0.0420.

**Change rate of modal strain energy of weighted element.** Equation (8) defines the modal strain energy rate of change index for weighted elements. During the modal analysis step, the natural frequency could be calculated in the case of resonance and the main mode shape of the structure are determined. Using the modal displacement of a node and the mode shape curve, which is fitted by interpolation, we can deduce the rotation angle of each element node. Then the weighted modal strain energy change rate (AMSECR) of the damage indicator is calculated at each modality order.

As shown in Fig. 5, element 9 has a higher weighted modal strain energy change rate when its cantilever beam is damaged. In the first three orders, it is evident that structural energy changes occur in the damaged part. Energy change rate increases with damage degree for modal strains. A cantilever beam with 45% damage has a first-order weighted modal strain energy change rate of 0.2276, a second-order of 0.3335, and a third-order of 0.7049.

**Table 2** First three orders of inherent frequency

(Hz)	No damage	Damage of 15%	Damage of 30%	Ddamage of 45%	Maximum ( $\Delta f_j$ )
First order	1.0073	1.0057	1.0035	1.0001	0.0071
Second order	6.3128	6.2801	6.2345	6.1667	0.0231
Third order	17.676	17.670	17.661	17.648	0.0016

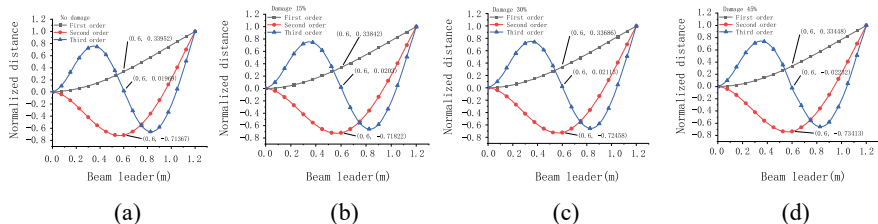


**Fig. 4** Third order vibration pattern

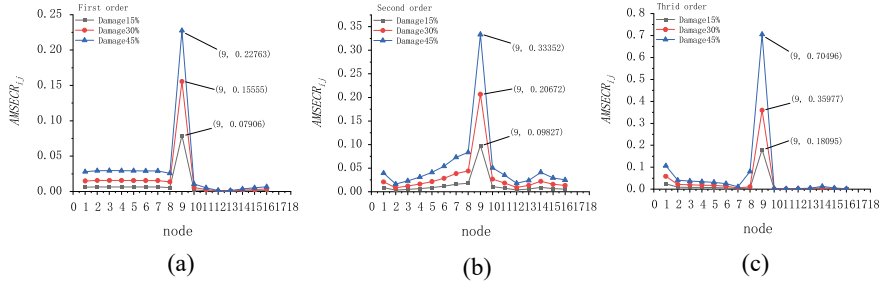


**Fig. 5** Weighted modal strain energy change rate line graph

## 5 Experimental Study on Damage of Cantilever Beam

### 5.1 Test Overview

To facilitate the comparison, this research employs the same rectangular cantilever beam as the numerical simulation. The steel bar is placed upright, with the upper end as the free end and the lower end welded to a rigid base of relatively high self-weight as the fixed end, thereby reducing the impact of self-weight on its bending. For this experiment, the cantilever beam was divided into 16 units with 17 measurement points. Based on the image sequence, 17 aliquots were selected as motion tracking targets. The location of the crack was located near point 9 (shown in Fig. 6). To reduce the influence of light changes, background noise, and other factors, no external lighting equipment was used during the experiment. Natural light was the only one adopted in the experiment. The instruments and related parameters are shown in Table 3.

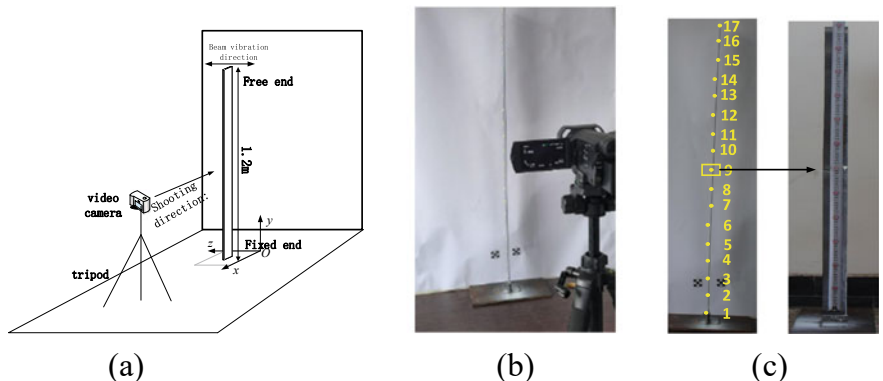


**Fig. 6** Schematic diagram and layout of the laboratory site

**Table 3** SONY FDR-AX700 video capture device parameters

Model	Camera lens	Total pixels	Frame rate (fps)	Resolving power (pixel)
SONY FDR-AX700	CMOS sensor	2 megapixels	100	1920 × 1080

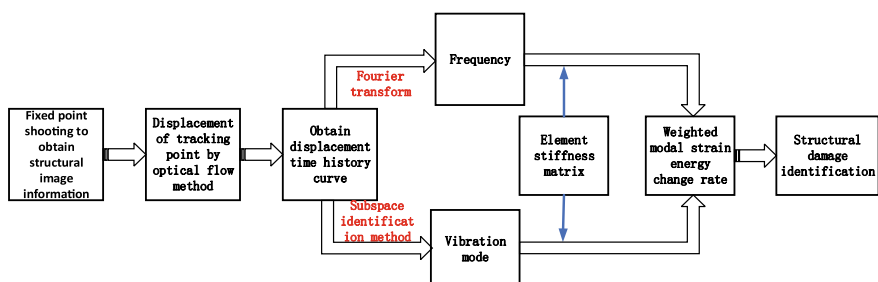
## 5.2 Test Conditions

For this test, an artificially excited cantilever beam is employed to create horizontal lateral displacement. Since the crack depth is linearly related to the section stiffness, and the thickness of the cantilever beams is thin, the crack depth is used to determine the degree of damage. The test involved three damage cases with crack depths of 6.6 mm (15%), 13.2 mm (30%), and 19.8 mm (45%), which corresponded to the numerical simulation conditions in 3.1.

## 5.3 Analysis of Results

Firstly, a program was written to track the displacement of 17 equal points of the cantilever beam using the optical flow method to track the displacement of the points and obtain their displacement time data. Next, to determine the frequency of a structure, the Fourier transform is used. Eventually, by using the modal subspace identification method, one can determine the mode shape of a structure (shown in Fig. 7).

**Displacement time curves.** Displacement time tracking based on image sequences for 17 measurement points in the whole domain of cantilever beam vibration. Displacement time-history curves for measuring points 1, 9, and 17 are shown in Fig. 8. Measurement point 1 has a small amplitude and a large high-frequency vibration, and measuring point 17 has a large amplitude and a small high-frequency vibration. The displacement value is also smaller the closer the measuring point is to the fixed end.

**Fig. 7** Flow chart for image sequence-based analysis

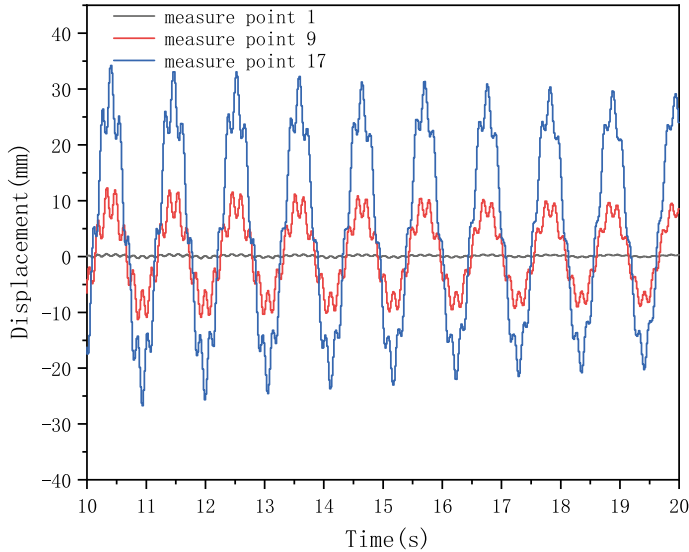


**Fig. 8** Vibration displacement time curve of different measuring points

**Inherent frequencies.** Based on the image sequences, Table 4 shows the natural frequencies of the first three orders of the cantilever beam without damage and under different damage conditions. Table 4 shows that the maximum error of the first-order frequency obtained by its frequency and numerical simulation is 4.83%, the second-order is 3.03%, and the third-order is 2.54%. Since the beams are welded, bent out of shape, or otherwise in practice, their frequencies will change accordingly. Therefore, the image measurement itself has a certain error with the finite element frequency. As a result of damage, the natural frequencies of each order of the beam will decrease. The frequency change rate increases and the frequency decreases more as the damage degree increases. There is a maximum frequency change rate when the damage level of unit 9 is 45%, the first-order frequency change rate  $\Delta f_j$  is 0.0682, the second-order  $\Delta f_j$  is 0.0562, and the third-order  $\Delta f_j$  is 0.0444.

**Table 4** First three orders of inherent frequency

(Hz)	No damage	The damage of 15%	The damage of 30%	The damage of 45%	Maximum percentage error (%)	Maximum ( $\Delta f_j$ )
First order	1.056	1.032	1.008	0.984	4.83	0.0682
Second order	6.336	6.216	6.12	5.98	3.03	0.0562
Third order	18	17.88	17.71	17.2	2.54	0.0444

**Regularized vibration patterns.** As shown in Fig. 9, the normalized mode shapes obtained at 17 measuring points with a 15% damage degree were compared with the numerical simulation structure. According to Fig. 9, photogrammetry results are in good agreement with numerical simulations. The vibration profile is not as smooth as that of the numerical simulation because of the inevitable noise effects in the experiment. The points tracked are not as accurate as those of the finite element. Compared with the numerical simulation, there is a certain error in the mode shape in the experiment.

**Weighted modal strain energy change rate.** Substituting the frequencies and mode shapes into Eq. (8) yields the weighted modal strain energy change rate. Figure 10 shows the results.

As shown in Fig. 10, the rate of change of the weighted modal strain energy of the damaged cell was significantly higher than that of the other cells when the damage occurred in the cantilever beam at cell 9. The structural energy changes are located in the damaged part where the energy changes. For 45% damage, the first-order weighted modal strain energy change rate is 0.3303, the second-order is 0.4369, and the third-order is 1.2003. The rate of change in weighted modal strain energy increases with damage severity. A weighted modal strain energy change rate derived from the image sequence, however, does not agree with the numerical simulation results. This problem is due to overly high numerical simulation accuracy, which reaches the thousandth level, unsatisfactory camera accuracy and frame rate, as well

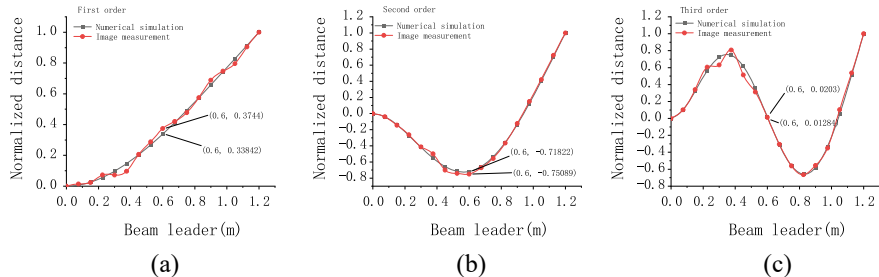


**Fig. 9** Third order vibration pattern before damage to 15% beam

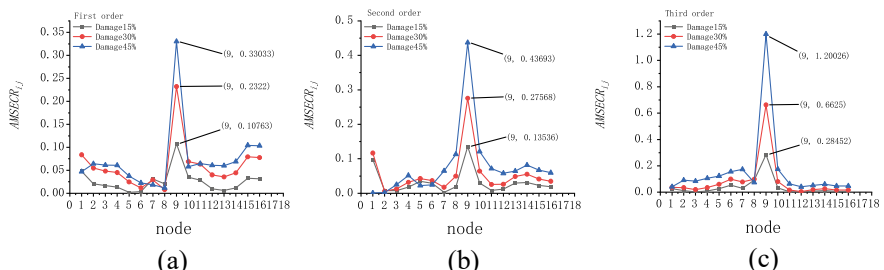


**Fig. 10** Weighted modal strain energy change rate line graph

as floating tracking points. A weighted modal strain energy change rate can be used to detect structural damage, and damage localization can be achieved when significant damage has occurred.

## 6 Conclusion

This research employs a weighted modal strain energy rate of change way and an optical flow method to identify damage in cantilever beam structures. As a result of theoretical derivations, numerical simulations, and cantilever beam tests, the following conclusions can be drawn:

1. With the optical flow method, a displacement time-history curve is obtained by tracking the dynamic displacement of any point of the structure. This approach overcomes the disadvantages of traditional measurement ways, including high labor costs, low efficiency, and traffic blocking.
2. Using Fourier transforms and modal subspace identification methods, the structure's frequency and mode shape are extracted. Suitable for structural health inspections, its frequency error is within 5%, and its mode shape curve is consistent.
3. Under low-order modal shape conditions, the weighted modal strain energy change rate index can be used to identify local damage in cantilever beam structures.
4. The rate of change of the weighted modal strain energy at the damaged unit is significantly higher than at other units, and the local damage location of the structure can be determined from the numerical magnitude of this index.

**Acknowledgements** This work was financially supported by the National Natural Science Foundation of China (51778094,51708068), Chongqing Jiaotong University Graduate Research Innovation Project (CYS22398).

## References

1. Yun Z, Yiting C (2021) Contactless structural displacement measurement method based on digital image correlation theory. *J Hunan Univ (NATURAL SCIENCE EDITION)* 48(05):1–9
2. Wei W (2021) Research on unmarked measurement method of bridge displacement based on image matching technology. Southeast University
3. Cawley P, Adams RD (1979) The location of defects in structures from measurements of natural frequencies. *J Strain Anal Eng Des* 14(2):49–57
4. Liu W, Guo L, He H, Yan L (2017) Damage identification method of breathing cracked beam based on natural frequency. *China Mech Eng* 28(06): 702–707 + 713
5. Niu Z (2020) Frequency response-based structural damage detection using Gibbs sampler[J]. *J Sound Vib* 470:115160

6. Chen JC, Garba JA (1988) On-orbit damage assessment for large space structures. *AIAA J* 26(9):1119–1126
7. Zhiyu S, Shaoxiang L, LingMi Z (1998) Element modal strain energy rate method for structural damage location. *J Vib Eng* 03:109–113
8. Wang S, Xu M (2019) Modal strain energy-based structural damage identification: a review and comparative study. *Struct Eng Int* 29(2):234–248
9. Nick H, Aziminejad A, Hosseini MH et al (2021) Damage identification in steel girder bridges using modal strain energy-based damage index method and artificial neural network[J]. *Eng Fail Anal* 119:105010
10. Wei J, Du Y, Wu Z, Huang D, Liu K (2019) Damage identification of beam structures based on modal strain energy and Bayes theory. *J Railw Sci Eng* 16 (08): 2052–2061
11. Peng L (2018) Research on damage identification method based on modal strain energy of DIC. *Guangdong University of Technology*
12. Miao B, Zhang Y, Huang Z, Zhang Z, Yang S (2022) Optimization method for structural damage identification using modal strain energy change rate [J/OL]. *J Vib Eng*: 1–10
13. Shen Q (2012) Research on structural damage identification based on experimental modal analysis. *Nanjing University of Aeronautics and Astronautics*
14. Fu'an L, Jun H, Lixin H (2021) Damage identification of functionally graded Eulerian Bernoulli beams based on modal strain energy and frequency fusion method. *Compos Sci Eng* 08:25–30
15. Ye X, Chuanzhi D (2019) A review of structural displacement monitoring based on computer vision. *J China High* 32(11):21–39

# Solution of the Full Potential Equation on an Airfoil by Physics-Informed Neural Network



Peiyuan Cong and Yunfei Gao

**Abstract** There are several fresh, promising approaches for solving partial differential equations (PDEs) based on machine learning techniques. In this study, the physics-informed neural network (PINN) is applied to approximate the solution of the full potential equation to simulate airfoil computation. To deal with a PDE system, PINN is capable of working without partial differentiation of the equation and specifically deals with shocks, which mainly uses the physical equations and other constraints like boundary conditions. The PINN method is efficient in solving PDEs, especially in higher dimensions, while it seems impossible to tackle them using traditional numerical methods due to the complex mesh generations and formulations. For the PINN method, the solution of this PDE system is predicted by DNN. The network architecture contains four hidden layers, using the tanh() function as the activation function. It is capable to take a spatial–temporal point as input so that the mean-square error is obtained to calculate loss terms. Then an optimizer is used to specify the mapping between the input and output. To show how well PINN performs in solving the full potential equation for various free-stream Mach number values, three examples are used. The predicted results show that PINN can find solutions successfully. Furthermore, several methods are proposed to optimize our model.

**Keywords** Physics-informed neural network · Full potential equation · Deep learning

---

P. Cong

Marine Science and Technology School, Tianjin University, Tianjin 300000, China

Y. Gao (✉)

College of Architecture and Environment, Sichuan University, Sichuan 610065, China

e-mail: [2019141410020@stu.scu.edu.cn](mailto:2019141410020@stu.scu.edu.cn)

## 1 Introduction

When simulating physical phenomena, partial differential equations (PDEs) are frequently used, especially in fluid dynamics. To numerically solve these PDEs, numerous techniques have been devised. For instance, based on Laplace-like transform and variational theory, Bekela et al. [1] proposed a numerical method for solving time-fractional nonlinear partial differential, showing great efficiency and accuracy. Besides, a new discretization method was obtained by Albuquerque et al. [2], which is capable of achieving the accuracy as the traditional one with lower computational cost. Utilizing HAM, the approximate solution of the partial differential equation (PDE) was obtained by Fallahzadeh et al. [3]. The methods mentioned above are novel and well-established. Nevertheless, they have to be tailored to the specifics of a particular PDE, which may include problems that are hard to solve using classical numerical approximations [4]. In the full potential equation case, shocks may be introduced.

With recent advances in computation power and software environments, Physics-informed neural networks (PINNs) [5] provide a brand-new perspective for solving PDEs. In terms of the training data and physical models, PINNs introduce the standard feed-forward neural networks (NNs) to approximate the solutions to the PDE systems. Using auto-differentiation, a method that works out the output's derivatives for the network's inputs, the formulation of the loss function is greatly simplified. Though PDE solvers based on neural networks are not as accurate and efficient as conventional solvers, they are easier to implement and can be applied to essentially any differential equation [6]. Take flow simulations in fluid mechanics as an example, the inverse and forward PINN formulate are the same: the code does not need to specifically deal with shocks, therefore this method is best used in the solution of PDEs that may introduce challenging physics features. PINNs have demonstrated promising performance in several nonlinear benchmark problems [7] and have been applied to many physical phenomena. For instance, Zapf et al. estimated the diffusion coefficient governing the long-term spread of molecules in the human brain from magnetic resonance images using PINNs and the finite element method [8]. Recently, Wang et al. studied the applicability of PINN in optical fiber communication and presented five potential solutions for time-domain, frequency-domain, and spatial-domain modeling [9].

In this paper, we use PINNs to solve the full potential equation, simulating the flow field around a thin airfoil. Before applying an appropriate optimizer to reduce the loss function by changing the parameters of the DNN, the loss function of the DNN is first used to encode the physical equations and other constraints [10]. After being trained, the neural network takes the spatial coordinate of a given point as the input and outputs the approximated value, which is our solution for the PDE. The rest of the paper is structured as follows: In Sect. 2, the full potential equation is described,

followed by the details of PINN. Then Sect. 4 shows the results of our approximation using this method compared with the finite element method approximation. Model discussion is then shown in Sect. 5.

## 2 Full Potential Equation

### 2.1 Full Potential Equation of Aerodynamic

To obtain the full potential equation of aerodynamics, the flow is assumed to be irrotational, steady, inviscid, and under the isentropic condition [11]. The equation can now be simplified as:

$$\nabla \cdot (\rho \nabla \phi) = 0 \quad (1)$$

where  $\phi$  is the velocity potential;  $\nabla$  is the gradient operator defined by  $\nabla \phi = \left( \frac{\partial \phi}{\partial x}, \frac{\partial \phi}{\partial y} \right)^T$ ;  $\rho$  is the local density as a function of  $\nabla \phi$ , which can be obtained by

$$\frac{\rho}{\rho_0} = \left[ 1 - \frac{(\nabla \phi)^2}{2H_0} \right]^{\frac{1}{\gamma-1}} \quad (2)$$

where  $\rho_0$  is the stagnation density;  $H_0$  is the stagnation entropy;  $\gamma$  is the specific heat ratio [12].

To derive the Mach number, considering the two-dimensional situation, this isentropic potential model is written in a non-conservative form by calculating the derivatives of the density,

$$(1 - M_x^2)\phi_{xx} + (1 - M_y^2)\phi_{yy} - 2M_x M_y \phi_{xy} = 0 \quad (3)$$

$$c^2 = (\gamma - 1) \left[ H_0 - \frac{1}{2} |\nabla \phi|^2 \right] \quad (4)$$

$$M_x = \frac{\phi_x}{c} M_y = \frac{\phi_y}{c} M^2 = \frac{|\nabla \phi|^2}{c^2} \quad (5)$$

where  $c$  is the speed of sound;  $M_x$ ,  $M_y$  refer to the Mach number components in the  $x$  and  $y$  directions, respectively.  $\phi_x$ ,  $\phi_y$  are partial differentiation of  $\phi$  with respect to  $x$ ,  $y$ .

## 2.2 Boundary Conditions

As for the external boundaries of a single airfoil, Dirichlet conditions are applied along the inlet section (on the left, right, and top of the airfoil) and Neumann conditions are applied along the outlet section (the bottom of the airfoil) [13]. Let  $\Omega \subset R^2$  be a two-dimensional computational airfoil domain,  $\Gamma_1$  denotes the Dirichlet boundary, and  $\Gamma_2$  denotes the Neumann boundary. Therefore, the initial condition and boundary conditions can be expressed as follows [12],

$$\phi(x, y) = g_0(x, y), (x, y) \in \Omega \quad (6)$$

$$\phi(x, y) = V_\infty \cdot \vec{x} + \phi_0, (x, y) \in \Gamma_1 \quad (7)$$

$$\nabla \phi(x, y) \phi n(x, y) = g_1(x, y), (x, y) \in \Gamma_2 \quad (8)$$

where  $g_0, g_1$  are the specified initial value and Neumann value, respectively;  $V_\infty$  is the free-stream velocity;  $\vec{x}$  is the distance to a point on the boundary with respect to a chosen reference.  $\Phi_0$  is an arbitrary constant; and  $n(x, y)$  notes the unit vector outward to  $\Omega$  on the Neumann boundary.

## 3 PINN Method

Physics-Informed Neural Networks nowadays have evolved so that they can be used to solve PDEs. The PINN approach uses neural network training to try to anticipate the results of a PDE system. A vanilla PINN consists of multiple fully-connected layers.

The process of solving a PDE system in PINNs can now be thought of as an optimization problem to minimize the loss function:

$$L(\theta) = L_{PDE}(\theta) + L_{BC}(\theta) + L_{IC}(\theta) \quad (9)$$

The term  $L_{PDE}$  imposes a penalty for the approximation results not respecting the governing equations. The other terms here penalize the deviation from the boundary conditions and the deviation from the initial conditions. Once the loss function is specified, it just needs to be minimized. In this case, to optimize the DNN's parameters, the Adam optimizer can be used. The parameters of the DNN are denoted by  $\theta$ :

$$\theta = \min_{\theta^*} L(\theta^*) \quad (10)$$

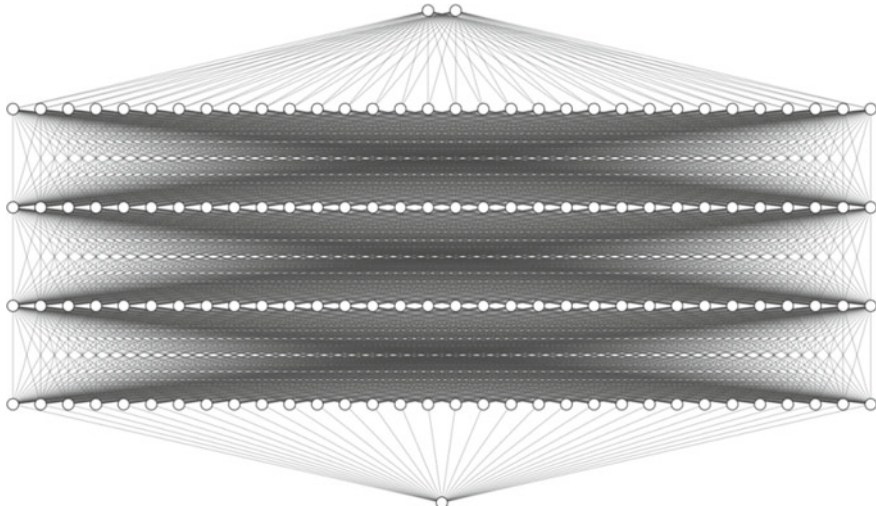


**Fig. 1** Schematic diagram of the neural network

One attractive feature of the PINN compared with conventional CFD solvers especially when it comes to fluid dynamics is that it is not required to be tailored to the specifics of a particular PDE [6]. In our case, the full potential equations, and shocks may be introduced, making it harder for conventional CFD codes to compute. However, PINN still couldn't replace CFD codes because its accuracy and efficiency are still lower than the existing CFD codes.

### 3.1 Network Architecture

With four hidden layers, our neural network is uncomplicated. Here, the activation function is the  $\tanh()$  function to introduce some non-linearity. Figure 1 is a schematic diagram of the neural network.

### 3.2 Problem Formulation

Describe the airfoil problem as the PDE system described in Sect. 2. From these formulas, we can derive the loss functions, which are the essence of the whole PINN methodology.

**Sampling strategy.** Since the 2-dimension full potential equation isn't time-dependent, it doesn't need sampling on the temporal domain, which means that sample points are only needed on the boundaries and the interior. Lattice hypercube sampling (LHS) is applied on the upper, left, right, and lower boundaries, and LHS is applied on the interior spatial domain. The sampling points then can be defined as our dataset.

**Loss functions.** As mentioned earlier, the key to solving our PDE system is to specify the loss function  $L(\theta)$ :

$$L(\theta) = L_{PDE}(\theta) + L_{BC}(\theta) + L_{IC}(\theta) \quad (11)$$

Then, once the spatial sampling points are obtained, the loss is calculated using the mean squared error. Loss terms can now be specified.

$$L_{PDE}(\theta) = \frac{1}{N_f} \sum_{(x_i, y_i) \in \Omega} \left( \frac{\partial (\rho(x_i, y_i) \frac{\partial}{\partial x} u(x_i, y_i, \theta))}{\partial x} + \frac{\partial (\rho(x_i, y_i) \frac{\partial}{\partial y} u(x_i, y_i, \theta))}{\partial y} \right)^2 \quad (12)$$

$$L_{BC1}(\theta) = \frac{1}{N_{BC1}} \sum_{(x_i, y_i) \in [0, 3] \times \{0\}} \left( \frac{\partial (u(x_i, y_i, \theta))}{\partial y} - U_{inf} \pi \beta \cos(\pi(x - 1)) \right)^2 \quad (13)$$

$$L_{BC2}(\theta) = \frac{1}{N_{BC2}} \sum_{(x_i, y_i) \in \{0\} \times [0, 1]} ((u(x_i, y_i, \theta) - U_{inf} x_i))^2 \quad (14)$$

$$L_{BC3}(\theta) = \frac{1}{N_{BC3}} \sum_{(x_i, y_i) \in \{0\} \times [0, 1]} ((u(x_i, y_i, \theta) - U_{inf} x_i))^2 \quad (15)$$

$$L_{IC}(\theta) = \frac{1}{N_{IC}} \sum_{(x_i, y_i) \in [0, 3] \times \{1\}} (u(x_i, y_i, \theta) - U_{inf} x_i)^2 \quad (16)$$

where  $\rho(x_i, y_i)$  is the local density,  $N_f$ ,  $N_{BC}$  and  $N_{IC}$  is the number of the interior sample points, the sample points on the boundaries, and the sample points where initial condition is enforced respectively.

With the use of automatic differentiation, it is now simple to calculate the partial derivatives of our output  $u$  using machine learning libraries such as TensorFlow or PyTorch. This makes the construction of loss function more convenient.

**Test cases.** Tried the code in several cases with several different values. The approximation of the spatial distribution of Mach numbers at  $M_{inf} = 0.3, 1.8$ , and  $2$  is tested to show the effectiveness of the standard PINN for modeling the computation of an airfoil. The differences are that shocks may be introduced as  $M_{inf}$  increases.

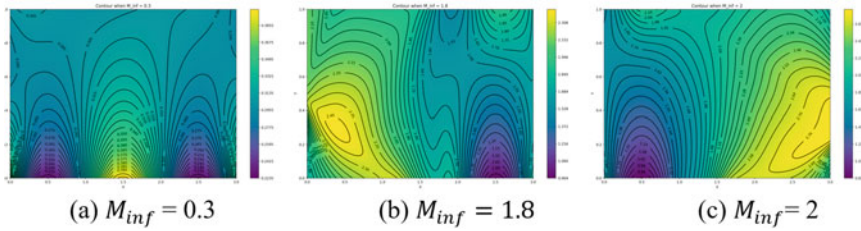


**Fig. 2** Mach contours of the flow with three different: **a**  $M_{inf} = 0.3$ , **b**  $M_{inf} = 1.8$  and **c**  $M_{inf} = 2$

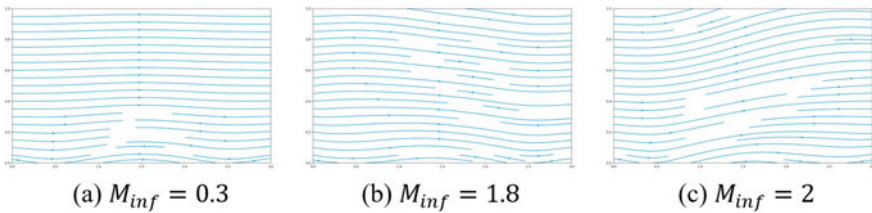


**Fig. 3** Streamline plots of the flow with three different  $M_{inf}$ : **a**  $M_{inf} = 0.3$ , **b**  $M_{inf} = 1.8$  and **c**  $M_{inf} = 2$

## 4 Experimental Results

The full potential equation previously discussed in Sect. 2 can be used to explain the flow around the airfoil, which is approximated in this section using the PINN method.

### 4.1 Calculation Results and Accuracy of PINN Method

For the full potential equation stated in part 2, then the PINN solution is obtained, with  $M_{inf} = 0.3, 1.8$  and  $2$ , representing the subsonic case, transonic case, and supersonic case of the flow respectively (Fig. 2).

In addition to Mach contours, streamline diagrams can also be obtained (Fig. 3).

Figure 4 below shows the history of the logarithm of our aggregate loss value with respect to the number of epochs. ( $M_{inf} = 0.3, 1.8, 2$  respectively).

### 4.2 Advantages and Disadvantages

The advantages of the PINN method are that it could be flexible and easy to implement with the recent advances in deep learning libraries, and it can be used to deal with

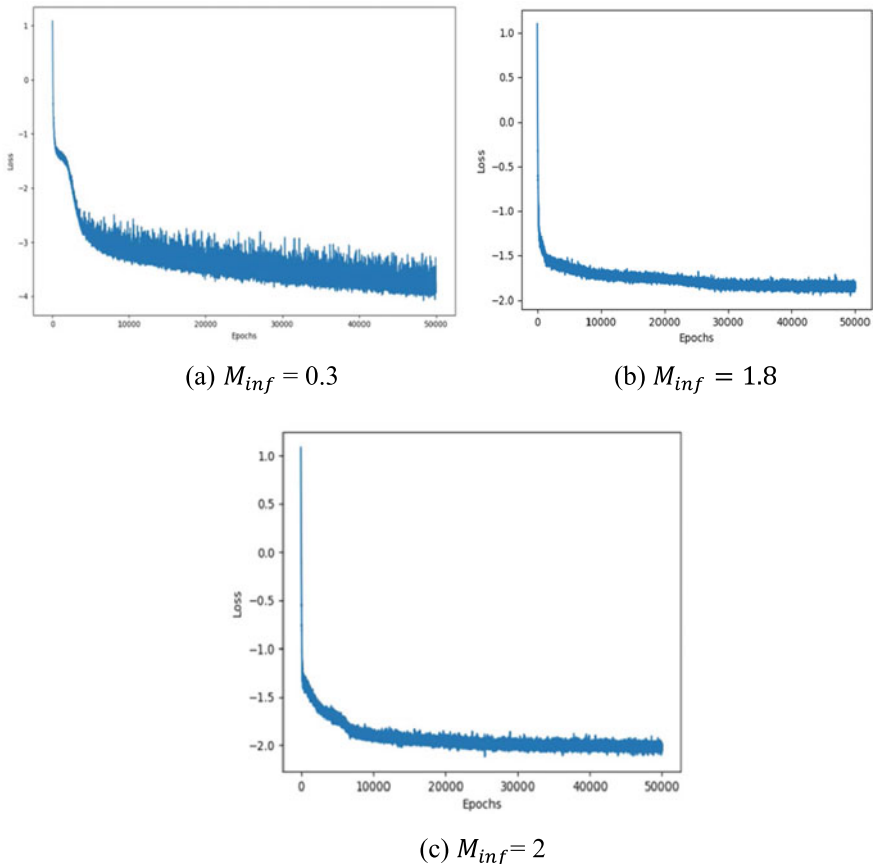


**Fig. 4** Training losses of the flow with three different: **a**  $M_{inf} = 0.3$ , **b**  $M_{inf} = 1.8$  and **c**  $M_{inf} = 2$

nonlinear PDEs with tricky physical characteristics. But the overall errors of our three cases were still at around  $1e-3$  after training for 50,000 epochs. The error is high, compared to the existing CFD codes. Also, potential equations are at a high approximation level, which is another limitation of our model. We also believe that this method is slower overall, so further research may be conducted to accelerate the training process of neural networks.

## 5 Model Optimization

### 5.1 Network Architecture

Though PINNs are capable to solve plenty of PDEs successfully, there's still room for improved precision and efficiency. DPINN, a distributed variant of PINN, can be used to enhance the network design. The DPINN approach can solve the potential vanishing gradients issue encountered by the original PINN. It has been tested that the DPINN approach can acquire more accurate results in PDEs and use data more efficiently compared with the PINN approach [10].

### 5.2 Training Data

The data are very important for training the neural network even if the PINN technique is data-efficient and doesn't require a lot of training data [6]. The training points in this paper were selected randomly from the Lattice Hypercube Sampling method. It's more likely to get better simulation results for airfoil flows by using accurate datasets obtained from the exact solution or carefully performed experiments [13].

### 5.3 Learning Rate

When it comes to solving PDEs, the PINN method requires a relatively long training time which reduces efficiency compared with traditional numerical methods like the finite element method. In this paper,  $\tanh()$  is used as the activation function to determine neurons' working patterns. To optimize the learning rate, adaptive activation functions can be applied to accelerate convergence in PINN. Hyper-parameter  $b$  is necessary to add in the activate function as

$$\sigma(bL_k(z^{k-1})) \quad (17)$$

A scale factor  $n \geq 1$  is also needed to multiply by  $\tanh()$ , which accelerates convergence towards global minima. Consequently, the activate function is produced in its final form by

$$\sigma(nb(z^{k-1})) \quad (18)$$

The way to find the minimum of a loss function is also changed for this adaptive activation function. We need to optimize the hyper-parameter  $b$  along with weights and biases [13].

## 6 Conclusion

To resolve the two-dimensional full potential equation, we describe the PINN technique and tested it for a range of  $M_{inf}$ . PINN is valid for inferring the flow speed, especially for the transonic case, where shocks may be introduced, suggesting that PINNs can be used to solve PDEs with more complex physical features. However, the efficiency and accuracy of the PINN method are rather low compared to the existing CFD methods. We believe the constant growth in the deep learning field may further stimulate the growth of using DNNs to solve PDEs, therefore it remains to be an exciting field of research.

## References

1. Bekela, A. S., Belachew, M. T., & Wole, G. A. (2020). A numerical method using Laplace-like transform and variational theory for solving time-fractional nonlinear partial differential equations with proportional delay. *Advances in Difference Equations*, 2020(1), 1–19. <https://gfbff1b13095ec5284139svck5uxuu5xbx6bn0fgab.eds.tju.edu.cn/10.1186/s13662-020-03048-3>
2. Albuquerque FAC, Ureña M, Ramos H (2022) A technique for generating adapted discretizations to solve partial differential equations with the generalized finite difference method. *Math Methods Appl Sci* 1. <https://gfbff1b13095ec5284139swkwop90nppf66p6pfgab.eds.tju.edu.cn/> <https://doi.org/10.1002/mma.8386>
3. Fallahzadeh A, Araghi MAF, Fallahzadeh V (2015) On the convergence of the homotopy analysis method to solve the system of partial differential equations. *J Linear & Topol Algebr* 4(2):87–100
4. He Q, Tartakovsky AM (2021) Physics-Informed neural network method for forward and backward advection-dispersion equations. *Water Resour Res* 57(7):e2020WR029479 (2021).
5. Raissi M, Perdikaris P, Karniadakis GE (2019) Physics-informed neural networks: A deep learning framework for solving forward and inverse problems involving nonlinear partial differential equations. *J Comput Phys* 378:686–707
6. Blechschmidt J, Ernst OG (2021) Three ways to solve partial differential equations with neural networks—A review. *GAMM-Mitteilungen* 44(2):e202100006
7. Dwivedi V, Parashar N, Srinivasan B (2019) Distributed physics informed neural network for data-efficient solution to partial differential equations. *arXiv preprint arXiv 1907.08967*
8. Zapf B, Haubner J, Kuchta M, Ringstad G, Eide PK, Mardal K-A (2022) Investigating molecular transport in the human brain from MRI with physics-informed neural networks. *Sci Rep* 7(1):1–11 <https://gfbff1b13095ec5284139sp5xp5b900ucq6vvqfgab.eds.tju.edu.cn/> <https://doi.org/10.1038/s41598-022-19157-w>
9. Wang D, Jiang X, Song Y, Fu M, Zhang Z, Chen X, Zhang M (2022) Applications of physics-informed neural network for optical fiber communications. *IEEE Commun Mag* 60(9):32–37. <https://gfbff1b13095ec5284139s6w69o9opxu9v6k9pfgab.eds.tju.edu.cn/> <https://doi.org/10.1109/MCOM.001.2100961>.
10. Meng X, Li Z, Zhang D, Karniadakis GE (2020) PPINN: Parareal physics-informed neural network for time-dependent PDEs. *Comput Methods Appl Mech Eng* 370:113250
11. Walale A, Chauhan AS, Satyanarayana A (2018) Analysis of shrinkage & warpage in ceramic injection molding of HPT vane leading edge core of a gas turbine casting. *Materials Today-Proceedings* 5(9):19471–19479

12. Davari M, Rossi R, Dadvand P, López I, Wüchner R (2019) A cut finite element method for the solution of the full-potential equation with an embedded wake. *Comput Mech* 63(5):821–833
13. Jagtap AD, Kawaguchi K, Karniadakis GE (2020) Adaptive activation functions accelerate convergence in deep and physics-informed neural networks. *J Comput Phys* 404(67):113–121

# Analysis and Research on Magnetic Leakage Simulation of Bimetallic Composite Pipe



Yilai Ma, Jinzhong Chen, Yaxing Wen, and Zhikun Xiong

**Abstract** In order to solve the problem of magnetization of bimetallic composite pipe, we establish a non-contact base pipe leakage detection model based on finite element simulation, determine the relationship between the magnetic field in the area where the tri-axis magnetic leakage sensor is located and the parameters of the magnetic excitation structure, quantitatively calculate the law of magnetization of the pipe wall under different excitation parameters, optimize the parameters of magnetic excitation structure, and obtain the range of excitation structure parameters required for the tri-axial magnetic leakage sensor to complete the non-contact base pipe detection. The magnetic excitation structure parameters required by the three-axis leakage sensor for non-contact base pipe detection can provide a basis for the design of the magnetic excitation device for bimetallic composite pipe detection.

**Keywords** Magnetic leakage · Bimetallic composite pipe · Magnetic excitation device · Finite element simulation

## 1 Introduction

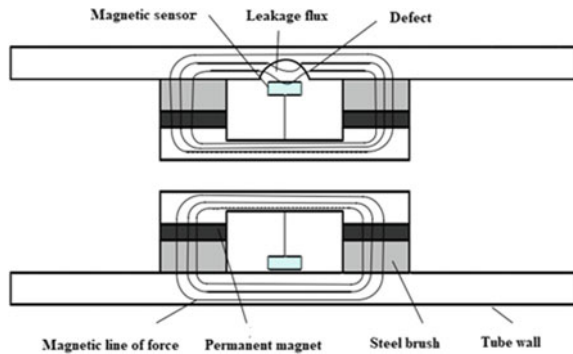
Bimetallic composite pipe has a high pressure-bearing capacity and excellent corrosion resistance, and has been widely used in the field of oil and gas pipeline transportation. The stainless steel lining of the bimetallic pipe enhances the corrosion resistance of oil and gas pipelines, while the carbon steel base pipe ensures excellent mechanical pressure-bearing performance, due to defects in the processing and manufacturing process, there are also composite pipe voids, air gap, weld cracks, base pipe corrosion and other forms of failure. The current domestic long-distance pipeline internal detection is mainly based on magnetic leakage detection, but the technology for the detection of bimetallic composite pipe has some limitations. Due to the weak magnetic conductivity of the inner stainless steel lined pipe, the air gap

---

Y. Ma · J. Chen · Y. Wen · Z. Xiong (✉)

China Special Equipment Inspection and Research Institute, Beijing 100029, China  
e-mail: [xiongzhikun@163.com](mailto:xiongzhikun@163.com)

**Fig. 1** The principle of magnetic flux inspection



between the detector and the magnetic circuit formed by the pipe wall increases, resulting in a series of problems such as reduced magnetization strength of the pipe wall, weak leakage signal in the area where the tri-axial magnetic leakage sensor is and reduced defect resolution, so the excitation magnetic circuit needs to be optimized [1–4]. After all parameters are optimized, we can better identify pipeline defects and improve the probability of defect detection, which is significant for pipeline operation safety.

## 2 The Principle of Pipeline Inspection on Magnetic Leakage

Pipeline leakage within the magnetic detection can be a more comprehensive detection of carbon steel pipeline metal loss defects and weld abnormalities and other information. The principle is shown in Fig. 1. When the leaky magnet detector moves in the pipe, the excitation structure consisting of a permanent magnet, steel brush and magnetic yoke forming a magnetic circuit with the pipe wall and magnetizes the carbon steel pipe wall; a leakage flux is generated at the defect in the pipe wall, and the leakage signal is collected using Hall sensors and further analyzed to determine the characteristics and size of the pipe defect [5, 6].

## 3 Establishment and Solution of the Bimetallic Pipe Magnetic Leakage Detection Model

A bimetallic composite pipe leakage detection model is established by ANSYS Maxwell finite element simulation software. The model contains the bimetallic composite pipe and the excitation structure which is established in a 1/4 axisymmetric way, as shown in Fig. 2.

**Fig. 2** 1/4 bimetallic composite pipe magnetic leakage detection model

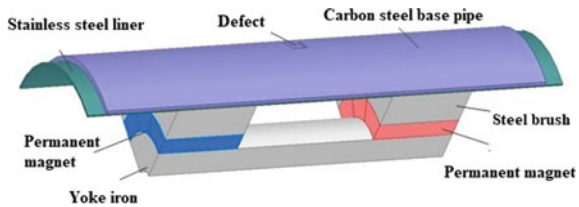


**Table 1** Bimetallic composite pipe geometry

Name	Inner/outer diameter(mm)	Length of pipe (mm)	Material
Base pipe	311/325	600	X52
Lined pipe	305/311	650	316L

### 3.1 Bimetallic Composite Pipe

A bimetallic composite pipe model of  $\varphi 325$  size was established in the finite element software Maxwell. The outer layer is a carbon steel base pipe with a maximum thickness of 7 mm and the inner layer is a stainless steel liner pipe with a maximum thickness of 3 mm, and the relative magnetic permeability is 1.05. A rectangular metal loss defect is set on the outside of the base pipe, the size of the defect is  $10 \times 10$  mm, and the depth is 10% of the base pipe wall thickness. The model dimensions are shown in Table 1.

### 3.2 Magnetic Excitation Structure

Permanent magnetization is used to excite the base pipe of the bimetallic composite pipe, and the excitation structure consists of a permanent magnet, magnetic yoke and steel brush. The initial parameters of the excitation structure are shown in Table 2.

**Table 2** Bimetallic composite pipe geometry

Name	Inner/outer diameter(mm)	Length of model (mm)	Material
Base pipe	165/305	100	10#
Lined pipe	135/165	100	N52
Magnetic yokes	75/135	400	Q235

### 3.3 Initial Magnetic Circuit Model Solving

The 3D distribution of magnetic induction lines of the model with the initial excitation magnetic circuit model parameters is shown in Fig. 3.

In pipeline leakage magnetic detection, the defect signal detected by the sensor probe consists of two parts: the leakage magnetic field generated by the defect itself and the air-coupled magnetic field (background magnetic field). The analysis and quantification of the defect mainly depends on the leakage magnetic field generated by the bending of the magnetic force lines of the defect itself, while the non-defect signals in the background magnetic field are all noise signals. When the detection object changes from an ordinary single-layer carbon steel pipe to a bimetallic composite pipe, the magnetic circuit gap becomes larger and the distance between the sensor probe and the carbon steel base pipe (lift-off value) becomes larger due to the presence of the stainless steel lined pipe, which can lead to changes in the detected defect signal [7].

Under the magnetic circuit constituted by the initial excitation structure, the relationship between the wall thickness of the liner pipe of the bimetallic pipe and the magnetization strength of the base pipe wall, the leakage magnetic field strength of the sensor area (with defects), and the background magnetic field strength is explored, and the results are shown in Figs. 4–7 [self draw].

In the initial excitation magnetic circuit model, the decrease of leakage magnetic intensity will reduce the signal-to-noise ratio of the sensor and the detection ability of defects, therefore, the magnetic circuit structure needs to be optimized to improve the leakage magnetic detection ability of base pipe defects in bimetallic pipe.

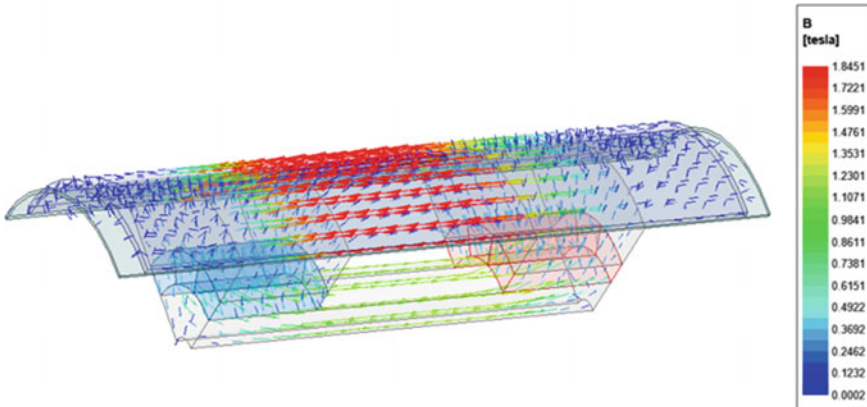


**Fig. 3** Excitation magnetic circuit model magnetic induction distribution

**Fig. 4** The relationship between the magnetic induction strength of the base pipe and the wall thickness of the liner pipe

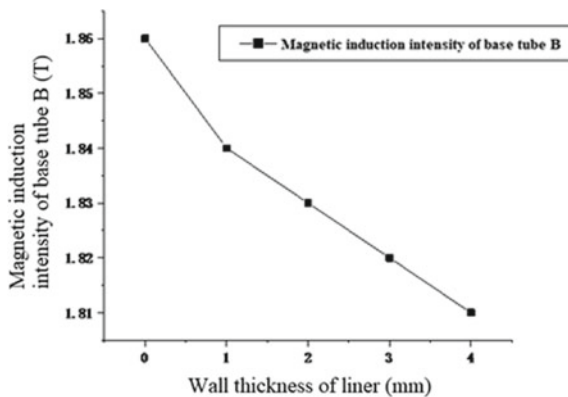


**Fig. 5** Relationship between background magnetic field in the sensor area and wall thickness of the liner pipe

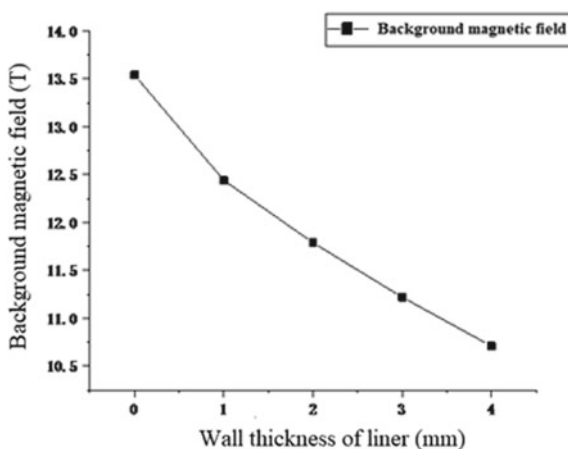


**Fig. 6** Relationship between axial magnetic leakage strength and wall thickness of liner pipe

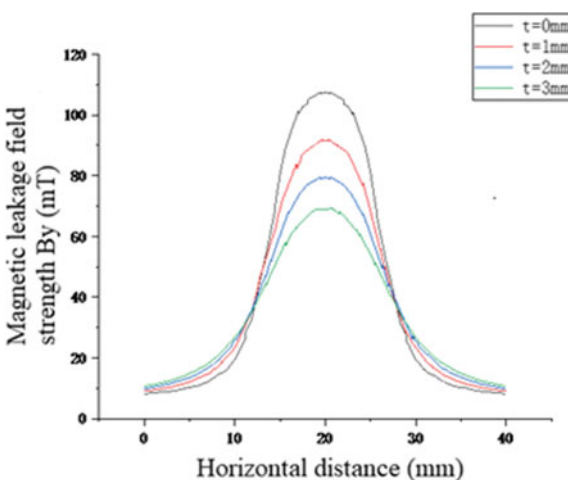
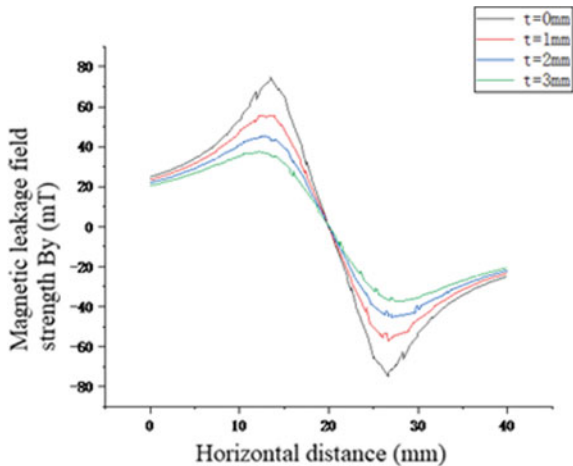


**Fig. 7** Relationship between radial magnetic leakage strength and wall thickness of liner pipe



## 4 Determination of the Relationship Between the Parameters of the Excitation Structure

If the pipe parameters are determined, the excitation structure can be optimized to increase the magnetization intensity of the pipe wall and improve the signal-to-noise ratio in the sensor area.

### 4.1 Permanent Magnet Thickness

According to the second equation of the magnetic circuit, the permanent magnet provides the total magnetic flux source  $F_m = H_m - L_m$  for the magnetic circuit, and the change of the thickness of the permanent magnet magnetization direction will affect the field strength distribution of each part of the magnetic circuit. Keeping the permanent magnet magnetization strength (200 kA/m) and other parameters of the magnetic circuit unchanged, the permanent magnet thickness, the magnetization of the pipe, the background magnetic field and the leakage field strength of the sensor area increase, the axial and radial component of leakage field increase [8], and the results are shown in Figs. 8–11 [self draw].

### 4.2 Permanent Magnet Cross-Sectional Area

The size of the cross-sectional area in the magnetization direction of the permanent magnet affects the reluctance and thus the flux in the magnetic circuit, while the total magnetic potential energy provided by the permanent magnet remains unchanged.

**Fig. 8** Thickness of the permanent magnet and magnetic induction of base pipe

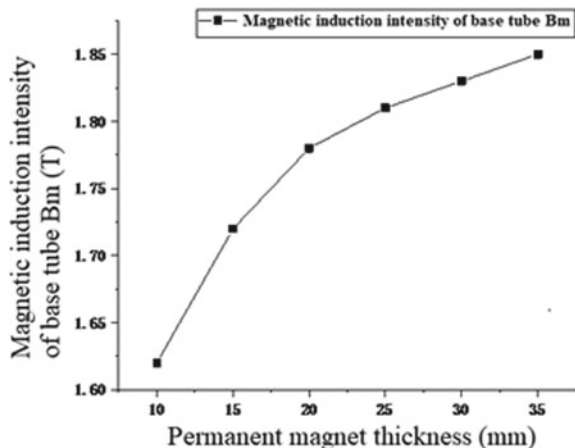


**Fig. 9** Permanent magnet thickness and background magnetic field

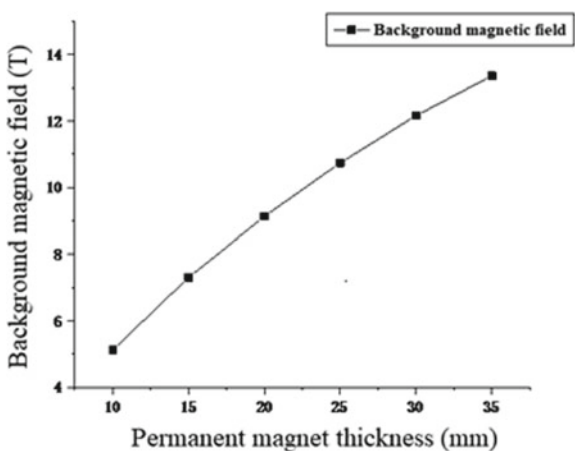


**Fig. 10** Thickness of the permanent magnet and axial component of leakage field

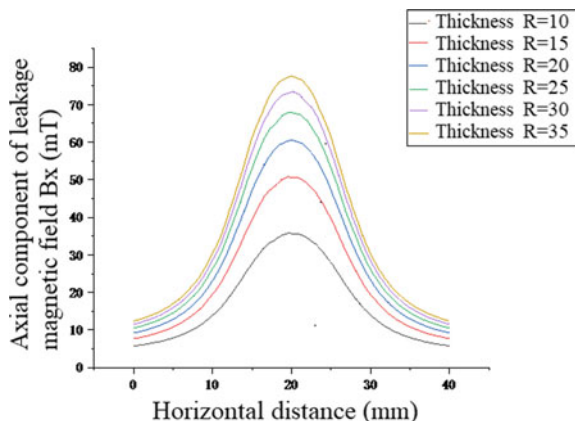


**Fig. 11** Thickness of the permanent magnet and radial component of leakage field Permanent magnet cross-sectional area

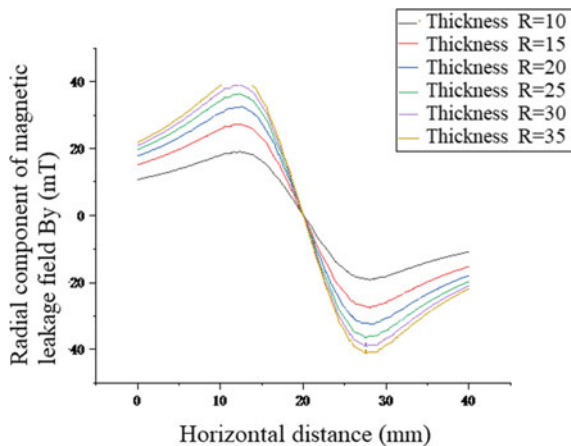
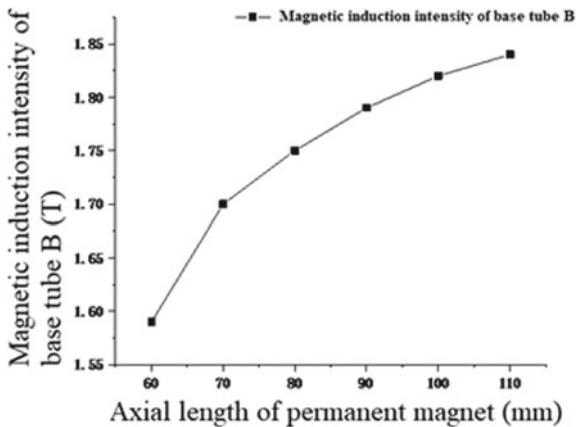


**Fig. 12** The cross-sectional area of the permanent magnet and the magnetic induction of the base pipe



The magnetic inductance of the base pipe wall, the background magnetic field and the axial and radial component pole of the leakage field in the sensor area increase. The results are shown in Figs. 12–15 [self draw].

### 4.3 Magnetic Yoke Length

Keeping the permanent magnet magnetization strength (250 kA/m) and other parameters of the magnetic circuit unchanged, the length of the permanent magnet yoke is increased, the magnetization of the pipe wall and the background magnetic field will be reduced, the axial component pole value of the leakage field strength in the sensor area  $B_x$  is reduced, and the radial component is decreased, as shown in Figs. 16–19 [self draw].

**Fig. 13** Permanent magnet cross-sectional area and background magnetic field

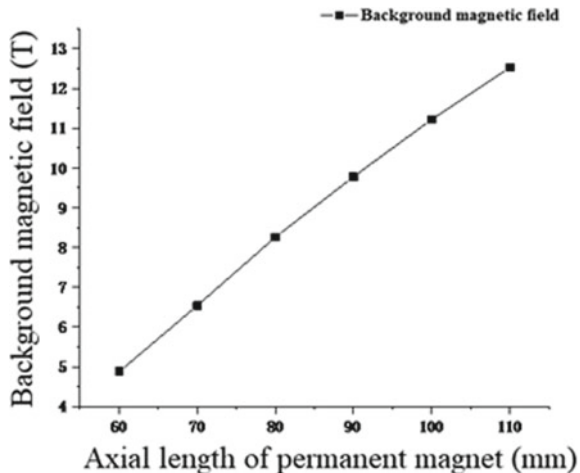


**Fig. 14** The cross-sectional area of the permanent magnet and the axial component of the leakage field

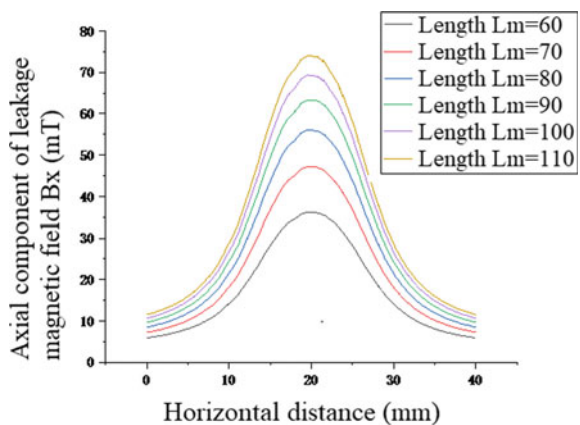


**Fig. 15** The cross-sectional area of the permanent magnet and the radial component of the leakage field Magnetic yoke length

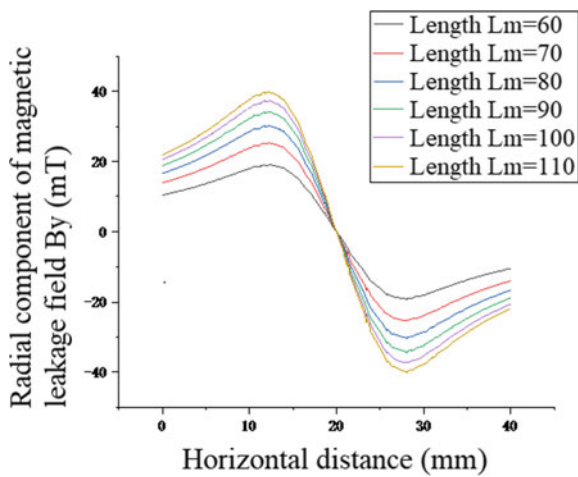


**Fig. 16** Magnetic yoke length and magnetic induction of base pipe

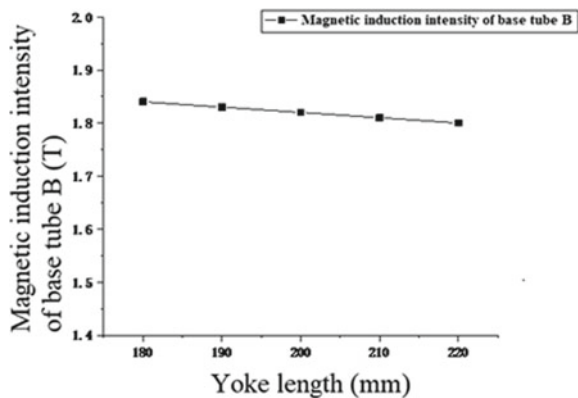


**Fig. 17** Magnetic yoke length and background magnetic field

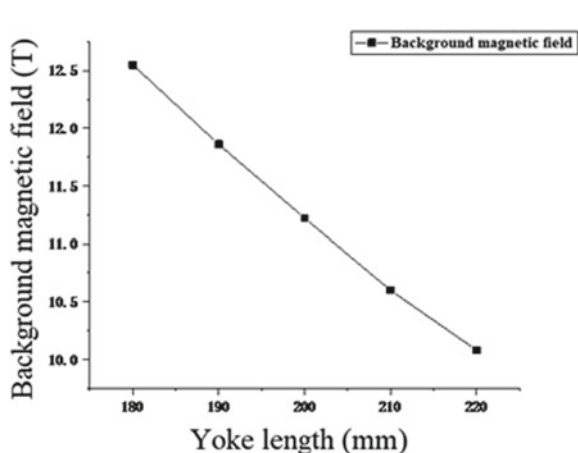


**Fig. 18** Magnetic yoke length and the axial component of leakage field

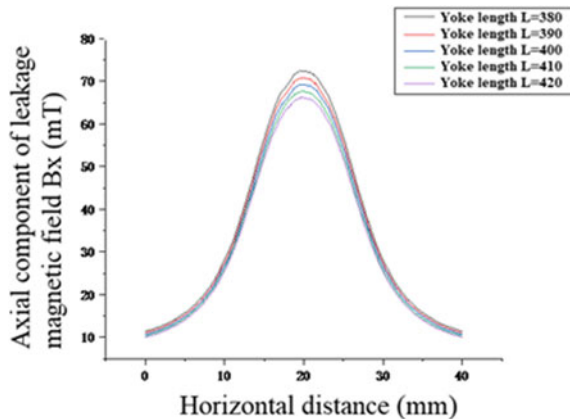
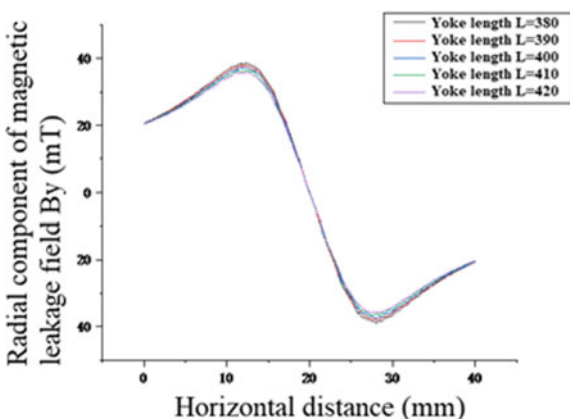


**Fig. 19** Magnetic yoke length and the radial component of leakage field



## 5 Conclusion

By simulating the magnetizing strength of the permanent magnet and the geometric parameters of the magnetic circuit, the parameter ranges and trends of the magnetization strength of the pipe wall, the leakage magnetic field strength of the sensor area, and the background magnetic field are obtained as follows.

- 1- The increasing of the liner thickness leads to the decreasing of the wall magnetization intensity, but the decrease is limited; the background magnetic field decreases slightly due to the lifting off value; the leakage magnetic field intensity in the tri-axial sensor area decreases significantly, and the resolution of the sensor to the defect depth decreases.
- 2- Increasing the thickness and cross-sectional area of the permanent magnet can both increase the magnetization strength of the pipe wall, while the background

magnetic field strength also increases, and the leakage magnetic field strength of the sensor area increases as well.

- 3- The changing of the yoke length has no obvious effect on the magnetization degree of the pipe wall, the background magnetic field does not change much, and the signal strength of the leakage magnetic field does not change significantly.

Based on our parameter simulation conclusions, it provides a design basis for the development of pipeline magnetic leakage detection equipment, thus it improves the probability of defect detection and further ensures the safety of pipeline operation.

**Acknowledgements** The work was financially supported by the National Key Research and Development Program of China (Project No. 2018YFF0215002) and the Science and technology plan project of China State Administration for Market Regulation (2020MK177).

## References

1. Yilai M, Lin L, Gao P, Gao X (2012) Improving SNR of MFL detecting defect signal of drill pipe by using pole piece. *Insight* 54(9):489–492
2. Gaunkar NP, Kypiris O, Nlebedim IC, Jiles DC (2014) Analysis of barkhausen noise emissions and magnetic hysteresis in multi-phase magnetic materials. *IEEE Trans Magn* 50(11):1–4
3. Ma YL, He RY, Chen JZ (2015) A method for improving SNR of drill pipe leakage flux testing signals by means of magnetic concentrating effect. *IEEE Trans Magn* 51(9):1–7
4. Adewale ID, Tian GY (2013) Decoupling the influence of permeability and conductivity in pulsed eddy-current measurements. *IEEE Trans Magn* 49(3):1119–1127
5. Song Q, Mao Y, Lei H (2011) Pulsed eddy current detection system based on DDS technology. *Comput Meas Control* 19(8):1817–1820
6. Ren J, Zhao L, Tang J, Yu J, Liao T (2009) Realization of pulsed eddy current signal source based on DDS technology. *Nondestruct Test* 31(8):643–646
7. Li C (2014) Research on In-pipeline inspection technology based on pulsed eddy current. Master Thesis of Inner Mongolia University
8. Liu Y, Han P, Qiao Z, Zhang J (2011) Design of DDS signal generator based on ARM. *Application World* 30:66–68

# Health State Assessment of Large Complex Equipment Based on Modified ER Algorithm



HaiYan Li, WenLi Li, and SongBin Liu

**Abstract** According to the characteristics of the influencing factors of the large-scale complex equipment health assessment system, a health state evaluation pattern based on the modified multi-attribute decision ER algorithm is proposed. The model can not only combine the assessment problems of multiple damage factors, but also deal with the uncertainty generated by uncertain information, and give trust in unknown information, which is an effective tool for the health status assessment of large-scale complex equipment. The evaluation results show that the model can comprehensively consider the uncertainty information in the evaluation process, which is of great significance for making scientific and reasonable large-scale complex equipment maintenance decisions.

**Keywords** Large complex equipment · ER algorithm · Health status · Evaluation

## 1 Introduction

The assessment of the health status of large-scale and complex equipment involves multi-index and multi-level assessment problems, and the assessment and decision-making process involves a lot of uncertain information or information lost due to the assessment subject, assessment environment and other reasons, and the indicator data for judging the health status in the environment of emergencies is often difficult to accurately determine. At the same time, there are many uncertainties and incomplete

---

H. Li

College of Weaponry Engineering, Naval University of Engineering, Wuhan, China

W. Li

Naval Armament Department, Major Special Equipment, Project Management Center, Beijing, China

S. Liu (✉)

Naval Security Assesment Guarantee Office, Beijing, China

e-mail: [731735206@qq.com](mailto:731735206@qq.com)

information in the evaluation process, which makes it difficult to assess the health status of large and complex equipment [1].

Among the current uncertainty reasoning methods, the subjective Bayes method uses probability as a measure of uncertainty, which is less applicable under the evaluation conditions of data scarcity, information ambiguity, and even uncertain assessment factors [2]. The ER (Evidential Reasoning) algorithm based on multi-attribute decision-making integrates many methods in decision theory, probability theory, set theory and D-S (Dempster Shafer) evidence theory [3–5], which has certain advantages for processing multi-indicator attribute decision evaluation problems under uncertain information conditions. In this paper, the ER algorithm is used to assess the health status of large-scale complex facility, and the facility results not only consider the qualitative and quantitative influence of the attribute information of the self-knowledge index on the health status of the entire large-scale complex equipment, but also describe the qualitative and quantitative influence of unknown information such as human cognition and damage influencing factors on the damage level of the entire weapon system.

## 2 Evaluation Model of ER Algorithm for Multiple Attribute Decision Making

### 2.1 Definition and Representation of Multi-Attribute Evaluation Problems

It is stipulated that the top event attribute in the index system is called the generalized attribute, and the index attribute below the top level is called the basic attribute. Define the collection of L essential properties as  $D = \{d_1, d_2, \dots, d_i, \dots, d_L\}$ ; The relative weight of the  $L$  basic property is estimated to be  $\omega = \{\omega_1, \omega_2, \dots, \omega_i, \dots, \omega_L\}$ . And it satisfies  $0 \leq \omega_i \leq 1$ ; Defining  $n$  significant assessment levels  $H = \{H_1, H_2, \dots, H_j\}$ . No, it's not general  $H_{j+1}$  but better than  $H_n$ . Index  $e_i$  represents:

$$S(e_i) = \{(H_j, \beta_{z,k}), n = 1, 2, 3, L, N\} \quad (1)$$

where:  $\beta_{z,k}$  Indicates that the  $i$ -th basic attribute is rated as the  $n$ th level of trust, and meets the  $\beta_{z,k} \geq 0, \sum_{z=1}^N \beta_{z,k} \leq 1$ .

## 2.2 Probability Assignment Function of Basic Attributes of ER Algorithm

Order  $k_{n,i}$  Assigns a function to the assigned probability, representing the  $i$ -th basic attribute,  $e_i$ s supports generalized attribute  $y$  that is rated as the  $n$ th grade  $H_n$ , the degree of  $k_{B,i}$  It is the unassigned probability assignment function, which indicates that the basic attribute has no support for the generalized attribute assigned to a specific level.  $k_{n,i}$  and  $k_{B,i}$  Calculation formula of

$$k_{n,i} = o_i \beta_{z,k} \quad (2)$$

$$k_{B,i} = 1 - \sum_{n=1}^N k_{n,i} = 1 - o_i \sum_{n=1}^N \beta_{z,k} \quad (3)$$

take  $k_{B,i}$  decompose into  $\bar{k}_{B,i}$  and  $\tilde{k}_{B,i}$  in which

$$\bar{k}_{B,i} = 1 - o_i \quad (4)$$

$$\tilde{k}_{B,i} = o_i (1 - \sum_{n=1}^N \beta_{z,k}) \quad (5)$$

where:  $\bar{k}_{B,i}$  is the first part of the residual probability quantity, which represents that the probability function is not allocated due to the weight;  $\tilde{k}_{B,i}$  is section two of the residual possibility quantity, which is caused by the incompleteness of the evaluation.

## 2.3 ER Information Fusion Algorithm

Referring to the evaluation aggregation table of the two basic attributes, the combined probability assignment function of the first  $i$  basic attributes can be given

$$k_{n,I_{i+1}} = K_{I_{i+1}} [k_{n,I_i} k_{n,i+1} + k_{B,I_i} k_{n,i+1} + k_{n,I_i} k_{B,i+1}]$$

$$\tilde{k}_{B,I_{i+1}} = K_{I_{i+1}} [\tilde{k}_{B,I_i} \tilde{k}_{B,i+1} + \bar{k}_{B,I_i} \tilde{k}_{B,i+1} + \tilde{k}_{B,I_i} \bar{k}_{B,i+1}]$$

$$\bar{k}_{B,I_{i+1}} = K_{I_{i+1}} [\bar{k}_{B,I_i} \bar{k}_{B,i+1}]$$

$$K_{I_{i+1}} = [1 - \sum_{a=1}^N \sum_{b=1,avb}^N k_{a,I_i} k_{b,i+1}]^{-1}, \quad i = 1.L, L-1 \quad (6)$$

where:  $I(i + I)$  indicates that it contains  $i + I$  basic index attributes;  $K$  is the scale factor, which reflects the degree of conflict among the evidences.

After aggregating all  $l$  estimates, the  $\bar{k}_{H,I(L)}$ , the combination trust can be obtained by properly assigning all evaluation levels.

$$\beta_n = \frac{k_{n,I_L}}{1 - \bar{k}_{B,I_L}} \quad (7)$$

$$\beta_H = \frac{\tilde{k}_{B,I_L}}{1 - \bar{k}_{B,I_L}} \quad (8)$$

$\beta_n$  represents the trust degree of the  $n$ th level of the generalized attribute;  $\beta_H$  represents the unassigned trust.

### 3 Normalization and Quantification of Health Status Assessment Information

The health status assessment information is normalized and quantified as the comparison value between the health status data and the standard data. The steps for normalization are as follows: First, calculate the health status data and standard data  $x_0$  deviation of.

$$\delta = x - x_0 \quad (9)$$

Then, the normalized quantitative data are calculated as  $\lambda$ . The calculation method is as follows.

- (1) If the standard data is a fixed value  $x_0$ , the Sum error limit is  $\delta_0$ , then  $\lambda$  is calculated according to the following function

$$\lambda = \begin{cases} 0 & |\delta| \geq \delta_0 \\ \frac{\delta_0 - |\delta|}{\delta_0} & 0 < |\delta| < \delta_0 \\ 1 & \delta = 0 \end{cases} \quad (10)$$

- (2) If the standard data is greater than a fixed value  $x_0$  then  $\lambda$  is calculated according to the following function

$$\lambda = \begin{cases} 0 & \delta < 0 \\ \frac{\delta}{x_0} & 0 \leq \delta \leq x_0 \\ 1 & \delta > x_0 \end{cases} \quad (11)$$

- (3) If the standard data is less than a fixed value  $x_0$  then  $\lambda$  is calculated according to the following function

$$\lambda = \begin{cases} 0 & \delta > 0 \\ \frac{-\delta}{x_0} & \delta \leq 0 \end{cases} \quad (12)$$

## 4 Time Correction of Health Status Assessment Information

Large complex installations can generally only get the health status of each test, and cannot reflect the health status and changing trends in the time period between each test. This article uses the time correction method to correct the health status information in real time, so that the health status can be evaluated at any time. Usually, in addition to the instantaneous overstress of equipment, there is generally a process of gradual degradation. Normal degenerative failures are usually a slow-first-then-fast process. So as to depict the changes in health status, the following time correction function is used.

$$\left\{ \begin{array}{ll} \lambda = 1 & T < T_1 \\ \lambda = \frac{\lambda_2 - \lambda_1}{T_2 - T_1}(T - T_1) + \lambda_1 & T_1 \leq T < T_2 \\ \lambda = \frac{-\lambda_2}{T_3 - T_2}(T - T_3) & T_2 \leq T < T_3 \\ \lambda = 0 & T \geq T_3 \end{array} \right. \quad (13)$$

$(T_1, T_2)$  For equipment slow failure time,  $(T_2, T_3)$  It is the equipment fast failure time.  $(T_1, \lambda_1) \sim (T_2, \lambda_2)$  According to the actual degradation data of the equipment and the experience of experts this paper mainly carries out time correction in the period of slow failure of equipment  $(T_1, \lambda_1) \sim (T_2, \lambda_2)$  by (2,1) ~ (12,0.8).

The assessment steps of health status information are as follows:

- (1) The health status data are normalized and quantified according to the method in Sect. 3.
- (2) Determine the weight of each key parameter.
- (3) According to what we got  $\lambda$ , modify the function according to time and weight.
- (4) The membership degree of the fuzzy function is determined.
- (5) The membership degree of each subsystem is obtained.
- (6) The confidence level was determined and the basic trust distribution function was calculated.
- (7) Calculate the basic probability assignment of basic attributes.
- (8) The combination probability assignment of generalized attributes is calculated.
- (9) The combination trust of generalized attributes is calculated.
- (10) The health status information level was determined by synthetic calculation.

In step (4), the membership degree is determined according to the triangular fuzzy number, and the triangular fuzzy number model is jointly obtained based on the actual degradation of the health state of large-scale complex equipment and expert experience, as follows.

$$y_1 = \begin{cases} \frac{\lambda-0.8}{0.2} & 0.8 \leq \lambda \leq 1 \\ 0 & \lambda < 0.8 \end{cases} \quad (14)$$

$$y_2 = \begin{cases} \frac{\lambda-0.5}{0.3} & 0.5 \leq \lambda < 0.8 \\ \frac{-\lambda+1}{0.2} & 0.8 \leq \lambda \leq 1 \\ 0 & \lambda < 0.5 \end{cases} \quad (15)$$

$$y_3 = \begin{cases} \frac{\lambda-0.2}{0.3} & 0.2 \leq \lambda < 0.5 \\ \frac{-\lambda+0.8}{0.3} & 0.5 \leq \lambda < 0.8 \\ 0 & \lambda < 0.2 \text{ or } \lambda > 0.8 \end{cases} \quad (16)$$

$$y_4 = \begin{cases} \frac{\lambda}{0.2} & 0 \leq \lambda < 0.2 \\ \frac{-\lambda+0.5}{0.3} & 0.2 \leq \lambda \leq 0.5 \\ 0 & \lambda > 0.5 \end{cases} \quad (17)$$

$$y_5 = \begin{cases} \frac{-\lambda+0.2}{0.2} & 0 \leq \lambda \leq 0.2 \\ 0 & \lambda > 0.2 \end{cases} \quad (18)$$

where,  $\lambda$  It is the normalized quantitative data;  $y_i (i = 1, 2, 3, 4, 5)$  The membership of “good”, “normal”, “attention”, “deterioration” and “sick” respectively.

## 5 Case Study of Large Complex Equipment Health Condition Assessment Based on ER Algorithm

On the basis of the achievement of research, the health assessment consequences of the test information, historical information and environmental information of large-scale complex equipment are respectively shown in Table 1.

Calculate the basic probability set according to Eqs. (2) to (5)  $k_{n,i}$  The results are as follows

$$\begin{aligned}
k_{I,I} &= 0, \quad k_{2,I} = 5.245 * 10^{-1}, \quad k_{3,I} = 9.48 * 10^{-2}, \quad k_{4,I} = 0, \quad k_{5,I} = 0, \\
\bar{k}_{B,I} &= 3.448 * 10^{-1}, \quad \tilde{k}_{B,I} = 3.59 * 10^{-2} \\
k_{1,2} &= 5.7 * 10^{-3}, \quad k_{2,2} = 1.116 * 10^{-1}, \quad k_{2,2} = 1.116 * 10^{-1}, \\
k_{3,2} &= 1.55 * 10^{-2}, \quad k_{4,2} = 0 \\
k_{5,2} &= 0, \quad \bar{k}_{B,2} = 8.524 * 10^{-1}, \quad \tilde{k}_{B,2} = 1.48 * 10^{-2} \\
k_{1,3} &= 0, \quad k_{2,3} = 1.775 * 10^{-1}, \quad k_{3,3} = 0, \quad k_{4,3} = 0, \quad k_{5,3} = 0 \\
\bar{k}_{B,3} &= 8.028 * 10^{-1}, \quad \tilde{k}_{B,3} = 1.97 * 10^{-2}
\end{aligned}$$

According to formula (6), the scale factor is calculated

$$K_{I_2} = [1 - \sum_{a=1}^5 \sum_{b=1, a \neq b}^5 k_{a,I_1} k_{b,2}]^{-1} = 1.0227$$

According to formula (6), the result of aggregation operation is as follows  $k_{1,I_2} = 2.2 * 10^{-3}$ ,  $k_{2,I_2} = 5.685 * 10^{-1}$ ,  $k_{3,I_2} = 9.16 * 10^{-2}$ ,  $k_{4,I_2} = 0$ ,  $k_{5,I_2} = 0$

$$\tilde{k}_{B,I_2} = K_{I_2} (\tilde{k}_{B,1} \bar{k}_{B,2} + \bar{k}_{B,1} \tilde{k}_{B,2} + \tilde{k}_{B,1} \bar{k}_{B,2}) = 3.71 * 10^{-2}$$

$$\bar{k}_{B,I_2} = K_{I_2} \bar{k}_{B,1} \bar{k}_{B,2} = 0.3006, \quad k_{B,I_2} = \bar{k}_{B,I_2} + \tilde{k}_{B,I_2} = 0.3377,$$

In order to get the combination probability, we need to aggregate with the third index attribute.

$$K_{I_3} = [1 - \sum_{a=1}^5 \sum_{b=1, a \neq b}^5 k_{a,I_2} k_{b,3}]^{-1} = 1.0169$$

$$\begin{aligned}
k_{1,I_3} &= 1.8 * 10^{-3}, \quad k_{2,I_3} = 0.6391, \quad k_{3,I_3} = 7.66 * 10^{-2}, \quad k_{4,I_3} = 0, \quad k_{5,I_3} = 0, \\
\tilde{k}_{B,I_3} &= 3.71 * 10^{-2}, \quad \bar{k}_{B,I_3} = 0.2454, \quad k_{B,I_3} = 0.2825
\end{aligned}$$

It can be obtained from Eq. (7)

$$\begin{aligned}
\beta_1 &= \frac{k_{1,I_3}}{1 - \bar{k}_{B,I_3}} = 2.4 * 10^{-3}, \quad \beta_2 = \frac{k_{2,I_3}}{1 - \bar{k}_{B,I_3}} = 0.85, \quad \beta_3 = \frac{k_{3,I_3}}{1 - \bar{k}_{B,I_3}} = 0.1015, \\
\beta_4 &= \frac{k_{4,I_3}}{1 - \bar{k}_{B,I_3}} = 0
\end{aligned}$$

The consequences was (0.0024, 0.8469, 0.1015, 0, 0), indicating that the health state assessment of large complex equipment based on the fusion of three kinds of information is 0.24%, the probability of the normal state is 84.69%, and the probability of “attention” state is 10.15%, which is basically consistent with the results of the separate evaluation of various types of information.

**Table 1** Health status assessment consequences of three kinds of information for large complex equipment [6]

Index	Weight	Good( $\beta_1$ )	Normal( $\beta_2$ )	Attention( $\beta_3$ )	Deterioration( $\beta_4$ )	Morbid( $\beta_5$ )	Not sure( $\beta$ )
Test information	0.6552	0	0.8257	0.1022	0	0	0.0797
Historical information	0.1476	0.0389	0.7564	0.1047	0	0	0.1
Environmental information	0.1972	0	0.9	0	0	0	0.1

## 6 Conclusion

ER algorithms can solve both deterministic and uncertain problems, and their contribution to uncertainty problems is particularly prominent. It solves the problem that the classical D-S evidence theory cannot solve the problem of the same multi-attribute weight and strict use scope (in some cases, the use of DS evidence theory will get a situation that does not match the reality), and can comprehensively use complete and incomplete information, improving the utilization and timeliness of information. The accuracy of the health status assessment results of large-scale complex equipment based on the ER algorithm is greatly improved, which reduces the uncertain information, improves the reliability, and provides a guarantee for system safety.

## References

1. Shen L, Ma J, Zili W (2016) Overview of PHM technology at home and abroad. Computer Meas Control 24(09):1–4
2. Yao Y, Wu Y, Feng Y et al. (2012) Research on evaluation method of equipment health status. Modern Defen Tech 40 (05):156–161
3. Li Q (2019) Health status assessment of motorized spindle based on multi-sensor data fusion. Jilin University
4. Mishra C, Samantaray AK, Chakraborty G (2017) Rolling element bearing fault diagnosis under slow speed operation using wavelet de-noising. Measurement 103:77–86
5. Hao Z, Ma L (2008) Damage assessment of submarine torpedo weapon system based on ER algorithm. Torpedo Tech 16(1):30–32
6. The data comes from internal research reports, which have not been disclosed and have been declassified

# Influence of the Modulus of Elasticity of the Jointed Material and Interlayers in Nodes with an Interlayer with a Low TCLE



Qi li, FengMei Liu, Haitao Gao, Huang He, and Viktor Kvasnytskyi

**Abstract** In this study, the influence of the modulus of elasticity of the jointed material and interlayers in the nodes with an interlayer with a low TCLE was investigated by computer simulation. In order to establish the general mode of SSS formation when loading cylindrical joints with soft stiffness layer and verify the adequacy of the simulation, the average elastic modulus of low TCLE layer was calculated. The results show that under thermal loading, in all variants, stresses are absent for the greater part of the node, a complex SSS is created only in small areas near the middle layer, near the joint edge (the outer surface of the cylinder), and in the middle layer. The stiffness coefficient is 0.8 on the outer surface of the interstory joint, decreasing to 0.62 near the joint in the nodes with a “soft” layer, and slightly increasing (to 0.82 ~ 0.91) in the nodes with “neutral” and “hard” interlayers. The interlayer material is in the volumetric stress state throughout its entire length. This provides reliability guidance for the theory of TLP diffusion welding under large gap.

**Keywords** TLP diffusion welding · Stiffness coefficient · Interlayer

## 1 Introduction

In the early 1970s, when Paulonic and others [1] were studying the welding of nickel-based superalloys, they proposed a new type of connection technology-transient liquid phase diffusion bonding. The technology has been successfully applied to the

---

Q. li · F. Liu (✉) · H. Gao (✉) · H. He

Guangdong Provincial Key Laboratory of Advanced Welding Technology, Institute of Welding, Guangdong Academy of Sciences, Guang Dong, Guangzhou 510650, China

e-mail: [liufm@gwi.gd.cn](mailto:liufm@gwi.gd.cn)

H. Gao

e-mail: [gaoht@gwi.gd.cn](mailto:gaoht@gwi.gd.cn)

Viktor Kvasnytskyi

National Technical University of Ukraine“Igor Sikorsky Kyiv Polytechnic Institute”, 37, Prospl. Peremohy, Kyiv 03056, Ukraine

blade welding of turbine engine, and the high temperature durability of the joint reaches 90% of the base material, realizing the practical application of the TLP connection technology [2]. So far, it has been widely used in nickel-based, cobalt-based, and oxide dispersion-strengthened high-temperature connections [3].

The prior studies mainly discusses the effects of factors such as TLP diffusion welding intermediate layer alloy, welding process parameters, and poor crystal orientation of welding assembly on welded joints, involving melting-reducing elements, intermediate layer alloy composition, form and thickness, welding temperature, heat preservation, welding pressure, post-weld heat treatment and poor crystal orientation of the base material, etc. [4–6]. The appropriate intermediate layer alloy can improve the interface contact, reduce the requirements for the surface preparation quality of the welded parts and the welding pressure, improve the diffusion conditions, accelerate the diffusion rate, and achieve the purpose of reducing the welding temperature and shortening the welding time [7]. To avoid or reduce the problems of diffusion holes and excessive thermal stress caused by the difference between the physical chemistry properties of the intermediate layer and base metal during welding.

There have been related theoretical studies and calculation formulas concerning the dissolution of base materials in TLP connection abroad [8]. However, after adding melting-reducing elements and strengthening elements on the basis of the composition similar to the base material, the elastic modulus of the intermediate layer will be different from that of the base material. The prior art mainly considers its phase composition and element diffusion during the welding process. However, the influence of the elastic modulus of the middle layer on the stress and strain state of the joint has not been studied. Based on the preliminary study of TLP diffusion welding, the stress and strain state of TLP diffusion welding interlayer with high elastic modulus are studied in order to optimize the interlayer composition.

## 2 Experimental Details

Considering the symmetry of the experimental samples, the top half of the sample taken from this model construction is divided into a reference. Model size: cylinder diameter  $d = 20$  mm, height  $H = 20$  mm, and the thickness of the middle layer is half of the total thickness of the middle layer. An overall view of the finite element (FE) of the sample and model and its adjacent layers is shown in Fig. 1.

For simulation the SSS under conditions of thermal loading (cooling) in the range  $1100 \sim 1270$  °C in all versions for the base metal, the average value of the elastic modulus  $E_{\text{OM}} = 0.5 \times 10^5$  MPa is adopted based on extrapolation of the available data from 20 to  $1100$  °C and approximation of the modulus of elasticity to zero at the melting point of the alloy. In this case, the elastic modulus of the “Soft” layer is less than 2 times that of the base metal, the “Neutral” layer is the same, and the elastic modulus of the “Hard” layer is twice as large, respectively (see Table 1). Extrapolating from the available data, take the Siméon Denis Poisson ratio between the primary material and the intermediate layer.

**Fig. 1** Overall view with intermediate layer specimens (a); Profsection of the finite element model (b)

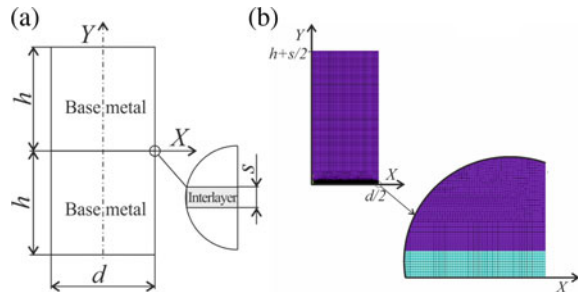


**Table 1** The FEM model type

No. of var	$\text{TCLE}_{\text{intlr}}, 10^{-6} \times 1/\text{deg}$	$E_{\text{intlr}}, 10^5 \text{ MPa}$	Thickness of interlayer, mm	Interlayer type
1	15	0.5	0.05	Neutral
2	15	0.25	0.05	Soft
3	15	1	0.05	Hard

Taking into account that elastic deformations at welding temperatures are small, some error in the initial data can be neglected. The thickness of the interlayer in all variants remained unchanged 0.050 mm. The obtained results can be applied to the loading by heating (temperature increase) in the same temperature range in the elastic stage. In this case, the stress fields and their magnitude do not change, only the sign is reversed.

### 3 Results and Discussion

#### 3.1 The Stress Field in a Small Area Near the Interlayer and the Base Metal

Analysis of the diagrams for individual components and equivalent stresses confirms that the width of most nodes (up to 70%) in almost all thickness variations remains almost constant as the material is connected and the middle layer, change the joint only at the edge of a small area.

The radial stress in the substrate metal is the tensile force (Fig. 2a, b). In most of the joints (Fig. 2a), they reached maximum values of 32, 42, and 60 Mpa, respectively, in the Soft", "Neutral", and "Hard" versions of the intercalation (Fig. 2b), that is, it increases linearly with the stiffness of the interlayer practically linearly ( $\sigma_x = 37 \cdot 10^{-5} \cdot E_{\text{intl}} + 23$ ).

In contrast, the radial stress in the intermediate layer is compressed. They are about -43, -85, and -170 MPa across most of the joint (Fig. 2c) and decrease

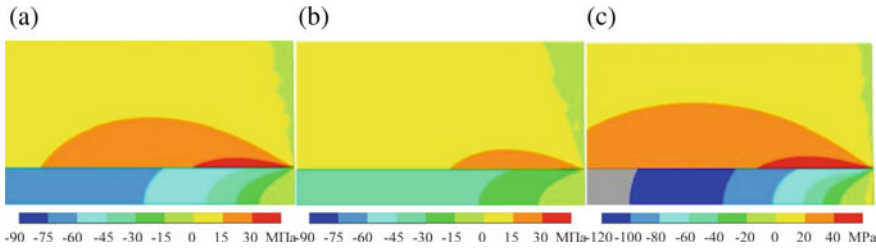


**Fig. 2** Radial  $\sigma_x$  stress fields in nodes with interlayers: “Neutral” (a), “Soft” (b), “Hard” (c) (X160) of the interlayer near the external surface of the node

to  $-17$ ,  $-26$  and  $-56$  MPa (Fig. 2d), i.e. in 3 times, at the edge joints in versions with “soft”, “neutral” and “hard” interlayers, respectively. Thus, in the material, the interlayers the stresses also increase with increasing rigidity both for the greater part of it inside the node ( $\sigma_x = -170 \cdot 10^{-5} \cdot E_{\text{intl}}$ ), and near the edge ( $\sigma_x = -56 \cdot 10^{-5} \cdot E_{\text{intl}}$ ).

There is axial stress along most of the joints in the substrate and interlayer, are absent (remain at the zero level) and appear and increase stretching to 18, 43 and 133 MPa is only at the edge of the joint in versions with “soft”, “neutral” and “hard” interlayers, respectively (Fig. 3). That is, the axial stresses at the joint edge also increase with increasing stiffness of the interlayer material, but with a somewhat more complex nonlinear dependence ( $\sigma_y = 90.5 \times 10^{-10} \cdot E_{\text{intl2}} + 41.8 \times 10^{-5} \cdot E_{\text{intl}}$ ).

The main stress  $\sigma_1$  in the main metal from zero in the middle part of the joint gradually grows as it approaches its edge, reaching 47, 73 and 127 MPa in the variants with soft, neutral and hard interlayers, respectively (Fig. 4a, b).

In this case, the lower the stiffness of the interlayer, the greater the zone of zero stresses and the smaller the zone of increase, which decreases from 3 mm at high rigidity (variant 3) to 1 mm at small (variant 2).

The main maximum stress  $\sigma_3$  in the intercalation is mostly kept at  $-43$ ,  $-85$  and  $-167$  MPa, and in the variation of “Soft”, “Neutral” and “Hard” intercalation, at the edge of the joint, they are reduced to  $-32$  MPa,  $-51$  MPa and  $-86$  MPa, respectively (Fig. 5c, d).

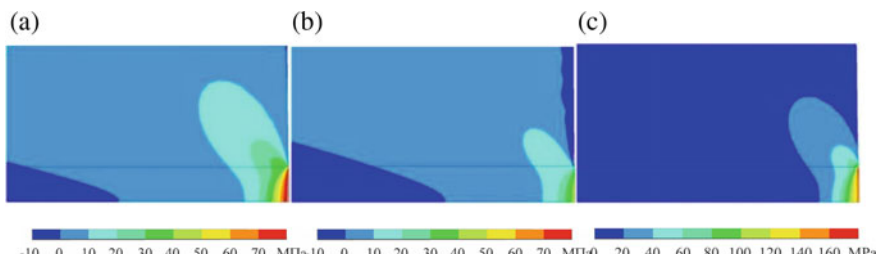


**Fig. 3** Axial stress  $\sigma$  fields between nodes: “Neutral” (a), “Soft” (b), “Hard” near the external surface of the node (c)(X160)

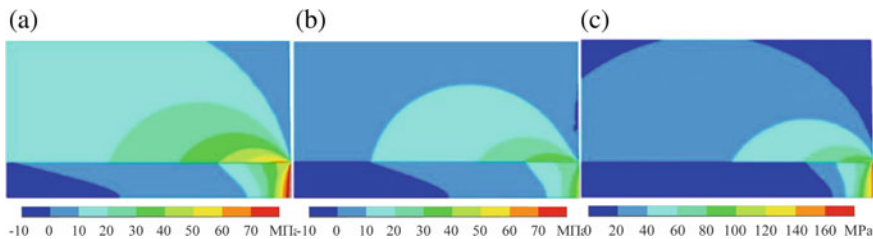


**Fig. 4** Maximum principal  $\sigma_1$  stress field of a node with an intermediate layer: ‘neutral’ (a), ‘soft’ (b), ‘hard’ of a sandwich near the external surface of the node (c) ( $\times 160$ )

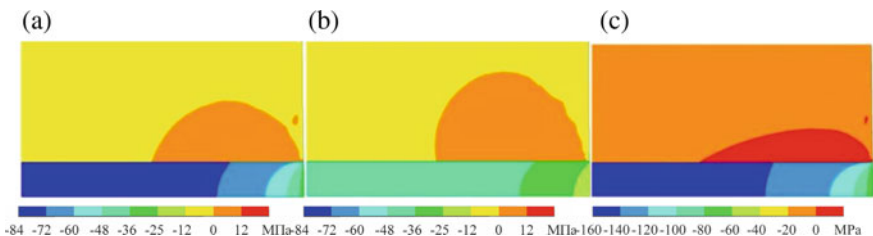


**Fig. 5** Maximum principal  $\sigma_3$  stress field of a node with sandwich: ‘neutral’ (a), ‘soft’ (b), ‘hard’ (c) ( $\times 160$ )

The circumferential stress distribution of the main material and the middle layer is similar to the radial stress. In the main metal, they are close to zero at most joints and increase only at their outer edges. Here, they are stretched at 16, 26, and 51 MPa (Fig. 6a, b, c), as in the radial direction, with “Soft”, “Neutral”, and “Hard” interlayers, respectively.

In the interlayer material, the circumferential stress is compressed, most of the joints are kept at the level of 43, -85 and -170 MPa, and the outer edge is reduced to -33, -51 and -86 MPa, respectively, that is, the “Soft”, “Neutral” and “Hard” intercalation of 1.5 ~ 2 times (Fig. 6c, d).

Most of the joint areas (about 95%) have no tangential stress, and in models with soft, neutral, and hard interlayers, this occurs only at their extreme edges and increases

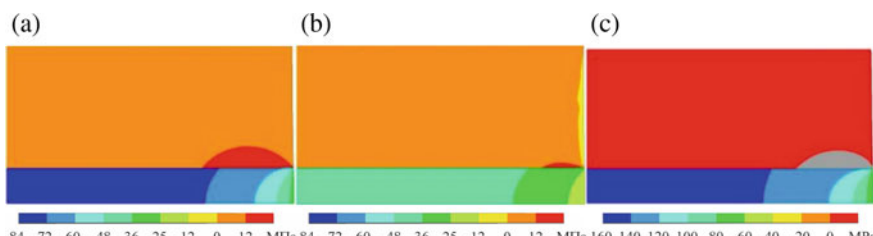


**Fig. 6** Fields of circumferential  $\sigma_z$  stresses in nodes with interlayers: ‘neutral’ (a), ‘soft’ (b), ‘hard’ (c) near the interlayer near the outer surface of the node ( $\times 160$ )

to  $-20$ ,  $-32$ , and  $-51$  MPa, respectively see Fig. 7, in other words, the maximum shear stress at the Joint Edge also increases with the increase of the interlaminar stiffness ( $\tau_{xy} = 29.5 \times 10^{-10} \times E_{int2} - 79.8 \cdot 10^{-5} \times E_{int1}$ ).

Depending on an individual component,  $\sigma_{eq}$  are also distributed (Fig. 8). They are constant along most of the joint, with the level of all the variants being close to zero in the main material (Fig. 8a, b). In the interlayer, the stress level increases linearly with the stiffness of the interlayer. In the “Soft”, “Neutral” and “Hard” interlayer, the stress level is 43 MPa, 85 MPa and 170 MPa respectively, which in magnitude completely coincides with the radial and circumferential ( $\sigma_{eq} = 170 \cdot 10^{-5} \cdot E_{intl}$ ) (Fig. 8c, d).

The equivalent stress of the base metal increases gradually and the middle layer decreases at the thickness of about 50 layers, only near the weld edge of the base metal, and reaches about 38, 57 and 92 MPa at the weld edge of the base metal, it reaches 39, 72 and 132 MPa at about 2 times the thickness from the outer surface of the module, and then increases to 53, 102 and 225 MPa at the edges of the “Soft”, “Neutral” and “Hard” interlayers, respectively.

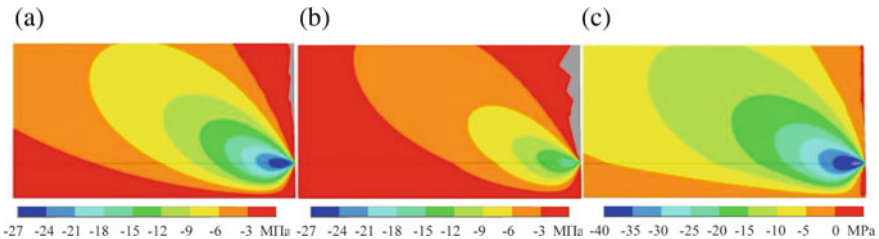


**Fig. 7** The fields of tangential stresses  $\tau_{xy}$  in the nodes with interlayers: “neutral” (a), “soft” (b), “hard” (c) near the interlayer near the outer surface of the node ( $\times 160$ )

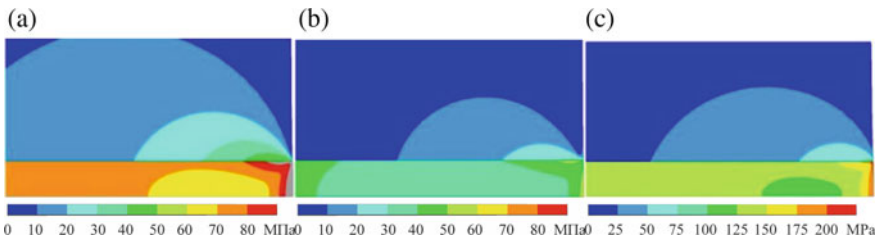


**Fig. 8** Equivalent stress fields  $\sigma_{eq}$  in nodes with intermediate layers: “Neutral” (a), “Soft” (b), “Hard” (c) ( $\times 160$ )

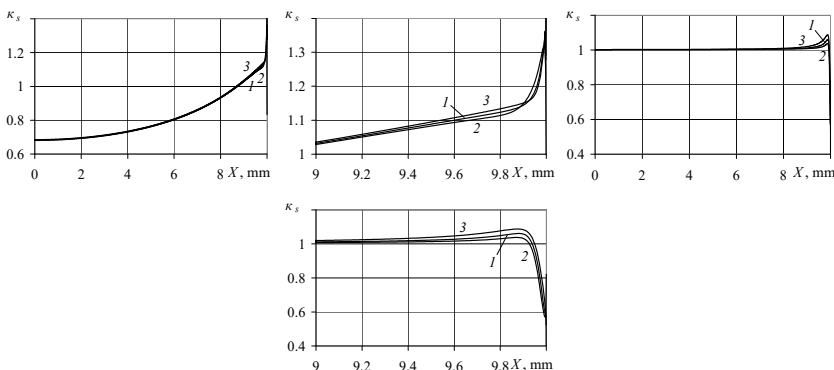
### 3.2 Effect of Volume SSS on Strength and Plasticity of Material in Joint

Figure 9 shows a graph of the stiffness coefficient of the body material (a, b) and the interlayer (c, d) along the entire joint (a, c) and its edges (b, d). The curve analysis shows that the distribution of stiffness coefficient  $K_{\text{stiff}} = \sigma_3/\sigma_{\text{eq}}$  [9] is virtually the same in all variants of joints, whether in the primary material or in the sandwich, that is, it does not depend on the stiffness of the intermediate layer.

In this case, in the base metal, the coefficient is less than 1 for most of the joint length of its inner portion, increasing gradually from 0.68 on the knob to 1 about 1.5 mm from the edge. At the edges of the joint, it was increased to 1.29, 1.32, and 1.36 in versions with “Soft,” “Neutral,” and “Hard” interlayers, respectively (Fig. 9a, b). That is, the SSS produced during thermal loading of the joint area reduces strength and increases the plasticity of the base metal, resulting in its hardening only near the outer surface, where the stiffness coefficient rises to 1.29 ~ 1.36 (Fig. 9b). In this case, the stiffness of the middle layer has little effect on the stiffness coefficient of the base metal, and the stiffness coefficient is reduced to some extent by the “Soft” middle layer.

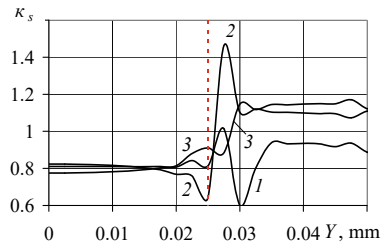
In the layer itself, the picture is different, at the most area of the joint length (up to 90%), the stiffness coefficient in the nodes with a layer of any stiffness remains at level 1. And only close to the edge of the joint, it first slightly increases to 1.04, 1.06 and 1.09 (Fig. 9, d) and then sharply reduced to 0.57, 0.59 and 0.63 on the lateral surface of the unit in variants with “soft”, “neutral” and “hard” interlayers, respectively. For the most part of the joint length, this SSS does not actually affect the strength and ductility of the DW Joint.

The distribution of the stress along the stiffness coefficient of the base axis near the joint is shown in Fig. 10.



**Fig. 9** The change of stiffness coefficient along the whole length of the joint (a, c) and the stress state near its edge (b, d) along the base metal (a, b) and  $K_{\text{stiff}} = \sigma_3/\sigma_{\text{eq}}$  interlayer (c, d)

**Fig. 10** The stiffness coefficient changes along the stress state of the unit in the middle layer 1, 2, 3 models



The analysis of the figure shows that the stiffness coefficient of the outer surface layer of the joint is 0.8, which drops to 0.62 near the “Soft” layer of the joint, and slightly increased ( $0.82 \sim 0.91$ ) node “Neutral” and “Hard” sandwich, that is, the metal some softening. In a “Soft” sandwich joint in a very narrow area near the joint, the stiffness coefficient rose sharply to 1.47, then decreased to nearly 1.1. In a node with a “Neutral” middle tier, it first increases to 1, then decreases to 0.59, then increases again, gradually approaching 1.

## 4 Conclusions

1. The stress field analysis obtained from the modeling results shows that the change of material stiffness combination in the site does not affect the properties of its SSS and changes the stress level to a certain extent. In all variants, there is no stress on most nodes. Only a small area near the middle layer near the edge of the joint produces a complex SSS in the middle layer itself.
2. As the stiffness of the interlaminar material decreases (variable 2), the stress level and the size of the zone decrease, and the opposite increases with the stiffness (variable 3). Outside this region, the radial, axial, circumferential, and tangential stresses in the substrate are negligible. The interlaminates are in the state of bulk stress throughout their length.
3. In the interlayer, for the greater part of the joint length (up to 90%), the stiffness coefficient in the nodes with a layer of any stiffness remains at level 1. And only close to the edge of the joint, it first slightly increases to 1.04, 1.06 and 1.09 and then sharply reduced to 0.57, 0.59 and 0.63 in variants with “soft”, “neutral” and “hard” interlayers, respectively in nodes with an interlayer, with low TCLE.

**Acknowledgements** This work was supported by the GDAS’ Project of Science and Technology Development (2020GDASYL-20200301001、2022GDASZH-2022010109、2021GDASYL-20210302008), the National Key Research and Development Program of China (2020YFE0205300), Science and Technology Planning Project of Guangdong Province (2022B1212050001).

## References

1. Lang B, Hou J, Teng J et al (2014) Diffusion welding of new aviation materials and structure[J]. Aviation Manufacturing Technology 464(20):74–75
2. Li X, Zhong Q, Cao C et al (2003) Research on TLP diffusion welding process of DD3 single crystal alloy split blades. Mater Eng 06:4–7
3. Kong Q, Qu S, Shao T et al (2010) Application and development of brazing and diffusion welding technology in aircraft engine manufacturing. Aeronaut Manuf Technol 24:82–84
4. Zhang Z, Teng J, Yang W et al. (2022) GH3230 alloy TLP diffusion welding process test. Welding, 2022 (06): 42–48 + 64.
5. Li Q, Liu F, Yue X et al (2021) Effect of heat treatment on microstructure and high temperature properties of IC10 superalloy TLP diffusion welding under 80  $\mu\text{m}$  gap. Trans China Weld Inst 42(05):36–44
6. Yue X, Liu F, Li Q et al (2020) Effect of post-bond heat treatment on microstructure and mechanical properties of the wide gap TLP bonded IC10 superalloy with a low boron Ni3Al-based interlayer. J Manuf Process 54:109–119
7. Wan D, Fang W, Chen H et al. (2016) Research progress of Ni-based superalloy TLP diffusion welding intermediate layer materials. Welding, 2016(08): 20–23+73
8. Haijian L, Xudong Y, Zhen K et al (2018) Finite element simulation and process research of TC4 titanium alloy rudder surface diffusion welding. Aerosp Manuf Technol 01:12–16
9. Kurrer KE (2018) The history of the theory of structures (searching for equilibrium). The first fundamental engineering science disciplines: theory of structures and applied mechanics

# Research on Aspect Ratio and Angle of Attack for Optimizing the Performance Of Airfoil NACA 24112



Ziyi Zhang

**Abstract** Airfoils produce lift force for aircrafts, and it is one of the most crucial components of the aircraft. For the purpose of better performance of the aircraft in the sky, it becomes important to design a suitable airfoil for sustaining a stable process of aviation. The overall objective of this very paper is to optimize the design of airfoil, specifically by exploring the effect of changing aspect ratio and angle of attack on aircraft performance, in a simplified case with certain initial conditions and boundary conditions that will be specified later. In order to realize the overall objective of this paper, the feature of flow simulation of Solidworks will be utilized to create a geometrical model and also run various computational fluid dynamics simulations (CFD), in company with python programming for numerical calculations to process various data. The original model of airfoil is the national advisory committee for aeronautics (NACA) 24112. As a consequence of the research and exploration process, it is discovered that under the condition of aspect ratio of 2 and angle of attack of 5°, the performance of airfoil NACA 24112 could be optimized with a lift force to drag force ratio of approximately 5.955.

**Keywords** Aircrafts · Suitable airfoil · Solidworks · Geometrical mode · Python programming

## 1 Introduction

Ever since the beginning of the information age, the advancement in technology and computer science has been made and facilitated as time passes by. In addition, various computational software is created and iterated to become more and more mature, with more efficient and accurate features generated. In the field of physics, engineering and aerospace industry, computational fluid dynamics (CFD), is one of the most popular and crucial subjects with various applications in real life situations,

---

Z. Zhang (✉)

Henry Samueli School of Engineering, University of California, Los Angeles, CA 92612, USA  
e-mail: [ziyiz19@uci.edu](mailto:ziyiz19@uci.edu)

for its capability of producing quantitative predictions of fluid-flow for objects based on certain initial or boundary conditions [1]. In this paper, the software of Solidworks will be utilized for the purpose of airfoil modeling, and for the purpose of CFD modeling, the flow simulation feature of Solidworks will be utilized, to obtain crucial information about the performance of airfoil. In addition to the computational simulation results obtained by the solidworks software, python programming has also been utilized to conduct numerical calculations, for lift coefficient and the final plotting.

For aircraft design, the airfoil is a critical component of the whole aviation system. One of the most important functions of an airfoil is to generate enough lift force, for the purpose of taking off and also sustaining a stable flight. In addition, it is important to minimize the drag during the flight time, since drag forces would require more energy input for the airplane to consume. In addition, the geometry of the airfoil is also particularly crucial as it determines various aspects of the flight performance. The geometry of the airfoil has been selected as NACA 24112 and in this paper, a comprehensive aerodynamic study of the airfoil will be conducted, with the consideration of the angle of attack and the aspect ratio [2]. The general purpose is to obtain the optimization of conditions for NACA 24112 to function; the parameters that will be utilized to evaluate the performance of the airfoil will include but are not limited to lift coefficient, drag coefficient and lift force to drag force ratio. The overall objective of optimization would be to maximize the lift and maximize the lift to drag ratio.

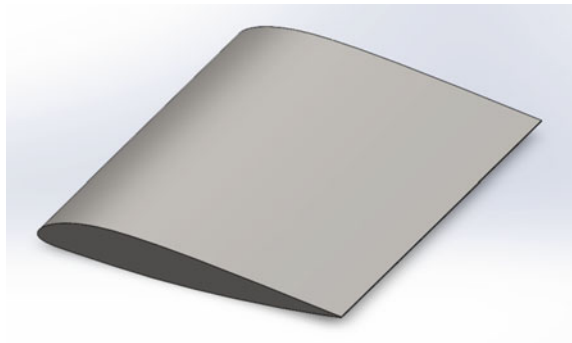
Regarding the methodology of this paper, two general approaches will be utilized for evaluating the parameters. Firstly, a computational fluid dynamics analysis will be conducted, utilizing solidworks for modeling purposes and solidworks flow simulation. Besides, an analytical method by calculating the lift coefficient numerically by python programming will also be conducted. The results of those approaches will be analyzed in order to evaluate under which scenario the optimization of airfoil NACA 24112 could be obtained.

## 2 Methodology

### 2.1 Geometric Model Creation of NACA 24112

To create the geometric model of NACA 24112, the coordinates of NACA 24112, in the two-dimensional (2D) form need to be imported. In this case, the credit of the 2D coordinates shall be given to “airfoil database research”, where the information regarding this NACA 24112 can be accessed [3]. The reasoning behind choosing NACA 24112 is because it is vertically unsymmetrical which would contribute to the creation of lift force. By utilizing the function of extrusion in solidworks, extruding the 2D face horizontally would create the final three-dimensional object of the NACA 24112, which is shown below in Fig. 1.

**Fig. 1** Three-dimensional form of NACA 24112 airfoil



There are two crucial parameters that would influence the performance of NACA 24112 airfoil, which are the aspect ratio and the angle of attack. Aspect ratio is defined as the ratio between the wingspan and the chord length, where wingspan is the average width of the airfoil and the chord length is the length of the surface [4]. The aspect ratio can be changed by adjusting the amount of extrusion of the airfoil and for the purpose of exploring its influence on the lift and drag force generation, five aspect ratios have been selected, which are 1, 1.25, 1.50, 1.75 and 2.00. The following Fig. 2 offers an example of aspect ratio of 2.

Angle of attack is defined as the angle between the incoming air and a reference line of the wing, which is the chord line of the airfoil in this case [5]. The angle of attack can be changed by adjusting the rotation of the airfoil, whereas the feature of “Body-Move/Copy” has been utilized. Specifically, the rotation around the z-axis has been selected for 0, 5, 10, 15, 20° for the rotation (angle of attack); an example of angle of attack of 15° is demonstrated below in the Fig. 3. The reasoning behind choosing 20° as the highest value is because a too high angle of attack might make the airfoil detached, resulting in the loss of lift so the increment only increases upon 20°, in order to avoid loss in lift generation [6].

**Fig. 2** Extrusion of NACA 24112 airfoil for aspect ratio of 2

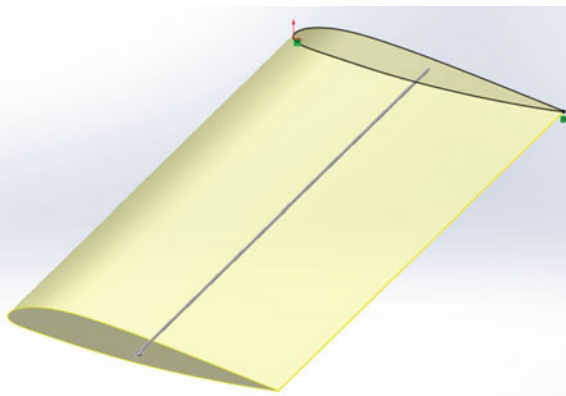


**Fig. 3** Rotation of 24112 airfoil for angle of attack of 15°

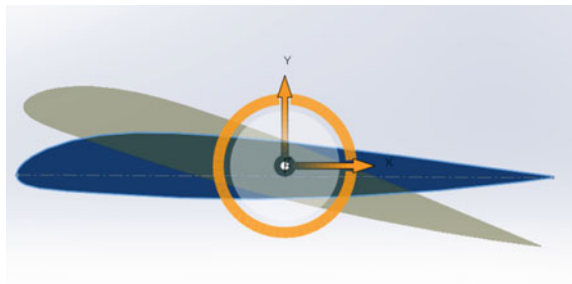


**Table 1** CFD simulation parameters

	Parameters	Value
1	Pressure	101325 Pa
2	Temperature	293.2 K
3	Fluid velocity	34.3 m/s
4	Airfoil	NACA 24112
5	Airfoil chord length	9.140 m

## 2.2 Flow Simulation of NACA 24112 (Physical Model)

After the three-dimensional NACA 24112 is constructed, the flow simulation could be run upon this model. It is important to firstly specify the initial conditions regarding various physical parameters. Here is the list of initial conditions, shown in the following Table 1.

As shown in Fig. 4, an example flow simulation results for 20° angle of attack and aspect ratio of 2 is shown; GG stands for global variable and “GG Force (X)” and “GG Force (Y)” correspond to the drag force and lift force, respectively. By repeating this flow simulation in a similar way to the other set of angle of attack and aspect ratio, the results of drag force and lift force could be obtained eventually and an analysis of them will be conducted in the results and discussion section of this paper [7].

## 2.3 Mathematical Model

The formula for calculating drag coefficient is expressed as the following:

$$C_d = \frac{2 * F_d}{\rho * v^2 * A_p} \quad (1)$$

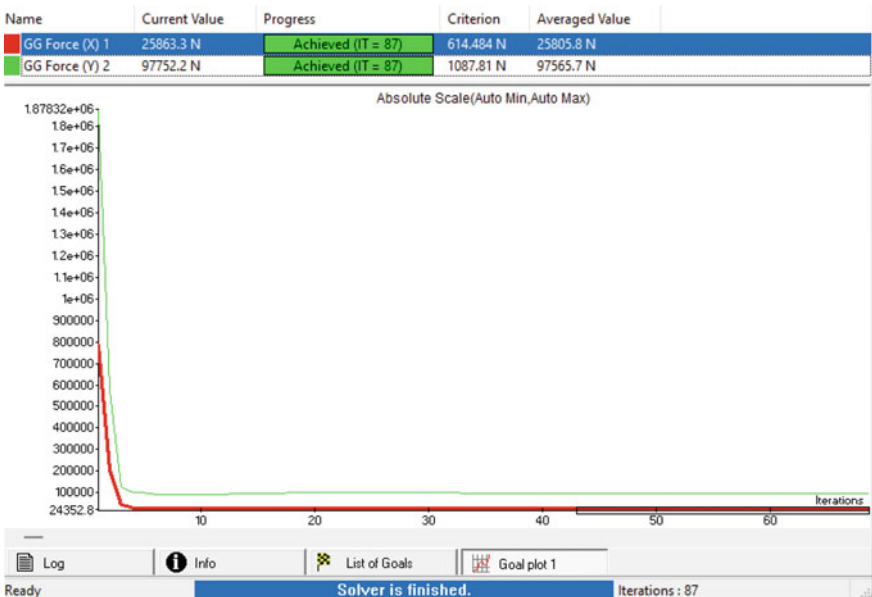


**Fig. 4** Example flow simulation results for 20° angle of attack and aspect ratio of 2

where,  $F_d$  is the drag force;  $\rho$  is the density of the fluid, which is air in this case of  $1.2004 \text{ kg} * \text{m}^3$ ;  $v$  is the velocity of the fluid, which is set as  $34.3 \text{ ms}^{-1}$  for the initial condition;  $A_p$  is the planform area of the airfoil.

For planform area of the airfoil, it can be expressed as:

$$A_p = c * l = AR * c^2 \quad (2)$$

where,  $C$  is the chord length of the airfoil, which is 9.140 m in this case;  $L$  is the wing span; AR is the aspect ratio that is defined as the ratio between wingspan to chord length.

Similarly, the formula for calculating lift coefficient is expressed as the following:

$$C_l = \frac{2 * F_l}{\rho * v^2 * A_F} \quad (3)$$

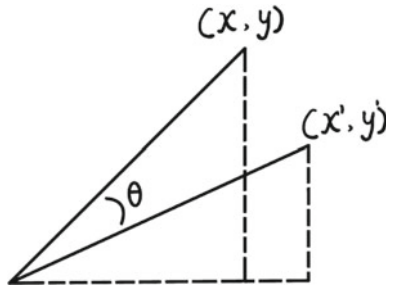
where,  $F_l$  is the lift force;  $A_F$  is the frontal area of the airfoil.

For frontal area of the airfoil, it can be expressed as:

$$A_p = t * l \quad (4)$$

where,  $T$  is the height of the airfoil, which is measured from the highest point to the lowest point of the airfoil vertically.

**Fig. 5** Rotation of the airfoil coordinate due to angle of attack



For calculating  $t$ , the height of airfoil, the following method of considering geometric location of coordinates is introduced. Figure 5 is rotation of the airfoil coordinate due to angle of attack.

In this case,  $(x, y)$  represents the coordinate of a particular point of the airfoil and  $(x', y')$  represents the corresponding coordinate after the rotation. The rotation due to angle of attack is expressed by the angle.

By using the Pythagorean Theorem, the following equation can be deduced, and  $s$  is introduced for the purpose of simplification for further derivation:

$$x^2 + y^2 = x'^2 + y'^2 = s \quad (5)$$

By using trigonometric identity, the following equations can also be deduced:

$$\theta_1 = \arctan\left(\frac{y}{x}\right) \quad (6)$$

$$\theta_2 = \arctan\left(\frac{y'}{x'}\right) \quad (7)$$

The angle of attack  $\theta$  can be expressed as:

$$\theta = \theta_1 - \theta_2 = \arctan\left(\frac{y}{x}\right) - \arctan\left(\frac{y'}{x'}\right) \quad (8)$$

By rearranging this equation, the following equation can be derived:

$$y' = x' * \tan\left(\theta - \arctan\left(\frac{y}{x}\right)\right) \quad (9)$$

By substituting this equation into Eq. (3), the following equations can be derived:

$$x'^2 + x' * \left[\left(\theta - \arctan\left(\frac{y}{x}\right)\right)\right]^2 = s \quad (10)$$

$$x' = \sqrt{\frac{s}{1 + (\theta - \arctan(\frac{y}{x}))}} \quad (11)$$

$$y' = \sqrt{\frac{s}{1 + (\theta - \arctan(\frac{y}{x}))}} * \tan\left(\theta - \arctan\left(\frac{y}{x}\right)\right) \quad (12)$$

Thus, knowing the angle of attack (for rotation) and also the initial coordinates of a particular point, the point's corresponding final coordinates can be calculated. As mentioned previously, the height of the airfoil, which is measured from the highest point to the lowest point of the airfoil vertically; knowing the  $y$  coordinates of all points of airfoil after rotation, the final formula for calculating the height is expressed as the following:

$$t = \max(Y) - \min(Y) \quad (13)$$

where  $Y$  is the set of all vertical coordinates of the airfoil point after rotation due to angle of attack.

By substituting the values of various parameters into Eqs. 1 and 2, the drag coefficient and lift coefficient under different input values of aspect ratio and angle of attack can be obtained. The results of the numerical results will be analyzed later in the discussion section.

### 3 Results and Discussion

#### 3.1 Result

By utilizing the methodology presented in the previous section, i.e. the flow simulation from solidworks and also the numerical calculation from python programming, the following results regarding the performance of NACA 24112 could be obtained.

It could be observed from Fig. 6 that universally, for all sets of angles of attack, the increase in aspect ratio would contribute to the better performance of airfoil NACA 24112 by increasing the lift to drag ratio (LDR). By increasing the angle of attack, the LDR would increase initially; however, after the angle of attack of  $10^\circ$ , the increase in AOA would correspond to a lower LDR. By considering the all possible scenarios presented by the different combinations of angle of attack and aspect ratio, the best alternative of geometry and rotation would be the aspect ratio of 2 at the angle of attack of  $5^\circ$ , which has the optimum LDR value of approximately 5.955.

From Fig. 7, it can be observed that both the increase in aspect ratio and angle of attack would contribute to the increase in drag coefficient. In this case, the maximum drag coefficient of the combination of aspect ratio of 2 and angle of attack of  $20^\circ$  is approximately 2.3207; the drag coefficient of optimum LDR value, i.e. aspect ratio of

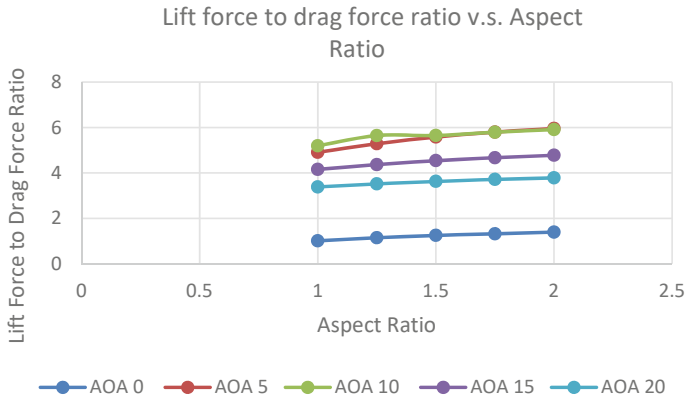
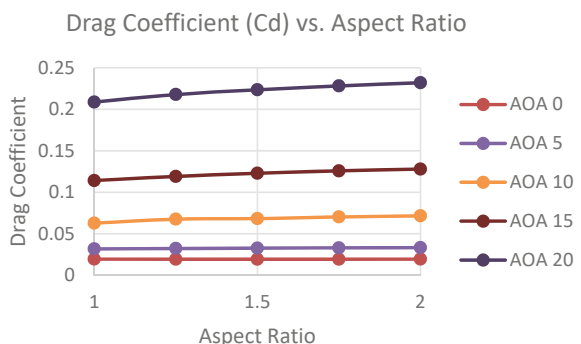


**Fig. 6** Lift force to drag force ratio versus aspect ratio

2 at the angle of attack of 5 is approximately 0.03327. The drag coefficient for typical streamlined body of 4-element (which is similar to the airfoil utilized on airplanes in real life situations) is approximately 0.05; this would signify at the optimum LDR case, the value of drag coefficient would be acceptable since it is lower than that of a typical streamlined body [8].

From Fig. 8, a similar trend of lift coefficient variation could be observed compared to that of the drag coefficient, which is that both aspect ratio and angle of attack have a positive correlation in regards to lift coefficient. In this case, the maximum lift coefficient of the combination of aspect ratio of 2 and angle of attack of 20 is approximately 2.2194; the lift coefficient of optimum LDR value is approximately 1.24868. This value of lift coefficient could also be acceptable as it is similar to the typical maximum values of lift coefficient for other NACA series airfoil, which is approximately 1.4 [9].

**Fig. 7** Drag coefficient versus aspect ratio (for different AOAs)



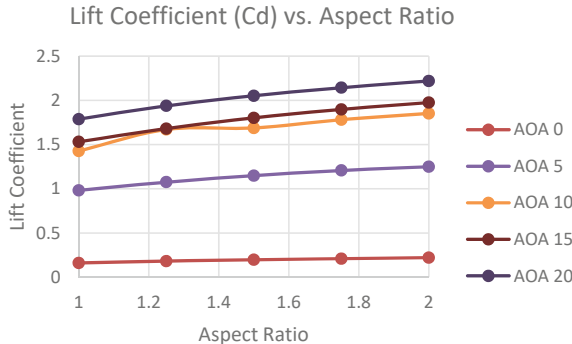


**Fig. 8** Lift coefficient versus aspect ratio (for different AOAs)

### 3.2 Evaluation

Even though a successful simulation and exploration of the optimum performance of NACA 24112 airfoil has been conducted in this paper, there is still room for improvement for the purpose of obtaining more accurate results and more generalized conclusions. The first strategy would probably be to increase the step size, i.e., to examine more values of angles of attack and aspect ratios since there are only 5 different values of angles of attack and 6 for that of aspect ratio.

The second strategy would be exploring the airfoil with more components or more variation regarding geometry in addition to changing the aspect ratio.

As shown by the Fig. 9, the airfoil lift coefficient could be enhanced by having additional components in different configurations of geometry, e.g. double slotted flap, plain flap etc. [10]. Those values are above that for the airfoil only of 1.4 (shown in the Fig. 4) or 1.249 for NACA 24112 airfoil only. For future exploration of the optimized performance for the NACA 24112, various additional components could be utilized e.g. flap. Nonetheless, the results obtained from this paper are still legitimate and could be considered as a preliminary test for airfoil optimization that would lay the necessary foundation for future exploration.

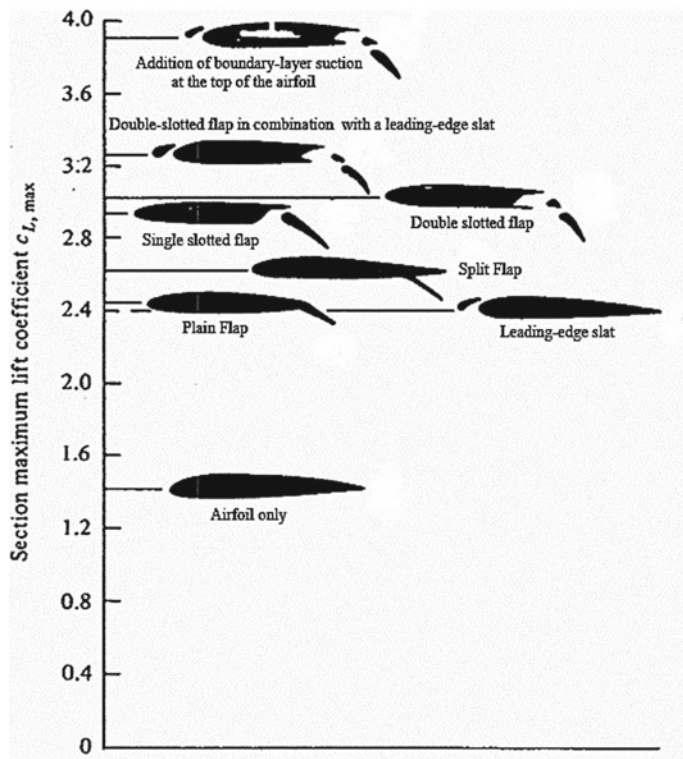


**Fig. 9** Typical values of airfoil maximum lift coefficient for various types of high-lift devices

#### 4 Conclusion

Because of the research on the performance of NACA 24112 airfoil, it can be concluded for the optimization of its performance, the aspect ratio and angle of attack shall be selected as 2 and  $5^\circ$ , respectively, with a LDR value of 5.955. In this case, the drag coefficient and lift coefficient are approximately 0.0333 and 1.249 approximately which are both acceptable values in comparison to the typical value of drag coefficient and lift coefficient for streamlined bodies. During the process of research, the solidworks flow simulation and python numerical calculation (for calculating the height of airfoil in particular) have been utilized, which contributed to the final data collection and following discussion of the results. There are certain limitations of the exploration of performance of NACA 24112 in this paper and for the purpose of better accuracy of the results, two alternatives could be applied for future work, which are having a smaller step size for aspect ratio and angle of attack and constructing additional components (to obtain a higher value of lift coefficient).

## References

1. Jian-Fei LI, Zhao TY, Zan SD (2016) Effect of angle of attack on the high-speed oblique penetration capability of long rod projectile. *Sci Technol Eng* 56(7):120–128
2. Yavuz K (2010) Performance analysis of the airfoil-slat arrangements for hydro and wind turbine applications. *Energy* 87(5):1591–1601
3. Zhaoyang S, Feng H, Jiancheng YU (2022) Influence of autonomous sailboat dual-wing sail interaction on lift coefficients. *J Ocean Univ China: English Edition* 21(3):13
4. Mobedi P, Lavasani AM, Abolfathi S (2022) The aspect ratio effect on the performance of a cam-shaped cylinder in crossflow of air. *Exp Heat Transf* 35(4):500–515
5. Giordano R, Ianiro A, Astarita T (2012) Flow field and heat transfer on the base surface of a finite circular cylinder in crossflow. *Appl Therm Eng* 49(1):79–88
6. Takahashi Y, Watanabe Z (2018) The positioning effect of air-passage-ports in a cylinder on the performance of an air rock-drill. *36(12):3240–3244*
7. Kagawa M (2013) A Study on the meter-out velocity control of a pneumatic cylinder Consideration of air temperature change effects. *Hydraul Pneum* 545:225
8. Kaufman DV, Ryabinin AN (2020) Effect of coaxially mounted disks on oscillations of a cylinder of large aspect ratio in air flow. In: IOP conference series: materials science and engineering, vol 927, no 1, p 012002
9. Hamidreza B, Arash B (2014) Experimental study of convective heat transfer from in-line cam shaped tube bank in crossflow. *Appl Therm Eng Des Process Equip Econ* 797:67
10. Mangrulkara CK, Dhoble AS, Deshmukha AR (2017) Numerical investigation of heat transfer and friction factor characteristics from in-line cam shaped tube bank in crossflow. *Appl Therm Eng* 110:521–538

# Experimental Analysis of Viscous Damping Wall Based on Free Vibration Response



Junxia Sun, Nana Liu, Yingjia Wang, Yan Zhang, and Wei Wang

**Abstract** Through the viscous damping wall test, the displacement time history data of the free vibration test is first obtained by means of the Vic-2D non-contact acquisition equipment. Then, based on the original displacement time history, the damping force time history and velocity time history are calculated by energy method and central difference method respectively. In order to filter the high-frequency noise in the signal, Butterworth low-pass digital filter is used to filter the time history curve, and then a smooth velocity damping force relationship curve is obtained. Select the key control points on the relationship curve to obtain the skeleton curve of velocity damping force. Linear fitting is performed based on the pure damping model to obtain the mechanical model parameters of the damping wall. Finally, Rosenbrock integration method is used for numerical simulation, and the displacement time history curve and displacement damping force relationship curve obtained from the test results and numerical simulation results are compared to verify the reliability of the mechanical model parameter identification method.

**Keywords** Viscous damping wall · Low pass digital filter · Rosenbrock integration method

## 1 Introduction

Viscous Damping Wall, as a new type of damper, was first proposed by Miyazaki [1], a Japanese scholar, in 1986. It has attracted extensive attention from scholars at home and abroad because of its remarkable damping effect. After more than 30 years of development, viscous damping walls have achieved many research results with practical significance [2–4]. The traditional test method is to fix the outer steel box of the viscous damping wall on the foundation beam on the ground, connect the top plate of the inner steel plate with the loading beam, connect the loading beam with

---

J. Sun · N. Liu · Y. Wang · Y. Zhang · W. Wang (✉)  
ChongQing College of Architecture and Technology, Chongqing, China  
e-mail: [773464815@qq.com](mailto:773464815@qq.com)

the actuator, and load through the actuator [5]. This method has high measurement accuracy and reliable test results. However, the problem is that the traditional test methods have high requirements for test equipment and devices, such as foundation beams, loading beams, and reaction walls that require high stiffness. Ordinary test equipment cannot meet the requirements.

At the same time, the traditional contact measurement method is used in the above research to measure the dynamic response parameters of the structure. The installation of sensors is more cumbersome, and additional mass and additional stiffness will be introduced, which will affect the accuracy of the measurement results. Compared with the contact measurement, the visual measurement technology based on computer system has significant advantages. The accuracy and reliability of non-contact measurement in system parameter identification has been verified. Zhou [6] and others put forward a non-contact measurement method based on computer vision, which realizes target motion tracking, has high measurement accuracy, and has good application prospects. Yang [7] and others used DIC technology to realize the rapid measurement of the time history of structural multi-point dynamic displacement and verified that the non-contact structural deformation measurement method based on fast DIC has engineering application value. Cabo et al. [8] proposed a displacement measurement method based on computer vision technology. Research indicates that the use of standard digital cameras and DIC methods can quickly, efficiently, and accurately measure the local displacement of structures. Based on the above research, this paper uses DIC method to identify the dynamic response parameters of viscous damping wall model with reliability.

In this paper, Butterworth filter is used to filter out the noise and error in the test data, and the velocity damping force relationship curve is fitted. Finally, in the Matlab program, Rosenbrock integral simulation method is used to analyze the data and other experimental theoretical analysis methods. The free vibration test of the scale viscous damping wall model is carried out, and the initial displacement is applied to the top plate of the damping wall for loading. At the same time, the displacement time history data of the steel plate at the top of the model is collected with the help of non-contact Vic-2D equipment. Based on the experimental data and the pure damping model, a parameter identification method for the mechanical model of the damper is proposed. Finally, based on Rosenbrock integration method [9], a MATLAB program was compiled to simulate the free vibration response of a single degree of freedom system with a damping wall. The experimental results were compared with the numerical simulation results, which verified the effectiveness of the parameter identification method.

## 2 Viscous Damping Wall Test

### 2.1 1Test Device

This test adopts a scaled damping wall model. The external dimensions of the box are 700 mm long, 600 mm high, and 150 mm thick. The whole test device is composed of upper and lower steel plates, damping wall box, channel steel, etc. The test device is shown in Fig. 1.

Fix the fabricated damping wall device on the upper and lower steel plates. The long rectangular plate welded with the shear plate is fixed with the upper steel plate by bolts. The two wings of the lower plate of the box are fixed with the lower steel plate by bolts. The clear width of the damping wall box is changed by installing a 20 mm thick acrylic plate with the same length and height as the box. The lower steel plate is not directly fixed on the ground, but on two C10 channel steels with a length of 3 m. The iron block is fixed on the top of the upper steel plate by bolts, and the number of iron blocks is adjusted to change the counterweight. The upper and lower steel plates are connected by four long screws, all of which are 10.9 grade high-strength screw rods with a diameter of 14 mm. Adjust the cutting height of the shear plate by changing the height between the upper and lower floors. In order to prevent the device from twisting, pull a rope at the diagonal position between the upper and lower plates on both ends of the device, and fasten it crosswise, as shown in Fig. 1.

Fix a perforated angle steel on the upper steel plate, and fix a strip steel plate sprayed with white paint and marked with black spots on the angle steel, as shown in Fig. 2. The strip dotting steel plate is perpendicular to the upper steel plate, which

**Fig. 1** Test devices-Damping wall

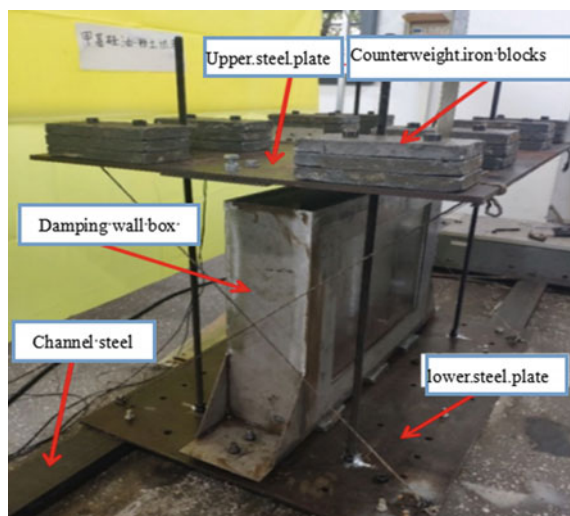
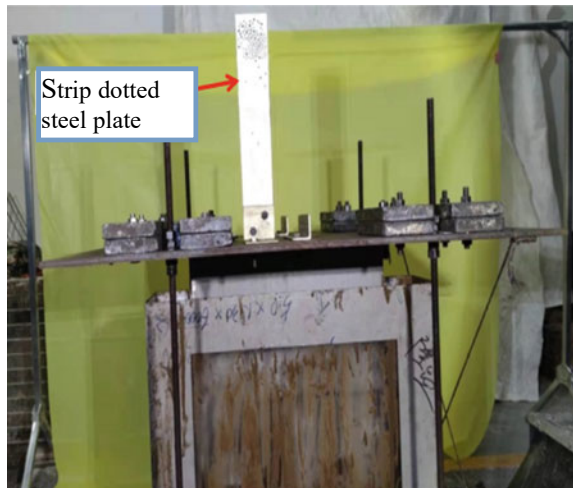


**Fig. 2** Test devices-Strip dotting steel plate



is mainly used to measure the displacement time history of the upper roof plate with the Vic-2D optical equipment.

In this test, the clear width of the damping wall box is 11 cm, the shear height of the shear plate is 4 cm, and the counterweight loaded on the top floor of the damping wall is 80 kg. The mixture of methyl silicone oil and silt with a mass ratio of 3:7 is used as a viscous damping material to fill the box of the damping wall, in which the grade of methyl silicone oil is 10000cs.

## 2.2 Test Process

After the equipment is installed, manually pull the rope tied to the top plate of the structure to make the top plate cycle for 4 to 6 cycles to reach a large displacement, and then suddenly release the rope, which is equivalent to giving an initial displacement, and the upper structure starts to vibrate freely. At the same time, start the high-speed camera, and start to collect the displacement time history data of the damping wall roof with the Vic-2D system based on the computer. During the test, the damping wall makes periodic left and right reciprocating motion. The shear plate in the box is subject to the damping force, and the speed of the upper roof gradually slows down until it stops. After the upper roof stops moving, sampling can be stopped.

### 3 Error Analysis

#### 3.1 Error Sources

The error analysis in this paper mainly includes test error and calculation error. The test error comes from the error of Vic-2D acquisition equipment due to its limited accuracy [10]; the calculation error comes from the derivation of displacement time history in the process of data processing, which amplifies the high-frequency noise in the test data. In the process of data processing, the original sampling time interval is uneven. After interpolation, the original time interval is reduced by ten times, which can improve the accuracy of the original data and achieve the smoothness of the original curve, which reduces high-frequency noise to a certain extent. However, in the calculation process, the derivation of displacement time history amplifies the amplitude of high-frequency noise, resulting in large fluctuations in the velocity time history curve, which is serrated. Therefore, it is necessary to use Butterworth low-pass digital filter to filter the high-frequency noise in the digital signal.

#### 3.2 Filter Performance Verification

As a key tool for processing the experimental data, Butterworth low-pass digital filter directly affects the results of this experiment. Therefore, it is very important to analyze its noise reduction characteristics. In order to study the filtering effect of the filter on the damped free vibration displacement response, the sine wave amplitude attenuation signal with artificial noise is selected for noise reduction. Compare the velocity time history and damping force time history before and after filtering, and compare with the results obtained from the original sine wave amplitude attenuation signal, and then analyze the filtering effect of the filter. To ensure that the input displacement time history is free of noise pollution, the smooth sine wave amplitude attenuation signal is selected as the original displacement time history, and the commonly used Gaussian noise [11] is selected as the digital noise source. In Matlab, use the imnoise function to add Gaussian noise to the original signal. The specific procedure is as follows:

```
imnoise(y,'gaussian',0,0.01)
```

In this formula,  $y$  is the original signal, 0 is the mean value of the added Gaussian noise, and 0.01 is the variance of the Gaussian noise.

The signal contrast before and after adding Gaussian noise of appropriate size is shown in Fig. 3. The signal added with Gaussian noise is selected for calculation, and the damping force time history and velocity time history are calculated according to energy method and central difference method respectively. The velocity time history curve before and after filtering is shown in Fig. 4. It can be seen from the figure that the

velocity time history curve before filtering is sawtooth shaped due to high-frequency noise, and the filtered curve is very smooth.

At the same time, the original signal without Gaussian noise is selected and calculated by energy method and central difference method respectively to obtain the velocity time history and damping force time history, as shown by the dotted line in Fig. 6. Similarly, the velocity time history and damping force time history are calculated from the displacement time history after adding noise, and filtered by Butterworth filter. The time history curve is shown as the solid line in Fig. 5.

It can be seen from Fig. 6 that the velocity time history curve processed by Butterworth low-pass digital filter and the velocity time history curve without Gaussian noise are highly consistent. The damping force time history curve processed by Butterworth low-pass digital filter is in good agreement with the rest of the curve except that there is a small error at the beginning and end of the damping force time history curve without Gaussian noise. It can be seen that the Butterworth digital filter designed in this experiment can effectively filter the high-frequency noise in the

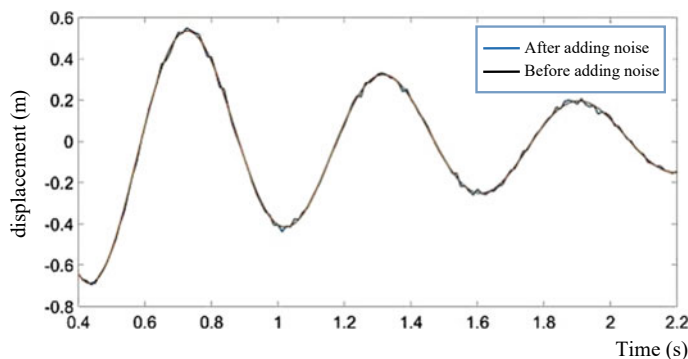


**Fig. 3** Displacement history before and after adding Gaussian noise

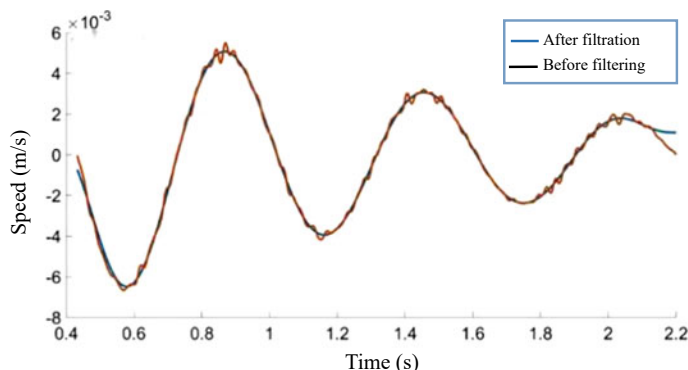


**Fig. 4** Velocity history curve before and after filtering

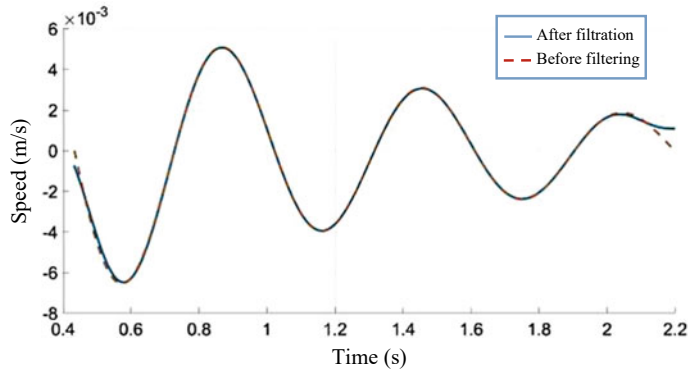


**Fig. 5** Speed time history comparison

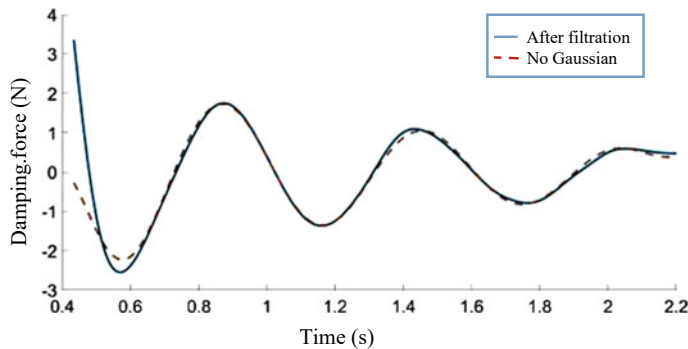


**Fig. 6** Time history comparison of damping force

digital signal and reduce the interference of high-frequency noise. Its noise reduction performance is good and can be used to process test data.

#### 4 Analysis of Test Results

The original test data collected by the Vic-2D equipment can be interpolated to obtain the displacement time history curve. Then the damping force and velocity are calculated respectively according to the energy method and the central difference method. The damping force time history curve and the velocity time history curve are both uneven serrated due to the interference of high-frequency noise. After filter processing, the high-frequency components in the digital signal are filtered out. The filtered velocity time history curve and damping force time history curve are smooth, as shown in Fig. 7. The filtered velocity time history curve can effectively avoid the

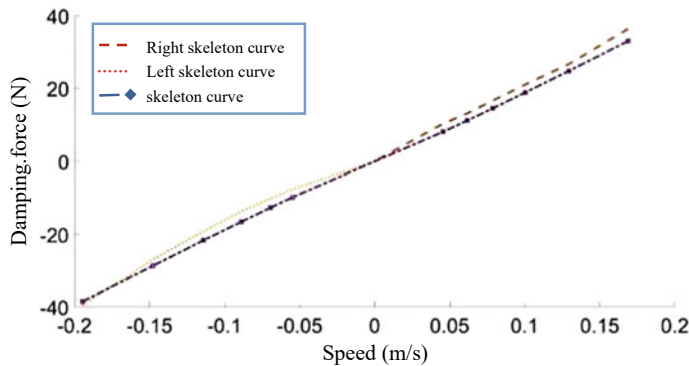


**Fig. 7** Velocity-damping force skeleton curve and fitting curve

interference of noise, and can truly reflect the response of the damping wall in the free vibration process. The filter designed in this experiment effectively realizes the low-pass filtering function and has good filtering performance.

## References

- Miyazaki M, Arima F et al (1986) Earthquake response control design of buildings using viscous damping walls. In: Proceedings of first East Asia Pacific conference. Bangkok, pp 1882–1891
- Robert JM, Douglas PT (2003) Fluid viscous dampers for high-rise buildings. *Struct Des Tall Spec Build* 12(2):145–154
- Elif CK, Kemal M (2017) An optimization study for viscous dampers between adjacent buildings. *Mech Syst Signal Process* 89:88–96
- Zhou Y, Chen P (2017) Shaking table tests and numerical studies on the effect of viscous dampers on an isolated RC building by friction pendulum bearings. *Soil Dyn Earthq Eng* 100:330–344. (in Chinese)
- Ou J, Liu W, Zhang Z (2005) Experimental study on dynamic performance of viscous damping wall. *Earthq Resist Eng Retrofit* 27(6):55–59. (in Chinese)
- Zhou Y, Zhang L, Liu T et al (2018) Structural system identification based on computer vision. *China Civ Eng J* 51(11):17–23. (in Chinese)
- Yang B, Li D, Xu G et al (2020) Structural deformation testing based on fast DIC and regularization smoothing technology. *Chin J Highw* 33(9):193–205. (in Chinese)
- Cabo C, Ordóñez C, Muñiz-Calvente M et al (2019) A hybrid SURF-DIC algorithm to estimate local displacements in structures using low-cost conventional cameras. *Eng Fail Anal* 104:807–815
- Ia C, Wang Z, Li Y et al (2012) Rosenbrock-based coupled time integration method and its application to real-time substructure testing. *Earthq Eng Eng Vib* 32(5):11–18. (in Chinese)
- Han J, Zhang Y, Zhang H (2019) Displacement measurement of shaking table test structure model based on computer vision. *Earthq Eng Eng Vib* 39(4):22–29. (in Chinese)
- Dominique P (2007) A theoretical result for processing signals that have unknown distributions and priors in white Gaussian noise. *Comput Stat Data Anal* 52(6):3167–3186

# Design and Analysis of Turnover Function of Nursing Bed Based on Ergonomics



Weiliang Zeng, Xinzui Wang, Fucheng Cao, Haibing Xin, Xihua Li, Zhaobo Li, and Hui Fu

**Abstract** In view of the present nursing bed turning over irrationally causes the human body local pressure to be excessively big, is difficult to prevent the bedsores situation, and so on. Based on the principle of ergonomics, establish the model of axial rollover and nursing bed, the complete parameters of the mechanism are determined by numerical simulation. The design has the safe reliable, the function diversification, and the automation degree high nursing bed.

**Keywords** Nursing bed · Ergonomics · Axial rollover · Kinematic simulation

## 1 Introduction

The problem of population aging is becoming more and more serious. According to official statistics, by the end of 2015, the number of senior citizens over 65 in China has reached 143.9 million, accounting for 10.5% of the total population. It is preliminarily estimated that the number of senior citizens over 65 in China will increase to 14% of the total population by 2026. In 2050, the population of our country will reach the peak, the proportion of the elderly aged 65 and above will be close to 30%, and the elderly population will be close to 500 million [1]. The aging of population will be a great challenge to our country in the future. The aging of population will not only bring negative impact on economic growth, but also bring great pressure to medical and health care [2]. In order to reduce the physical burden and psychological pressure of the elderly, using nursing beds, wheelchairs, and other nursing supplies has gradually become an irreplaceable means in health care [3, 4].

---

W. Zeng · X. Wang (✉) · F. Cao · H. Xin · X. Li · Z. Li  
Ji Hua Laboratory, Foshan 528200, China  
e-mail: [wangxz@jihualab.com](mailto:wangxz@jihualab.com)

W. Zeng · H. Fu  
Guangdong University of Technology, Guangzhou 510006, China

As one of the three common functions of nursing beds, turning-over function still has some deficiencies in the design of existing nursing beds [5]. Through investigation, we found that most of the nursing beds use V-turn, which has the problems of squeezing human body, increasing local force and weakening the support of the bed [6]. Based on the pressure distribution test of human body, a turning-over mechanism with sufficient support, irregular adjustment of local force and prevention of extrusion was designed and manufactured. Design and manufacture of bedsore prevention function, safety and comfort of the nursing bed prototype.

## 2 Overall Design and Functional Distribution of Nursing Bed

The study of nursing bed solves the problems of single function, excessive dependence on nursing staff and independence of bed and chair. Figure 1 is the whole of the nursing bed, where Fig. 1a is a three-dimensional model drawing and Fig. 1b is a physical drawing. Firstly, the combination of bed and chair is realized by modular design. The bed mainly has three modules: bed body, wheelchair and defecation system. The bed body mainly realizes the nursing bed the elevation as well as the wheelchair and the bed body butt joint provides the bigger space for the human body; after the chair is separated from the bed, the automatic molding of the wheelchair is realized by bending the legs and lifting the back. In addition to the wheelchair to achieve rollover, back and curved leg functions, but also equipped with defecation system, it is in order to enhance the versatility of nursing beds. The utility model adopts the linear actuators as the power source to realize the functions of automatic rollover, back lifting and crouching, and the defecation system is arranged at the bottom of the wheelchair to automatically recover urine and feces, and to clean and dry the buttocks, the automation and diversity of functions effectively reduce the working intensity of nursing staff.

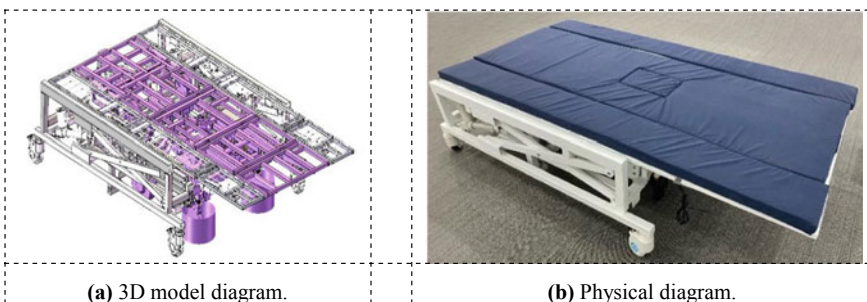


**Fig. 1** Overall structure of nursing bed

### 3 Human Pressure Distribution Test

The main function of the nursing bed is to assist in caring for the elderly. Most of the nursing beds on the market have the basic functions of turning over, starting back and bending knees. Different brands of nursing beds have different ways to realize the three functions. V-turn is the main way of turning over. In order to verify the reliability of V-turn, the pressure distribution test is conducted.

#### 3.1 Test Method

Buy the mattress material that is often used in nursing beds, the mattress material that the home uses, and new mattress materials altogether 7 kinds. Choose one male and one female volunteer from the social group according to the average height and weight level of China. The BPMS is designed and manufactured by Tekscan Corporation of the United States, and the thickness of the pressure measuring pad is only 0.2 mm, to minimize the error impact of the experimental equipment. The pressure measuring pad is connected to the computer terminal through a USB interface and powered by a USB interface. The sampling frequency is set to 10 Hz and the data resolution is 8bit.

#### 3.2 Data Analysis

Data on static pressure distributions of volunteers lying flat on different mattresses were collected, and the data were cleaned and visualized to obtain a heat map of pressure distributions. Figure 2 is a heat map of human pressure distributions, with Fig. 2a being male and Fig. 2b being female. The figure shows that no matter which mattress the body is lying on, the back and buttocks of the human body are most stressed, and the most pressure is concentrated on the back and buttocks.

Through the analysis and calculation of the data, the pressure ratio of the back and buttocks of the human body is shown in Table 1. For men, the pressure ratio of the back is 33.10–36.91%, the buttocks pressure ratio is 37.24–46.07%; for women, the back pressure ratio is 28.20–38.17%, and the buttocks pressure ratio is 39.92–50.36%; for both men and women, the average back pressure ratio is more than 32%, the average buttocks pressure ratio is more than 41%, and the total back and buttocks pressure ratio is more than 76%. From the data, we can see that the back and buttocks of the body lie flat bear most of the pressure, so the design of the motion mechanism should fully consider the impact of the motion mechanism on the back.

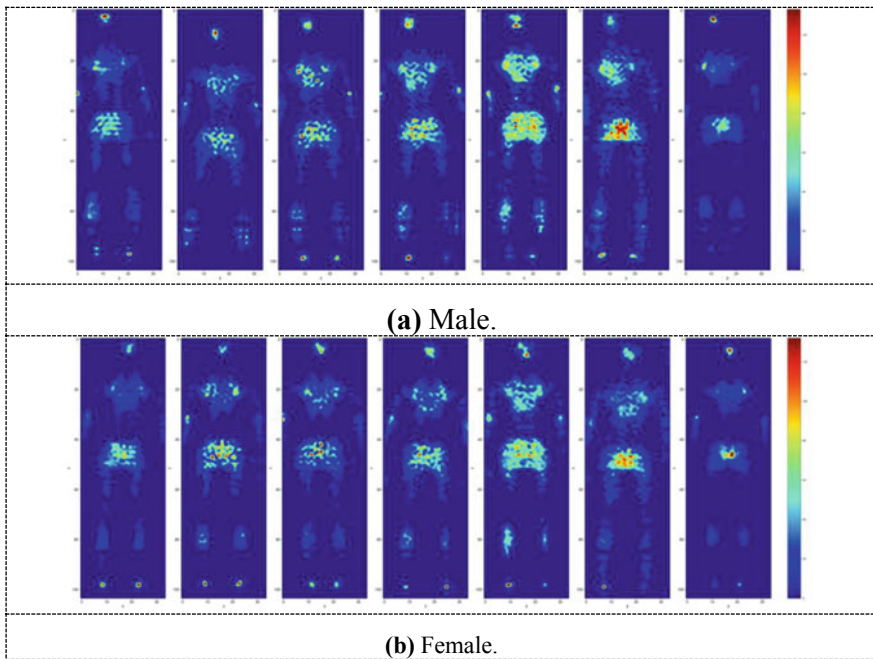


**Fig. 2** Heat map of human pressure distribution

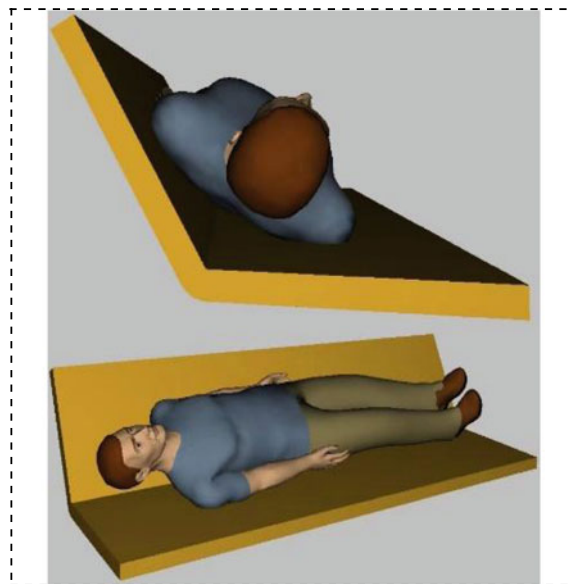
#### 4 The Argument and Choice of Turning Over Way

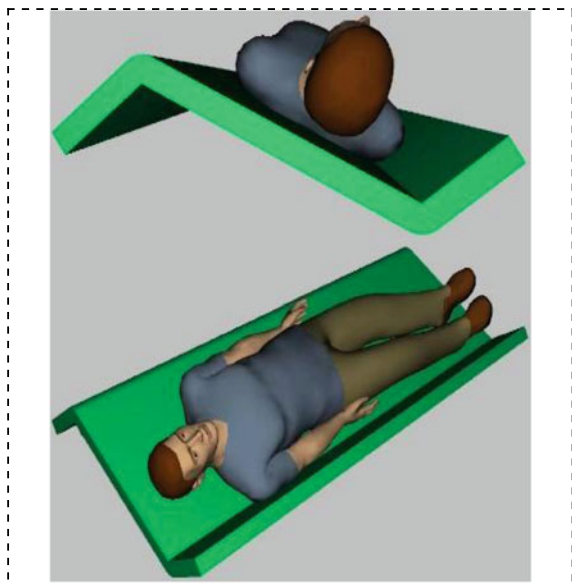
V-turn simulation is shown in Fig. 3, V-turn rotation axis is located under the middle axis of human body. When the turn-up module rotates around the axis, the rotation module provides support for the two points and one line of shoulder and hip of the same side of human body, and flips over the two points and one line of shoulder and hip of the other side to achieve the effect of turning over. The biggest disadvantage of the turning-over mode is that the contact area between the bed surface and the body is small, and the back and buttocks are aerial by the V-shaped bed surface, so that the human body pressure mainly concentrates on the shoulders and hips. When the turning angle of the turning-over module gradually increases, the body is squeezed, or even causes secondary injury to the body [7, 8].

Based on the pressure distribution test of human body and the insufficiency of V turning over, the bed surface shall provide sufficient support and contact surface for the back and buttocks of human body when turning over. The nursing bed adopts the axial rollover, the Fig. 4 is the simulation of the axial rollover, which is divided into three parts. When turning over, the left and right rollover modules mainly provide protection and support for human body, and the rotating axis of the central support module is located on the central axis of the wheelchair, which provides a larger contact area for human body.

**Table 1** The pressure ratio of the back and buttocks of the human body

The mattress material	Proportion of back pressure	Proportion of buttocks pressure	Sum
<i>Male</i>			
A (%)	33.32	37.24	70.56
B (%)	33.10	40.86	73.96
C (%)	35.21	41.73	76.94
D (%)	34.58	41.92	76.50
E (%)	36.91	39.99	76.90
F (%)	34.41	43.52	77.93
G (%)	35.44	46.07	81.51
Average (%)	34.71	41.67	76.33
<i>Female</i>			
A (%)	28.20	48.52	76.72
B (%)	31.74	46.22	77.96
C (%)	37.71	39.92	77.63
D (%)	31.10	45.25	76.35
E (%)	38.17	41.32	79.49
F (%)	33.33	44.20	77.53
G (%)	29.99	50.36	80.35
Average (%)	32.89	45.11	78.00

**Fig. 3** V-turn

**Fig. 4** Axial rollover

Long-term bedridden elderly local skin long-term pressure, leading to blocked blood circulation, resulting in tissue ischemia and hypoxia, inadequate nutrition, prone to bedsore. Daily care in order to prevent local skin pressure for a long time, every two hours during the day turn over once, no more than three hours at night turn over once. Simulation of artificial turning over can effectively relieve the problem of pressure concentration in bed and improve the effect of bedsore prevention in nursing bed.

## 5 Design of Axial Rollover

As the module with the most integrated functions, wheelchair has many functions and small space, which is one of the main difficulties in nursing bed design. The defecation system is installed under the hip of the wheelchair and occupies most of the space, so this design uses the linear actuators as the power source to achieve the rolled-over function of the wheelchair. In order to save space and select the most suitable electric pusher, numerical simulation method is used to complete the design of the axial rollover, and the selection of linear actuator must be calculated and checked.

## 5.1 The Numerical Simulation

The model of the axial rollover mechanism located in the wheelchair is shown in Fig. 5. The mechanism is mainly composed of linear actuator hinge base, linear actuator, rollover bracket and wheelchair support hinge base. When the linear actuator is expanded, it will drive the rollover bracket to rotate around the axis center, so as to realize the left-right rollover of 0–20°.

The motion diagram of the axial rollover mechanism is shown in Fig. 6. A, B and C are the coordinate points of the linear actuator hinge base, the hinge point between the rollover bracket and the linear actuator, and the hinge base of the wheelchair support, respectively. The position of the linear actuator hinge base and wheelchair support hinge base is fixed due to space limitation. The length of the connecting rod of the BC segment shall not exceed the vertical distance between the point of A and C. When the bed surface is in the horizontal state, in order to provide the least thrust when the linear actuator starts, the connecting rod of the BC segment and the electric push rod are perpendicular to each other.  $B_1$  and  $B_2$  are the limiting positions of point B when the bed surface rotates 20° clockwise and counter clockwise, respectively. The main parameters studied in the rollover mechanism are the length of the BC and the choice of the linear actuator.

According to the principle of moment balance  $M = L \times F$ , BC should take the maximum value in a limited range. The stroke S of the linear actuator is 90 mm and the load thrust is 3000N.

Minimum installation distance of linear actuator:  $L = S + 175$ ;

Calculated, A  $B_1 \leq 355$  mm, A  $B_2 \geq 265$  mm;

- In  $\triangle ABC$ ,  $\angle CBA = 90^\circ$ ,  $AC = 336$  mm,  $\angle BCA = \arccos \frac{BC}{AC}$
- In  $\triangle A B_1 C$ ,  $A B_1^2 = B_1 C^2 + A C^2 - 2 B_1 C * AC * \cos(\angle BCA + 20^\circ)$
- In  $\triangle A B_2 C$ ,  $A B_2^2 = B_2 C^2 + A C^2 - 2 B_2 C * AC * \cos(\angle BCA - 20^\circ)$
- $B_1 C = BC$ ,  $B_2 C = BC$

According to the above formula and restriction conditions, the length change curve of the linear actuator is drawn, as shown in Fig. 7, there are two intersection points

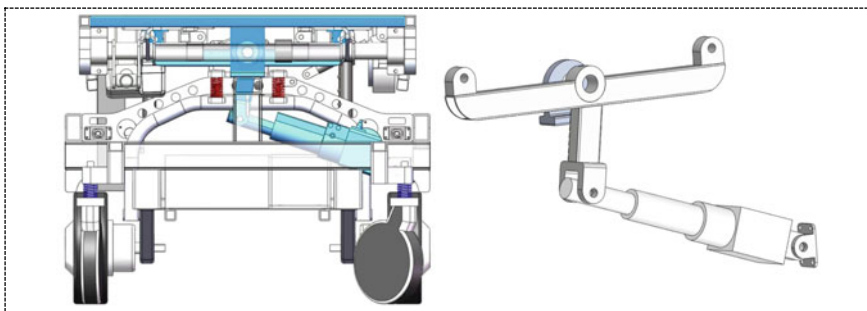


**Fig. 5** Axial rollover mechanism

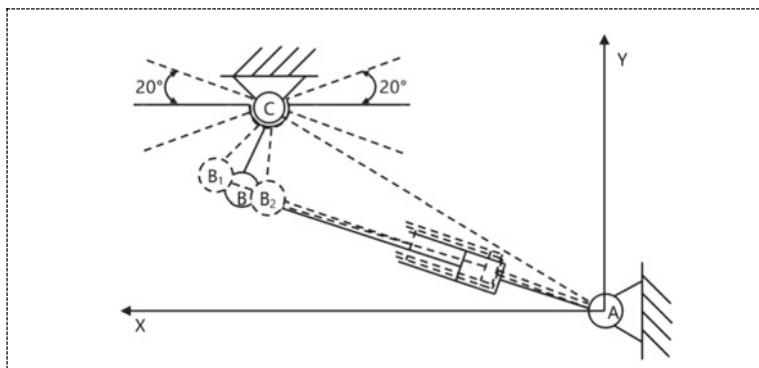


**Fig. 6** The motion diagram of the axial rollover mechanism

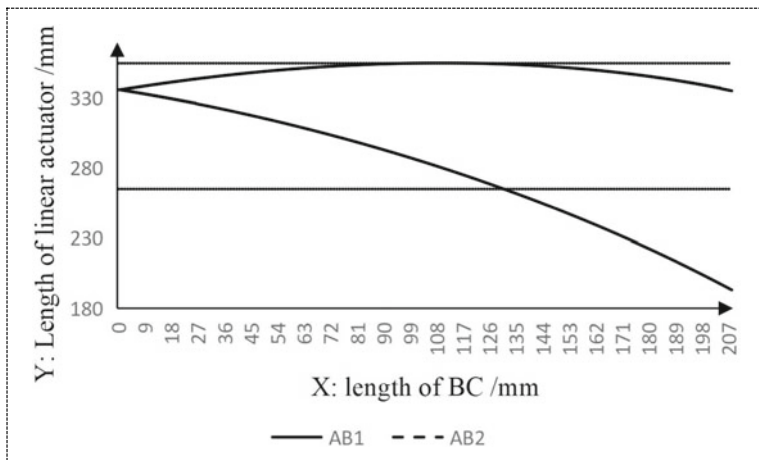


**Fig. 7** The linear actuator length change curve

between the change curve of A B<sub>1</sub> and the line Y = 355, which are respectively (99.17,355) and (118.84,355). There is an intersection point between the change curve of A B<sub>2</sub> and line Y = 265 is (130.64,265). The maximum value of BC is 130.64 mm, the angle of  $\angle BCA = 67.12^\circ$ , and the angle between BC and bed surface is 105.37°.

## 5.2 Linear Actuator Calculation Check

The normal body mass index of the elderly ranges from 18.5–24, which refers to the quotient of weight to the square of height. The length of the nursing bed is 2 m,

which can be used by people under 1.8 m in height. In combination with the use of obese people, 900N load is used in this simulation as the force of the human body on the rollover mechanism. The width of the wheelchair is 600 mm. According to the principle of moment balance  $M = L \times F$  can check whether the load thrust of the linear actuator meets the use requirements.

When the rollover mechanism rotates  $20^\circ$  counter clockwise, the moment arm of the linear actuator acting on the rollover mechanism is the shortest, so just check this situation.

According to the principle of moment balance, it can be known that:  $L_D \times F_{la} = L_M / 2 \times M \times \cos 20^\circ$ ,

Type:

$L_D$  is the vertical distance between the wheelchair support hinge base and the linear actuator, that is, the vertical distance from point C to A  $B_2$ ,  $L_D=121.38$  mm;

$L_M$  is the width of the wheelchair,  $L_M=600$  mm;

$M$  is the load of the human body on the wheelchair,  $M = 900$ N.

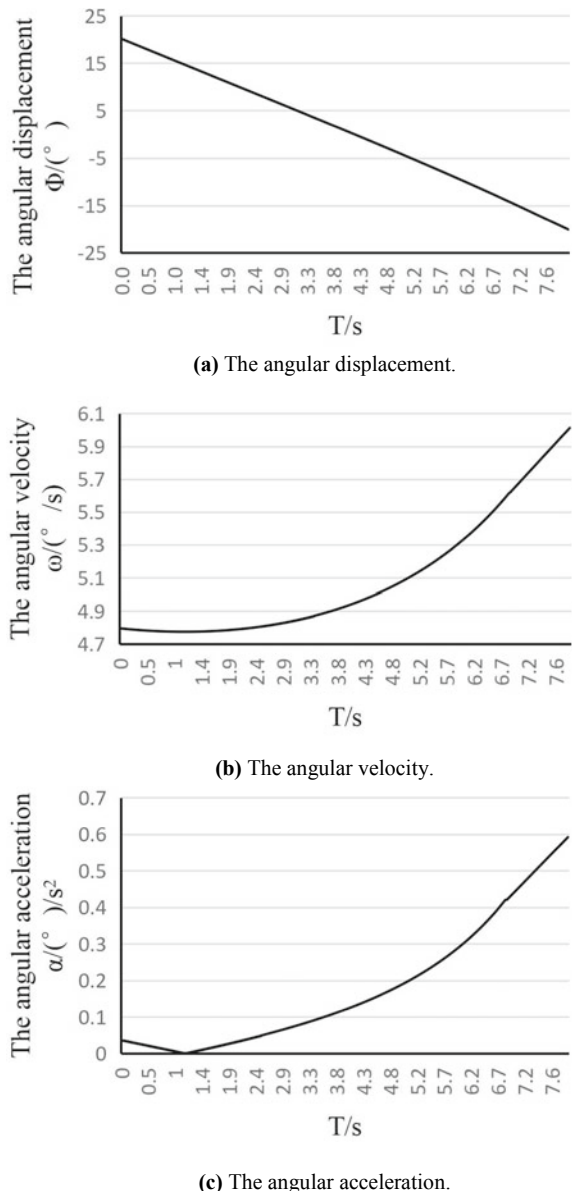
Calculated: The maximum thrust required by the linear actuator  $F_{la} = 2090.27$ N is less than the load thrust of the linear actuator 3000N. Therefore, the linear actuator meets the use requirements.

Through the numerical simulation to determine the complete parameters of the axial rollover mechanism, check the load and stroke of the linear actuator, provide the numerical simulation result support for the prototype nursing bed, ensure the correctness of nursing bed parameter design.

## 6 Simulation of Virtual Prototype

Automatic dynamic analysis of the axial rollover mechanism was carried out. The main work includes the simulation of angular displacement, angular velocity, and angular acceleration of the rollover mechanism. Add a sliding pair and linear drive between the guide tube of the linear actuator and the push rod to achieve linear motion, add a rotating pair in the linear actuator hinge seat and the ground, and add a rotating pair in the rollover bracket and the linear actuator hinge, add a rotating pair in the rollover mechanism and the wheelchair support hinge base. After simulation, the angular displacement, angular velocity, and angular acceleration of the rollover mechanism can be measured. Figure 8 shows the three measurement results, where Fig. 8a is the angular displacement, Fig. 8b is the angular velocity and 8c is the angular acceleration, from which it can be found that the angular velocity of the rollover mechanism is controlled within  $4.8\text{--}6.0(^{\circ})/\text{s}$ , and the angular acceleration is controlled within  $0.6(^{\circ})/\text{s}^2$ . The changes of the three factors are stable without sudden changes. The simulation results show that the parameter design of the axial rollover mechanism is reasonable, which provides the motion simulation result support for the prototype nursing bed, and ensures the feasibility of the nursing bed.

**Fig. 8** Motion simulation of axial rollover mechanism



## 7 Conclusion

From the point of view of ergonomics, this paper makes a comparative study of V-turn and axial rollover through experiment and data analysis. As the realization form of turning over function, the function has the advantages of protecting the human body

from secondary injury, providing stronger support and larger contact area for the human body, so that the user can get reasonable, comfortable and reliable nursing experience. For the nursing bed, the use of axial rollover to regularly adjust the distribution of human pressure, simulate artificial turning over effectively alleviates the problem of long-term bed pressure concentration, so that the nursing bed to prevent bedsores more obvious, further slowing down the work intensity of nursing staff.

In the further design of the axial rollover mechanism, considering the lack of solid space and other factors, the complete parameters of the mechanism were obtained by numerical simulation, and the kinematics simulation of the model was carried out. The simulation results showed that the angular displacement, angular velocity and angular acceleration of the axial rollover mechanism were smooth, which verified the correctness and feasibility of the mechanism. The above demonstration results and simulation results provide a theoretical basis for further optimization of the nursing bed prototype.

**Acknowledgments** Supported by the Jihua Laboratory of China (Grant No. X190341TD190). Suzhou Institute of Biomedical Engineering and Technology Chinese Academy of Sciences (Grant No. 2021SYHZ0020).

2020 Sui Talent Program No. 9.

## References

1. Xiang X, Wang Y (2021) Current situation, characteristics, causes and countermeasures of population aging in China Chin J Gerontol 41(18):4149–41
2. Zhao Y (2021) The effect of predictive nursing intervention on the formation of bedsores and psychological state of long-term bedridden patients Psychologies 16(11):195–196
3. Liu J, Zhu LY, Gou XF (2019) Status and development trend of multi-functional nursing bed. Chin Med Equip J 40(07):94–98+103
4. Xu H, Li CG, Guo Q, Zhou NC, Mo SL (2015) Survey and analysis of function requirement for senior's nursing bed. Packag Eng 36(20):74–78
5. Zhou ZR, Yu CT, Zhou XY, Sun XB (2022) Design and analysis of backplane mechanism for new nursing bed chair. J Mech Transm 46(03):74–80
6. Su N, Reyihanguli M, Muyesaier M, Li ZB, Tao Q (2021) Comparison of sitting postures based on motion capture, pressure distribution and sEMG for finding the optimal sitting posture 2021. J For Eng 6(02):176–182
7. Qin SH, Zhao XH, Yang YW, Liu L (2017) Optimal design and simulation on back-part-lifting mechanism of multi-functional nursing bed based on MATLAB. Manuf Autom 39(10):146–151
8. Wang YD, Yu N (2019) Research on the optimization design of nursing bed for the elderly Furnit Inter Des (04):22–23

# Cumulative Damage Study of Air-Dropped Vehicles with Multiple Drops Impact



Xudong Wang, Yubo Zhou, and Ming Zhang

**Abstract** The vehicle landing process is simulated by dropping the air-dropped vehicle, establishing the vehicle finite element model based on the drop test and verifying the accuracy of the model, and deriving the weak components in the vehicle drop process by transient response analysis of LS-DYNA. Based on the complete restart technology, we propose the simulation method of cumulative damage of vehicle fall and realize the simulation analysis of multiple vehicle falls and the cumulative analysis of vehicle stress state and plastic deformation. Finally, the Johnson–Cook failure damage model was combined to calculate the cumulative damage caused by the fall impact; the variation law of the damage was derived, and the structural damage was evaluated according to the failure model, which has certain guiding significance for the study of the cumulative damage of vehicle airdrop.

**Keywords** Airdrop vehicle · Multiple falls · Cumulative damage · Damage assessment

## 1 Introduction

At present, several vehicles are put into combat after an airdrop. These combat vehicles must have reusable capabilities in terms of airdrops. Since, the cumulative damage after multiple airdrops exists, there should be a maximum number of airdrops of these airdropped combat vehicles upto which these vehicles operate efficiently. How to maximize the number of airdrops puts forward high requirements for the structure and maintenance guarantee of airdrop vehicles. The research methods for airdrop vehicles can be divided into tests and simulations. There are many inconveniences in airdrop vehicle tests, and it is difficult to obtain relatively complete test data for analysis. Simulation can shorten the development cycle and solve relatively

---

X. Wang · Y. Zhou (✉) · M. Zhang

School of Mechanical Engineering, Nanjing University of Science and Technology,  
Nanjing 210094, China

e-mail: [yunbo31983@163.com](mailto:yunbo31983@163.com)

difficult problems in experiments. The cumulative damage of the airdrop vehicle is mainly simulated by the finite element method, and the finite element software provides the possibility for the simulation of the cumulative damage of the airdrop vehicle from multiple falls.

In this paper, the finite element model of the airdrop vehicle is established, and the accuracy of the established model is verified by the real vehicle test. The landing process of the vehicle is simulated by LS-DYNA, and the multiple landings of the airdrop vehicle are simulated by the method of full restart [1] combined with the J-C damage model to evaluate, find out the maximum number of times the vehicle can be dropped, and provide certain guidance for the cumulative damage of subsequent vehicles after multiple airdrops.

## 2 Airdrop Vehicle Analysis Process

### 2.1 Material Failure Model

In the process of high-speed collision or impact, vehicle components often undergo large deformation. The Johnson–Cook failure model is based on the strain failure phenomenon [2], which takes into account the effects of stress triaxiality, strain rate, and temperature on materials. Its failure strain expression is as follows:

$$\varepsilon_f = [D_1 + D_2 \exp(D_3 \sigma^*)] \left[ 1 + D_4 \ln\left(\frac{\varepsilon_p}{\varepsilon_0}\right) \right] [1 + D_5 T^*] \quad (1)$$

$$\sigma^* = \frac{\sigma_m}{\sigma_{vm}} \quad (2)$$

$$\sigma_m = (\sigma_1 + \sigma_2 + \sigma_3)/3 \quad (3)$$

$$D = \sum \frac{\Delta \varepsilon_p}{\varepsilon_f} \quad (4)$$

$\varepsilon_p$  represent plastic strain;  $\Delta \varepsilon_p$  represent the difference between plastic strain;  $\varepsilon_f$  reflects fracture Strain at current stress, temperature, and strain rate;  $\sigma^*$  represent stress triaxial degree,  $\sigma_m$  represent hydrostatic (mean) stress;  $\sigma_{vm}$  represent VonMisess stress;  $\sigma_1$ ,  $\sigma_2$ , and  $\sigma_3$  is first, second, and third principal stress;  $D$  represents cumulative damage. Material destruction when  $D$  is 1,  $D_1$ ,  $D_2$ ,  $D_3$ ,  $D_4$ , and  $D_5$  are failure parameters.

Table 1 shows the Johnson–Cook failure model parameters of the main material used in this vehicle [3, 4], available through material test  $D4$  and  $D5$  are 0.

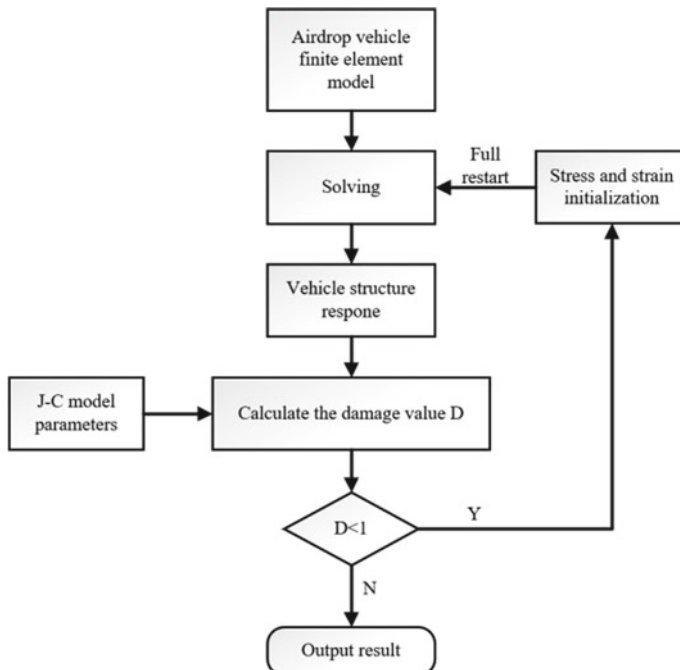
**Table 1** The Johnson–Cook failure model parameters for the main materials of the vehicle

Material	$D_1$	$D_2$	$D_3$	$D_4$	$D_5$
TC4	−0.09	0.25	0.5	0	0
DC03	0.15	0.11	−1.4	0	0
Aluminum 6061	0.17	8.54	−3.99	0	0

## 2.2 Vehicle Drop Cumulative Damage Simulation Process

Airdrop vehicles will suffer a large ground impact during the landing process. Under the action of the ground impact load of each drop, the vehicle parts will undergo local plastic strain and stress. It should be noted that the plastic strain and stress needs of the vehicle can be transmitted and accumulated. Figure 1 shows the simulation flow of the vehicle drop cumulative damage [5].

Firstly, the airdrop vehicle finite element model was established in Hypermesh, and then the simulation analysis of LS-DYNA was used. Then, the residual stress and plastic strain were transferred to the next fall to reach the cumulative effect. Finally, the vehicle damage was evaluated by the Johnson–Cook failure model.

**Fig. 1** Vehicle drop cumulative damage simulation process

## 2.3 Finite Element Model Verification

### Airdrop Vehicle Finite Element Model

A finite element model of the airdrop vehicle is established according to material definition, mesh division, contact setting [6], constraint setting, load setting, card control, etc.

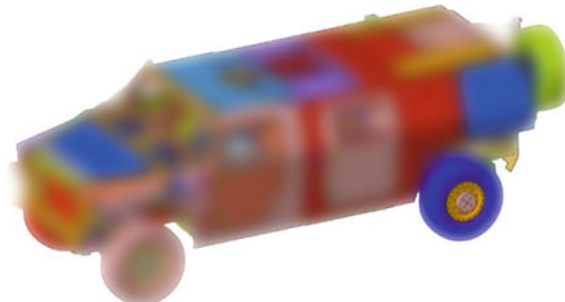
The mesh size of the vehicle parts is generally 10 mm. The shell elements are generally divided into meshes with quadrilaterals as the main triangles. The vehicle is divided into 1,940,193 grid units and 1,785,761 nodes. The vehicle model is shown in Fig. 2.

### Accuracy Validation of the Simulation Model

Use LS-DYNA software to perform drop simulation on the above-established model, set the drop speed to be consistent with the test drop speed of 4.9 m/s, and obtain the simulation data. The acceleration time history curve is compared with the test data as shown in Fig. 3.

In the test, the peak acceleration of the main driving position is basically the same as the peak value of the acceleration of the center of mass and the peak value of the acceleration obtained by the simulation. The peak value of the simulated acceleration of the main driving position is 19.18 g, which has a 7% error compared with the peak value of the test acceleration of 20.67 g; the peak value of the simulated acceleration of the center of mass is 18.8 g, the acceleration peak value of 18.03 g in the comparison test has a 4% error. The overall motion trends are very similar, so the finite element simulation model of the complete vehicle is credible.

**Fig. 2** Vehicle finite element model



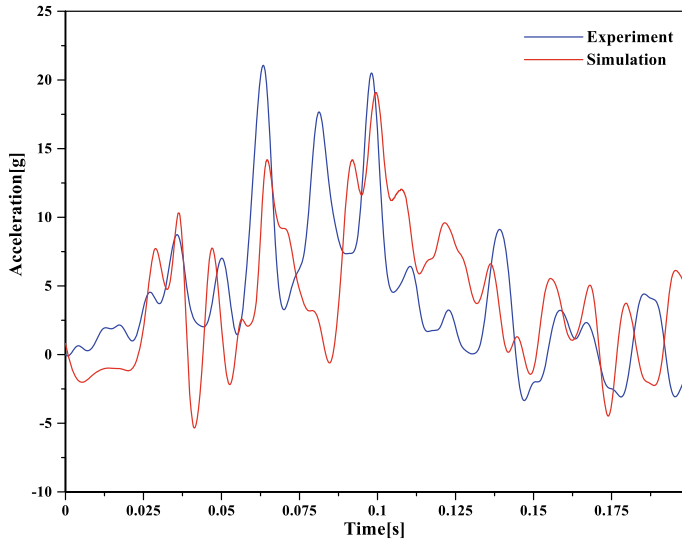


**Fig. 3** Center of mass position acceleration comparison

### 3 Simulation of Multiple Drops of Airdrop Vehicles

#### 3.1 *Simulation Analysis of Cumulative Damage of Airdrop Vehicles from Multiple Falls*

After the vehicle falls, it will cause certain damage to the vehicle. This damage is mainly reflected in the components that generate certain residual stress and residual strain, which in turn affects the damage caused by the next drop of the vehicle, showing a cumulative form of damage. Therefore, in the simulation, the previous damage value must be transferred to the next simulation, and the last simulation result is the initial state of the next simulation. This paper adopts the technology of full restart [7] in LS-DYNA to realize the transfer of damage value and the initialization of stress and strain.

Based on the above description, the airdrop vehicle is simulated for many times, and the cumulative damage value of each component of the vehicle is obtained as shown in Table 2.

It can be seen from Table 2 that after the airdrop vehicle has been dropped for four consecutive times, most of the vehicle components have not reached the stage of material failure, but the damage value of the column and the left front upper swing arm exceeds the failure value 1, so it is considered that these two components are in the first stage. Material failed after four drops. However, after the failure of the column material, the vehicle still has the ability to drive, so the following will only analyze the swing arm on the front axle that affects the normal running of the vehicle.

**Table 2** Cumulative damage from multiple dropped vehicle parts

Time of airdrop	Typical damage part	$\sigma_{vm}$ (MPa)	$\varepsilon_p$	$\sigma_m$ (MPa)	$\varepsilon_f$	$\Delta\varepsilon_p$	$\Delta D$	$D$
The 1st time	Roof	413	0.003	247.8	0.2474	0.003	0.012	0.012
	Middle floor of vehicle	409.3	0.019	213.4	0.2345	0.019	0.081	0.081
	Cab front baffle	174.6	0.015	120.4	0.1849	0.015	0.081	0.081
	Left front hem arm	381.2	0.017	270.1	0.2662	0.017	0.063	0.063
	Left front top swing arm	496.8	0.043	465	0.3142	0.043	0.136	0.136
	Left back hem arm	340.1	0.011	274.9	0.2845	0.011	0.038	0.038
	Left back top swing arm	442.4	0.026	352.7	0.2824	0.026	0.092	0.092
	Central column	55.9	0.053	53	0.3391	0.053	0.145	0.145
The 2nd time	Roof	460	0.008	259.6	0.2415	0.005	0.020	0.032
	Middle floor of vehicle	478.9	0.045	338.2	0.2658	0.026	0.092	0.173
	Cab front baffle	175.4	0.048	141.7	0.2844	0.029	0.101	0.182
	Left front hem arm	494.7	0.043	384.9	0.2788	0.024	0.086	0.167
	Left front top swing arm	500.1	0.105	402.3	0.2837	0.062	0.218	0.354
	Left back hem arm	473.2	0.031	377.8	0.2826	0.020	0.070	0.108
	Left back top swing arm	450.3	0.059	372.7	0.2881	0.033	0.114	0.206
	Central column	54.9	0.127	50.4	0.3880	0.074	0.193	0.338
The 3rd time	Roof	516.8	0.021	257.4	0.2307	0.013	0.563	0.585
	Middle floor of vehicle	502.7	0.083	253.2	0.2315	0.038	0.164	0.337
	Cab front baffle	174.1	0.085	145.3	0.1841	0.037	0.200	0.382
	Left front hem arm	493.6	0.078	376.7	0.2761	0.035	0.137	0.304
	Left front top swing arm	498.4	0.202	396.1	0.2820	0.097	0.343	0.697

(continued)

**Table 2** (continued)

Time of airdrop	Typical damage part	$\sigma_{vm}$ (MPa)	$\varepsilon_p$	$\sigma_m$ (MPa)	$\varepsilon_f$	$\Delta\varepsilon_p$	$\Delta D$	$D$
The 4th time	Left back hem arm	475.3	0.065	393.5	0.2882	0.034	0.118	0.285
	Left back top swing arm	447.9	0.111	360.1	0.2837	0.052	0.183	0.389
	Central column	54.6	0.235	50.7	0.3795	0.108	0.284	0.622
	Roof	554.6	0.059	274.1	0.2300	0.038	0.165	0.75
	Middle floor of vehicle	534.4	0.155	353.4	0.2579	0.072	0.279	0.616
	Cab front baffle	175.8	0.136	154.9	0.1820	0.051	0.280	0.662
	Left front hem arm	494.2	0.156	409.8	0.2884	0.064	0.221	0.525
	Left front top swing arm	493.7	0.326	398.9	0.2844	0.124	0.435	1.132
	Left back hem arm	472	0.124	382.6	0.2849	0.059	0.207	0.492
	Left back top swing arm	445	0.204	348.9	0.2800	0.093	0.332	0.721
	Central column	55	0.37	53.4	0.3474	0.135	0.361	1.010

### 3.2 Analysis and Evaluation of Cumulative Damage Results

After the simulation analysis of the vehicle for multiple drops according to Sect. 3.2, the left front upper swing arm is further analyzed. Figure 4 is the response cloud map of the four drops of the upper swing arm on the front axle of the airdrop vehicle (see Figs. 5 and 6).

The results of the four drops of the vehicle are further analyzed, and the data of the four drops are superimposed to obtain the four-drop stress change and the cumulative time history curve of plastic deformation as shown in Figs. 7 and 8.

The calculation time of each drop is 0.2 s, and the results of the last simulation analysis are read every 0.2 s at the start of the next simulation analysis. From the whole stress change, in the early stage of each vehicle landing, the stress change is relatively gentle, and then the stress value increases steeply to reach the peak value, and the maximum peak value of each vehicle drop shows an upward trend with the increase of the number of drops. From the time history of plastic deformation, it can be seen that after the sharp increase of plastic deformation, with the gradual decrease of the stress value, the plastic deformation amount tends to be stable, and the difference between the residual strain and the initial strain of each drop of the vehicle is also obvious with the increase of the number of drops rising trend.

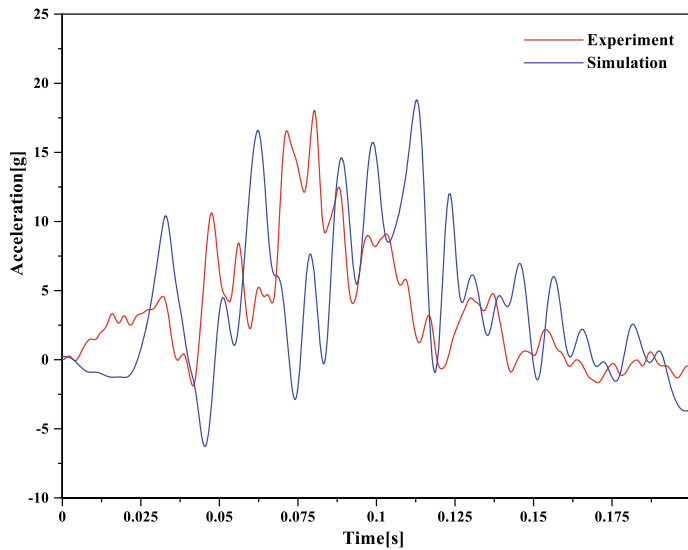


**Fig. 4** Acceleration comparison of the main driving position

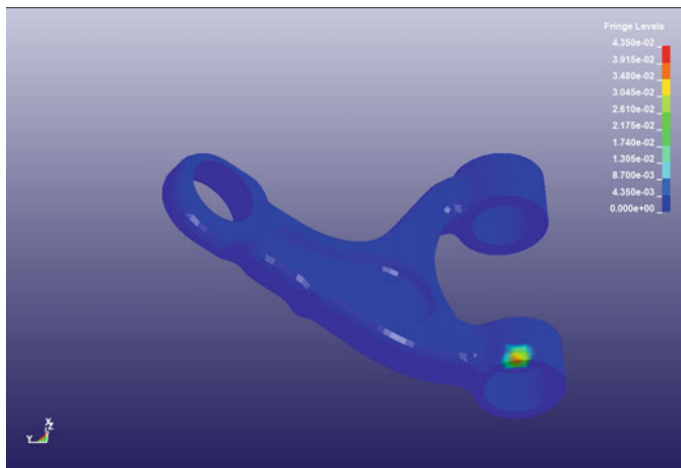


**Fig. 5** Plastic strain cloud map of the first time

## 4 Conclusion

Through the simulation analysis of multiple drops of the airdrop vehicle, and according to the calculation and evaluation method of the cumulative damage of the airdrop vehicle proposed in this paper, the cumulative damage calculation of

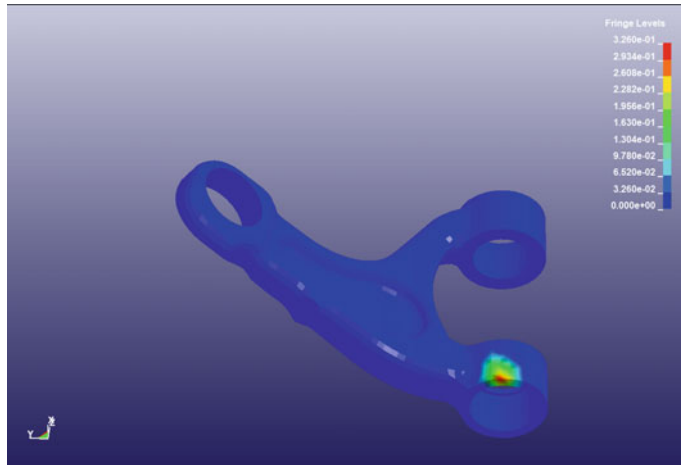


**Fig. 6** Plastic strain cloud map of the fourth time

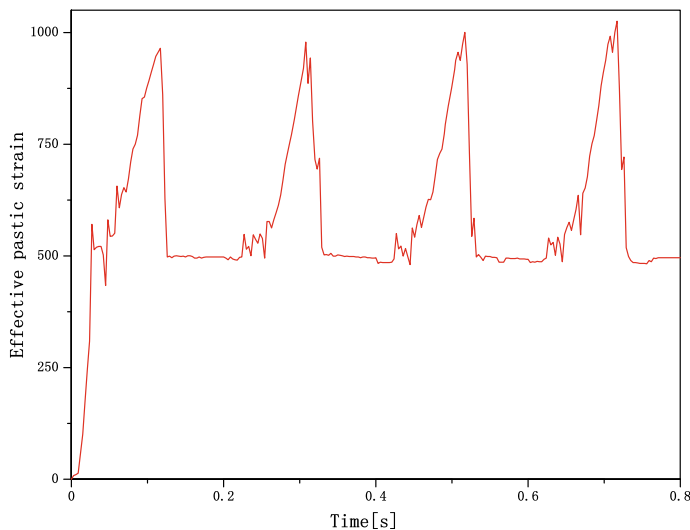


**Fig. 7** Stress change curve

the weak parts of the vehicle is completed, and the damage value is obtained. The increase showed a clear upward trend.

According to the calculated cumulative damage results, local materials of the upper swing arm and the vehicle center column will fail after the fourth drop of the vehicle. The vehicle column has little effect on the normal driving ability of the vehicle, while the upper swing arm has a more obvious impact. The normal driving ability of the vehicle, so that the maximum number of drops of the vehicle is three

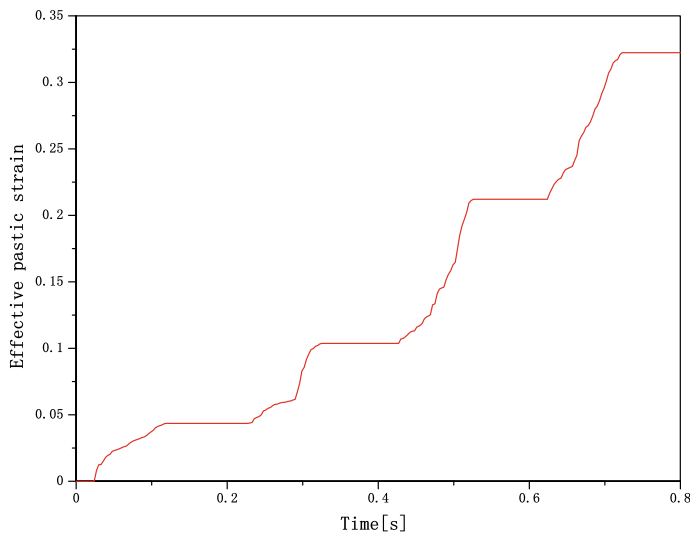


**Fig. 8** Plastic strain change curve

times. It is recommended to strengthen the upper structure of the connection between the upper swing arm and the frame, and the column structure can also be strengthened at the same time.

## References

1. Dua A, Braimah A (2020) Assessment of reinforced concrete slab response to contact explosion effects. *J Perform Constr Facil* 34(4):04020061
2. Umbrello D, M'saoubi R, Outeiro JC (2007) The influence of Johnson–Cook material constants on finite element simulation of machining of AISI 316L steel. *Int J Mach Tools Manuf* 47(3):462–470
3. Xin CL, Xue ZQ, Tu J et al (2020) Common material parameter manual for finite element analysis. Machinery Industry Press, Beijing, pp 139–143
4. Ou HG, Fang XJ, Hong QQ (2013) RADIOSS theoretical foundation and engineering application. Theoretical Foundation and Engineering Application of RADIOSS
5. Lin JB (2016) Study on the impact and cumulative damage of the power battery pack. Dalian University of Technology
6. Xu KF (2020) Research on air drop protection technology of a light vehicle carrier. Nanjing University of Science and Technology
7. Hu YZ, Zeng YQ, Xie SG (2011) Vehicle safety simulation and analysis based on LS-DYNA and HyperWorks

# Research on Detonation Wave Analysis Model of Composite Charge



Huiming Shen, Wenli Yu, Tao Wang, Weibing Li, Jintao Wang,  
and Guiyun Hang

**Abstract** In order to analyze the detonation wave action process, the variation of detonation pressure and the evolution law of the detonation waveform, of the composite charge structure, established a theoretical analysis model of the composite charge structure with inner and outer layers explosives superimposed. Based on the detonation wave collision theory, the pressure distribution, size, and detonation waveform changes of the detonation wave on the plate under the single-point initiation of the center of the end face of the composite charge structure were carried out; the research obtained the calculation method of the pressure distribution area and the pressure magnitude of the composite charge structure and the waveform difference of the horn-shaped detonation.

**Keywords** Composite charge · Inner and outer layer explosives superimpose · Detonation wave · Theoretical analysis

## 1 Introduction

Improving the damage power of ammunition has always been the goal of researchers, under certain conditions of charge type and processing technology, the ammunition power is closely related to the charge structure. A composite charge is one of the hot research issues in recent years. It is a kind of charge structure that combines two or more explosives by the superposition of inner and outer layers or the superposition of upper and lower layers. The composite charge has shown a certain application prospect in the high-efficiency damage warhead. For example, the United States [1] conducted in-depth research on the double-layer composite charge composed of

---

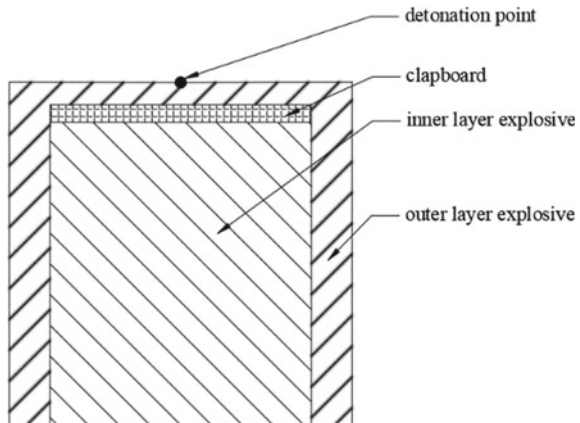
H. Shen (✉) · W. Yu · T. Wang · J. Wang · G. Hang  
Department Automat, Xi'an Inst High Tech, Xian 710025, Shanxi, China  
e-mail: [shenhuiming202@163.com](mailto:shenhuiming202@163.com)

W. Li  
Ministerial Key Laboratory of ZNDY, Nanjing University of Science and Technology,  
Nanjing 210094, Jiangsu, China

B2249 (outer)/WFQ (inner). Studies have shown that the double-layer composite charge can not only meet the requirements of rapid roasting, slow roasting, gunshot, friction sensitivity, and detonation tests, but more importantly, as an underwater explosive, its bubble energy can be increased by 15%; Arthur Spencer, John D. Corley, etc. [2] studied the effect of composite charge on fragmentation velocity and shock wave overpressure performance of explosives. The results show that the double-layer charge significantly improves the acceleration ability of the fragments. Mayseless et al. [3] studied the formation characteristics of the jets formed by inner and outer composite charge. It was found that the head velocity of the jet was increased by about 30%; Kato et al. [4, 5] studied the composite charge composed of high-density explosives with tungsten powder and high-explosive-velocity explosives, It was found that the detonation speed of the composite charge was significantly improved, and the pressure was more than doubled. Chinese researchers have also carried out some researches on the composite charge. Zhang et al. [6] and Xian Feng et al. [7, 8] pointed out that the inner charge of the inner and outer layer composite charge formed a relatively obvious overpressure detonation phenomenon,.The detonation pressure can reach up to 65GPa, which is much higher than the C-J detonation pressure of the explosive; Mei [9] pointed out that the composite charge which inner layer is high-energy explosive and outer layer is insensitive explosive, can obtain higher energy output than a single insensitive explosive. Yu Lei et al. [10] studied the energy output characteristics of composite charge explosive; Gang et al. [11] proposed that under the condition of eccentric initiation, the front of the detonation wave of the composite charge is a concave converging wave. The converging wave can improve the speed of the detonation wave of the inner charge, and the detonation waveform propagation process on the surface of the charge is measured by the slit scanning technology of the rotating mirror high-speed camera, the scanning curve of the detonation wave at the slit position, the space-time coordinates and the distribution map of the detonation wave front are obtained. Kai Shu et al. [12] designed an inner and outer composite charge structure composed of high-explosive velocity ideal explosives and aluminum-containing explosives, use a pressure sensor to test the shock wave overpressure, and the initial velocity of the fragments was measured by the target net, the results show that compared with a single aluminum-containing explosive, the composite charge structure composed of an outer high-explosive-velocity explosive and an inner layer of aluminum-containing explosives can significantly increase the detonation wave overpressure value and the initial velocity of fragments. In general, the research on composite charges is still in the exploratory stage. For the formation, propagation law, and action mechanism, the distribution of the detonation pressure field and the evolution of the overpressure detonation waveform, etc., of the detonation wave of the composite charge were rarely reported.

In this study, the detonation energy output characteristics of the composite charge structure were studied by theoretical analysis. To study the interaction and propagation law and the evolution of detonation waveforms of detonation waves of composite charges, the detonation analysis model of composite charge was constructed which can provide technical support for the application of composite charge technology in warhead.

**Fig. 1** Composite charge structure



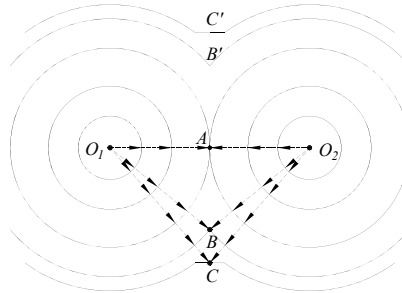
## 2 Establish the Model of Composite Charge

In this paper, the composite charge structure of inner and outer layers that are widely used in conventional warheads (the inner layer is low-explosive velocity explosive, and the outer layer is high-explosive velocity explosive) is used as the research object, as shown in Fig. 1. The composite charge is a cylindrical structure, the center single-point detonation.

The detonation point of the composite charge detonating, the outer layer high-explosive velocity explosive detonates first, the detonation wave propagates to the inside of the charge and to both sides of the cylinder. Due to the blocking of the clapboard, the detonation wave propagating inward cannot continue to propagate, so the detonation wave can only propagate to both sides of the charge, the detonation wave propagates to the side of the charge in a very short time, and detonates the inner layer of explosives, and the inner layer of explosives forms a ring-shaped detonation effect.

## 3 Analysis of Propagation and Action of Detonation Wave in Composite Charge Structure

According to the detonation wave collision theory [13], when two detonation waves propagate head-on, the detonation waves positive collision first, the pressure at the collision point rises sharply, and at the same time, two shock waves are formed to propagate to the detonation products on both sides, respectively. The schematic diagram of the collision process is shown at point A in Fig. 2. When the two detonation wave fronts form a certain angle, the oblique reflection of the detonation wave occurs at this time, the pressure at the reflection point also increases, and two shock waves are also formed that travel back into the detonation products. The phenomenon of



$O_1 O_2$ —detonation points;  $A$ —positive collision;  $B B'$ —regular oblique reflection;  $C C'$ —Mach reflection

**Fig. 2** Two detonation waves collide

oblique reflection is different depending on the angle of reflection. When the angle between the two detonation wavefronts is small, the flow deflection angle of the detonation product is consistent with the flow deflection angle of the reflected shock wave, and the reflected shock wave is generated at the reflection point, which is called regular oblique reflection. With the increase of the angle between the two detonation wavefronts, the flow deflection angle of the detonation product and the flow deflection angle of the reflected shock wave both increase, and when the angle between the two detonation wavefronts reaches a certain angle, the two turning angles are inconsistent, will force the reflected shock wave up a certain distance from the point of reflection, it is called irregular oblique reflection, also known as Mach reflection.

Figure 3 is detonation wave propagation and action in the inner layer explosive of cylindrical composite charge (detonation ring is replaced by eight points). Since the detonation point is closer, the detonation wave has not yet formed a stable detonation, that is, the interaction and the end face constraint is small, the detonation pressure decreases sharply under the action of the expansion wave, it is considered that the pressure at initiation points is C-J pressure relative to the pressure at the axis of the charge. The detonation wave is colliding at point  $O$ ,  $OA$  is a normal oblique reflection, and Mach reflection begins to occur at point  $A$ . Then the collision of the detonation wave will eventually form an overpressure region with a diameter of  $BC$  and a peripheral C-J pressure region, as shown in Fig. 3.

Take any cross section of the charge axis to study; Fig. 4 shows a schematic diagram of the flow of the Mach-reflected detonation wave inside the shaped charge. The detonation waves in the cylindrical charge collide with each other to form Mach reflection, the two parts  $B_1CB$ ,  $AB$ , and  $A_1B_1$  on the plate are subjected to two different detonation pressure loads, respectively. Among them,  $B_1CB$  is affected by the Mach wave in the (3) area, and  $AB$  and  $A_1B_1$  are affected by the C-J detonation wave in the (1) area.

**Fig. 3** Schematic diagram of the detonation wave action of the inner charge (3D)

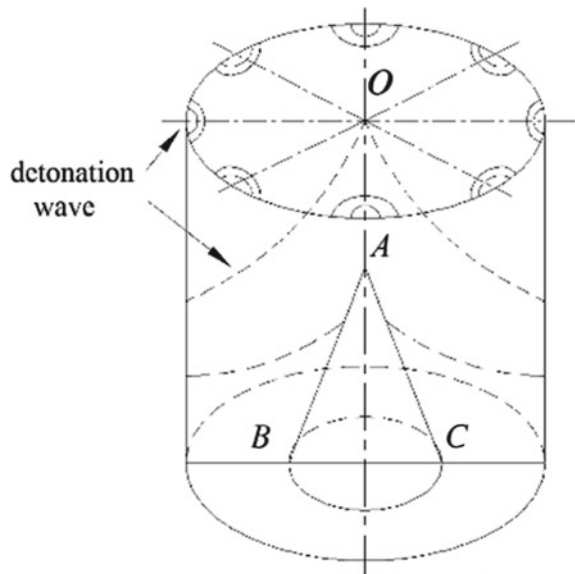
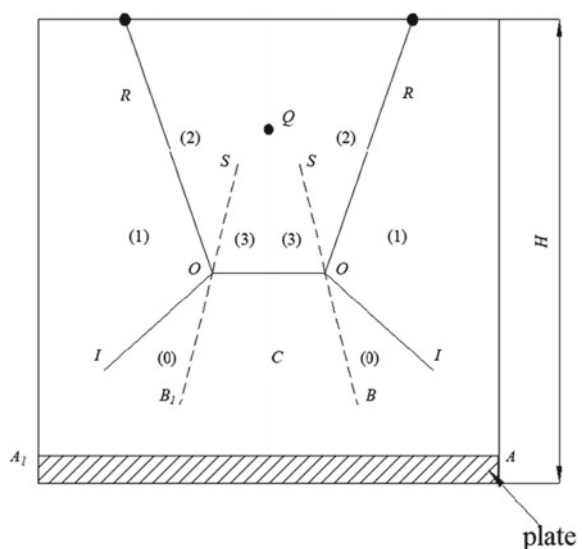


**Fig. 4** Distribution of Mach reflection flow field of the detonation wave action of the inner charge (2D)



### 3.1 Pressure Distribution Area on the Surface of the Plate

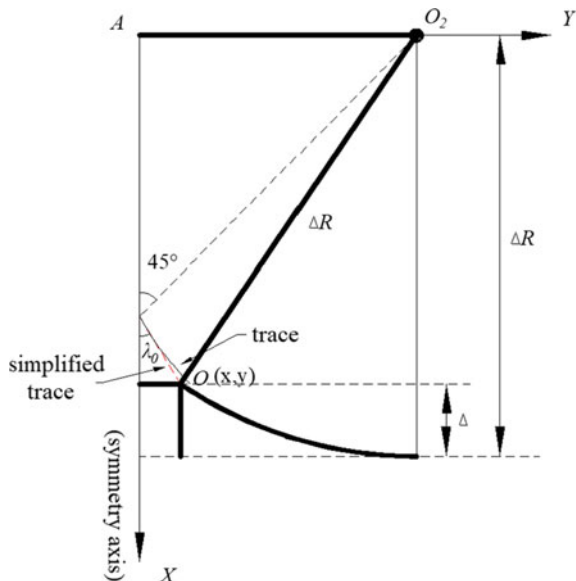
In order to calculate the pressure distribution of the Mach wave on the plate, the following assumptions are made:

- (1) The three-wave point trace is simplified as a straight line. Because the size of the conventional warheads is small, the composite charge is small, the three-wave point trace of the Mach reflection can be simplified to a straight line, and the Whitham iteration method can be simplified to obtain the numerical solution of the Mach rod height.
- (2) The transition from normal oblique reflection to Mach reflection is a continuous process.
- (3) The Mach rod is perpendicular to the solid wall.
- (4) Ignore the edge sparsity effect.

The Adiabatic index  $k = 3$  of the condensed explosive, the AX axis is the collision surface of the detonation wave, when  $t = 0$ ,  $O_2$  emits a scattered spherical detonation wave. As the wave moves forward, the three-wave points advance toward the plate, and the height of the Mach rod is also increasing, assume that the angle between the trace of the three-wave points and the axis of the charge is  $\lambda_0$ . The coordinates of the three-wave point  $O$  is  $(x, y)$ , as shown in Fig. 5.

In the coordinate system (XAY), from the geometric relationship shown in Fig. 5, the coordinates  $(x, y)$  of the three-wave points at any position can be obtained:

**Fig. 5** Three-wave point trace and waveform difference



$$\begin{cases} \frac{x-r}{y} = \cot \lambda_0 \\ x^2 + (r-y)^2 = \Delta R^2 \end{cases}$$

Solving the system of two-variable equations, taking only the positive roots, we get:

$$\begin{cases} x = \frac{r \cot \lambda_0 (\cot \lambda_0 - 1)}{1 + \cot^2 \lambda_0} \left[ \sqrt{1 + \frac{1 + \cot^2 \lambda_0}{(\cot \lambda_0 - 1)^2} \left( \frac{\Delta R^2}{r^2} - 2 \right)} - 1 \right] + r \\ y = \frac{r (\cot \lambda_0 - 1)}{1 + \cot^2 \lambda_0} \left[ \sqrt{1 + \frac{1 + \cot^2 \lambda_0}{(\cot \lambda_0 - 1)^2} \left( \frac{\Delta R^2}{r^2} - 2 \right)} - 1 \right] \end{cases}$$

The condition for the solution is  $\Delta R^2 > 2r^2$ , Mach reflection occurs only when this condition is met. Given the charge height  $\Delta R$ , the initiation radius  $r$ , and  $\lambda_0$ , the position  $(x, y)$  of the three-wave point can be calculated.

The angle between the trace of the three-wave points and the axis of the charge is  $\lambda_0$ , which can be measured through experiments in the project.

For the cylindrical composite charge structure, the coordinates of the Mach reflection starting position  $Q$  are  $(r, 0)$ . The height of the charge is  $H$ , then the Mach wave travels  $(H-r)$  distance and acts on the plate.

Then the pressure area of the Mach detonation wave act on the plate is:

$$S_{\text{Mach}} = \pi [(H - r) \tan \lambda_0]^2 \quad (1)$$

The pressure area where the C-J detonation wave act on the plate is:

$$S_{\text{CJ}} = S - S_{\text{Mach}} = \pi \left( \frac{D}{2} \right)^2 - \pi [(H - r) \tan \lambda_0]^2 \quad (2)$$

### 3.2 Pressure Calculation on the Surface of the Plate

The post-wave pressure of the Mach detonation wave. According to the detonation wave collision theory [13]:

$$\frac{p_3}{p_H} = \frac{1}{\sin^2 \alpha_0} + \frac{1}{\sin \alpha_0} \left( \frac{1}{\sin^2 \alpha_0} - \varepsilon \right)^{\frac{1}{2}} \quad (3)$$

where  $\varepsilon$  is a constant, generally  $\varepsilon = 1.1-1.2$ .  $\alpha_0$  is the incident angle of the Mach wave, when the incident wave is a spherical detonation wave, the incident angle  $\alpha_0$

of the Mach wave varies with time, so the Mach pressure  $p_3$  is, therefore, a function of time.

From the geometric relationship in Fig. 5, we get:

$$\cos \alpha_0 = \frac{r - y}{\Delta R} = \frac{r}{\Delta R} \left\{ 1 - \frac{\cot \lambda_0 - 1}{1 + \cot^2 \lambda_0} \left[ \sqrt{1 + \frac{1 + \cot^2 \lambda_0}{r^2(\cot \lambda_0 - 1)^2} (\Delta R^2 - 2r^2)} - 1 \right] \right\} \quad (4)$$

Therefore, as long as  $\Delta R(t)$  is given, the corresponding  $p_3$  can be obtained.

### 3.3 Detonation Waveform Difference

Assuming that point  $O$  emits a spherical detonation wave, at the same time, a train of plane detonation waves must also be emitted, and advancing along the  $X$ -axis direction, the two detonation speed is the same. At a certain moment, the spherical detonation wave propagates to the  $\Delta R$  position and forms the Mach wave  $OT$ , at the same time, the plane detonation wave propagates to the  $BC$  position. Therefore, there is a distance  $\Delta$  between the Mach wave  $OT$  and the plane wave  $BC$ .

From the geometric relationship shown in Fig. 5, it is clear that:

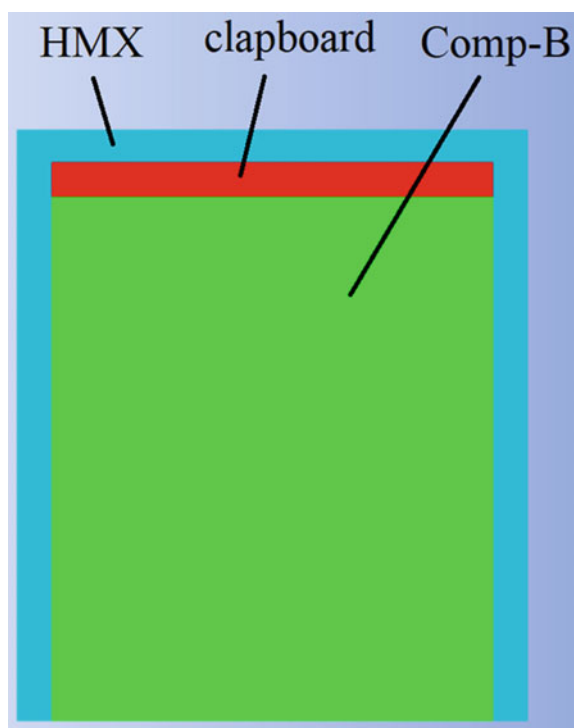
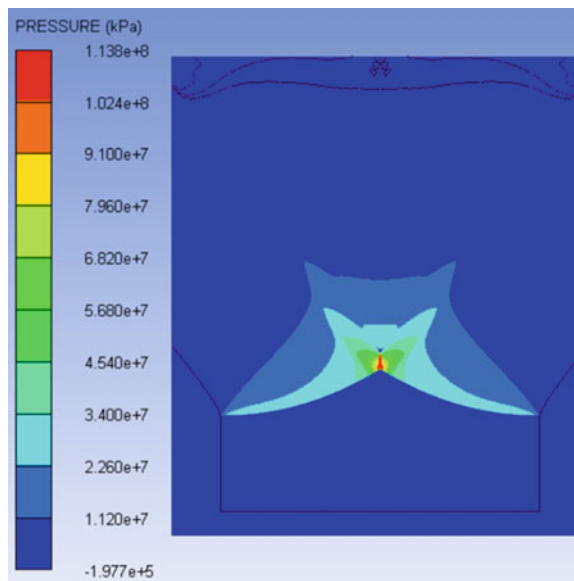
$$\Delta = \Delta R - x = \Delta R - \frac{r \cot \lambda_0 (\cot \lambda_0 - 1)}{1 + \cot^2 \lambda_0} \left[ \sqrt{1 + \frac{1 + \cot^2 \lambda_0}{(\cot \lambda_0 - 1)^2} \left( \frac{\Delta R^2}{r^2} - 2 \right)} - 1 \right] - r \quad (5)$$

$\Delta$  is the reason why the composite charge structure forms a horn-shaped detonation wave. Different detonation waveform difference has certain guiding significance for the improvement of the damage power of conventional warheads.

## 4 Simple Simulation Example

To verify the reliability of the theoretical model. An example of a composite charge structure explosion simulation model is established, as shown in Fig. 6. Among them, HMX is a high-explosive explosive, Comp-B is a low-explosive explosive, and the clapboard material is nylon. Figure 7 is the pressure cloud diagram of the simulation result, the pressure gradually decreases from red to green to light blue. It can be found that there is a central region with high pressure, that is, the  $p_3$ , and the edge is the C-J pressure region.

To calculate the value of  $S_{\text{Mach}}$ ,  $p_3$  and  $\Delta$  need to know the value of  $\lambda_0$ . Based on the literature [13],  $\frac{\rho_0}{\rho_3} = \frac{k-1}{k+1} + \frac{\varepsilon}{k+1} \frac{p_H}{p_3}$ ,  $k$  is the adiabatic exponent of the explosive,

**Fig. 6** Simulation model**Fig. 7** Pressure cloud diagram

**Table 1** Theoretical and numerical results comparison

	$S_{\text{Mach}}$ (cm <sup>2</sup> )	$p_3$ (Gpa)	$\Delta$ (mm)
Theoretical results	29.1	40.32	35.5
Simulation results	19.9	34	40.05

generally taking  $k = 3$ ,  $\varepsilon$  is the excessive compression coefficient, generally taking  $\varepsilon = 1.1\text{--}1.2$ . The maximum pressure in the Mach reflection zone is about 3.45 times the C-J pressure,  $q_0$  is the velocity of the medium flowing into the incident wave in Mach reflection zone (0), which can be simplified as the detonation velocity of the explosive. For Comp-B explosive with density  $\rho_0 = 1.717 \text{ g/cm}^3$ ,  $q_0$  is taken as 7.98 km/s.  $p_0$  is the pressure of the medium in the zone (0), that is, the pressure of the unreacted explosive, which is negligible compared to  $p_3$ . At the same time, the material size in the simulation is  $H = 200 \text{ mm}$ ,  $r = 130 \text{ mm}$ . It is easy to obtain from the above parameters,  $\lambda_0$  can be found, bringing into Eqs. (1), (3), (4) and (5) can get  $S_{\text{Mach}}$ ,  $p_3$ , and  $\Delta$ . The numerical simulation of detonation parameters at typical moments is also listed in Table 1.

There are deviations between theoretical calculation and numerical simulation results of  $S_{\text{Mach}}$ . Because, in the numerical simulation, the area size of the high-pressure area is greatly affected by the time step of the software,  $p_3$  and  $\Delta$  deviations is within a reasonable range. The Simulation result of  $p_3$  is less than the theoretical result, because of the infinite air domain modeled in the simulation, the pressure is affected by air thinning.

## 5 Conclusion

The detonation wave interaction theory is applied to the inner and outer layer composite charge structure, simplified the three-wave point trace of Mach reflection to a straight line, derive the detonation wave pressure distribution area, pressure calculation, detonation waveform difference under the composite charge structure, the following conclusions are obtained:

- (1) The overpressure part in the center of the plate is  $p_3$ , the pressure distribution area  $S_{\text{Mach}} = \pi[(H - r) \tan \lambda_0]^2$ ; The edge is C-J pressure and the distribution area is  $S_{\text{CJ}} = \pi\left(\frac{D}{2}\right)^2 - \pi[(H - r) \tan \lambda_0]^2$ .
- (2) Detonation waveform difference  $\Delta = \Delta R - x = \Delta R - \frac{r \cot \lambda_0 (\cot \lambda_0 - 1)}{1 + \cot^2 \lambda_0} \left[ \sqrt{1 + \frac{1 + \cot^2 \lambda_0}{(\cot \lambda_0 - 1)^2} \left( \frac{\Delta R^2}{r^2} - 2 \right)} - 1 \right] - r$

## References

1. Kernen P (1994) Way and methods to insensitive munitions, IM Recipes Version. In: Insensitive munitions technology symposium
2. Spencer A, Corley JD (1999) Blast and fragmentation enhancing explosive, US5996501
3. Mayselessm HE, Harvey WB et al (2011) Is higher detonation velocity needed for shaped-charges. In: Baker E, Temelton D (eds) 26th international symposium on ballistics, Miami, FL, United States: DE Stech Publications Inc., pp 155–166
4. Kato H, Murata K, Itoh S et al (2007) Application of overdriven detonation in high density explosive to shaped charge. Galvez F, Sanchez-Galvez V (eds) 23rd international symposium on ballistics, Tarragona, Spain: IBC, pp 223–230
5. Kato H, Murata K, Itoh S et al (2008) Investigation of jet formation with overdriven detonation in high density explosive. Mater Sci Forum 566:327–332
6. Zhang X, Huang Z, Qiao L (2011) Detonation wave propagation in double-layer cylindrical high explosive charges. Propellants Explos Pyrotech 36(3):210–218
7. Xian Feng Z, Xiao Ning Z (2011) Review on overdriven detonation of double layer high explosive charge. Chin J Energ Mater 19(3):352–360
8. Xian Feng Z, Jian Bao D, Xiao Ning Z (2009) Numerical simulation of double layer shaped charge. Explos Shock Waves 29(6):617–624
9. Mei X (2012) Investigation on safety rules and energy output of composite charge. Nanjing University of Science and Technology, Nanjing
10. Yu Lei N, Xiao Feng W, Ran Y (2009) Characteristic of energy output of underwater explosion for dual explosive charge. Chin J Energ Mater 17(4):415–419
11. Gang D, Bao Hui Y (2009) Detonation wave characteristics of dual explosive under asymmetrical initiation. Chin J Explos Propellants 32(1):79–82
12. Kai Shu H, Hong Zheng P, Li Lun W et al (2018) Test analysis on power performance of composite explosive charge. Ordnance Ind Autom 37(1):83–84, 96
13. Shou Zhong Z (1993) Explosion and impact dynamics. Ordnance Industry Press, Beijing

# Influences of Element Types on Nonlinear Finite Element Analysis of a Concrete Column Under Near-Field Blast Loading



Jie Xu, Max A. N. Hendriks, Jan G. Rots, and Apostolos Tsouvalas

**Abstract** Due to the accompanying severe consequences of explosions, the blast puts a great threat to public security. Nonlinear finite element analysis is a possible method for civil engineers to check the integrity of the structures under blast loading without underestimating the limit of the structures. However, different choices of element types would generally put a great influence on the analytical results and the corresponding computational expenses. Therefore, how should civil engineers simplify their physical model into finite element models to gain relatively accurate numerical results with acceptable computational expenses is of great interest. In this article, 6 different types of elements are discussed with different orders and shapes for a certain physical situation, and the corresponding experimental results and the numerical results for a very detailed finite element model are used as the baseline for judgement, which could be helpful for civil engineers to make proper simplifications in the set-up of finite element models.

**Keywords** Nonlinear finite element analysis · Blast · Solution strategy

## 1 Introduction

Explosions, having a low probability of occurrence in daily life, the accompanying consequences are extremely severe in most cases due to the potential collapse of structures, are known as “Low Probability and High Consequences (LP-HC)” events.

---

J. Xu (✉)

College of Aerospace Science and Engineering, National University of Defense Technology,  
Changsha 410073, Hunan, China

e-mail: [vitavitalopez@icloud.com](mailto:vitavitalopez@icloud.com)

Hunan Key Laboratory of Intelligent Planning and Simulation for Aerospace Missions,  
Changsha 410073, Hunan, China

M. A. N. Hendriks · J. G. Rots · A. Tsouvalas

Faculty of Civil Engineering and Geosciences, Delft University of Technology, Delft, Zuid  
Holland 2628 CN, The Netherlands

Not only the accidental explosion, but also the premeditated attack puts a great threat to public security [1]. For this reason, it could be of great necessity for civil engineers to take the structural integrity of structures under blast loading into consideration during the design process.

Nonlinear finite element analysis is a potentially helpful tool for civil engineers to predict structural integrity without underestimation of the capacities of structures. However, before the set-up of the nonlinear finite element models, different civil engineers would have different choices in the element types, which would lead to considerable differences in the numerical results and the corresponding computational expenses.

For nonlinear finite element analysis of reinforced concrete structures under blast loading, Toy et al. did a series of experiments and numerical analyses for reinforced concrete slabs and reinforced concrete retaining walls [2–4]. Most of the comparisons between the analytical results and the experimental observations focused on the deformed shapes and cracking patterns.

Siba did 16 experiments on reinforced concrete columns with different reinforcement detailings and different stand-off distances. During the experiments, pressure gauges and string potentiometers were used to record the blast pressure–time histories and displacement–time curves [5].

Existing methods for predicting blast loading on a structure are generally based on the analytical work of Brode [6] or the Kingery/Kingery and Bulmash semi-empirical relations [7, 8], which is widely used in commercial finite element analysis software like LS-DYNA and ABAQUS. These methods are accurate for simple scenarios with spherical or semi-spherical explosives under free-air bursts. Nevertheless, cylinders are known as one of the most common shapes of explosives. Jordan et al. did a series of research on the blast shock wave generated by cylindrical charge, and it has been certificated that the characteristics of the stress distribution and wave propagation of cylindrical explosives are very different from spherical explosives [9–12].

Based on Siba’s experiments, 6 finite element models are established with different element types and orders, and 5 groups are divided to make the comparison between the analytical results.

## 2 Experiments

The column named CONV-7 from Siba’s experiments is selected as the baseline of comparison. Figure 1 presents the set-up of the experiment. Two columns were tested in pairs, and a 100 kg cylindrical ANFO with 1.30 m height was denoted to create the shockwave.

Pressure gauges were attached to both the front and the rear surfaces of the column to record the blast pressure–time diagrams and string potentiometers were attached to the rear surface of the column to record the displacement–time curves. Figure 2 demonstrates the detailed locations of pressure gauges and string potentiometers.

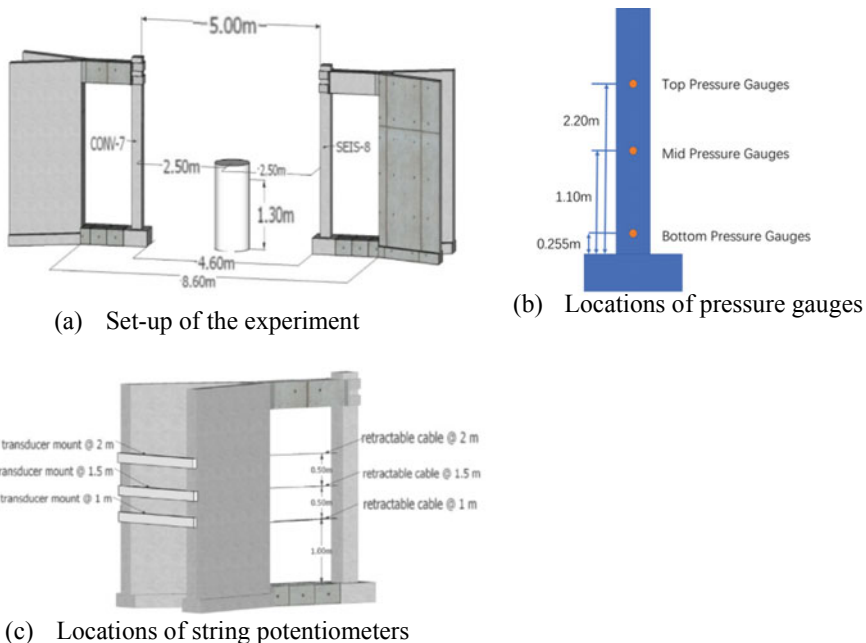


**Fig. 1** Set-up of the experiment [5]

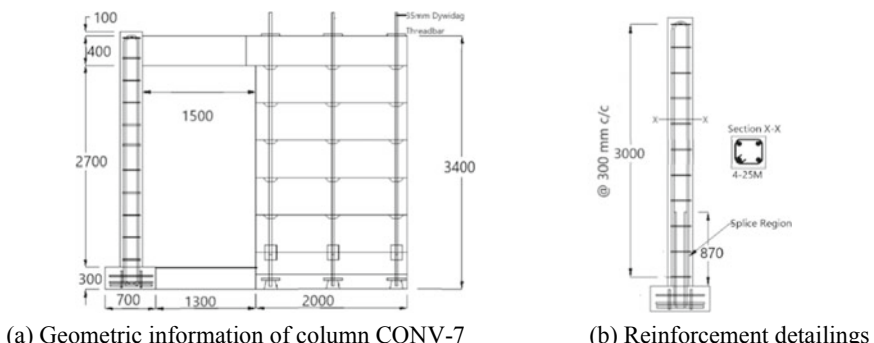


**Fig. 2** Detailed information of the column CONV-7 for modelling set-up [5]

C35 was used for the column and C70 was used for the support structures. Tensile tests were executed for the reinforcement rebars, which give detailed information about the mechanical properties of the rebars. 10 M rebars with 11.3 mm diameter were used as the ties, and 25 M rebars with 19.5 mm diameter were used as the longitudinal rebars. Pre-tensioned DYWIDAG Threadbars were used in the support structures with 35 mm diameter. Detailed information about the reinforcements and

**Table 1** Material properties of reinforcements [5]

Rebar size	Yield strength (MPa)	Yield strain	Ultimate strength (MPa)	Ultimate strain
10 M	465.2	0.0022	731.1	0.11
25 M	474.7	0.0024	673.2	0.11

geometries of the columns and the support structures is illustrated in Fig. 2 as well. The mechanical properties of 10 M rebars and 25 M rebars are listed in Table 1.

### 3 Modelling Set-up

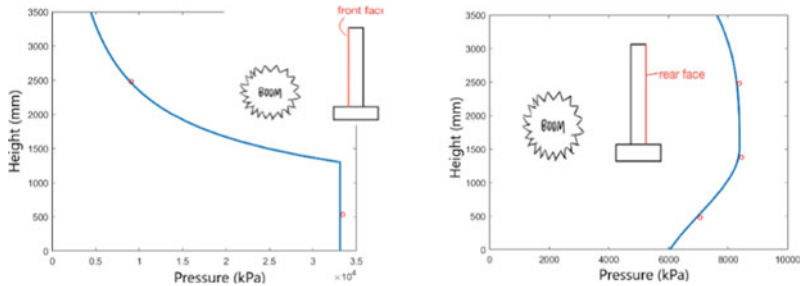
DIANA FEA is applied in this article to perform the nonlinear finite element analysis as it could help to unify the iteration scheme and the convergence criteria, which could help to eliminate the influences of the solution strategies on the numerical results. At the same time, the CPU occupation could be recorded during the nonlinear finite element analysis, which helps to make a detailed comparison of the computational expenses.

#### 3.1 Simplifications of Blast Loads

The negative phase of the explosive pressure–time history is usually not taken into consideration for the design purpose as it has been verified that the main structural damage is connected to the positive phase [13].

The simplification of the blast pressure–time diagrams is based on the assumption that a cylindrical explosive could be regarded as a combination of a set of small spherical explosives. With the recorded blast pressure–time diagrams, the blast pressure profiles could be interpolated. The peak overpressure value distribution of the front surface is assumed to be uniform within the lower 1.30 m of the surface, and Hopkinson-Cranz scaling law [14] is applied to interpolate the distribution of the upper front surface of the column. For the rear surface of the column, there are limited theories for the peak value distribution, and therefore, curve-fitting is used to interpolate the distribution of the peak overpressure. Figure 3 demonstrates the distribution of the peak overpressure among the front and rear surfaces of the column.

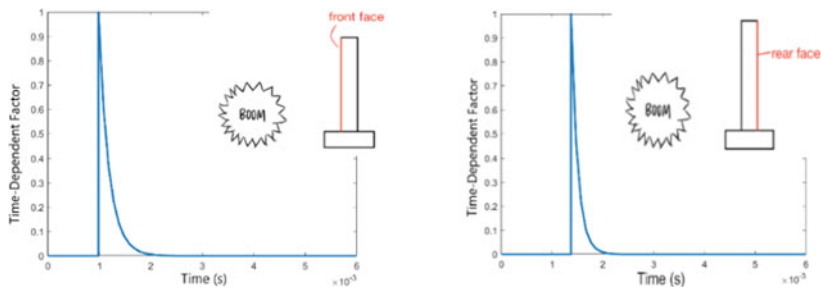
Due to the limitation of the DIANA FEA, the time-dependent factors of the front and rear surfaces could not be set as a function of the height. Therefore, uniform time-dependent factors are applied for both the front and rear surfaces [15]. Figure 4 presents the time-dependent factors of the front and rear surfaces, respectively. The rate-dependent factor is considered for the material model of concrete to take the strain-rate dependency into consideration, and based on Sluys' report, the rate-dependent factor is assumed to be 0.1 [16].



(a) Distribution of the peak pressure of the front surface

(b) Distribution of the peak pressure over the rear surface

**Fig. 3** Interpolated peak pressure distributions



(a) Time-dependent factors of the front surface

(b) Time-dependent factors of the rear surface

**Fig. 4** Time-dependent factors

### 3.2 Modelling Set-up

In this article, 6 finite element models are established and divided into 5 groups. Detailed information on the finite element models is listed in Table 2. And the detailed information for the group designation is given in Table 3. Due to the inclusion of the nonlinearity, with rapid change in loadings, there are difficulties in reaching convergence, therefore, different iteration schemes must be adopted for different models. The iteration schemes and convergence criteria are listed in Table 4.

For the 6 finite element models, the interpretation of the boundary conditions is demonstrated in Fig. 5a, and the bond-slip effect between the concrete and the rebars are not considered. For the detailed finite element model, based on which the comparison is made, the support structure is included and the boundary conditions are demonstrated in Fig. 5b, the bond-slip effect is included at the same time.

**Table 2** Model designation

Model designation	Element type	Element Order	Mesh size (mm)
1	Solid	Linear	100
2	Plane stress	Linear	100
3	Beam	Linear	100
4	Solid	Quadratic	100
5	Plane stress	Quadratic	100
6	Beam	Quadratic	100

**Table 3** Group designation

Group designation	Models
1	Model 1 & 2 & 3
2	Model 4 & 5 & 6
3	Model 1 & 4
4	Model 2 & 5
5	Model 3 and 6

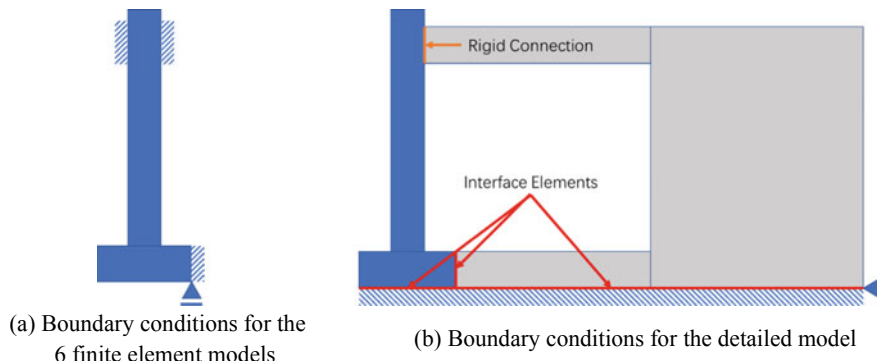
**Table 4** Iteration schemes and convergence criteria

Model	Self weight	Iteration method	Convergence criteria	Time steps	Iteration method	Convergence Criteria
1	1 step	RTNR <sup>a</sup>	Displ.:0.01 Force:0.01	0.05 ms 600 steps	MLNR <sup>b</sup>	Displ.:0.01
2	1 step	RTNR <sup>a</sup>	Displ.:0.01 Force:0.01	0.05 ms 600 steps	MLNR <sup>b</sup>	Displ.:0.01
3	1 step	RTNR <sup>a</sup>	Displ.:0.01 Force:0.01	0.05 ms 600 steps	MLNR <sup>b</sup>	Displ.:0.01
4	1 step	RTNR <sup>a</sup>	Displ.:0.01 Force:0.01	0.05 ms 600 steps	MLNR <sup>b</sup>	Displ.:0.01
5	1 step	RTNR <sup>a</sup>	Displ.:0.01 Force:0.01	0.05 ms 600 steps	MLNR <sup>b</sup>	Displ.:0.01
6	1 step	RTNR <sup>a</sup>	Displ.:0.01 Force:0.01	0.05 ms 600 steps	RTNR <sup>a</sup>	Displ.:0.01

<sup>a</sup>Notes refers to the regular tangential Newton–Raphson iteration method

<sup>b</sup>Notes refers to the modified linear Newton–Raphson iteration method

However, for the detailed model, there is difficulty in reaching convergence, therefore, a combination of the iteration scheme is made. The information for the detailed finite element model is listed in Table 5.

**Fig. 5** Interpretations of boundary conditions**Table 5** Information on the detailed finite element model

	Self-weight	Post-tension	Time steps		
	1 step	1 step	0.045 ms 2 steps	0.05 ms 60 steps	0.05 ms 522 steps
Iteration method	RTNR	RTNR	MLNR	RTNR	MLNR
Convergence criteria	Displ.:0.01 Force:0.01	Displ.:0.01 Force:0.01	Displ.:0.01	Displ.:0.01	Displ.:0.01

## 4 Results and Discussion

The numerical results of the 6 finite element models are summarized in Table 6. The first 30 ms after the detonation of the explosive are focused and the largest deformation of the point that locates on the rear surface of the column and 1.0 m away from the footing is compared. The maximum stresses and maximum crack widths are compared as well. The numerical results are given in Table 7.

**Table 6** Summary of the numerical results

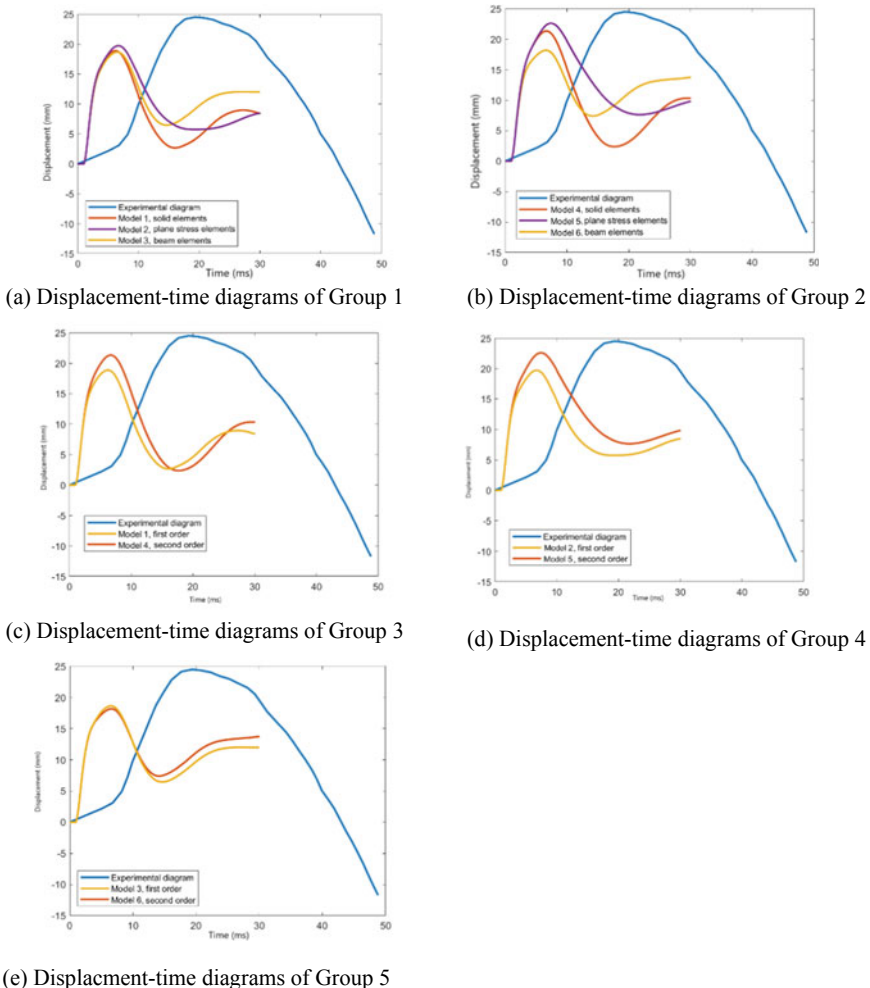
Model	1st natural Freq. (Hz)	2nd natural Freq. (Hz)	CPU	Largest Def. (mm)	Largest Def. at 1.0 m (mm)	Error (%)
1	97.498	102.52	747.28	22.51	18.8857	21.31
2	97.928	167.20	351.03	23.20	19.7247	17.814
3	114.26	149.75	289.33	23.26	18.6758	22.184
4	95.686	99.906	2272.42	24.69	21.3419	11.075
5	95.958	149.71	411.48	23.4	18.2059	24.142
6	97.498	161.43	355.17	26.16	22.6104	5.79
Detailed	72.210	89.438	4259.95	20.50	16.9420	29.408

**Table 7** Summary of maximum stresses and crack widths

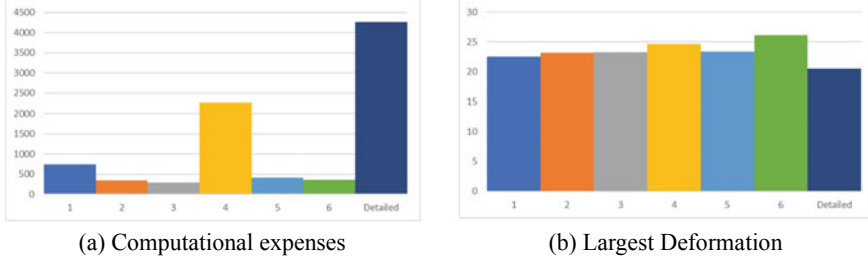
Model	Maximum stress (MPa)	Maximum crack width (mm)
1	492.57	1.60
2	494.69	2.31
3	493.44	1.31
4	540.06	2.86
5	552.17	2.76
6	521.39	4.35
Detailed	484.57	1.40

The displacement–time diagrams are presented in groups in Fig. 6. The curve in deep blue represents the recorded displacement–time curves during the experiment. And the computational expenses are illustrated in Fig. 7.

Based on the numerical results of Group 1 and Group 2, it could be observed that the finite element models with beam elements have the highest natural frequencies, which is the reason the translational constraints on models with beam elements are applied at the central axis of the column which restrain the rotations of the columns and the footings in a degree and therefore, introduce higher stiffness into the finite element models.



(e) Displacement-time diagrams of Group 5

**Fig. 6** Displacement-time diagrams**Fig. 7** Differences in numerical results

## 5 Conclusion

The choice of dimensions and orders of elements shows a great influence on the numerical results and the corresponding computational efforts.

First-order elements are more recommended for nonlinear finite element analysis of structures under dynamic loadings due to the uniform mass distributions that would introduce fewer model uncertainties.

Plane stress elements are recommended at the preliminary design stage, which is extremely helpful in lowering the computational expenses and would generally yield conservative results with acceptable accuracies.

For models with beam elements, modifications of boundary conditions are required to ensure the rotations of the models would not be over-restricted.

Rayleigh damping coefficients based on the 1st and 2nd natural frequencies of finite element models are not proper enough for the structures under blast loading. For structures under blast loading, the loads should be considered as dynamic loads with extremely short periods, rather than impact, therefore, higher-order natural frequencies should be applied for the calculation of damping coefficients.

Further studies on solution strategies of nonlinear finite element analysis of structures under near-field explosions could focus on the calculation of the damping coefficients and the influence of the simplification of the blast pressure–time histories to help civil engineers gain more accurate numerical results on the displacement–time diagrams.

## References

1. Olmati P, Petrini F, Bontempi F (2013) Numerical analyses for the structural assessment of steel buildings under explosions. *Struct Eng Mech* 45(6):803–819
2. Toy AT, Sevim B (2017) Numerically and empirically determination of blasting response of a RC retaining wall under TNT explosive. *Adv Concr Constr* 5:493–512
3. Wang F, Wan YKM, Chong OYK, Lim CH, Lim ETM (2008) Reinforced concrete slab subjected to close-in explosion. In: LS-DYNA Anwenderforum, pp 21–28
4. Carey NL, Myers JJ, Asprone D, Menna C, Prota A (2018) Polyurea coated and plane reinforced concrete panel behavior under blast loading: numerical simulation to experimental results. *Trends Civ Eng Archit* 1(4):87–98
5. Braimah A, Siba F (2017) Near-field explosion effects on reinforced concrete columns: an experimental investigation. *Can J Civ Eng* 45(4):289–303
6. Brode HL (1955) Numerical solutions of spherical blast waves. *J Appl Phys* 26(6):766–776
7. Kingery CN (1966) Air blast parameters versus distance for hemispherical TNT surface burst. Army Ballistic Research Lab Aberdeen Proving Ground MD
8. Kingery CN, Bulmash G (1984) Airblast parameters from TNT spherical air burst and hemispherical surface burst. US Army Armament and Development Center, Ballistic Research Laboratory
9. Jordan DW (1962) The stress wave from a finite, cylindrical explosive source. *J Math Mech* 503–551
10. Price MA (2005) Effects of cylindrical charge geometry and secondary combustion reactions on the internal blast loading of reinforced concrete structures (No. LA-14209-T). Los Alamos National Lab. (LANL), Los Alamos, NM (United States)

11. Knock C, Davies N (2013) Blast waves from cylindrical charges. *Shock Waves* 23(4):337–343
12. Rigby SE, Osborne C, Langdon GS, Cooke SB, Pope DJ (2021) Spherical equivalence of cylindrical explosives: effect of charge shape on deflection of blast-loaded plates. *Int J Impact Eng* 155:103892
13. Karlos V, Solomos G (2013) Calculation of blast loads for application to structural components. Publication Office of the European Union, Luxembourg
14. Hopkinson B, Cranz C (1915) Cube root scaling law
15. Diana FEA BV. Diana finite element analysis user's manual. <https://dianafea.com/manuals/d102/Analys/Analys.html>. Last Accessed 15 Sep 2022
16. Sluys LJ, de Borst R, Mühlhaus H-B (1993) Wave propagation, localization and dispersion in a gradient-dependent medium. *Int J Solids Struct* 30(9):1153–1171

# Experimental Study on the Mitigation Effects of Water Mist on Quasi-Static Pressure



Qi Li, Yan-Wei Chen, Liang Zhang, Ping-Hui Li, Ya-Wei Wang,  
and Ya-Bin Liu

**Abstract** In this study, the mitigation effects of water mist with different characteristics on quasi-static pressure were studied experimentally in a confined chamber. Experimental results demonstrated that the water mist considerably mitigated the quasi-static pressure and reflected waves when a blast occurred in a confined chamber. The water spray could absorb the energy released by the detonation of charge by means of evaporation and heat absorption. The primary determinants of the mitigation effects were the water's surface area and the diameter of droplets. The mitigation of the quasi-static pressure was made better by increasing the water's surface area and reducing the diameter of the droplets.

**Keywords** Blast · Quasi-static pressure · Water mist · Mitigation effects

## 1 Introduction

The blast can be classified as confined blast or air blast depending on where it occurred. Confined blasts include explosions that occur in ammunition depots, warship cabins, underground bunkers, and so on. The internal explosion is the most common damage method for ships, buildings, and other targets with chamber structures. In these circumstances, shock wave pressure and quasi-static pressure are two different types of pressure. The structure is damaged differently in a confined blast than in an open space. After the charge is detonated, the structure of the confined space is firstly affected by the high-frequency shock wave, resulting in cracks, throwing, tearing, and other pre-damage, and then the low-frequency quasi-static pressure continues to act on the target, resulting in structural disintegration, flight, and other more serious damage. The final damage effect of the target is closely related to the effective strength of the quasi-static pressure. Accurately measuring the quasi-static

---

Q. Li (✉) · Y.-W. Chen · L. Zhang · P.-H. Li · Y.-W. Wang · Y.-B. Liu

713th Research Institute of China State Shipbuilding Corporation Limited, Zhengzhou 450015, China

e-mail: [921910005@qq.com](mailto:921910005@qq.com)

pressure in a limited region is crucial. The blast generates a shock wave that strikes the inner wall, and the detonation products accumulate in the confined space to form a gradually decreasing pressure that continues to squeeze the inner wall. The gradually decreasing pressure is called quasi-static pressure. The quasi-static pressure is generated because the gas products with a high temperature and high pressure generated by the explosion expand outward and are constrained by the confined space. It rises relatively slowly and becomes stable to a certain low pressure, and the peak value is far less than the maximum value of shock wave overpressure. When a blast occurred in a confined chamber, the inner wall's typical pressure history is depicted in Fig. 1 [1]. The incident shock wave and the reflected shock wave are the first stages of the pressure curve, as shown in Fig. 1. The second stage is characterized by a period of stable quasi-static pressure. Quasi-static pressure is significantly less than overpressure in terms of value. Equation (1) is the theoretical equation of quasi-static pressure derived by Feldgun et al. [2]:

$$p_{q-s} = \left( \frac{P_0}{(\gamma_0 - 1)} (V - V_E) + \Delta E_{TOTAL} \rho_E V_E \right) \frac{(\gamma - 1)}{V} \quad (1)$$

where  $P_{q-s}$  and  $P_0$  are the quasi-static pressure and atmospheric pressure;  $V$  and  $V_E$  are the volume of the confined chamber and the volume of the charge;  $\rho_E$  is the density of the charge;  $\gamma$  and  $\gamma_0$  are the adiabatic index of air and the adiabatic index of a mixture of air and detonation products.  $\Delta E_{TOTAL}$  is the energy generated when a unit mass of charge detonates.  $\Delta E_{TOTAL}$  can be calculated by the proportion of the explosive's mass  $W$  to the chamber's volume  $V$ . This is evident from Eq. 1 that the quasi-static pressure mainly depends on the mass of the charge and the confined space' volume.

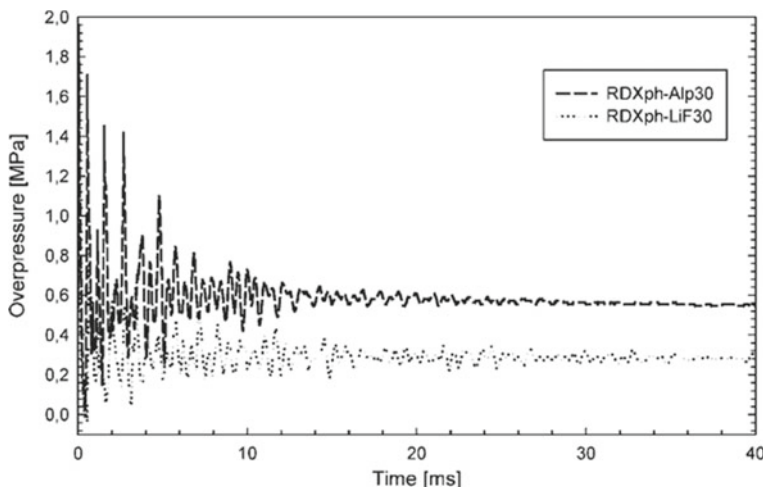


**Fig. 1** Typical pressure–time history for a blast happened in a confined space [by author]

Researchers have long been interested in how to reduce the destructive effects of blast in confined spaces. Water has a latent heat of 2.25 MJ/kg, and the energy released by detonating 1 kg TNT is 4.45 MJ. As a result, the energy released by the detonation of 1 kg TNT can ideally be completely absorbed by 2 kg water via evaporation. The surface area of water increases dramatically when it is atomized into mist. Water mist can improve heat transfer efficiency and allow water to absorb blast energy more efficiently. Furthermore, water is inexpensive, easy to obtain, and non-polluting to the environment. Therefore, the application of water spray to lessen blast damage has drawn the attention of researchers. Water mist is highly capable of reducing blast damage, according to a huge number of experimental studies. The NRL (Naval Research Laboratory) carried out experiments on blast mitigation by water mist. Water mist with a droplet diameter of 35–550  $\mu\text{m}$  was sprayed in a chamber. 900 g, 2200 g, and 3200 g TNT placed in the chamber were detonated, respectively. Results revealed a 47% decrease in quasi-static [3]. Subsequently, NRL used charges with higher energy density to conduct experiments. A water mist with a concentration of 70 g/m<sup>3</sup> was sprayed into the chamber. The charges were detonated after 60 s. The blast load inside the chamber was measured using a pressure transducer. The experimental results showed that compared without water spray, the impulse, over-pressure, and quasi-static pressure generated by the detonation of 50 kg TNT were reduced by 40%, 36%, and 35%, respectively [4]. Ananth et al. found latent heat absorption was the main mitigation mechanism through numerical calculation [5]. Grujicic et al. believed that water vapor in the gas phase could inhibit the combustion of detonation products, which was also one of the attenuation mechanisms [6].

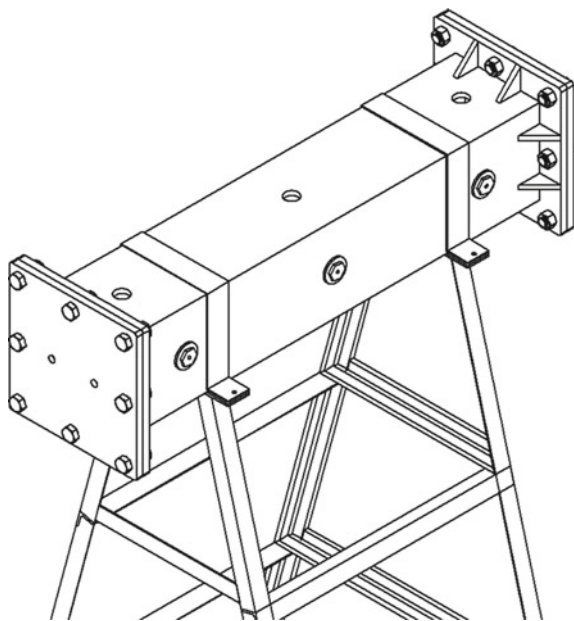
Existing research indicates that, while water mist can reduce quasi-static pressure, the effect of water spray characteristics on the attenuation effect is not well understood. The effect of different types of water mist on quasi-static pressure was investigated experimentally in this paper. Six blast tests were conducted in a confined chamber. The effect of water spray with different properties on quasi-static pressure was investigated.

## 2 Experimental Tests

### 2.1 Apparatus

The experimental setup consisted of a confined chamber, a pressure measuring system, and a water spray system. Stainless steel was used to create the chamber. The chamber's entire length was 1000 mm, and its wall thickness was 10 mm, as seen in Fig. 2. The chamber had a square 180 \* 180 mm cross section, and its interior volume was 0.0324 m<sup>3</sup>. Both ends of the chamber were sealed by flanges. In order to avoid the shaking of the chamber during the blast and affecting the test results, the chamber was fixed on a support.

**Fig. 2** Schematic of the confined chamber [by author]



As shown in Fig. 3, two pressure transducers (Model PCB 113B26) were installed on the wall of the chamber. The positions of the two pressure transducers were 400 mm and 750 mm from the charge, respectively. The pressure transducers' sensitive area was mounted flush against the chamber's inside wall. The pressure transducers were connected to a signal amplifier, a data collector, and a computer in turn through signal cables. In this experiment, the sampling rate of the data collector was 1 MHz.

The water spray system consisted of three nozzles, a water pump, and a segregator. Two nozzles were installed at the top of the chamber and one was installed at the bottom of the chamber. The position of the nozzles is shown in Fig. 3. The water pump was a submersible pump with a power of 2.5 kW. In this experiment, two different kinds of spray nozzles were utilized. The fine atomization nozzle A can create a fine atomization effect. The spray angle is 45°. The diameter of atomized particles is 500 um. The stainless steel guide blade and nozzle core that are integrated into the nozzle have an anti-drip system. Under water pressure of 20–120 kg, the liquid flows rapidly, creating a centrifugal vortex in the guide blade and ejecting extremely thin hollow mist particles through the nozzle. Nozzle B produces solid conical spray forms; it is a solid cone. There is a 120° spray angle. This type of nozzle has a circular spray area and can create a medium to large droplet size, evenly spread spray at a variety of flow rates and pressures. This even spray dispersion results from the special blade design, the broad, smooth flow channel, and the sophisticated jet control features. It can play an excellent role in the application field of jet which requires covering an area.

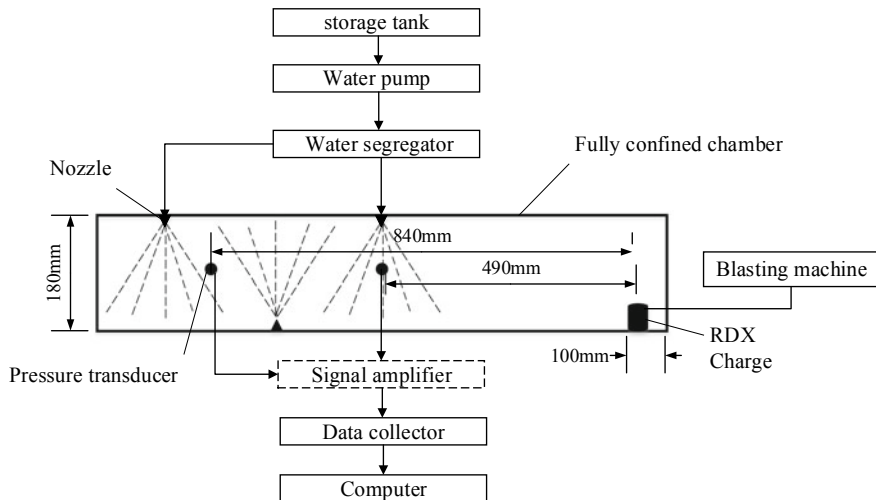


**Fig. 3** Schematic of experimental configuration [by author]

**Table 1** Test cases [by author]

Cases	Mass of RDX (g)	Theoretical value of quasi-static pressure (MPa)	Water mist
1	3	0.41	None
2	7	0.75	None
3	3	0.41	Nozzle A
4	7	0.75	Nozzle A
5	3	0.41	Nozzle B
6	7	0.75	Nozzle B

## 2.2 Experimental Test Cases

In this experiment, two different kinds of nozzles were employed to study the effects of water spray characteristics on quasi-static pressure. Table 1 displays the experimental test cases. The type of charge used in this experiment was RDX (Hexogen), which was detonated by an electric detonator.

## 3 Results and Discussion

The pressure histories produced by the detonation of 3 g and 7 g of RDX in the enclosed chamber without water spray are shown in Figs. 4 and 5. Many reflected shock waves followed the initial overpressure, and as time passed, the peak value of these reflected shock waves gradually decreased. As the shock wave reflection

diminished over time, the pressure curve stabilized. The stable pressure was the quasi-static pressure. According to Eq. 1, the theoretical values of the quasi-static pressure created by the detonation of 3 g RDX and 7 g RDX in the chamber are 410 kPa and 750 kPa. The value obtained in the experiment were 400 kPa and 700 kPa. The errors were 2.4% and 7.1%, respectively.

Figures 6 and 7 present the time-dependent curves of the pressure generated by the detonation of 3 g RDX and 7 g RDX in the confined chamber with water spray generated by nozzle A. As shown in Figs. 6 and 7, the number of reflections and the amplitude of the reflected shock waves were significantly reduced relative to

**Fig. 4** Pressure profile versus time for 3 g RDX detonated in the chamber without water mist [by author]

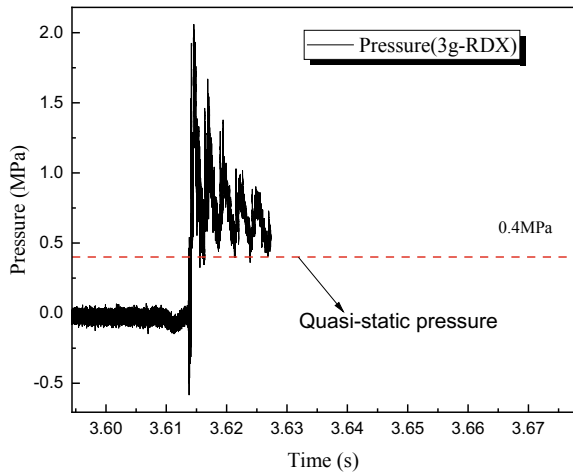
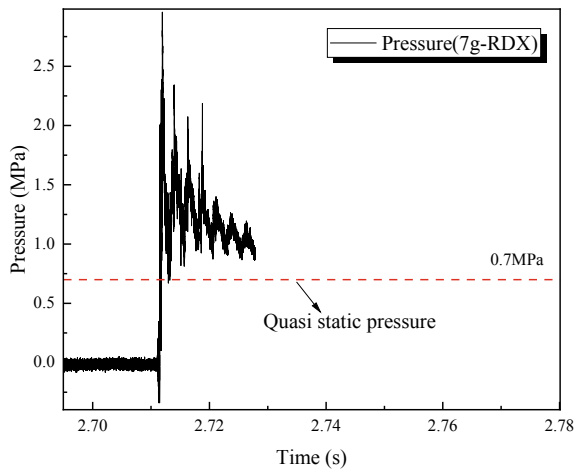


**Fig. 5** Pressure profile versus time for 7 g RDX detonated in the chamber without water mist [by author]



cases 1 and 2. The pressure gradually tended to zero after the reflected shock wave, indicating that the water mist absorbed the energy generated by the blast through evaporation.

The pressure produced by the explosion of 3 g and 7 g RDX in the enclosed chamber with water mist produced by nozzle B is shown in Figs. 8 and 9. Similar to case 3 and 4, the number and amplitude of reflections of the reflected shock waves were significantly smaller than those in case 1 and case 2. As shown in Figs. 8 and 9, there was a quasi-static pressure in the chamber, and the values of the quasi-static pressure were 0.03 MPa and 0.025 MPa, respectively. The flow rate of nozzle B was greater than that of nozzle A. Under the same spray time, the total mass of water in the chamber in cases 5 and 6 was greater than that in cases 3 and 4. In theory,

**Fig. 6** Pressure profile versus time for 3 g RDX detonated in the chamber with water mist generated by nozzle A [by author]

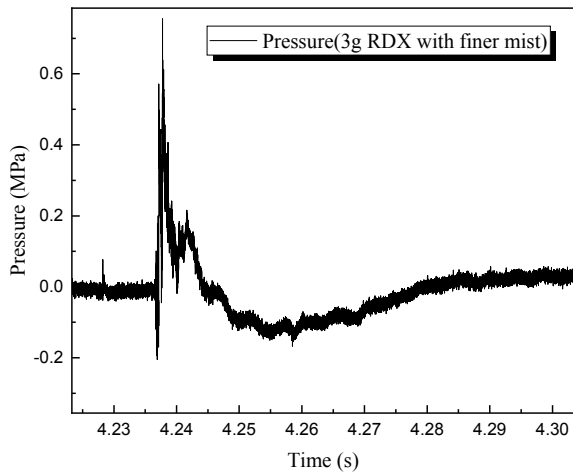
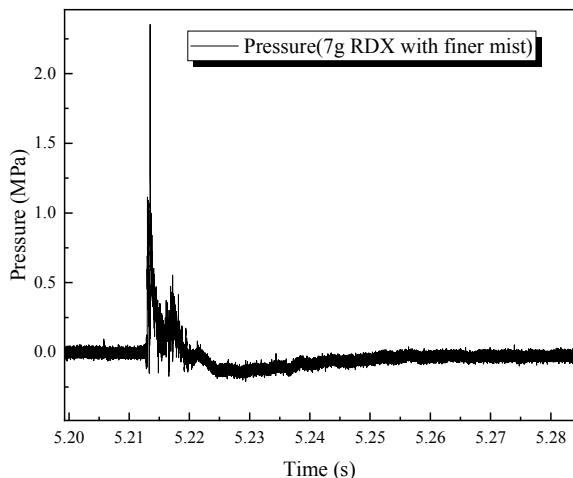


**Fig. 7** Pressure profile versus time for 7 g RDX detonated in the chamber with water mist generated by nozzle A [by author]



there should be no quasi-static pressure in the chamber. In fact, in cases 5 and 6, a considerable part of the mass of water in the chamber was attached to the side wall and deposited on the bottom of the chamber, which caused the surface area of the liquid to be smaller than that in cases 3 and 4. The smaller surface area meant that the efficiency of evaporation and heat absorption was lower, and the water could not evaporate in time in cases 5 and 6, resulting in the existence of quasi-static pressure in the chamber. The initial shock wave and the subsequent reflected shock waves caused the droplets to undergo secondary atomization, but the larger the droplet diameter, the longer it took for the droplet to become fully atomized. The diameter of droplets generated by nozzle B was larger than that of nozzle A, which also retarded the process of droplet evaporation.

**Fig. 8** Pressure profile versus time for 3 g RDX detonated in the chamber with water mist generated by nozzle B [by author]

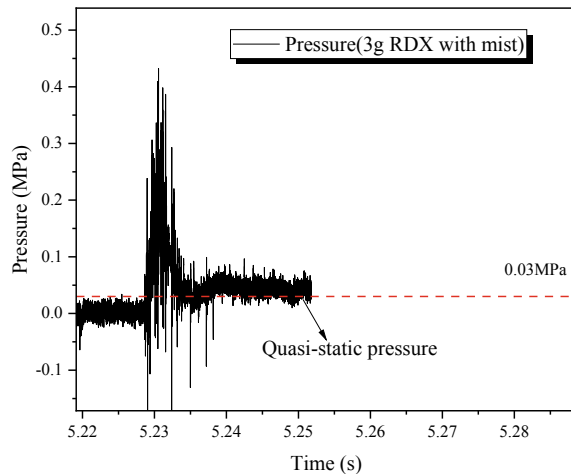
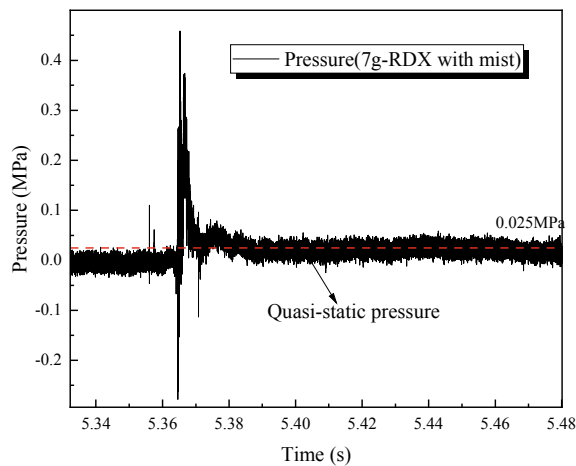


**Fig. 9** Pressure profile versus time for 7 g RDX detonated in the chamber with water mist generated by nozzle B [by author]



## 4 Conclusion

Six blast tests were conducted in a confined chamber to investigate the effect of different types of water mist on pressure mitigation. The effects of water mist with two different properties on quasi-static pressure were compared. (1) The water mist significantly reduced the quasi-static pressure and reflected wave when the blast occurred in the confined space. (2) Water mist can absorb the energy released by charge detonation via evaporation and heat absorption. (3) The key factors influencing the mitigation effects are the water's surface area and the droplet diameter of the water mist. By increasing the water's surface area and reducing the droplet's diameter, the mitigation effect was enhanced.

## References

1. Waldemar AT, Stanislaw C, Józef P (2007) Studies of free field and confined explosions of aluminium enriched RDX compositions. *Propellants, Explos, Pyrotech* 32(6)
2. Feldgun VR, Karinski YS, Edri I et al (2016) Prediction of the quasi-static pressure in confined and partially confined explosions and its application to blast response simulation of flexible structures. *Int J Impact Eng* 90:46–60
3. Bailey JL, Farley JP, Williams FW et al (2006) Blast mitigation using water mist. *NRL/MR/6180-06-8933*
4. Willauer HD, Ananth R, Farley JP et al (2009) Blast mitigation using water mist: test series II. *NRL/MR/6180-09-9182*
5. Ananth R, Willauer HD, Farley JP et al (2012) Effects of fine water mist on a confined blast. *Fire Technol* 48(3):641–675
6. G M, P B, L Z C et al (2007) A computational investigation of various water-induced explosion mitigation mechanisms. *Multidiscip Model Mater Struct* 3(2)

# Research on the Method of Compiling the Normalized Fatigue Load Spectrum of Motorized Transportation



Chunjuan Shi, Zhiyong Sun, and Gang Feng

**Abstract** Aiming at the fatigue load design technology of motorized transportation, the compiling method of fatigue load spectrum and the present research situation of fatigue load design of motorized transportation were introduced in this article. The deficiencies of the key technology of fatigue load design of motorized transportation were clarified. A method of compiling the normalized fatigue load spectrum of motorized transportation is researched. Based on the normalization process, the equivalent load model, the synthesis method of multi-transportation conditions, and the bench fatigue test spectrum of key structural components are established, which can provide a reference for the structural fatigue design in motorized transportation.

**Keywords** Fatigue design · Load spectrum · Motorized transportation · Normalization

## 1 Introduction

At present, the maneuvering mode of large-scale structures is mainly the organic combination of railway transportation and road transportation, among which the railway transportation mode has the advantages of high speed and good stability, as it is suitable for large-scale campaign mobile transportation. The road transportation mode has the advantages of flexible route planning, easy camouflage and protection, and good quick reaction. It is suitable for small-scale mobile transfer [1].

The vibration of the system caused by road excitation has a great influence on the safety of the structure, especially on off-road road transportation. The vibration may cause the connection to be loose, the reliability of the instrument and equipment to become worse, may cause the structure stress are bigger, which causes the distortion, the breakage and destructive fault. Moreover, the fatigue problem may be caused by

---

C. Shi (✉) · Z. Sun · G. Feng

Air Force Engineering University, Air and Structure Defense College, Xi'an 710051, Shaanxi, China

e-mail: [scj-003@163.com](mailto:scj-003@163.com)

periodic excitation, and the fatigue crack may develop into fatigue failure. The fatigue problem is not easy to detect and find, it will not only affect the safety and reliability of the structure, but also reduce the life of the structure. Therefore, the structural anti-fatigue load design in highway transportation has become the key content of structural system design.

The test method of fatigue load spectrum of motorized transportation and the overall scheme of compilation will be put forward in this article, which can promote the innovation of structural design technology and the replacement of equipment to improve the adaptability and reliability of structures under complex maneuvering conditions and the high maneuvering performance of structures.

## 2 Research Status of Fatigue Load Spectrum Compilation Method

The load spectrum is the result of statistical treatment and analysis of random load-time history under various typical actual conditions by using a data processing algorithm, it can be described by numbers, formulas, graphs, tables, matrices, probability distributions, etc., for theoretical analysis and engineering applications [2]. The load spectrum is the basic content of structural dynamic strength research, which can provide a load basis for structural dynamic research, structural fatigue design, and reliability design. It is used to evaluate the fatigue strength of the structure and to predict the fatigue crack growth life of the structure to establish the structural reliability test standard and design code lay the load foundation [3]. Therefore, the study of the load spectrum is a key step to promote the transformation of the load-bearing structure from the traditional infinite life design to the finite life design.

In 1850, Vaire invented the constant amplitude fatigue testing machine, which was used in the fatigue test of the railway wheel and axle, the constant amplitude fatigue test spectrum was generally used in fatigue test, and the corresponding load spectrum has appeared successively in the fields of automobile, agricultural machinery, aviation, and railway. Veers use the first three moments of the sample to describe the rain-flow counting results of the load amplitude and apply the regression method to predict the probability of the large-amplitude load [4]. By fitting the cumulative frequency curve, the extrapolation frequency of each stage load was obtained. At present, the most widely used method is to estimate the parameters of the distribution of the amplitude and mean of the load, respectively. The cumulative frequency can be extrapolated to a certain frequency by using the results of the rainfall cycle count and the joint probability density function. The extrapolation method of rain-flow counting matrix parameter estimation has been widely used in the life prediction of vehicle components [5].

The research on load spectrum in China is relatively late, which began in the twentieth century since the 1980s, but the important role of load spectrum in various fields has been paid more and more attention, in aviation, vehicle transmission systems,

railway freight cars, high-speed trains, construction machinery and other fields of relatively full research, technology is relatively mature. In the field of aviation, many common key technical problems in the process of aircraft load spectrum compilation have been solved, and a lot of achievements have been made in the measurement and processing of aircraft load spectrum data, the compilation of random spectrum and program block spectrum, the counting and statistical analysis of fatigue load under single or multiple working conditions, the conversion of damage equivalent of accelerated test spectrum, the truncation criterion of high and low loads, etc. Xiong J.J. and Gao Z.T. discussed the parameter estimation and hypothesis test of the load distribution when the measured load spectrum data were processed In 2008, which put forward the method of whole life acceleration load-time history generation, which provided a good idea for greatly reducing the fatigue test time, the method of measuring and compiling the load spectrum of aircraft landing gear proposed by Liu K.G. and Yan C.L. have greatly improved the efficiency of compiling the load spectrum. The fatigue reliability of aircraft structures is required highly in the aviation field. Many units and scholars have improved and innovated the technology of load spectrum test and compilation after many years of hard work, it is of great significance to the study of the load spectrum of structures in other fields.

Field of construction machinery, at the beginning, focuses on the relative system and sufficiency of the technical problems such as the accurate measurement and reliable transmission of the load spectrum of the loader transmission system, the synthetic extrapolation of the multi-working conditions, the inference of the extreme load and the mixed distribution in the process of programming the load spectrum Lei. X.J. collected and tested the load spectrum of the concrete pump truck boom under multiple working conditions, and analyzed the damage caused to the boom based on the load spectrum obtained, the whole life load spectrum considering both load sequence effect and interaction effect is compiled, and a new method for obtaining the stress spectrum of bridge crane is proposed, the key characteristic parameters of the stress spectrum were measured and analyzed in situ, and the probability distribution model was established. Based on the distribution model, the characteristic parameters with longer periods were obtained by Latin hypercube sampling, the stress spectrum of concern can be obtained by dynamic simulation. Taking the excavator as the research object, considering the loading characteristics of the key structural members, the fatigue failure mode, and the feasibility of the test scheme, the program load spectrum of each key structural member under single working condition is obtained by LV P.M. The validity of the program spectrum of the bench fatigue test is evaluated by synthesizing the program load spectrum under multiple operating conditions, and the consistency of the random spectrum, the program spectrum of the bench fatigue test and the original load spectrum is verified, the program spectrum can reproduce the fatigue damage state of the key structural components, and the accelerated load spectrum of the bench fatigue test can be compiled [6].

### 3 Research Status and Deficiency of Fatigue Load Spectrum of Structure Maneuvering Transportation

Due to the secret protection of the basic data of the load spectrum, the research on the fatigue load spectrum of the structure transportation is seldom reported in foreign countries. In the development of structural engineering in our country, the existing transportation vibration environment conditions in GJB 150A and MIL 810G are mainly adopted without the measured data. However, GJB 150A and MIL 810G only proposed the environmental test conditions and did not give too much detailed explanation of their application and scope of application.

In practical application, designers usually directly use these standard conditions to carry out vibration tests on products or equipment without distinguishing different objects such as structures, structure-mounted equipment or vehicle-mounted equipment, this may be very different from the actual vibration environment of product transportation, and even lead to the test or lack of test.

At present, the research on the fatigue load spectrum of tactical structure maneuvering transportation is mainly carried out by China Academy of Launch Vehicle Technology Institutions and universities, and the fatigue life prediction of tactical structure maneuvering transportation is carried out and certain research results were obtained. The research contents mainly include the measurement method of the transportation vibration fatigue test, the selection of the fatigue dangerous parts, the transportation vibration test simulation, and the transportation environment condition acceleration simulation.

In the field of aviation, many common key technical problems in the process of aircraft load spectrum compilation have been solved. A lot of achievements have been made in the measurement and processing of aircraft load spectrum data. The compilation of random spectrum and program block spectrum, the counting and statistical analysis of fatigue load under single and multiple working conditions, the conversion of damage equivalent of accelerated test spectrum, the truncation criterion of high and low loads, etc.

The research on the key technology of the fatigue load spectrum of motorized transportation is lacking, and the fatigue design method and experimental technology of the structure are still in the primary stage at present. Compared with the research on the fatigue load spectrum design of other fields, the design method of load spectrum for motorized transportation is not perfect and has some limitations.

The main disadvantages are as follows:

- (1) Due to the harsh environment and the complex working conditions, the loads on the structure during the actual maneuvering cannot be measured completely, so the influence degree cannot be analyzed quantitatively.
- (2) The load spectrum test cannot include the actual transport load of the structure under various typical working conditions, and there is almost no universal load spectrum test technology.
- (3) The strength design of static load and defect-free material is mostly used in the design. The environmental conditions of transportation vibration are considered

in the design of structural engineering. They are not different from the actual fatigue load of structural transportation. Such as the structure, the structure and the vehicle.

- (4) In the structural design, the load spectrum is usually obtained by the field test, which verifies the adaptability and fatigue reliability of the key structural components under the actual transportation vibration environment and does not aim at the key structural details of the structural transportation. The compiled load spectrum is difficult to be generalized as it is not universal. There is no relevant standard to refer to in the test compilation of the structural load spectrum.
- (5) There is no systematic and universal research achievement on the testing method of load spectrum, fatigue load spectrum and test spectrum, structure fatigue test technology, fatigue design method, and verification method for the key structure of motorized transportation.

## 4 A Normalized Method for Compiling Standard Fatigue Test Spectra

Taking the missile road mobile transport as the research object, on the basis of the statistical analysis of the load environment data of missile mobile transport, puts forward the normalized standard fatigue test spectrum testing and compilation method, focusing on the missile transport fatigue load spectrum and the compilation method of the test spectrum, and the compilation method of the missile transport fatigue test spectrum.

### 4.1 *Fatigue Load Spectrum Test Method for Missile Transportation*

When researching the fatigue problem of the key structural parts or the whole missile, whether an indoor bench simulation test, theoretical analysis method or simulation method is used, the real load information of the structure is indispensable. Especially for indoor simulation load test, the key to test effectiveness is whether the load spectrum that can reflect the actual transportation conditions is available. Therefore, the accurate measurement of the load spectrum is a key step in fatigue research. The technology involves technical difficulties such as research on synchronous identification method of complete spatial load on key structural members, development of special sensors, design of measuring point layout, evaluation of load identification effect, etc.

Factors such as different transportation roads, driving speeds, and drivers' operating habits directly affect the stress state of the key structural parts of the missile. Therefore, the technical route shown in Fig. 1 is used to analyze the load spectrum

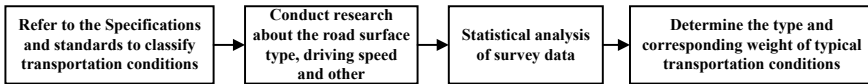


**Fig. 1** Load spectrum test conditions under typical transportation conditions

test conditions, that is, the typical transportation conditions are investigated to determine the type and corresponding weight of the typical transportation conditions in the load spectrum test.

#### 4.2 Preparation Method of the Normalized Standard Fatigue Test Spectrum

Different types of missiles are similar in structure, and their typical mobile transport conditions are also consistent. Therefore, in order to solve the problem of fatigue load spectrum and test spectrum of missile mobile transport, this paper proposes a standardized test spectrum compilation method for key structural components of missile mobile transport. There are many links in the preparation of the fatigue test spectrum, so the fatigue test spectrum of key structural parts of missiles is prepared according to the technical route shown in Fig. 2.

**Fig. 2** A method of compiling the standardized fatigue test spectrum of the key structural components

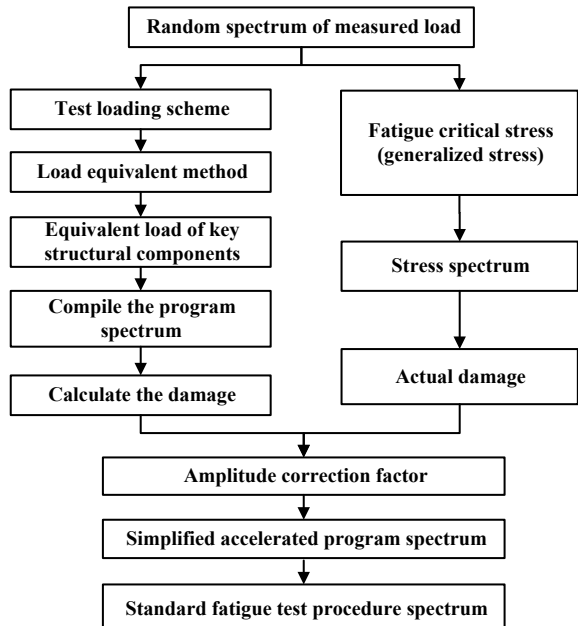
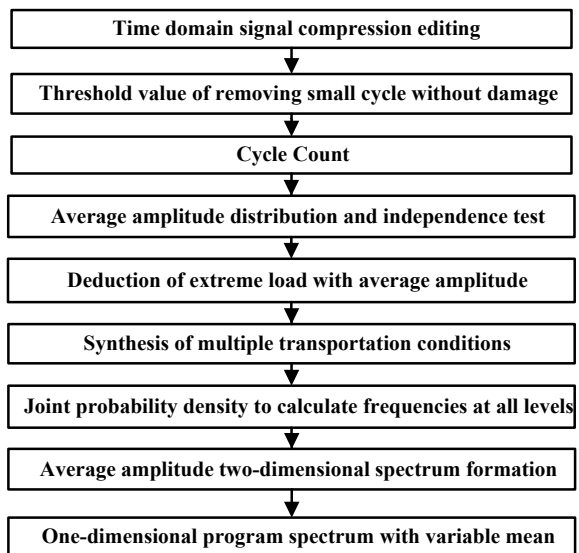


**Fig. 3** Compilation process of fatigue program spectrum



Then, take the compilation of the time domain spectrum as an example to compile the equivalent load of key structural members, as shown in Fig. 3.

- (1) Firstly, the load spectra are compiled separately in the respective local coordinates according to the key structural components.
- (2) The fatigue test spectra of key structural components were constructed by establishing the equivalent load model and synthesizing the multi-transportation conditions.
- (3) Based on the normalization processing, the generalization of the test spectrum is realized, and the acceleration and standardization of the test spectrum are solved.
- (4) The formed fatigue load spectrum is a normalized standard load spectrum, which can be used in the fatigue design of structures with similar structures of different types.

## 5 Conclusion

In this article, a method for compiling the normalized standard load spectrum of the fatigue load spectrum of motorized transportation is presented, by establishing the equivalent load model and the synthesis method of multi-transportation conditions, the fatigue test spectrum of the key structural components is constructed, and the generalization of the test spectrum is realized based on the normalization treatment. It solves the important technical problem of acceleration and standardization of test spectrum and can be effectively applied and reasonably extended to structural fatigue design.

## References

1. Wang BH, Xiang QY, Chen YX (2022) Research status and prospect of fatigue reliability of excavator structure. *J Chang'an Univ (Natural Science Edition)* 42(1):115–126
2. Xiang QY, Lv PM, Wang BH (2018) Equivalent load method for fatigue test of bucket rod bench of hydraulic excavator. *China J Highw Transp* 31(6):317–326
3. Shi X, Wu FQ, Luo QW (2021) Calculation of fatigue life of lugs of structural joints under common load and vibration environment. *Tactical Struct Technol* 5(1):57–64
4. Shang L, Zhang HR, Li P (2019) Compilation of fatigue load spectrum and life prediction of road maneuvering transportation for structure front directional parts. *J Vib Shock* 38(9):88–93
5. Feng K, Nangong ZJ, WANG L (2018) Research on screening method of tactical structure structure fatigue risk parts. *Tactical Struct Technol* 2018(6):26–34
6. Ma MN, Yu Q (2019) Fatigue life analysis of a structure rack under random load. *Equip Manuf Technol* 2019(4):171–174+189

# Research on the Reliability Design Method of the Typical Mechanism of Naval Gun Based on Failure Form



Fei Zhao

**Abstract** This paper proposes a reliability design method for the typical mechanism of naval gun based on failure form, selects a typical mechanism to analyze its failure mode and failure form, and carries out research using finite element analysis, dynamics simulation, and reliability analysis to provide theoretical support and engineering methods for the development of mechanism reliability design.

**Keywords** Failure forms · Typical mechanisms · Reliability design

## 1 Introduction

The reliability design determines the inherent characteristics of the product, and the reliability factor must be considered in the design of naval gun equipment. Naval gun equipment is an electromechanical-hydraulic integrated product. The reliability theory and methods of electronic products have a certain foundation. Mingzhu [1] analyzed and compared the reliability prediction methods of electronic products, and gave the scope of application of various methods. Qiong [2] proposed the principles that should be followed in the reliability design of electronic products and introduced the reliability design methods of electronic products. Yuzhen [3] analyzed the inherent reliability and use of reliability design of electronic components and proposed measures to further improve the reliability of electronic components. In addition, almost every item of electronic reliability design work has a relatively mature national standard or national military standard. The essence of electronic card bank design is to apply a series of published electronic reliability standards [4]. However, due to the characteristics of mechanical mechanism reliability such as multiple failure modes and complex distribution types, the reliability theory and methods of electronic products cannot be fully applied to mechanical mechanisms

---

F. Zhao (✉)

No. 713 Research Institute of China Shipbuilding Industry Corporation, Zhengzhou, China  
e-mail: [z1261310329@163.com](mailto:z1261310329@163.com)

[5]. Therefore, this paper takes a certain type of naval gun in my country as the research object and proposes a reliability design method based on failure form for typical mechanical mechanisms.

## 2 The Working Mechanism of the Switch Latch Mechanism [6]

The main function of the switch latch mechanism is to complete the action of switching the latch body after the gun fires into position. With the vertical wedge-shaped latch body, the gun compresses the latch spring to store energy at the beginning of the reentry. The gun continues to re-enter, forcing the left and right extractor barrels to move backward through the rocker's arm, and the latch opening roller drives the crank arm to rotate downward, completing the latch opening and shell extraction action. When the open latch is in place, the latch body moves upward under the action of the closing latch spring and is hung by the backward extractor barrel template to keep it in the open latch position for the next round of ammunition delivery. After the delivery round is chambered, the extractor barrel is released and the closing latch action is completed under the action of the closing latch spring, the basic composition is shown in Fig. 1.

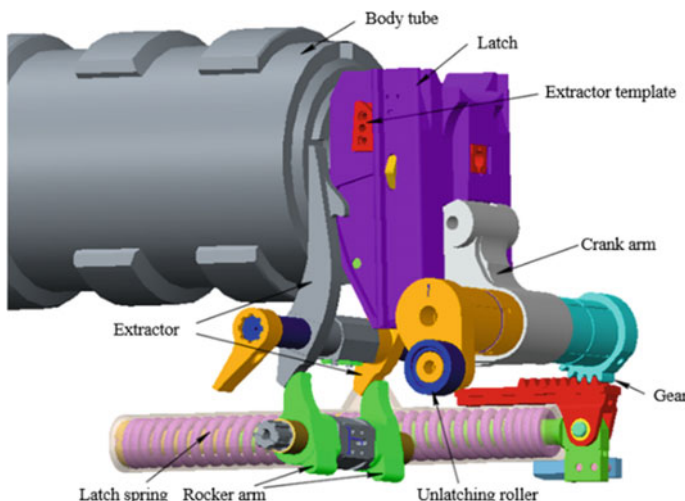


**Fig. 1** Schematic diagram of the basic components of the latching mechanism

### 3 Latching and Unlatching Mechanism Failure Form Analysis

#### 3.1 Latching and Unlatching Mechanism Failure Mode Effects Analysis

Failure Mode Effects Analysis (FMEA) is the most widely used analytical method and effective tool to carry out quality design using a general inductive approach to accomplish a qualitative analysis of system reliability and safety [7]. The failure mode and effect analysis work were carried out on the latching and unlatching mechanism according to its stress and motion patterns, and the failure modes of each component, causes of failure, and effects caused by the failure on higher levels were analyzed, as shown in Table 1.

**Table 1** Latching and unlatching mechanism failure mode effects analysis

Name	Products or functions	Failure mode	Failure cause	Task phases and working methods	Failure effects				
					Local effects	Higher level effects	Final effects		
Latching and unlatching mechanism	Complete the action of unlatching, extracting the shell, discharging the shell, etc., and completing the latching after the bullet delivery	Latching in advance	Extractor self-locking angle anomaly	Unlatching	Extractor and extractor template self-locking unreliable	The latch closes prematurely, causing other subsequent mechanism movements to stall	Guns stop firing		
			Inadequate machining precision	Unlatching					
			Latching spring force decreases	Unlatching					
			Latch spring breakage	Unlatching					
	Latching action abnormal	Rack stalling	Latching	Latch closure not in place	The latch cannot be closed, and ammunition cannot be fired	Guns stop firing			
		Crank arm deformation	Latching						
		The extractor is not relieved	Latching	The latch does not move					
		Rack breakage	Latching						

**Table 2** Latching and unlatching mechanism failure form classification

Serial No	Part name	Failure cause			
		Insufficient rigidity	Poor wear resistance	Poor fatigue performance	Poor relative motion precision
	Latch spring			✓	
	Extractor		✓		
	Extractor template		✓		
	Rack	✓			
	Unlatching roller	✓			✓
	Crank arm	✓		✓	✓
	Latch	✓			

### 3.2 *Latching and Unlatching Mechanism Failure Form Analysis*

Through the failure mode and effects analysis of the latch mechanism, the failure causes and manifestations that affect the reliability of the latch mechanism are obtained, and these failure causes are sorted out, which can be summarized into four typical failure forms, namely: insufficient design of structural parts for rigidity and strength, poor wear resistance of parts, the poor fatigue resistance of parts, and poor relative motion accuracy of parts, as shown in Table 2.

## 4 Reliability Design Based on Different Failure Forms

Combining different failure forms, targeted design and calibration work is carried out to effectively reduce the probability of failure of parts due to this type of cause and improve reliability.

### 4.1 *Reliability Design of Stiffness of Structural Parts*

In this section, the stiffness design process of the structural member is described as an example of the stiffness design of the latch body. The solid model of the latch body is imported into the simulation software ANSYS for stress analysis. After dividing the mesh, set the boundary conditions: the constraint mode is a full constraint of the contact surface between the latch body and the gun tail, the force is  $1.06 \times 10^7 N$ ,

and the location of the action point is shown in Fig. 2. The cloud diagram of the stress distribution on the latch body obtained from the simulation is shown in Fig. 3.

It can be seen from the figure that the stress values of the stressed parts of the latch body are below 460 MPa, so the designed latch mechanism meets the design

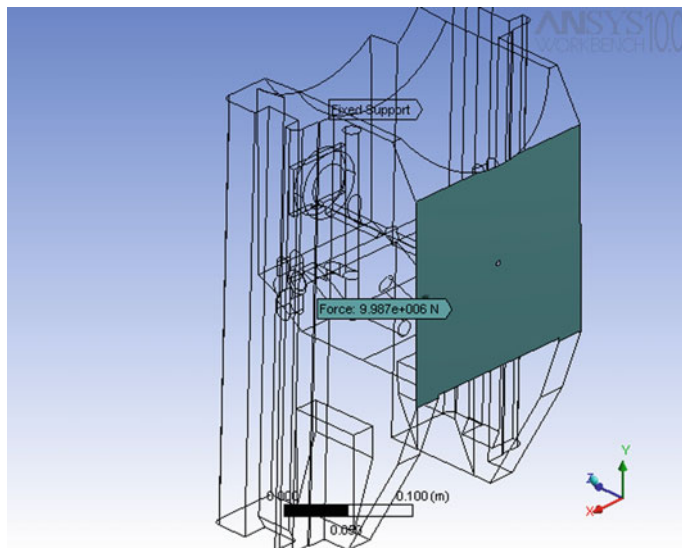


**Fig. 2** Location of action points

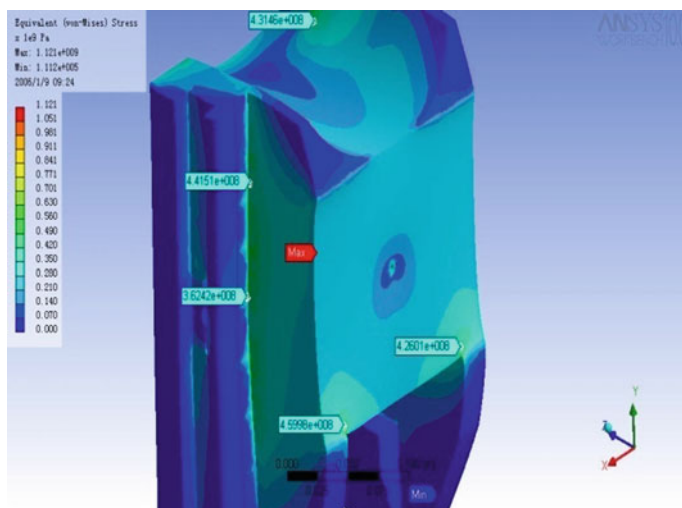


**Fig. 3** Stress distribution cloud diagram

requirement that the latch body is subjected to a stress value  $\sigma \leq 460$  MPa, and the maximum stress value of the latch body can be 460 MPa.

According to the stress–strength interference model [8, 9], it is known that the latch body's stiffness (denoted by  $S$ ) and the applied stress ( $\sigma_j$ ) exhibit some statistical distribution due to the variation of some factors, and the product will fail when the distribution of its strength and the applied stress overlap. Due to factors such as the working environment and the unstable quality of the ammunition, the stress values on the latch body obey a normal distribution,  $\sigma_j \sim N(\mu_\sigma, \delta^2_\sigma)$ . The latch body's strength is determined by its material properties, but the randomness of the production process and machining process can lead to the latch body strength  $S$  showing a normal distribution,  $S \sim N(\mu_S, \delta^2_S)$ , from which the stress-strength distribution of the latch body is shown in Fig. 4.

The latch reliability is expressed as:

$$R = P(S > \sigma) = \Phi\left(\frac{\mu_S - \mu_\sigma}{\sqrt{\delta^2_S + \delta^2_\sigma}}\right) \quad (1)$$

To improve the reliability of the latch body, we can start from three aspects: reduce the variation of the use environment; reduce the individual variation of the latch body strength; and improve the design margin of the product, the improvement effect is shown in Fig. 5.

From the figure, we can see that reducing the working environment and individual differences of the latch can improve the latch reliability, but the effect is small and difficult to operate, while the method of improving the design margin can significantly improve the latch reliability, and the purpose of improving the design margin can be achieved by increasing the safety factor of the latch design.

When PCrNi3MoVQE is selected as the latch body design material, its allowable stress is 1104 MPa, and its reliability is close to 1 according to the above stress–strength interference model, which meets the latch body reliability design requirements.

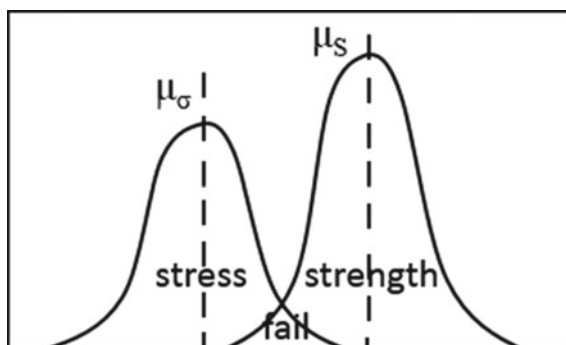


**Fig. 4** Latch body stress–strength distribution

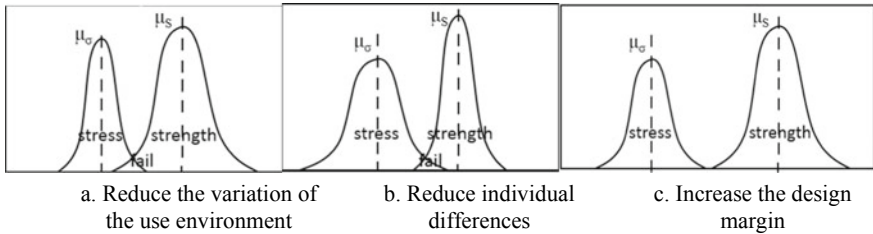


**Fig. 5** Reliability improvement effect diagram

By analogy, for the reliability design of other structural parts such as rack and roller, the stress–strength interference model can also be used to predict their reliability, and when the designed structural parts cannot meet the design requirements, the design margin should be increased until the reliability design requirements are met.

## 4.2 Design for Fatigue Reliability of Crank Arm

For the crank arm carrying the working load, and for the failure mode of fatigue, the following functional function is obtained according to the fatigue failure criterion:

$$g(X) = R - S \quad (2)$$

$$R = \frac{cb}{k} \sqrt{\frac{1+r^2}{2}} S_{-1} \quad (3)$$

$$S = \sqrt{S_m^2 + S_a^2} \quad (4)$$

where  $R$  is the fatigue limit,  $S$  is the equivalent fatigue stress,  $c$  is the size factor,  $b$  is the surface finish factor,  $k$  is the stress concentration factor,  $r$  is the stress cycle ratio,  $S_{-1}$  is the fatigue limit of the material when the stress ratio  $r = -1$ ,  $S_a$  is the stress amplitude, and  $S_m$  is the average stress value. Therefore, the fatigue reliability of the crank arm is the probability of the functional function  $g(X)$ .

To obtain the stress amplitude and average stress value of the crank arm under the working environment, the finite element simulation calculation of the working process of the crank arm is carried out, and the simulation results are shown in Figs. 6 and 7.

From the figure, the maximum stress amplitude of the crank arm is 389.2 MPa and the average stress is 21.1 MPa. the equivalent fatigue stress value  $S$  can be obtained by substituting into Eq. (4). Except for the maximum stress amplitude and the average stress value which are not random variables, the other variables in

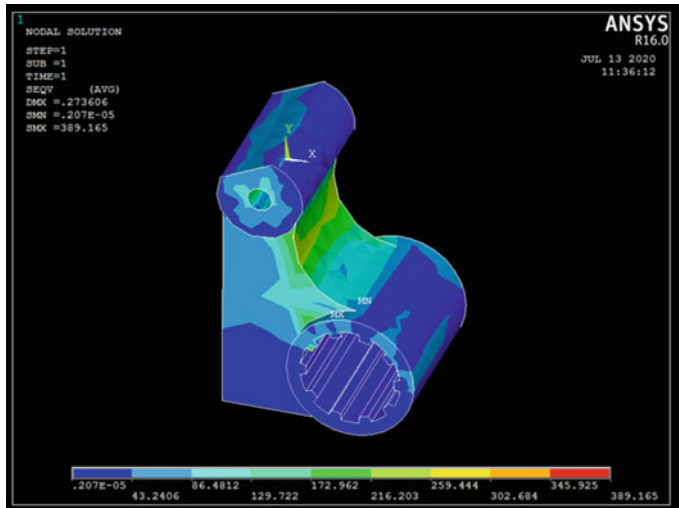


**Fig. 6** Crank arm tensile stress distribution

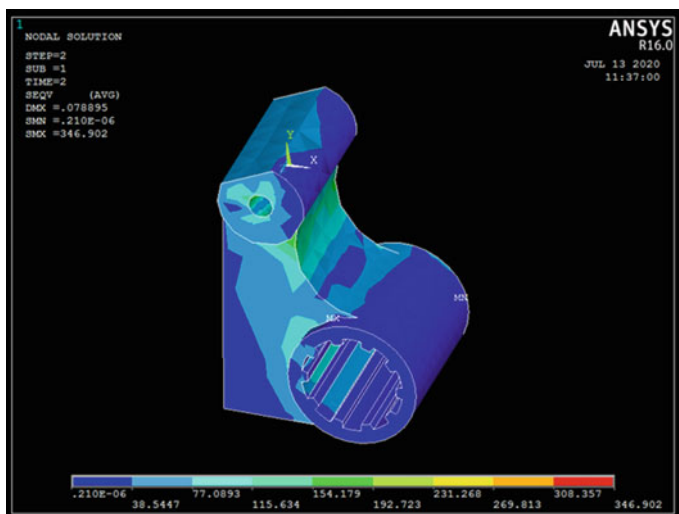


**Fig. 7** Crank arm compressive stress distribution

the function will also show random changes due to the instability of the working environment. The distribution table of each variable obtained from the empirical data is shown in Table 3.

Reliability calculations were performed using the variables in Table 3, and the results did not meet the reliability design requirements. After optimizing the fatigue limit  $S_{-1}$  of the material, the fatigue limit of 490 MPa was finally selected and

**Table 3** Variable distribution table

Variable names	Distribution types	Average value	Variance
Modulus of elasticity $E/\text{MPa}$	Normal distribution	210,000	1000
Compression load $P_1/\text{MPa}$	Normal distribution	80	8
Tensile load $P_2/\text{N}$	Normal distribution	70	7
Maximum stress amplitude $S_a$	–	389.2	–
Average stress $S_m$	–	21.1	–
$c$	Normal distribution	0.79	0.068
$b$	Normal distribution	1.1	0.043
$k$	Normal distribution	1.18	0.032
Fatigue limit $S_I/\text{MPa}$	Normal distribution	400	8.7

the reliability calculation was carried out again. From the calculation results, after optimizing the fatigue limit of the material of the crank arm, the fatigue strength reliability of the crank arm is 1, which meets the reliability design requirements of the crank arm.

### 4.3 Latching and Unlatching Mechanism Motion Reliability Design

The relevant parameters of the latch mechanism are random and the response is random due to machining errors, assembly errors, and environmental factors during its operation, which can have an impact on the reliability of the mechanism [10].

According to the working principle of the latch mechanism, the closing of the latch body is powered by a latching spring, and the fluctuation of the latching spring force will directly affect the reliability of the latch body closing movement. If the spring force is too large, it will cause the latch body to move too fast and impact other parts of the machine when it is closed; if the spring force is too small, it will cause the latch body to move slowly and fail to meet the requirement of closing time. Therefore, in this paper, the stiffness of the latching spring is input into the kinematic model as a variable parameter for kinematic simulation. Assuming that the initial value of the stiffness coefficient is  $100 \text{ N/m}$ , the stiffness coefficient of the latching

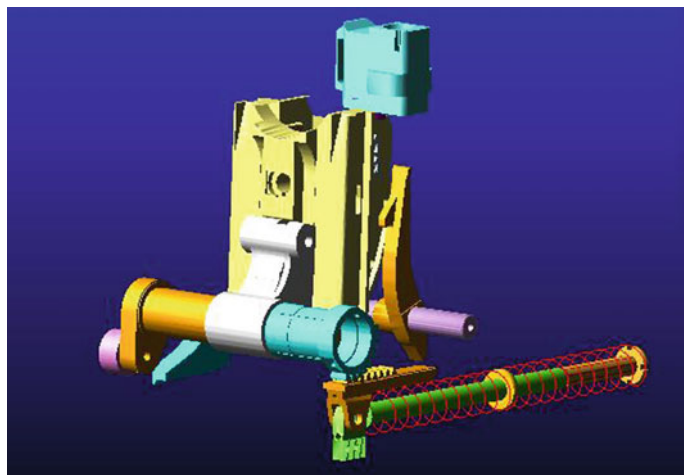


**Fig. 8** Kinematic model of the latch mechanism

spring can be expressed by  $K = (1 + a) \times 100$ , where  $a (-1, 1)$  is the variable coefficient.

The kinematic model of the latch mechanism built in ADAMS is shown in Fig. 8.

The variable  $a$  is used as input to simulate the motion state under different stiffnesses. According to the simulation results, when  $a$  is 0.1, the latching time meets and is closest to the design requirement of 0.12 s. When  $a < 0.1$ , the latching spring force is too small, resulting in a latching failure of more than 0.12 s, which cannot meet the use requirements; when  $a > 0.1$ , the latching time is within the required range, but due to the excessive spring force, the impact on the latch body buffer at the end of the latching stroke is larger, which is not conducive to the reliability of other parts, so the stiffness coefficient at  $a = 0.1$  is chosen as the design value.

## 5 Conclusion

This paper takes the reliability design of a type of naval gun latch mechanism as an example and starts from the aspects of mechanical engineering, stress analysis, failure causes, and failure form analysis to form a reliability design method for a typical mechanism of naval gun based on different failure forms. The aim is to solve the problem of weak reliability in the design stage of naval gun products in the past and improve its reliability level comprehensively, thus improving the practicality and sustained combat capability of naval guns, and at the same time providing a technical method for engineers to carry out reliability design work.

## References

1. Luo MZ (2014) Overview of reliability prediction methods for electronic products. Electron Sci Technol
2. Cao Q (2016) Reliability design of electronic products. Electron Test
3. Wang YZ (2018) Reliability design and analysis of aerospace electronic components. Sci Technol Innov Guide
4. Fu YM (2014) Reliability theory research and application of electromechanical equipment. Beijing University of Posts and Telecommunications
5. Lu TX (2011) Reliability design and analysis. National Defense Industry Press
6. Fu CY (2018) Fault tree-based fault analysis of a ship's gun early latch-off fault. Military Autom
7. Wang JW (2013) Fundamentals of reliability engineering. Science Press, Beijing
8. Wang YC (2019) Reliability analysis of ship machinery and equipment based on stress-strength interference model. Naval Electron Eng
9. Hu QG (2014) Mechanical reliability design and application. Electronic Industry Press, Beijing
10. Ke XW (2013) Action reliability analysis of caliber naval gun swing mechanism. Comput Simul

# Computer Aided Mechanical Mechanism Design for Industrial Design



Yanxia Liang

**Abstract** A mechanism rapid solving method was proposed based on motion mechanism coding aiming at black-box problems of mechanism design from designers. The mechanism was expressed as directed network models and saved as matrices. A mechanism database was built based on network models. A prototype system that could search mechanism units and combine units to achieve some solutions according to input and output conditions was developed based on CAD software. The system could provide schematic diagrams of mechanism for designers to perform evaluation, selection, and improvement. A typical design task test indicated that this method could search out or combine effective mechanism design cases, reduce requirements of designer mechanical design abilities, and improve design efficiency.

**Keywords** Industrial design · Mechanism design · Motion mechanisms · Coding · CAD

## 1 Introduction

In the conceptual design stage, industrial designers often need to carry out product creative design at the level of the mechanism principle. Most of the mechanisms in the product are the deformation or combination of several universal mechanisms, so you can refer to the design manual, case atlas, and other materials for design. This puts forward higher requirements for the mechanism design experience of industrial designers, which greatly limits the creativity of conceptual design.

Lanyun et al. [1] used object-oriented technology to carry out motion analysis and design of user-defined planar mechanisms. Weijuan et al. [2] developed a planar four-bar mechanism design system based on VB visual programming technology and realized the simulation and structural design of crank rocker, double crank, double rocker, crank slider, and other mechanisms based on user input. Yiling et al.

---

Y. Liang (✉)

Jiangsu Normal University, Xuzhou 221116, Jiangsu, China

e-mail: [745898591@qq.com](mailto:745898591@qq.com)

[3] established the mathematical model of the basic linkage group based on the mechanism composition principle, gave the design algorithm of the multi-linkage mechanism, and realized the rapid design and modification of the planar linkage mechanism based on the graphic simulation technology. Koza et al. [4] proposed the concept of constructive genetic programming through the study of 76 mechanism schemes, expressed the mechanism by tree coding, and gradually evolved a complex mechanism that met the design requirements. Lipson [5] applied the genetic programming method to the intelligent design of two-dimensional mechanisms and proposed two tree structure coding representation methods, namely, the top-down representation method for transforming existing mechanisms and the bottom-up representation method for assembling sub-mechanisms. Both methods can systematically explore the innovation of mechanisms with a certain degree of freedom. Hong [6] expressed the hinge mechanism and slider mechanism with the mechanism coding method of genetic programming, defined the connection rules between components and components with the terminator set and function set in genetic programming, and established an extensible mechanism library to solve the innovative design problem of mechanisms. Xiping [7] proposed an automatic generation method of motion chain graph based on matrix storage form in the mechanism trajectory design of agricultural machinery.

Most of the above documents are for mechanical designers or automatic solving programs. Facing the needs of industrial designers, the goal of this paper is to search the case base of the mechanism, then deform and combine them to get some schemes that meet the creative concept of designers, and then the designers will further screen and design in detail.

## 2 Coding of Motion Mechanism

The coding design principle of motion mechanism is oriented to three uses: (1) it is convenient for designers to manually code and create case bases; (2) The mechanism code is automatically generated based on the digital motion sketch drawn by the designer; (3) Based on the input and output conditions given by the designer, the coded mechanism library is searched, combined, and the mechanism diagram is drawn.

### 2.1 Network Model of Motion Mechanism

Referring to the current motion characteristics in electronic circuit design [8], the mechanism is reorganized around the transmission route of mechanism motion to form a tree or mesh structure, and the basic characteristics of mechanism motion are maintained while taking into account the intuitive visual characteristics. Taking the

planar linkage mechanism as an example, the expression method of the main design elements of the mechanism is as follows:

- (1) Fixing member. It refers to the reference components that do not participate in the movement, such as the ground and the rack, which are expressed as fixed nodes in the network model and identified by the number “0”. The kinematic pair relationship between the fixed member and other member nodes is represented by a solid line connection.
- (2) Moving member. A member that has a relative motion with a fixed member and has the function of transmitting motion is expressed as a node in the network model of the mechanism.
- (3) Input and output components. Input and output members also belong to moving members. Since these two kinds of components are the purpose of mechanism design, they are expressed separately. Since colors are easily recognized by programs in EXCEL documents or vector graphics documents, input and output components are represented by blue and red nodes, respectively.
- (4) Direction of motion transmission. The driving relationship between components (nodes) is indicated by arrows on the connecting lines between nodes: the beginning of the arrow is the driving part, and the end is the driven part. The arrow points in the direction of motion transmission.
- (5) Sports pair. In the network model, it is represented as the connection between two nodes. The model in this paper is mainly oriented to planar mechanisms, and there are three types of kinematic pairs involved: rotating pairs, moving pairs, and high pairs. In the network model diagram, they are expressed in different line types of node connecting lines: solid lines represent rotating pairs, dashed lines represent moving pairs, and double solid lines represent high pairs.
- (6) Composite hinge. The composite hinge involves at least three components connected together. In the conventional network, a connecting line can only connect two nodes. If more than three nodes are connected, the composite hinge is simplified, that is, it is treated as two independent hinges on the same component.

Taking the mechanism diagram of the long handle umbrella as an example, according to the description rules of the node expression, the network model expression can be obtained [9], as shown in Fig. 1.

## 2.2 Matrix Expression of Kinematic Mechanism

The network model of the mechanism is convenient for designers to understand the mechanism rationally in a certain degree of abstraction. At the same time, in order to realize the understanding of the program and facilitate the retrieval and other operations of the mechanism library, the network model is expressed in the equivalent matrix form and saved in the form of Excel.

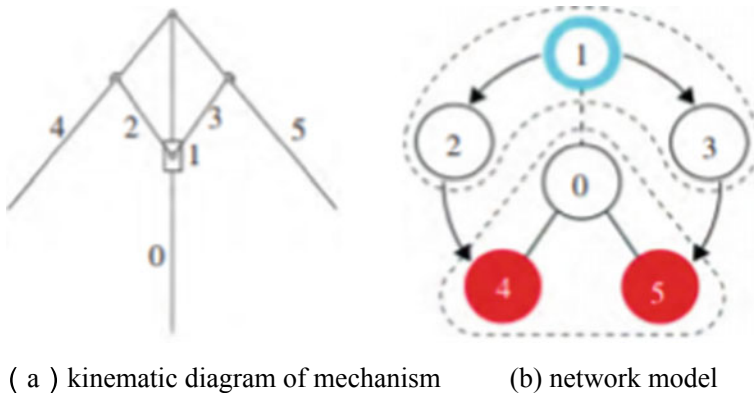


**Fig. 1** Network model of long handle umbrella mechanism

As shown in Fig. 2, in the Excel table, the first column on the left is the type information of each component in the mechanism, in which the input component is marked with blue (letter R), the output component is marked with red (letter C), and other components are marked with yellow. The green area in the second column and the first row is the code of each part of the mechanism in the mechanism diagram, where the code of the rack is represented by the letter D. The cells in the purple area record the types of kinematic pairs connected by the two parts.

In the purple area, the cells at the diagonal are used to identify the motion type of the component itself. The cell at the intersection of rows and columns of different parts identifies the type of kinematic pair at its connection point: G identifies the fixed frame, FG identifies the non-fixed axis rotation; Identify the moving pair with Y and the rotating pair with Z. If GZ indicates that the component rotates on a fixed axis, FGY indicates that the component rotates on a non-fixed axis. If there is no connection between components, the cell intersection is empty.

For multi-component motion, in order to distinguish the master–slave relationship between components, the corresponding marking rules are designed: use “+” to represent the active motion and “−” to represent the slave relationship. In the Excel

component type	component	D			
fame ( D )	D				
input component					
connecting rod					
connecting rod					
output component					

**Fig. 2** Area division of mechanism motion matrix expression in Excel

**Table 1** Motion matrix expression of long handle umbrella mechanism

Component type	Component	D	Component1	Component2	Component3	Component4	Component5
Frame	D	G	Y	-	-	Z	Z
Slider (R)	Component1	Y	GY	-Z	-Z	-	-
Connecting rod	Component2	-	+Z	FGZ	Z	-Z	-
Connecting rod	Component3	-	+Z	Z	FGZ	-	-Z
Connecting rod (C)	Component4	Z	-	+Z	-	GZ	-
Connecting rod (C)	Component5	Z	-	-	+Z	-	GZ

table, the uniform specification is to drive the components in the row direction by the components in the column direction. If member 1 drives member 2 to move through the rotation pair, the cell at the intersection of the column direction member 1 and the row direction member 2 in the table is marked with “+Z”, indicating that member 1 is actively moving toward the member 2. And the cell at the intersection of the column direction member 2 and the row direction member 1 is marked with “-Z”, indicating that member 2 is driven to member 1. If the two components are connected but there is no or unclear master-slave relationship, then “+” or “-” will be discarded.

Taking the long handle umbrella as an example, the mechanism is coded by using the matrix expression coding rules of the Excel table, as shown in Table 1.

### 3 Mechanism Innovation Design Based on Coding

Based on the definition of mechanism code described in this paper, various known mechanisms can be stored in Excel according to the coding rules for the computer to call. The designer draws the known mechanism diagram in the graphic design software CorelDRAW according to the preset drawing rules. The program automatically identifies the components and connection relationships of the mechanism, such as rods, sliders, moving pairs, hinges, and high pairs, and generates an Excel matrix based on the identified information and stores it in the mechanism Library. In this way, designers can easily and quickly expand the mechanism resource base, and entrust the task of understanding the mechanism to the program. Designers only need to draw a sketch according to the drawing rules.

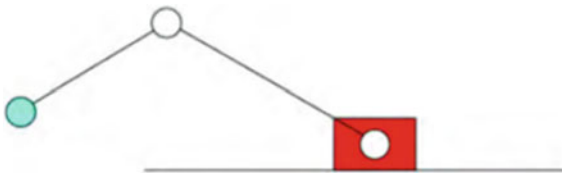


**Fig. 3** The schematic diagram of the mechanism drawn by the designer according to the design concept

Taking the planar linkage mechanism as an example, the rules for designers to draw the mechanism diagram in CorelDRAW software are as follows:

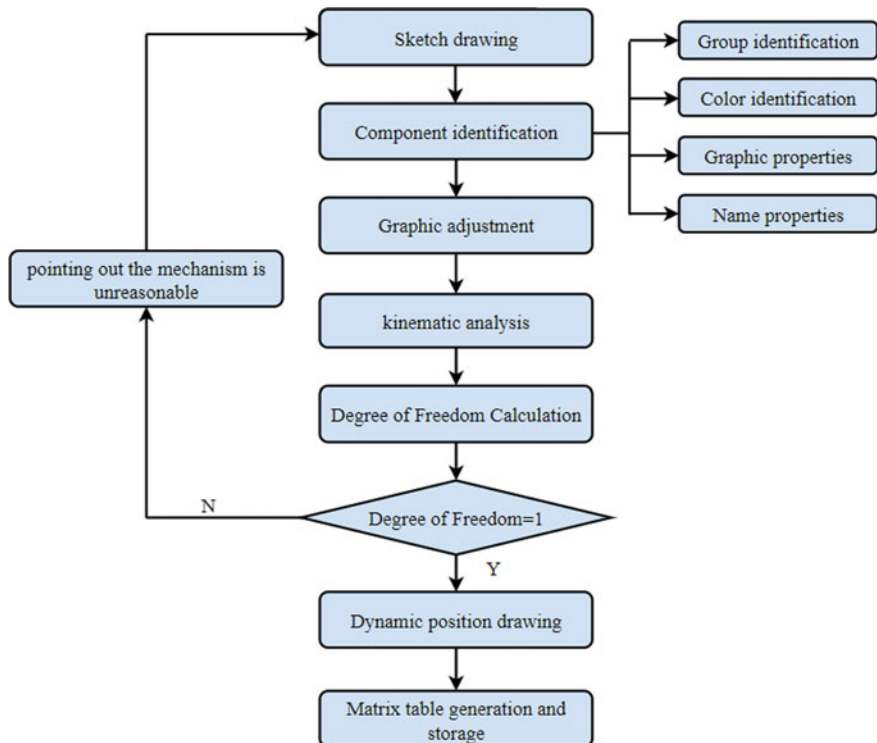
- (1) All components are expressed as a group, including component entities and motion pairs: entities can be a line or a closed figure; The rotation pair (hinge) is expressed by a small circle; The moving pair uses a straight line to represent the contact surface of the two components.
- (2) The expression figure of the kinematic pair is recognized by setting its name attribute, such as setting the name attribute to “hinge”.
- (3) Fixed hinge and movable auxiliary fixed guide rail shall be preceded by “fixed”, such as “fixed hinge”.
- (4) The input member and the output member are identified by the outline color or the fill color.

Figure 3 is a schematic diagram of the mechanism drawn by the designer according to the design concept.

For the sketch drawn by the designer, the program will automatically understand and adjust the inaccurate part of the design. When two components are connected, such as hinge connection, as long as the center positions of the hinge circles of the two components are close enough (such as smaller than the diameter of the hinge circles), they can be considered as hinged. The program automatically aligns and connects the hinge circles of the two components; if it is a moving pair, as long as the straight lines representing the contact surfaces of the two components are basically coincident, they will automatically align and fit together. After adjustment and improvement, the program automatically calculates the degree of freedom and judges the rationality of the mechanism. For a reasonable mechanism, the program will draw several dynamic positions according to the motion rules. Finally, according to the coding format designed in this paper, excel table information is automatically generated and stored.

Figure 4 is a flow chart of the designer expanding the institutional resource base.

The process for designers to use the mechanism resource library to obtain innovative mechanism design schemes is shown in Fig. 5.



**Fig. 4** Flow chart of designers expanding the institutional resource base

When using the mechanism case base for mechanism design, the designers first give the requirements for input and output components. The program searches the mechanism base according to the requirements, selects several unit mechanisms that meet the requirements, and then combines the unit mechanisms to obtain a variety of innovative mechanism design schemes. Then, the computer draws the mechanism sketch of the obtained mechanism scheme in the plane CAD software. Finally, the designers evaluate the advantages and disadvantages of the schemes generated by these intelligent technologies according to the mechanism diagram and select the appropriate scheme to apply to the product design.

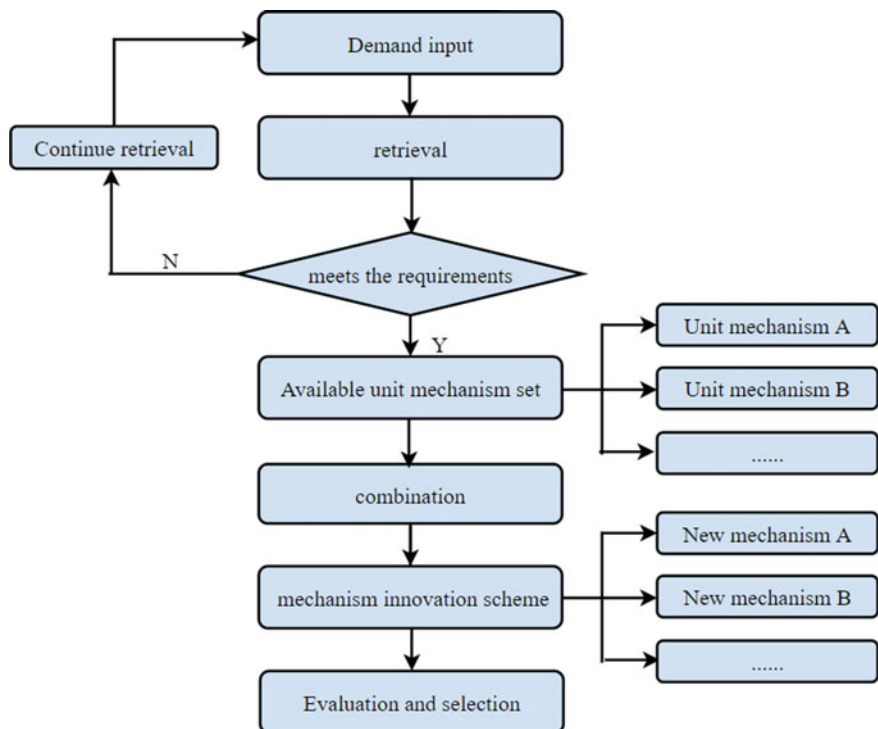


**Fig. 5** The process for designers to use the mechanism resource library to obtain innovative design schemes of mechanisms

## 4 Conclusion

The existing mechanism design research mainly explores the realizable mode and specific mechanical design. This paper explores a method of mechanism coding and a solution for industrial design. The coding mode and combination rules of the designed motion mechanism can be recognized and operated by the computer so that the industrial designers can easily obtain the required mechanism and expand the mechanism library, and reduce the requirements for the industrial designers' mechanism design knowledge. The method of establishing a unit mechanism database combined with computer-aided technology is proposed, which can provide a more convenient way for mechanism realization in industrial design, and save time and communication cost for designers to realize their creativity.

In this paper, some simple planar linkage mechanisms and low pairs are used as reference indexes for induction and treatment. Limited by the variability in the specific implementation of mechanism design, many mechanism movements in real life usually involve relatively complex categories such as spatial mechanisms and high pairs. In this case, the coding and connection rules of components will change

more. In order to deal with this situation, the coding and connection rules of the mechanism can be expanded and enriched according to the ideas provided in the paper, or supplemented by classification, so as to improve the functions of the prototype system, so that it can serve the innovative design of the mechanism more comprehensively.

## References

1. Lanyun S, Mei L, Bo Y et al (2001) Intelligent analysis of planar mechanism motion. *J Shandong Univ Architect* 16(4):70–73
2. Weijuan D, Hongmin Z, Yong Z (2011) Computer aided planar linkage design. *Digit Technol Appl* 29(6):52–53
3. Yiling Y, Fengyi L, Zhihong Z (2009) Computer aided design and simulation of planar linkage mechanism. *J Taiyuan Univ Sci Technol* 30(4):333–337
4. Koza JR (2010) Human-competitive results produced by genetic programming. *Genet Progr Evolvable Mach* 11(3):251–284
5. Lipson H (2008) Evolutionary synthesis of kinematic mechanisms. *Artif Intell Eng Des Anal Manuf* 12(22):195–205
6. Hong X (2007) Genetic programming and its application in mechanism innovation design. Jingdezhen Ceramic Institute, Jingdezhen
7. Xiping Y (2017) Application of innovative design of agricultural machinery mechanism trajectory. *Heilongjiang Sci Technol Inf* 20(2):18
8. Wenfang Y, Qi M (2005) VLSI power/ground grid design method. *Electron Packag* 5(6):31–34
9. Manzoni L, Castelli M, Vanneschi L (2013) A new genetic programming framework based on reaction systems. *Genet Progr Evolvable Mach* 14(3):457–471

# Research on Parameter Identification of the Mechanical Model of Damping Wall Based on Free Vibration Response



Wei Wang, Nana Liu, Yingjia Wang, Yan Zhang, and Junxia Sun

**Abstract** Research on the identification method of mechanical model parameters of damping wall based on free vibration response was carried out. This paper uses a silicone oil silt mixture as the viscous damping material for damping wall free vibration test based on a single degree of freedom system, introduces the basic idea of mechanical model identification method, and derives the calculation formula of damping force based on the energy method in the analysis of test theory method. In order to filter the high-frequency noise in the velocity time history and damping force time history, Butterworth low-pass filter is designed to filter the data. Draw the relationship curve between speed and damping force, and select the key control points on the curve for fitting to obtain the damping parameters and. Numerical simulation analysis is conducted based on Rosenbrock numerical integration method. The final analysis of the theoretical method is consistent with the experimental results, which shows that the application of the model parameter identification method is good.

**Keywords** Parameter identification method · Low pass filter · Numerical simulation · Rosenbrock integral method

## 1 Introduction

Viscous Damping Wall, as a new type of damper, was first proposed by Miyazaki [1], a Japanese scholar, in 1986. It has attracted extensive attention from scholars at home and abroad because of its remarkable damping effect. After more than 30 years of development, viscous damping walls have achieved many research results with practical significance [2–4]. However, due to the complex energy dissipation mechanism of the damping wall and the limitations of the test site conditions and test equipment, it is often difficult to accurately measure the damping force provided by the damping wall. In order to further deepen the research on viscous damping wall

---

W. Wang · N. Liu · Y. Wang · Y. Zhang · J. Sun (✉)  
ChongQing College of Architecture and Technology, Chongqing, China  
e-mail: [773464815@qq.com](mailto:773464815@qq.com)

and promote its application in practical projects, it is necessary to find appropriate test methods and model parameter identification methods to accurately measure the energy dissipation performance of the damping wall. As the basis of obtaining the test data, parameter identification is extremely important for building the mechanical model of the damping wall and calculating the energy dissipation performance of the damping wall. How to accurately measure the modal parameters of the damping wall is the key point of the current research. Some effective methods for identifying the parameters of the damper have been proposed by existing scholars. Ren Yichun [5] and others obtained the instantaneous amplitude and frequency of the response based on the nonlinear system identification method based on the adaptive sparse time–frequency analysis method. Research shows that this method can effectively identify the parameters of typical nonlinear systems. Xie Liyu [6] and others proposed a method for identifying structural parameters and unknown excitation based on an adaptive extended Kalman filter and applied it to the identification of damper characteristics of energy dissipation structures. Liu Yongqiang [7] and others proposed a new method for identifying the model parameters of magnetorheological dampers. This method does not require any prior knowledge of the model parameters and can evaluate the impact of each parameter on the output damping force, so as to select the best damping force control parameters. Zhang Lingling et al. [8] obtained the characteristic data of the metal rubber damper through experiments and proposed two methods to identify the hysteretic restoring force parameters of the damper: two-dimensional Lagrangian interpolation method and artificial neural network. Zhou Ying et al. [9] used Wen plastic element and viscous damping element to identify the parameters of viscoelastic damper, and compared with the test results, verified the rationality of the identification model. Yang et al. [10] used Bouc Wen model to identify the parameters of a magnetorheological damper, which has good adaptability to smooth curves. The above research methods have high accuracy and reliability for the parameter identification of dampers, but the applicability for the parameter identification of damping walls is not high, so it is necessary to further study the parameter identification methods of damping walls.

## 2 Introduction to Mechanical Model Identification Method

The acquired image is processed by the digital image correlation method (DIC) [11] through the Vic-2D equipment processing system to obtain the test data of displacement time history. Due to the limited sampling frequency, it is necessary to interpolate the displacement time history in the calculation process to obtain the interpolated displacement time history curve, making the time step smaller. Then, damping force time history and velocity time history are obtained by the energy method and central difference method, respectively. The acquisition error of original data introduces a high-frequency signal, which causes the damping force time history curve and velocity time history curve to be serrated, so filtering is required. Considering that the Butterworth low-pass digital filter has the characteristics that low frequency can

pass through high-frequency filtering and can achieve the maximum smoothness of the curve, Butterworth low-pass digital filter is used to filter the damping force time history curve and velocity time history curve, filter out the high-frequency components, and get a smooth curve. From the smooth displacement time history and damping force time history, the smooth speed damping force relationship curve is obtained, and then the key control points of the curve are selected to draw the skeleton curve of speed damping force. The curve is fitted by the self-compiled MATLAB program to determine the damping force parameters of the damping wall, so as to obtain the functional relationship between the velocity and the damping force.

When the Rosenbrock integration method is used for numerical simulation, the Jacobian matrix is obtained according to the sum of damping force parameters, and the appropriate integration step is selected according to the natural vibration period of the structure. A peak or valley value of displacement in the process of free vibration is selected as the initial displacement, and the initial velocity is selected as 0. Then, the displacement and velocity are gradually integrated to obtain the simulated displacement time history curve. Then, according to the damping force time history curve and displacement time history curve, the simulated hysteresis curve is obtained and compared with the displacement time history curve and hysteresis curve of the test.

### 3 Analysis of Test Theory and Method

#### 3.1 Derivation of Damping Force Calculation Formula Based on Energy Method

In this paper, a new algorithm for calculating the damping force of the damping wall by using the law of conservation of energy is derived. Here, the idea of the energy method is introduced. The kinetic energy and potential energy of any free vibration single degree of freedom structural system can be expressed as:

$$T = \frac{1}{2}mv^2 \quad (1)$$

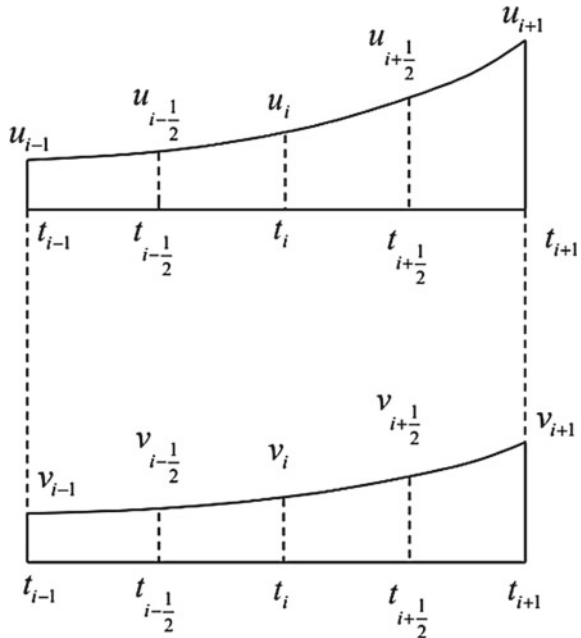
$$V = \frac{1}{2}ku^2 \quad (2)$$

The total energy of the system is:

$$E = T + V = \frac{1}{2}mv^2 + \frac{1}{2}ku^2 \quad (3)$$

As shown in Fig. 1, it is assumed that the displacement and velocity at time  $i$  are respectively  $\mu_i$  and  $v_i$ ; The displacement and velocity at time  $i + 1$  are respectively

**Fig. 1** Displacement time history curve and velocity time history curve within any two-time steps



$\mu_{i+1}$  and  $v_{i+1}$ ; The displacement and velocity at time  $i + 1$  are respectively  $\mu_{i-1}$  and  $v_{i-1}$ .

Then the displacement and velocity at  $v_{i-1}$  and  $\frac{i-1}{2}$  are:

$$u_{i+\frac{1}{2}} = \frac{1}{2}(u_i + u_{i+1}) \quad (4)$$

$$v_{i+\frac{1}{2}} = \frac{1}{\Delta t}(u_{i+1} - u_i) \quad (5)$$

$$u_{i-\frac{1}{2}} = \frac{1}{2}(u_{i-1} + u_i) \quad (6)$$

$$v_{i-\frac{1}{2}} = \frac{1}{\Delta t}(u_i - u_{i-1}) \quad (7)$$

Then the total energy of the system at the moment  $\frac{i+1}{2}$  is:

$$E_{i+\frac{1}{2}} = \frac{1}{2}mv_{i+\frac{1}{2}}^2 + \frac{1}{2}ku_{i+\frac{1}{2}}^2 = \frac{1}{2\Delta t^2}m(u_{i+1} - u_i)^2 + \frac{1}{8}k(u_i + u_{i+1})^2 \quad (8)$$

Similarly, the total energy of the system at the moment  $\frac{i-1}{2}$  is:

$$E_{i-\frac{1}{2}} = \frac{1}{2}mv_{i-\frac{1}{2}}^2 + \frac{1}{2}ku_{i-\frac{1}{2}}^2 = \frac{1}{2\Delta t^2}m(u_i - u_{i-1})^2 + \frac{1}{8}k(u_i + u_{i-1})^2 \quad (9)$$

The energy difference between the system from  $\frac{i+1}{2}$  time to  $\frac{i-1}{2}$  time is:

$$\begin{aligned} \Delta E &= E_{i+\frac{1}{2}} - E_{i-\frac{1}{2}} = \frac{1}{8}k(u_{i+1} - u_{i-1})(u_{i+1} + 2u_i + u_{i-1}) + \\ &\quad \frac{1}{2\Delta t^2}m(u_{i+1} - u_{i-1})(u_{i+1} - 2u_i + u_{i-1}) \end{aligned} \quad (10)$$

The displacement difference between the system from  $\frac{i+1}{2}$  time to  $\frac{i-1}{2}$  time is:

$$\Delta u = u_{i+\frac{1}{2}} - u_{i-\frac{1}{2}} = \frac{1}{2}(u_{i+1} + u_{i-1}) \quad (11)$$

The energy reduction value of the system from  $\frac{i-1}{2}$  time to  $\frac{i+1}{2}$  time is the work done by the damping force, which makes the total energy of the system attenuate. Therefore, the damping force at the i time can be calculated according to the energy difference and displacement difference of the system as follows:

$$F_D = \frac{\Delta E}{\Delta u} = \frac{1}{4}k(u_{i+1} + 2u_i + u_{i-1}) + \frac{1}{\Delta t^2}m(u_{i+1} - 2u_i + u_{i-1}) \quad (12)$$

At the same time, the velocity of the system at the moment can also be calculated according to the central difference method as follows:

$$v_i = \frac{1}{2\Delta t}(u_{i+1} - u_{i-1}) \quad (13)$$

### 3.2 Butterworth Filter

Butterworth filter [12] is a frequency selective filter. In order to filter the noise and error in the test data and obtain more accurate test analysis data, a Butterworth low-pass filter is introduced for processing.

### 3.3 Butterworth Low-Pass Filter Characteristics

The modulus of the frequency response of an n-order Butterworth low-pass filter [13] is:

$$|H(jw)| = \frac{1}{\sqrt{1 + (w/w_c)^{2n}}} \quad (14)$$

In this formula, n is the order of the Butterworth filter, and  $w_c$  is the cut-off frequency.

The ideal low-pass filter can pass through all frequencies below the cut-off frequency  $w_c$  (including  $w_c$ ) without attenuation, and completely filter out all frequencies in the stopband (above  $w_c$ ). However, an ideal low-pass filter is impossible to achieve, so some attenuation in the passband is allowed. The attenuation function of the Butterworth low-pass filter is:

$$\alpha = -20\lg|H(jw)| \quad (15)$$

The design indexes of the actual low-pass filter are  $\alpha_p$  and  $\alpha_s$ , which are respectively defined as the maximum allowable attenuation in the passband.

$\alpha_p = -20\lg|H(jw)|_{w=w_p}$ ; Minimum attenuation required in the stopband.

$\alpha_s = -20\lg|H(jw)|_{w=w_s}$

### 3.4 Design of Butterworth Low-Pass Filter

A butterworth low-pass digital filter is designed in a MATLAB environment by using three functions: butterd, butter, and filtfilt. Butord function can select the nth order of Butterworth filter N and 3 dB cut-off frequency  $w_c$  under the condition of the given filter performance, and use the butter function to design the transfer function of the filter. The main parameters of the Butterworth low-pass digital filter are as follows:

$$[N, w_c] = \text{butord}(w_p, w_s, R_p, R_s)$$

In this formula,  $W_p = 2/(F_s/2)$  is the passband cut-off frequency,  $W_p = 20/(F_s/2)$  is the stopband cut-off frequency,  $R_p$  is the maximum allowable attenuation of 2 dB in the passband,  $R_s = 20$  is the minimum allowable attenuation, 20 dB in the stopband, and  $F_s$  is the data sampling frequency determined according to the step size;

The coefficient of the transfer function can be calculated by the n-order number of the filter and the 3 dB cut-off frequency  $w_c$ ,  $[b, a] = \text{butter}(N, w_c)$ ;

The input signal is filtered according to the obtained transfer function coefficient. For example, the process of filtering the speed can be expressed as  $\text{velf} = \text{filyfilt}(b, a, vel)$

### 3.5 Curve Fitting of Speed Damping Force Relationship

In order to determine the functional relationship between velocity and damping force, it is necessary to calculate the performance parameters  $c$  and  $a$  of nonlinear viscous damping walls. Use MATLAB software to program, calculate the speed and damping force based on the formula derived above, and draw the speed damping force relationship curve. Select the leftmost point and rightmost point of each motion cycle relationship curve as the key control points of the skeleton curve. Connect the control points, get the skeleton curve of velocity damping force, and perform fitting analysis. Analyzing the relationship between damping force  $F_D$  and velocity  $v$ , the following calculation formula is given:

$$F_D = cv^\alpha \quad (16)$$

In this formula,  $c$  is the damping coefficient and  $\alpha$  is the damping index. Then take the logarithm of both sides to get the following formula:

$$\ln F_D = \ln c + \alpha \ln v \quad (17)$$

In this way, the nonlinear relationship between damping force  $F_D$  and speed  $v$  is converted into a linear relationship between  $\ln F_D$  and  $\ln v$ , and then the linear fitting is performed to obtain the performance parameters, and thus the functional relationship between the damping force  $F_D$  and speed  $v$  is determined.

### 3.6 Analysis of Numerical Simulation Methods

In the MATLAB program, the Rosenbrock integration method is used for numerical analysis. In order to meet the requirements of calculation stability and accuracy, the LRST2 algorithm with second-order accuracy is used in numerical simulation.

According to the test results of free vibration, a peak value or valley value is selected as the initial displacement, and the initial speed is selected as zero. In order to facilitate the program calculation, the initial speed is taken as a positive value that is small enough.

$$y(t_0) = y_0 \dot{y} = f(y, t) \quad (18)$$

In this formula,  $y$  is the state variable of the structure.

Divide the total time  $T$  into  $N$  equal time steps  $\Delta t$ , that is,  $\Delta t = T/N$ . Let  $t_k = k\Delta t$ , then  $y_k$  mean State variables for  $t_k$  time. Use LRST2 algorithm to calculate the state variable value  $y_{k+1}$  at time  $t_{k+1}$ :

$$y_{k+\frac{1}{2}} = y_k + \frac{1}{2}k_1 \quad (19)$$

$$y_{k+1} = y_k + k_2 \quad (20)$$

In these formulas:

$$k_1 = [I - \gamma \Delta t J]^{-1} f_k \Delta t \quad (21)$$

$$k_2 = [I - \gamma \Delta t J]^{-1} (f_{k+\frac{1}{2}} - J \gamma k_1) \Delta t \quad (22)$$

$I$  is the n-order identity matrix, and  $J$  is the Jacobian matrix at time  $t_k$ , that is,  $J = \partial f / \partial y|_{t=t_k}^{y=y_k}$ ,  $\gamma$  is the algorithm parameter. This simulation takes  $\gamma = 1 - \sqrt{2}/2$ .

This time, the integration step  $\Delta t = 0.002s$  is taken, and the simulated displacement time history curve is obtained through gradual integration under the condition that the initial displacement and initial velocity are known. Then the relationship curve between displacement and damping force can be drawn according to the time history curve of damping force.

## 4 Summary

In this paper, the above experimental theoretical analysis method is applied to the free vibration test based on the damping wall, and the parameter identification method of the mechanical model of viscous damping materials is analyzed. The original displacement time history curve and hysteresis curve obtained from the test are compared with the numerical simulation results, and the following conclusions are drawn:

(1) The energy method is used to derive the damping force calculation formula, which is suitable for calculating the damping force of the single degree of freedom viscous damping wall. The MATLAB program is compiled with this formula to calculate the damping force, and the calculation result has high accuracy.

(2) Through the verification of Gaussian noise, the Butterworth digital filter designed in this paper can effectively filter the high-frequency noise in the digital signal, and its noise reduction performance is good.

(3) By fitting and analyzing the relationship curve between velocity and damping force, damping parameters can be obtained, which can better reflect the functional relationship between the shear velocity of the steel plate of viscous damping wall and damping force.

(4) Rosenbrock integral method is used to conduct numerical simulation analysis, and the simulation results are in good agreement with the experimental results, which verifies the effectiveness and correctness of the model parameter identification method in this paper.

## References

1. Miyazaki M, Arima F, et al. Earthquake response control design of buildings using viscous damping walls[C]. Proceedings of first East Asia Pacific Conference. Bangkok :[s,n], 1986: 1882–1891
2. Robert J M, Douglas P T. Fluid viscous dampers for high-rise buildings[J]. The Structural Design of Tall and Special Buildings, 2003, 12(2): 145 - 154.
3. Elif C K, Kemal M. An optimization study for viscous dampers between adjacent buildings[J]. Mechanical Systems and Signal Processing, 2017, 89: 88–96
4. ZHOU Ying, CHEN Peng. Shaking table tests and numerical studies on the effect of viscous dampers on an isolated RC building by friction pendulum bearings[J]. Soil Dynamics and Earthquake Engineering, 2017, 100: 330–344.
5. Yichun REN, Dong XU (2020) JIANG Youbao, Identification of nonlinear vibration system by adaptive and sparsest time-frequency analysis[J]. Chinese J Appl Mech 37(3):1233–1238
6. XIE Liyu, LI Xianzhi, ZHANG Rui, et al. Identification of passively-controlled energy dissipation structure and additional damping force based on adaptive extended Kalman filter[J]. Journal of Hunan University(Natural Sciences), 2020, 47(11):66–73.
7. Yongqiang LIU, Shaopu YANG, Yingying LIAO (2018) A new method of parameters identification for magnetorheological damper model[J]. Journal of Mechanical Engineering 54(06):62–68
8. ZHANG Lingling, YANG Zhichun, SUN Hao. Modeling of a type of nonlinear metal rubber damper and its parameter identification[J]. Mechanical Science And Technology For Aerospace Engineering, 2007, 26(05):558–562.
9. Ying ZHOU, Rui LI, Xilin LV (2013) Experimental study and parameter identification of viscoelastic dampers[J]. Structural Engineers 29(1):83–91
10. Yang G, Spencer BF, Carlson JD et al (2002) Large-scale MR fluid dampers modeling and dynamic performance considerations[J]. Eng Struct 24(3):309–323
11. Baldi A (2020) Robust Algorithms for Digital Image Correlation in the Presence of Displacement Discontinuities. Optics and Lasers in Engineering, 133
12. Oppenheim AV, Willsky AS, Nawab SH et al (2013) Signals and systems (Second Edition)[M]. Publishing House of Electronics Industry, Beijing
13. Shibendu M, Suman KS, Rajib K et al (2018) Optimal design of fractional order low pass Butterworth filter with accurate magnitude response. Digital Signal Processing

# Experimental Study on Electrical Discharge Precision Orbital Machining of Closed Impeller Based on Response Surface Optimization



Yicong Qiu

**Abstract** EDM orbital machining is often used for a large number of precision structure machining due to its good inter-electrode discharge state and high machining accuracy. Aiming at a rough-machined closed impeller blank with inter-blade channels, the electric discharge clean-up machining of the leading edge of the blade was studied. After analysis and univariate comparison experiments to determine the electrode orbiting mode and orbiting axis, the orbiting machining parameters were optimized based on the response surface method, and the orbiting machining parameter combinations with the smallest surface roughness and the smallest profile error were obtained. Finally, the leading edge of the blade was cleaned with comprehensive optimal process parameters, and the machining leading edge met the design requirements, which verified the feasibility of the optimized scheme. The research results of this paper will serve as a reference for the future development and engineering application of EDM orbital machining and have important value.

**Keywords** Electrical discharge machining · Leading edge of blade · Response surface methodology · Closed impeller · Orbital machining

## 1 Introduction

The closed integral impeller is a key component of an aero engine [1], and the leading-edge surface needs to be smoothly connected with the main profile surface of the blade, so as to avoid the interference of the leading-edge flow and the generation of separated bubbles, and it can also minimize the stagnant pressure drop from the inlet to the outlet of the channel [2]. At present, the main machining technologies include multi-axis CNC milling [3–5], welding [6–8], casting, forging, grinding [9, 10], additive manufacturing [11], electrochemical machining, and electric discharge machining [12–14].

---

Y. Qiu (✉)

Nanjing University of Aeronautics and Astronautics, Nanjing 210016, China

e-mail: [qiyicong@nuaa.com](mailto:qiyicong@nuaa.com)

The EDM machining parameters have a direct impact on the forming accuracy and surface quality of the leading edge of the blade. However, the optimal results cannot be obtained by evaluating the machining parameters only through experiments, hence the combination of multiple optimization algorithms is usually used to optimize the strategy. Jafarian [15] and Moganddam et al. [16] optimized the machining through the combination of artificial neural network and non-dominated sorting genetic algorithm or particle swarm algorithm. Kumar et al. [17] used the Taguchi method and regression equation to generate a database of EDM machining parameters, which provide references for a reasonable selection of machining parameters.

However, during the machining of the leading edge of the blade, due to the narrow discharge gap and the existence of the corner, the product obtained by discharge will be difficult to eject, which will seriously affect the quality of the machined surface and even cause arcing to burn the leading-edge surface. There are usually two ways to solve this problem. One is to lift the tool (electrode); the other is to use orbital machining. The research of Mathai [18] shows that orbiting machining is more suitable for machining titanium alloy components than traditional EDM.

Different from normal EDM parameters, orbital machining parameters mainly refer to electrode movement parameters, such as orbiting period, orbiting radius, etc. The optimization of orbital machining parameters can improve the discharge state between electrodes and further improve the machining quality. Dave et al. [19–21] obtained the best combination of orbital machining parameters through the Taguchi method and dimensional analysis method.

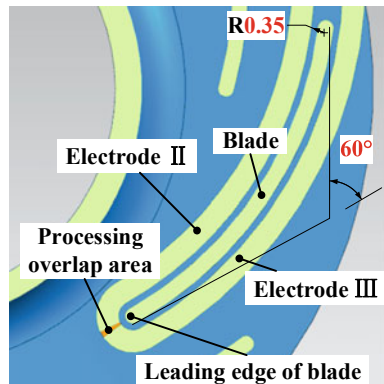
Due to the response, surface law can establish a linear regression equation about the parameters to be optimized to obtain the optimal parameters, hence it has been applied in new material mechanical drilling [22, 23], EDM boring [24], EDM micromachining and other fields, but it is relatively less used in EDM orbiting machining [25].

In view of the above-mentioned research deficiencies, this paper intends to use different orbital machining techniques to conduct comparative machining experiments on the leading edge of a closed impeller blade. Through the analysis of the machining results, the optimal orbiting technique is obtained, and the orbiting technique parameters are optimized by the response surface method. Finally, actual machining experiments are carried out to verify the feasibility of the above-mentioned orbital machining parameters.

## 2 Research Object Analysis

Figure 1 is a cross-sectional view of the leading edge of the blade and machining plan. Two long and narrow electrodes are used to clean up the machining of the leading edge. The blades are two-dimensionally curved and twisted, the twist angle of the side at the leading edge and outlet is  $60^\circ$ . The radius of the leading edge is only 0.35 mm; hence the thickness of the blade is only 0.7 mm, which is a thin-walled

**Fig. 1** Cross-sectional view of the leading edge of the blade and machining plan



structure. The gap between the channels is small, only 2.3 mm at the narrowest position. The difficulties of using EDM are as follows:

- (1) The channel is long and narrow, and the machining accessibility is bad, especially when the leading edge of the blade is close to the hub of the impeller, the clean-up machining electrode is not easy to reach.
- (2) The channel between the leaves is closed up and down, and the electrode can only enter the channel from the outside.
- (3) Due to the blade thickness being very small, it is easy to produce over-cutting during machining, so the requirement of the shape and size accuracy of the electrode is extremely high. Meanwhile, the electrode is also a thin-walled structure, and it is easy to affect the machining accuracy due to its own deformation during manufacturing and clamping.
- (4) When using sub-area machining, it is easy to form a machined trace at the junction of the machining area.

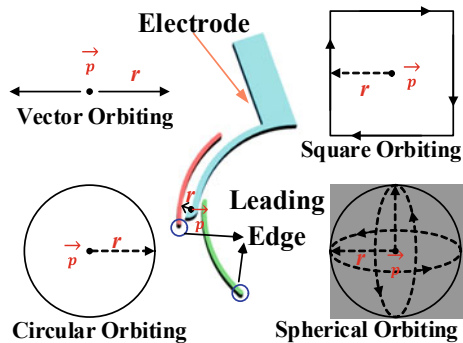
The above-mentioned difficulties show that in addition to the design of the electrode and the feed path, the selection of the orbital machining method and the orbiting axis is also extremely important to the quality of the leading edge. Furthermore, it is vital to reasonably design the discharge parameters when using the clean-up machining electrode to prevent excessive electrode wear and arc discharge.

### 3 Orbital Machining of the Leading Edge of the Blade

#### 3.1 Orbiting Method Selection

As shown in Fig. 2, EDM orbital machining technology can be divided into vector orbiting, circular orbiting, square orbiting, and spherical orbiting according to orbiting methods. In both vector orbiting and square orbiting, the electrode makes

**Fig. 2** Four forms of orbital machining



periodic reciprocating linear motion relative to the workpieces, and the error is relatively large when machining curved and twisted surfaces, so it is not suitable for leading edge processing.

In spherical orbiting, the electrode moves along a small-radius spherical surface centered on a fixed point on the main axis. The orbiting radius can be adjusted to adapt to changes in the curvature of different curved surfaces. Therefore, spherical orbiting can be used for almost all surface machining. However, it has high requirements on the machine tool servo control system, and compared with other orbiting methods, the effective discharge time of spherical orbiting at the same time is shorter, and the machining efficiency is lower.

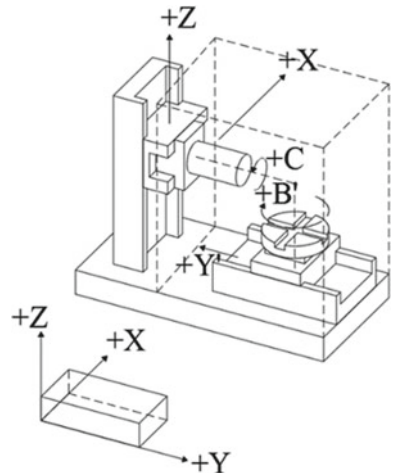
The circular orbiting can be regarded as the projection movement of the spherical orbiting in the plane perpendicular to the feed direction. Circular orbiting can not only change the orbiting radius step by step to change the discharge parameters and achieve semi-finishing or finishing, but also when used in conjunction with an electrode with a guide chute, the discharge products are easier to eject. But compared with spherical orbiting, circular orbiting has higher flexibility in use, so it is suitable for machining blade leading edges similar to round corners. Considering factors such as machining accuracy, machining efficiency, and cost, the circular orbital machining technology is finally selected for the leading edge shown in Fig. 1.

In the actual test, based on the machine tool structure shown in Fig. 3, the orbiting axis was selected, and the leading edge was orbitally machined. The sample block in Fig. 3 will be fixed on a disk-shaped table with cross grooves, and the electrode is driven by the self-orbiting of the machine spindle to realize the orbiting machining of the sample block.

### 3.2 Determination of Orbiting Axis

As shown in Fig. 4, CNC code is used to control the electrode to make a circular orbiting around the orbiting axis to realize the back-and-forth machining around the

**Fig. 3** Schematic diagram of machine tool structure



center of the circle. In order to compare the machining accuracy and surface roughness differences of the channels machined by different orbiting axes, the electrodes were made to circulate the X, Y, and Z axes and the X plus Y axes at the same time, and the sample was subjected to an orbital machining comparison test. The orbiting axis is determined by comparing the forming accuracy and surface roughness of channels machined by different orbiting axes.

Figure 5 shows the results of machining using different orbiting axis. It can be seen that the surface roughness processed without orbiting is significantly bigger than that with orbiting. At the same time, there are local burns in the deep part of the channel, which is mainly due to the narrow and large degree of twisting of the channel, and a large amount of erosion products accumulate, resulting in the phenomenon of arcing.

A three-coordinate measuring instrument and a surface roughness meter were used to measure the maximum profile error and surface roughness after orbiting. Table 1 shows the roughness and the maximum profile error of the channel machined

**Fig. 4** CNC code format of orbiting machining

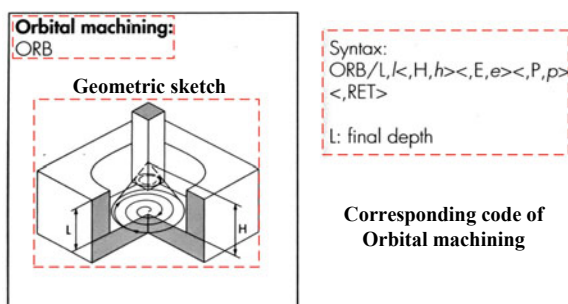


**Fig. 5** Channels machined by different orbiting axis

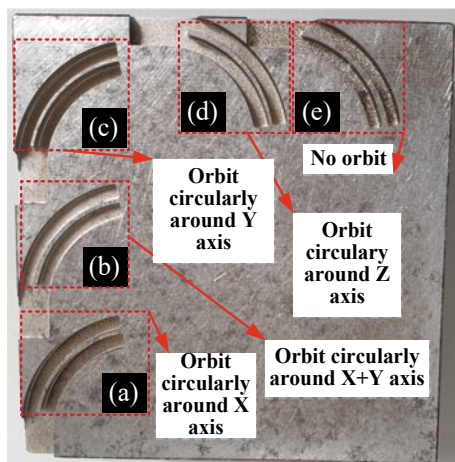


**Table 1** Accuracy and surface quality of different axis of orbiting

Orbiting axis	Maximum error (mm)	Roughness (Ra)
X axes	0.1139	2.863
X + Y axes	0.0602	2.665
Y axes	0.1054	2.816
Z axes	0.1448	2.901
No orbiting	0.3251	3.147

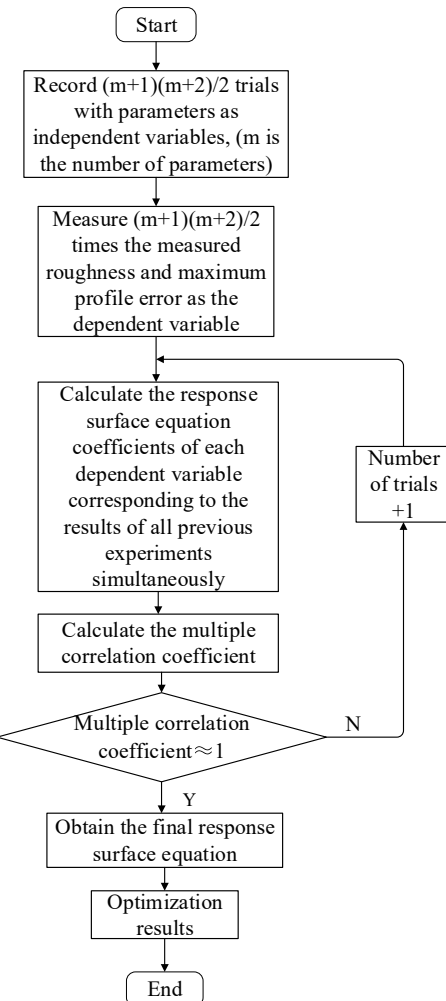
by different orbiting axis. Since the surface roughness and the maximum profile error obtained by the orbiting of the X + Y axis are the smallest, the final choice of the orbiting axis is the X + Y axis.

### 3.3 Orbital Machining Parameter Optimization

The general process of parameter optimization by the quadratic response surface method is shown in Fig. 6. The general expression of the quadratic response surface can be expressed as Eq. (1).

$$y(x) = c + \sum_{j=1}^k c_j x_j + \sum_{j=k+1}^{2k} c_j x_{j-1}^2 + \sum_{j=1, j < i}^k c_{j+2k} x_j x_i \quad (1)$$

**Fig. 6** Optimization process of quadratic response surface method



where  $k$  is the number of input independent variables, that is, the number of orbital machining parameters that need to be optimized, so  $k$  is taken as 3. Let  $x_1$ ,  $x_2$ , and  $x_3$  denote the three machining parameters of discharge gap, orbiting period, and orbiting- radius, respectively, then the secondary response surface function of the orbital machining parameters can be expressed as Eq. (2).

$$y_2(x) = c_0 + c_1x_1 + c_2x_2 + c_3x_3 \quad (2)$$

In Eq. (2),  $y(x)$  represents the fitting value of the surface roughness or profile error of the leading edge of the blade after machining. When the secondary response surface function reaches a certain fitting accuracy, the fitting value can approximately

replace the actual measured value of surface roughness or machining error. Therefore, the response surface function can be directly used for the optimization of machining parameters. The final expression of the response surface function can be obtained by fitting the coefficients before each item by least squares, which can be expressed as:

$$\mathbf{c} = [c_0, c_1, \dots, c_{10}]^T. \quad (3)$$

$$\boldsymbol{\alpha} = [1, x_1, \dots, x_2 x_3]^T \quad (4)$$

$$\mathbf{y} = [y_1, y_2, \dots, y_{10}]^T \quad (5)$$

When  $y_1, y_2, \dots, y_{10}$  represent the roughness value measured in 10 tests, the response surface function of the roughness with respect to the discharge gap, orbiting period, and orbiting radius can be obtained after fitting. In the same way, the response surface function of processing error with respect to machining parameters can be obtained.

$$\boldsymbol{\alpha}_i = \left[ 1, x_1^{(i)}, \dots, x_2 x_3^{(i)} \right]^T \quad (6)$$

$$\mathbf{A} = [\boldsymbol{\alpha}_1, \boldsymbol{\alpha}_2, \dots, \boldsymbol{\alpha}_{10}]^T \quad (7)$$

In Eq. (6),  $\boldsymbol{\alpha}_i$  indicates the combination of machining parameters used in the  $i$ -th test, and the combination of parameters used in all 10 tests can be represented by Eq. (7). And  $\mathbf{c}$  should be able to minimize the second norm of  $\mathbf{y} - \mathbf{Ac}$ . According to the projection theorem Eq. (8), Eq. (9) is obtained.

$$\langle \mathbf{y} - \mathbf{Ac}, \mathbf{A} \rangle = 0 \quad (8)$$

$$\mathbf{c} = (\mathbf{A}^T \mathbf{A})^{-1} \mathbf{A}^T \mathbf{y} \quad (9)$$

In order to obtain the value of  $\mathbf{c}$ , it is planned to use different parameter combinations to perform 10 trial machining on a test sample and calculate the fitting accuracy according to the measured surface roughness and the maximum profile error after machining. If the fitting accuracy is low, the number of tests should be appropriately increased. Table 2 shows the parameter combination used for 10 trial machining and the measured values of roughness and maximum error after machining.

**Table 2** Trial machining parameters and results

NO	Discharge Gaps (mm)	Orbiting Period(s)	Orbiting Radius (mm)	Maximum Error (mm)	Surface Roughness(Ra)
1	0.05	0.2	0.25	0.0823	2.669
2	0.05	0.4	0.25	0.1019	2.816
3	0.10	0.4	0.20	0.0944	2.774
4	0.10	0.6	0.20	0.1207	2.906
5	0.15	0.4	0.15	0.0904	2.676
6	0.15	0.8	0.15	0.1325	2.975
7	0.20	0.6	0.10	0.1267	2.913
8	0.20	1.0	0.10	0.0948	2.791
9	0.25	0.8	0.05	0.1093	2.859
10	0.25	1.0	0.05	0.0896	2.770

$$\mathbf{c} = \begin{bmatrix} 2.4261 \\ -9.4926 \\ -12.0799 \\ 14.2484 \\ -71.2776 \\ 13.0419 \\ 5.5426 \\ 31.1534 \\ -70.2688 \\ -42.4509 \end{bmatrix} \quad (10)$$

$$y_1(x) = 2.4261 - 19.4926x_1 - 12.0799x_2 + 14.2484x_3 \quad (11)$$

When  $y$  is the roughness, Eq. (10) can be obtained from Table 2, and Eq. (11) represents the roughness response surface function of the machining parameters.

The complex correlation coefficient can be obtained from the measured values shown in Table 2 and the corresponding fitting function value, and the fitting accuracy is represented by the complex correlation coefficient. When the value of the coefficient is closer to 1, it indicates that the fitting accuracy is higher. The multiple correlation coefficient can be expressed as [19].

$$R^2 = S_n/S_y \quad (12)$$

$$S_n = \sum_{i=1}^N \left( \tilde{y}_i - \bar{y} \right)^2 \quad (13)$$

$$S_y = \sum_{i=1}^N \left( y_i - \bar{y} \right)^2 \quad (14)$$

$$\bar{y} = \left( \sum_{i=1}^N y_i \right) / N \quad (15)$$

In Eq. (12),  $\tilde{y} = y(x)$ . Therefore, the complex correlation coefficient of the roughness response surface function is approximately 1, and no additional tests are needed.

From the above process, the maximum machining error response surface function of the machining parameters can also be expressed as Eq. (16).

$$y_2(x) = 0.1214 - 0.8606x_1 - 0.9147x_2 + 1.6921x_3 \quad (16)$$

The multiple correlation coefficient is approximately 1, and no additional experiments are required. Because the smaller the roughness and the maximum machining error value, the higher the quality of the machined workpieces. Therefore, the optimization machining parameter is transformed into orbital machining parameters  $x_i$  when the two response surface functions are minimized under the constraints of Eq. (17).

$$x_{i \min} < x_i < x_{i \max}, \quad i = 1, 2, 3 \quad (17)$$

As shown in Figs. 7 and 8, it can be concluded that the optimal machining parameter of each other are as follows: when the minimum surface roughness is required, the discharge gap is 0.02 mm, the orbiting period is 0.34 s, and the orbiting radius is 0.09 mm for machining; when the highest machining accuracy is required, the discharge gap is 0.06 mm and the orbiting period is 0.6 s, the orbiting radius is 0.08 mm for machining. Due to the little difference between the discharge gap and the orbiting radius of the minimum surface roughness and the highest machining accuracy, the major difference is the orbiting period. Considering the precondition of improving machining accuracy as much as possible, the comprehensive orbital machining parameter is adjusted as follows: the discharge gap is 0.15 mm, the orbiting period is 0.6 s, and the orbiting radius is 0.15 mm for machining.

## 4 Orbital Machining of the Leading Edge of the Blade

In order to verify the feasibility of the comprehensive optimal orbital machining parameters obtained before, based on the schematic diagram of the leading edge of blade orbital machining technology shown in Fig. 9, the leading-edge machining test was carried out on the open blank and the closed blank using a clean-up machining electrode.

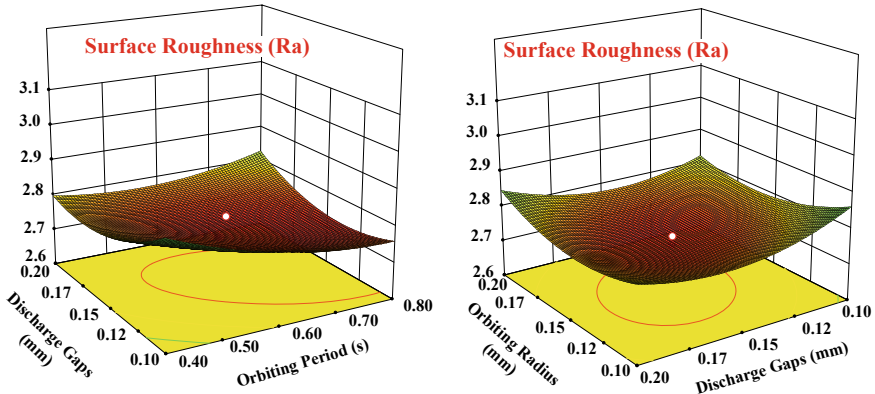


**Fig. 7** Response surface of surface roughness

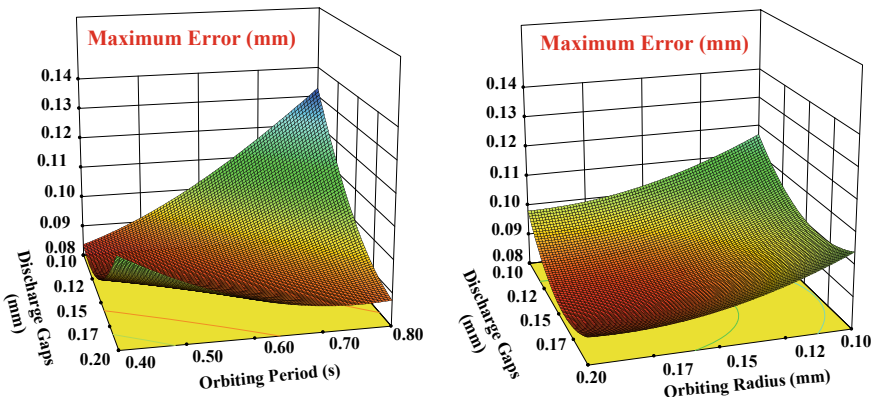


**Fig. 8** Response surface of maximum error

#### 4.1 Trial Machining of the Leading Edge of the Blade

Appropriate electrical parameters can reduce electrode loss and improve accuracy. When the peak current is constant, the pulse width decreases, the electrode loss will increase, and the narrower the pulse width, the more obvious the trend of electrode loss increase; when the pulse width is very large, the peak current has little effect on the electrode loss [20]. Table 3 is partial discharge parameters of leading-edge trial-machining.

In order to ensure the reliability of the orbital machining for clean-up, firstly, the open blank is machined for testing, and then the closed blank is actually machined. The inter-blade channel after clean-up machining is shown in Fig. 10. It can be seen that the leading-edge arc surface processing results are good.

**Fig. 9** Orbital machining technology sketch

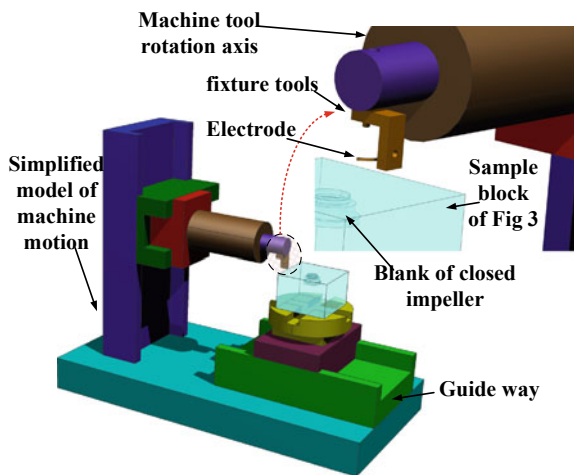
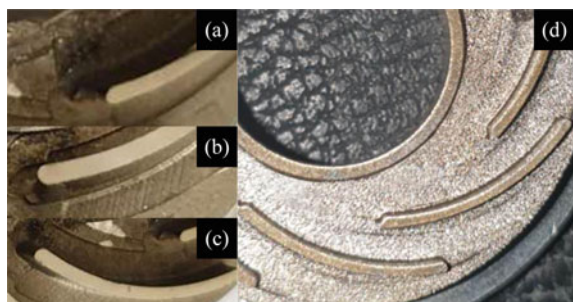


**Table 3** Partial discharge parameters of leading-edge trial machining

Machining parameters	Setting value
Processing voltage	200 (V)
Peak current	3 (A)
Pulse width	25 ( $\mu$ s)
Pulse interval	25 ( $\mu$ s)
Gap voltage	29 (V)

**Fig. 10** The interleaf channel after clean-up machining



The results of Fig. 10a–c show that the machining accuracy of the leading edge can be effectively improved by using the orbital machining parameters optimized by the response surface. Figure 10d shows the leading edge of the blade in the cut-away closed twisted channel. It can be seen that the clean-up result is good, and the leading-edge profile is smooth.

## 5 Comparative Analysis of Test Results

After measurement, the maximum profile error of the leading edge of the blade machined by the optimal machining parameters meets the requirements of the design ( $\pm 0.02$  mm), and the surface roughness  $R_a = 2.7$ . Comparing the machining results measured in Table 2 simultaneously, when the discharge gap is the smallest, the orbiting radius is the largest, and the orbiting period is as small as possible, the maximum profile error and surface roughness reach the minimum value at the same time, the machining quality is the highest.

The profile accuracy of Fig. 10a–c is generally better than that of Fig. 10d. The reason is that in closed condition, the accumulation of machining products in orbital machining is more serious than that in open condition. In the actual machining process, the short circuit phenomenon caused by excessive accumulation of machining products can be greatly reduced by slightly reducing the orbiting period to increase the orbiting times per unit time.

When the discharge gap is equal to the orbiting radius, the surface roughness is improved greatly, and as the difference between the two gradually increases, the maximum error is also improved. At the same time, the surface roughness is worse when the orbiting period is larger, which is because, when the size of the orbiting area is the same, the larger orbiting period corresponds to the slow orbiting, which makes the ejection of the discharge products more difficult and the discharge conditions in the channel are bad. This leads to a decline in processing quality.

## 6 Conclusion

1. By comparing the profile error and surface roughness of different orbital machining, the forming laws of different orbiting axes are mastered: from the perspective of morphology, the channel profile without shaking is rougher than others, and the machining surface finish of the X-axis circular shaking mode and the Y-axis circular shaking mode is not much different, and the X-axis + Y-axis circular shaking mode is more sufficient than the above single axis machining.
2. Orbital machining parameters of the leading edge of the blade are optimized by the optimization method based on the quadratic response surface function optimizes. The rule of discharge gap, orbiting period, and orbiting radius is mastered. Orbiting machining parameters of the leading edge based on the profile error and surface roughness are obtained.
3. The trial manufacturing of the leading edge of the blade shows that when the discharge gap is consistent with the orbiting radius, the machining accuracy is the best, and the surface roughness can be further improved by adjusting the shaking period.

4. Then, there is still room for further optimization of the above research methods. Subsequently, artificial intelligence algorithms will be used to improve the accuracy of iteration and better jump out of the local optimal solution. In addition, for the orbital machining, the mechanism behind it is still unclear, so further analysis of its mathematical model is needed.

## References

1. Li J, Wang X, Wang Y (2020) Effects of a combination impeller on the flow field and external performance of an aero-fuel centrifugal pump. *Energies* 13(4):13–18
2. Hamakhan, I. A., Korakianitis.: I Aerodynamic performance effects of leading-edge geometry in gas-turbine blades. *Applied Energy* 87(5), 1591–1601 (2010).
3. Huang W, Chen ZT, Chen WY (2012) Principle of machining variant curvature blending surfaces with counter t-orus cutter. *J Beijing University Aeronautics Astronaut* 38(8):1118–1123
4. Shan CW, Zhang DH, Liu WW (2009) A novel spiral machining approach for blades modeled with four patches. *Int J Advanced Manufacturing Technol* 43(6):563–572
5. Wan N, Liu P, Chen ZZ (2019) Constructing process models of engine blade surfaces for their adaptive machining: An optimal approach. *J Manufacturing Sci Eng* 141(1):501–508
6. Brandt M, Sun S, Bishop M (2009) Laser repair of steam turbine blades. *Chin J Lasers* 36(12):3240–3244
7. Muangson N, Wongsa S, Phung-on I (2013) Optimization of induction brazing parameters for stellite strip of steam turbine blade using Taguchi-Neural Network. *Key Eng Mater* 545:225
8. Walale A, Chauhan AS, Satyanarayana A (2018) Analysis of shrinkage & warpage in ceramic injection molding of HPT vane leading edge core of a gas turbine casting. *MATERIALS TODAY-PROCEEDINGS* 5(9):19471–19479
9. Liu ZY, Huang W, Wei HP (2013) Research on the technology of NC abrasive belt grinding for the leading and trailing edges of aero-engine blades. *Advanced Materials Research* 797:67
10. Li X, Ma S, Meng FJ (2015) Surface integrity of GH4169 affected by cantilever finish grinding and the application in aero-engine blades. *Chin J Aeronaut* 28(5):1539–1545
11. Ealy B, Calderon L, Wang WP (2017) Characterization of laser additive manufacturing-fabricated porous superalloys for turbine components. *Journal of Engineering for Gas Turbines and Power-Transactions of the ASME* 139(10):89–93
12. Yu LG, Zhu D, Yang YJ (2020) Improvement of leading-edge accuracy by optimizing the cathode design plane in electrochemical machining of a twisted blade. *Proceedings of the Institution of Mechanical Engineers Part B-Journal of Engineering Manufacture* 234(4):814–824
13. Zhu D, Yu LG, Zhang RH (2018) Design of the cross-structural cathodes in electrochemical machining of aero-engine blades. *Mach Sci Technol* 22(5):851–864
14. Wang H, Zhu D, Liu J (2019) Improving the accuracy of the blade leading/trailing edges by electrochemical machining with tangential feeding. *CIRP Ann Manuf Technol* 68(1):165–168
15. Jafarian F (2020) Electro discharge machining of Inconel 718 alloy and process optimization. *Mater Manuf Processes* 35(1):95–103
16. Moghaddam M, Azadi D, Kolahan F (2020) Modeling and optimization of the electrical discharge machining process based on a combined artificial neural network and particle swarm optimization algorithm. *Scientia Iranica* 27(3):1206–1217
17. Kumar S, Dave S, Harshit K, Desai D, Kayur P (2018) Methodology for database development for electro discharge boring of aerospace material. *Int J Mater Prod Technol* 56(4):295–312

18. Mathai V, Dave H, Desai K (2016) Study on effect of process parameters on responses during planetary edm of titanium grade 5 alloy. International Journal of Modern Manufacturing Technologies 8(1):53–60
19. Dave HK, Desai KP, Raval HKA (2013) Taguchi approach-based study on effect of process parameters in electro discharge machining using orbital tool movement. Int J Mach Mach Mater 13(1):52–66
20. Dave HK, Desai KP, Raval HK (2012) Optimisation of multiple response characteristics in orbital electro discharge machining of Inconel 718 using Taguchi's loss function. Int J Manuf Technol Manage 25(1–3):78–94
21. Dave HK, Desai KP, Raval HK (2013) Development of semi empirical model for predicting material removal rate during orbital electro discharge machining of Inconel 718. Int J Mach Mach Mater 13(2):215–230
22. Ahmad, N., Khan, S., Ali, S.: Raza Syed Farhan. Influence of hole diameter, workpiece thickness, and tool surface condition on machinability of CFRP composites in orbital drilling: a case of workpiece rotation. International Journal of Advanced Manufacturing Technology 103(5–8), 2007–2015 (2019).
23. Geier N, Szalay T (2017) Optimisation of process parameters for the orbital and conventional drilling of uni-directional carbon fibre-reinforced polymers (UD-CFRP). Measurement 110:319–334
24. Kumar S, Dave HK, Desai KP (2017) Application of radial tool movement in electrical discharge machining process for boring operation. International Journal of Materials, Mechanics and Manufacturing 5(3):178–182
25. Kumar P, Hussain M (2020) Optimization of micro-electro discharge drilling parameters of Ti6Al4V using response surface methodology and genetic algorithm. Adv Intell Syst Comput 56:449–456

# Influence of Vibration on Noise Measurement and Correction Method



Yuan-ming Zhao, Ya-hui Song, Sheng Shen, and Gao-yu Fan

**Abstract** When measuring the noise level of the aircraft in flight, the vibration generated by the aircraft in flight will be directly transmitted to the noise sensor fixed on the aircraft body. The generated vibration noise results in inaccurate noise measurement. This paper used the control variable method to study the influence of vibration on noise measurement during flight noise measurement. A large number of laboratory measurements and analyses were performed, and it is found that the vibration acceleration of the noise sensor, vibration direction, and noise sensor type are the main factors affecting the magnitude of vibration noise. And the vibration noise correction curve of the common noise sensor is obtained. According to the vibration noise correction curve, the noise flight measurement data of a certain aircraft is corrected. Comparing the sound pressure levels before and after correction, shows that vibration noise has a great impact on the accuracy of aircraft noise measurement. The proposed method can effectively correct the measurement results and provide a reference for the noise measurement test in flight.

**Keywords** Vibration noise · Noise measurement · Correction curve · Noise flight test

## 1 Introduction

As China's large military transport aircraft are widely used, the ride comfort of military aircraft has received more and more attention. Noise is one of the key factors of ride comfort [1, 2]. How to accurately measure the noise in the cabin of aircraft in flight is of great importance to the noise reduction of aircraft. The complexity of the noise test environment of military aircraft such as atmospheric temperature, humidity, and

---

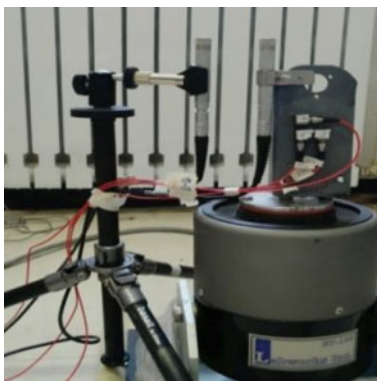
Y. Zhao (✉) · Y. Song · G. Fan  
Flight Test Establishment, Xian, China  
e-mail: [993620483@qq.com](mailto:993620483@qq.com)

S. Shen  
Beijing Institute of Control and Electronics Technology, Beijing, China

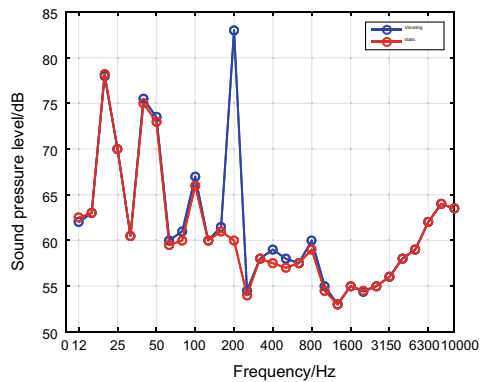
vibration have a significant impact on the measurement accuracy. Before the noise data processing, it is necessary to correct the error caused by temperature, air pressure, vibration, and other factors.

Corresponding methods and standards had been specified for sound pressure level correction at atmospheric conditions [3–5]. In which, vibration is a factor that needs to be considered only in special measurement environment. As for flight tests, the impact of vibration on noise measurement is a factor that cannot be ignored. As shown in Fig. 1, under laboratory conditions, two identical noise sensors were used in the same noise environment; when 200 Hz vibration was applied to one of the sensors, the sound pressure level was very different at 200 Hz, but completely the same at other frequencies. This difference in sound pressure caused by vibration is called vibration noise. The flight noise measurement data showed that the noise sensor was hard to avoid the influence of aircraft structural vibration. The national military standard (General requirements for modification of aircraft flight test system) and product technical documents have requirements for correcting the influence of vibration on noise measurement, however, there was no corresponding method and standard.

In this paper, three types of noise sensors which are commonly used in aircraft noise measurement in flight were tested in the laboratory. A large number of tests were performed using the control variable method. According to the test data, the main factors affecting the magnitude of vibration noise were analyzed. The vibration noise correction curves of the three types of noise sensors were obtained. The tests verified the necessity of vibration noise correction. Finally, according to the vibration noise correction curve, the real flight test data were obtained.



(a) Fixing method of vibration exciter and noise sensors



(b) Comparison of sound pressure levels in frequencies domain

**Fig. 1** Test and octave band diagram of sound pressure level

## 2 Generation Mechanism of Vibration Noise

Assume that the core of the noise sensor is rigidly fixed on the shell, and the external vibration is applied in the direction perpendicular to the diaphragm, as shown in Fig. 2. The acceleration of the whole noise sensor is  $\alpha'$ , the velocity is  $v'$ , and the displacement is  $x'$ . Although the diaphragm is fixed on the shell, its effective mass  $m$  is supported by force. Therefore, the acceleration  $a$ , velocity  $v$ , and displacement  $x$  of the diaphragm are different from the shell. Therefore, there is a relative velocity  $v - v'$  and displacement  $x - x'$  between the diaphragm and the shell.

In general, there is a windproof layer around the diaphragm. When the noise sensor is vibrated, the air around the diaphragm has the same speed as the shell, and the load impedance of the air is very small for the diaphragm impedance. Therefore, the external air has a weak effect on the diaphragm.

Based on the above assumptions, the motion equation of the diaphragm can be expressed as follows:

$$am + r(v - v') + \frac{1}{c}(x - x') = 0 \quad (1)$$

The form written with displacement  $x$  as a variable is:

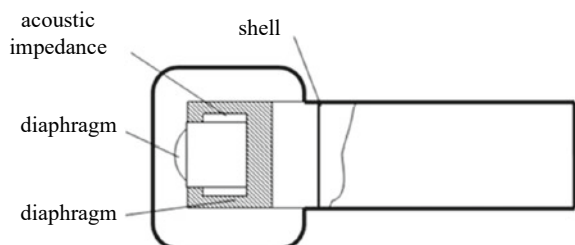
$$m \frac{d^2x}{dt^2} + r \frac{d(x - x')}{dt} + \frac{1}{c}(x - x') = 0 \quad (2)$$

The vibration of the noise sensor is unstable, but this vibration can also be seen as a combination of numerous sinusoidal vibrations. So it is necessary to study the application of sinusoidal driving force. We introduce  $x = Ae^{j\omega t}$ ,  $x' = A'e^{j\omega t}$  into Formula (2):

$$x - x' = \frac{ma'}{\frac{1}{c} + jwr - w^2m} \quad (3)$$

When the noise sensor is at the speed type, the output voltage is given by the relative speed, we can differentiate formula (3) and introduce  $v' = \frac{a'}{jw}$  into it:

**Fig. 2** Internal structure diagram of noise sensor



$$v - v' = \frac{ma'}{\frac{1}{jwc} + r + jwm} \quad (4)$$

If the electromechanical conversion coefficient of this noise sensor is  $k$ , the absolute value  $|E|$  of the output voltage can be expressed as:

$$|E| = k |v - v'| \quad (5)$$

If the total force impedance of the noise sensor is  $Z$ , the output voltage  $|E_v|$  can be obtained by introducing formula (4) into formula (5):

$$|E_v| = \frac{kma'}{|z|} \quad (6)$$

It can be seen from the above formula that the vibration noise voltage of the noise sensor is directly proportional to the effective mass of the diaphragm [5, 6]. The mechanism of vibration noise generation through mathematical principles has been analyzed above. Since the physical quantity on the right side of formula (6) is difficult to obtain through measurement or sensor operation manual, and the derivation of the formula is based on some assumptions, it is very difficult to accurately calculate the vibration noise through the formula. In the real noise measurement test in flight, the environment of the noise sensor is relatively complex, such as the noise sensor type, fixed mode, background noise, spectrum characteristics of the measured noise source, etc. All these factors will affect the magnitude of vibration noise. To sum up, a large number of tests in the laboratory could be performed to obtain the vibration noise level of the noise sensor.

### 3 Vibration and Noise Test

#### 3.1 Experimental Design

In the aircraft noise measurement test in flight, the random vibration of the noise sensor, types of noise sensors, and test environments are potential factors affecting the magnitude of vibration noise. Based on this, these factors are decomposed into six variables for experimental investigation from two aspects of vibration and noise sensor. They are vibration frequency, vibration acceleration, vibration combination frequency, noise sensor type, environmental background noise, and vibration direction.

Figure 3 shows the connection mode of the test equipment. The red and green parts indicate two noise sensors, respectively. The red microphone was fixed on the ground and the green microphone was fixed on the vibration table. Two sensors had

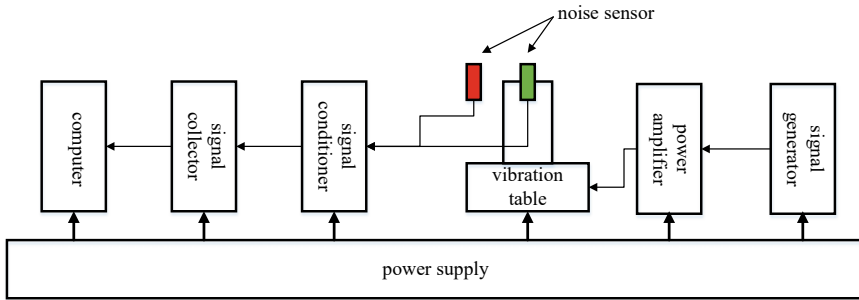


**Fig. 3** Schematic diagram of the test equipment connection

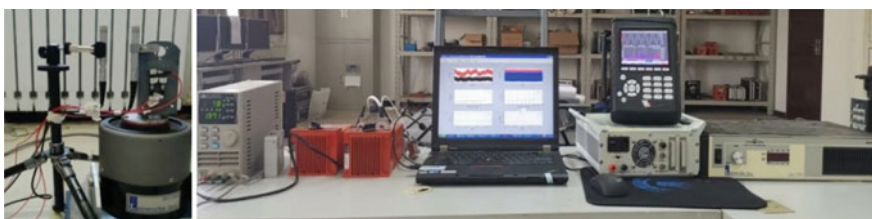
the same type and property and were measured in the same acoustic environment. The vibration table output a certain frequency of vibration, and the sound pressure level measured by the noise sensor fixed on the ground is  $L_1$ , the sound pressure level measured by the noise sensor on the vibration table is  $L_2$ . Then, the vibration noise sound pressure level is  $L_{VIB}$ .

$$L_{VIB} = L_2 - L_1 \quad (7)$$

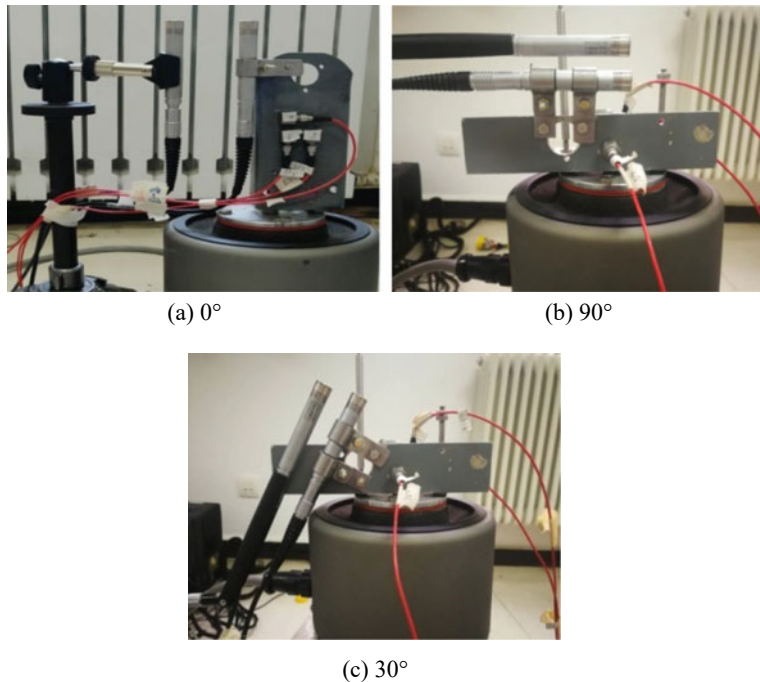
### 3.2 Test Implementation

Figure 4 shows the test situation. The whole test system includes vibration signal generator, miniR700 acquisition recorder, computer, CoCo80 dynamic signal analyzer, power amplifier, noise sensor, vibration sensor, vibration table, speaker, triangular bracket, etc. When the vibration noise was tested in the laboratory, the background noise shall be stable.

During the test, the three vibration sensors were vertically fixed on the rigid support on the vibration table. As shown in Fig. 5a, the true vibration of the noise



**Fig. 4** Test equipment



**Fig. 5** Included angle between noise sensor and vibration direction

sensor on the vibration table could be measured. Each test ensured that the vibration acceleration in the vertical direction was far greater than the vibration acceleration in the two horizontal directions. Otherwise, the test point data was invalid. Two identical noise sensors shall be selected each time, one fixed on the triangular bracket and placed on the ground, and the other fixed on the vibration table, as shown in Fig. 5a. One-third octave spectrum measured by the two noise sensors was recorded under different vibration accelerations, vibration frequencies, vibration directions, and environmental background noise. The vibration noise characteristics of three types of noise sensors were measured, namely B&K 4192, B&K 4948, and ENDEVCO 2510M4A. Figure 5 is the equipment layout to test the influence of different vibration directions on the vibration noise of B&K 4192. Since the vibration from the vibration table is vertical, different fixed angles of the noise sensor correspond to different vibration angles.

### **3.3 Analysis of Measured Data**

The vibration direction was adjusted to parallel to the axial direction of the microphone while keeping other test conditions were completely the same. As shown in

Fig. 5a, the vibration table output vibrations with frequencies of 50 Hz, 100 Hz, and 200 Hz, respectively, and the vibration acceleration was in the range of 0.1 g to 3.5 g. The vibration noise curves of the three types of noise sensors under two acoustic environments were compared to when pink noise was used as the noise source or not.

Figure 6a is the vibration noise curve of B&K 4192 with pink noise as a noise source and without pink noise at vibration frequencies of 50 Hz, 100 Hz, and 200 Hz, Fig. 6b, c are the vibration noise curve of B&K 4948 and ENDEVCO 2510M4A, respectively. From the test results of the above three different types of noise sensors, for the same type of microphone, the vibration noise curve is completely consistent in the environment with pink noise and without pink noise, which indicates that the measured environmental noise does not affect the vibration noise. We also find that different types of noise sensors have different vibration noise curves.

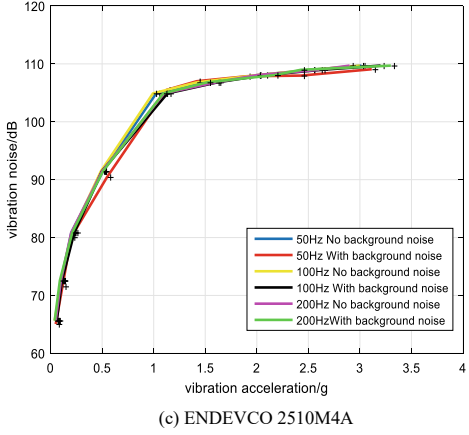
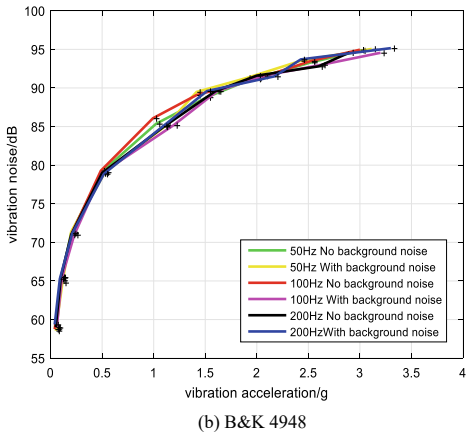
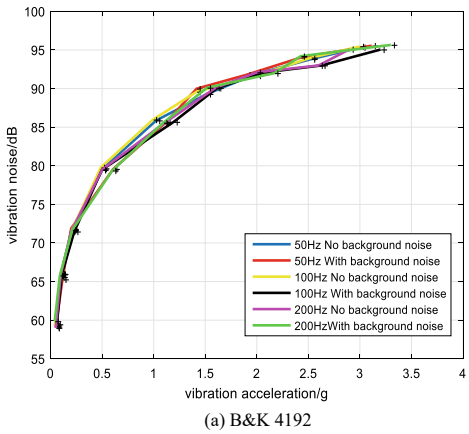
In the aircraft noise measurement test in flight, the vibration transmitted from the airframe to the noise sensor is a broadband signal, so it is necessary to consider whether the vibration noise values obtained in the case of combined frequency vibration and single frequency vibration are consistent. The combined frequency and vibration acceleration are shown in Table 1.

Comparing the vibration noise measured under combined frequency and single frequency vibration, the difference between them was very small. It can be concluded that the vibration noise measured by the B&K 4192 was the same when the combined vibration frequency was the same as the corresponding single vibration frequency, so the combined frequency vibration had no effect on the vibration noise. By extension, when there are enough combined frequencies, it is a broadband vibration situation, so this conclusion is also applicable to the general vibration situation. B&K 4948 and ENDEVCO 2510M4A were tested in the same way and the same conclusion was obtained.

According to the included angle between the noise sensor axis direction and the vibration direction, the included angle can be divided into 0°, 90°, and between the two angles. In order to explore whether the vibration direction will affect the vibration noise, a vibration noise test was carried out with B&K 4192 noise sensor at three angles of 0°, 30°, and 90°.

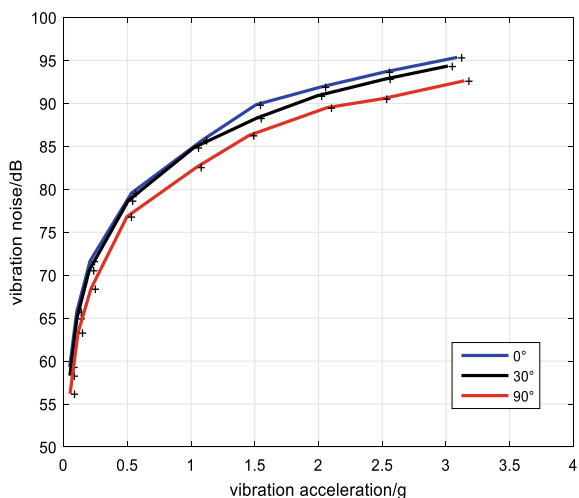
It can be seen from Fig. 7, for B&K 4192, that the vibration noise curves obtained when the vibration direction was 0°, 30°, and 90° from the noise sensor axial direction were all different, but still have certain regularity. First, in the three directions of vibration, within a certain range of vibration acceleration (less than 3.5 g), vibration noise increases with the increase of vibration acceleration. Secondly, when the vibration direction was at 0° to the axial direction of the noise sensor, the vibration noise was the largest, when the vibration direction was at 90°, the vibration noise was the smallest.

**Fig. 6** The vibration noise curves with pink noise as a noise source and without pink noise



**Table 1** Comparison of vibration noise under combined frequency and single frequency vibration

	20 Hz	50 Hz	100 Hz	200 Hz	315 Hz	Remarks
Vibration noise under Combined frequency (20 + 50 + 100 + 200 + 315)Hz vibration(dB)	84.252	90.087	86.788	84.872	88.598	Vibration acceleration at each frequency: 20 Hz: 0.993 g 50 Hz: 1.504 g 100 Hz: 1.113 g 200 Hz: 1.024 g 315 Hz: 1.431 g
Vibration noise under single frequency vibration(dB)	84.380	90.114	85.739	84.194	89.057	
Difference	-0.130	-0.113	1.049	0.678	-0.459	

**Fig. 7** Vibration noise curves measured in different vibration directions of B&K 4192 noise sensor

### 3.4 Test Conclusion

In the laboratory tests, three main factors affecting the vibration and noise were obtained: The first factor is the type of microphone. The effective mass of the diaphragm of different types of noise sensor is different, and there are different vibration noise correction curves. The first factor is the vibration direction. When the vibration direction is parallel to the axial direction of the noise sensor, the vibration noise is the largest; when the vibration direction is perpendicular to the axial direction of the noise sensor, the vibration noise is the smallest. The third factor is vibration acceleration. Within a certain vibration acceleration range, the larger the vibration acceleration, the greater the vibration noise.

## 4 Test Data Correction

Through theoretical analysis and laboratory tests, the vibration noise correction curve was obtained. According to the correction curve, a section of noise data in the noise measurement test in flight was corrected. The noise measurement point was in the missile cabin outside the aircraft. At the same time, the vibration data of the installation position of the noise sensor was extracted for analysis.

The vibration acceleration at each frequency can be obtained by spectrum analysis of the vibration data at the corresponding time period of the measurement point. The type of noise sensor was B&K 4948 in the test, and the vibration noise correction curve is shown in Fig. 6b. The vibration noise correction amount at each frequency can be obtained from Fig. 8 and Fig. 6b, as shown in Fig. 9.

The blue histogram in Fig. 10 is the one-third octave chart of noise data without vibration noise correction, and the yellow is the corrected spectrum chart. By comparison, it can be seen that the measured sound pressure level in some frequency bands is higher than the true value due to the presence of vibration noise.

Figure 11 shows the absolute difference in sound pressure level before and after correction. It can be seen from the absolute difference that the correction amount reaches 2.3 dB in the 1400 Hz frequency band, which indicates that the vibration noise cannot be ignored in the aircraft noise measurement test in flight and must be corrected.

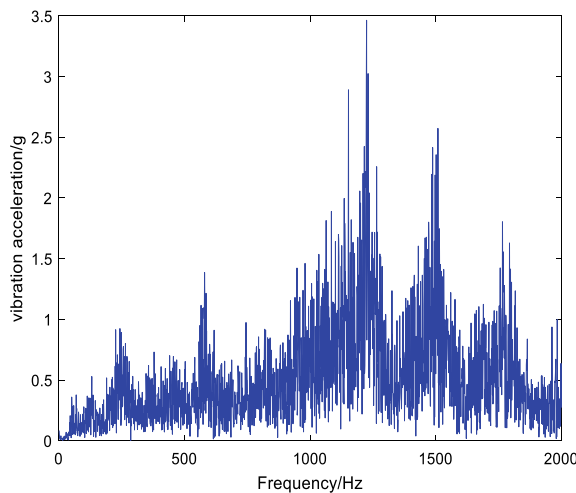


**Fig. 8** Frequency spectrum of vibration acceleration

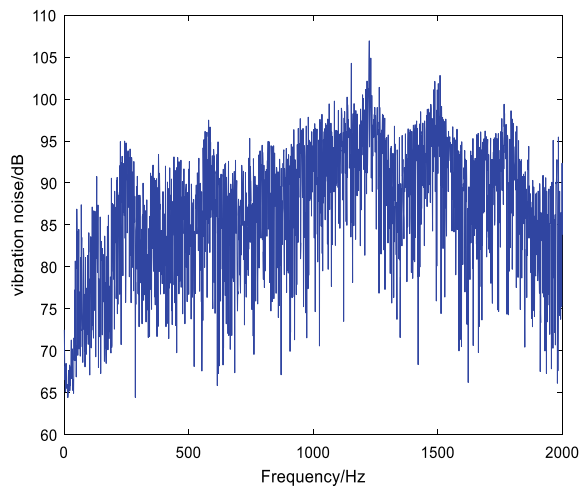


**Fig. 9** The vibration noise correction amount at each frequency

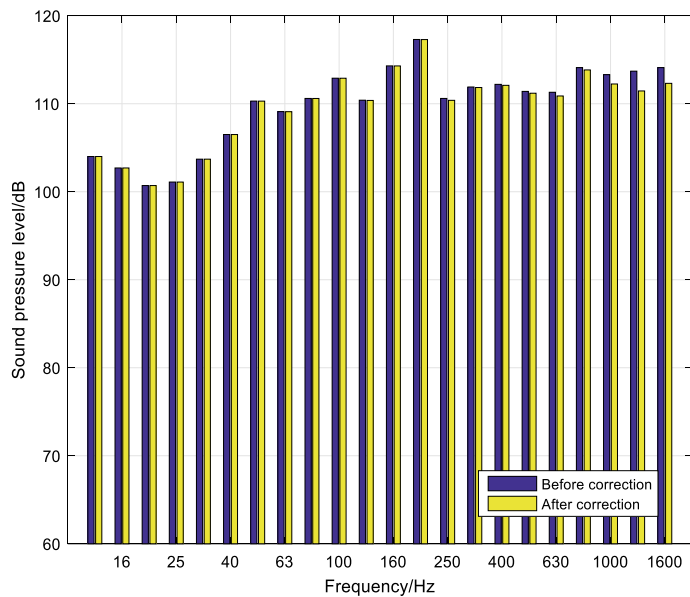


**Fig. 10** 1/3rd Octave spectrum before correction, after correction, and vibration noise

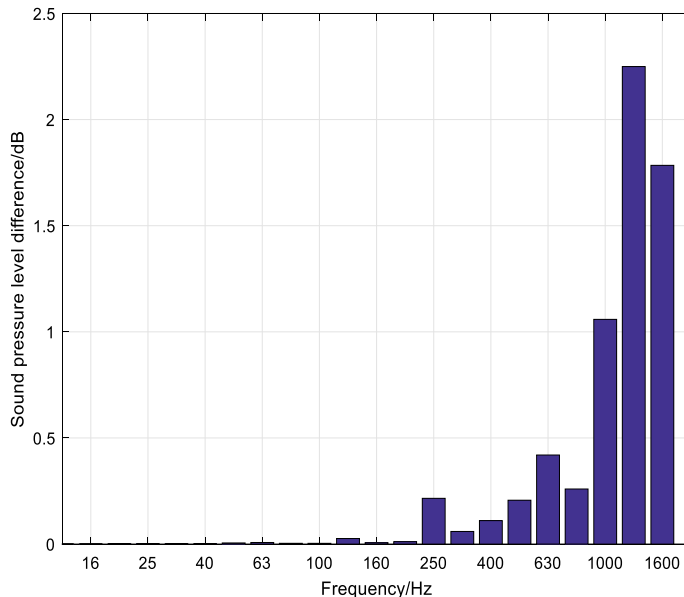


**Fig. 11** The absolute difference in sound pressure level before and after correction

## 5 Conclusion

In this paper, the vibration noise generated by the noise sensor is studied. Firstly, the physical mechanism of the vibration noise is explained through theoretical analysis. Secondly, the laboratory test of the three types of noise sensors used in the aircraft noise flight test, it is verified that the magnitude of the vibration noise is affected by the type and direction of the noise sensors, and the vibration noise correction curve of the three types of noise sensors is obtained. Finally, according to the vibration noise correction curve obtained from the test, the flight test data are corrected, which shows the necessity of vibration noise correction. The proposed method can effectively correct the measurement results and provide a reference for the noise measurement test in flight.

## References

1. Kongcheng Z, Peng C, Zheng W, Hao T, Daofeng T (2016) Research status of aircraft interior noise[J]. *Acta Aeronautica et Astronautica Sinica* 37(8):2370–2384
2. Lindvallj, Vastfall D (2013) The effect of interior aircraft noise on pilot performance. *Perceptual & Motor Skill* 116(2),472–490
3. CCAR-36-R2, Noise Regulations for Aircraft Type and Airworthiness Certification
4. Yishan J (2013) Introduction to the qualification examination of civil aircraft noise[M]. Shanghai Jiao Tong University Press, Shanghai

5. Acoustical Society of America National Standard, "Method for the Calculation of the Absorption of Sound by the Atmosphere," ANSI S1.26-1978.
6. Bai C (1984) Vibration noise of microphone and its reduction method [J]. Electroacoustic Technology(02), 46-51

# Flex-Structural Embedded Flexible Strain Sensor via 3D Printing



Hongyu Han, Xuminyang Xie, Bo Li, and Facai Ren

**Abstract** Fused Deposition Modeling (FDM) 3D printing is one of the most commonly used additive manufacturing techniques, especially for flexible sensors. At present, there are few researches on flexible sensors that use carbon-based conductive fillers to prepare composite materials and form sensing structures through FDM 3D printing. In this paper, ABS wire drawing extruder is used to mix carbon black to prepare conductive wire. Then, flexible piezoresistive strain sensors with various three-dimensional structures were fabricated by FDM dual-nozzle printing technology. Finally, the sensitivity experiment results are discussed in combination with the sensing principle. The results prove the feasibility of FDM technology to prepare flexible sensors with integrated sensing structure.

**Keywords** Flexible strain sensor · 3D printing · Conductive filler · Structural integration

## 1 Introduction

A sensor is a device that can sense measured information and convert the information into the desired signal output [1]. The research of sensors is developing in the direction of lightweight, high flexibility, and fast response speed. Fused deposition modeling (FDM) additive manufacturing technology can process complex structures with high precision that are difficult to manufacture by traditional processing methods [2]. The principle of FDM 3D printing technology is that the hot-melt filament is heated and melted, and then the filament is extruded on the substrate or the material formed

---

H. Han · X. Xie · B. Li (✉)

School of Mechanical and Power Engineering, East China University of Science and Technology, Shanghai 200237, China  
e-mail: [libo@ecust.edu.cn](mailto:libo@ecust.edu.cn)

F. Ren

Shanghai Institute of Special Equipment Inspection and Technical Research, Shanghai 200062, China

in the previous layer through the nozzle according to the preset trajectory and is stacked layer by layer to form the required parts. FDM 3D printing can also use a dual-nozzle printing mode [3]: different materials are loaded into the dual nozzles, and the printer prints two materials at the same time in one process. This work takes advantage of this feature to print the sensor substrate and the sensing structure with non-conductive substrates and materials with excellent electrical conductivity, to realize the integrated molding process of the sensor sensing structure [4]. This work explores the feasibility of preparing a variety of three-dimensional structures of dual-material and flexible piezoresistive strain sensors filled with conductive paste by FDM 3D printing technology. This work also conducts experimental tests and simulation analysis on the fabricated sensors. Based on the results, the performance of the sensor is evaluated.

## 2 Design and Fabrication of Embedded Flex-Sensor Structure

The materials used in the experiment are thermoplastic polyurethane elastomer rubber (TPU), conductive CB/TPU particles prepared by mixing TPU and carbon black (CB), and carbon nanotube (CNT) water-based conductive paste. According to the theory of conductive fillers [5], conductive TPU particles can be made by adding a certain amount of CB to pure TPU raw materials. According to previous studies, when the CB content is 12%, the conductivity of the composite material increases significantly due to the formation of a conductive network. Using a desktop ABS wire drawing extruder, through the five-step operation of extrusion, feeding, cooling, pulling, and winding, the pure TPU raw material and CB are uniformly mixed to prepare conductive TPU wire. FDM printers provide two independent extrusion nozzles that can use two independent materials during the printing process. In this paper, the FDM dual-material printing nozzles 1 and 2 extrude pure TPU filament and conductive TPU filament, respectively. In order to demonstrate the capability of dual-nozzle FDM-printed flexible strain sensors and to compare the sensor performance of different structural designs, five sensors with different shapes of CB/TPU conductive structures are designed in this paper: long bond shape, stepped shape, flat shape, 24-sided helix, and leaf-shaped. The long key shape, stepped shape, flat shape, 24-sided helix, and blade body are printed with pure TPU, and the rest of the five configurations including the central void at the top of the 24-sided helix are printed with conductive CB/TPU. Both straight microchannels and curved microchannels were fabricated by extruding pure TPU silk from nozzle 1, and the CNT conductive paste was injected into the microchannels through a 1 mm needle. The preparation process of the FDM-printed flexible strain sensor includes the following steps: loading the filament, leveling the substrate, slicing the model, printing the model, and removing the support. The final shaped FDM-based CB/TPU flexible piezoresistive sensor and microchannel configuration piezoresistive sensor are shown in Fig. 1.

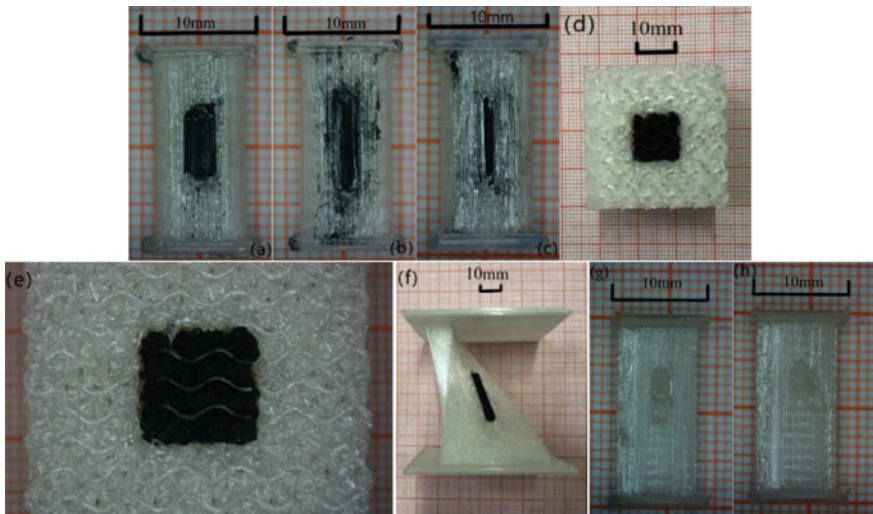


**Fig. 1** FDM-based CB/TPU flexible piezoresistive sensor and microchannel configuration piezoresistive sensor: **a** long bond shape; **b** stepped shape; **c** flat plate shape; **d, e** 24-sided helix; **f** blade shape; **g** straight microchannel; **h** curved microchannel. [self drawn]

Each strain sensor was fabricated in a single print of the FDM printer, and the conductive CB/TPU and pure TPU material interfaces were well bonded in the fabricated strain sensor. Among a large number of printed samples, only a few samples have the phenomenon that the interface between conductive TPU and pure TPU is not firmly bonded. In order to improve the data accuracy of the subsequent experiments, all the prepared sensors were put into a vacuum drying oven and subjected to heat treatment at 130 °C for 30 min. After heat treatment, the interface between conductive TPU and pure TPU is more closely combined. It should be noted that due to the FDM dual-nozzle printing mode, when the nozzle 1 extruding the pure TPU is working, the nozzle 2 that extrudes the conductive TPU stops extruding, but it still moves with the extruder carriage of the nozzle 1. As shown in Fig. 1a–c, any dark spots or blurred areas in pure TPU are the result of applying a small amount of residual conductive TPU to the TPU surface on the substrate as the parked nozzle 2 moves with the carriage. The amount of applied conductive TPU is small. It is difficult to be continuous so that a better conductive loop cannot be formed. Therefore, they do not affect piezoresistive sensor performance. This is an aesthetic defect that can be reduced or avoided by optimizing print parameters and print paths.

### 3 Compression Testing Results and Discussions

On the universal tensile testing machine, the strain sensors of long key shape, stepped shape, plate shape, 24-sided helix, blade shape, straight microchannel, and curved microchannel filled with conductive paste were tested at a fixed speed of 1.2 mm/min compression, and the compression amount is 1.2 mm, 1.2 mm, 1.2 mm, 2 mm, 3.3 mm, 1.2 mm, and 1.2 mm, respectively. Use a resistance tester to measure the change in resistance of the strain sensor with strain. From the amount of compression and the size of the piezoresistive sensor, the strain range of the compression experiment is 0–6%. The relationship between the rate of change of resistance and the strain variable is drawn and fitted, and the slope of each segment of the curve is obtained, that is the sensitivity of each segment (Fig. 2). It can be seen from Fig. 2 that the sensitivity of the long bond structure in the range of 0 to 1.5% is 0.36077, and in the range of 1.5 to 6% is 0.12404; the sensitivity of stepped shape structure in the range of 0–1.5% is the smallest, which is 0.15336, in the range of 1.5–4% is 0.39239, and in the range of 4–6% is the largest, which is 0.8553; the sensitivity of flat structure in the range of 0–1.5% is 0.05991, and in the range of 1.5–3% is 0.45553; the sensitivity of 24-face helix in the range of 0–0.5% is −0.41781, and in the range of 0.5–6% is −0.07774; the sensitivity of the blade-shaped structure in the range of 0–2.25% is 0.25588, and in the range of 2.25–3% is 5.35958; the sensitivity of straight microchannel in the range of 2.5–4.5% is the smallest, which is 0.00559, in the range of 0–2.25% is 0.10472, and in the range of 4.5–6% is 0.01954; the sensitivity of the curved microchannel structure in the range of 0–4% is 0.39831, and in the 4–6% range is −1.83451.

The action mechanism of the piezoresistive response in the piezoresistive sensor based on the integrated printing of the FDM dual-nozzle sensing structure is the change of the conductive network structure in the CB/TPU. The CB particles are uniformly dispersed in the flexible TPU matrix and contact with each other to form a conductive path and finally form a complete conductive network, which endows the CB/TPU wire with conductive properties. When the CB/TPU structure is compressed and deformed, the inner conductive network is deformed and destroyed together. When an object is compressed in one direction, there is a tensile strain in the direction perpendicular to the direction of compression due to the Poisson effect. Due to the higher elastic modulus of CB/TPU compared to TPU matrix (measured about 2.5 times), the tensile strain of conductive TPU under compression perpendicular to the compression direction is smaller than the strain of TPU matrix in this direction. In addition, the conductive CB/TPU in the strain sensor is embedded and confined in the TPU platform with different dimensions and mechanical properties, and the connection part with the TPU substrate will also deform during compression. Therefore, the CB/TPU conductive sensing structures of the long bond, stepped, plate, 24-face helix, and blade-shaped piezoresistive sensors have complex shape and size changes during compression, as well as complex changes in the internal CB/TPU conductive network. Piezoresistive sensors with different configurations have different resistivity changes in compression experiments, which leads to differences in sensitivity

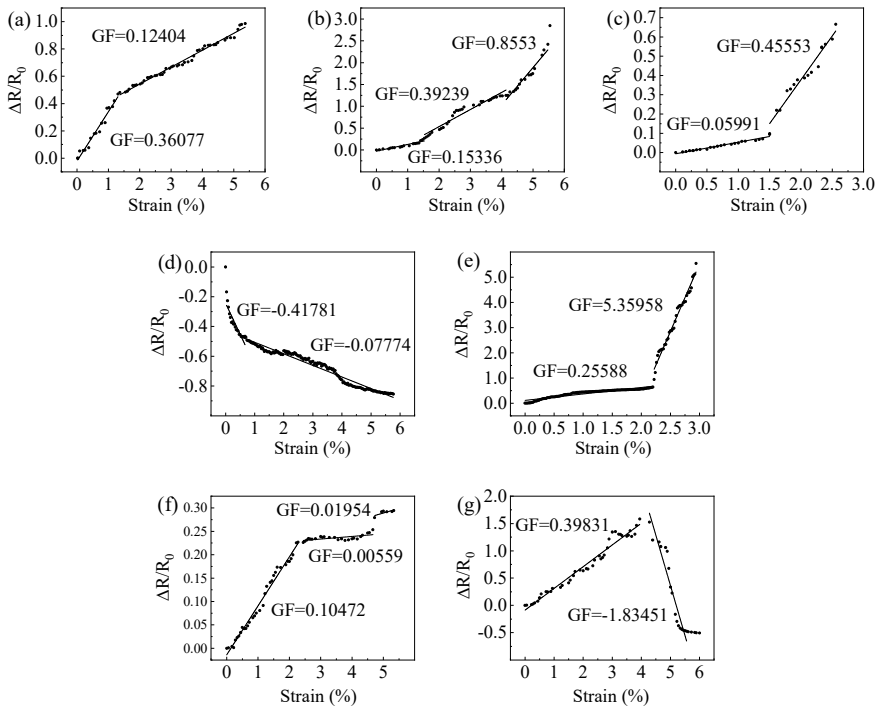


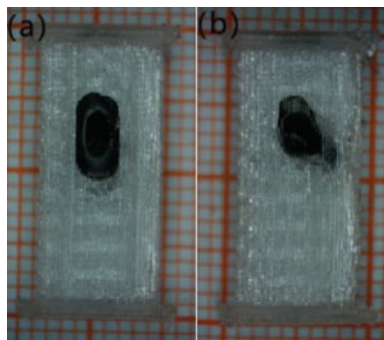
**Fig. 2** Sensitivity of the flexible piezoresistive sensor formed based on FDM and its multi-segment linear fitting curve: **a** long bond shape; **b** stepped shape; **c** flat shape; **d** 24-face helix; **e** blade shape; **f** straight microchannel; **g** curved microchannel. [self drawn]

among piezoresistive sensors. In the test results of the sensitivity experiment, the phenomenon of different sensitivities under different strains also appeared, mainly because the complex deformation of the CB/TPU structure occurred under different strains. That is to say, the complex changes in the internal conductive network of CB/TPU may be different, and the degree of damage and reconstruction of the conductive path will also be different, which ultimately affects the sensitivity test results.

For the microchannel configuration, it is very important to select an appropriate filling rate and perform appropriate heat treatment. It was comprehensively decided to select 80% filling rate for FDM printing and heat treatment at 170 °C for 30 min after printing. After heat treatment, the CNT conductive paste was injected into the microchannel with a 1 mm diameter needle until the microchannel was filled with the conductive paste, as shown in Fig. 3.

The working principle of the microchannel sensor is as follows: when the conductive paste is compressed, the diameter of the middle part of the conductive path formed by the conductive paste decreases, and the resistance increases. The difference between the configuration of the curved microchannel piezoresistive sensor and the straight microchannel piezoresistive sensor is that under the same height difference, the middle part of the curved microchannel and the microchannel holes on both

**Fig. 3** Microchannel configuration piezoresistive sensor: **a** straight microchannel; **b** curved microchannel. [self drawn]



sides are in the plane direction. They are perpendicular to each other, which is equivalent to a 90° rotation of the flow channel compared with the straight microchannel in space, which prolongs the length of the conductive path and reduces the influence of gravity. Therefore, the curved microchannel piezoresistive sensor has higher sensitivity. After the compression experiment, due to the viscosity and incompressibility of the conductive paste, the conductive paste in the microchannels of the two configurations will naturally return to its original state under the action of gravity. However, due to the influence of gravity, the straight microfluidic sensor will return to its original state faster than the curved microfluidic sensor. It is also found from the sensitivity graph of the curved microchannel piezoresistive sensor that when the amount of compression is too large, the measured resistance of the curved microchannel sensor will decrease. It is speculated that it may be that the resultant force of the stress on the conductive paste at the connecting parts of the curved microchannel on both sides and the straight in the middle causes the conductive paste to be squeezed into the pure TPU matrix, while the compression is larger. Since there is less conductive paste in the middle part, the conductive paste squeezed into the connection part is sucked into the middle part again, so that the conductive path is connected again, resulting in a decrease in resistance.

In order to observe the change of the sensitivity of the designed piezoresistive sensor with the strain more intuitively, the work selects the long bonded sensing structure and uses the finite element simulation to analyze the stress and strain of the piezoresistive sensor during compressive deformation. First, the pure TPU and CB/TPU wires were tensile tested by the universal tensile testing machine. From the stress-strain curve, the tensile modulus of CB/TPU was 14.236 MPa, and the tensile modulus of pure TPU was 5.694 MPa. Assuming that Poisson's ratio of the two kinds of wires is 0.49, the finite element analysis is performed using the ABAQUS simulation software. Set the left bearing surface of the model to be fixed, apply deformation to the right bearing surface, apply 2%, 4%, and 6% deformation to the model, respectively, and observe its stress and strain distribution cloud map. As shown in Fig. 4, with the increase of the compression amount, the stress and strain of the long bond-shaped sensing structure increase accordingly.

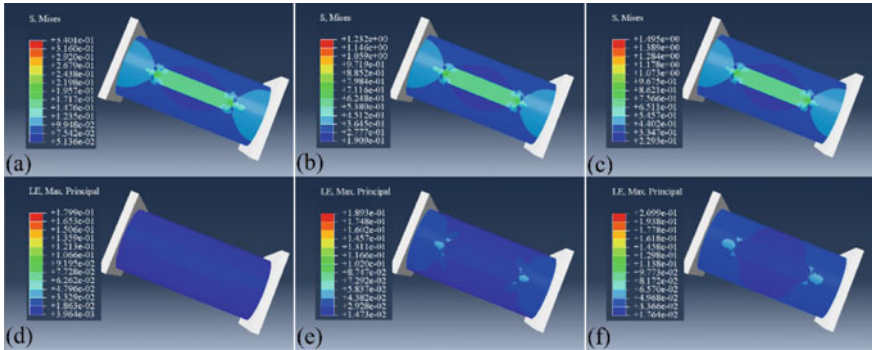


**Fig. 4** Long-key flexible piezoresistive sensors under different deformations stress distribution: **a** 2%; **b** 4%; **c** 6%; strain distribution: **d** 2%; **e** 4%; **f** 6%. [self drawn]

It can be seen from Fig. 4a–c that under different compression amounts, the stress at the long bond structure formed by CB/TPU printing is the largest, and it increases with the increase of compression amount; the cylindrical matrix formed by pure TPU printing, the stress at both ends of the axis where the long bond is located is larger, and the stress on the TPU near the center of the long bond is the smallest. It can be seen from Fig. 4d–f that under different compression amounts, the strain of the piezoresistive sensor is concentrated at both ends of the cylinder, and the strain in the middle is the smallest; as the amount of compression increases, the connection between CB/TPU and TPU will also produce relatively large strain. Because the finite element simulation is also an ideal situation, and some constraints are added at the same time, the deformation of long bond piezoresistive sensor is more complicated in practice, so there is a certain deviation between the simulation results and the actual situation.

## 4 Conclusion

In this work, a dual-nozzle printed CB/TPU flexible piezoresistive strain sensor based on FDM molding and a microfluidic flexible piezoresistive strain sensor filled with conductive paste are proposed. The two strain sensors forming methods are low cost, simple, and efficient and have good repeatability, which proves that flexible piezoresistive strain sensors with three-dimensional complex structures can be formed by FDM 3D printing technology.

The sensing mechanism and sensitivity data of the two sensors are combined, indicating that a flexible piezoresistive strain sensor with integrated sensing structure and filled with conductive paste can be fabricated based on FDM 3D printing technology, and both sensors are reproducible and have excellent sensing performance. The change of stress and strain of the designed long bond flexible strain sensor during compression is verified by finite element simulation. The sensor is

connected to the data acquisition card and the host computer, which can realize the real-time transmission of the signal. It proves that the designed sensor has certain practicability.

**Acknowledgements** This work is sponsored by the Research Project of the Shanghai Municipal Administration for Market Regulation, in China (Grant No. 2021–22), and Carbon Dioxide Peaking & Carbon Neutrality Fund from Shanghai Science and Technology Innovation Action Plan, in China (Grant No. 21DZ1207800).

## References

1. Ghosh R, Song MS, Park JB et al (2021) Fabrication of piezoresistive Si nanorod-based pressure sensor arrays: a promising candidate for portable breath monitoring devices. *Nano Energy* 80:105537
2. Dong X, Xuezhong Z, Yuntao L, Harkin-Jones E, Yongfeng Z, Lei Wang, Chunxia Zhao, Ping Wang. Enhanced performance of 3D printed highly elastic strain sensors of carbon nanotube/thermoplastic polyurethane nanocomposites via non-covalent interactions. *Composites Part B*, 2019, 176(5)
3. Kim K, Choi J, Jeong Y et al (2019) Highly sensitive and wearable liquid metal-based pressure sensor for health monitoring applications: integration of a 3D-printed microbump array with the microchannel. *Adv Healthcare Mater* 8(22):1900978
4. Al-Rubaiai M K, Tsuruta R, Gandhi U, et al (2019) A 3Dprinted stretchable strain sensor for wind sensing. *Smart Mater Struct* 28(8), 084001
5. Amjadi M, Yoon YJ, Park I (2015) Ultra-stretchable and skin-mountable strain sensors using carbon nanotubes–Ecoflex nanocomposites. *Nanotechnology* 26(37):375501

# Research on Pre-tightening Force of Filament-Wound Composite Barrel of Railgun



Xuan Li

**Abstract** To study the influence of the pre-tightening force of the carbon fiber composite barrel of the electromagnetic railgun on the overall performance of the barrel, this paper has built a local finite element model of the fiber composite barrel and analyzed the stress and deformation of the rail after it is prestressed based on the ANSYS element birth and death technology and the multi-step continuous solution method. On this basis, this paper has studied the stress and deformation of each part of the barrel after the electromagnetic expansion force is applied to the barrel, and the relationship between the condition for the stable operation of a form of railgun barrel and the pre-tightening force has been obtained. The results show that the appropriate pre-tightening force of the barrel is necessary for the stable operation of the railgun. The conclusions of this paper can guide railgun design.

**Keywords** Railgun · Pre-tightening force · Composite barrel

## 1 Introduction

The electromagnetic railgun is a new concept weapon with high kinetic energy. It is based on the electromagnetic principle and uses the current advanced engineering technology. At present, the electromagnetic railgun has passed the proof-of-principle stage and is developing toward equipment application. A barrel is the core component of the electromagnetic railgun; thus, designing a lightweight and high-strength barrel has become the key technology for railgun design and manufacture. The housing material of the railgun barrel should be able to provide sufficient rigidity and strength. It should be able to withstand the electromagnetic force transmitted from the rail and the insulator to guarantee the insulation strength and improve the inductance gradient. It should also be able to stabilize the inner bore parts such as the guide rail and the insulation supporter to ensure the horizontal and vertical rigidity of the barrel. If

---

X. Li (✉)

The 713th Research Institute of CSSC, Zhengzhou 450000, Henan, China  
e-mail: [695048914@qq.com](mailto:695048914@qq.com)

there is space between the armature and the guide rail, the electric arc will occur and ablate the guide rail or the armature. If there is space between the parts of the barrel, the insulating materials will be ablated, affecting the insulation performance of the launch device. To avoid the above situations, a certain pre-tightening force should be applied to the barrel. There are mainly three methods to apply the pre-tightening force to the barrel currently: Continuous sealing and continuous pre-tightening with steel bushing, discrete sealing and discrete pre-tightening with bolt connection, and carbon fiber wound pre-tightening [1].

Carbon fiber material technology has developed rapidly in recent years with widening applications. Compared with traditional gun steel materials, carbon fiber materials have the advantages of low magnetic permeability, high strength and high modality, and the designability of fiber lay-up. At present, medium and large-caliber electromagnetic railgun barrels adopting carbon fiber winding enhancement technology have been studied domestically and abroad [2]. Root J B and Littlefield A G compared the rigidity of elliptically encapsulated barrels with the rigidity of flat encapsulated barrels on the basis of taking into consideration the anisotropy of carbon fiber composites. Liudas T et al. analyzed the structural characteristics of the electromagnetic railgun barrel macroscopically. Shi Jiangbo established electromagnetic railgun barrel analysis models with the same die structure adopting the continuous sealing with steel bushing mode and the discrete sealing with bolt connection mode to study the influence of different sealing modes on railgun encapsulation performance. Xiao Hongcheng et al. introduced the structure optimization and design method for the filament-wound encapsulation of the electromagnetic railgun's composite barrel. The optimization results of the winding thickness, winding angle, and stacking order of the 50 mm-diameter composite barrel's fiber layer were provided in their study. J.T.Tzeng studied the fracture behavior caused by the dynamic response of composite barrels under moving loads [3]. In this paper, the barrel structure of a form of the railgun is modeled and analyzed. This paper uses the "element birth and death" technology of the finite element method combined with the "temperature difference method" of the multi-step continuous solution to simulate the pre-tightening force of the filament-wound composite barrel and the relevant methods are studied. The changing pattern of the railgun's caliber under the electromagnetic expansion force with different barrel pre-tightening forces is analyzed in this paper.

## 2 Pre-tightening Model of Railgun Composite Barrel

### 2.1 *Overall Structure of the Composite Barrel*

The carbon fiber modulus is higher than the average modulus of the inner bore material. The carbon fiber wound outside the inner bore can improve the rigidity of the barrel to resist more deformations during launch. During the winding process of the filament-wound composite barrel, a certain winding tension is applied to the

carbon fiber filaments of the encapsulation layer, which is converted into the pre-compression stress on the inner bore structure, achieving the pre-tightening effect on the barrel. Taking the 40 mm-caliber composite barrel developed by the French and German ISL laboratories as an example, the specific structure of the barrel is shown in the figure below. The material of the pre-tightening encapsulation layer is T700 carbon fiber; the material of the insulation winding layer is Kevlar fiber; the material of the insulation supporter is glass fiber composite material G10; the material of the supporter of the copper guide rail is steel. The mechanical property parameters of each part are shown in the table below.

## 2.2 *Finite Element Modeling of the Filament-Wound Layer*

ANSYS Composite PrePost module (ACP module) is a professional tool for layered modeling and failure analysis of composites. It provides all the necessary functions for composite structural analysis and allows users to effectively define material properties, layer domains, and stacking order. This paper uses this tool to model the lay-up of the filament-wound layer. Since the barrel shape is axisymmetric with a center line, only one-fourth of the barrel model is analyzed to reduce calculation.

According to the material mechanics theory of composite materials and the material performance parameters of the single-layer board, nine parameters (3 resilient moduli, 3 Poisson coefficients, and 3 shear moduli) of the T700 carbon fiber orthotropic material are calculated and defined in the material library of Ansys.

The thickness of the material lay-up is set according to the table below, and the filament-winding direction: A single layer is made of 0.2 mm composite fiber bundles, and a sublayer is made of 20 single layers. There are a total of five sublayers and the total thickness of the winding layer is 20 mm. The winding angle is changed according to 0 degrees, 45 degrees, 90 degrees, and -45 degrees for every three single layers. Adhesive contact pairs are established between each winding layer. The lay-up model is shown in the figure below.

## 3 Analysis of the Pre-tightening Force of the Composite Barrel

### 3.1 *Element Birth and Death Technology and Multi-step Continuous Solution Algorithm for Winding Process Simulation*

The “element birth and death” doesn’t refer to adding and deleting certain elements. It makes elements ineffective or return to normal in the structure by multiplying the term describing these elements by an attenuation factor A in the stiffness matrix.

The basic idea of simulating the winding process of the composite using the “element birth and death” method of Ansys finite element software is as follows. First, during modeling, conduct multi-layer modeling of composite materials in the thickness direction based on the actual situation of the winding process. After the material parameters are set and the mesh is divided, “kill” the composite elements of all layers. Use the multi-step calculation in the calculation process. Activate a layer of “killed” composite elements in each calculation step, apply the corresponding prestress load to the activated composite layer, and perform the calculation. Activate the composite elements layer by layer until the calculation is completed. The composite materials use cured material parameters in the calculation. The changes caused by different winding directions are reflected by creating material models with different properties. A flow chart is used below to describe the nonlinear simulation process of composite winding calculation. It is shown in the flow chart below:

### 3.2 Temperature Difference Method to Simulate Filament-Winding Tension

Filament-wound composite materials inevitably cause prestress after the housing is formed during the material forming process. The prestress magnitude, the uniformity of the stress of each fiber bundle, and the prestress distribution on each layer of the formed housing have an important influence on the structure and strength of the housing. The equivalent force method and the temperature difference method can be used to simulate the prestress. The equivalent force method is commonly used for prestressing rebars, but it cannot be used for circumferential prestress. Using the temperature difference method to generate equivalent prestress is a common method to apply the circumferential prestress.

Pre-tension stress generated from fibers during the winding process:

$$\sigma = \frac{T}{A} \quad (1)$$

T—winder tension; A—fiber bundle area.

Axial pre-tension stress:

$$\sigma_\theta = \sigma \cos(\theta) \quad (2)$$

Circumferential pre-tension stress:

$$\sigma_r = \sigma \sin(\theta) \quad (3)$$

The so-called temperature difference method adds pre-tension stress as required. A virtual linear expansion coefficient and temperature difference load are set for the material to make it deform from the inside, thus generating the prestress.

In subsequent models, the material needs to be shortened in the axial direction. Therefore, a negative linear expansion coefficient is given in the axial direction as follows:

$$\alpha_\theta = -\frac{\sigma_\theta}{\Delta T E_\theta} \quad (4)$$

In the formula,  $E_\theta$  refers to the resilient modulus of the composite material in the length direction;  $\alpha_\theta$  refers to the linear expansion coefficient;  $\sigma_\theta$  refers to the pre-tension stress applied;  $\Delta T$  refers to the temperature difference.

For the sake of simplicity, the initial temperature is set to 0 °C. Assuming that when the temperature rises by one degree, the material shrinkage in the axial direction will generate 1 MPa pre-tension stress. Thus, a linear expansion coefficient is obtained. Different temperatures applied to each layer of the composite material can generate corresponding pre-tension stresses and pre-tension stress effects.

To verify the correctness of the temperature difference method for pre-tension stress simulation, when the model, mesh division, and boundary conditions are consistent, the comparison between the temperature difference to be applied that is calculated by the temperature difference method and the solution results of the prestress applied with Ansys is as follows:

The maximum error of the maximum circumferential stress is within 5%, and the stress distribution is consistent. Therefore, the temperature difference method can be used to simulate the pre-tension stress of filament winding.

## 4 Equal-Strength Winding Theory

The process of winding the composite material on the outer surface of the inner bore structure is the process of adding the composite material to the inner bore structure after stretching it in the length direction. Since the winding tension of the fibers has a relaxing effect on the wound fibers of the inner layer, the stress of the winding layer fiber changes. Thus, the winding tension of the fibers must be reduced gradually to achieve equivalent stress winding. The stress distribution within the composite tends to be uniform after the winding. The equal-strength winding theory is required for the general filament winding, and the prestress of each filament-winding layer is based on the equal-strength winding theory as follows:

$$T_i = \frac{\sigma_M \delta_M}{\delta_1} \frac{E_c \delta_c + E_M \delta_M}{(i-1)E_c \delta_c/N + E_M \delta_M} \quad (5)$$

In the formula,  $T_i$  refers to the prestress used for the  $i$ -th layer winding;  $N$ —the number of winding layers;  $E_c$ ,  $E_M$  refers to the resilient modulus of the composite material and the metal mandrel;  $\sigma_M$  refers to the expected stress of the metal mandrel

after winding (negative value);  $\delta_c$ ,  $\delta_M$  refers to the thickness of composite and mandrel.

The stress distribution within the composite tends to be uniform after the winding, and the average stress is

$$\sigma_c = \frac{\sigma_M \delta_M}{\delta_c} \quad (6)$$

## 5 Determination of the Winding Tension of Each Layer

Referring to the equal-strength winding theory, the pre-tension stress of the winding follows the law of diminishing. The first layer has the maximum winding tension and the outermost layer has the minimum winding tension. The tension decreases averagely as the number of the winding layers increases, as shown in the following formula.

$P$  = Pre-tension stress -  $N \times 5$  (MPa).

Specifically,  $N$  is the number of winding layers.

## 6 Analysis and Discussion of the Results of Applying Pre-tightening Force to the Barrel

### 6.1 When the Barrel isn't Withstanding the Electromagnetic Expansion Force

Based on the “element birth and death” of the finite element method and the temperature difference method, 100, 200, 300, and 500 MPa pre-tightening forces are applied to the winding layers of the composite barrel in this paper. The following figures show the barrel stress and deformation under partial pre-tightening forces.

### 6.2 When the Rail is Withstanding the Electromagnetic Expansion Force

For electromagnetic railguns, the classical electromagnetic force calculation formula is as follows:

$$F = L' I^2 / 2 \quad (7)$$

Calculate the electromagnetic force generated when the armature is launched at the initial muzzle velocity of 2000 m/s, under the conditions that the barrel length is 3 m, the projectile mass is 0.35 kg, and the current is 1 MA. The empirical value of the inductance gradient is  $L' = 0.46 \mu H/m$ .

$$F = 2.3 \times 10^{-5} \approx ma$$

In this formula, the current is considered to be a constant value  $I$ , thus the armature is in uniform acceleration. Acceleration:  $a = \frac{2}{3} \times 10^6 m/s^2$ . The armature moves on the rail for 3 ms. According to the principle of electromagnetic action, the electromagnetic repulsion force on the unit rail length is equal to the electromagnetic force of the armature on the unit span, thus

$$\frac{F}{z} = \frac{1}{2} \frac{\partial}{\partial y} L' I^2 = \frac{L' I^2}{2s} \quad (8)$$

The intensity of pressure withstood by the rail where the current flows is

$$p = \frac{1}{2} \frac{L' I^2}{2s} / h$$

In the formula,  $s$  is the inner distance of the rail,  $h$  is the height of the rail, and the intensity of pressure withstood by the rail is 144 MPa. Calculate the change of the barrel caliber with a unilateral load of 150 MPa. The common method is loading the results of analysis and calculation to the structure field to simulate the caliber changes and take the caliber change percentage of no more than approximately 1% as the necessary condition for the stable operation of the launcher. After the electromagnetic expansion force of 150 MPa is evenly loaded on the surface of the arc-shaped rail, solve the equations, and the results are as follows.

The structural states of the barrel under 100, 300, and 500 MPa pre-tightening force are shown in the figures below.

Simulation results show the following:

- (1) Caliber expansion decreases gradually as the pre-tightening force increases. Under the conditions of no pre-tightening force and 100 MPa pre-tightening force, the unilateral rail caliber expansions are 0.27 mm and 0.23 mm, respectively. The caliber change rates are all greater than 1%. There is a clear separation trend between the rail and the supporter, and the maximum stresses of the insulation layer are 753 MPa and 613.6 MPa. Under such a state, the excessive expansion of the rail will lead to the fact that the armature cannot contact the rail properly, which may also cause adverse consequences such as rail ablation, and the requirements for stable operation of the railgun cannot be met. The results show that applying reasonable pre-tightening force on the railgun barrel is an important part of railgun design.

- (2) The maximum stress on the rail decreases as the pre-tightening force increases gradually. The maximum stress on the supporter rises gently as the pre-tightening force increases. Their maximum stresses are both within the reasonable range, which is beneficial to the reduction of rail ablation and insulating supporter damage during launch.
- (3) The maximum equivalent stress of the barrel shows a rebound trend of rising after decreasing. After analyzing the equivalent stress nephogram, it is found that the maximum stress location shifts during the rising process of the pre-tightening force. The location gradually shifts from the intersection of the insulation layer, the rail, and the supporter to the inner side of the winding layer. The analysis shows that the separation trend between the rail and the supporter caused by the electromagnetic expansion force gradually decreases as the pre-tightening force increases. The concentration effect of the stress at the intersection of the insulation layer, the rail, and the supporter weakens. The stabilization effect of the carbon fiber composite layer on the barrel structure strengthens as the pre-tightening force increases. Therefore, the carbon fiber layer withstands the main load and restricts the caliber expansion effectively. So the change is reasonable.

## 7 Experiments and Results

### 7.1 Experiment Method

Use the GO gauge experiment to verify the overall bore caliber. Cut a sample from the wound barrel and smooth its cutting surface. Attach strain gauges to different positions of the barrel to test caliber strain. Fix the sample on the jig. Preset the tensile tension to 1000 N, set the strain gauge to zero, and eliminate the gap error. After that, set the maximum tensile force, which is equal to the tensile force required when the rail is withstanding 150 MPa pressure in the theoretical calculation. Activate the tensile machine and record the stress and strain. Observe the cross-sections of the rail and the supporter. Record the caliber size of the maximum tension. Slowly unload to complete the experiment.

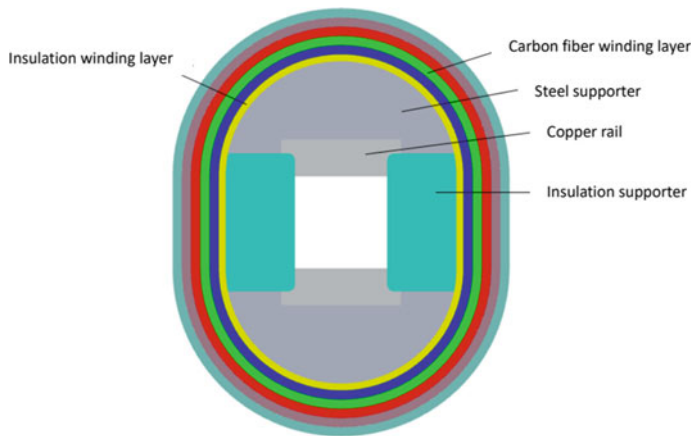
### 7.2 Tensile Test Results

The experiment was carried out step by step according to the pre-tension and rated load. The changes in the barrel structure during the test were recorded.

It was found in the test of samples with 200 MPa and 500 MPa pre-tightening forces, the error between the simulation value and the test value was within 10%.

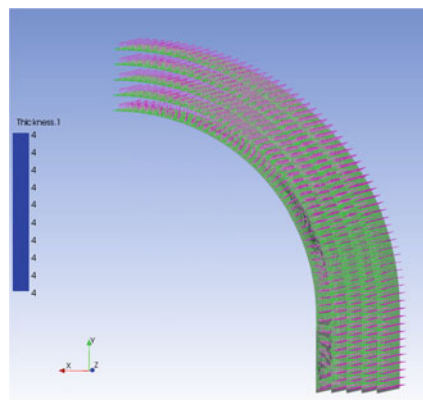
### 7.3 Conclusion

The local finite element model of the filament-wound composite barrel of railgun was built. This paper gave a simulation method of the filament-wound pre-tightening force of the composite barrel based on “element birth and death” and the multi-step continuous solution algorithm. It also analyzed the pattern of stress and deformation generated after the barrel’s inner bore structure was pre-tightened. On this basis, the stress and deformation of each part of the barrel after the electromagnetic expansion force was applied were studied, and the relationship between the pre-tightening force and the condition for the stable operation of a certain electromagnetic railgun was obtained. The results showed that appropriate barrel pre-tightening force was necessary for the stable operation of the railgun. The conclusion can provide a basis for the design of the railgun composite barrel.

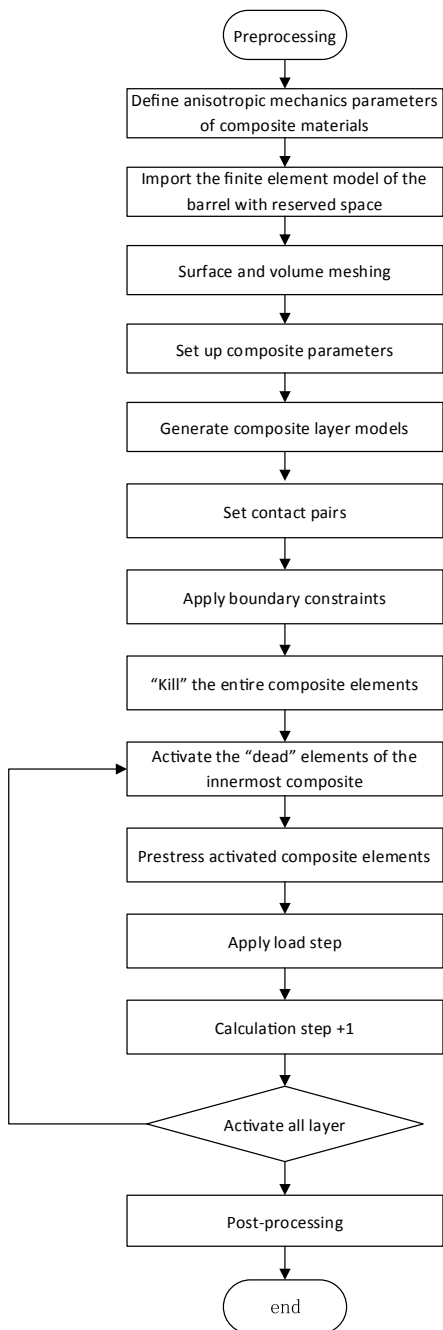


**Fig. 1** Cross-section of the barrel structure

**Fig. 2** The lay-up mode of the filament-winding layer



**Fig. 3** The algorithm flow of simulating the winding process of composite



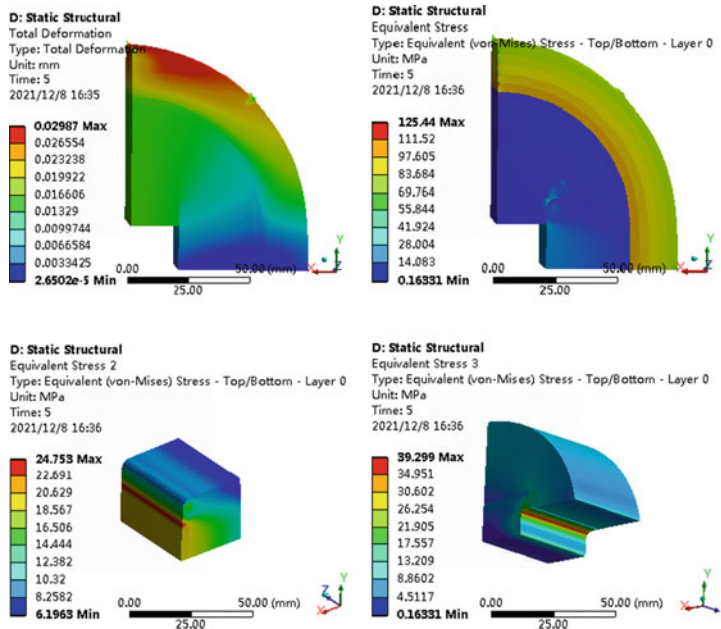


**Fig. 4** The stress and deformation of the barrel when the 100 MPa pre-tightening force is applied to the winding layer of the barrel

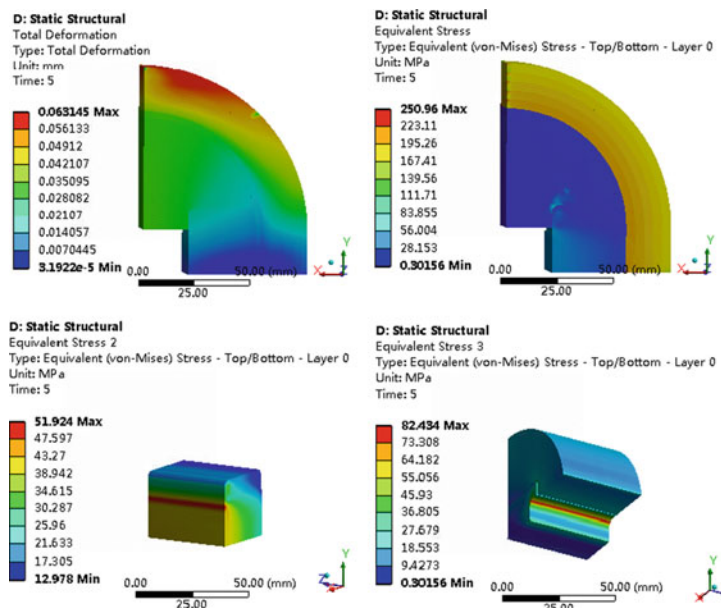


**Fig. 5** The stress and deformation of the barrel when the 200 MPa pre-tightening force is applied to the winding layer of the barrel

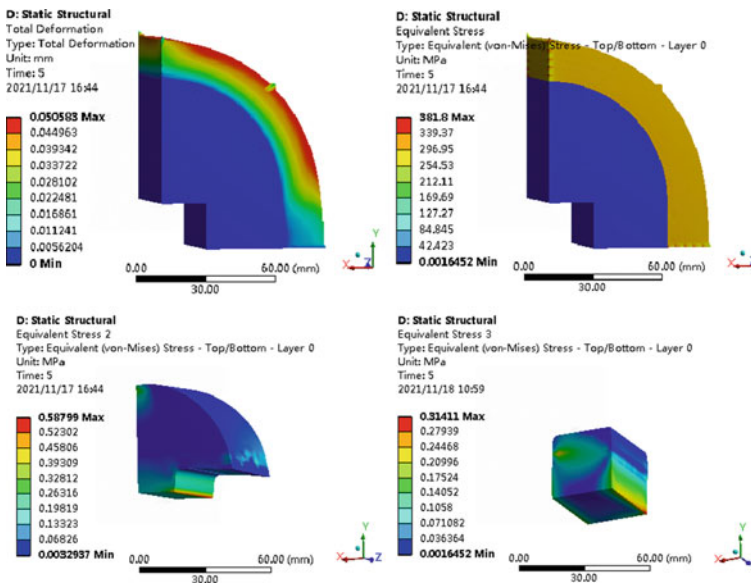


**Fig. 6** The stress and deformation of the barrel when the 300 MPa pre-tightening force is applied to the winding layer of the barrel

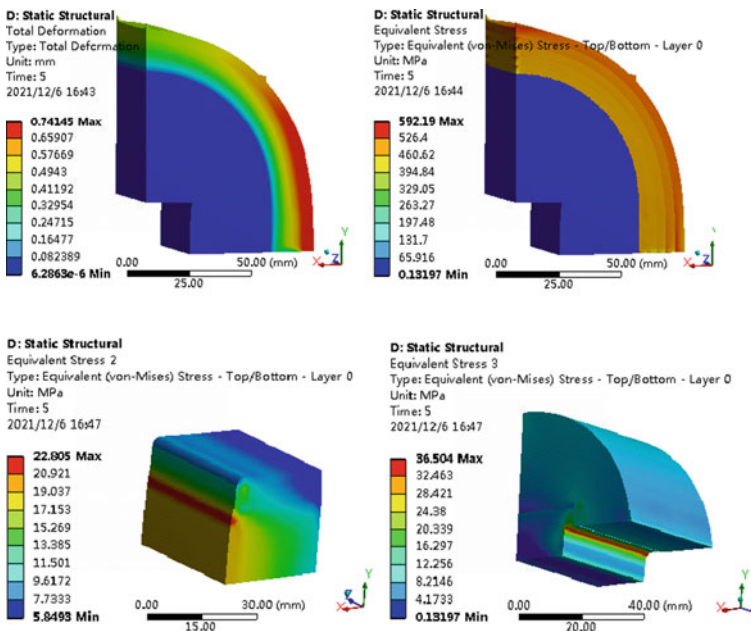


**Fig. 7** The stress and deformation of the barrel when the 500 MPa pre-tightening force is applied to the winding layer of the barrel

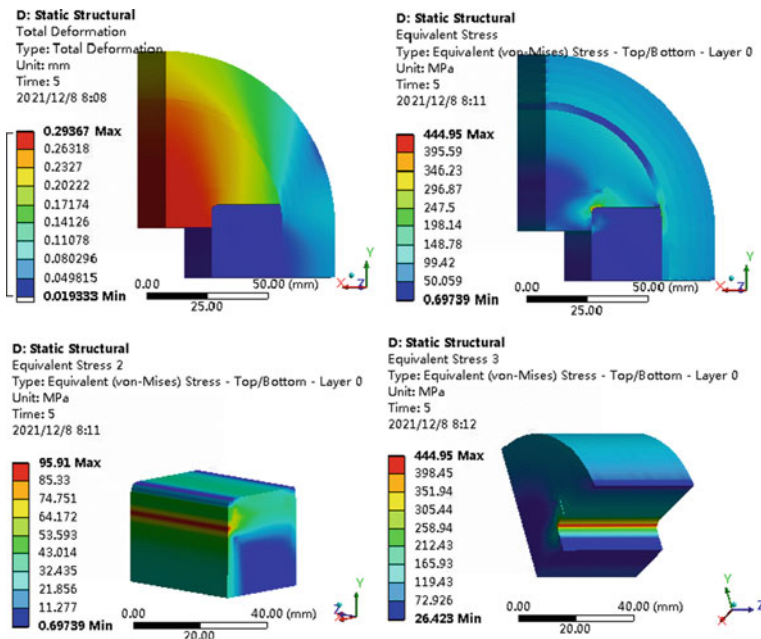


Fig. 8 After withstanding the electromagnetic expansion force under 100 MPa pre-tightening force

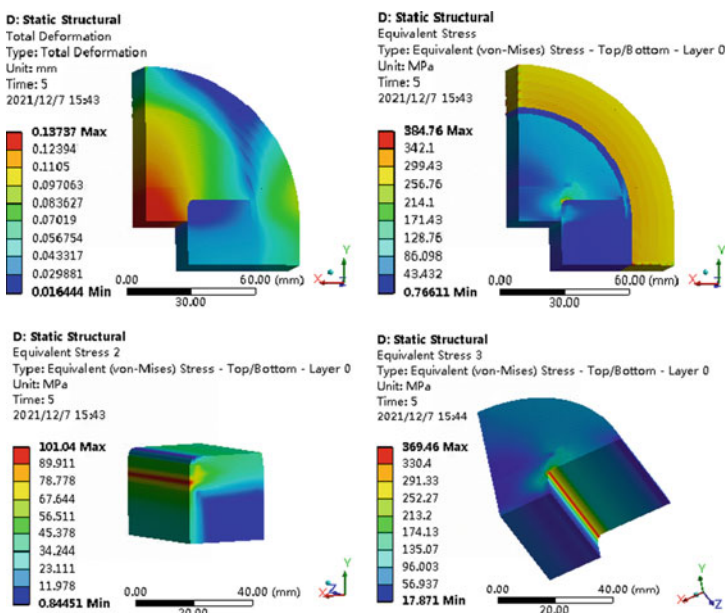
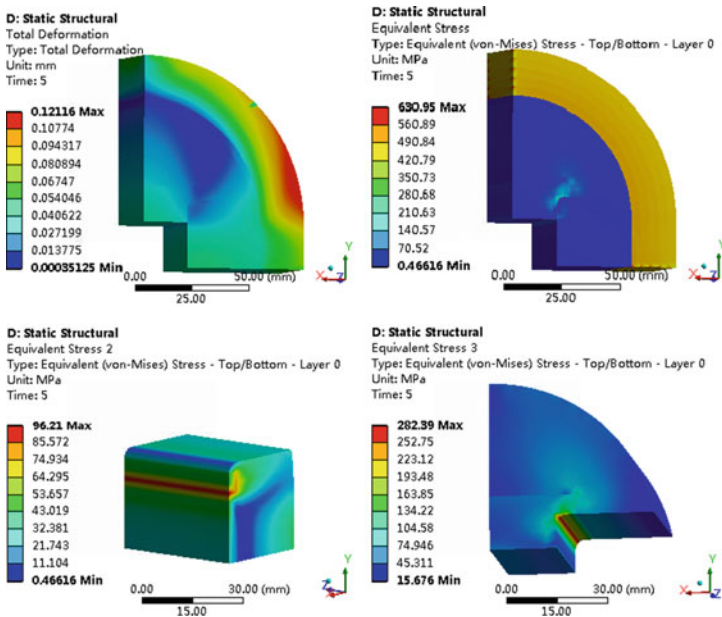
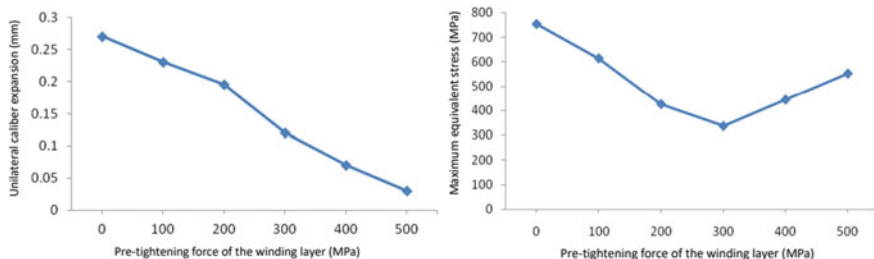


Fig. 9 The stress and deformation of the barrel when 300 MPa pre-tightening force is applied to the winding layer of the barrel



**Fig. 10** The stress and deformation of the barrel when 500 MPa pre-tightening force is applied to the winding layer of the barrel



**Fig. 11** Change curve of relevant parameters



**Fig. 12** GO gauge Experiment

**Table 1** Material Properties of Barrel Parts

Main Parts	Material	Density (g/cm <sup>3</sup> )	Resilient Modulus (MPa)
Rail	Copper alloy	8.25	1.3e + 5
Insulation supporter	G10	1.8	1.5e + 4
Winding layer	Carbon fiber T700	1.85	1.54e + 5 (main direction)
Insulation layer	Kevlar	1.3	9.0e + 4
Rail supporter	Steel	7.85	2.06e + 5

**Table 2** Anisotropic Elastic Mechanical Parameters of T700 Carbon Fiber/Epoxy Resin after Parameter Transformation

Fiber	Ex(GPa)	Vxy	Vyz	Vxz	Gxy(GPa)	Gyz(GPa)	Gxz(GPa)
T700	154.2	0.33	0.49	0.49	7.1	3.8	7.1

**Table 3** Comparison between the Circumferential Stress Generated by the Temperature Difference Method and that Generated by Direct Prestressing

Name	Prestress (temperature difference)	Maximum circumferential stress (MPa)	Minimum circumferential stress (Mpa)
Temperature difference method	300 °C	354	52
Prestressing	300 MPa	365	48

**Table 4** Mechanical Properties of the Barrel under Different Prestresses

Prestress (MPa)	Caliber deformation (mm)	Maximum barrel stress (MPa)	Caliber change rate	Maximum rail stress (MPa)
100	0.013	125.4	0.03%	39.3
200	0.028	251.0	0.07%	82.4
300	0.017	330.7	0.043%	110
400	0.024	440.9	0.06%	148
500	0.060	551	0.075%	185

**Table 5** Barrel Mechanical Parameters of Different Prestresses under the Action of Electromagnetic Force

Pre-tightening force (MPa)	Unilateral expansion in the Y-direction (mm)	Maximum rail stress (MPa)	Maximum supporter stress (MPa)	Caliber change rate (%)
0	0.27	348.7	47.5	1.35
100	0.23	344.5	47	1.15
200	0.195	308	49.7	0.975
300	0.12	271.8	54.6	0.6
400	0.07	240.9	67.7	0.35
500	0.03	214.7	80.7	0.15

**Table 6** Barrel Mechanical Parameters

Sample No	Pre-tightening force (kN)	Rail expansion in the Y-direction (mm)	Maximum rail stress (MPa)	Maximum supporter stress (MPa)
1	200	0.208	319	53
2	500	0.068	232	71

## References

1. Yanhui C, Wei G, Zhouzi S (2018) Analysis and discussion on the problems faced by the engineering of electromagnetic rail gun barrel. Ordnance Material Science and Engineering (02), 41
2. Guimin L, Zhongxu Y, Tao Y, Xiaoying Z (2015) Current Situation and Prospect of the Research on the Guide Failure of Electromagnetic Railgun. Mater Rev 29(07), 63–70
3. Yan L, Zening R, Hongyan Z (2012) Current Situation and Prospect of the Research on the Guide Failure of Electromagnetic Railgun. Ordnance Mater Sci Eng 35(1), 93–96

# A Study on the Outfield Application of Nondestructive Testing Technologies for Stealth Coating



Xiaohuan Guo, Faliang Sun, Xiaoju Yong, and Minghua Chen

**Abstract** The internal debonding occurring in the inlet stealth coating in use will cause the coating to peel off, thereby seriously impacting the overall stealth performance of an aircraft. In order to address this problem, this paper has introduced the nondestructive testing technologies that apply to the detection of the internal debonding defect in stealth coating. Additionally, experiments with infrared thermal imaging and phased array ultrasonic testing technologies and equipment have been carried out in this paper, which will facilitate the real-time testing and maintenance of the stealth coating in service.

**Keywords** Stealth coating · Nondestructive testing · Internal defect

## 1 Introduction

External physical defects in the stealth coating in use, such as cracking, peeling, and blistering, can be visually inspected and timely corrected, whereas debonding occurring inside such coating cannot be detected visually. Moreover, if the stealth coating of key parts (such as the inlet) is identified with internal debonding, it will peel off, thereby impairing the overall stealth performance of the aircraft and even threatening flight safety. Therefore, testing and locating the damage inside the stealth coating plays a significant role in safeguarding the stealth performance of the aircraft. Nondestructive testing (NDT), based on multiple physical and chemical principles, is a testing method for evaluating the discontinuous area, physical properties, and chemical composition of the materials to be tested, on the premise that the original status, physical properties, and chemical composition of such materials are not impaired [1, 2]. It will not damage the materials and can visualize the internal damage. Accordingly, this paper has introduced the NDT technologies that apply to the detection of the internal debonding defect in the stealth coating. Besides, in this paper, stealth coating specimens with pre-set internal debonding damage have been designed and

---

X. Guo (✉) · F. Sun · X. Yong · M. Chen

Sergeants School of Aviation Locomotive, Air Force Engineering University, Henan, China

made for analyzing the critical technical parameters and testing effects of infrared thermal imaging and phased array ultrasonic testing technologies and equipment, which will guide the application of NDT technologies in safeguarding the outfield support of stealth coating.

## 2 NDT Technologies for Coating Damage Detection

The NDT technologies for detecting coating damage at home and abroad at present include mainly ultrasonic testing technologies, infrared thermal imaging testing technology, and laser shearography.

### 2.1 Ultrasonic Testing Techniques

#### 2.1.1 Ultrasonic Microscope Technology

The ultrasonic microscope technology uses the high-frequency or ultra-high-frequency ultrasound incident on the near-surface of the material to be inspected and projects the acoustic differences of the material to produce a characteristic image that reflects the relation between the resolution and ultrasonic frequency. Then the characteristic image is used to perform nondestructive testing and evaluation of the material. When testing the internal quality of special coatings with the ultrasonic microscope technology, Wu et al. [3] discovered that the technology could detect internal defects in coatings, such as cracks, porosity, and debonding from the substrate. However, due to the difficulties in producing high-frequency ultrasonic probes, high requirements for relevant supporting instrumentation, the complexity of the testing system, and high requirements for the roughness of the surface of the materials to be inspected, the ultrasonic microscope technology is mainly used for testing precision components, biological tissues, and ultra-thin film.

#### 2.1.2 Laser-ultrasonic Technology

The laser-ultrasonic testing technology uses the thermoelastic effect and ablation mechanism generated through laser irradiation on the structure's surface to excite the ultrasonic guided waves in the structure, thereby carrying out structural testing. Due to its non-contact excitation, the high spatial resolution of the testing, and relaxed requirements for the surface of the machine elements, the technology has become a trending topic in the NDT field. Qiu et al. [4], based on the laser-ultrasonic technology, carried out an in-depth discussion and exploration into the damage testing method for

the laminated structure. However, in light of the low photoacoustic conversion efficiency, weak echo signal, and low testing sensitivity, the laser ultrasound technology does not apply to high-attenuation materials.

### 2.1.3 Ultrasonic Pulse Echo Technology

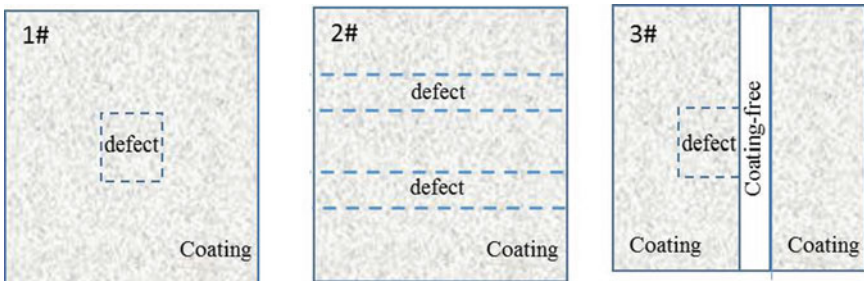
The ultrasonic pulse echo technology is the first ultrasonic testing technology to have been applied, with simple testing means and low requirements.

## 2.2 *Infrared Thermal Imaging Testing Technology*

The infrared thermal imaging testing technology is a new NDT testing method that has been developed rapidly in recent years. It has been widely used due to its convenience and efficiency. Besides, it has become one of the main NDT testing methods of the National Aeronautics and Space Administration (NASA) for quality testing in regard to aerospace. Li et al.'s studies showed that the thickness and defects of the 0.35–2 mm-thick coating specimen with a carbon fiber substrate could be tested with the infrared thermal imaging NDT technology, and the precision of the coating's thickness tested was 0.1 mm. Naval University of Engineering [5] created a pulse phase testing model for thermal barrier coating in axisymmetric cylindrical coordinates to analyze the influences of different factors on the testing results. Relevant studies indicated that if the coefficient of the thermal conductivity was lower or the material was thinner, the sensitivity of the infrared thermal imaging technology used for testing the bonding quality and thickness of the laminated material would be higher.

## 2.3 *Laser Shearography*

Laser Shearography, also known as speckle pattern shearing interferometry, is a non-contact, full-field measurement optical testing technology evolving in recent years. When the load is increased on the defective coating, the debonding area between coatings will result in abnormal strain distribution on the coating surface. A pair of speckle interferometric images is acquired before and after loading to create a difference. By doing so, a strip image characterizing the abnormal strain can be obtained. Then the phase difference information is extracted via the phase shift technology. In this way, the information on the coating surface deformation brought about by the external loading on the internal defects in the materials can be directly reflected. However, the testing system is relatively sensitive to disturbances, thereby setting a high requirement for testing conditions.



**Picture 1** Design diagrams of the debonding defects in the materials [self drawn]

### 3 Analysis of the Applicability of NDT Technologies for Stealth Coating

#### 3.1 Experiment with Infrared Thermal Imaging Testing Technology

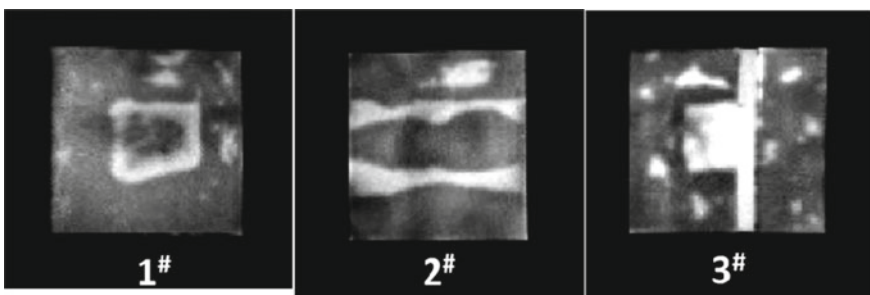
In this experiment, infrared thermal imaging testing equipment was used to carry out the NDT of the pre-made defective stealth coating materials to check whether the testing results were consistent with the pre-made defects. Picture 1 shows the design diagrams of the debonding defects in the materials. It can be found in the picture that three types of defects are designed, namely the central defect, penetration defect, and boundary defect. In Picture 2, the three defective specimens are depicted in the pictures, and the artificial defects in the specimens cannot be detected visually. Picture 3 displays the thermograms of the three defective specimens. The testing results were completely consistent with the designed defects. As the defects led to a difference in the internal conduction of the thermal waves after the coatings were thermally excited, the intensities of the thermal waves reflected onto the surface were different, thereby causing the surface temperatures to vary. Since the debonding defect belongs to the thermal-insulation defect, the temperature of the surface of the defective part is higher than that of the normal coating surface. Additionally, the results showed that the boundaries of the defective areas were irregular, mainly because the 914 epoxy resin used for sticking the adhesive film of the pre-made coatings extended after being pressed during the specimen-making process.

#### 3.2 Experiment with Phased Array Ultrasonic Testing Technology

Picture 4 shows the pre-made coatings with internal defects, which simulate the debonding of the coating from the substrate. Between the coating of the defective

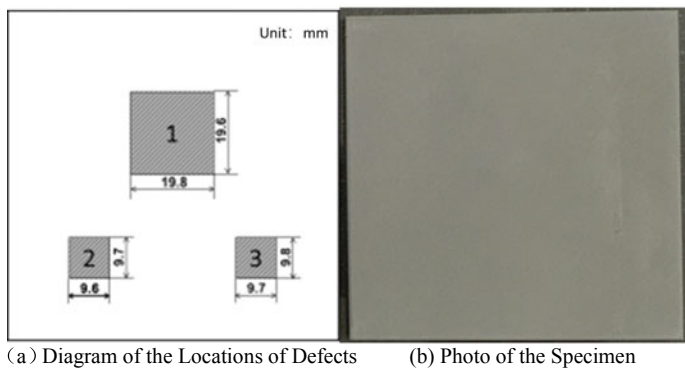


**Picture 2** Pictures of the specimens of the defective materials [self drawn]

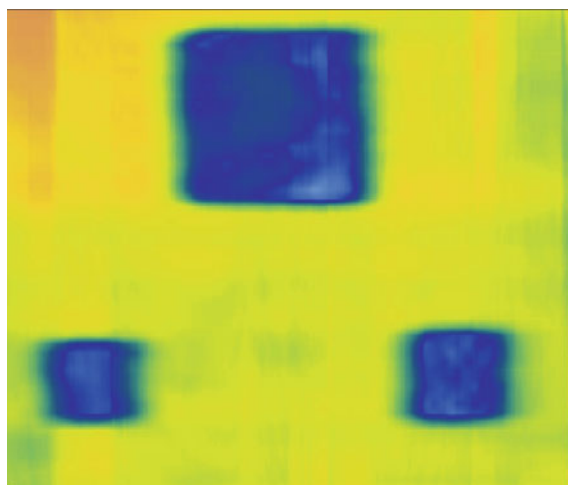


**Picture 3** Thermograms of the three defective specimens [self drawn]

part and the substrate is the air layer. Picture 4a shows the locations of the defects in the specimens; Picture 4b is a photo of the specimen of the absorbing coating with artificial defects, and the specimen, by visual inspection, is identical to a defect-free coating. In Picture 4a, the dimensions of the defect at Location 1 are 19.8 mm × 19.6 mm, while the dimensions of the defects at Locations 2 and 3 are 9.6 mm × 9.7 mm and 9.7 mm × 9.8 mm, respectively. Picture 5 presents the defects detected by the phased array ultrasonic testing equipment. The dimensions of the defects are measured based on the ultrasonic A-scan signal with the –6 dB method. In Table 1, the quantitative results of the phased array ultrasonic testing of the defects' dimensions are presented. Statistically, the maximum absolute error and the maximum relative error between the testing result for the defect at Location 1 and its actual dimensions are 0.6 mm and 3%, respectively; for the defect at Location 2, they are 0.3 mm and 3%, respectively; for the defect at Location 3, they are 0.4 mm and 4%, respectively. Therefore, for the three defects, the relative errors between the testing results and their actual dimensions are all  $\leq 4\%$ , complying with the engineering requirements.



**Picture 4** Absorbing coating specimen with debonding defect [self drawn]



**Picture 5** Result of phased array ultrasonic imaging testing of stealth coating defects [self drawn]

**Table 1** Quantitative results of phased array ultrasonic testing of defects' dimensions [self drawn]

Defect No	Actual dimensions (mm)	Dimensions tested (mm)	Maximum absolute error (mm)	Maximum relative error (%)
1	$19.8 \times 19.6$	$20.0 \times 19.0$	0.6	3
2	$9.6 \times 9.7$	$9.8 \times 10.0$	0.3	3
3	$9.7 \times 9.8$	$10.0 \times 10.2$	0.4	4

### 3.3 Applicability Analysis

According to the above results of the simulative testing of the internal defects in the absorbing coating with the infrared thermal imaging testing system and the ultrasonic testing method, it is considered that the two methods apply to the NDT of the internal defects in the absorbing coating. Nevertheless, in light of the characteristics of the outfield, they are preliminarily believed to be different in terms of the scope of application to the stealth coating of the surface of an aircraft. The entire infrared thermal imaging testing system requires a thermal exciter, a high-energy flashlight, and a box cover simultaneously. Besides, the size of the system is very large and can hardly be reduced. Therefore, the infrared thermal imaging testing system applies to the fast and large-area inspection of the defects in the external surface coating of an aircraft, not the testing of the internal defects in the stealth coating of the inlet. In comparison, by the testing results of ultrasonic testing of defects, the phased array ultrasonic testing technology can effectively identify the defects in the stealth coating, the relative errors between the testing results and the actual dimensions of the defects are all below 4%, and the testing results are basically consistent with the pre-made defects in terms of location and dimensions. Besides, the portable design applies to the phased array ultrasonic testing technology, the weight of the whole machine is no more than 5 kg, and the ultrasonic probe can be roller-shaped. Thus, the phased array ultrasonic testing technology is applicable to the inspection on the engineering sites and to the rapid inspection of internal defects in the stealth coatings of the inlet and external surfaces.

## 4 Conclusion

This paper has summarized the NDT technologies applicable to coating testing and selected the infrared thermal imaging and phased array ultrasonic testing technologies based on the characteristics of stealth coatings. According to the experiment results and the requirements for the application of NDT technologies in the outfield and for the testing, it is considered that the phased array ultrasonic testing technology is the optimal outfield testing method, especially for testing the inlet coating damage, while the infrared thermal imaging testing applies to the fast and large-area inspection of the defects in the coating of the external surface of an aircraft.

## References

1. Li J (2006) The principle and experimental research of ultrasonic characterization for layered medium. Master's degree thesis, Dalian University of Technology, Dalian

2. Liu P (2018) Research on defect identification of stealth materials based on laser shearing speckle interferometry. Master Thesis, Library of University of Electronic Science and Technology of China, Chengdu
3. Wu SH (2005) A study on the application of the ultrasonic microscope system in coating testing. *Aerospace Mater Technol* 4:55–57
4. Zhu Q (2016) Nondestructive testing research based on laser ultrasonic technique for laminated structure. Dissertation, Nanjing University of Aeronautics and Astronautics, Nanjing
5. Chen L, Yang L et al (2015) Infrared quantitative identification of the thickness and debonding defect of the thermal barrier coating based on phase. *Infrared Laser Eng* 44(7):2050–2056

# Simulation Analysis of the Maneuverability Limit of a Certain Type of Military Vehicle Based on Adams/Car Under Semi-Circular Obstacles



Rui Tao, Ming Zhang, Yaoyu Fu, Yunbo Zhou, Jianing Bai, Jun Zhou,  
and Yongguang Yu

**Abstract** Taking a certain type of off-road vehicle as the research object, the corresponding high-fidelity multi-body dynamics whole vehicle model is constructed based on Adams/car, combined with the test approach of U.S. Army TOP01-1-014A, the vertical peak acceleration and vertical vibration dose value (VDV) obtained from simulation are plotted as a function of velocity, and the maneuverability performance limit of a certain type of tactical wheeled vehicle through each size of semi-circular obstacles is obtained through nonlinear interpolation, which provides test, simulation, and analysis experience for China's off-road vehicle maneuverability limit evaluation program.

**Keywords** Off-Road vehicles · Vertical peak acceleration · Vibration dose value (VDV) · Maneuverability evaluation

## 1 Introduction

The maximum maneuvering speed of an off-road vehicle on the ground depends in part on the driver's tolerance limit for riding uncomfortably through uneven ground. The surface undulations of rough terrain can cause internal vibrations in the vehicle, and the vibrations generated by the vehicle driving over rough terrain are transmitted to the driver through the tires, suspension, and body, and when the driver feels the discomfort, a speed reduction occurs to mitigate the vibrations [1].

---

R. Tao (✉) · M. Zhang · Y. Zhou · J. Bai

School of Mechanical Engineering, Nanjing University of Science and Technology,

Nanjing 210094, Jiangsu, China

e-mail: [hputaorui@163.com](mailto:hputaorui@163.com)

Y. Fu · J. Zhou · Y. Yu

Chinese People's Liberation Army Unit 63969, Nanjing 211113, Jiangsu, China

Domestic and foreign research on the maneuverability of vehicles considering occupant vibration impact mainly focuses on the absorbed power of occupants. Han Yu et al. studied the maneuverability of off-road vehicles under E-class road surface by taking the average vehicle speed under the human absorbed power of 6 W as an evaluation index [2]; Wang Zhang et al. used the vehicle speed corresponding to the average absorbed power of occupants when driving on different classes of road surface as an evaluation index and simulated its smoothness [3]; Chen Xin et al. took a domestic  $8 \times 8$  independent suspension heavy vehicle as an example to study the relationship between the root mean square value of occupant seat acceleration and vehicle speed and the relationship between the average absorbed power and vehicle speed on different classes of road surface [4].

At present, the mobility evaluation method of domestic off-road vehicles is mainly based on the absorbed power, but the absorbed power is the average value of time, which reflects the intensity of the vibration amount on a macro level, but cannot reflect the rapid change of the vibration amount, and is not suitable for instantaneous acceleration. vibration. However, there are many foreign studies on this situation. Vibration dose value VDV and vertical acceleration peak are commonly used evaluation indicators. Therefore, in order to study the mobility limit of a certain type of high-mobility off-road vehicle, we will use the fallen trees, telephone poles, and other pillars commonly found in the battlefield environment as obstacles, using the test method of TOP01-1-014A in the United States [5], through test verification, and the simulation predicts the limit speed of the vehicle passing through four semi-circular obstacles of 4 inches, 6 inches, 8 inches, and 10 inches.

## 2 Vehicle and Terrain Modeling

### 2.1 Adams/car-Based Modeling of the Entire Vehicle

Before carrying out the mobility performance limit simulation of the whole vehicle, it is necessary to establish the whole vehicle model of the vehicle, by obtaining the basic parameters of each component required for the whole vehicle, divide the whole vehicle into subsystems according to the modeling ideas in ADAMS/car [6], modify the hard points and relevant performance parameters of the subsystem model, write relevant property files, and finally assemble the whole vehicle multi-body dynamics model of the military vehicle as shown in Fig. 1.

**Fig. 1** Whole vehicle multi-body dynamics model

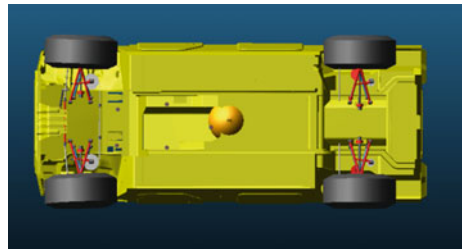
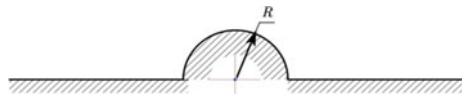


**Fig. 2** Cross-sectional view of semi-circular barrier pavement



## 2.2 Terrain Modeling

It is necessary to make four sizes of semi-circular pavement with radius  $R$  of 4 inches, 6 inches, 8 inches, and 10 inches, respectively. The cross section of semi-circular pavement is shown in Fig. 2 below.

In order to generate a more realistic pavement, it is necessary to use the Adams software 3D pavement modeling ideas, with the help of the equivalent volume method to establish the pavement model, the specific idea is three nodes constitute a triangular pavement unit, a series of pavement units combined to form the entire road.

The semi-circular pavement was first modeled by Hypermesh finite element software, then the pavement was triangulated, and the pavement file was prepared by extracting all node serial numbers and coordinates and using volume pavement files such as Adams/Car [7].

## 3 Experimental Validation

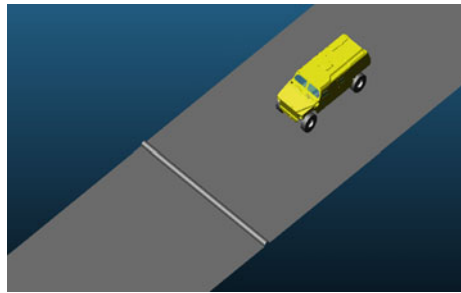
The acceleration measurements at the driver's seat cushion and seat floor were performed at a test site using a triaxial seat cushion accelerometer. For a given semi-circle size, the test recorded the z-directional vibration acceleration at the driver's seat base at a high sampling rate (500 Hz). The test data was low-pass filtered (30 Hz, fourth-order low-pass filter) in accordance with the requirements of the U.S. Army TOP01-1-014A test method. At the same time, the test analysis software Dewe-soft has a whole body vibration (WBV) analysis module for real-time recording of vibration dose values VDV (Figs. 3 and 4).

The simulation can directly obtain the floor vertical vibration acceleration, but the vibration dose value VDV is obtained by frequency-weighting the floor vertical vibration acceleration and then integrating it. The Frequency-Weighted Acceleration

**Fig. 3** Impact semi-circular barrier



**Fig. 4** .Simulation of impacting a single semi-circular barrier



module is used in DIADEM for frequency-weighting the signal, which provides digital filters for all frequency-weighting curves specified in ISO2631 and ISO5349 [8].

As shown in Fig. 5, the test data at the driver's seat floor when the vehicle passes through an 8-inch (15 cm) semi-circle obstacle at 10 km/h is filtered by a low-pass filter and the simulation results are plotted. As shown in Fig. 6 below, the time course  $a(t)$  of the driver's seat floor vertical vibration acceleration from the above simulation is weighted in the frequency domain to obtain the floor vertical weighted acceleration time course  $aw(t)$ .

The resulting weighting results are calculated to obtain the value of VDV under the impact once semi-circular barrier. The simulation and test results of the peak floor vertical acceleration and vibration dose value VDV under the 10 km/h impact 8-inch semi-circular condition are shown in Table 1 below.

**Fig. 5** Driver's floor vertical acceleration test and simulation curve

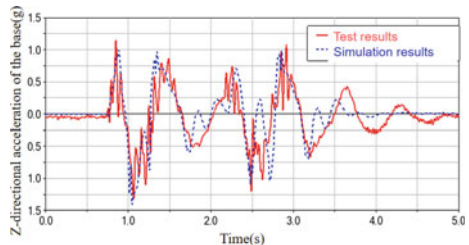


**Fig. 6** Simulation data of driver's floor vertical acceleration and its weighted acceleration

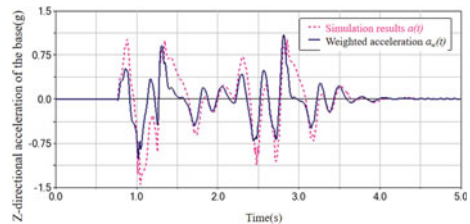


**Table 1** Experimental and simulation results under various evaluation indexes

Evaluation Indicators	Half circle size (inch)	Vehicle speed (km/h)	Simulation results	Test results	Error (%)
Peak vertical acceleration	8	10	1.32 g	1.41 g	6.8
Vertical vibration dose value VDV	8	10	4.61 m/s <sup>1.75</sup>	4.81 m/s <sup>1.75</sup>	4.1

The simulation and test errors of the peak vertical acceleration and vertical vibration dose value VDV obtained are within 10%, indicating that the model accuracy meets the requirements of subsequent simulations.

## 4 Vehicle Mobility Limit Simulation

The simulation was performed using the Adams/car whole vehicle analysis module, and the vibration acceleration in the vertical direction of the driver's seat floor was recorded at the same 500 Hz sampling frequency through a pre-prepared road with different initial speeds set through the semi-circular obstacle.

The peak acceleration and vibration dose values of the vehicle through each size of semi-circular obstacle were plotted as a function of velocity, and the simulation results were obtained by nonlinear fitting as shown in Figs. 7 and 8 below.

According to the requirements of the U.S. Army on the half-circle obstacle test in the peak vertical acceleration and ISO 2631-1 used vibration dose value (VDV) warning area upper limit value, the use of vertical peak does not exceed 2.5 g and vertical vibration dose value does not exceed 8.5 m/s<sup>1.75</sup> two evaluation index to explore the size of the half-circle obstacle under a certain type of military vehicles mobility limit, to reach the limit value of the vehicle speed will be determined by The above nonlinear interpolation curve to determine the speed of the vehicle at this time as the limit speed of this type of obstacle road, the simulation results obtained are shown in Table 2 below.

From the above results, it can be seen that when the vehicle through the equivalent profile of 4-inch semi-circle or smaller obstacles, the vehicle maneuverability will not be significantly limited, in the vehicle speed greater than 35 km/h when the

**Fig. 7** Driver floor z-direction peak acceleration versus vehicle speed

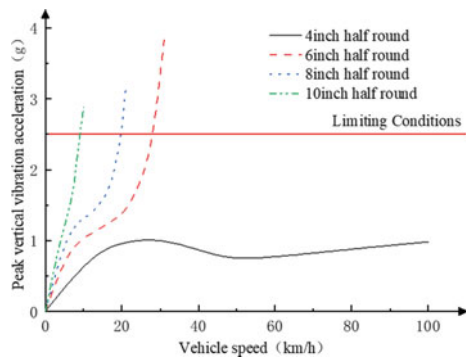


**Fig. 8** Driver floor vertical vibration dose value VDV versus vehicle speed

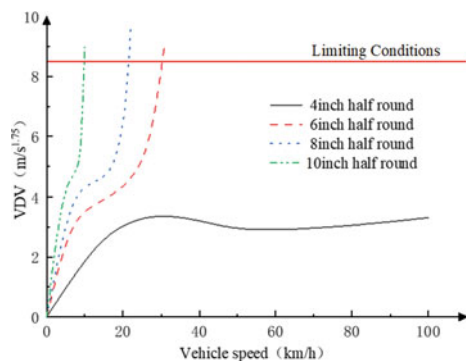


**Table 2** Velocity limit results for impact semi-circular barriers

Half circle size (inch)	Limit speed based on vertical vibration acceleration not exceeding 2.5G (km/h)	Limit speed based on vertical vibration dose value VDV not exceeding 8.5 M/S <sup>1.75</sup> (km/h)
4	100	100
6	28.8	25.4
8	20.7	17.9
10	9.3	8.5

impact is reduced, mainly because the low speed, the road to the vehicle excitation frequency is low, close to the vehicle damping system inherent frequency, not easy to play the damping system damping effect, and high speed, the road to the vehicle Excitation frequency is relatively high, greater than the damping system's inherent frequency, most of the impact energy is absorbed by the damping system, so that the impact transmitted to the human body is greatly reduced, which is why the vehicle through the 4-inch semi-circular obstacles, the impact on the occupants with the speed increase first increase and then decrease and then increase; and for more than 4 inches of semi-circular obstacles, vehicle mobility will be significantly limited,

so in the vehicle through similar size. Therefore, the vehicle should be limited to a certain speed when passing through obstacles of similar size to avoid transferring the danger to the driver.

## 5 Summary

In this paper, a high-mobility off-road vehicle is taken as the research object, and a vehicle maneuverability evaluation model is established through multi-body dynamics modeling and experimental registration. This paper predicts the limit speed of passing through semi-circular obstacles of different sizes when the dose value of vertical vibration exceeds 2.5 g and the dose value of vertical vibration does not exceed  $8.5 \text{ m/s}^{1.75}$ . The simulation results show that the evaluation results of the two evaluation indicators are basically similar under the restriction of the vehicle's maneuverability by semi-circular obstacles, but when the equivalent contour is between 4 and 10 inches of semi-circular obstacles, the VDV value-based evaluation results are basically similar. The evaluation is more severe.

## References

1. Durst PJ, Baylot A, Mckinley B (2011) Techniques for inferring terrain parameters related to ground vehicle mobility using UAV born IFSAR and LIDAR data. In: Proceedings of SPIE - The International Society for Optical Engineering, 8020
2. Han Y, Guangwei M, Chaosheng H et al (2015) Research on the mobility of off-road vehicles. Vib Shock 34(2):5
3. Zhang W, Lei W, Mingfeng Z, et al. (2021) Mobility simulation analysis and evaluation of an off-road vehicle. Veh Power Technol (02):7–10+17
4. Xin C, Q, Tao, L, Shuancheng et al (2008) Research on the analysis method of off-road ride comfort of high mobility vehicles. Automot Eng 30(9):7
5. Test Operations Procedure 01-1-014A (2011) Ride Dynamics and Evaluation of Human Exposure to Whole—body Vibration
6. Song NX et al (2019) Vehicle ride comfort analysis and optimization based on ADAMS/Car software. J Jinan Univ: Nat Sci Ed 33:5
7. Zhu MT, et al. (2010) Reproduction of 3D virtual road based on ADAMS. Mech Des Manuf (6):3
8. Xu ZM, Zhou XL, Yu F, Zhang F, Tan JL (2012) Comparison of time domain method and frequency domain method in vehicle ride analysis. Automot Eng (4):5

# An Extraction Method of Resistance Characteristics in Different Microchannels Using Numerical Method



Yang Tang

**Abstract** The resistance characteristics of four positive multi-deformations at microscale were studied numerically with an inlet velocity of 1 m/s. The study involved four sizes of 0.04 mm, 0.06 mm, 0.08 mm, and 0.1 mm pipe inner tangent circle diameters to study the effect of circular pipe expansion boundary in this particular way. The common resistance characteristics among different pipes with the change of pipe diameter and inlet velocity are investigated. For the shape effect of different micro-pipes, the differences in the resistance stability characteristics with diameter and the inlet velocity change are analyzed in a new way, while the resistance distribution at the outlet is also analyzed. The results show the stability of the outlet velocity with pipe diameter changing is related to the shapes of pipes. Besides that, with a unique way to analyze the data, it is found that the positive-even polygon has a special distribution different from that of the integer-odd polygon, and a detailed way to describe the effects of different locations on resistance in pipes.

**Keywords** Micro-pipes · Resistance · Numerical simulation

## 1 Introduction

Micro devices have a strong attraction to manufacturing enterprises with their batch processing, low price, and excellent microscale effect. Different shapes of micro-channel devices are widely used in various fields to achieve different functions, such as machinery, aerospace, biomedical, and chemical analysis.

First of all, the most important issue is to define the micro-pipe. However, there is no consensus about the boundary for the microscale effects. Mehendale et al. give a way to differentiate the size of systems based on their shape [1]. It shows that micro-channels are in 1 to 100  $\mu\text{m}$ , while the mini-channel is in range of 100  $\mu\text{m}$  and 1 mm with a small channel of size 1–6 mm and a conventional channel above 6 mm.

---

Y. Tang (✉)

School of Energy and Power Engineering, Xi'an Jiaotong University, Xi'an, China

e-mail: [tangyang2021@stu.xjtu.edu.cn](mailto:tangyang2021@stu.xjtu.edu.cn)

In addition, Kandlikar showed that the hydraulic diameter in the range of 1–10 m can be converted from micron to nanometer [2]. The hydraulic diameter of the channels in the range of 10  $\mu\text{m}$ –200  $\mu\text{m}$  and 200  $\mu\text{m}$ –3 mm are respectively classified as meter channels and millimeter channels, and conventional channels are more than 3 mm.

Many scholars have also studied micro-channels for different shapes. Araki studied the gas flow characteristics of circular pipes with diameters of 5–100  $\mu\text{m}$ , triangular and trapezoidal pipes with hydraulic diameters of 3.92–10.3  $\mu\text{m}$  and rectangular pipes with dimensions of  $1.33 \times 52.25 \times 7500 \mu\text{m}$  [3–5]. It is concluded that the drag coefficients in the micro-channels were reduced in all shapes of pipes, except for the triangular pipes. Although these properties were obtained experimentally, this is not a general phenomenon. Flockhart and Dhariwal studied pure water in trapezoidal microchannels with diameters of 50–120  $\mu\text{m}$  and concluded that for  $\text{Re} < 600$  [6], the resistance characteristics of the microchannels were consistent with those of conventional channels. Pfund studied the resistance of rectangular microchannels with diameters of 128–521  $\mu\text{m}$  at different roughness characteristics [7]. It was found that for a channel size of  $D_h = 521 \mu\text{m}$  and a relative roughness of 0.57%, the coefficient of friction of the microchannels matched the conventional value, while for higher roughness there appeared to be an increase of 10–25% compared to the conventional channel. In the microchannel, Reynolds number and pipe roughness are important factors influencing microchannel resistance characteristics. Currently, there are different modeling approaches proposed by researchers for different pipe types. For example, Colin established a second-order slip model in rectangular micro-channels, Li established a first-order slip model, and Hsieh experimentally verified the accuracy of the first-order model for rectangular micro-channels [2, 8]. From the present research results, the current comparison of different shaped micro-channels is limited to the comparison of specific flow parameters.

This paper presents the water resistance characteristics of microchannels with different geometries. Circular microchannels with constant velocity distribution at the inlet flow are selected as the standard channel condition, and the velocity distribution of the channels at the outlet is chosen to be the comparison criterion among different channels in order to find the pipes with the same resistance as circular pipes. During the process of finding the same outlet velocity as the circular pipes in other kinds of pipes, some resistance characteristics about the shape effects can be shown, and a way to analyze hydraulic characteristics data is given.

## 2 Micropipe Hydraulic Model

In this part, the physical models and some hydraulic effects are shown, which will be used in the numerical simulation. Besides that, it is the part that is used for the explanation of why we chose these effects or pipe shapes.

## 2.1 Pipeline Model

The 3D physical model was created in Catia and the figure shows the pipes analyzed in this simulation. These pipes are divided into four size series, which have the same inner tangent circle diameters among the specific series, including 0.04 mm, 0.06 mm, 0.08 mm, and 0.1 mm, which is shown in Fig. 1.

Based on the previous background, it can be judged that these pipes are in the micro-pipe range. First, it is assumed that the round pipe is a perfect shape pipe. This is because the round pipes don't have specific effects of boundary shapes on the flow pattern. It is a good idea to set them as control series or reference series. By comparing the non-circular pipe with the same series of circular pipes, the influence of the expanded pipe boundary can be analyzed in a new way, rather than using the hydraulic diameter approach. We believe this way is more valid in the analysis towards the shape influence. Based on the series of pipes listed above, it is possible to explore the different effects of different angular boundaries of non-circular pipes and the interaction effects of the same angular boundaries. In this simulation, some effects are taken into consideration.

Diameter of inscribed circle	0.04mm	0.06mm	0.08mm	0.10mm
Circle				
Quadrangle				
Pentagons				
Hexagons				

**Fig. 1** Shapes of micro-pipes

## 2.2 Continuous Media

It has been shown that when the scale of the study object is fine-tuned to a range of size, the flow law appears significantly different with the scale effect. The most important point for the modeling analysis of this study is whether the N–S equation is applicable. The validity of the assumption of a continuous medium assumption is therefore a very important issue.

There are two key points to the assumption of a continuous medium. First, the scale of the molecular clusters must be sufficiently large compared to the scale of molecular motion, so that molecules can be accommodated in the cluster and a determined value can be obtained by averaging statistics over the cluster. Secondly, the scale of the molecular clusters must be small enough in relation to the scale under study, in which the average physical quantities can be regarded as uniformly constant. To deal with the problem, the dimensionless parameter Knudsen number is used as a criterion for the division [9, 10]. Knudsen number depends on the size of the molecular mean free path and the channel characteristics of size, shown as follows.

$$Kn = \Lambda/D_h \quad (1)$$

The  $\Lambda$  is the molecular mean free path and  $D_h$  is the channel size. In the case of Knudsen, the value is less than 0.001, the flow state of the fluid is continuous, in which situation macroscopic theories and laws such as the Navier–Stokes equations can be applied.

Knudsen number, therefore, can be used to determine the effectiveness of microtubes in the continuum hypothesis. The pipes we used are in a small hydraulic diameter, less than 0.1 mm. (2) The typical calculations of pipes show that the Knudsen number is far less than 0.001, so it is reliable to use the assumption of N–S equations for continuous fluid in this situation. Besides that, no slip boundary condition is used in the flow boundary condition.

## 2.3 Boundary Layer

It is acknowledged that there is a region between the mainstream and the wall with the radial velocity gradient, in which the viscous effects have an influence on the flow nearby, and that is the boundary layer. The boundary layer divides the fluid into two areas. The mainstream area is outside the boundary layer. For laminar flow, this boundary is at the point where the fluid velocity almost reaches the velocity in the mainstream with a tiny pressure gradient. There is an equation to calculate the boundary layer thickness [10]:

$$\delta \approx 2.4 \sqrt{\frac{v}{B}} \quad (2)$$

where,  $v$  is the velocity in the mainstream region. In general practical engineering problems, the boundary layer is so thin that its effect on the flow in the channel is negligible. However, for the fluid flow in tiny size channels, the boundary layer thickness has become non-negligible relative to the real small channel size. So it is vital to consider it in the physical modeling.

## 2.4 Resistance

Resistance in pipes is an important research problem in hydraulics, and resistance in microtubes can be affected by microscale effects which will lead to a deviation in the process of the resistance simulation. Mala GM, Qu WL et al. found that the microscale flow is mechanically very different from the conventional scale flow [11, 12]. Some researchers did some numerical simulations to study this problem. Wang Wei et al. studied the microscale flow law of the rough surface by artificially setting the rough element in the pipe wall. Jin Wen et al. made a simulation study on the surface roughness of straight micropipes by using Fluent and found that using porous parts to achieve wall roughness shows more accurate results. Jin Wen used a porous layer to replace the wall roughness of the straight micropipes and additional momentum source terms (viscous and inertial drag) of the porous medium to simulate the flow near the linear microtubular wall [13, 14]. In this case, the thickness of the porous medium is set in direct relation to the roughness of the tube wall. Therefore, in our study, the thickness of the porous medium is taken to be approximately equal to the average height of the rough element, and the thickness of porous is set to 0.15D (D is the diameter of the inscribed circle of the pipes). Besides that, the same pipe material design is used as Jin Wen's research. Unfortunately, due to the lack of actual experimental data, it is a regret that we cannot use the same method as Jinwen used to derive the inertial resistance coefficient of the straight channel. In this study, the calculation was done directly using the sand grain roughness module in Fluent and the fixed value of roughness constant 0.5 in it.

## 2.5 Other Effects

**Entrance effect.** Viscous incompressible fluid flow in the inlet pipe is different from the flow of a full development situation [15]. Therefore, the flow at the inlet has its own special laws. (1) Inlet section: Inlet section is the area from the inlet to the confluence of the flow boundary layers. For laminar flow, the inlet length-diameter ratio is given by  $l/d \approx 0.5RePr$ , while the ratio for turbulent flow is  $l/d < 60$ . (2) Fully

developed part: This part begins with the point where the flow boundary confluences [16]. This study focuses on the effect of pipe shapes on the fully developed section, so the pipe length is chosen to be 20 mm, which is much longer than the diameter of the pipes, to ensure that the effect of inlet effect is eliminated.

**Capillary force.** The flow of liquid in the micropipe will show a clear capillary phenomenon, which is a curved moon-like partition interface. Capillary action is caused by the apparent action of surface tension between the fluid phase in the microchannel and the solid wall [17]. To avoid this influence caused by the surface tension of the microchannel, the free outflow is used in this study to eliminate the capillary force brought by the pipe outlet.

### 3 Numerical Simulation

#### 3.1 Governing Equations

Numerical simulation software is used to solve the quality, momentum and energy conservation equations. Jin wen et al. investigated the accuracy of three typical  $k-\epsilon$  models and two typical  $k-\omega$  turbulence models with a porous model used to achieve the wall roughness. By comparison, it is reported that the Realizable  $k-\epsilon$  model can effectively reflect the micro-scale flow field variation, and the reason is that the Realizable  $k-\epsilon$  model has good correction for the flow with strong cyclonic flow and curved walls. Although the conditions for these pipes are in laminar flow, in order to get the results as close as possible to the real situation, this paper selects the method Jin wen et al. used.

#### 3.2 Governing Equations

Therefore, in order to simplify the calculation and considering the influence of the small size, the microtubes resistance is established with the following assumptions: (1) Although the microtubes are laminar incompressible flow, K-epsilon model is used to get a more accurate results. (2) Considering water as a Newtonian fluid is a basic requirement. (3) The physical parameters of the fluid and the physical properties of the solid are constant. (4) The effects of natural convection and radiation between the wall and the air are ignored. From this, we can get the transport equations for single-phase flow in the micropipes.

$$\frac{\partial}{\partial t}(\rho k) + \frac{\partial}{\partial x_j}(\rho k u_j) = \frac{\partial}{\partial x_j} \left[ \left( \mu + \frac{\mu_t}{\sigma_k} \right) \frac{\partial k}{\partial x_j} \right] + P_k + P_b - \rho \epsilon - Y_M + S_k \quad (3)$$

$$\frac{\partial}{\partial t}(\rho \epsilon) + \frac{\partial}{\partial x_j}(\rho \epsilon u_j) = \frac{\partial}{\partial x_j} \left[ \left( \mu + \frac{\mu_t}{\sigma_\epsilon} \right) \frac{\partial \epsilon}{\partial x_j} \right] + \rho C_1 S \epsilon - \rho C_2 \frac{\epsilon^2}{k + \sqrt{v \epsilon}} + C_{1\epsilon} \frac{\epsilon}{k} C_{3\epsilon} P_b + S_\epsilon \quad (4)$$

where

$$C_1 = \max \left[ 0.43, \frac{\eta}{\eta+5} \right], \eta = S_{\epsilon}^k, S = \sqrt{2S_{ij}S_{ij}}, \mu_t = \rho C_{\mu} \frac{k^2}{\epsilon}.$$

In this equation,  $k$  is the turbulent kinetic energy,  $\epsilon$  is the kinetic energy dissipation rate, and  $\mu$  is viscosity.  $P_k$  is the turbulent kinetic energy caused by the laminar velocity gradient,  $P_b$  is the turbulent kinetic energy given by the buoyancy.  $Y_M$  is the fluctuation generated by the diffusion of the transition in compressible turbulence.  $\mu_t$  is the vortex viscosity.  $C_2$  and  $C_{1\epsilon}$  are constant.  $\sigma_{\epsilon}$  and  $\sigma_k$  are the turbulent Prandtl numbers of the  $\epsilon$  and  $k$  equations.  $S_{\epsilon}$  and  $S_k$  are user-defined parameters.

Therefore, first use Mesh software to perform mesh partitioning on the 3D model, and then solve it using the finite volume method. The pressure and velocity equations are coupled by using the PRESTO! The inlet condition of the straight micropipes is set as a velocity inlet with a constant velocity. The outlet condition is set as a pressure outlet, and the outlet pressure is set as the atmospheric pressure. The wall boundary is calculated by using the standard wall function method in the near-wall area using the no-slip condition.

### 3.3 Results and Discussion

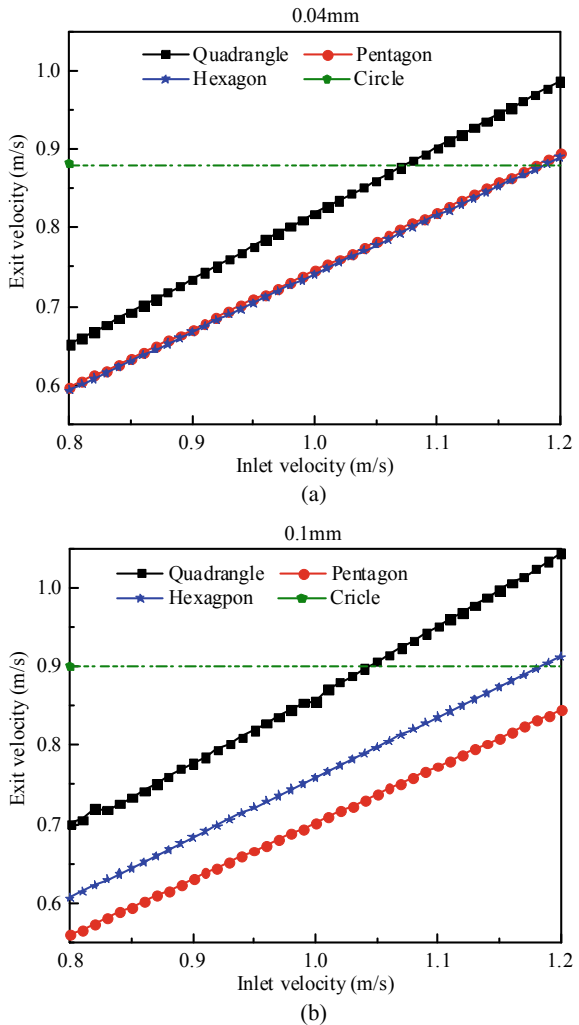
The simulation results were analyzed to determine the average flow rates at the different pipe outlets, and the results are shown as follows. Firstly, in Fig. 2, it illustrates the variation of outlet velocity with inlet velocity change in four size series of pipes.

The outlet velocity increases with the growth of the inlet velocity in four series, respectively. However, although the outlet velocity shows the process of increasing and then decreasing with increasing pipe diameter, which we consider the influence of increased frictional resistance caused by more fluid in the pipes, there are also some different characteristics among these series. The pentagon pipes are more sensitive to changes in increasing pipe size, while the quadrangle is the most stable series, with hexagon pipes not so stable as them. We can see that there is a best size for the least resistance for different pipes, and this size is related to the shape of the pipes. Besides that, a positive even polygon outlet velocity is less affected by the pipe diameter than the positive odd polygon. And it seems there is no direct relationship between the angle of the pipes and the resistance.

To have a clear view, Fig. 3 shows the outlet velocity of different pipes at inlet speeds of 0.8 m/s, 1.1 m/s, and 1.2 m/s. Figure 4 shows the inlet velocity, while the non-circular pipes have the same outlet velocity as the circular pipes in different sizes.

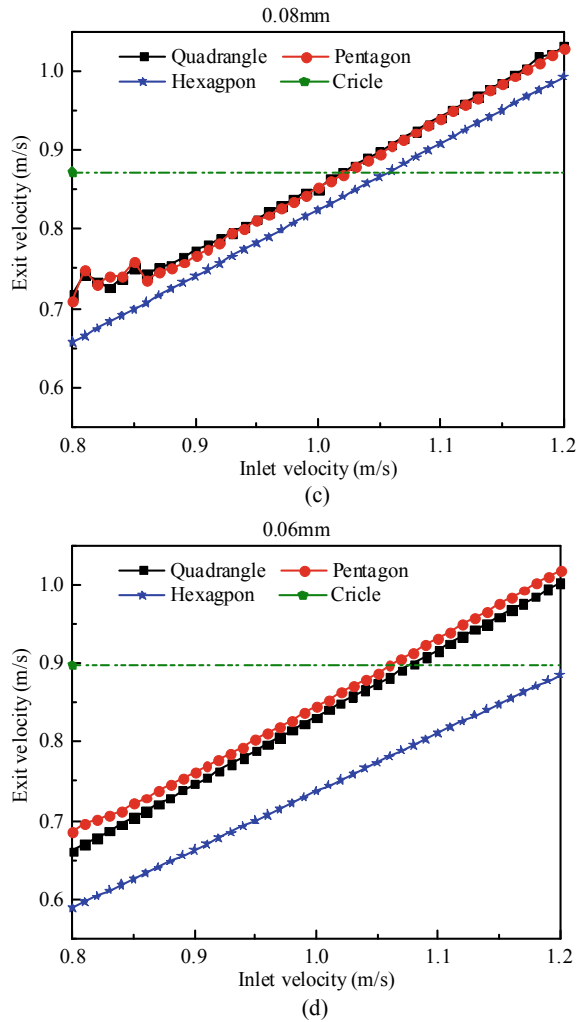
From Fig. 5, it is obvious that the velocity distribution of the inner circle is deformed to different degrees due to the influence of the walls. This must have impeded the flow of fluid, but we cannot figure it out from Fig. 3. By subtracting the velocity distribution in the circular pipes from the velocity distribution in the

**Fig. 2** Average outlet velocity in different sizes of pipes. (Inner tangent circle diameter: **a** 0.04 mm, **b** 0.06 mm, **c** 0.08 mm, **d** 0.1 mm)



non-circular pipes of the same series, a more intuitive distribution can be obtained, as shown in Fig. 6.

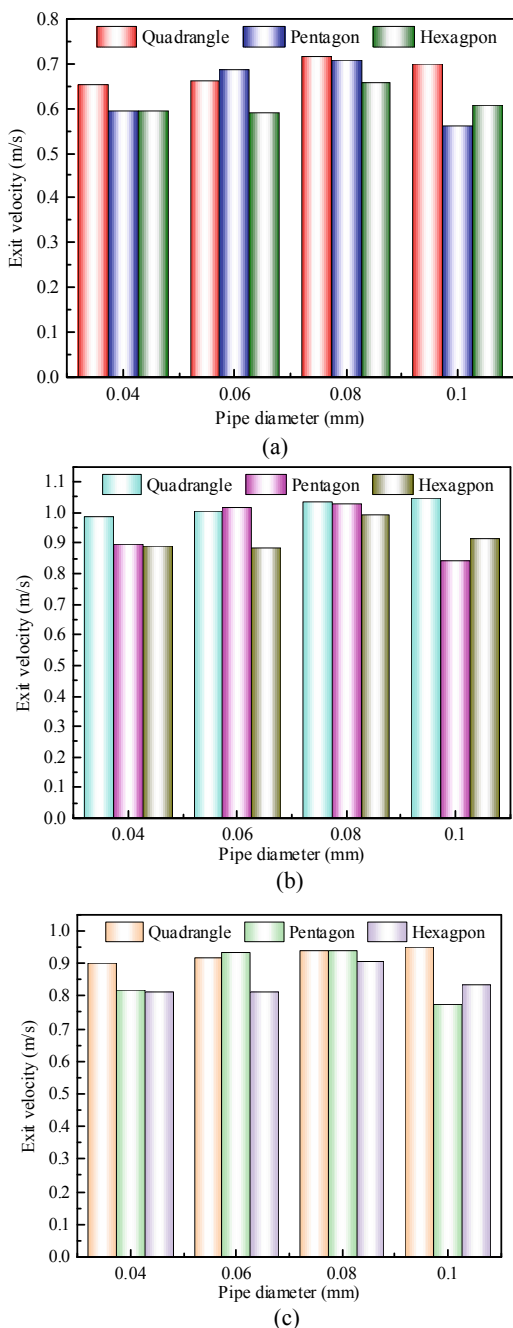
From Fig. 4, the most attractive phenomenon is the area in the middle of quadrangle pipes. This indicates that this area in the square pipes is consistent with the velocity distribution of the circular pipes. However, the hydraulic diameter of the square pipes is larger than that of the circular pipes. Therefore, this indicates that the resistance of this area is significantly larger than that of the circular pipes, and we named the similar area as the inner tangent circular resistance boundary (ITCRB). However, this situation does not occur in other pipes. In the positive pentagonal pipes, all ITCRBs

**Fig. 2** (continued)

are located at the wall in pentagon pipes, and an approximate ITCRB exists at the right-hand boundary. In the hexagonal pipes, only four ITCRBs are present.

However, it should be noted that it does not show the region in less resistance, when the calculation results are bigger than zero. First, this treatment does not calculate the area outside the inner tangent circle, but that area results in a higher pipe resistance. Next, since the hydraulic diameter of the positive multi-deformation pipes is larger than that of the circular pipes, the actual resistance boundary should be larger than ITCRB. Based on the above two points, the middle horizontal area of the hexagon pipes can also be seen as a relatively large resistance area. To get more digitizing features, a Fourier fit is performed with radius and outlet velocity, after polarizing the

**Fig. 3** Average outlet velocity in different inlet velocities. (Inlet speed: **a** 0.8 m/s, **b** 1.1 m/s, **c** 1.2 m/s)



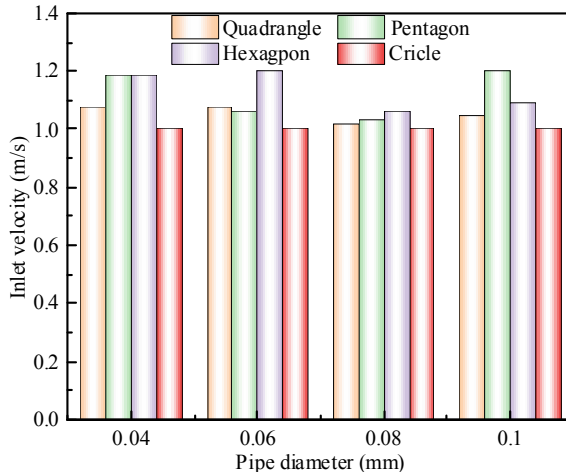


**Fig. 4** Inlet velocity with the same outlet velocity of pipes

data points, and the curves of different pipes at horizontal line positions are selected for presentation in Fig. 7.

It can be seen that the boundary of the positive-even polygon shows a special distribution different from that of the integer-odd polygon. Since gravity is considered in the numerical simulation, this is most likely due to gravity, which remains to be explored. Combined with the stability of the mean velocity, it can be conjectured that the special distribution form can slow down the variation of the mean velocity influenced by pipe diameter. In addition to this, the increase in resistance of the positive multi-deformed pipes is compared to the resistance of the circular pipes, which suggests that the mitigation effect of the resistance at the center is less than the increase of the resistance boundary (including the ITCRB) together with the region outside the inner tangent circle. However, the distribution remains to be further explored.

## 4 Conclusions

A comparative analysis was performed for four different shapes of pipes. In the average velocity line charts of the outlet section, the relationship between the pipe outlet velocity and pipe inner tangent circle size is first analyzed to get the connection between pipe size and pipe resistance. Then, the trend of velocity variation with pipes of different sizes is analyzed to get the relationship between pipe shapes and the magnitude of resistance change of pipes at different sizes. Moreover, the resistance distribution characteristics are analyzed by plotting images of the data after subtracting the velocity distribution between non-circular pipes and circular pipes.

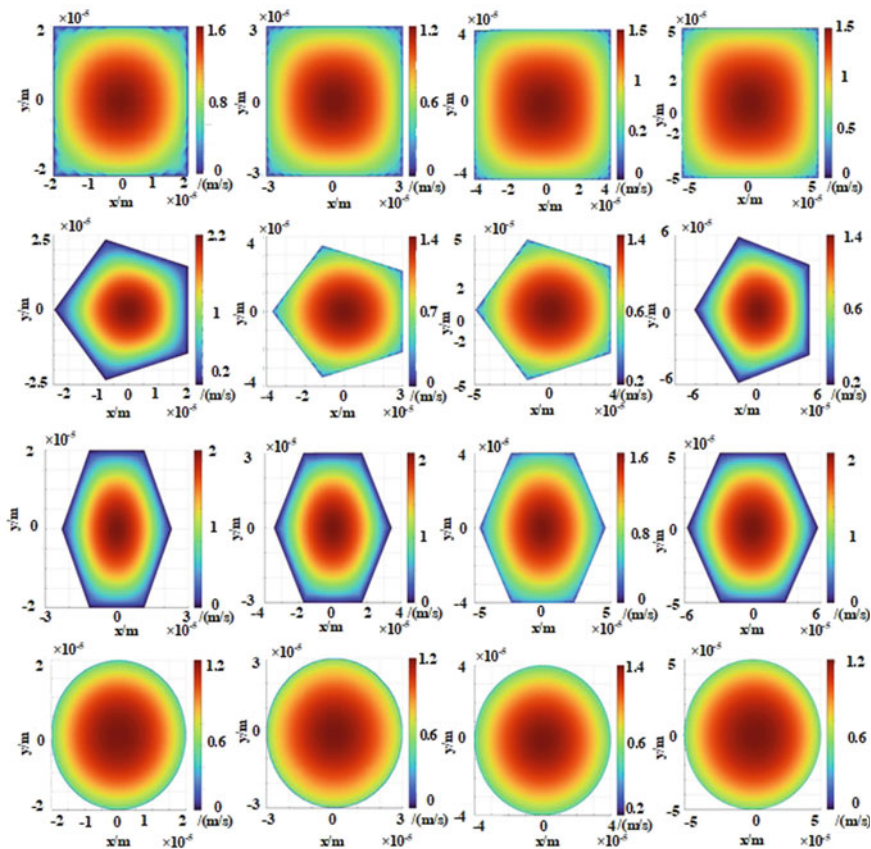


Fig. 5 Pipeline exit velocity cloud

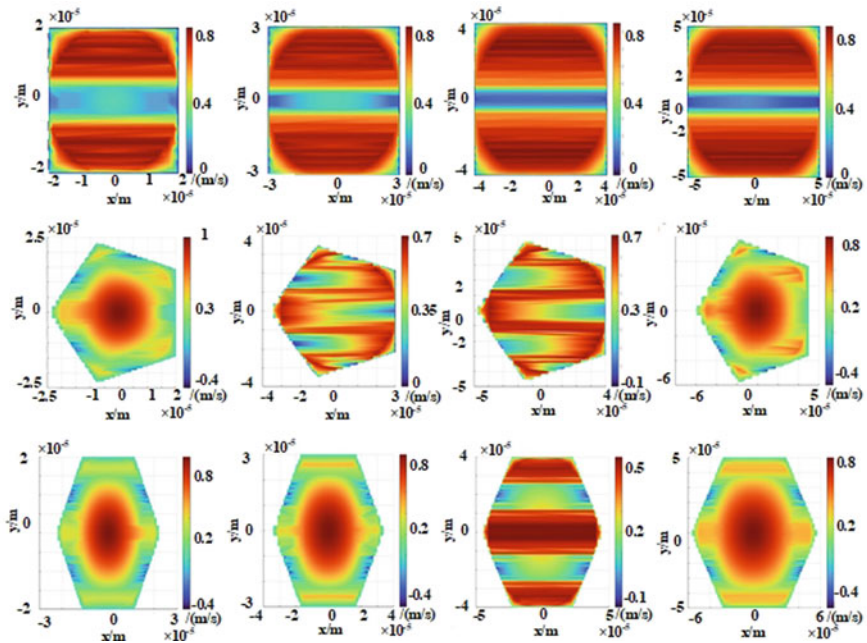
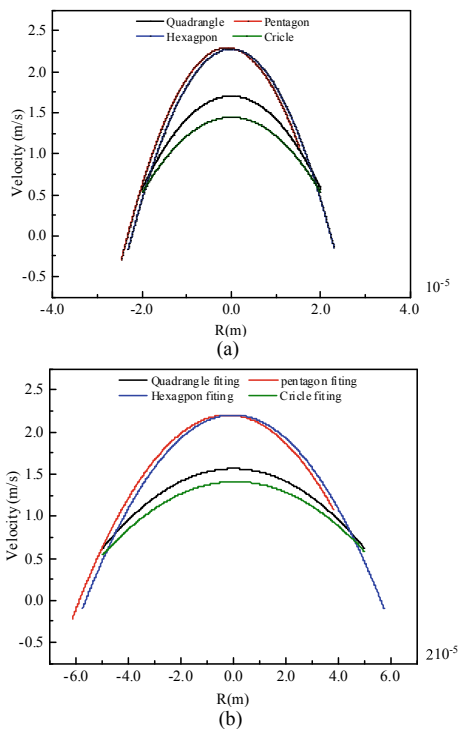
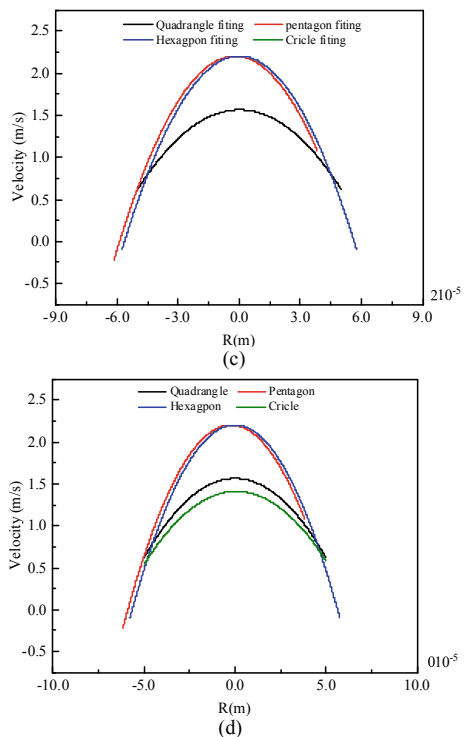


Fig. 6 Pipeline exit velocity cloud after calculation

**Fig. 7** Horizontal velocity points fitting diagram in different pipes. (Inner tangent circle diameter:  
**a** 0.04 mm, **b** 0.06 mm,  
**c** 0.08 mm, **d** 0.1 mm)



**Fig. 7** (continued)

## References

1. Mehendale SS, Jacobi AM, Shah RK (2000) Fluid flow and heat transfer at micro-and meso-scales with application to heat exchanger design. *Appl Mech Rev* 53(7):175–193
2. Kandlikar SG, Grande WJ (2003) Evolution of microchannel flow passages—thermohydraulic performance and fabrication technology. *Heat Trans. Eng.* 24(1):3–17
3. Araki T, Kim MS, Iwai H, Suzuki K (2002) An experimental investigation of gaseous flow characteristics in microchannels. *Micromech Therm Eng* 6(2):117–130
4. Arkilic EB, Breuer KS, Schmidt MA (2001) Mass flow and tangential momentum accommodation in silicon micromachined channels. *J Fluid Mech* 437:29–43
5. Flockhart SM, Dhariwal RS (1998) Experimental and numerical investigation into the flow characteristics of channels etched in (100) silicon. *J Fluids Eng* 120(2):291–295
6. Pfund D, Rector D, Shekarriz A, Popescu A, Welty J (2000) Pressure drop measurements in a microchannel. *AICHE J* 46(8):1496–1507
7. Li X, Lee WY, Wong M, Zohar Y (2000) Gas flow in constriction microdevices. *Sens Actuator A Phys* 83(1–3):277–283
8. Hsieh SS, Tsai HH, Lin CY, Huang CF, Chien CM (2004) Gas flow in a long microchannel. *Int J Heat Mass Trans* 47(17–18):3877–3887
9. Steinke ME, Kandlikar SG (2006) Single-phase liquid friction factors in microchannels. *Int J Thermal Sci* 45(11):1073–1083
10. Mala GM, Li D (1999) Flow characteristics of water in microtubes. *Int J Heat Fluid Flow* 20(2):142–148
11. Qu WL, Mohiuddin M, Li DQ (2000) Pressure-driven water flows in trapezoidal silicon microchannels. *Int J Heat Mass Trans* 43(3):353–364
12. Wang W, Li ZX (2003) Numerical analysis of the effects of rough surfaces on microscale flows. *J Eng Thermophys* 1:85–87
13. Jin W, Zhang HY (2010) Microscale internal flow field numerical simulation method and experiment. *J Agr Mach Sci* 3(41):6771
14. Wang H, Wang Y, Zhang J (2007) Flow in the microchannel with flow pattern and pressure drop. *J Micromech Microeng* 17(3):589–596
15. Pan SB (1987) Pipeline entrance effect. *J Xinyang Normal Univ* 2:12–15
16. Zhang MY, Jing SR, Li GJ (2006) Advanced engineering fluid mechanics. Xi'an Jiaotong University Press, Xi'an
17. Zhang JG (2009) Oil and gas layer permeability mechanics. China University of Petroleum Press, Beijing

# Vibration Analysis of Airplane Wing Under Fuel Weight



Zihao Zhou

**Abstract** Airplane wing will experience vibration from various sources due to airflow during flight and mechanical equipment. Vibration is the major consideration to the safety of airplanes since it can lead to resonance, structure failures and system breakdown. Resonance will increase vibration deformation which can cause structure failure. One of the vibration sources is the abnormal vibration resulting from imbalance of fuel weight. Therefore, this project investigates the vibration deformation of a plane wing (Airfoil NACA 2415) under a harmonic load caused by fuel weight. Finite element methods like modal analysis and harmonic response analysis are used. From the results, the first six order natural frequencies of the wing are from 4.5168 Hz to 119.63 Hz, which are much smaller than the harmonic response frequency (around 150 Hz). So resonance will not happen. The maximum deformation of the fourth order of the plane wing is the largest (1.5329 mm) compared to other orders. The fuel weight during a flight is treated as a harmonic load, which is applied to the middle of the wing. The maximum harmonic response is  $4.7929e^{-3}$  mm. H-convergence study are conducted to verify the numerical results are accurate. Theoretical results from Euler–Bernoulli Beam Theory are in comparison with the numerical results from modal analysis and errors between two results are very small (2.608%), indicating that the results from modal analysis are precise.

**Keywords** Resonance · Modal analysis · Harmonic response analysis · Mode shape · Maximum deformation

---

Z. Zhou (✉)

School of Mechanical and Manufacturing Engineering, University of New South Wales, Kensington, NSW 2052, Australia

e-mail: [sjsywz@sina.com](mailto:sjsywz@sina.com)

## 1 Introduction

Vibration is the major consideration to the safety of airplanes, since the air current during a flight can cause periodic and non-periodic loads to the airplane [1]. These loads can lead to resonance, structure failures and system breakdown. Resonance takes place when the frequency of an external load is approximate to the natural frequency of a physical structure and it will increase vibration amplitude which can directly cause structure failure [2]. Air turbulence, normal vibration and abnormal vibration are three main vibration types for an airplane during a flight in the sky [3]. Finite element analysis (FEA) is an effective way to conduct vibration analysis of a plane wing since finite element analysis is appropriate for real-life engineering problems with sophisticated geometries, boundaries conditions and materials.

Cui and Han [4] investigate aeroelastic behavior of the MAVRIC wing model using FEA methods. Chaitanya et al. [5] use FEA methods to study the structural frequency and the behavior of AGARD 455.6 wing under various pressure on the surface of the wing. Ali and Meral [6] conduct modal analysis of an aircraft wing under free vibration condition and investigate the mode shapes and related natural frequency. Kuntoji and Kuppast et al. [7] focus on the structural analysis of wing structures under buffet and obtain the natural frequency and deformation of the wing. Although the above research has played an important role in the design of the wing, it does not take into account the abnormal vibration caused by the unbalanced fuel weight during flight. Therefore, this paper will study the wing vibration behavior caused by the fuel weight. The design of the wings serves as a reference.

Imbalance fuel weight during a flight can cause abnormal vibration which can cause resonance, so it is of great significance to investigate the vibrational behavior of the wing caused by fuel weight. The main aim of this paper is to study natural frequencies and mode shapes of the wing structure under free vibration condition and investigate behavior of the wing structure (maximum deformation and corresponding frequency) under harmonic load caused by fuel weight.

## 2 Model Definition

### 2.1 Geometry

This project researches on the plane wing of Cessna 172 Skyhawk, an extremely popular single-engine aircraft shown in Fig. 1. It has a wingspan of 11 m and the usable fuel weight is 144 kg [8].

The airfoil of Cessna 172 Skyhawk is NACA 2415, which is shown in Fig. 2.

Since the wings from two sides are identical, this project will be only researched on half of the plane wing. Dimensions of NACA 2415 airfoil are shown in Table 1.



**Fig. 1** Cessna 172 Skyhawk [8]

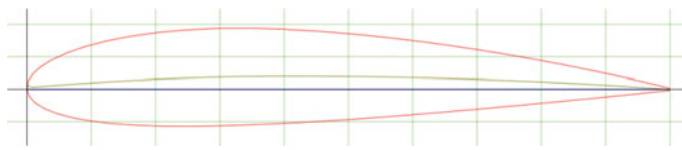


**Fig. 2** NACA 2415 cross-sectional airfoil plot [9]

**Table 1** Dimensions of NACA 2415 airfoil [8, 8]

Dimension	Value
Length	5.5 m
Airfoil chord length	1 m
Airfoil thickness	0.2016 m

The aircraft model of the wing is simplified to a solid cross section with no taper. Some structures, like fuel tank, electronics, ribs, spars, stringers and wing flap are neglected in the model. The simplified wing model is shown in Fig. 3.

**Fig. 3** Wing model

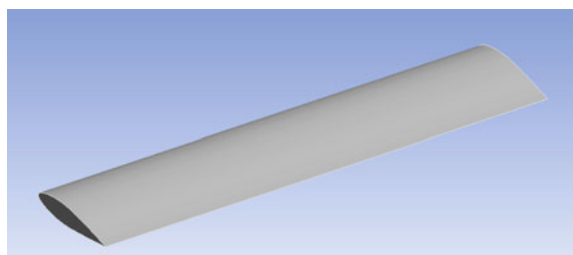


**Table 2** Material properties [10]

Property	Value
Ultimate tensile strength	310 MPa
Density	2770 kg/m <sup>3</sup>
Young's modulus	68.9 GPa
Poisson's ratio	0.33

## 2.2 Material Properties

The material of the aircraft wing is aluminum alloy. Table 2 shows the material properties.

## 2.3 Assumption

Several assumptions are made in this project.

- (1) The usable fuel weight during flight is under vibration and is modeled as a harmonic load on the vertical direction. Forces and vibrations on other direction are neglected.
- (2) The fuel tank and engine are neglected in the model.
- (3) The aircraft wing is assumed to be in a fixed position of fuselage and it is assumed to be a cantilever beam.
- (4) Internal components and surface irregularities are neglected.
- (5) Heat exchange and temperature change of the wing during flight are not considered.
- (6) Material is isotropic and homogenous.
- (7) The wing is assumed to be parallel to the ground with no tilt.
- (8) The harmonic load applied to the middle of the wing is assumed to be 1440 N.
- (9) The cross-section of the wing is assumed to be constant.

## 3 Analysis and Numerical Approach

### 3.1 Analysis Methods

Modal analysis is used for researching on the dynamic properties of a structure, comprising of structural modes and corresponding natural frequencies. Modal analysis of the plane wing under free vibration will be conducted.

Harmonic response analysis is aimed to research on the mechanical characteristics of the wing when subjected to a weight of fuel as a harmonic load. The load will

be applied at the middle of the wing. Frequency responses of deformation under harmonic load will be investigated.

### 3.2 Element Types

The element type of the wing model is SOLID 185, which is commonly used in modeling 3D structure [11].

The mesh size is 30 mm, which can reach mesh convergence. For uniform geometry, mesh elements use Hex 20 and Wed 15 and Fig. 4 shows the meshed model.

The element metrics is shown in Fig. 5. It can be found that the mesh of the element is of high quality.

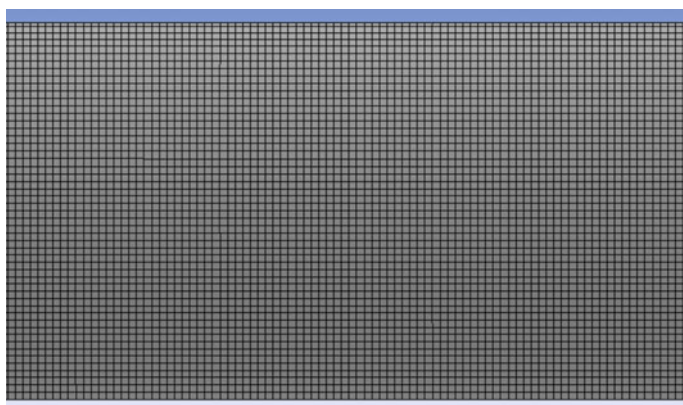


**Fig. 4** Meshed model

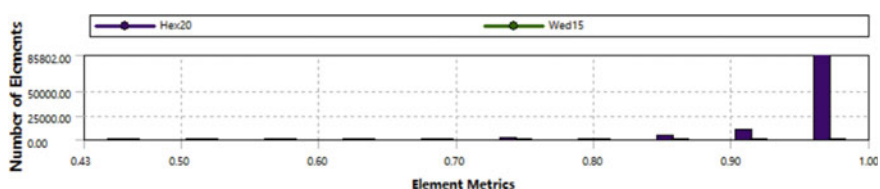


**Fig. 5** Element metrics

### 3.3 Boundary Conditions

The boundary condition for the plane wing is a fixed end as it is connected with the fuselage. Therefore, a fixed support is applied to aerofoil cross section at the end of the plane wing. The fuel weight during a flight is treated as a harmonic load and it is applied to the middle of the plane wing.

## 4 Results

First six order natural frequencies and the corresponding maximum deformations of the wing by modal analysis are presented in Table 3.

Table 4 shows the first six order vibration mode shapes of the wing, from which maximum deformation of the fourth order (1.5329 mm) is the largest compared to other orders and the maximum deformation occurs at the edge of the wing.

Figure 6 shows the frequency response plots (amplitude vs. frequency). It can be found that the maximum deformation appears at around 150 Hz, which is  $4.7929e^{-3}$  mm.

## 5 Discussions and Conclusion

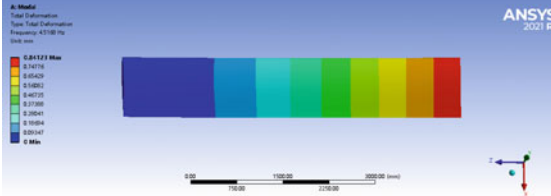
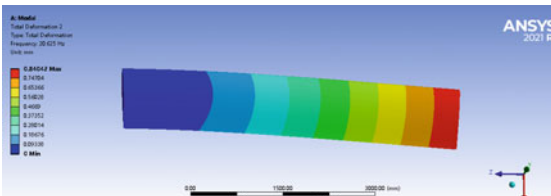
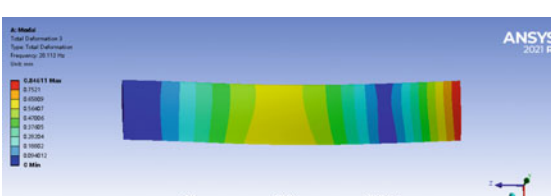
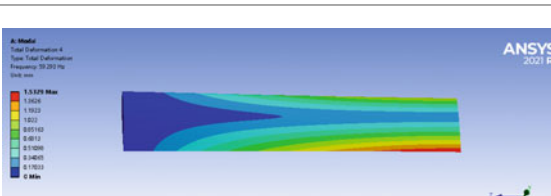
### 5.1 Verification

H-mesh convergence study is aimed to verify the mathematical results is precise by altering the mesh element size. The parameter for H-mesh convergence study is total deformation frequency. Figure 7 illustrates the results and it can be found that mesh reaches convergence after mesh element size reaches 30 mm.

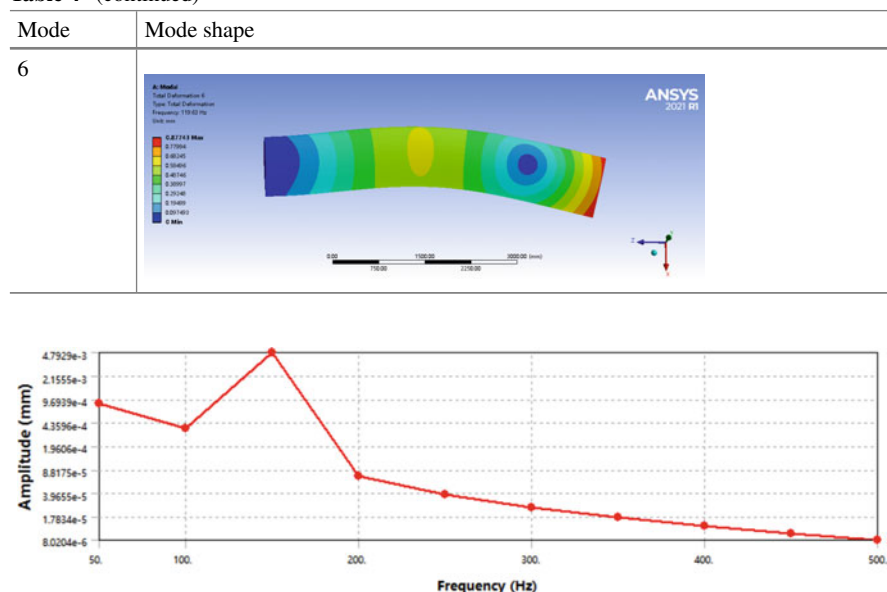
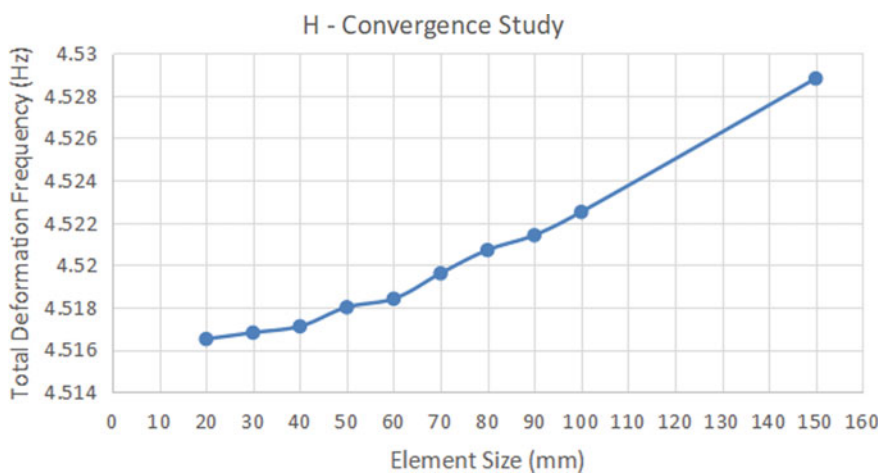
**Table 3** First six order natural frequencies and corresponding maximum deformation of the wing

Mode	Frequency (Hz)	Maximum deformation (mm)
1	4.5168	0.84123
2	20.625	0.84042
3	28.113	0.84611
4	59.293	1.5329
5	77.907	0.84704
6	119.63	0.87743

**Table 4** First six order vibration mode shapes of the wing

Mode	Mode shape
1	
2	
3	
4	
5	

(continued)

**Table 4** (continued)**Fig. 6** Frequency response of the wing**Fig. 7** H-Convergence study by different element sizes

## 5.2 Validation

Euler–Bernoulli Beam Theory is the fundamental method to calculate the theoretical natural frequency. The wing model is simplified and assumed to a solid cantilever beam under the transverse loading. Table 5 shows dimensions of the wing.

The moment of inertia can be obtained from [11]:

$$I = 0.036c^4t(t^2 + h^2) \quad (1)$$

From Euler–Bernoulli Beam Theory [12], natural frequency of a cantilever beam under the transverse loading can be obtained by:

$$w_n = (\beta_n L)^2 \sqrt{\frac{EI}{\rho A L^4}} \quad (2)$$

$\beta_n L$  values are satisfied to the following equation [12]:

$$\cosh(5.5\beta_n L) \cdot \cos(5.5\beta_n L) + 1 = 0 \quad (3)$$

By substituting the corresponding values into the equation, the natural frequencies are calculated and the comparison of the theoretical results (from calculation) and the numerical results (from software simulation) is shown in Table 6. It can be found that the errors are very small and lower than 3%, which means that the numerical results are validated.

**Table 5** Dimensions of the wing

Property	Value
Chord length of the wing (c)	1 m
Cross-sectional area (A)	0.1318 m <sup>2</sup>
Maximum chamber of the wing (h)	0.1008 m
Wing length (L)	5.5 m
Maximum thickness of the wing (t)	0.2016 m

**Table 6** Comparison of the theoretical and numerical results

Mode	Natural frequencies (Hz)		Error (%)
	Theoretical results	Numerical results	
1	4.402	4.5168	2.608
2	20.357	20.625	1.317
3	27.584	28.113	1.918
4	58.824	59.293	0.797
5	77.221	77.907	0.888
6	118.204	119.63	1.206

## 6 Conclusion

By doing finite element analysis of the plane wing (airfoil NACA 2415) comprised of modal analysis and harmonic response analysis, the first six order natural frequencies are from 4.5168 Hz to 119.63 Hz and the harmonic response frequency is around 150 Hz. From the results, the resonance will not happen because first six order natural frequencies is much smaller than harmonic response frequency. From the mode shapes of the plane wing, the forth order natural frequency witnesses maximum deformation (1.5329 mm).

The fuel weight during a flight is treated as a harmonic load, which is applied to the middle of the wing. The maximum harmonic response is 4.7929e-3 mm. H-convergence study verifies the numerical results are accurate and the error between theoretical results and numerical results are less than 3%, indicating that the numerical results are validated.

## References

1. Srividhya S, Nehru K, Rago A, Selvan P (2020) Vibrational analysis of an aircraft wing model using ANSYS workbench. *Int J Eng Dev Res* 8(3):280
2. Faidh-Allah MH, Hamzah AA (2019) Vibration analysis of aircraft wing under gust load. *J Eng Appl Sci* 14(11):67–71
3. Ansari A (2021) Modal and harmonic analysis of aircraft wing. *Ijsart.com* 56:601–608
4. Cui P, Han J (2016) Prediction of flutter characteristics for a transport wing with wingtip devices, Institute of Vibration Engineering Research, State Key Lab of Mechanics and Control for Mechanical Structures, Nanjing University of Aeronautics and Astronautics, Nanjing 210016, China
5. Chaitanya JS, Prasad A, Pradeep B, Sri Harsha PLN, Shali S, Nagaraja SR (2017) Vibrational Characteristics of AGARD 445.6 Wing in Transonic Flow, Amrita University, India
6. Ali D, Meral B (2016) Free vibration analysis of an aircraft wing by considering as a cantilever beam, Department of Mechanical Engineering, Mechanical Engineering Faculty, Yildiz Technical University, Besiktas, 34349 Istanbul, Turkey
7. Kuntoji N, Kuppast VV (2017) Study of aircraft wing with emphasis on vibration characteristics, Basaveshwar Engineering College, Bagalkot, India
8. Duan TT, Liu JH, Yang LW (2014) Failure diagnose and analysis of joining structure of airplane under vibration. *Fail Anal Prev* 78:89–93
9. George JS, Vasudevan A, Vinayagam M (2020) Vibration analysis of interply hybrid composite for an aircraft wing structure. *Mater Today: Proc* 78(7):501–508
10. Costley RD, McKenna MH, Diaz-Alvarez H (2015) Vibration and acoustic analysis of trussed railroad bridge under moving loads. *J Vib Acoust: Trans ASME* 56:20–27
11. Demirtas MB (2019) Free vibration analysis of an aircraft wing by considering as a Cantilever beam. *Sci Technol* 7(8):12–21
12. Agrawal P (2021) Comparative study on vibration characteristics of aircraft wings using finite element method. *Mater Today: Proc* 46:176–183

# Selection and Research of Common Waste Water Tank Mixer



Chun-Yu Tian

**Abstract** The waste water tank is one of the indispensable main equipment in the wet flue gas desulfurization process. Waste water tank is widely used in FGD industry, so the selection of waste water tank agitator is very important. Both companies and research institutes have done a lot of experiments and practices on the mixing of waste water tank, and it is acknowledged that some progress and results have been achieved. In the current FGD industry, the selection of mixers relies heavily on tests and practical engineering experience, which leads to a variety of types of mixers for waste water tanks in the market. Based on many years of engineering experience, this paper selects and optimizes each component and internal component of waste water tank mixer, including stirring blade shape, blade diameter, rotational speed, stirring shaft size, etc. Using the existing performance analysis and comparison, determine the common specifications and models of waste water tank applicable mixer.

**Keywords** Desulfurization and denitrification · Waste water tank · Mixer · Type selection · Optimize design

## 1 Introduction

Mixing and stirring is common in the FGD industry. With global warming, environmental governance issues in various countries have become increasingly prominent, and environmental protection has become a topic of concern for everyone. And China's March 5, 2021, the State Council government work report, clearly pointed out that "do a solid job in carbon peak", carbon neutrality, strive to achieve the goal of carbon neutrality by 2030, Desulfurization denitrification industry at the present stage in China, the major processing waste gas of power plant, most of the limestone-gypsum method flue gas desulfurization technology, according to the relevant units, the limestone-gypsum method flue gas desulfurization technology has occupied 85%

---

C.-Y. Tian (✉)

School of Mechanical Engineering, Southeast University, Jiangsu 211189, China  
e-mail: [13810485984@163.com](mailto:13810485984@163.com)

of China's market share [1], its operation difficulty is small, reliable technology, development history in China for decades. It has been widely used and recognized [2–5]. By means of coagulation and precipitation treatment, the quality of waste water in accordance with the standard (DL/T 997–2006) is finally reached, and the standard of Comprehensive Sewage discharge is implemented according to GB8978-1996. Therefore, the setting of waste water tank including waste water tank mixer has become an indispensable part of the flue gas treatment in each power plant. With the progress of technology, waste water tanks are developing toward standardization, specialization and high efficiency and energy saving. Therefore, it is very important to study the waste water tank mixer.

## 2 Working Condition

The selection of waste water tank mixer, one of the most important input conditions is the specific slurry parameters, only clear the concrete slurry material properties on the basis of the correct selection of mixer. In the following, the author takes the waste water tank in the “Guodian XX Power Plant Ultra-low Emission Transformation Desulphurization EPC Project”, which he successfully participated in and implemented in the past, as the research background, to design the waste water tank jack-in mixer. Table 1 shows the water quality of raw water and waste water tanks.

The size diameter (m) x height (m) of the five waste water tanks in this study are  $\varphi 1 \times 1$ ;  $\varphi 2 \times 2$ ;  $\varphi 3 \times 3$ ;  $\varphi 4 \times 4$ ;  $\varphi 5 \times 5$  (Fig. 1).

The general blender design program can be represented by the following block diagram 1:

**Table 1** Waste water tank operating environment (self drawn)

Number	Project parameters	limestone slurry
1	Velocity, $m s^{-1}$	0~3,0
2	Operating pressure, MPa	$\leq 0, 7$
3	Density, $kg m^{-3}$	1020~1200
4	Temperature, °C	$\leq 65$
5	pH	8~10
6	Viscosity, $m(Pa s)$	$\leq 2, 3$
7	Particle size, $\mu m$	43 (90% ass)
8	Solid content, %(mass fraction)	5~10
9	$Cl^-$ , $\mu L L^{-1}$	40,000

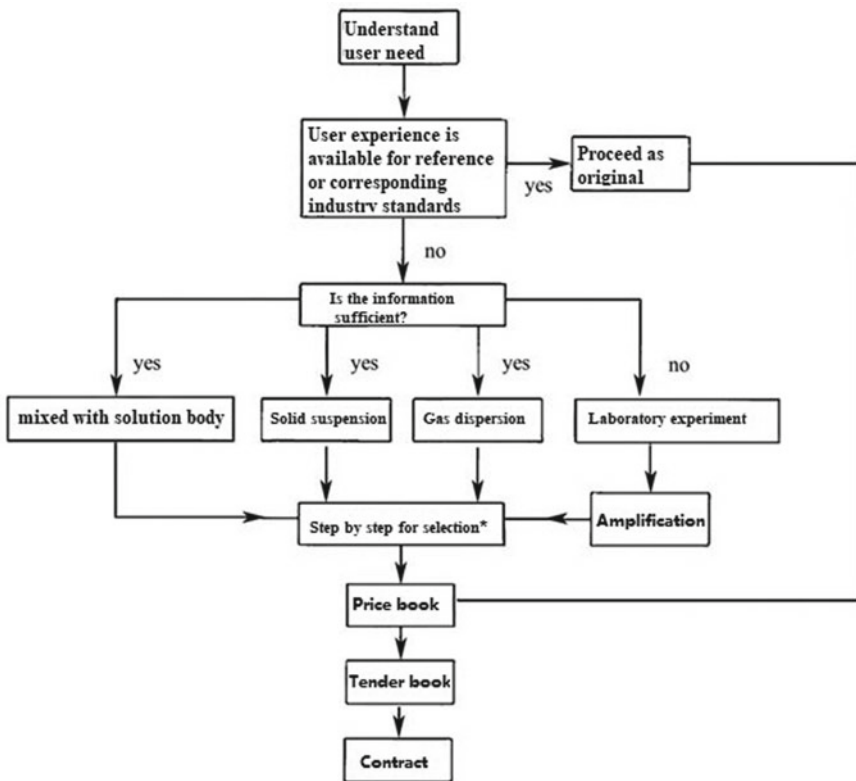


**Fig. 1** Selection flow chart

### 3 Speed of Mixer

Agitator rotational speed computation formula is as follows (1):

$$NC = K \times D^{-2/3} \times dp^{1/3} \times (\Delta\rho / \rho)^{2/3} \times (\mu / \rho)^{-1/9} \times (V_p / V)^{-0,7} \quad (1)$$

After consulting the reducer sample and calculating one by one, the speed of the five specifications of waste water tank agitator is selected as 85 r/min, 76 r/min, 67 r/min, 52 r/min and 44 r/min. The blade end line speed of the agitator is 1,78 m/s, 2,78 m/s, 4,03 m/s, 3,81 m/s and 3,91 m/s.

Compare to the blender selection that has been completed in reality, the rotation speed is not different from the actual selection of the manufacturer, which indicates that the selection of waste water tank mixer is preliminary correct.

## 4 Blade Type and Blade Diameter

The stirring effect of the mixer is generated by the moving impeller. Therefore, the shape, size and quantity of the impeller affect the stirring effect of the mixer. According to the different sizes of waste water tank, the waste water tank mixer selected are three narrow blade detachable plate propeller (HZCX) and arc oblique blade detachable paddle type (HXCJ) [6–8]. The blade processing diagram is as follows (Figs. 2 and 3).

Considering the specific slurry requirements of the waste water tank, because the slurry viscosity of the waste water tank is not large, the diameter ratio of the paddle diameter tank  $D/D = 0.25\sim0.5$ . In general,  $D/D = 1/3$  is the most appropriate.

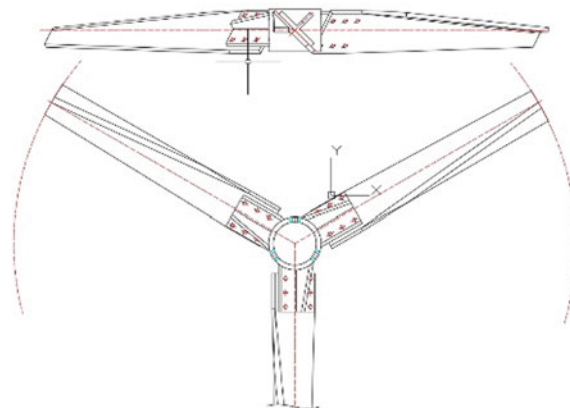


**Fig. 2** Machining drawing of arc three narrow blade detachable plate propeller (HZCX) (self drawn)

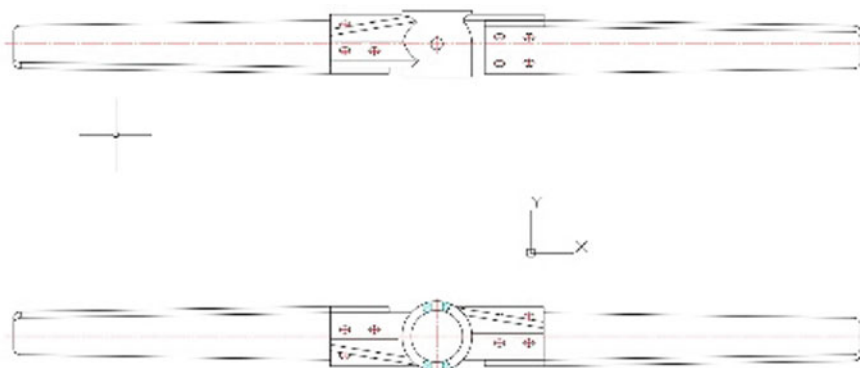


**Fig. 3** Processing drawing of arc inclined blade detachable paddle (HXCJ) (self drawn)

It is believed that under the condition of this ratio of propeller diameter to tank diameter, when the power consumption is fixed, the mass transfer rate is larger. Through calculation, the impeller diameters of the neutralizing box and settling box in five specifications are, respectively, selected as HZX400mm, HZX700mm, HXCJ1150mm, HXCJ 1400 mm and HXCJ 1700 mm.

Footnotes should be avoided whenever possible. If required they should be used only for brief notes that do not fit conveniently into the text.

## 5 Power of Mixer Motor

The calculation formula of motor power is shown in Eq. (2)

$$P = Np \times \rho \times (n/60)^3 \times Dj^5 \quad (2)$$

The mixer of neutralizing box and settling box in five specifications is, respectively, selected as 1,1KW, 2,2KW, 4KW, 5,5KW and 7,5KW. Specific statistics of motor power are as follows (Table 2).

Through the two verification of the existing achievements, it is found that the motor power is not different from the actual selection. From the side also confirm the validity of the motor power to choose.

## 6 Diameter of Stirring Shaft

The diameter and torque are calculated as follows (3)–(4):

$$D = 155,4 \times (M/\gamma/E)^{0.25} \quad (3)$$

$$M = 9553 \times P \times \eta/n \quad (4)$$

**Table 2** Motor power statistics table(self drawn)

Box specifications (mm)	The motor power	Protection grade	Temperature level	Insulation class
φ1 × 1	1,1, KW	IP55	B	F
φ2 × 2	2,2, KW	IP55	B	F
φ3 × 3	4, KW	IP55	B	F
φ4 × 4	5,5, KW	IP55	B	F
φ5 × 5	7,5, KW	IP55	B	F

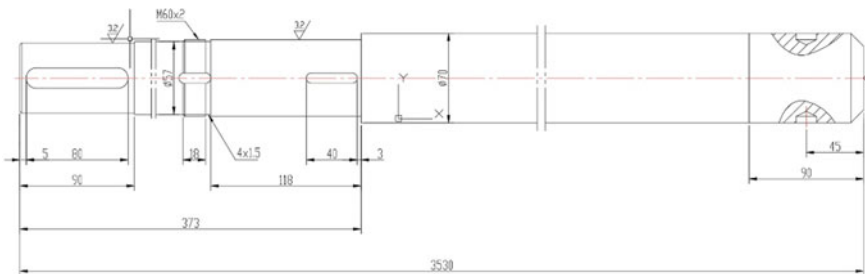


**Fig. 4** Axis processing drawing (self drawn)

The mixing shaft of waste water tank mixer adopts solid shaft in the form of ladder shaft, and it is a whole shaft, and there is sufficient calculation margin on the calculated value. This kind of solid shaft can be on the basis of ensuring enough stiffness, minimizing the stirring shaft deflection and prolonging actual service life of the stirring shaft. After calculation, the mixing shaft of five kinds of waste water tank agitator is respectively selected as 50 mm, 60 mm, 70 mm, 80 mm and 90 mm. The length of the cantilever shaft is 1000 mm, 2000 mm, 2700 mm, 3800 mm and 4800 mm (Fig. 4).

## 7 Conclusion

Currently, in view of the waste water tank agitator selection, now rely on the domestic and foreign successful experience and the case, or laboratory after successful experiments, in proportion to further enlarge. In this paper, five kinds of waste water tank specifications are selected by referring to the previous successful performance. These specifications almost cover the common sizes of waste water tanks seen in desulfurization and denitrification industry, which can help design and process personnel, quick positioning and selection reference.

In the stirring process of waste water tank, there is not only simple mixing of materials, but also reaction, heat and mass transfer. In addition, the automatic climbing of materials in the stirring process of waste water tank results in a very complex flow state [9]. Its principle involves flow field, fluid mechanics, etc., which also determines that it is difficult to select waste water tank mixer under the guidance of a strict and strict system. In this paper, through a lot of calculations and combined with the previous successful performance, five kinds of common specifications of waste water tank mixers are designed and selected. In addition to the selection of a similar size waste water tank mixer of the same slurry, the corresponding model and demonstration are also provided for stirring other media with similar density and solid content.

## References

1. Jing Z, Liang M, Dengfei Z (2020) Structure optimization of magnet mold electromagnetic stirrer. *China Mech Eng* 31(10):1148–1154
2. Lei W, Yongfeng S, Jungang R, Li H, Song Z (2017) Fatigue behavior and crack propagation behavior of 2A12 aluminum alloy repaired by friction stir. *China Mech Eng* 28(13):1628–1632
3. Zhao Z, Jun B (2008) Full thermodynamic coupling model for numerical simulation of friction stir welding process. *China Mech Eng* 19(10):0–1257
4. Jiaxing W, Yanbing N, Na D et al (2016) Prediction of working load and stiffness analysis of friction stir welding equipment. *China Mech Eng* 27(2):258–264
5. Fusheng M, Peng Y (2012) Stirring mill medium movement discrete element numerical simulation analysis of. *China Mech Eng* 23(20):2465–2468
6. Zhiping Z, Xinghua L, Xuwen Z (2004) Design and selection manual of mixing and mixing equipment. Chemical Industry Press, Beijing, pp 124–128
7. Kai W, Jun Y (2011) Chemical equipment design book–stirring equipment. Chemical Industry Press, Beijing, pp 6, 45
8. Bangchun W (2011) Mechanical design manual (fifth edition-fourth volume). China Machine Press, Beijing, pp 154–159
9. Prakash M, Cleary PW, Ha J et al (2007) Simulation of suspension of solids in a liquid in a mixing tank using SPH and comparison with physical modeling experiments. *Prog Comput Fluid Dyn* 7(2):91–100

# Study on Grease Elasto-Hydrodynamic Lubrication of Deep Groove Ball Bearings



Hao Wu, Shenghan Zhang, Haoyang Sun, Jirong Wang, and Hongxin Zhang

**Abstract** Deep groove ball bearings are widely applied and usually work in the Elasto-hydrodynamic lubrication (EHL) state. Grease lubrication is widely used and the analysis of grease lubrication is more complex than oil lubrication. In this paper, the EHL properties of deep groove ball bearings are studied by using an exponential rate rheological model, and a complete numerical solution is obtained. The results show that, for lubrication condition, the roller element and the outer ring are worse than that between the roller element and the inner circle. Regardless of the rheological index value, there is a relatively obvious second pressure peak in the pressure distribution, and the second pressure peak decreases as the rheological index increases.

**Keywords** Deep groove ball bearing · EHL · Exponential rate rheological fluid

## 1 Introduction

Deep groove ball bearings are widely used in a variety of mechanical systems because of their advantages of small friction and high speed, and their life will directly affect the life of the whole machine [1]. The study of elasto-hydrodynamic lubrication can better reveal its tribological state, then carry out targeted tribological design to improve its serviceability. A lot of researches have been carried out on oil lubrication [2, 3]. Although grease is widely used in engineering as it is not easy to lose, grease lubrication has not been well studied due to the complexity of rheology. Morales-Espejel obtained oil film thickness on the contact surface of grease lubrication points for different greases [4] and concluded that under the condition of low enroler speed, the oil film thickness is much larger when using grease compared to lubricating oil. However, the effect of the maximum Hertz contact pressure on the film thickness was not considered. Cyriac studied the influence of the geometric size and concentration

---

H. Wu · S. Zhang · H. Sun (✉) · J. Wang · H. Zhang

College of Mechanical and Electrical Engineering, Qingdao University, Qingdao Shandong, China  
e-mail: [haoyangnew@163.com](mailto:haoyangnew@163.com)

of thickener particles on the thickness of the grease lubrication film at medium entrainment speed through experiments [5] but ignored the influence of bearing speed on the pressure distribution on contact points surface. This paper carried out a grease thermal EHL analysis for deep groove ball bearings.

## 2 Point Contact EHL Analysis Model

From the perspective of lubrication analysis, a deep groove ball bearing can be equivalent to the point contact friction pair composed of plane a and ball b, and there is flow in both the  $x$ -direction and  $y$ -direction. Moreover, considering the thermal effect, dividing the grid in  $x$ ,  $y$ , and  $z$ -directions, as shown in Fig. 1.

Under the condition of point contact, the Reynolds [6] equation is

$$\frac{\partial}{\partial x} \left[ \left( \frac{\rho}{\eta} \right)_e h^3 \frac{\partial p}{\partial x} \right] + \frac{\partial}{\partial y} \left[ \left( \frac{\rho}{\eta} \right)_e h^3 \frac{\partial p}{\partial y} \right] = 12u_e \frac{\partial}{\partial x} (\rho^* h) \quad (1)$$

where  $\rho$  is the density of lubricant,  $\eta$  is the viscosity of lubricant,  $h$  is film thickness,  $p$  is film pressure, and entrainment velocity  $u_e = (u_a + u_b)/2$ , each equivalent symbol is defined as follows:

$$\left( \frac{\rho}{\eta} \right)_e = 12 \left( \frac{\eta_e \rho'_e}{\eta'_e} - \rho''_e \right), \quad \rho^* = \frac{\rho'_e \eta_e (u_b - u_a) + \rho_e u_a}{u_e},$$

$$\rho_e = \frac{1}{h} \int_0^h \rho dz, \quad \frac{1}{\eta_e} = \frac{1}{h} \int_0^h \frac{1}{\eta^*} dz,$$

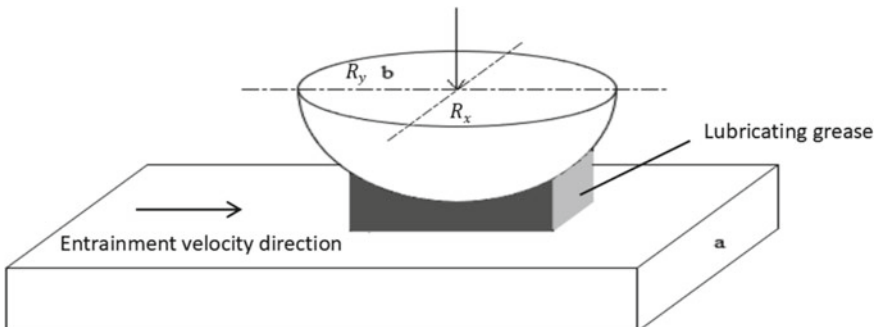


**Fig. 1** Schematic diagram of point contact elasto-hydrodynamic lubrication (Self-drawn)

$$\frac{1}{\eta'_e} = \frac{1}{h^2} \int_0^h \frac{z}{\eta^*} dz, \rho'_e = \frac{1}{h^2} \int_0^h \rho \int_0^z \frac{dz'}{\eta^*} dz, \rho''_e = \frac{1}{h^3} \int_0^h \rho \int_0^z \frac{z'}{\eta^*} dz' dz.$$

The boundary conditions for Reynolds equations at the oil film entrance are that the pressure is equal to 0, and the Reynolds boundary condition is used at the outlet where the oil film breaks naturally. In order to ensure that the boundary conditions can be satisfied during iteration, it is only necessary to assume that the boundary conditions at the outlet are pressure equal to 0, but the negative pressure is always set to 0 in the bearing area. Then Reynolds boundary condition can be summarized as

$$\begin{cases} p(x_{in}, y) = p(x_{out}, y) = p(x, -y_{out}) = p(x, y_{out}) = 0 \\ p(x, y) \geq 0, x_{in} < x < x_{out}, -y_{out} < y < y_{out} \end{cases}$$

where  $x_{in}$ ,  $x_{out}$ ,  $y_{out}$  are the starting point coordinates of the calculation domain.

The film thickness equation is

$$h(x, y) = h_{00} + \frac{x^2}{2R_x} + \frac{y^2}{2R_y} + \frac{2}{\pi E'} \iint \frac{p(x', y')}{\sqrt{(x - x')^2 + (y - y')^2}} dx' dy' \quad (2)$$

where  $h_{00}$  represents the central film thickness of rigid element,  $R_x$ ,  $R_y$  are equivalent radii in x- and y-directions, and  $E'$  is reduced elastic modulus.

The load equation is

$$\iint p dx dy = w_{load} \quad (3)$$

where  $w_{load}$  is applied load.

The viscosity equation is

$$m = m_0 \exp \left\{ (\ln m_0 + 9.67) \left[ (1 + 5.1 \times 10^{-9} p)^{Z_0} \left( \frac{t - 138}{t_0 - 138} \right)^{-S_0} - 1 \right] \right\} \quad (4)$$

where  $m$  is the viscous function and  $m_0$  is the viscous function under environmental pressure  $Z_0 = \alpha / (\ln \eta_0 + 9.67)(1 + 5.1 \times 10^{-9} P)$ ,  $S_0 = \beta(t_0 - 138) / (\ln \eta_0 + 9.67)$ .

The density equation is

$$\rho = \rho_0 \left[ 1 + \frac{0.6 \times 10^{-9} p}{1 + 1.7 \times 10^{-9} p} - 7.0 \times 10^{-4}(t - t_0) \right] \quad (5)$$

where  $\rho_0$  is the ambient density of lubricant,  $t$  is time, and  $t_0$  is the ambient temperature.

The heat conduction equation of the two solids is

$$\begin{cases} c_a \rho_a u_a \frac{\partial t}{\partial x} = k_a \frac{\partial^2 t}{\partial z_a^2} \\ c_b \rho_b u_b \frac{\partial t}{\partial x} = k_b \frac{\partial^2 t}{\partial z_b^2} \end{cases} \quad (6)$$

where  $c_a, c_b$  are specific heat of solids,  $\rho_a, \rho_b$  are densities of solids,  $u_a, u_b$  are velocities of surface a, b, and  $k_a, k_b$  are thermal conductivity of solids.

Where the condition of the boundary of heat conduction equations of the two solids is

$$\begin{cases} t(x_{in}, y, z_a) = t_0, & t(x, y, -d) = t_0 \\ t(x_{in}, y, z_b) = t_0, & t(x, y, d) = t_0 \end{cases}$$

Considering the continuity equation, the energy equation with oil film can be written as follows when the influence of heat radiation and heat conduction in  $x$ - and  $y$ -directions is ignored.

$$\begin{aligned} & c \left[ \rho u \frac{\partial t}{\partial x} + \rho v \frac{\partial t}{\partial y} - \left( \frac{\partial}{\partial x} \int_0^z \rho u dz' + \frac{\partial}{\partial y} \int_0^z \rho v dz' \right) \frac{\partial t}{\partial z} \right] \\ &= k \frac{\partial^2 t}{\partial z^2} - \frac{t}{\rho \partial T} \left( u \frac{\partial p}{\partial x} + v \frac{\partial p}{\partial y} \right) + \eta^* \left[ \left( \frac{\partial u}{\partial z} \right)^2 + \left( \frac{\partial v}{\partial z} \right)^2 \right] \end{aligned} \quad (7)$$

where the oil film entrance is a non-countercurrent zone, and the condition of boundary of the energy equation is

$$t(x_{in}, y, z) = t_0$$

The interface between oil film solid should meet heat flow continuous conditions:

$$\begin{cases} k_a \cdot \partial t / \partial z_a |_{z_a=0} = k \cdot \partial t / \partial z |_{z=0} \\ k_b \cdot \partial t / \partial z_b |_{z_b=0} = k \cdot \partial t / \partial z |_{z=h} \end{cases}$$

The flow rates of the oil film along the  $x$ - and  $y$ -directions are

$$u = \left( \int_0^z \frac{z'}{\eta^*} dz' - \frac{\eta_e h}{\eta'_e} \int_0^z \frac{1}{\eta^*} dz' \right) \frac{\partial p}{\partial x} + \frac{\eta_e (u_b - u_a)}{h} \int_0^z \frac{1}{\eta^*} dz' + u_a \quad (8)$$

$$v = \left( \int_0^z \frac{z'}{\eta^*} dz' - \frac{\eta_e h}{\eta'_e} \int_0^z \frac{1}{\eta^*} dz' \right) \frac{\partial p}{\partial y} \quad (9)$$

Suppose the grease is an exponential rate fluid, and its constitutive equation is

$$\tau_e = m \left( \frac{\partial V}{\partial z} \right)^n \quad (10)$$

where  $m$  is the viscosity function and  $n$  is grease rheological index.

Equivalent viscosity  $\eta^*$  is

$$\eta^* = m^{1/n} |\tau_e|^{(n-1)/n} \quad (11)$$

The detailed solution method of  $\eta^*$  can be found in reference [7].

### 3 Processing of Mathematical Models

#### 3.1 Dimensionalization of Mathematical Model

The mathematical model of lubrication of exponential rate grease is similar to that of Newton fluid, in dimensionalization, in order to ensure that after dimensionalization, except for the three newly introduced functions  $\bar{m}$ ,  $\bar{\tau}_e$ , and  $\bar{\eta}^*$ , all the other dimensional-one expressions can be consistent with the dimensional-one expressions in Newton's fluid mathematical model, an equivalent environmental viscosity  $\eta_0 = m_0 (p_H / \eta_0)^{n-1}$  should be introduced. To replace the Newton fluid mathematical model of the environment viscosity  $\eta_0$ , on this basis, the parameters of each dimension are as follows:

$$\begin{aligned} P &= p / p_H, \bar{h} = h R_x / b^2, T = t / t_0, \bar{u} = u / u_e, \bar{u}_a = u_a / u_e, \bar{u}_b = u_b / u_e, \\ \bar{v} &= v / u_e, X = x / b, Y = y / b, Z = z / h, Z_a = z_a / b, Z_b = z_b / b, \bar{\eta}^* = \eta^* / \eta_0, \\ \bar{m} &= m / m_0, \bar{\rho} = \rho / \rho_0, \bar{\tau}_{xa} = \tau_{xa} / p_H, \bar{\tau}_{ya} = \tau_{ya} / p_H, \bar{\tau}_e = \tau_e / p_H. \end{aligned}$$

See reference [8] for details.

#### 3.2 Multigrid Solution Method

The multigrid method can not only see better details of the real solution on the grid but also have a good convergence speed [8], so the W cycle is selected.

The multigrid method was used for iterative calculation, which was set as a 5-layer grid, and the solution domain in the X-direction was  $[-4.5, 1.5]$ . In the Y-direction, the calculation scope is  $[0, 2]$  according to symmetry. In the solution area, the grid is divided. On the top grid, set 257 nodes in X-direction and 97 nodes in Y-direction on the fifth grid.  $i$  is the node ID of X-direction,  $j$  is Y-direction, and let the spacing between each node is  $\Delta X$  and  $\Delta Y$ , where  $\Delta X$  and  $\Delta Y$  are not required to be equal. Since the grid in the Z-direction is composed of two solids a and b and the oil film, the coordinates in the two solids a and b in the Z-direction are taken as  $Z_a$  and  $Z_b$ , respectively, and the sittings in the oil film are marked as  $Z$ . Its node number is denoted as  $k$ , node spacing is denoted as  $\Delta Z$ , and its serial number ranges from 1 to 9. In solids a and b, the node serial number is from -6 to -1 and 11 to 16, respectively, and the node serial number 0 is located at the solid interface, and the node serial number 10 is located at the oil film interface. It is divided into two adjacent nodes of the distance between the common ratio of two equal series of the unequal grid. The distance between nodes closer to the oil film is smaller.

### 3.3 Numerical Method

Since the main difference between the exponential rate grease and Newton fluid is the introduction of an equivalent viscosity  $\bar{\eta}^*$ , only  $\bar{\eta}^*$  is required, and the rest is similar to the method of Newton fluid. Refer to Reference 8 for specific mathematical expressions.

Iterate between the pressure field and the temperature field. The elastic deformation term in the thickness equation of the film is obtained by the multigrid integration method. The basic idea is to transfer the information from the node dense grid to the sparse grid, integrate the results on the sparse grid, and then transfer the results to the dense grid for correction. In this way, we can obtain the value that satisfies the accuracy requirement on the grid with dense nodes. A column scanning technique is used to solve the temperature field [9]. The complexity of the solution is greatly reduced, and the computational speed is improved. In the point contact problem, each solution scans a system of equations consisting of the temperature of the unknown of a column of nodes, where X- and Y-coordinates are the same but Z-coordinates are different. The above difference scheme is used to solve the tridiagonal matrix written by the coefficient matrix of the equations of equations, which can obtain a high efficiency of catching up speed.

Through the above method, after each pressure calculation, the viscosity function, density function, and other pressure-related quantities can be updated and then used to solve the temperature field. After each temperature calculation, the quantity related to temperature is also updated and then used to solve the pressure field until the pressure and temperature converge.

## 4 Lubrication Performance Analysis of Bearings

The selected grease is compound lithium base grease, which is analyzed by 6206 bearings. Table 1 shows the basic calculation parameters.

According to the data in Table 1, the distribution diagram of the pressure and film thickness of the bearing under lubrication of the selected lithium base grease can be obtained. Pressure distribution and film thickness at the contact point between the roller element and the outer ring and that between the roller element and the inner circle are shown in Figs. 2 and 3, respectively.

It can be seen from Figs. 2 and 3 that a relatively obvious second pressure peak appears in the pressure distribution diagram because the viscosity of grease is much greater than that of lubricating oil. The initial viscosity of the grease selected here is  $11 \text{ Pa S}^n$ , while the initial viscosity of the lubricating oil in general oil lubrication condition is only between  $0.02 \text{ Pa S}^n$  and  $0.05 \text{ Pa S}^n$ . So you have this high second pressure peak. From the film thickness distribution diagram, under the lubricating action of grease, the thickness of oil film has a necking phenomenon.

Comparing Figs. 2 and 3, the peak pressure at the contact point between the roller element and the outer ring is higher than that at the contact point between the roller element and the inner circle. This is because the roller element in contact with

**Table 1** Calculation parameters (Self-drawn)

Name and Unit	Value
Load $w_{\text{load}}/\text{N}$	1327
Entrainment velocity $u_e/\text{m} \cdot \text{s}^{-1}$	0.0069
The environment temperature $t_0/\text{K}$	303
Maximum Hertz contact pressure $p_H/\text{GPa}$	2.0
Equivalent viscosity of grease $\eta^*/\text{Pa} \cdot \text{s}^n$	11
Viscosity coefficient of lubricating oil $\alpha/\text{GPa}^{-1}$	22
Viscosity, temperature, and viscosity of lubricating oil $\beta/\text{K}^{-1}$	0.054
Ambient density of grease $\rho_0/\text{kg m}^{-3}$	910
Specific heat of grease $c/\text{J} \cdot \text{kg}^{-1} \cdot \text{K}^{-1}$	2000
Thermal conductivity of grease $k/\text{W} \cdot \text{m}^{-1} \cdot \text{K}^{-1}$	0.14
Grease rheological index $n$	0.9
Equivalent elastic modulus of friction pair $E'/\text{GPa}$	225
Thermal conductivity of friction pair $k_a k_b/\text{W} \cdot \text{m}^{-1} \cdot \text{K}^{-1}$	46
Friction pair density $\rho_a \rho_b/\text{kg} \cdot \text{m}^{-3}$	7850
Specific heat of friction pair $c_a c_b/\text{J} \cdot \text{kg}^{-1} \cdot \text{K}^{-1}$	470
Equivalent radius of curvature $R_x/\text{m}$	0.016
Equivalent radius of curvature $R_y/\text{m}$	0.025
Slide-roll ratio $S = (u_a - u_b)/u_e$	0.032

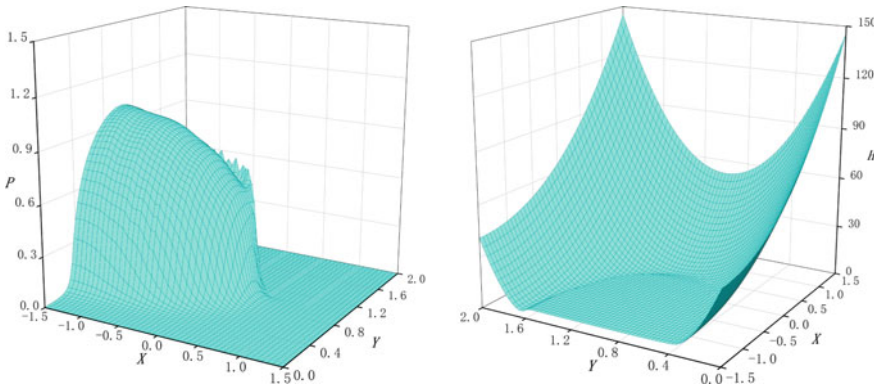


**Fig. 2** Distribution of pressure and film thickness at contact zone between roller element and outer ring (Self-drawn)

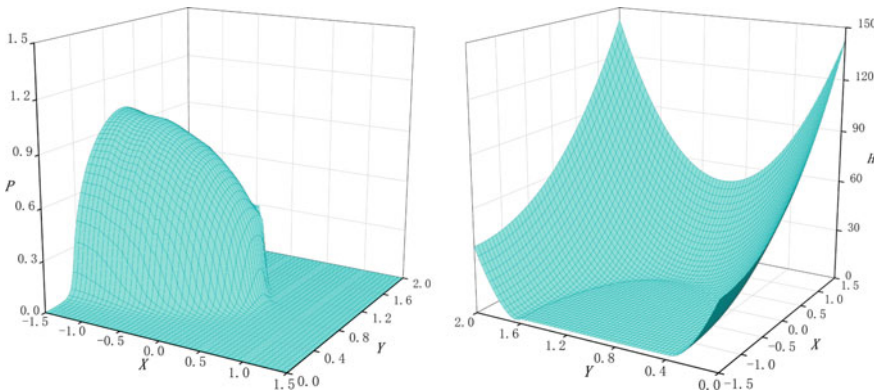


**Fig. 3** Distribution of pressure and film thickness at contact zone between roller element and inner circle (Self-drawn)

the outer ring is under greater pressure than that in contact with the inner circle. For lubrication condition, the roller element and the outer ring is worse than that between the roller element and the inner circle.

Rheological index  $n$  of grease is a non-negligible factor when considering the lubrication properties of the lubricant. The rheological index was set as 0.7, 0.8, 0.9, and 1.0, when the maximum Hertz contact pressure  $p_H$  was 2.0GPa, the pressure distribution diagram at the contact point between the roller element and the outer ring was obtained, as shown in Fig. 4.

As can be seen from Fig. 4, no matter what value the rheological index takes, a relatively obvious second pressure peak appears in the pressure distribution. One of the main features of elasto-hydrodynamic lubrication analysis is the second pressure peak. Through research, it can be known that the height of the second pressure peak

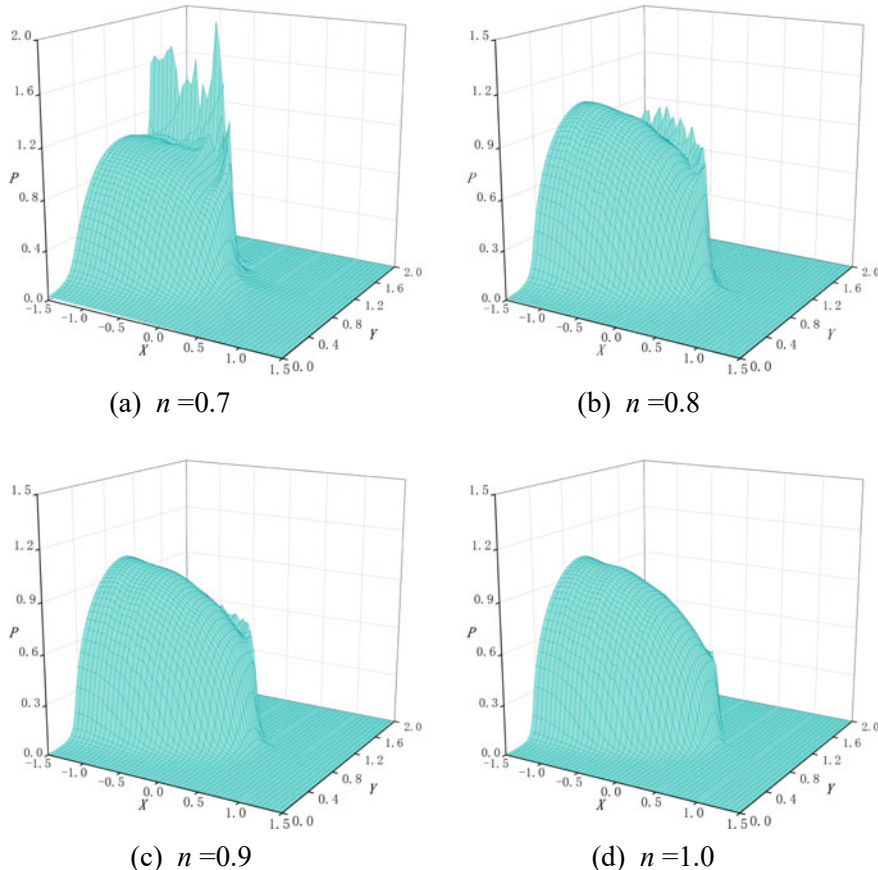


**Fig. 4** Pressure distribution under different rheological indices (Self-drawn)

is related to the viscosity of the lubricant and the maximum Hertz contact pressure  $p_H$  and other factors. Due to the high viscosity of grease, a high second pressure peak will appear when the  $p_H$  is not large. It can be seen from the figure that the smaller the rheological index is, the higher the second pressure peak is. This is because the lower the rheological index of the lithium-based lipids selected, the higher their apparent viscosity in operation, and the higher the viscosity, the higher the second pressure peak in the pressure distribution.

## 5 Conclusion

The thermal elasto-hydrodynamic lubrication mathematical model of point contact exponential rate grease of deep groove ball bearings is established and solved by Fortran programming. By importing the results into Origin software, lubrication between the roller element and the outer ring is worse than lubrication between the roller element and the inner circle. Regardless of rheological index value, there is a relatively obvious second pressure peak in the pressure distribution, and the second pressure peak decreases as the rheological index increases.

**Acknowledgements** This work is supported by the National Natural Science Foundation of China (52075278/E0506; 50905090).

## References

1. Gulzar M (2016) Tribological performance of nanoparticles as lubricating oil additives. *J Nanopart Res* 18(8):1–25
2. Meng F (2021) Solution of thermal deformation and its effects on high-speed point-contact elastohydrodynamic lubrication. *Tribology* 41(05):680–689
3. Wang X (2021) Speed scope of inlet dimple under elastohydrodynamic lubrication point contacts. *Lubr Eng* 45(11):41–45
4. Morales-Espejel G (2014) Film thickness in grease lubricated slow rotating roller bearings. *Tribol Int* 74(4):7–19
5. Cyriac F (2016) Effect of thickener particle geometry and concentration on the grease EHL film thickness at medium speeds. *Tribol Lett* 61(2):1–13
6. Yang P (1990) A generalized Reynolds equation for non-newtonian thermal elastohydrodynamic lubrication. *ASME J Tribol* 112(4):631–636
7. Zhang S (2020) Elastohydrodynamic study and life analysis of index rate grease lubricated deep groove ball bearing. Qingdao University
8. Lu H (2010) An approach for accurately calculating the EHL film thicknesses with multi-grid method. *Lubr Eng* 35(4):5–9
9. Shi X (2013) Single asperities transient thermal elastohydrodynamic lubrication analysis of power law water-based ferrofluid journal bearing. *Lubr Eng* 38(7):36–40

# Influence of Shock Load on Performance of Mixed Lubrication Sliding Bearings



L. C. Qin, X. M. Miao, H. Guo, and M. H. Shi

**Abstract** The principal objective of this research is to analyze the axis trajectory evolution process of sliding bearing under nonlinear shock. Therefore, a transient mathematical model coupled with the average flow equation, G-T contact model, and rotor kinetics equation was established in this paper and was solved by a numerical algorithm. The computations were in comparison with the program results of reference to demonstrate the dependability of the model. This paper analyzed the variation of the mixed lubricated bearing behavior under a pair of shocks in opposite directions. The calculation result shows that when the bearing is subjected to a vertical sinusoidal shock, both the minimum lubricant film gap and the capacity load change sinusoidally. The axis trajectory is a closed curve. And the variation trend of each parameter is opposite and the change range is similar when the shock is in the opposite direction.

**Keywords** Elastic deformation · Mixed lubrication · Euler stepwise integration · Sinusoidal shock · Axial trajectory

## 1 Introduction

Mechanical equipment in an environment with changing natural conditions may be affected by many factors, for instance, strong winds or waves. That would result in the deterioration of the behavior of the sliding bearings supporting the rotor system which may indeed cause the journal bearing failure or wear. Therefore, it is supposed to analyze the parameters change pattern of the impacted bearing. But at present, only a few researchers have used numerical methods to study the trajectory of bearings subjected to nonlinear shocks [1–4].

Thence, a transient mixed lubricated bearing model considering shock load was established in the research and was solved by over-relaxation iterative method and

---

L. C. Qin · X. M. Miao · H. Guo (✉) · M. H. Shi

College of Machinery and Power Engineering, Zhengzhou University, Zheng Zhou 450001, China  
e-mail: [ghhletter@zzu.edu.cn](mailto:ghhletter@zzu.edu.cn)

Euler stepwise integration. The evolution result of parameters concluding axis trajectory, hydrodynamic load, and contact load was discussed. The research results of this paper will provide a reference for practical engineering applications.

## 2 Mathematical Model

### 2.1 Average Flow Reynolds Model

Regardless of the density change of the lubricant, the Reynolds lubricated model considering the roughness can be obtained according to the coordinate system of Fig. 1, the equation is

$$\frac{\partial}{r\partial\phi} \left( \phi_x \frac{h^3}{12\mu} \frac{\partial P_h}{r\partial\phi} \right) + \frac{\partial}{\partial z} \left( \phi_z \frac{h^3}{12\mu} \frac{\partial P_h}{\partial z} \right) = \frac{U}{2} \phi_c \frac{\partial h}{r\partial\phi} + \frac{U}{2} \sigma \frac{\partial \phi_s}{r\partial\phi} + \phi_c \frac{\partial h}{\partial t} \quad (1)$$

where  $h$  is the actual fluid film thickness including roughness peak,  $P_h$  is the fluid pressure,  $\phi_x$  and  $\phi_z$  are the pressure flow factor along  $x$ -direction and  $z$ -direction, respectively,  $\mu$  is the initial lubricant viscosity,  $U$  and  $r$  are the shaft sliding linear velocity and the journal radius, respectively, and  $\sigma$  is the integrated root mean square deviation of roughness.  $\phi_s$  and  $\phi_c$  are the shearing flow factor and contact factor.

Pressure is solved by using the Reynolds boundary conditions:

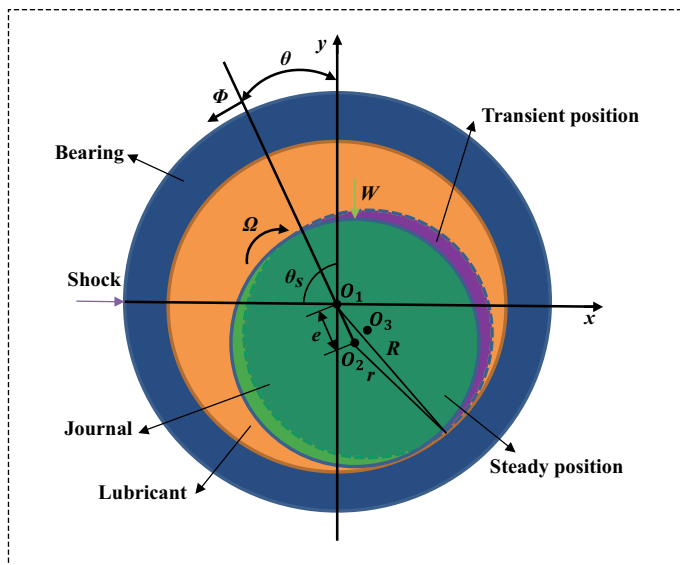


**Fig. 1** Journal bearing subjected to shock

$$\begin{cases} P_h = 0, \phi = 0 \text{ or } z = \pm \frac{l}{2} \\ P_h = 0 \text{ and } \frac{\partial P_h}{\partial \phi} = 0, \phi = \phi_2 \end{cases} \quad (2)$$

which  $\phi_2$  is boundary between oil film and cavitation.

## 2.2 Roughness Peak Contact Model

The model (G-T model) proposed by Greenwood and Tripp is used for analysis in the research, which is on account of the micro-bulge contact theory. Assuming that the height of the asperity follows a normal distribution and the texture direction of the asperity is isotropic, the resulting contact pressure and area are

$$\begin{cases} P_c = \frac{16}{15} \sqrt{2\pi} (\eta \beta \sigma)^2 \sqrt{\frac{\sigma}{\beta}} E' F_{\frac{5}{2}}(H) \\ A_c = \pi^2 (\eta \beta \sigma)^2 A F_2(H) \end{cases} \quad (3)$$

where  $P_c$  is the contact pressure,  $A_c$  is the contact area,  $\eta$  is the distribution density of the roughness peak,  $\beta$  is the curve radius of the roughness peak,  $E'$  is the comprehensive elastic modulus, and  $H$  is the ratio of oil film thickness to roughness.  $A$  is the nominal contact area, which can be regarded as the area where the contact pressure exists.  $F_n(H)$  is the rough peak probability distribution function related to the film thickness ratio [5].

## 2.3 Fluid Film Thickness Equation

On the basis of the geometry relationship in Fig. 1, the lubricant film gap after considering deformation of elasticity can be written as

$$h = c(1 + \varepsilon \cos \phi) + h_\delta \quad (4)$$

where  $c$  and  $\theta$  are the radius clearance from sliding bearings fit and attitude angle, respectively.  $\varepsilon$  is the eccentricity ratio, that is, the ratio of eccentric distance to clearance.  $h_\delta$  is the shell deformation of elasticity, and this paper uses the Winkler equation to calculate the elastic deformation [4]

$$h_\delta = \frac{(P_h + P_c)B}{E_1} (1 - v_1^2) \quad (5)$$

where  $B$  is the bearing shell thickness and is usually set to 1–2 mm.

## 2.4 Rotor Kinetics Equation

According to the rotor kinetics theory, the load balance equation considering the shock is as follows:

$$\begin{cases} m\ddot{e}_x = F_x - F_{fx} + F_s \sin \theta_s \\ m\ddot{e}_y = F_y + F_{fy} - W - F_s \cos \theta_s \end{cases} \quad (6)$$

where  $\ddot{e}_x$  and  $\ddot{e}_y$  are, respectively, the accelerations of the shaft along the horizontal and vertical orientation. And  $m$  is the equivalent mass of journal,  $(F_x, F_y)$  are components of capacity load,  $(F_{fx}, F_{fy})$  are the components of friction force,  $W$  is the external force on the shaft,  $F_s$  is the shock load, and  $\theta_s$  is shock direction. The formula for each force is as follows:

$$\begin{cases} F_x = \int_0^{2\pi} \int_{-l/2}^{l/2} (P + P_c)r \sin(\phi + \theta) dz d\phi \\ F_y = - \int_0^{2\pi} \int_{-l/2}^{l/2} (P + P_c)r \cos(\phi + \theta) dz d\phi \end{cases} \quad (7)$$

$$\begin{cases} F_{fx} = \int_{-l/2}^{l/2} \int_{0_1}^{2\pi} \left[ (\phi_f + \phi_{fs}) \frac{\mu U}{h} + \frac{h}{2} \phi_{fp} \frac{\partial P_h}{\partial x} + \mu_B P_c \right] \sin(\phi + \theta) r d\phi dz \\ F_{fy} = \int_{-l/2}^{l/2} \int_0^{2\pi} \left[ (\phi_f + \phi_{fs}) \frac{\mu U}{h} + \frac{h}{2} \phi_{fp} \frac{\partial P_h}{\partial x} + \mu_B P_c \right] \cos(\phi + \theta) r d\phi dz \end{cases} \quad (8)$$

$$\begin{cases} F_s = W_S \sin\left(\frac{2\pi}{T_s} t\right), 0 \leq t \leq \frac{T_s}{2} \\ F_s = 0, t > \frac{T_s}{2} \end{cases} \quad (9)$$

where  $\mu_B$  is the boundary friction factor,  $W_S$  is the shock load amplitude, and  $T_s$  is the cycle time of shock. This paper only considers a vertical shock and the shock load amplitude is 600N. The shock angle is 0 and 180° and the cycle time is set as 0.04 s.

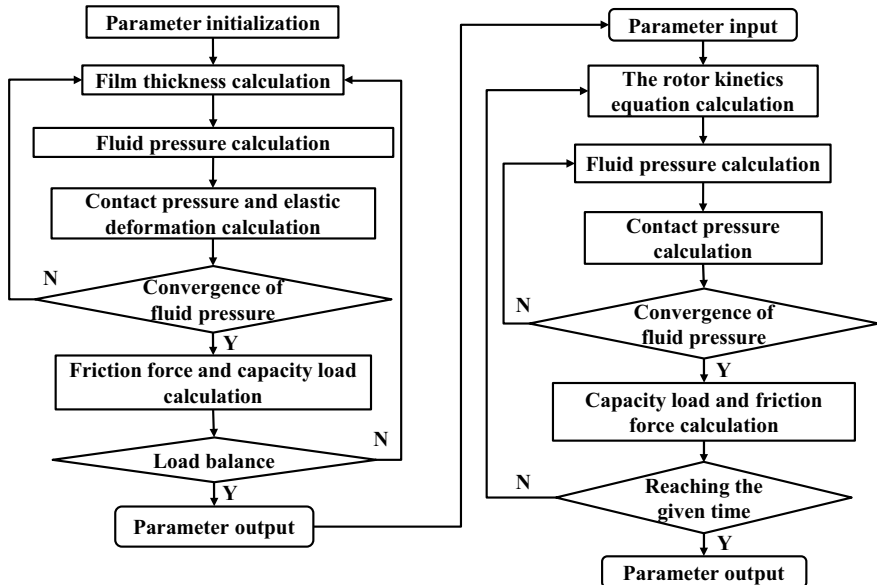


**Fig. 2** Flowchart of the calculation process

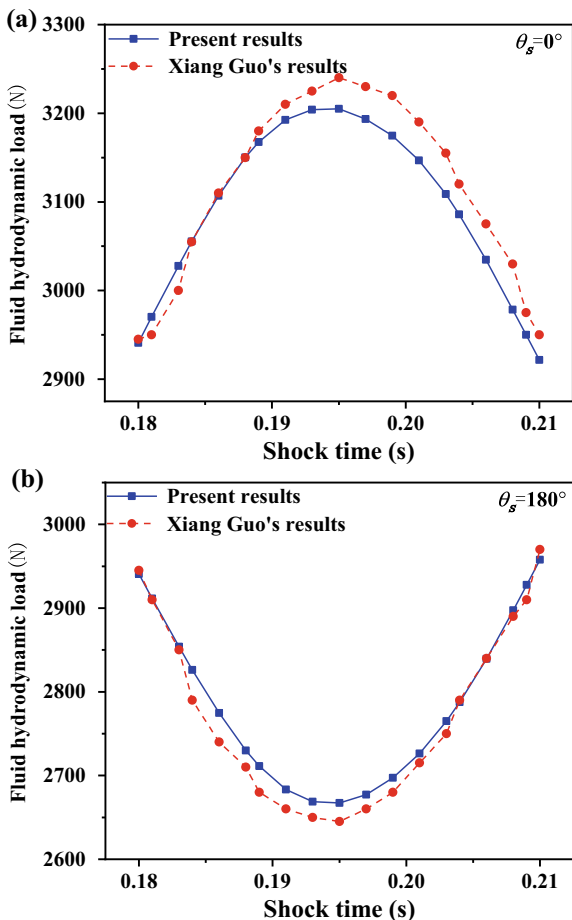
### 3 Numerical Calculation

The algorithm process is shown in Fig. 2. The steady-state position and parameters of the bearing are determined firstly to calculate the transient part subsequently. If the shock moment is reached at this time, the parameters including bearing capacity and friction force are input into the rotor kinetics equation to obtain the new axial position by the Euler stepwise integration. After determining the rotor center position after each impact time node, the lubricant film thickness can be calculated and then substituted into each model to obtain the fluid and contact pressure, bearing capacity load, and friction force. These parameters will later be utilized to calculate the shock performance results of the next time node. After the shock is over, it is necessary to judge whether the given termination time has been reached. For the sake of guaranteeing the correctness of the computation results, the pressure convergence accuracy in this paper is  $1 \times 10^{-4}$  and the time step is set as  $1 \times 10^{-5}$ .

### 4 Model Verification

The accuracy of the established model should be discussed first. Hence, the calculation results during shock with the literature [3] results were compared. As shown in Fig. 3, the variation trend of the capacity load caused by shock in different directions

**Fig. 3** Comparison of variation of capacity load under different shock directions: a  $\theta_s = 0^\circ$ ; b  $\theta_s = 180^\circ$



was first compared. It can be seen from the picture that the results have good consistency. The effect of grooves was removed during model consequence comparison, so the results were biased and the error is within 5%.

## 5 Result Discussion

The parameters utilized in the simulation computation are displayed in Table 1. The position of the axis is obtained by the method in Sect. 2.4. The hydrodynamic pressure, contact pressure, and other parameters are obtained by the calculus of five-point difference and the over-relaxation iteration algorithm.

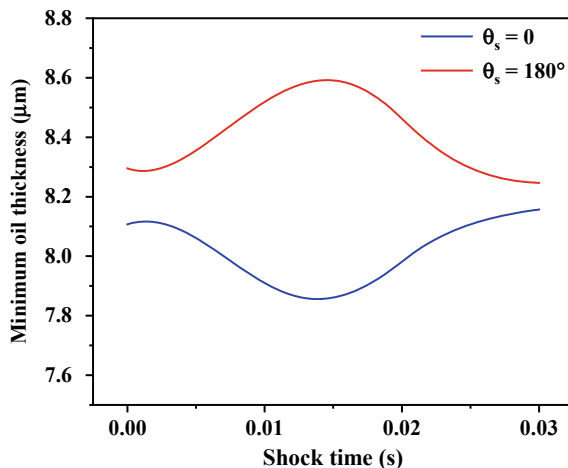
Figure 4 illustrates the minimum film thickness curve when the shock angle is 0 and  $180^\circ$ , respectively. As shown, when  $t = 0.01$  s, the thickness value reached

**Table 1** Computation parameter

Parameters	Value	Parameters	Value
Journal semidiameter/ $r$ (m)	0.05	Bearing Poisson ratio/ $\nu_1$	0.3
Bearing width/ $l$ (m)	0.08	Journal Poisson ratio/ $\nu_2$	0.3
Radius gap/ $c$ (mm)	0.060	Lubricant viscosity/ $\mu$ (Pa s)	0.0189
Bearing elastic modulus/ $E_1$ (GPa)	100	Load/ $W$ (N)	6000
Shaft elastic modulus/ $E_2$ (GPa)	210	Rotation speed/ $n$ (r/min)	1000
Shock period $T$ (s)	0.04	Composite roughness/ $\sigma$ ( $\mu\text{m}$ )	2.6

the peak, while the film thickness gradually stabilized after the impact when  $t = 0.03$  s. The version of the minimum film geometry gap is opposite to the shock force function curve. And the film thickness variation mode is the opposite when the shock direction is converse. The above phenomena are caused by the extrusion or expansion of the lubricant by the shock load. Though the vertical downward impact will cause the continuous reduction of the film thickness ratio, the film thickness ratio is still within a reasonable limit in the whole shock process. Because of this, the Reynolds equation is still applicable.

Figure 5 illustrates the variation of the hydrodynamic and contact force when shock angle is 0 and  $180^\circ$ , respectively. As shown, the variation trend of the fluid capacity load and contact load is similar to the shock function when the bearing is subjected to a vertical sinusoidal shock. Although the impact from two directions makes the capacity load evolution trend opposite, the variation value and change time node are similar. And the pressure will return to the initial values after 0.02 s due to the bearing stability characteristics. The minimum lubricant film gap is inversely correlated with the dynamic pressure effect and contact pressure, so the variation trend of the two capacity loads and the minimal film gap is opposite.

**Fig. 4** Variation of oil thickness with time in different directions

**Fig. 5** Capacity load variation in different shock directions: **a** hydrodynamic load and **b** contact load

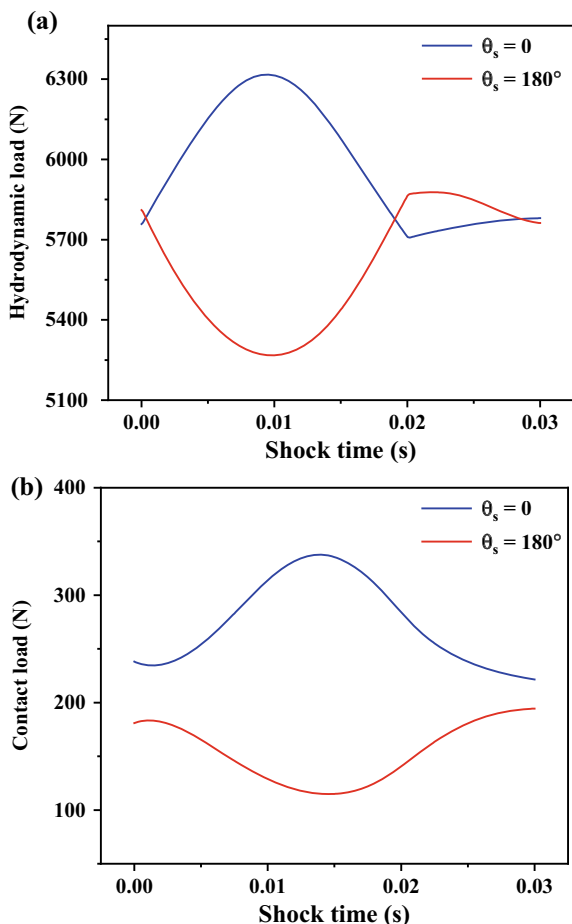
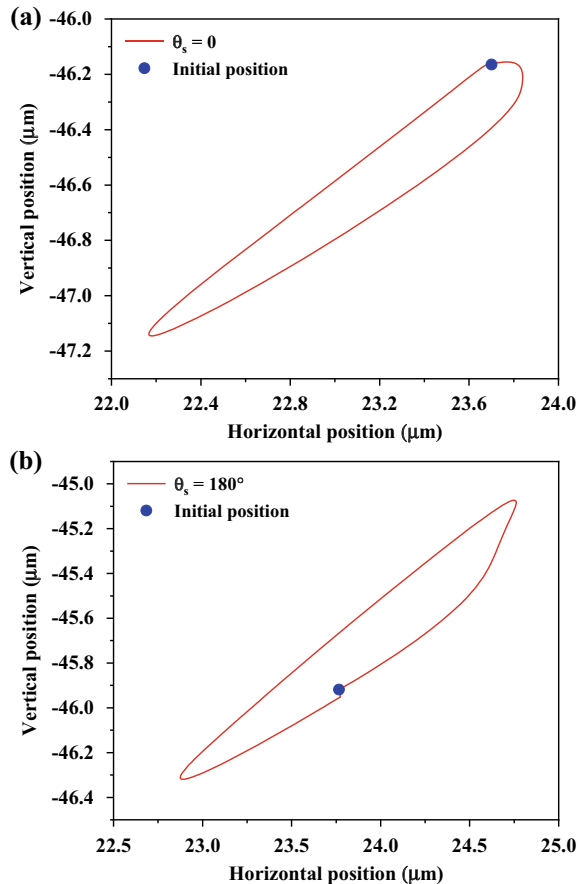


Figure 6 is the axis trajectory variation in different shock directions. As shown, due to the bearing being impacted, the axis trajectory changes nonlinearly. And the bearing almost returns to its original position after the shock. Because the film thickness and capacity load change oppositely when the shock direction is converse, the journal movement trend is first down and then up when the shock angle is 0, while the journal movement trend is first up and then down when the shock angle is  $180^\circ$ . Despite the two impact directions lead to the opposite trend of parameters variation, their variation range is almost tantamount.

**Fig. 6** Variation of axis trajectory with time: **a**  $\theta_s = 0$ ; **b**  $\theta_s = 180^\circ$



## 6 Conclusion

After analyzing the results, the main conclusions are as follows:

- (1) Nonlinear shock causes nonlinear changes in the parameters of the bearing concluding capacity load and film thickness, and these parameters can nearly restore to their initial values after the shock due to the stiffness and damping of the lubricant film itself;
- (2) variation of all parameters is due to the shock changes in the film thickness. The reduction of lubricant film thickness enhances the dynamic pressure effect and increases the probability of rough peak contact;
- (3) the axis trajectory during the entire shock cycle is almost a closed curve. And a pair of shocks in opposite directions makes the parameters change conversely but has almost no effect on the change time.

**Acknowledgements** The study is supported by the National Natural Science Foundation of China (51575498) and the China Postdoctoral Science Foundation (2021M692913).

## References

1. Zhang SL, Pei SY, Xu H, Zhang YB, Zhu J (2018) Journal bearing properties and dynamic response under transient impact load and elastic deformation. *J Xi'an Jiaotong Univ* 52(01):100–106+114 (2018)
2. Ren T, Feng M (2017) Anti-shock characteristics of water lubricated bearing for fuel cell vehicle air compressor. *Tribol Int* 107:56–64
3. Xiang G, Yang TY, Ning Q, Zhou CD, Wang C, Lv ZL (2021) Numerical study on transient mixed lubrication response for multiple grooves water-lubricated bearings under non-linear shock with 3D thermal effect[J]. *Surf Topogr Metrol Prop* 9(3):35014
4. Liang P, Li XY, Guo F, Cao YZ, Zhang XH, Jiang FL (2022) Influence of sea wave shock on transient start-up performance of water-lubricated bearing. *Tribol Int* 167:107332
5. Wang HW, Ma B, Li HY (2014) A study on the mixed lubrication characteristics of journal bearing for high-speed planet gears in tracked vehicles. *Automot Eng* 36(03):328–333

# Experimental Study on Direct Measurement of the Air–Water Interface at High-Speed Condition



Sheng-Zhe Shi, Teng-Jiao Sang, Fei Wei, and Gang Sun

**Abstract** In order to accurately obtain the air–water interface characteristics of the high-speed ship, such as the spray height and the wake profile, a model test of the planned hull was carried out. A probe driven by a motor is used to measure the interface, when the probe pins are in contact with water, a short-circuit form is used as a trigger to stop the electric probe, and the coordinates of each point on the wake profile can be directly measured. The test results show that, at the same speed, the wake height increases gradually with the increase of the abscissa; the wake height at the same position increases gradually with the increase of the flow velocity. This method is suitable for the measurement of the water mist generated by the planned hull on the water surface, especially for the direct measurement of the wake of the high-speed ship.

**Keywords** Model test · Air–water interface · Spray height · Wake profile · Planning hull

---

S.-Z. Shi (✉) · T.-J. Sang · F. Wei · G. Sun

AVIC Special Vehicle Research Institute, Key Aviation Scientific and Technological Laboratory of High Speed Hydrodynamic, JingMen, China  
e-mail: [shishengzhe05011232@126.com](mailto:shishengzhe05011232@126.com)

T.-J. Sang  
e-mail: [hshl\\_jiangting@163.com](mailto:hshl_jiangting@163.com)

F. Wei  
e-mail: [weifei605@163.com](mailto:weifei605@163.com)

G. Sun  
e-mail: [sungang7211@126.com](mailto:sungang7211@126.com)

## 1 Introduction

During the planning process of the amphibious aircraft on the water surface, the main splash generated by the stagnation line will impact the propeller, flap, and tail, affecting the normal use of these components, and even causing damage, directly reducing the attendance rate of the amphibious aircraft, even affecting the amphibious aircraft safety. Tang [1–3] uses the photographic grid method to measure the coordinate position of the spray on the grid, obtains the spray profile, studies the spray performance of the amphibious aircraft, and uses the grooved fog suppressor to reduce the spray intensity and Probability of the spray hitting the propeller. Li [4] used high-speed photography technology to obtain the evolution characteristics of spray and cavitation in the high-speed water entry of trans-media vehicle. Aiming at the problem of liquid spurt caused by the hydrodynamic ram, Chen [5] designed a set of test equipment and researched the corresponding relationship between cavity and spray, as well as the velocity and shape characteristics of spray by using high-speed camera. Wei [6] used a constant-speed camera (25 frames per second) and a high-speed camera (250 frames per second) to record the shaking impact process and the air–water interface. Li [7] collects undisturbed images of the vortex flow field by introducing image recognition technology, and the velocity distribution of the vortex under different working conditions is obtained. The photography grid method estimates the coordinate based on the comparison and analysis of the pictures. There are many factors affecting the test results, and it is easy to produce large errors. High-speed photography technology is the only feasible method for dynamic and unsteady spray, but it is still not enough to accurately describe stable and steady spray.

This article uses a motor-driven probe with pins attached to the end of the probe. At the beginning of the test, the probe moves downward and stops when the probe's pins come into contact with the water to form a short circuit. By changing the position of the probe, the coordinates of each point on the wake profile are directly recorded; on this basis, the model test of the planned hull at high speed is carried out. The test results show that the test technique is effective for high-speed ship wake measurements.

## 2 Direct Measurement of Two-Phase Flow

### 2.1 Model Test

The model is made of acrylic material with a thickness of 20 mm. The length of the model is 1.4 m, the width is 0.5 m, the slope angle is 20°, the pitch angle is 3°, and the maximum draft of the keel is 58 mm.

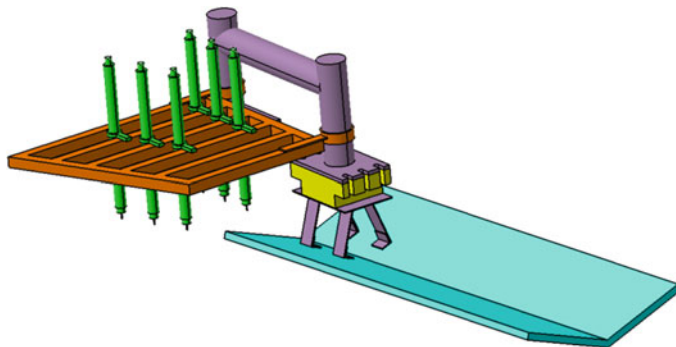


**Fig. 1** Test device

## 2.2 Test Device

The mounting platform is fixed to the rear of the model. The model is made of transparent material. The installation platform is fixed on the trailer bracket by bolt connection, so that the trailer drives the test model forward. Series probes are mounted on the rear of the test model to measure wake profiles. The probe is fixed on the mounting platform. The probe is driven by an electric motor. During the test, the probe moves down automatically. When the needle touches the water, the probe stops automatically. The test setup is shown in Fig. 1.

## 2.3 Two-Phase Flow Height

Before the test, record the height  $z_1$  between the top of the probe and the installation platform, and the height  $z_2$  between the bottom of the probe and the water surface. After the test, record the height  $z_3$  between the top of each probe and the installation platform at each section.

The height of the spray profile at each probe can be calculated.

$$z = (z_3 - z_1) + z_2 \quad (1)$$

## 3 Model Test

The test object is a prismatic planned hull in a fixed state. The interface height was calculated from the height recorded when the probe stopped touching the water surface. Test speeds are 6, 8, and 10 m/s.

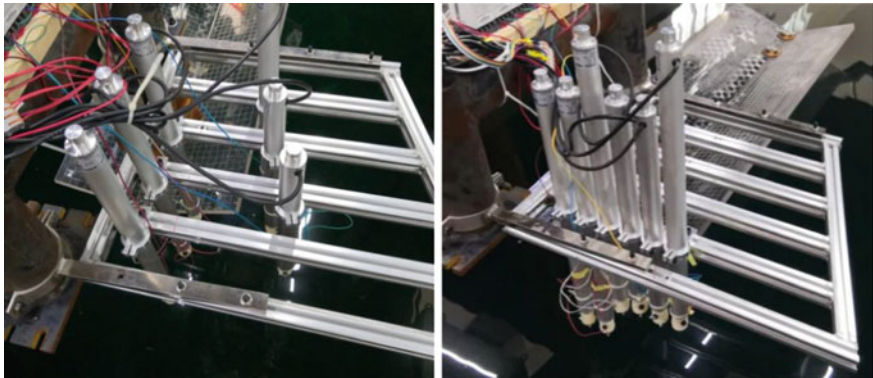


**Fig. 2** The arrangement of electric probe in two-phase flow test

In test case 1, three points are located in the spray zone and three points are located in the wake zone. In case 2, points 1–6 are located in a transverse section, in the spray zone and the wake zone. The left side of Fig. 2 shows the arrangement of the electric probe in test case 1, and the right side of Fig. 2 shows the arrangement of the electric probe in test case 2.

Table 1 shows the coordinates of the electric probes in test case 1 and test case 2. The origin of the coordinates is the round point of the pipe, the x-axis points to the tail of the model, and the y-axis points to the starboard of the model.

The spray area is mainly composed of gas–water mixture and has no obvious interface; the wake is concave and the boundary is clear (Fig. 3).

The spray pattern of test case 2 is shown in Fig. 4. The spray is a high-speed, white, and gas–water mixture. The probes start to move from top to bottom after the model reaches the stable test speed and stop automatically after the probes touch the water. Whether the wake zone of the water surface or the spray zone of the gas–water mixture, it can be accurately measured.

As can be seen from Table 2 and Fig. 5, the stop trigger of the probe is not perfect. Sometimes it's too sensitive. A small spray of water in the spray area will cause the probe to stop moving. Sometimes it's too slow. After exposure to water, the probe continues to move a certain distance until the pin is completely shorted. Therefore,

**Table 1** Coordinates of electric probes in two-phase flow test (unit: mm)

Electric probe	Case 1	Case 2
Point 1	(235, 150)	(435, 160)
Point 2	(335, 150)	(435, 210)
Point 3	(435, 150)	(435, 255)
Point 4	(235, 345)	(435, 300)
Point 5	(335, 380)	(435, 345)
Point 6	(435, 415)	(435, 390)

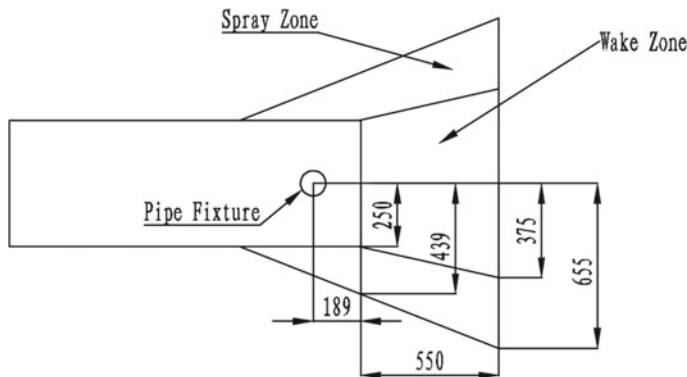


**Fig. 3** Zone diagram of two-phase flow test



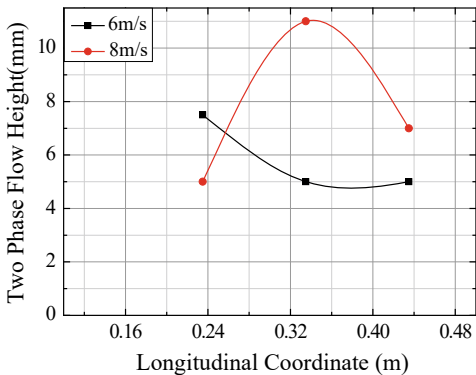
**Fig. 4** Two-phase flow interface test diagram

there are deviations in the results of multiple detections. When the speed is 8 m/s, the three test results of point 2 are 12 mm, -25 mm, and 10 mm, respectively. The result of the second test is obviously deviated, which belongs to the excessive movement of the probe, and the probe does not stop in time. The result of the second test is the wrong result and should be removed. The test results of other points are relatively stable at different speeds and can be used for simulation comparison.

**Table 2** Test results of two-phase flow height in case 1

Velocity (m/s)	Spray height (mm)					
	Point 1	Point 2	Point 3	Point 4	Point 5	Point 6
6	5	5	5	55	80	65
6	10	5	5	55	75	65
8	5	12	1	53	91	95
8	5	-25	10	53	83	85
8	0	10	10	55	87	95

**Fig. 5** Two-phase interface height of different longitudinal coordinates at 150 mm from the middle section in case1



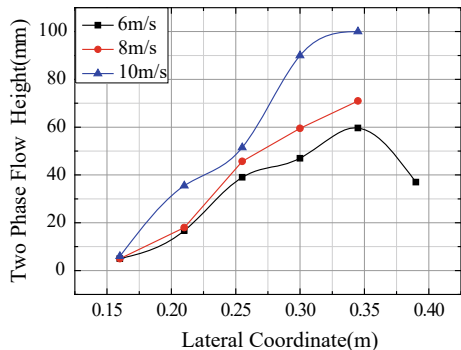
As can be seen from Table 3, some probes do not move after activation. The reason is that the relay fails, and some points have no measurement results. As can be seen from Fig. 6, after removing invalid data, the abscissa is the x-axis, and the interface height is the y-axis. The height of the two-phase flow on the water surface increases gradually with the increase of the abscissa at the same speed; the height of the two-phase flow on the water surface increases gradually with the increase of the velocity at the same position.

In the direct measurement test of the two-phase flow, due to the reliability of the trigger, relay, and other components, some invalid data appeared, but the overall operation was good, and the high-speed spray could be directly measured.

**Table 3** Test results of two-phase flow height in case 2

Velocity (m/s)	Spray height (mm)					
	Point 1	Point 2	Point 3	Point 4	Point 5	Point 6
6	5	10	34	31	65	54
6	—	20	—	—	47	20
6	5	20	44	63	67	—
8	5	17	47	68	—	—
8	5	—	47	—	55	—
8	5	19	43	51	87	—
10	6	47	55	—	109	—
10	6	24	48	90	91	—

**Fig. 6** Two-phase interface height of different lateral coordinates at 435 mm from the longitudinal section in case 2



## 4 Conclusions

- (1) After the model reaches a stable speed, the probe starts to move up and down, and the probe stops automatically when it touches the water. Whether it is the wake area or the spray area of the gas–water mixture, it can accurately measure the water–air interface.
- (2) The height of the air–water interface increases gradually with the increase of the abscissa at the same speed; the height of the interface at the same place increases gradually with the increase of the flow velocity.
- (3) This test method is suitable for the measurement of the two-phase interface generated by the planned hull on the water surface. It can be extended to the wake and spray profiles of amphibious aircraft.

## References

1. Tang B-B, Zhang, J-X Li C-H, Zuo X-B, Xu J-F (2015) Study on analytical method for spray peaks of amphibious aircraft. *Aeronaut Comput Tech* 6(45):45–46, 51
2. Tang B-B, Zhang, J-X Li C-H, Zuo X-B, Xu J-F (2015) Comparative test study for the effect of groove type spray suppressor heights on amphibious aircraft spray performance. *Sci Technol Eng* 33(15):249–252
3. Tang B-B, Wu B, Wang M-Z, Zuo Z-B (2015) Comparative test study for the effect of groove type spray suppressor widths on amphibious aircraft spray performance. *Aeronaut Sci Technol* 1(26):73–78
4. Li Y-G, Wang C, Wu Y, Gao W, Lu J, He Q (2022) On the motion characteristics of cavity wall in the high-speed water entry of trans-media vehicle. *Acta Armamentarii* (43):574–585
5. Chen A-R, Li X-D, Zhou L-W, Ji Y (2021) Experimental study on the characteristics and influencing factors of liquid spurt caused by hydrodynamic ram. *J Natl Univ Defense Technol* (43):144–152

6. Wei Z-J, Shen L-M, Wang Z-M, Zhou M-F, Ruan S-I, Yue Q-J (2020) Experimental investigation on the similarity relationship of the free-surface wave elevation due to the liquid sloshing. *J Ship Mech* 3(24):283–293
7. Li W-H, Mu D-W, Zhang D (2021) Experiment of free surface vortex characteristics based on image recognition. *Mar Equip/Mater Mark* 4(29):32–34

# Experimental Study on Fatigue Life of Four Typical Aircraft Connectors



Hongwei Qiao, Yunyan Ren, and Hui Zhang

**Abstract** This study compares the fatigue performance of several connections using theoretical and experimental methodologies to forecast the fatigue life of aviation connectors. To determine the matching yield strength and fatigue life of the four specimens, static tensile tests and fatigue tests were performed on four different types of porous single-shear lap joint specimens. Three example S–N models were produced in accordance with the fatigue life determined by the test. The effect that best fits the data is the three-parameter power function S–N model. When the fatigue life of the four different types of specimens is compared, it is clear that each type of specimen has excellent fatigue properties and can fatigue up to  $3 \times 10^7$  times. In general, the high-lock bolt specimen has a longer fatigue life than the rivet specimen. The fatigue limit is reached by the high-lock bolt specimen, and the associated loading stress is higher than for the rivet specimen.

**Keywords** Hi-lock bolt · Rivet · S–N model · Fatigue life

## 1 Introduction

Predicting the fatigue life of structural connections is crucial because fatigue cracks in aircraft body structures nearly always start and spread at fastener connections. The structure of an airplane is made up of several connections, most of which are fastened together by screwing or riveting. The structure's strength and fatigue characteristics are necessarily diminished as a result of the extreme stress concentration around the attaching hole [1, 2]. One of the most typical types of damage to airplanes in service is fatigue cracking of fastening holes. Statistics show that it is responsible for 50–90% of all failures. The way holes are configured, the materials used, the

---

H. Qiao (✉) · Y. Ren  
Beijing Institute of Technology, Beijing, People's Republic of China  
e-mail: [qhw18406583361@163.com](mailto:qhw18406583361@163.com)

H. Zhang  
Avic China Aero-Poly Technology Establishment, Beijing, People's Republic of China

surface conditions, and the methods of assembly used between fasteners and mating plates, Galling between fasteners and holes, and localized stress variations brought on by external loads are two factors that significantly affect how structural connectors operate under fatigue [3, 4]. In engineering structures, bolted connections are a common type of connection. It has a lot of benefits, including a big transfer load, a dependable connection, an easy process, and more. The tension around the hole is more complicated when the components are fastened together by bolts because it includes both an extrusion zone and a tensile zone at the hole's border. Fracture caused by stress concentration at the hole's edge is the most common manifestation of the failure form of metal bolted connection structures [5]. The connector's fasteners will be loaded unevenly due to the asymmetry of certain factors, such as material and size, which may cause excessive stress to concentrate around one or more fastening holes and finally cause structural damage.

Currently, there is a lot of study being done on the fatigue performance and longevity of structures joined by bolts and rivets. In order to predict the fatigue life of the single-bolt single-shear lap joint/single-bolt double-shear lap joint with an interference fit and clamping force, the Chakherlou [6] team used various multi-axis fatigue criteria. The predicted results are in good agreement with the experimental data, but the research primarily focuses on the lap joint specimen of a single bolt, and its stress mode is relatively simple, while the bolts are typically used in groups in practical applications. Zhao [7] used the finite element simulation method to analyze the fatigue characteristics of the two aluminum alloy composite lap joints to determine the fatigue failure position and the estimated life under the fly-continuous-fly spectrum. Chengcheng [8] equivalent the fasteners and the surrounding balance load system in the connecting piece obtained by finite element as two uniaxial loads, through the superposition of the stress fields under the action of the two uniaxial loads, and introducing complex geometry and load boundaries for the influence of SSF, the equivalent SSF method is proposed. Tianyu [9] first carried out a dynamic analysis of the pressure riveting process, obtained the deformation from an interference amount of the nail and hole after riveting, established the nail element in ANSYS, and realized the parametric modeling to calculate the nail load, using the stress Severity factor method for estimating fatigue life of connectors.

## 2 Test Specimen and Test System

### 2.1 Test Piece Structure

The sample structure used in this study is shown in Fig. 1. Figure 1a includes two 7050T7451 aluminum alloy plates with a length of 140 mm and a thickness of 4 mm, the width of the test section is 40 mm, and the upper and lower plates are milled. There are 4 round holes with a diameter of 5 mm on the plate, the distance between the centers of the two circular holes is 20 mm (4 times the diameter of the bolt hole),

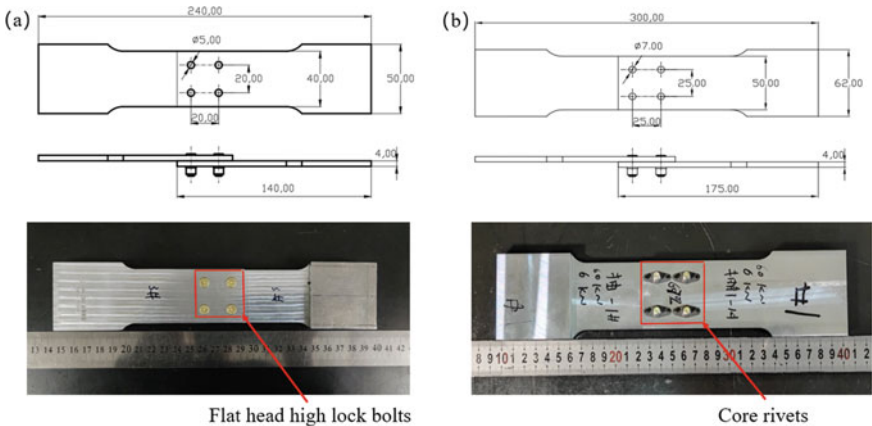


**Fig. 1** Specimen of lap plates **a** High-lock bolt specimen **b** Rivet specimens [self drawn]

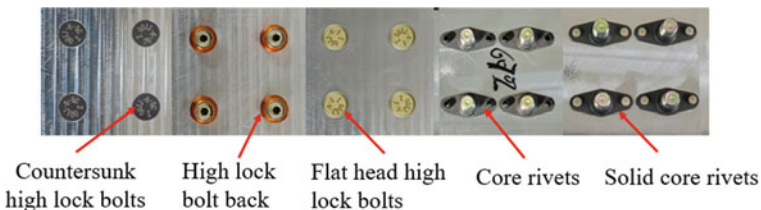


**Fig. 2** 4 typical connection test pieces [self drawn]

and the two plates are connected with 4 MJ titanium alloy flat head hi-lock bolts or countersunk head hi-lock bolts. The total length after the connection is 240 mm, and the material used in Fig. 1b is the same as that in Fig. 1a, but the dimensions are different. The aluminum alloy plate is 175 mm long, 4 mm thick, and 50 mm wide. It is 25 mm, and the total length of the test piece is 300 mm. The actual picture is shown in Fig. 2.

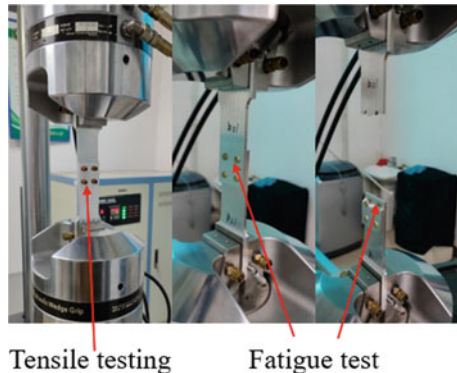
## 2.2 Test System

The test is divided into two parts: static tensile test and fatigue test; the static tensile test is the preparation for the fatigue test of the bolted connection, providing load data for the fatigue test; tensile tests and fatigue tests were carried out on the MTS370.1 hydraulic universal material testing machine produced by MTS Company in the United States.

**Table 1** Static tensile test results [self drawn]

Specimen type	Yield strength (MPa)
Flat head hi-lock bolt connection	216
Countersunk head hi-lock bolt connection	191
Blind rivet test piece	380
Solid rivet test piece	380

**Fig. 3** Tensile and fatigue tests [self drawn]



### 3 Static Tensile Test

#### 3.1 Static Tensile Test Procedure

The flat head hi-lock bolt specimens and the countersunk head hi-lock bolt specimens were taken, respectively, for static tensile tests. The test is carried out in MTS according to GB/228.1–2010 “Tensile Test for Metal Materials Part I: Test Method at Room Temperature” on board. The test scheme of the static tensile test is shown in Table 1, and the test process is shown in Fig. 3.

#### 3.2 Static Tensile Test Results

The yield strength of the four specimens was obtained through the test, and the test results are shown in Table 1.

**Table 2** Fatigue test protocol [self drawn]

Serial number	Specimen type	67%P quantity	50%P quantity	30%P quantity	20%P quantity	15%P quantity
1	Flat head hi-lock bolt	6	6	6	3	2
2	Countersunk head hi-lock bolt	5	5	5	1	1
3	Blind rivet test piece	5	5	5	5	5
4	Solid rivet test piece	5	5	5	5	5

The fatigue test process is shown in Fig. 3

## 4 Fatigue Test

### 4.1 Fatigue Test Process

The fatigue test of the hi-lock bolt specimen is carried out according to the GJB715.9 “fastener test method-shear joint fatigue” method, using the MTS material testing system to conduct the test, using force control loading, the highest stress level of the fatigue test passes the yield strength of the specimen P is sure, the maximum stress  $S_{max}$  is 0.67P, and the minimum stress level is the stress value when the specimen fails about 3 million times. The lifting method was used to select 50, 30, and 20 of the yield strength, etc., respectively, as the applied stress for the fatigue test. Because the fatigue was loaded with a uniaxial sine wave constant amplitude, the above-selected stress was the maximum value of the sine wave loading, and 10% of it was selected. It is the minimum value of sine wave loading, so the stress ratio is 0.1, the frequency of the experimental process is generally 5–20 Hz, and cyclic loads are then applied following relevant technical requirements until the specimen fails. If the sample fails, it is considered that the sample has been damaged. For high-life specimens, it is considered that the fatigue limit (permanent life) is reached when  $3 \times 10^7$  times and above are reached. In order to reduce the bending moment of the specimen, a gasket is attached to the clamping section of the specimen. The test scheme of the fatigue test of the bolted joint is shown in Table 2, where P is the yield strength of the static tensile test, and the load level of the fatigue test is divided into 67%P, 50%P, 30%P, 20%P, and 15%P.

### 4.2 Fatigue Test Results

The fatigue life of the four specimens under different stress levels was obtained through the test. The test results are shown in Tables 3, 4, 5, and 6:

**Table 3** Fatigue test results of flat head hi-lock bolt specimens [self drawn]

Stress (MPa)	145	108	65	43	33
Fatigue life (cycle)	14,506	38,228	252,186	1,111,330	$3 \times 10^7$
	15,745	40,656	283,299	2,607,418	$4 \times 10^7$
	18,648	45,511	289,122	$4 \times 10^7$	—
	20,027	46,228	295,107	—	—
	21,141	52,893	302,788	—	—
	25,406	67,982	392,685	—	—

**Table 4** Fatigue test results of countersunk head hi-lock bolt specimens [self drawn]

Stress (MPa)	128	96	58	38	33
Fatigue life (cycle)	15,268	45,145	439,942	1,893,233	$4 \times 10^7$
	16,528	65,995	451,911	—	—
	17,871	85,253	472,938	—	—
	18,321	85,462	503,126	—	—
	20,718	89,504	537,064	—	—

**Table 5** Fatigue test results of blind rivet specimens [self drawn]

Stress (MPa)	253	188	113	76	57	45	30
Fatigue life (cycle)	1127	3929	17,925	37,284	142,122	1,466,298	$3 \times 10^7$
	1218	4108	18,923	45,163	148,844	—	—
	1329	4254	19,326	51,520	156,283	—	—
	1391	4517	20,085	57,630	163,968	—	—
	1422	4632	22,318	63,292	172,130	—	—

**Table 6** Fatigue test results of solid rivet specimens [self drawn]

Stress (MPa)	253	188	113	76	57	45	30
Fatigue life (cycle)	1837	4340	17,326	33,215	102,931	404,436	$4 \times 10^7$
	1930	4428	18,732	48,926	117,824	620,024	—
	2011	4566	19,621	52,317	125,782	—	—
	2103	4639	20,275	62,754	136,709	—	—
	2241	4715	21,530	63,459	146,308	—	—

#### 4.3 Specimen Fracture Surface

If you look at the specimen's fracture surface, like in Fig. 4, you can see that the crack always starts at the bolt hole and then spreads outward from the connection

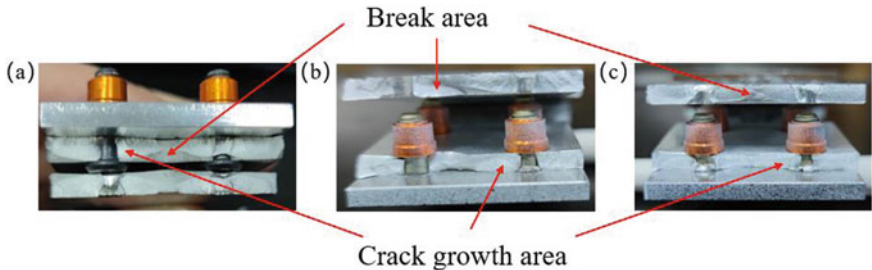


**Fig. 4** Condition of the fracture surface of the specimen **a** 67%P specimen, **b** 50%P specimen, and **c** 30%P specimen [self drawn]

between the two plates to the center and edge of the connecting plate. However, due to the phenomenon of stress concentration, the stress decreases with distance from the bolt hole, so when the crack widens to a certain point and the specimen is unable to withstand the loading stress, it will immediately break close to the outer surface. Figure 4 illustrates this specific phenomenon. Fractures that start out in the corners of bolt holes eventually spread into penetrating cracks that fail structurally. This is the failure mode.

## 5 S–N Model

There are three S–N curve models commonly used to characterize material stress fatigue: Basquin S–N model, exponential S–N model, and three-parameter power function S–N model. Different models have different abilities to describe the fatigue curve. Therefore, it is necessary to obtain three models of connectors first and then select the model with a better description ability to complete the subsequent analysis.

### (1) Basquin S–N model

$$S^m N = C \quad (1)$$

### (2) Exponential S–N Model

$$e^{mS} N = C \quad (2)$$

### (3) Three-parameter power function S–N model

$$(S - S_0)^m N = C \quad (3)$$

Among them,  $m$  and  $C$  are constants related to the material;  $S$  is the maximum cyclic load under a certain stress level, MPa;  $N$  is the corresponding fatigue life under a particular stress level  $S$ , cycles.  $S_0$  is the theoretical stress fatigue limit, MPa.

For the Basquin S–N model and the exponential S–N model, the stress level S and the fatigue life N under the corresponding stress have been obtained through experiments, and then m and C are fitted by the least square method, and finally, the S–N curve equation is established [10].

The three-parameter power function S–N model has m, C, and  $S_0$  three parameters; due to the difficulty in obtaining the parameters of the three-parameter power function S–N model, this paper adopts the Gao Zhentong method, [11] it makes full use of the characteristics of Python, and can accurately and efficiently give the three parameters of the Weibull distribution at the same time. It is briefly summarized that under a certain stress level, if the fatigue life N of the fatigue specimen obeys the Weibull distribution, then its probability density function for

$$f(N) = \frac{b}{N_a - N_0} \left( \frac{N - N_0}{N_a - N_0} \right)^{b-1} \exp \left[ - \left( \frac{N - N_0}{N_a - N_0} \right)^b \right] \quad N \geq N_0 \quad (4)$$

In the formula,  $N_0$  is the position parameter, the minimum life parameter;  $N_a$  is the characteristic life parameter; b is the shape parameter.

The probability of fatigue life  $n \leq N$ , that is, the unreliability function, is

$$F(N) = P(n \leq N) = \int_{N_0}^N f(N) dN \quad (5)$$

Then the expression of the fatigue life reliability functions obeying the three-parameter Weibull distribution:

$$P = \exp \left[ - \left( \frac{N - N_0}{N_a - N_0} \right)^b \right] \quad (6)$$

The mathematical expectation and variance of Weibull-distributed variables are

$$E(N) = N_0 + (N_a - N_0) \Gamma \left( 1 + \frac{1}{b} \right) \quad (7)$$

$$\text{var}(N) = (N_a - N_0)^2 \left[ \Gamma \left( 1 + \frac{2}{b} \right) - \Gamma^2 \left( 1 + \frac{1}{b} \right) \right] \quad (8)$$

Let the probability of fatigue life  $n \leq N$  be

$$P(n \leq N) = p \quad (9)$$

In the formula,  $p$  is the reliability, and the fatigue life of the reliability corresponding to  $p$  can be expressed as  $N_p$ . The classic S–N curve has a reliability P of 50% on the P-S–N curve, also known as the median S–N curve.

When the reliability is  $p = 0.5$ ,  $N_p = N_{50}$ ,  $N_{50}$  which corresponds to the median of the fatigue life sample, substitute  $N_p = N_{50}$  into

$$\ln 0.5 = - \left( \frac{N_{50} - N_0}{N_a - N_0} \right)^b \quad (10)$$

According to the fatigue life data of a group of test samples under a certain stress level, the mean, variance, and median of the samples can be calculated, and a nonlinear equation system can be established; solving this nonlinear system of equations yields estimates of the values of the three parameters of the Weibull distribution.

### 5.1 Flat Head Hi-Lock Bolt Test Piece

Basquin S–N model:

$$m = 3.457, C = 548276964, S^{3.457}N = 548276964 \quad (11)$$

Exponential S–N Model:

$$m = 0.0347, C = 7.8547, e^{0.0347S}N = e^{7.8547} \quad (12)$$

Three-parameter power function S–N model:

$$m = 2.094, C = 363989, S_0 = 35, (S - 35)^{2.094}N = 363989 \quad (13)$$

By analyzing the three S–N models, as shown in Fig. 5, before the fatigue life is  $3 \times 10^5$  times, the three models have strong prediction and fitting ability and can accurately describe the fatigue life. However, after  $3 \times 10^5$  times, the exponential function S–N model has a sharp decrease in fatigue life prediction, and the accuracy is weaker than the other two models. Comparing the curves and test results for the other two S–N models reveals that the Basquin S–N model predicts fatigue life conservatively, while the three-parameter power function S–N model, which is the best of the three S–N models, has the best ability to accurately describe fatigue life. As a result, the following countersunk head high-lock bolt specimen's fatigue life fitting uses the three-parameter power function S–N model, and the fatigue performance of the two types of high-lock bolts is determined by contrasting their S–N models.

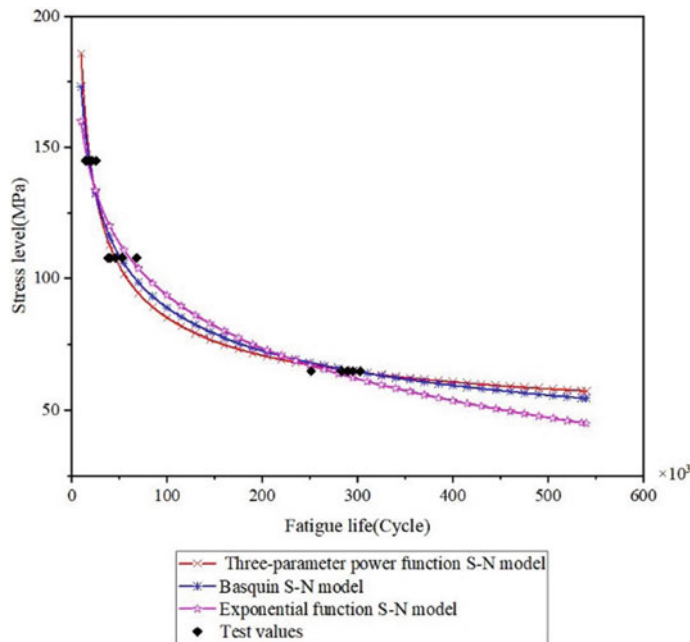


**Fig. 5** S-N curve of flat head hi-lock bolt specimen [self drawn]

## 5.2 Comparison of Flat Head and Countersunk Head Hi-Lock Bolt Specimens

Figure 6 shows the three-parameter power function S-N curves of the two specimens. By comparison, it can be found that, before  $9 \times 10^4$  times, the fatigue life of the flat head high-lock bolt specimen was higher than that of the countersunk head high-lock bolt specimen. After  $9 \times 10^4$  times, the fatigue life of the two specimens is almost the same.

## 5.3 Blind Rivets and Solid Rivets

Basquin S-N model:

$$\begin{aligned} m &= 3.0918, C = 39715290, S^{3.0918}N = 39715290 \quad (\text{core pull}) \\ m &= 2.754, C = 8398840.8, S^{2.754}N = 8398840.8 \quad (\text{solid core}) \end{aligned} \quad (14)$$

Exponential S-N Model:

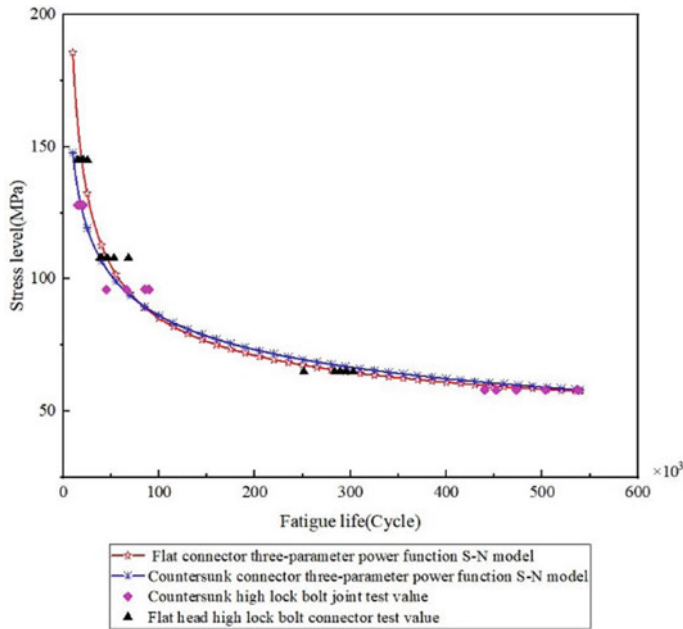


**Fig. 6** Comparison of S-N curves of three-parameter power functions for flat and countersunk bolt specimens [self drawn]

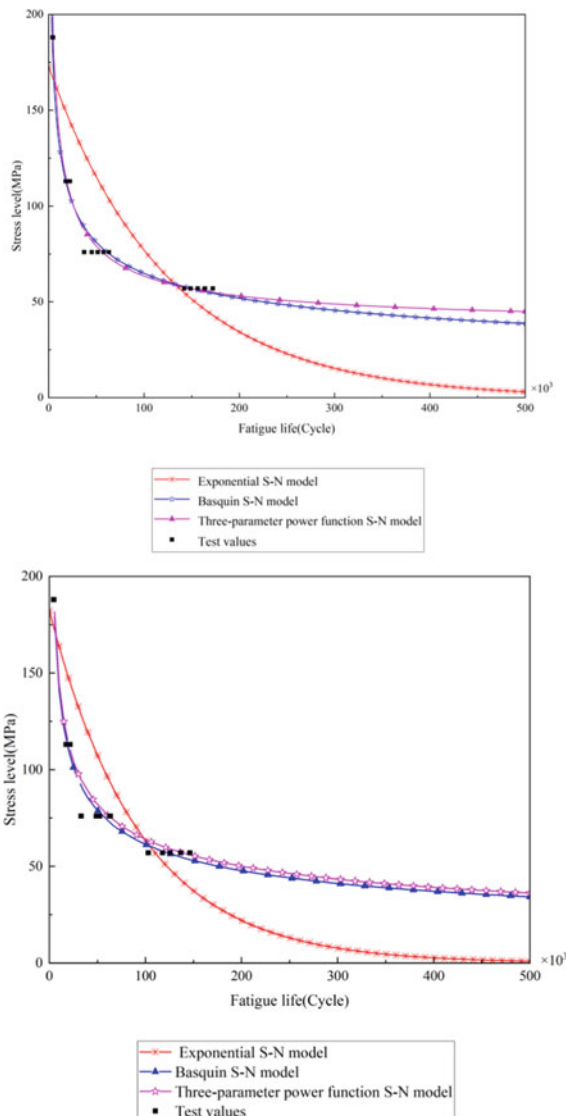
$$\begin{aligned} m &= 0.023, C = e^{5.903729565}, e^{0.023S} N = e^{5.903729565} \quad (\text{core pull}) \\ m &= 0.0204, C = e^{5.599836655}, e^{0.0204S} N = e^{5.599836655} \quad (\text{solid core}) \end{aligned} \quad (15)$$

Three-parameter power function S-N model:

$$\begin{aligned} m &= 0.724, C = 77408, S_0 = 28, (S - 28)^{0.724} N = 77408 \quad (\text{core pull}) \\ m &= 0.7847, C = 182305, S_0 = 20, (S - 20)^{0.7847} N = 182305 \quad (\text{solid core}) \end{aligned} \quad (16)$$

By analyzing the three S-N models of blind rivets and solid rivets, respectively, as shown in Fig. 7, the exponential function S-N model deviates from the test value, and the fitting effect is very poor, so it is not considered. The other two S-N models, both can describe the fatigue life of the specimen well. Among them, the three-parameter power function S-N model accurately describes the fatigue life. The ability is the best, which is the best among the three S-N models. Therefore, the three-parameter power function S-N model is directly selected for the fatigue life fitting of the two specimens in the next comparison.

**Fig. 7** S-N curve of the blind rivet and solid rivet specimens [self drawn]



#### 5.4 Comparison of Blind Rivets and Solid Rivets

Figure 8 shows the three-parameter power function S-N curves of blind rivets and solid rivets. By comparison, it can be found that before  $3 \times 10^4$  times, the fatigue lives of the two are equal, and after  $3 \times 10^4$  times, the fatigue life of blind rivets is slightly higher than that of solid rivets, but the fatigue life of the two specimens is not much different, and the fatigue properties of the two are close.

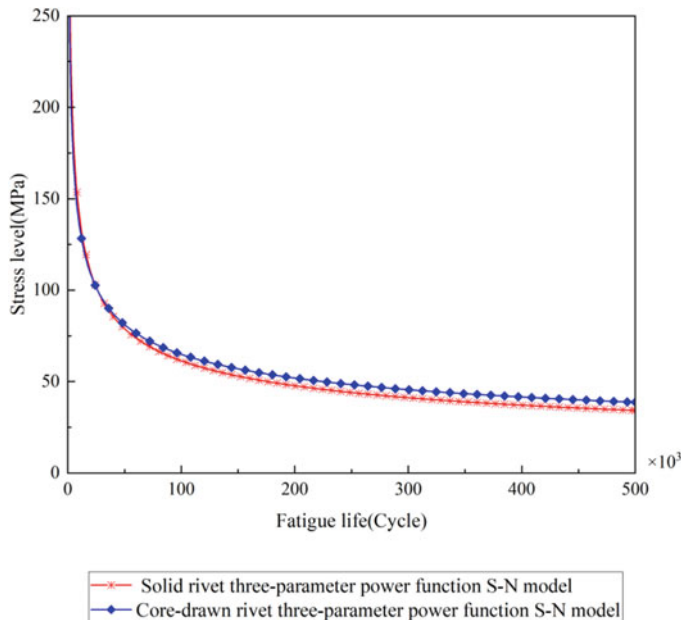


**Fig. 8** Comparison of three-parameter power function S-N curves of blind rivets and solid rivets [self drawn]

### 5.5 Comparison of High-Lock Bolt Specimens and Rivet Specimens

Figure 9 shows the three-parameter power function S-N curves of four types of high-lock bolt specimens and rivet specimens. By comparison, it can be found that under the same stress level, the fatigue life of high-lock bolt specimens is higher than as the applied stress decreases, the difference between the fatigue life of the rivet specimen is greater, and the high-lock bolt specimen reaches the fatigue limit when the applied stress is greater than that of the rivet specimen, which can be obtained in engineering applications. The fatigue performance of the locking bolt specimen is better than that of the rivet specimen.

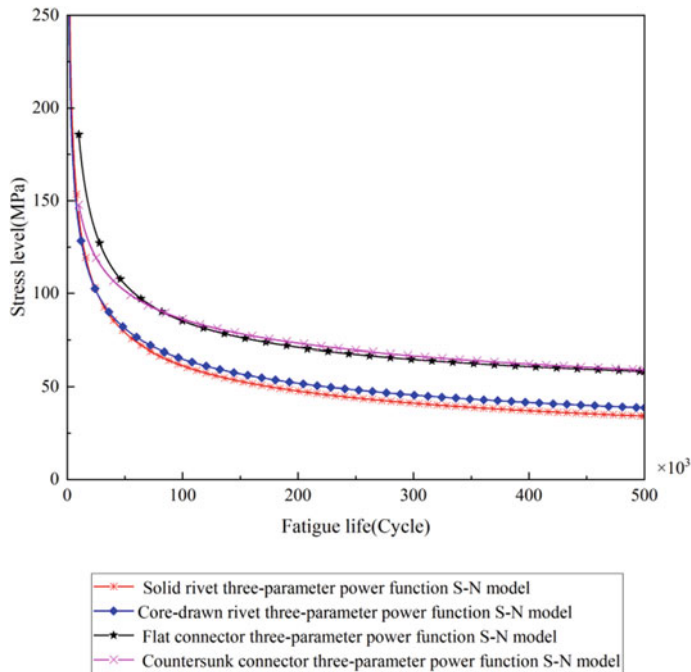


**Fig. 9** Comparison of S-N curves of three-parameter power functions of four specimens [self drawn]

## 6 Conclusion

By performing static tensile tests and fatigue tests on four kinds of specimens, and comparing the specimens with the S-N model, the following conclusions can be drawn:

1. The four kinds of connectors all have good fatigue characteristics, which can meet the requirements of GJB and reach the fatigue limit of  $3 \times 10^7$  times.
2. Among the three S-N models, the predicted life obtained by the three-parameter power function S-N model is in the best agreement with the test results.
3. Before  $9 \times 10^4$  times, the fatigue performance of the flat head high-lock bolt specimen is better than that of the countersunk head high-lock bolt specimen, and after  $9 \times 10^4$  times, the fatigue performance of the two is close.
4. Before  $3 \times 10^4$  times, the fatigue properties of blind rivets and solid rivets are similar. After  $3 \times 10^4$  times, the fatigue performance of blind rivets is better than that of solid rivets.
5. The fatigue life of the high-lock bolt specimen is generally better than that of the rivet specimen, and the corresponding loading stress of the high-lock bolt specimen reaching the fatigue limit is greater than that of the rivet specimen.

6. The failure mode is that cracks are first generated at the corners of the bolt holes and gradually expand into penetrating cracks, eventually leading to structural failure.

## References

1. Ireman T, Ranyik T, Eriksson I (2000) On damage development in mechanically fastened composite laminates. Compos Struct 49(2):151–171
2. Xiaofei X, Weixing Y (1998) Research on detail design of anti-fatigue of machine structure. Mech Strength 20(1):70–73
3. Liu J, Xu HL, Zhai HB et al (2010) Effect of detail design on fatigue performance of fastener hole. Mater Des 31(2):976–980
4. Qiqing H, Caifeng Z, Zhiping Y (2005) Study on the stress intensity factor of multi-crack crack tip in porous connection structure with contact problem. Mech Strength 27(5):661–665
5. Urban MR (2003) Analysis of the fatigue life of riveted sheet metal helicopter airframe joints. Int J Fatigue 25(9–11):1013–1026
6. Esmaeili F, Zebsaz M, Chakherlou TN et al (2015) Fatigue life estimation of double lap simple bolted and hybrid(bolted/bonded) joints using several multiaxial fatigue criteria. Mater Des 67:583–595
7. Zhao H, Jinjie Y, Qinghua L, Zhiyuan Z (2014) Analysis of fatigue characteristics of two kinds of aluminum alloy composite lap joints. Hot Work Technol 43(12):83–86+95. <https://doi.org/10.14158/j.cnki.1001-3814.2014.12.024>
8. Chengcheng Z, Weixing Y, Bin Y (2009) Equivalent SSF method for fatigue life analysis of connectors. Acta Aeronaut Sinica 30(02):271–275
9. Tianyu Z, Yuting H, Tao C, Xu D, Xiangfei T, Kai L (2018) A fatigue life analysis method for multi-nail riveted joints. J Beijing Univ Aeronaut Astronaut 44(09):1933–1940. <https://doi.org/10.13700/j.bh.1001-5965.2017.0689>
10. Dan L (2011) Weibull distribution model and its application in mechanical reliability. University of Electronic Science and Technology
11. Jiajin X, Zhentong G (2021) method in fatigue statistics intelligence. J Beijing Univ Aeronaut Astronaut 47(10):2024–2033. <https://doi.org/10.13700/j.bh.1001-5965.2020.0373>